Methane Activation and Functionalisation using Zinc-Modified Zeolites

This thesis is submitted in partial fulfilment for the degree of PhD at the University of Durham

by Meera Shah

February 2020

Supervisor: Dr Russell A. Taylor

Chapter 1: Introduction

Includes published work, S. Raynes, M. A. Shah and R. A. Taylor, *Dalton Trans.*, 2019, **48**, 10364-10384, with permission from all authors. The paper can be found in Appendix 7.

Chapter 1: Introduction

Methane, the principal component of natural gas, continues to play an ever increasing role as a feedstock for the production of energy and chemicals.[1-3] While energy production remains the primary use of methane, it is also the feedstock for some of the most important inorganic and organic bulk chemicals produced by the chemical industry. However, bulk chemicals are not produced directly from methane, but are instead produced indirectly through the intermediacy of synthesis gas (also known as syngas), a mixture of carbon monoxide and hydrogen. Scheme 1 shows some of the diverse bulk chemicals that are produced from synthesis gas, either by utilising hydrogen or carbon monoxide alone, or by using syngas.

Syngas can be produced from methane in a number of ways,[4] but steam reforming (SR) and autothermal reforming (ATR, a combination of steam reforming and partial oxidation) remain the most practised methods.[5, 6] Historically it is steam reforming that has been most commonly implemented for producing syngas for the manufacture of important basic chemicals (*e.g.*, ammonia and methanol), oil refining, and in many other industrial applications.[7]

The industrially practised approach for converting methane to chemicals *via* syngas has a number of drawbacks. Both SR and ATR of methane utilise catalysts and operate at elevated temperature (800 °C and above) and pressures (30 barg and above).[7] Due to these extreme conditions, plant construction costs are high and the catalysts are prone to deactivation due to sintering or the formation of carbonaceous deposits.[4] Furthermore, depending on the degree of heat exchange, it is estimated that approximately between 20% and 50% of the natural gas feedstock is consumed through energy losses in order to reach the high reaction temperatures required during SR.[5] Further it is reported that trying to improve the energy efficiency of SR would detrimentally impact the syngas production cost.[8] Given the points above, syngas production plants are typically constructed at large scales to optimise material throughput and thus maximise the return on investment. As it stands today, the conversion of methane to

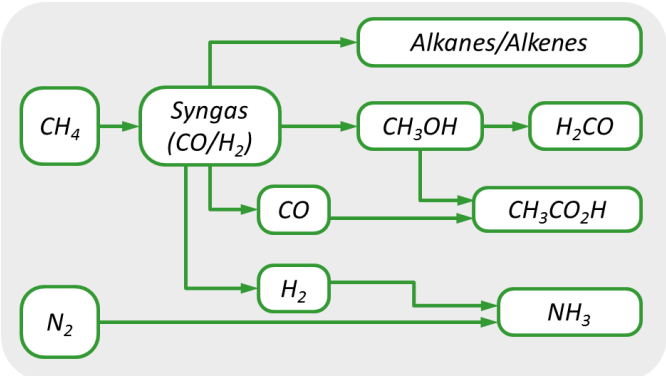

Scheme 1: Flow scheme showing some of the primary products formed from syngas.

chemical products requires a minimum of two chemical manufacturing plants, of which syngas production reportedly accounts for the majority of the investment required. For instance, the production of methanol from methane requires a syngas production plant and a methanol synthesis plant, where the latter most commonly utilises a $Cu/ZnO/Al_2O_3$ catalyst to produce the desired product.[9] For methanol production, the syngas plant accounts for approximately 60% of a new production facility.[5] This multistep, large scale approach consequently limits the number of opportunities for deployment of indirect methane conversion technology.

The direct conversion of methane to higher value chemical products has been an area of industrial and academic interest ever since the turn of the 20th century.[10] Moreover the prospect of direct conversion to liquid products has the allure of being able to address two important areas that indirect production cannot. Firstly, associated natural gas (gas produced at oil reservoirs) is often flared on site for environmental and safety reasons, however, in 2015, this amounted to approximately 3.5% of global gas production.[11] Secondly, it is estimated that 40% of natural gas reserves are not economically viable resources as the cost of production is too significant compared to the perceived financial reward.[12] Such reserves are known as stranded gas. The direct conversion of methane to higher value chemicals has the potential to tap into these resources should the requisite plants have lower associated costs than indirect production. There are of course serious concerns regarding the exploitation of coal, oil and gas for fuels and chemicals, mainly due to the risks of global warming and other environmental issues.[13-15] However, natural gas is regarded as the cleanest of all the fossil-based resources and is championed to be the preferred resource in the global transition to lower carbon economies.[16] Therefore, developing technologies that enhance the portfolio of products derived from methane will help to alleviate our reliance on oil for chemical production.

The direct conversion of methane to chemicals has three main areas of interest 1) methane to ethylene, 2) methane to aromatics and 3) methane to methanol (Scheme 2).[17] Substantial progress has been made in all three areas however it is probably methane to ethylene that shows the greatest promise of a commercial process given recent announcements from Siluria Technologies that they have been running a pilot facility in La Porte, Texas since

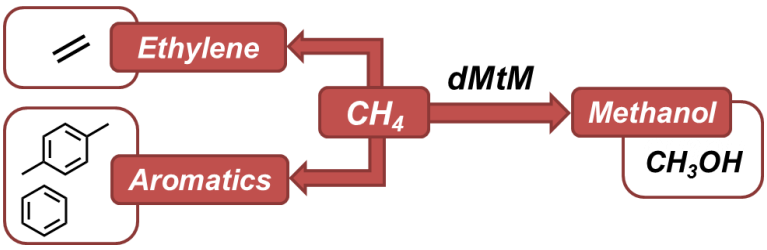

Scheme 2: Main products of dMtM process

2015[18] and have recently executed a multi-plant technology license with Saudi Aramco to deploy the technology at existing sites.[19]

Catalytic methane aromatisation has received significant attention since Wang *et al.* demonstrated high selectivity to benzene, via non-oxidative methane upgrading at 700 °C, using a Mo modified H-ZSM-5 zeolite catalyst.[20] Since these initial findings, methane aromatisation has been studied extensively with conversion rates of 17% achieved over Mo/H-ZSM-5.[21] Unfortunately, rapid catalyst deactivation and high selectivity to coke hinder commercialisation. Greater clarification of the active species and reaction mechanism is required for progress into large scale catalyst development.[22]

However it is direct methane to methanol (dMtM) that has been described as the holy grail of catalysis,[23] and has been intensely tackled by both homogeneous and heterogeneous catalyst researchers. Perhaps what makes dMtM so tantalising is the very fact that nature has already been able to master this challenging chemistry in the form of methantropic bacteria. These bacteria contain an enzyme, methane monooxygenase (MMO), which is capable of converting methane to methanol at physiological conditions.[24] Two types of MMO enzymes exist, so called *particulate* and *soluble* forms, pMMO and sMMO respectively. The sMMO enzyme contains a dinuclear Fe centre in the active site while pMMO contains Cu.[25] The proposed structures of these active sites have inspired much research to develop laboratory mimics and have been a significant source of inspiration in the development of catalysts for dMtM.

1.1 Introduction to Zeolites

The term zeolite, from the Greek *zeo* – to boil and *lithos* – stone, was coined in 1756 by Cronstedt. Constedt discovered stilbite, a naturally occurring zeolite, which when rapidly heated produced large amounts of steam from adsorbed water.[26] However, it was not until Richard Barrer prepared the first solely synthetic zeolite in the early 20th century that research into zeolites accelerated.[27] Since the initial discovery there has been extensive research into developing and understanding zeolites, from new synthetic methodology to catalytic applications.

Since Barrer's initial discovery, 245 different zeolite frameworks have been developed.[28] These frameworks are made up of corner-sharing $[SiO_4]$ and $[AlO_4]^-$ tetrahedra, which form a continuous three dimensional structure with interconnecting pores, channels or cages. It is this unique network of channels which make zeolites particularly valuable as molecular sieves, ion exchange materials and, in particular, catalysts. Five common, commercially available zeolite

framework types: MFI, FER, MOR, FAU and Beta which are made up of different ring sizes are used widely in scientific research and in catalytic applications (Figure 1).

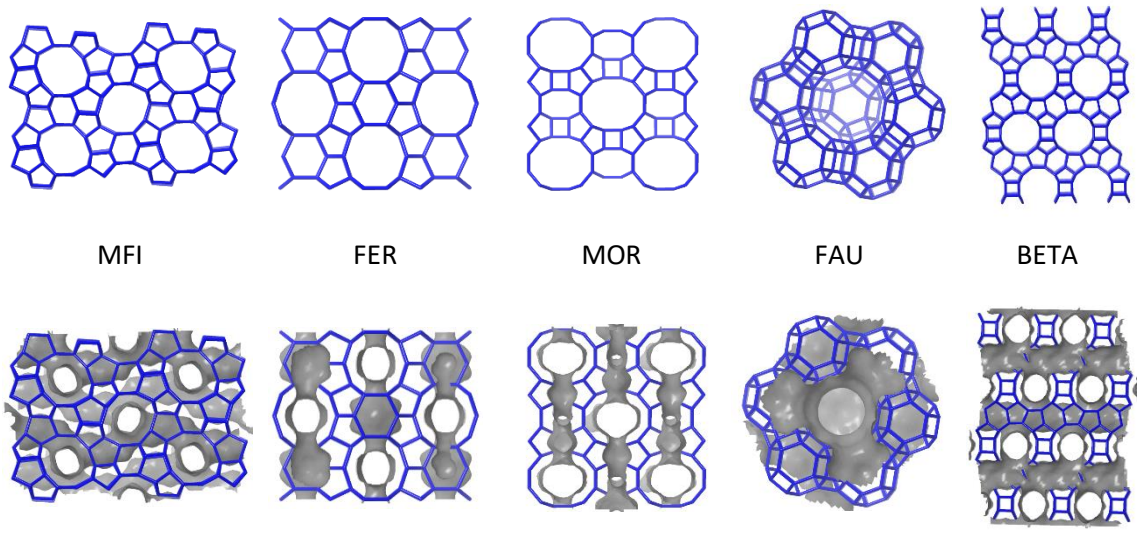

Figure 1: 'Big Five' zeolite topologies with channel systems highlighted in grey. Images taken with permission from IZA[17]

In 1948, Barrer formed a synthetic analogue of the naturally occurring MOR under hydrothermal conditions.[29] The first fully synthetic zeolite framework A was reported in 1959.[26] This synthesis method forms the foundation of most modern syntheses, where a source of silica and alumina are combined and dissolved in the presence of a mineraliser to form a gel. This gel phase is subsequently placed in an autoclave at elevated temperature to crystallise. The resulting zeolite structure is dependent on factors such as temperature (80-200 ^{o}C), time for crystallisation (hours to weeks), structure directing agent (SDA) and pressure. [26] Figure 2 illustrates these factors as well as many other synthesis parameters that may control the outcome of a zeolite synthesis.

Whilst pure silica zeolites can be formed, the presence of $[AlO_4]^-$ tetrahedra, which require a charge balancing cation, drastically change the chemistry of the materials. Inorganic cations or organic SDAs are used in synthesis to balance this charge. Additional post synthetic treatments are carried out: calcination to remove the organic SDA or ion exchange to form solely acidic zeolites. The zeolite can also be loaded with metal ions which can help promote catalytic reactions.

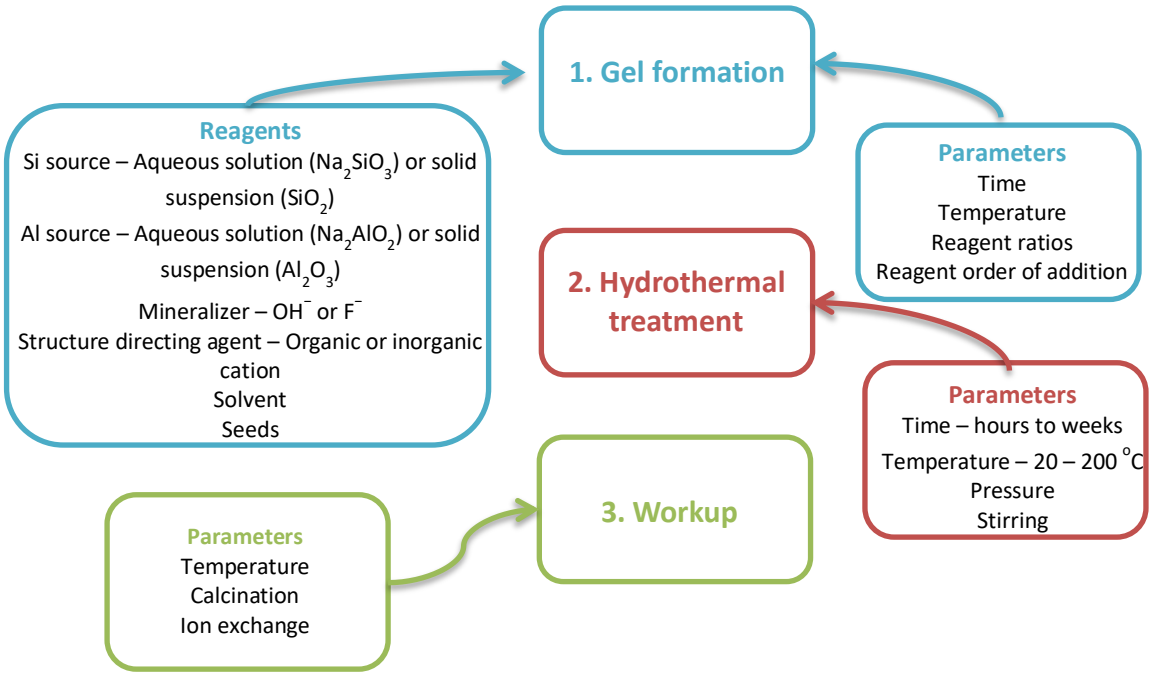

Figure 2: Factors effecting zeolite formation under hydrothermal synthesis conditions.

Zeolites have three main applications in industry: catalysis, gas separation and ion exchange. The largest volume use for zeolites is in detergent formulations where the ion exchange properties are exploited to remove calcium and magnesium from hard water.[30] However, the introduction of zeolites into refinery operations was groundbreaking and since their success in catalytic cracking, zeolites have found many applications in petroleum processing.[31] Fluid catalytic cracking (FCC) uses USY to convert high boiling fractions of crude oil primarily into gasoline with around 15 million barrels processed around the world per day.[30, 31] Other catalytic processes such as isomerisation and hydrocarbon synthesis rely on the shape-selective properties provided by 3D zeolite pore networks or the utilisation of acidic zeolites as effective solid-state acid catalysts.[32] These valuable properties also allow zeolites to be used in applications involving drying, purification and gas separation. The porous structures that often have similar kinetic diameters to gases allows precise separation, for example removing impurities such as CO_2 and SO_2 impurities from natural gas streams.[33] Both natural and synthetic zeolites have found wide-ranging application in chemical industry due to their diverse and valuable properties.

1.2 The direct conversion of methane

1.2.1 Brief history of Direct Methane to Methanol dMtM

Since the beginning of the 20th century efforts to effect dMtM have been recorded. Articles in 1902 and 1903 reported on gas phase (homogeneous) partial oxidation of methane,[10] while one of the first dMtM patents dates from 1905 when Lance and Elworthy described the synthesis of methanol by oxidizing methane with hydrogen peroxide in the presence of ferrous sulfate.[34] Although efforts to effect dMtM over heterogeneous catalysts were reported in 1928,[35] the vast majority of subsequent research focussed on dMtM through partial combustion/oxidation in the absence of an added heterogeneous catalyst. However, by the 1960s a range of different supported metals had been identified as competent for dMtM.[36] In 1969, Shilov reported that when methane was heated to 100 °C in a sealed ampoule containing $PtCl_4$ and a D_2O/CH_3COOD mixture, H/D exchange was observed to occur, indicating that methane activation could occur under mild conditions with a homogeneous catalyst.[37] This was the birth of so-called 'Shilov chemistry' and resulted in the first example of direct methane to methanol using homogeneous platinum complexes under remarkably mild conditions (120 °C, in water).[38] Mechanistic studies of the Shilov system elucidated the key steps involved[39] and numerous efforts have been made to improve the system by ligation.[40] [41, 42] The Shilov cycle, shown in Scheme 3, consists of three main steps: the electrophilic activation of the C-H bond, oxidation of the Pt complex and nucleophilic oxidation of methane. However, it has not been possible to bring the aqueous Shilov system close to commercial levels.

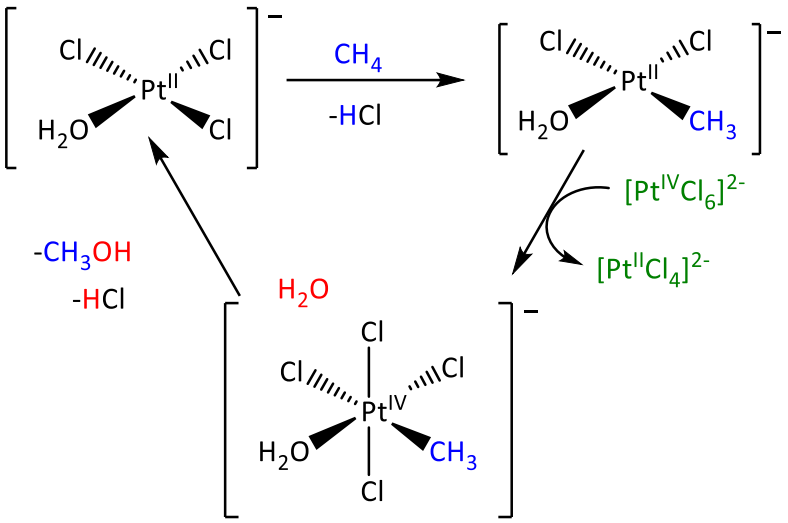

Scheme 3: Shilov mechanism for methane activation catalysed by a Pt salt

While not a direct conversion process, an important breakthrough in methane conversion came in 1998, with the report from Catalytica that utilised a ligand modified Pt

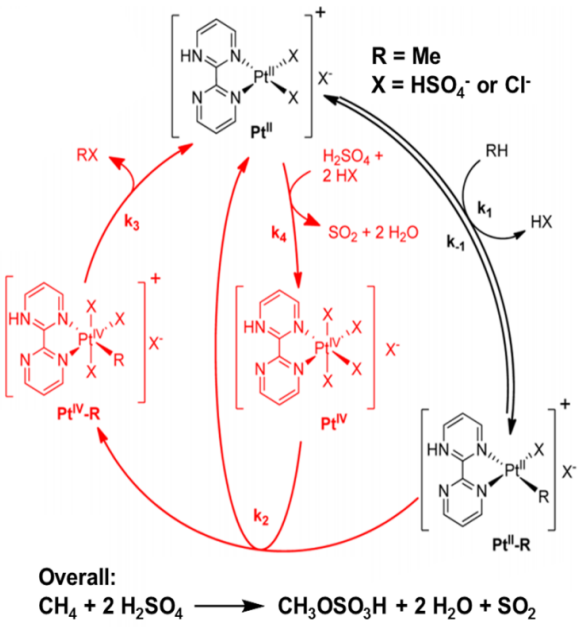

Figure 3: Proposed mechanism for the functionalisation of methane using (bpym)Pt(TFA)$_2$ in H_2SO_4 in the Catalytica system. Adapted with permission from reference 42. Copyright 2014 American Chemical Society

system in fuming sulfuric acid to oxidise methane to methane bisulfate (Figure 3).[43, 44] The system gave a single pass yield of 72% for methane bisulfate. Subsequent hydrolysis of methane bisulfate to methanol gave an overall selectivity of 81%. More recently, Schüth has shown that the Catalytica system can be substantially improved upon by controlling the level of SO_3 in the oleum used and by using K_2PtCl_4 as a catalyst precursor in the absence of additional ligands.[45, 46] The improvements led to turnover frequencies (TOFs) three orders of magnitude higher than the original system, giving process parameters which the authors showed are comparable to industrial processes such as the Cativa™ process (methanol carbonylation to acetic acid). However challenges remain in separating methane bisulfate from the reaction mixture and recycling the SO_2 by-product.[45] Furthermore, the inventory of oleum required may be off-putting, though it should be noted that refinery alkylation processes often use concentrated sulfuric acid on very large scales.[47] Although methanol is not produced directly, it is this exact feature of the reaction which prevents over oxidation, giving very high selectivities. This is a result of the methane bisulfate being deactivated with respect to further Pt mediated, electrophilic C–H activation due to the electron withdrawing effect of the sulphate group.

It is unsurprising to note that substantial heterogeneous catalysis research on dMtM has been conducted over early transition metal oxides, which find much use as oxidation catalysts through Mars-van Krevelen type mechanisms.[48] In particular, the commercial production of maleic anhydride *via* partial oxidation of either benzene or n-butane has utilised oxides of molybdenum or vanadium as catalysts.[49] Correspondingly, both vanadium oxide as well as

molybdenum oxide catalysts have been studied for dMtM. Interestingly, catalysts based on MoO_3 and V_2O_5 can also form substantial quantities of formaldehyde during the process.[50-52] By the late 1980s heterogenised molybdenum catalysts were some of the most active materials available for the dMtM reaction.[53-55] In 2008 very impressive methane conversion and methanol selectivity values (13.2% and 78.8% respectively) were reported over an Fe/SiO_2 catalyst.[56] Mössbauer spectroscopic analysis of the catalyst indicated that 81% of the iron is present as supported hematite (Fe_2O_3), while 19% of the iron is embedded into the silica matrix as tetrahedral, Fe^{3+} sites.[56] No further articles on the system have been reported, but these impressive results over Fe/SiO_2 highlight the continuing improvements that are being made using heterogeneous catalyst systems.

By 1990 and beyond, metal-modified zeolites were being reported for the catalytic, direct partial oxidation of methane to methanol with molecular oxygen under flow conditions.[57,58] These pioneering results showed that methanol could be formed selectively under the right conditions. For example, the selectivity reported by Lyons *et al.* was 64% at 4.6% conversion[57] while Walsh reported 20.6 % selectivity at 5.5% conversion.[58] These initial catalytic dMtM studies did not ascertain the nature of the active site, but did show that enhanced MeOH yield and selectivity was attainable over such materials (by comparison Walsh reported 47% selectivity at 0.2% conversion over glass beads).[58] In 1995 Panov showed that methanol could be formed from methane by contact with the so-called α–Fe site, supported on ZSM–5.[59] The active site was at this stage unknown. However, the selectivity, after aqueous extraction, was shown to be 75%. This inspired others to further study these stoichiometric reactions in a bid to uncover the mechanism and active site requirements such that the yield and selectivity of the catalytic reaction may be improved.

Despite the progress in heterogeneous and homogeneous systems towards direct (and indirect) methane conversion to methanol, no system has yet been commercialised. This is indicative of the substantial hurdles that remain. In his 2015 article evaluating a dMtM production plant using current catalyst technologies, de Klerk highlights the areas where improvements need to be made in order to challenge the practiced syngas based route.[60] These areas are namely in improving MeOH selectivity/reducing CO_2 selectivity, reducing the need for pure oxygen (which introduces an air fractionation step) as well as keeping the reaction pressure to a minimum to reduce the compressor duty. These areas can all be tackled by catalyst understanding and improvement, and serve as the basis for focus areas for further research.

1.2.2 Brief history of Methane Dehydroaromatisation (MDA)

Aromatics, such as benzene, toluene and xylene (BTX), are in high demand as feedstocks for fine-chemicals, commodity chemicals and the plastic industry.[61] Like dMtM, direct non-oxidative conversion of methane to higher hydrocarbons without multistep processes is extremely attractive to industry. However, as for dMtM, the reaction is hindered by thermodynamic limitations.[62] It is clear from Equation 1 and the graphs in Figure 4 that formation of benzene is extremely unfavourable. At equilibrium, benzene formation is only significant at very high temperatures and solid carbon (C_s) is the thermodynamically favoured product. This coke formation leads to rapid catalyst deactivation, limiting MDA catalyst lifetime. Two approaches can be taken to address the equilibrium limitations on benzene formation: the use of oxygen or the addition of other alkanes/alkenes.[21] Whilst the addition of oxygen results in a thermodynamically favourable reaction, in practice, over oxidation CO_x results in selectivity challenges. Addition of further alkanes/alkenes results in methane activation at temperatures less than 600 °C, but this could hinder benzene selectivity.[63]

$$6\ _{4(\ )} \rightarrow 9\ _{2(\ )} +\ _{6}\ _{6(\ )} \qquad \Delta^{\circ} = +433\ \text{kJ}^{-1}$$

$$\Delta^{\circ} = +531\ \text{kJ}^{-1}$$

Equation 1: Benzene formation from methane with ΔG and ΔH energy values.[62]

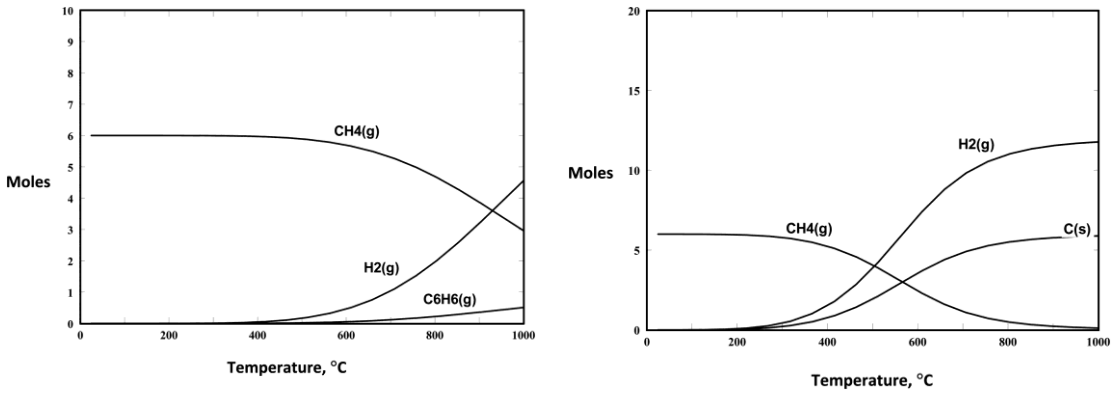

Figure 4: Left: Equilibrium amounts (moles), 1 bar, starting with 6 mol CH_4 and allowing only H_2 and benzene as components. Calculated using HSC 7.1 software. Right: Equilibrium amounts (moles), 1 bar, starting with 6 mol CH_4 and allowing $C_{(s)}$, H_2, and benzene as components. Adapted with permission from reference 60. Copyright 2014 Royal Society of Chemistry

Following the pioneering results achieved by Wang *et al.* in the direct non-oxidative aromatisation of methane to benzene over Mo/H-ZSM-5,[20] numerous studies have been undertaken using a variety of metals (V, Cr, Fe, Mo,[64] W,[65] Re,[66] Zn,[67] Mn,[68] Ga,[69] *etc.*). Mo/H-ZSM-5 and Mo/H-MCM-22 are the most promising systems to date, achieving 10-12% methane conversion with 60-70% benzene selectivity at 700 °C.[70] Factors such as the Brønsted acidity of

the zeolite, the channel structure, and the state, location and method of Mo introduction, seem crucial for the catalytic performance in MDA.[71]

Although the mechanism of MDA over Mo/ZSM-5 has yet to be fully clarified, a two-step bifunctional pathway is generally accepted. Firstly, methane is converted to C_2 hydrocarbons over Mo sites within the catalyst (ethylene or acetylene have been proposed as intermediates). The C_2H_y is subsequently dehydrogenated and oligermerised on the BAS sites of the zeolite support.[21, 72] The mechanism, shown in Figure 5, is very similar to the hydrocarbon pool mechanism for the methanol-to-hydrocarbon reaction, except MDA proceeds through a radical intermediates, not *via* carbocations.

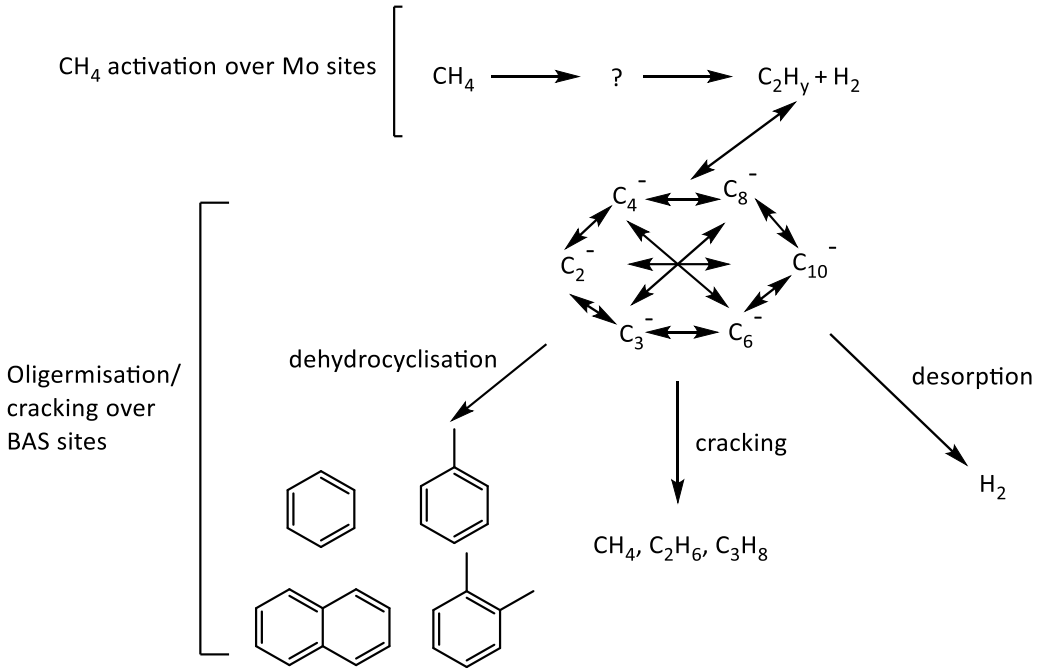

Figure 5: Mechanism for MDA over Mo/H-zeolites demonstrating the bifunctional pathway involving CH_4 activation over Mo sites and aromatisation over BAS.[62]

Although the mechanism for the non-oxidative transformation of methane to benzene is clearly very complex, some important mechanistic factors have been established. The production of aromatics from methane over Mo/H-ZSM-5 occurs in three overlapping stages. The first, the activation period, is associated with the reduction of Mo (most likely present as MoO_3) by methane to form Mo_2C.[73] The induction period accompanies the formation of the hydrocarbon pool derived from C_2 hydrocarbons reacting at BAS sites to build up higher products.[70, 74] This results in carbonaceous deposit, either on the acid sites or on the partially reduced Mo species which leads to catalyst deactivation. This organo-mediated mechanism was further evidenced by ^{13}C isotope studies and pulse reactions by Hensen *et al.,* which demonstrated that the benzene is synthesised from secondary reactions of confined

polyaromatic carbon species with the initial products of methane activation.[75] Gascon *et al.* also observe that carbon from the active site is incorporated into the final products.[70] Hence, the carbon species formed inside the micropore are integral to the MDA reaction, akin to the hydrocarbon pool mechanism operative in the methanol-to-gasoline reaction.

The main intermediate of the reaction, *i.e.* the initial product of methane activation, is usually considered to be ethylene. Xu *et al.* suggest ethylene as the initial product as they observed the formation of ethylene at similar times to benzene and with increasing space velocity, ethylene selectivity increased.[20, 71] Furthermore, Rosynek *et al.* established that when using ethylene as the reactant, a similar hydrocarbon product distribution to methane over Mo/H-ZSM-5 was observed.[73] However, Meriaudeau *et al.* consider acetylene as an important intermediate in MDA as the amount of acetylene formed decreases with increased reaction time whilst the yields of ethylene and benzene increased.[76] They believe that the bifunctional mechanism is less important, and the principle route for the aromatisation of methane is the formation of C_2H_2 over Mo_2C which forms benzene over the same Mo_2C sites. Kapteijn *et al.* also conclude that ethylene is not likely to be the primary product of MDA, as upon reaction of ethylene under MDA conditions, the hydrocarbon pool formed was more dense and contained less hydrogenated species than when using methane.[72] Furthermore, the coke deposits formed from MDA when using methane were found to be more reactive than those formed from ethylene. A very recent paper by Bhan *et al.* reports that ethane is the sole primary product of methane pyrolysis and this is subsequently dehydrogenated to ethylene and acetylene before aromatisation to benzene occurs.[77] Overall, the mechanism of MDA over Mo/H-ZSM-5 has not yet been fully understood and questions such as the exact involvement of carbonaceous deposits in the formation of benzene still require answers.

Understanding the state of the Mo species within the zeolite is crucial to controlling catalytic behaviour. Mo/zeolite catalysts are usually prepared through impregnation using $(NH_4)_6Mo_7O_{24}$ as the Mo source (2-5 wt% Mo).[21] Upon calcination, MoO_3 is formed and migrates into the zeolite channels.[71] This migration has been evidence by numerous techniques: BET, NH_3-TPD, XRD, XAS and NMR spectroscopy.[78-82] Iglesia *et al.* have pioneered the investigation into the structure of Mo species using a vast array of analysis techniques. Their results show that at 350 °C MoO_x species are distributed over the external surface of the zeolite.[80] Upon heating, these species migrate into the zeolite channels and can undergo ion exchange at BAS. The exchange reaction results in the formation of $[MoO_2(OH)^+]$ species which can condense to form dimers (Scheme 4a). Iglesia showed these $[Mo_2O_5^{2+}]$ dimers are reduced to the active MoC_x species upon exposure to CH_4.[81] The $[MoO_2(OH)^+]$ species can also react with a BAS to form a $[Mo_2O_5^{2+}]$ cation

bridging two framework oxygen atoms (Scheme 4a). However, XPS studies by Rosynek *et al.* demonstrate that following calcination, Mo exists principally as Mo^{6+}, likely as MoO_3.[73] Exposure to CH_4 at 700 °C resulted in gradual reduction of the Mo^{6+} until complete transformation to Mo_2C occurred. XRD analysis indicated that the carbide was highly dispersed within the zeolite channels and this Mo_2C species was found to be critical for the activation of methane.[73, 83] This is supported by Xu *et al.* who demonstrate using extraction of Mo species with NH_3(aq) that small MoO_3 crystallites with octahedral co-ordination are active for MDA.[84] Once again, the nature of the Mo active sites is highly debated and the exact active species is yet to be elucidated.

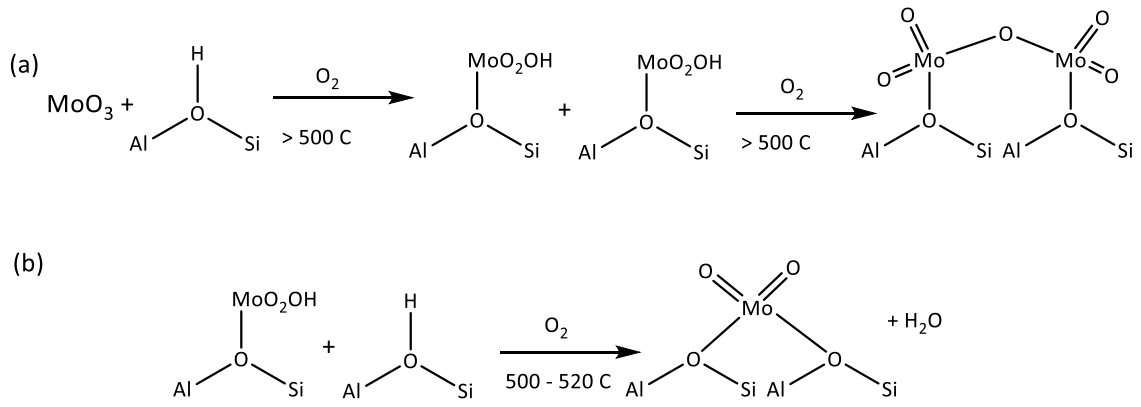

Scheme 4: Interactions between Mo species and BAS resulting in Mo dimers and bridged species.

In order to maximise benzene selectivity whilst minimising the effects from coking, numerous Mo exchanged zeolite and zeotype frameworks have been studied for MDA. Lln *et al.* screened several frameworks and concluded that protic silica-alumina zeolites, such as ZSM-5, ZSM-8, ZSM-11 and beta, containing 2D channel structures with pore diameters close to the dynamic diameter of benzene (6 Å) were the best supports for the MDA reaction.[85] No hydrocarbon products were formed from Mo/H-SAPO-5 or Mo/SAPO-11 catalysts.[85] Other frameworks (X, Y, MOR) demonstrated low levels of methane conversion and were rapidly deactivated due to the formation of coke.[86] However, only Mo loaded HMCM-22 and H-MCM-49 produced high MDA activity that was comparable to Mo/H-ZSM-5[21] hence, MCM-22 and ZSM-5 have been studied extensively. H-MCM-22 consists of two independent pore systems: a 2D sinusoidal 10 MR pore system and a larger 3D 12 MR super-cage system interconnected by 10 MR windows. The smaller sinusoidal system is not dissimilar to the 3D channel structure of ZSM-5 (Figure 6). This pore structure and the presence of supercages allows MCM-22 to

accommodate high levels of coke whilst retaining shape selectivity for benzene, hence, high MDA activity is achieved using Mo/H-MCM-22 with higher catalyst stability than Mo/H-ZSM-5.[87, 88]

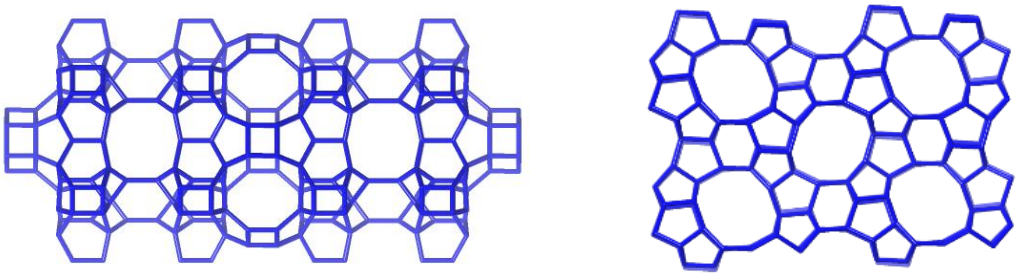

MCM-22 (MWW)

10 MR: 4.1 x 5.1 Å

10 MR windows: 4.0 x 5.5 Å

ZSM-5 (MFI)

10 MR: 5.1 x 5.5 Å

10 MR: 5.3 x 5.6 Å

Figure 6: Structure and channel dimensions of MCM-22 and ZSM-5, both promising catalysts for MDA. Images and dimensions from IZA database.

Although the exact nature of the active species and mechanism for MDA has not yet been established, one fact is clear for MDA reactions over Mo/zeolites: deactivation is caused by severe carbon deposition, which limits the practically of MDA reactions industrially. Three types of coke have been observed on Mo/H-ZSM-5 using XPS: graphite-like carbon in the zeolite channels, carbidic coke as a component of Mo_2C on the zeolite surface and hydrogen poor sp-type coke which gradually covers the zeolite surface.[21, 61] Evidence for these types of coke is supported by temperature-programmed techniques performed by Bao *et al.*[87, 89, 90] and UV-Raman spectroscopy.[91] The coke levels increase with time on stream and with temperature.[92] Generally, the dehydrogenation of CH_x on the metal catalyst results in amorphous coke, whilst the polymerisation of C_2H_x and C_6H_5 on the BAS sits results in polyaromantic deposits.[93] It is this polyaromatic type carbon that is thought to be the main cause of catalyst deactivation.[21, 61] Furthermore, under excessive Mo loading and extended time on stream, the zeolite framework can collapse forming $Al_2(MoO_4)_3$ and under the harsh reaction conditions, sintering of the Mo_2C species can also cause deactivation.[94]

Whilst formation of carbon deposits is somewhat inevitable, catalyst deactivation within a few hours of contact with methane under MDA reaction conditions is not suitable for practical applications. Therefore, a number of groups are working on regeneration protocols and also reducing the deposition of coke during MDA reactions. The catalysts can be regenerated by

oxidation or hydrogenation of the coke. Oxidative treatments result in the removal of coke by forming CO_x but high temperature air calcination cannot be carried out as this results in zeolite dealumination.[21] Low temperature (300 – 500 °C) oxidation can remove polyaromatic deposits and Hensen *et al.* have developed a novel isothermal air regeneration protocol for MDA.[95] Periodic oxygen pulses into the methane feed resulted in full restoration of catalytic activity, a doubled cumulative benzene yield and considerably lower overall coke formation. However, the regenerative effects diminish with time on stream as harder to oxidise polyaromatic coke, which cannot be removed at 700 °C under oxidative conditions, forms. Other groups have further developed this pulsing method, under oxygen or hydrogen, leading to enhanced benzene yields and more stable catalyst performances.[96-98] This method shows great potential in tackling the coking issues of the MDA reaction, though a suitable reactor has yet to be developed.

Since the initial report of MDA over Mo/H-ZSM-5 in 1993, substantial progress has been made in understanding various aspects of the reaction. However, the inherent inertness of methane, rapid catalyst deactivation due to coke formation and thermodynamic limitations of the reaction hinder the industrialisation of MDA. Mo/H-ZSM-5 and Mo/H-MCM-22 remain the most active and selective catalysts due to their 10 MR channel. Though the exact mechanistic details remain debated, it is generally accepted that Mo migrates into the zeolite channels during calcination where the Mo_2C phase is formed upon methane exposure. Methane is believed to form C_2H_x species on the Mo sites, though the precise nature of these sites remains unknown, and subsequent oligomerisation occurs on BAS sites of the zeolite framework. However, results from Hensen and Meriaudeau demonstrate that BAS sites are not necessarily required for MDA. Further advances in reaction procedure, reactor design and fundamental understanding of mechanism and active sites will hopefully lead to the development of an efficient, practical MDA process.

1.3 Metal-modified Zeolites for dMtM

Zeolites are already extensively utilised for refinery and petrochemical processes[99] and are also well known to be able to induce reaction selectivities which differ to those predicted on thermodynamics alone. This can be achieved through the well-known reactant, product and transition state selectivity.[100] Additionally zeolites can impart remarkable reaction selectivity through confinement, where the free energy of the transition state is lowered by interactions with the framework, commonly van der Waals interactions and charge stabilisation by anionic T-sites.[101] The capacity to alter reaction selectivities through subtle substrate-framework interactions has drawn parallels with enzymes,[102] exemplified by the carbonylation of dimethyl ether to methyl acetate, which has been shown to selectively take place in the 8 membered ring (MR) side pockets of MOR.[103, 104] Given that zeolites are already made and utilised on industrial scales, and demonstrate a remarkable capacity to control reaction selectivity, it is fair to say that zeolite based catalysts have the potential to be industrial catalysts for dMtM. Subsequently, since Panov reported the highly selective conversion of methane to methanol over iron-modified ZSM-5 (Fe/ZSM-5),[59] although not catalytic, the field has grown enormously to become one of the most promising approaches to dMtM.

1.3.1 Fe-modified zeolites

Perhaps the most historic system within this field, Fe-modified zeolites have been known to be active in the oxidation of methane since the pioneering work of Panov *et al*. in the early 1990s.[105] Early reports concluded that Fe/ZSM–5 is able to efficiently decompose N_2O at relatively low temperatures (< 300 °C) resulting in a highly reactive iron/oxygen species bound to the zeolite surface, termed α–oxygen (α–O), which is active for the direct partial oxidation of benzene to phenol at ambient temperature,[105-107] and was later deduced to be the active species in direct partial oxidation of methane to methanol. The formation of α–O is found to possess first order kinetics with respect to N_2O and cannot be formed by reaction with O_2 or NO.

Due to the presence of inactive spectator iron species, the nature of the active site and factors determining reactivity have been difficult to prove spectroscopically. Originally it was thought that the active precursor associated with the decomposition of N_2O (known as α–Fe) was a binuclear iron species, similar to that observed in MMO enzymes.[108] However, the α–Fe site was later determined to be a mononuclear Fe^{II} species formed *via* irreversible auto-reduction of impregnated Fe^{III} species upon thermal treatment.[109, 110] A substantial contribution from Snyder *et al*. reports the use of magnetic circular dichroism (MCD) to elucidate significant structural and electronic information about both the α–Fe and α–O sites in zeolite beta (ß).[110] It

was found that α–Fe is a mononuclear, high spin Fe^{II} species residing within a square planar co-ordination environment. Further density functional theory (DFT) studies suggest that this square planar environment resides within a β–6 MR (Figure 7). Similarly, the α–O site is a mononuclear, high spin species which contains an Fe^{IV}=O centre adopting a square pyramidal geometry within the same β–6 MR.

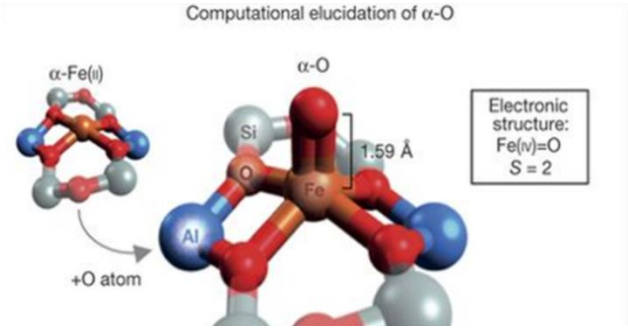

Figure 7: DFT-optimized structure of α-Fe(IV)=O in the S = 2 ground state and its formation. Adapted with permission from reference 108. Copyright 2016 Nature

The general consensus regarding the methane-to-methanol reaction pathway over α–O sites is that it follows a radical-based hydrogen atom abstraction mechanism, although steps following this are debated. Briefly, active α–O species are introduced into the catalyst by N_2O decomposition before methane is subsequently introduced. A hydrogen atom is abstracted from methane by the α–O resulting in an Fe^{III}–O–H fragment and a CH_3 radical. This CH_3 radical may then either react with a further α–O to form Fe^{III}–O–CH_3 that may be extracted *via* hydrolysis or the CH_3 radical may 'rebound' to form an associated Fe^{II}–O(H)–CH_3 which may then desorb forming CH_3OH (Figure 8).[109, 111] Formation of dimethyl ether (DME, CH_3OCH_3) has also been observed *via* the proposed reaction of a CH_3 radical with an already formed Fe^{III}–O–CH_3 group.[109] Kinetic isotope effect experiments suggest that initial C–H bond cleavage is the rate-limiting step in this process.[108] Fourier-transform infrared spectroscopy (FTIR) further supports the presence of the hydrogen atom abstraction process with computational evidence strongly suggesting that the C–H cleavage is performed *via* a radical mechanism with the Fe^{IV}=O species elongating and gaining significant radical character at the transition state, becoming closer to an Fe^{III}–$O^{\bullet-}$ species.[109, 110]

The remarkable activity of the α–O site is partially attributed to confinement effects within the zeolite channels.[49, 111] Periodic and cluster modelling of an α–O site in SSZ–13 have shown that the confining effect of zeolite channels may reduce the energetic barrier to methane activation by over 50%.[111] It is suggested that the confinement effect is predominantly electrostatic in nature and stabilises reaction intermediates and transition states to a further degree than that of the initially adsorbed methane molecule.[111] The key effect is stated to be

the stabilisation of the intermediate species, suggesting that tighter confinement leads to lowered C–H bond activation energy owing to a Brønsted−Evans−Polanyi relationship.

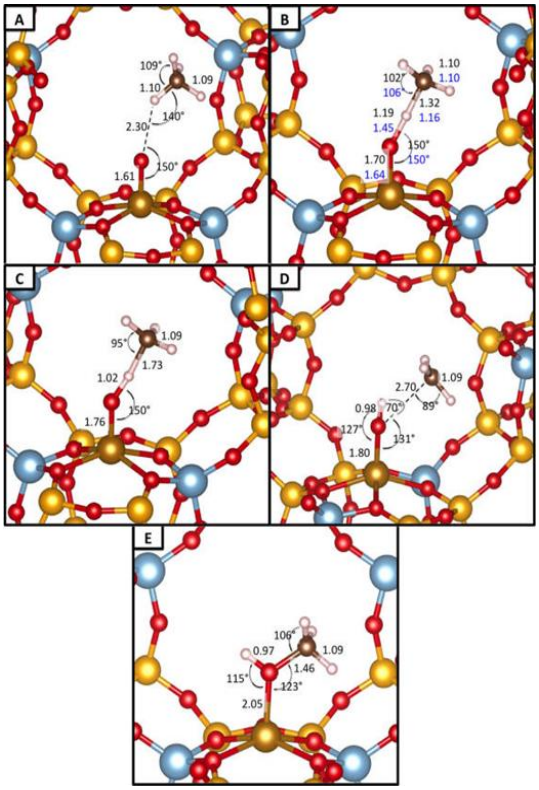

Figure 8: Structures and the most important intermediates (adsorbed molecule (A), reaction intermediate (C), and adsorbed methanol (E)) and transition states (abstraction transition state (B) and rebound transition state (D)) along the reaction pathway of dMtM over the α–O site. Colour legend: Si atoms, yellow; O atoms, red; Al atoms, blue-grey; Fe atoms, gold; H atoms, white; and C atoms, brown. Black numbers represent PBE-D2 distances (in Å) and angles (in degrees); blue numbers in panel (B) show the optimized RPA geometry. Adapted with permission from reference 109. Copyright 2016 American Chemical Society

In order to become more viable at large-scale, the requirement for batch-style oxidative pre-treatments and liquid phase extraction should be avoided. Hence, several attempts have been made to produce methanol from methane over Fe–modified zeolites under a continuous or catalytic regime, although success has been limited. The reaction has been reported to occur in a "quasi-catalytic" manner at 160 °C over Fe/ZSM–5 under an atmosphere of CH_4:N_2O with stoichiometry of 1:1 and single site turnover number (TON) of 3.6, although liquid phase extraction of products was still required.[112] The >1 TON is attributed to methanol spill over, suggesting that methoxy species can migrate within the framework, reforming the α–Fe site and allowing another catalytic cycle to take place. It is suggested that the reaction temperature (160 °C) is insufficient to promote methanol desorption. A later contribution describes the continuous flow reaction of N_2O and CH_4 over Fe/ZSM–5 at 300 °C.[113] Methanol was observed with only very low selectivity (~1%) while CO is observed as the major product. This is attributed to the inability of methanol to desorb from the catalyst, instead migrating to nearby Brønsted acid sites and

rapidly producing coke in subsequent reactions akin to those seen in the methanol-to-olefins process. Upon introduction of water in a co-feed, the selectivity to methanol is seen to greatly improve, reaching around 16%. It is thought that the additional water hydrolyses adsorbed methanol and methoxy species, allowing them to leave the catalyst, a hypothesis that is concordant with an observed decrease in coke formation. Activation of N_2O by extra-framework iron species is not experimentally limited to MFI framework types alone with evidence for N_2O decomposition over MOR, FER and FAU having been reported.[114-117] In each case it has been shown that framework oxygen atoms are able to be isotopically exchanged with $N_2{}^{18}O$. N_2O decomposition and subsequent methane activation have also recently been observed to take place on both Fe/BEA and Fe/CHA, resulting in the production of methanol which was able to be recovered by liquid extraction.[110, 118] From computational studies, it is found that in the CHA case the α–O site is also stabilised within a 6 MR, similar to that of BEA but with subtle differences in their geometries. The mononuclearity of the CHA α–O site was confirmed by Mössbauer spectroscopy.[81]

Ferrisilicate, a zeotype material containing only Si and Fe tetrahedral atoms and adopting an MFI framework type, has been shown to be active in the direct conversion of methane to methanol using O_2 as an oxidant as opposed to N_2O.[119] This is of significant interest as α–O sites in aluminosilicates are unable to form from O_2, always requiring N_2O instead. In contrast to Fe–modified aluminosilicate systems which are able to activate methane and form methanol at ambient temperatures, the ferrisilicate systems require much greater temperatures (350 °C) for reaction to take place although the observed methane conversion at this temperature is only around 0.1%. Temperatures even higher still (630 °C) are needed for substantial methane conversion to be observed where methane conversions up to around 30% are seen, although at significant cost of methanol selectivity. The requirement for much higher temperatures to achieve even low-level conversion coupled with the ability to utilise dioxygen as an oxidiser strongly suggest that the ferrisilicates system contains an active site different to that of Fe–modified aluminosilicate zeolites. No mechanism has been suggested as to how this transformation takes place over ferrisilicates and hence a mechanistic comparison with respect to the α–O site cannot be made as yet. For the ferrisilicates system, a higher Si/Fe ratio was shown to result in higher methanol selectivity, although at the expense of percentage methane conversion. Both H– and Na–form ferrisilicates were compared, with Na–forms demonstrating higher selectivity for methanol.

In addition to gaseous phase activation by O_2 or N_2O, several recent contributions have investigated the use of an aqueous phase oxidant, H_2O_2, in the dMtM reaction over Fe-modified

zeolites.[120-124] In contrast to what has been highlighted previously, this system is not thought to proceed *via* α–O formation (Fe^{II}/N_2O system), but instead by a mechanism that utilises extra-framework Fe^{III} oxides, intermediately forming methyl hydroperoxide (CH_3–OOH) which is subsequently transformed into the desired methanol product alongside further oxidised products, namely formic acid and carbon oxides.[121]

Overall, the active sites (α–Fe and α–O) in Fe-modified zeolite systems have been well characterised, whereas the mechanism of C–O bond formation following initial hydrogen abstraction requires further elucidation. Although a well-established system, potential for exploration of methanol production over different framework types and expansion to continuous flow processes is ripe. A major factor determining the success of Fe-modified zeolite systems will be the ability to use O_2 as an oxidant as opposed to N_2O, which, owing to its energetic nature, is generally undesirable for large-scale industrial usage. In this regard, investigation of methane partial oxidation over ferrisilicates holds promise within this area.

1.3.2 Cu-modified zeolites

Since the first report of methane partial oxidation to methanol over copper-modified zeolites in 2005, the field has been subject to intense scientific interest and research.[125] Methanol formation has since been shown to be possible over a wide range of copper-modified zeolite frameworks including: MFI, MOR, FER, CHA, FAU, BEA, LTL, EON, MAZ, MEI, BPH, HEU, SZR, AFX and AEI.[126-128] Within these frameworks, a wide variety of active sites have been proposed for this important transformation.

1.3.2.1 Active sites for methane partial oxidation in copper-modified zeolites

Unlike iron-modified zeolites in which it is thought that only one site (the so-called α–Fe site) is active for methane partial oxidation to methanol, there have been multiple active sites proposed to exist in copper-modified zeolites. The first site to be proposed for methane C–H bond activation in Cu/ZSM–5 was the bis(μ-oxo)dicopper core (Figure 9A) that had previously been identified for the decomposition of NO[129] and was thought to be characterised by a strong absorption band at 22700 cm^{-1} in the ultraviolet-visible-near infrared (UV-Vis-NIR) spectrum.[125] Another active site, a (μ-η^2:η^2-peroxo)dicopper core (Figure 9B) which is active in nature for O_2 transport by the protein hemocyanin, was also suggested, but was not observed to be active in NO reduction.[125, 129, 130]

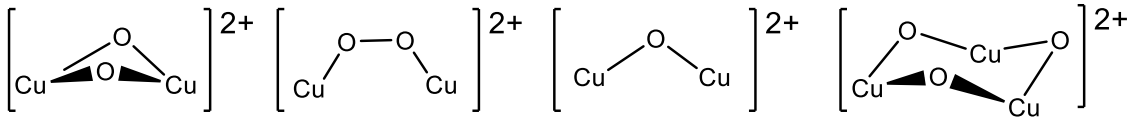

A. $Cu_2(\mu\text{-}O)_2^{2+}$ B. $Cu_2(\mu\text{-}O_2)^{2+}$ C. $Cu_2(\mu\text{-}O)^{2+}$ D. $Cu_3(\mu\text{-}O)_3^{2+}$

Figure 9: Cu-oxo complexes proposed as the active sites for methane activation in Cu-containing high-silica zeolites.[131]

A considerable contribution by Woertink *et al*. utilised resonance enhanced Raman spectroscopy (rR) to further elucidate the active site structure in Cu/ZSM-5.[132] By tuning a laser to the characteristic absorption feature identified with the active site (22700 cm^{-1}), the Raman vibrations associated with this feature are enhanced, enabling the ~5% active species to be distinguished from spectator Cu. As a result, the bis(μ-oxo)dicopper and (μ-η^2:η^2-peroxo)dicopper cores were able to be discounted due to inconsistencies with the observed rR stretching frequencies. Instead, a bent mono(μ-oxo)dicopper core (Figure 9C) was proposed as the active site owing to a series of isotope-sensitive fundamental vibrations at 456 cm^{-1} ($\Delta^{18}O_2$ = 8 cm^{-1}) and 870 cm^{-1} ($\Delta^{18}O_2$ = 40 cm^{-1}) alongside an intense overtone of the latter at 1725 cm^{-1} ($\Delta^{18}O_2$ = 83 cm^{-1}). This intensity pattern closely resembles that seen for mono(μ-oxo)diferric cores.[132, 133] The mono(μ-oxo)dicopper species is suggested to exist within the 10 MR channel of ZSM–5, bridging two framework aluminium sites separated by two silica tetrahedra. Each copper atom of the mono(μ-oxo)dicopper core is ligated by two oxygen atoms associated with the framework aluminium alongside the bridging oxygen. Normal co-ordinate analysis predicts a Cu–O–Cu bridging angle of 140°. The copper species are proposed to be formally Cu^{II}, as Cu^{III} cannot be stabilised without co-ordination of a further –OH group of which no evidence was detected by IR spectroscopy.[132]

The mono(μ-oxo)dicopper core can be formed by activation in both N_2O and O_2 as evidenced by observation of the UV-Vis-NIR band at 22700 cm^{-1} that is associated with this active site.[134, 135] Activation by N_2O can occur at room temperature by liberation of N_2 with the lowest energy pathway for N–O cleavage — the oxygen bridging mode (μ-1,1-O).[136] Activation by O_2 proceeds at room temperature *via* the formation of a (μ-η^2:η^2-peroxo)dicopper core which can be characterised by a strong UV-Vis-NIR absorption band at 29000 cm^{-1}.[135] Heat treatment in flowing He or O_2 results in the decrease of the 29000 cm^{-1} band and a coincidental increase of the 22700 cm^{-1} band from approximately 448 K, demonstrating formation of the mono(μ-oxo)dicopper core (Figure 10). This conversion results in the deposition of an oxygen atom on other remote Cu sites within the zeolite as evidenced by $^{18}O_2$ TPD.[135] It has been further

proposed that spectator Cu^+ ions in ion exchange sites provide the necessary electrons to reduce the peroxo-bridge.[135]

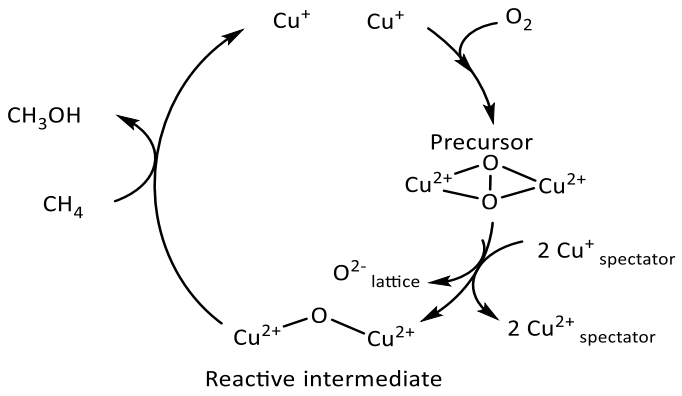

Figure 10: Formation of the mono(μ-oxo)dicopper core in the presence of O_2. Adapted from reference 133. Copyright 2010 American Chemical Society

Larger copper clusters have been both evidenced and predicted as active sites for the partial oxidation of methane in copper-modified zeolite systems. A trinuclear copper core, $[Cu_3(\mu O)_3]^{2+}$, has recently been proposed to exist at the mouth of the 8 MR side pocket of Cu/MOR (Figure 9D).[137] Extended X-ray absorption fine structure (EXAFS) measurements suggest that more than one Cu–Cu scattering path exists within the cluster, suggesting a nuclearity >2. From investigations into the change in acidity of the zeolite upon active site formation, it was shown that two Brønsted acid sites are displaced for every three Cu atoms incorporated into the structure. As a result, it is suggested that the trinuclear cluster is balanced between two aluminium atoms, each separated by three silica tetrahedra.

DFT simulations of mono(μ-oxo)dicopper and $[Cu_3(\mu O)_3]^{2+}$ cores in Cu/ZSM–5 have shown that under standard activation protocols (high temperature calcination in O_2) the trinuclear species is more stable than the binuclear species, whereas the binuclear species is preferentially formed under low partial pressures of O_2.[138] Previously identified binuclear and trinuclear cores alongside clusters of higher nuclearity ($[Cu_nO_{n-1}]^{2+}$ and $[Cu_n(\mu O)_n]^{2+}$, where n = 2,3,4,5) in Cu/MOR have also been simulated by DFT calculations in order to compare their stability and reactivity.[139] It was found that as the cluster increases in size, it becomes both more stable as a cluster and that increased reactivity with methane is strongly correlated with this increased stability.

In small pore zeolites such as CHA, several potential mononuclear extra-framework Cu cations have been identified both experimentally[140] and using DFT calculations.[141, 142] Specifically, $[CuOH]^+$ has been suggested to be active for methane partial oxidation in Cu/SSZ–13 and is predicted to be stabilised within an 8 MR CHA that contains only one charged

aluminium species.[141, 142] This species is believed to be formed upon dehydration of hydrated Cu^{2+} species and is characterised by a FTIR stretch at ν(O–H) = 3657 cm^{-1}.[143, 144]

1.3.2.2 Reaction mechanism for the partial oxidation of methane over copper-modified zeolites

Typically, methane partial oxidation over copper-modified zeolites is observed to take place in three distinct steps. Initially, the copper-exchanged zeolite is activated in an oxidative atmosphere using either O_2, at elevated temperature (typically 723–823 K), or N_2O, at from as low as room temperature.[125, 145, 146] The activated material is then exposed to methane at a moderate temperature (approx. 473 K) followed by subsequent extraction of the strongly bound products through contact with water vapour or a suitable solvent, such as a 1:1 mixture of acetonitrile and water.[125, 147]

Thus far, methane activation over copper-modified zeolites has only been proposed to occur *via* a radical type mechanism with DFT calculations having proved crucial for elucidation of this mechanism and kinetic isotope experiments proving important for determination of the rate-limiting step.[132, 138, 146, 148] The mono(μ-oxo)dicopper core, formally denoted as Cu^{2+}–O^{2-}–Cu^{2+}, is thought to be in resonance with what is effectively a cupric-oxyl species, Cu^{2+}–$O^{\bullet-}$–Cu^{+} (Figure 11), which possesses significant radical character owing to its singly occupied molecular orbital (SOMO) that is directed into the zeolite channel.[132, 138] This resonance form is aptly poised to perform hydrogen atom abstraction from methane to form an intermediate Cu–OH–Cu species and a CH_3 radical. This preliminary step shows a considerable H/D kinetic isotope effect of 3.1 at 448 K when the activation energies of CH_4 and CD_4 are compared.[132] This has been further confirmed when the products of a mixed substrate (CH_2D_2) were reacted over Cu/ZSM–5 at 403 K (as analysed by ^{1}H NMR spectroscopy, following extraction into D_2O).[132] In this analysis, a greater product integral is observed for CD_2HOD than for CDH_2OD implying that the rate of C–H cleavage is greater than that of the C–D bond. In a separate study an H/D KIE of 1.6 was determined when CH_4 was substituted by CD_4 in the extracting gas at 483 K over Cu/Na–

ZSM–5.[145] These observations alongside DFT predictions show that hydrogen abstraction is the rate limiting step in methanol formation from methane.

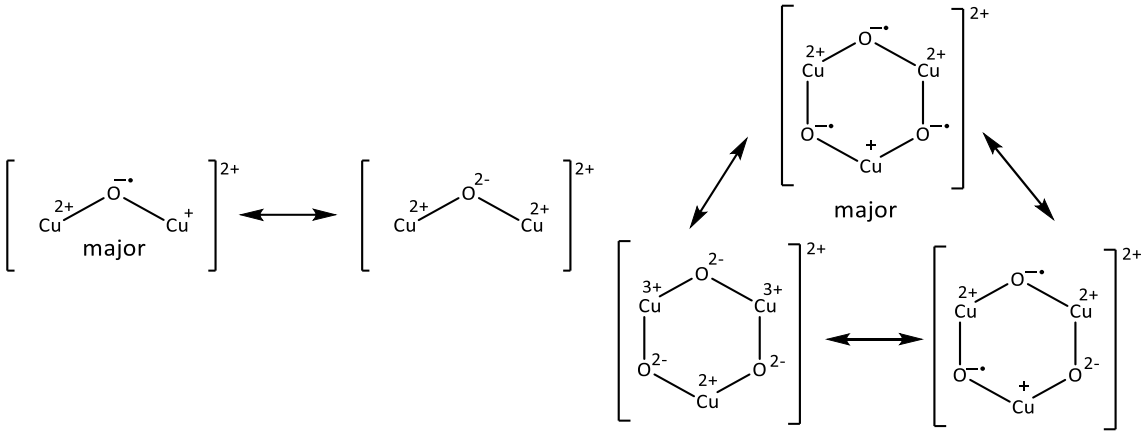

Figure 11: Possible resonance structures that could be proposed to describe the formal charge configuration in the extra-framework copper species. [131]

The newly formed "free" CH_3 radical intermediate has been predicted to collapse in several ways to form bound intermediates of various stability.[138] Two potential pathways can lead to the formation of a strongly bound, yet desired, methanol molecule (Figure 12). The first pathway is known as the "rebound mechanism" in which the CH_3 radical reacts directly with the bridging Cu–OH–Cu and forms a sorbed methanol molecule, Cu–(CH_3)OH–Cu. It is also possible that the CH_3 radical reacts with one of the copper atoms before migrating to the bridging oxygen atom; this pathway proceeds *via* an intermediate CH_3–Cu–OH–Cu species. However, the lowest energy pathway calculated proceeds *via* reaction between the CH_3 radical and framework oxygen atoms. This results in formation of a zeolite grafted methoxy group (CH_3–O_{FW}) and reduced copper cluster, Cu^{I}–O–Cu^{I}. The production of methanol from this state is predicted to be highly unlikely owing to the need to spontaneously reform the CH_3 radical.[138] It should be noted that alternative mechanistic intermediates have been proposed previously. Prior reports utilised DFT calculations to predict formation of both Cu–OH–Cu and Cu–OCH_3–Cu species as stable intermediates upon hydrogen atom abstraction, resulting in an exothermic methane activation step as opposed to an endothermic step associated with Cu–(CH_3)OH–Cu formation.[132, 149] Introduction of water vapour then allows desorption of the methoxy intermediate as methanol.

The mechanism of action for methanol production for the trinuclear $[Cu_3(\mu O)_3]^{2+}$ core is predicted to occur in a similar fashion to the binuclear equivalent. Although formally identified as a mixed Cu^{III}/Cu^{II} species owing to the formal O^{-II} charge of the bridging oxygen atoms, DFT,

Bader charge and spin-polarized charge density calculations suggest that the trinuclear species is more aptly described as a radical species, similar to that seen for the binuclear equivalents.[137, 138] Therefore this species is proposed to exist as a mixed Cu^{II}/Cu^{I} system possessing radical anionic oxygen ligands in resonance with the formally charged species and one other form (Figure 11).

The initial step of methane partial oxidation over $[Cu_3(\mu\text{-}O_3)]^{2+}$ remains to be H-atom abstraction, however, unlike the binuclear mechanism, direct methanol formation (rebound mechanism) is thermodynamically strongly favoured over the formation of grafted, framework methoxy groups (CH_3–O_{FW}) and copper bound methyl species (CH_3–Cu–OH–Cu). The most-energetically favoured pathway in this system, however, is the combination of the CH_3 radical with another μ-oxo bridge associated with the cluster. From this point, adsorbed methanol can be formed by intermolecular proton transfer (Figure 12).[138]

Methane partial oxidation over mononuclear copper sites, $[CuOH]^+$, has also been predicted by DFT calculations to occur *via* a radical hydrogen atom abstraction pathway.[142] Initially in this pathway, a hydrogen atom is abstracted from methane to form a hydrated copper species and a CH_3 radical. The formed CH_3 radical may then directly insert into $[Cu–OH_2]^+$ to form a bound methanol molecule, although the calculated activation barrier to this transformation renders it unlikely. Formation of $[CH_3–Cu–OH_2]^+$, however, is facile. Experimentally, NIR spectroscopic analysis supports the latter pathway, providing evidence for the existence of a $[CH_3–Cu–OH_2]^+$ or $[CH_3–Cu–OH]^+$ intermediate.[150]

As the methanol produced is strongly adsorbed in all cases, co-adsorption of water is required to either hydrolyse the methoxy intermediate or desorb the formed methanol. It is not

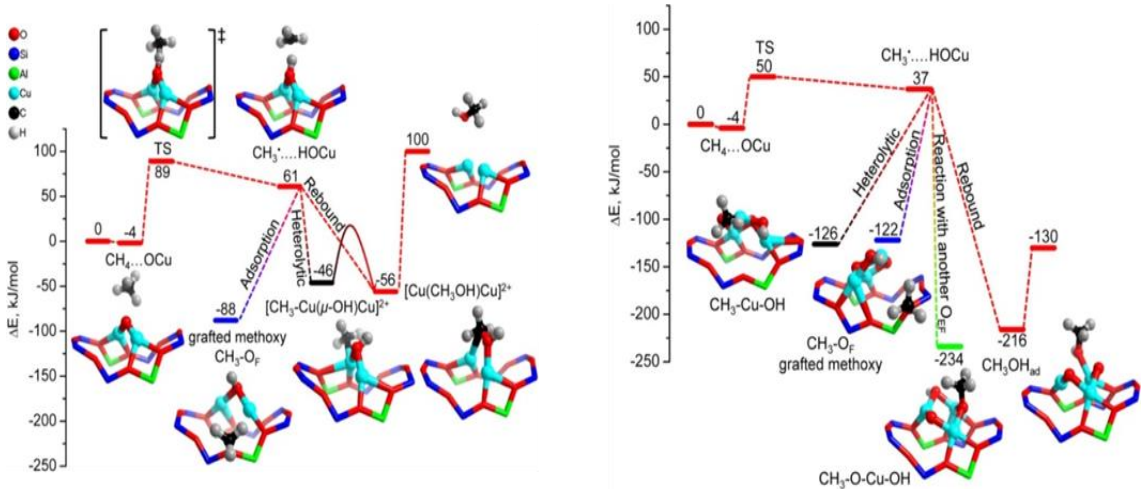

Figure 12: Reaction pathways for methane oxidation to methanol, and alternative CH_3 recombination routes over binuclear $[Cu_2(\mu O)]^{2+}$ (left) and trinuclear $[Cu_3(\mu O)_3]^{2+}$ (right) sites. Adapted with permission from ref 137. Copyright 2016 Elsevier

considered possible to thermally desorb methanol as increased reaction temperatures may result in further oxidation to CO_2. Following removal of products, it is possible to regenerate both binuclear and trinuclear copper species by reactivation in O_2, hence the reaction pathway may be described as a stepwise cycle as opposed to continuous. In the case of the trimeric active site, $[Cu_3(\mu\text{-}O_3)]^{2+}$, DFT calculations predict that a second C–H activation reaction may occur prior to regeneration of $[Cu_3(\mu\text{-}O_2)]^{2+}$ proceeding *via* an analogous pathway that is similar energetically to the first reaction.[151]

1.3.2.3 Alternatives to stepwise methanol production: Isothermal and direct catalytic conversion of methane to methanol over copper-modified zeolites

As previously stated, most systems that convert methane to methanol over copper-modified zeolites occur in three distinct steps that are performed over a variable temperature range. This represents a significant barrier to commercial exploitation as substantial temperature changes lower both the production efficiency (time is wasted waiting for the reactor to heat or cool) and thermal efficiency (heat is wasted repeatedly heating and cooling the reactor) of the process, hence resulting in reduced profitability.[152] Several recent reports, however, have shown the ability to run this reaction in an isothermal regime using O_2 or NO as an oxidant at 473 K and 423 K, respectively. [152, 153] Within this mode of operation, both activation and methane exposure steps are run at the same temperature. It is found in the case of isothermal activation with O_2 that methanol yield depends greatly on methane inlet pressure; increasing the inlet pressure from 50 mbar to 37 bar resulted in an increase of methanol yield per gram of catalyst of approximately two orders of magnitude (0.3 μmol g^{-1} and 56.2 μmol g^{-1} respectively). The dependence of methanol yield on methane partial pressure indicates that the active sites present are non-uniform in nature.[152] This may be either due to the presence of additional active species (e.g. higher nuclearity clusters, as suggested by the authors),[152] and/or potentially in the extraframework distribution of the clusters present (such as at channel intersections). It is also feasible that the specific distribution of framework aluminium sites can alter the active site potency as observed for Zn^{2+} sites in ZSM-5.[154]

The overarching objective of methane partial oxidation research, however, is to provide a system in which methanol can be produced in a catalytic fashion under continuous flow conditions using O_2 as an oxidant. At the time of writing, literature surrounding methanol production over copper-modified zeolites within a catalytic regime is relatively sparse, yet promising none the less. A recent contribution reports testing of various copper-modified zeolite and silica frameworks for the production of methanol from methane using a feed gas mixture of $CH_4/O_2/H_2O$ at moderate temperatures (483–498 K).[145] Methanol production values of

approximately 0.30–3.12 $\mu mol_{MeOH}\ g_{cat}^{-1}\ h^{-1}$ were observed over different frameworks and are suggested to be the result of various topologies better stabilising transition states and active sites. Isotopic pulsing by the introduction of $^{13}CH_4$ into the feed gas resulted in detection of a pulse of ^{13}C enriched methanol ($^{13}CH_3OH$) within the mass spectrum; similarly, isotopically enriched $^{13}CO_2$ was observed as a side product during a pulse. While a very valuable contribution to the field, major limitations of the catalytic system are apparent by the fact that approximately 300 hours of time on stream (TOS) were required to generate a cumulative 1.4 $mol_{MeOH}\ mol_{Cu}^{-1}$. Furthermore, the high selectivities reported for methanol formation are due to the limited concentration on oxygen in the feed (25 ppm), which clearly limited the maximum possible yield of methanol in order to prevent over-oxidation to carbon oxides.

1.3.2.4 Effect of framework topology and composition on methane partial oxidation over copper-modified zeolites

The varying topologies and compositions of copper-modified zeolites are thought to have a large effect on not only their ability to produce methanol, but also the nature of the active sites responsible. As a general observation, frameworks containing a higher Si/Al ratio in which the Al atoms are more dispersed are more likely to support monomeric active sites, whereas those with a lower Si/Al ratio are likely to have several Al atoms within close proximity that are able to stabilise multinuclear copper clusters.[155] Thus far, ZSM–5 and MOR frameworks have been studied most intensively, although many small pore frameworks, such as SSZ–13, have recently been subject to intensified investigation.

Although not as efficient as other copper-modified zeolites in terms of methanol production, Cu/ZSM–5 has been used to great extent to help characterise the active sites involved in methane partial oxidation, their formation and the reaction mechanism. Cu/ZSM–5 is suggested to host various active sites depending upon the Cu loading and Al distribution with the framework which can have a major effect on methanol production.[131] The major active site within Cu/ZSM–5 is suggested to be the bent mono(μ-oxo)dicopper species (Figure 9C), characterised by the UV-Vis-NIR band at 22700 cm^{-1}.[89] However, the Cu species within the channel and at channel intersections reside in different local environments, and hence have differing reactivity towards methane partial oxidation.[131]

Whilst ZSM–5 was the first zeolite framework to be investigated for dMtM, the vast majority of the research regarding methane partial oxidation over copper-modified zeolites has been performed with regard to Cu/MOR as it is typically observed to produce a higher methanol yield.[125] At the 8 MR windows of the side pockets, Cu/MOR has been suggested to possess both

binuclear and trinuclear clusters capable of performing methane partial oxidation.[125, 137] Recent spectroscopic observations[156] and DFT simulations[151] have further suggested that Cu/MOR possesses two mono(μ-oxo)dicopper species (Figure 9C) predicted to be distinct with respect to their siting within the 8 MR side pocket.[151] Interestingly, these two different sites demonstrate substantial reactivity differences despite very similar geometric and electronic structures. It was further noted that only one of the two active sites is stable above 603 K.[156] Very recently it has been reported that the two species observed are the result of confinement within the multidimensional structure of MOR.[157] Confinement of the $[Cu_2O]^{2+}$ dimer in the 8 MR side pocket of MOR gives rise to a lower activation barrier as a result of stabilisation of the transition state through van der Waals contacts with the framework. This effect of confinement, sometimes known as the nest effect,[158] is substantially less well known than the other shape selective effects imparted by zeolite micropores. Interestingly, confinement in the 8 MR side pockets of MOR has been shown to give rise to a remarkable increase in reaction rate, and therefore selectivity, in the carbonylation of carbon monoxide to form methyl acetate.[103, 159] Additionally, the role of confinement within zeolites in a number of other catalytic systems has been recognised by the Iglesia group.[101, 160, 161] The ability of confinement to selectively enhance the rate of one reaction over another through transition state stabilisation is an enticing mechanism by which to "break" the themordynamic limitations on methane partial oxidation (or change the selectivity outcome of the partial oxidation of methane).

Owing to the amount of methanol extracted, it was previously determined that approximately 5% of Cu atoms were active in the conversion of methane to methanol over Cu/ZSM–5.[132] However, X-ray adsorption near edge structure (XANES) studies have demonstrated that over Cu/MOR approximately 60% of Cu^{II} species change structure upon methane introduction and are reduced to Cu^{I}.[162, 163] In a later contribution, it has been shown that the fraction of copper species that undergo reduction correlates well to the amount of methanol produced.[164] It was also observed that multiple oxidation/reduction cycles were required to obtain a representative view of long-term performance of methane partial oxidation over Cu/MOR, as it is suggested that the copper species present equilibrate over many cycles.

Recent *operando* X-ray absorption spectroscopy (XAS) and high-energy-resolution fluorescence-detected (HERFD) XANES spectroscopy investigations into the active sites of Cu-exchanged MOR strongly suggest that the active species in the systems tested is a dicopper species.[165] This hypothesis is supported by two crucial pieces of evidence; first, a Cu–MOR material was tested in which approximately one methane molecule was activated for every two Cu ions within the material. Subsequently, the methanol productivity across a range of materials

and reaction procedures was observed to increase with a slope of 0.5 as the concentration of what is identified spectroscopically as the active Cu species increases. Within this contribution, the highest methanol yield to date over Cu-modified zeolites is reported at 170 $\mu mol_{MeOH}\ g_{cat}^{-1}$ using a Cu-exchanged mordenite with Si/Al = 7 and Cu/Al = 0.18.[165]

Recently, copper-modified small pore zeolites, such as SSZ–13, have gained substantial interest as potential materials to facilitate methane partial oxidation.[128, 150, 166] In particular, Cu/SSZ–13 has been reported to produce competitive quantities of methanol per copper atom to both previously spotlighted zeolites, Cu/ZSM–5 and Cu/MOR, at similar Si:Al ratios.[128, 145, 166] Much of the recent literature suggests that isolated copper ions, in the form of $[CuOH]^+$, are responsible for the transformation of methane to methanol over Cu/SSZ–13 (as mentioned in section 2.2.1) as opposed to the multinuclear clusters observed for larger-pore zeolites.[141, 142, 165]

Importantly, Cu/SSZ–13 has not only been shown to produce methanol in the standard stepwise process, but has also shown great potential in a continuous regime utilising both O_2[145] and N_2O[166] as oxidants. Maximum methane conversion and methanol production rates over Cu/SSZ–13 (H–form parent) and using N_2O as an oxidant were observed when employing a gas composition of 30% CH_4, 30% N_2O, 3% H_2O (balance He) at 573 K, resulting in production of 55 $\mu mol_{MeOH}\ g_{cat}^{-1}\ h^{-1}$. The greatest methanol selectivity, however, was observed at a lower temperature of 543 K and lower Cu loading, implying that at a higher temperature, selectivity is sacrificed for production rates.[166] When using O_2 as an oxidant and a feed gas mixture of $CH_4/O_2/H_2O$, the maximum yield recorded over several different frameworks was 3.12 $\mu mol_{MeOH}\ g_{cat}^{-1}\ h^{-1}$ as a result of catalysis over Cu/CHA.[145]

Given the potential realised for confinement to promote the partial oxidation of methane, we expect that additional progress in the field will be made by exploiting zeolites that have small pores, or more importantly, small channels and side pockets.[167] Interestingly, until recently, the highest reported methanol yield to date, 86.1 $\mu mol_{MeOH}\ g_{cat}^{-1}$, utilised zeolite omega (MAZ structure), which contains an intersecting 8 MR small pore network alongside a discrete 12 MR channel.[126] However, this has now been surpassed once again by MOR which notably contains an 8 MR side pocket.[165]

1.3.3 Other d-block metals in zeolites

Unlike iron and copper, the literature surrounding the partial oxidation of methane to methanol over Co–modified zeolites is relatively sparse. There are two major products of methane partial oxidation over Co–modified zeolites, methanol and formaldehyde, and their

relative selectivities depend upon the active Co species. Cobalt oxide species, Co_3O_4 and CoO, throughout the zeolite are typically selective towards methanol production whilst Co^{2+} cations within the zeolite channels show a general selectivity towards formaldehyde production.[168] As a result, the effect of modification method on methanol selectivity over Co/ZSM–5 may be dramatic; it was found that Co/ZSM–5 prepared by incipient wetness impregnation (IWI) typically contains more surface Co oxide species and is more selective towards methanol, whilst Co/ZSM–5 prepared *via* ion exchange (IE) contains more Co^{2+} species within the zeolite channel system and is more selective towards formaldehyde.[168]

It has been reported that increasing the surface area of Co/ZSM–5 by the introduction of mesoporosity *via* alkaline treatment can improve methanol selectivity by increasing the number of potential Co oxide sites.[169, 170] A contribution from Beznis *et al*. shows that a linear correlation between the zeolite surface area and number of Co oxide species can be established and (owing to the selectivity for methanol of Co oxides) a linear correlation between zeolite surface area and methanol selectivity also results.[169] The authors also suggested that increased methanol selectivity could be attributed to the reduced ability to form Co^{2+} sites as a result of extra-framework alumina blocking the channel system. Hence, a subsequent acid treatment to remove extra-framework alumina was applied to the previously alkali treated zeolites before Co introduction. As expected, the relative amounts of Co^{2+} species within the zeolite channels increased and methanol selectivity decreased.[169]

Partial oxidation of methane conducted in a small-scale batch reactor at 150 °C under an atmosphere of methane (0.75 bar) and 5% oxygen in nitrogen (2 bar), respectively demonstrated the effect of exposure time and oxygen presence on the direct conversion of methane to methanol over Co-impregnated mesoporous H–ZSM–5.[171] It was found that the optimum extracted methanol yield (79%) was obtained at a reaction time of 60 minutes with longer reaction times resulting in a substantial decrease in yield which the authors suggest may be resultant from complete oxidation of methane to CO_2 and water. It is further suggested that the presence of molecular oxygen as an oxidant causes an increased reaction rate when compared to the base reaction in which oxygen (O^{2-}) from cobalt oxides or the ZSM-5 surface acts as the oxidising agent.

In all reports, a preliminary calcination step is required to introduce active oxygen species into Co modified zeolite materials (similar to Cu, *vide supra*) before being exposed to methane at 150 °C. Additionally, it is worth noting that the reaction products remain strongly

adsorbed to the catalyst and must be extracted into the liquid phase resulting in a process that, at present, has not been demonstrated to run in a continuous regime.

DFT studies of the direct oxidation of methane to methanol over Co/ZSM–5 in the presence of N_2O have determined a reaction mechanism similar to that observed for α–Fe species.[172] Co/ZSM–5 is predicted to efficiently decompose N_2O resulting in an α–O species which is highly reactive towards radical hydrogen abstraction from methane. The mechanism follows the same pathway as that for Fe (*vide supra*) but with notably lower activation barriers for each step. As with Fe, the presence of water substantially decreases the energy barrier to the methanol formation step.

Ni–modified ZSM–5 has been reported to be active for the direct production of methanol from methane with an anchored mono(μ-oxo)dinickel, $[Ni_2(\mu O)]^{2+}$, motif reported as the active site, analogous to that observed for Cu-ZSM-5.[173] The modified zeolite must be thermally activated in O_2 before methane introduction, but produces methanol as the major product at 150 °C, after aqueous extraction into the liquid phase from the catalyst. DFT studies, however, suggest that this active site motif is not plausible, as no activity in methane to methanol conversion was able to be simulated under reasonable conditions.[174] This conclusion corroborates with a recent contribution that utilises a combination of density functional theory with Coulomb interaction potential calculations to simulate an array of plausible Ni-oxo motifs in the periodic MFI framework structure, namely $[NiO]^{2+}$, $[Ni_2(\mu O)]^{2+}$, $[Ni_2(\mu O)_2]^{2+}$, and $[Ni_3(\mu O)_3]^{2+}$ (Figure 13).[175] It is suggested that the reactivity of the $[Ni_2(\mu O)]^{2+}$ centre is insufficient to be the active site owing to its respective energy of activation for hydrogen atom abstraction from methane being both considerably higher than that observed experimentally and that calculated for the other motifs examined.[173, 175] Conversely, the energy of activation for hydrogen atom abstraction calculated for the $[Ni_2(\mu O)_2]^{2+}$, and $[Ni_3(\mu O)_3]^{2+}$ centres is in good agreement with that observed experimentally. Furthermore, the authors suggest that, based on the calculated values for energy of methanol desorption for both active sites, the energetics are within the range that may enable spontaneous, solvent-free and online product extraction.[175] As alluded to in the contribution, the use of experimental resonance Raman spectroscopy (rR) (as used to discern the active species in Cu-modified zeolites) could prove invaluable in assigning the true nature of the active Ni species.

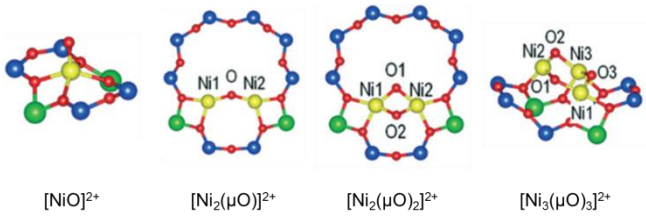

Figure 13: Optimised ground state structures of $[NiO]^{2+}$, $[Ni_2(\mu O)]^{2+}$, $[Ni_2(\mu O)_2]^{2+}$, and $[Ni_3(\mu O)_3]^{2+}$ in MFI. Adapted with permission from reference 173. Copyright 2018 Royal Society of Chemistry

Mn/ZSM–5 has been shown to be active in the decomposition of N_2O resulting in the suggested formation of an α–O species.[176] Similar to Fe/ZSM–5, this site cannot be generated directly using O_2. At the time of writing, no activation of methane (or any other alkane) over this species has been reported, however the suggested similarity to the α–O in Fe/ZSM–5 could prove promising in methane partial oxidation.

1.3.4 Zn-modified zeolites

In 2004, Kazansky *et al.* demonstrated heterolytic CH_4 bond dissociation over Zn exchanged zeolites.[177] Since then, a number of groups have gone on to show that methane can be partially oxidised in the presence of dioxygen over zinc modified zeolites. A major advantage of these zinc-based systems is the ability to form an active species without an initial high temperature oxidation step, which is required for iron- and copper-modified zeolites. Hence, these materials are of great interest industrially as an isothermal process could be developed.

Framework bound Zn^{2+} cations are believed to be responsible for C–H activation but the mechanism involved is still highly debated. The zinc species introduced in to the zeolite is dependent on a number of factors: the zeolite topology, Si/Al ratio, method of zinc introduction and also any further thermal treatment carried out.[178]

Two key ways of introducing zinc into zeolites are incipient wetness impregnation and ion exchange using a decomposable zinc salt. These methods can introduce a variety of zinc species into the zeolite: isolated Zn^{2+} ions which sit at cation exchange sites within the zeolite, $[Zn–O–Zn]^{2+}$ clusters formed through the condensation of partially hydrolysed $[Zn–OH]^{+}$ extraframework ions and ZnO clusters, though ion exchange methods result in predominantly the introduction of Zn^{2+} cations.[178, 179] The presence of multiple zinc species makes it difficult to determine which exact species is responsible for C–H activation and subsequently a variety of different mechanisms have been proposed.

Chemical vapour deposition (CVD) methods can also be used to introduce zinc into zeolites. Vapour deposition with Zn^0 powder involves the exchange of Brønsted acid sites (BAS) for Zn^{2+} ions *via* a redox reaction evolving H_2.[180] Under certain zinc vapour deposition conditions,

additional zinc species have been detected. A small fraction of paramagnetic isolated Zn^{+} ions have also been detected by EPR spectroscopy upon contact of metallic zinc vapours with H–ZSM–5 but these have not been reported to react with methane.[181] CVD of dimethyl zinc leads to surface grafted $[Zn–CH_3]^{+}$ species which can be converted to Zn^{2+} ions through reaction with H_2 or oxidised to ZnO clusters.[178]

Decamethyldizincocene, $Zn_2(\eta^5\text{-}C_5Me_5)_2$, an organometallic compound of Zn^{I} formally derived from the dimetallic $[Zn–Zn]^{2+}$ unit, was the first instance of the covalent zinc-zinc bond successfully synthesised in 2004.[182] Since this discovery, several studies have been carried out to understand the nature of the Zn-Zn bond.[183, 184] In 2015, Kuroda *et al.* were able to stabilise a $[Zn_2]^{2+}$ species in the pores of ZSM-5 through introduction of zinc by CVD where an excess of metallic zinc was present.[185] However, the reactivity of this dimeric species has not yet been explored in the confines of a zeolite micropore.

The levels of zinc exchange can vary with the method of zinc introduction. Through collection of molecular H_2 produced upon zinc vapour deposition, Kazansky *et al.* showed that full exchange of BAS occurs.[177] Substitution through impregnation or ion exchange methods normally results in lower exchange levels.[178] This is particularly evident in high silica zeolites where there is a low framework charge and potentially a high degree of separation between framework Al tetrahedra. Reduced zinc loading is often ascribed to the difficulty of stabilising the formal 2+ charge associated with the Zn^{2+} ions in high silica zeolites.[186, 179]

1.3.4.1 Mechanism of C–H activation in zinc-exchanged zeolites

Understanding the mechanism of CH_4 activation in zinc-exchanged zeolites is essential for the progress of the fundamental and applied chemistry of these materials. Zinc-exchanged into the MFI micropore network, Zn/ZSM–5, has been the most studied system for C–H activation. However, the mechanism of activation is still under debate. In 2004, Kazansky *et al.* were the first to report that heterolytic CH_4 bond dissociation can occur at room temperature on isolated Zn^{2+} sites in Zn/ZSM–5 as determined through diffuse reflectance infrared Fourier transform spectroscopy (DRIFTs) studies, having observed the formation of a zinc methyl species and a framework BAS as illustrated in Scheme 5.[177]

Solid-state NMR spectroscopy has also been a key technique in confirming the formation of the $Zn–CH_3$ species. Kolyagin *et al.* were the first to observe a signal at $\delta = -20$ ppm from the reaction of CH_4 within Zn/ZSM-5 at ambient temperature.[187] The upfield chemical shift is characteristic of methyl groups in different organozinc compounds implying the presence of a surface zinc methyl.[188] The peak position was found to be independent of methane loading suggesting the

presence of a well-defined surface species. The intensity of the line increased considerably in a $^{1}H–^{13}C$ CP/MAS NMR spectrum in comparison to a direct excitation spectrum. This indicates the signal corresponds to a rigid surface species strongly attached to the surface. This spectroscopic evidence presented by Kolyagin *et al.* strongly suggests that methane activation at ambient temperature takes place by dissociative adsorption over Zn sites resulting in the formation of a $Zn–CH_3$ species and a framework BAS. DRIFTS and NMR spectroscopy have shown that upon exposure to methane, an initial complex is formed in which a methane molecule is adsorbed onto an isolated zinc cation.[177, 189] At room temperature or following thermal treatment, a C–H bond of this intermediate is heterolytically cleaved between the zinc centre and a framework oxygen atom. The Zn^{2+} species acts as a Lewis acid with the CH_4 σ(C–H) orbital donating electron density into the Zn–4s orbital, while the framework oxygen atom acts as a Lewis base, leading to C–H bond cleavage.[154] This mononuclear Zn^{2+} species is also reported to be active for H_2 dissociation as shown through IR spectroscopic studies.[154]

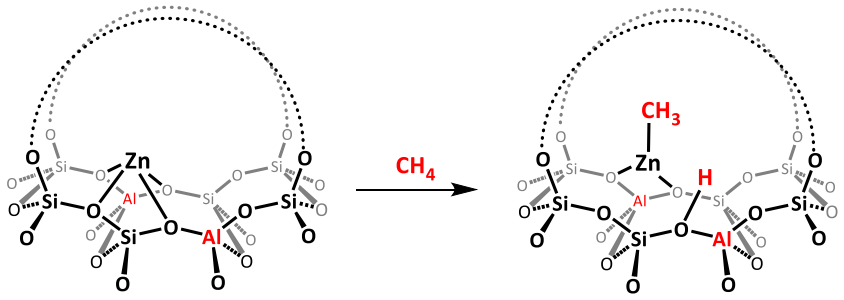

Scheme 5: C–H activation step for dissociative adsorption of methane over Zn^{2+} forming a $Zn–CH_3$ and new BAS.

However, other mechanistic theories for the activation of methane have been presented involving different active sites. A ^{13}C NMR signal at δ = 58 ppm corresponding to a zinc methoxy species ($ZnOCH_3$) led Xu *et al.* to suggest homolytic C–H bond cleavage is possible over a $[Zn–O–Zn]^{2+}$ dimer.[190] This Zn/ZSM–5 sample was interestingly prepared through Zn vapour deposition which should lead to the presence of predominantly Zn^{2+} ions only. The suggested mechanism involved the formation of a methyl radical ($\cdot CH_3$), which can then interact with the zinc cluster to produce the zinc methoxy species. This zinc methoxy species was reportedly formed in a 3:1 ratio to the zinc methyl. As both species were present, Xu *et al.* suggests that both heterolytic cleavage over Zn^{2+} sites forming the zinc methyl species alongside the homolytic cleavage forming the zinc methoxy species on $[Zn–O–Zn]^{2+}$ dimer can occur, with the zinc methoxy species being favoured according to the 3:1 ratio stated above.[190]

The concept of both activation mechanisms occurring simultaneously is supported by Wang *et al.* who also observed the presence of oxygenated species (zinc methoxy and zinc formate groups) in ^{13}C NMR spectra whilst predominately observing the zinc methyl species in ZSM–5.[191] However, in this case, the zinc was introduced through incipient wetness impregnation, which can lead to a variety of zinc species within the zeolite.[191] The signals from the zinc methoxy and zinc formate groups disappeared upon further heating of the sample implying additional reactions occurring at higher temperatures.

On the other hand, Stepanov *et al.* have provided strong evidence that the appearance of zinc methoxy and formate species are in fact not due to the radical-based homolytic cleavage suggested above, but actually due to the presence of adventitious oxygen, as shown in Scheme 6.[180] When Zn/ZSM-5 prepared by vapour deposition was exposed to labelled methane ($^{13}CH_4$) at room temperature, two signals at δ = −4 and −6 ppm, corresponding to physisorbed methane, were observed in the ^{13}C NMR spectrum.[180] The two signals correspond to two Zn^{2+} sites of different Lewis acidity caused by a non-homogeneous aluminium distribution.[177] Upon heating to 250 °C, the zinc methyl signal is observed as expected, while no zinc methoxy or zinc formate species are formed. Signals corresponding to oxygenated species only appeared through the addition of molecular oxygen after methane exposure. The intensity of these NMR signals increased upon heating and the presence of NMR signals from further oxygenated species such as carbonates, ethers and aldehydes were also subsequently detected. This study therefore supports heterolytic cleavage as the principle method of CH_4 activation by Zn^{2+} ions contrary to the findings of Xu *et al*.

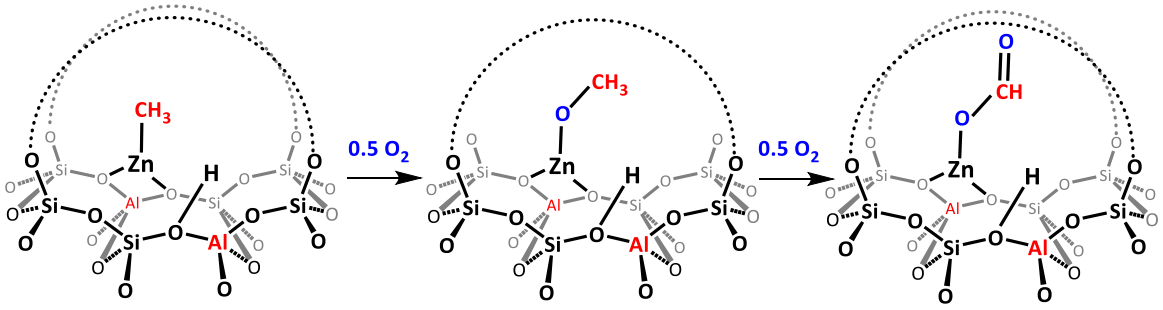

Scheme 6: Formation of zinc methoxy and zinc formate species upon addition of O_2 to [Zn^{II}-CH_3] species.

Very recently, Kuroda *et al.* have reported room-temperature activation of methane over a Zn^{II}-oxyl species in ZSM-5.[192] The Zn^{II}-oxyl species is formed by irradiation of a Zn^{II}-H species using UV light under an O_2 atmosphere.[193] The photoreaction results in the formation of

Zn^{II}–($O_3^{\bullet}$) which liberates O_2 resulting in a Zn^{II}–$O_t^{\bullet}$ species. This radical Zn^{II}-$O^{\bullet}$ species is able to oxidise methane to methanol with a very high selectivity of 94% and a methanol yield of 29 µmol g^{-1} at room temperature,[192] remarkable for zinc species at room temperature.

It has been determined that as few as 5-15% of ion-exchanged sites are active for CH_4 heterolysis in MFI zeolites.[194] Hence, understanding the role of Al distribution in zeolites is key to maximising metal-ion exchange levels. DFT studies have suggested this reactivity is dependent on a specific Al array within the zeolite.[195] A recent theoretical paper by Kuroda examines the spontaneous heterolytic cleavage of H_2 on Zn^{2+}/MFI to investigate this dependence.[2] It was found that heterolysis was more favourable on a circumferentially-arrayed Al–Al site compared with a straight channel axis in MFI as shown in Figure 14. This is due to the formation of a favourably aligned Lewis base–Zn^{2+} pair resulting in a suitable position to activate H_2, even at room temperature. Therefore, the Al arrangement alongside the curvature created by the zeolite pores may be seen to have an impact on the activity of metal ions within zeolite frameworks.

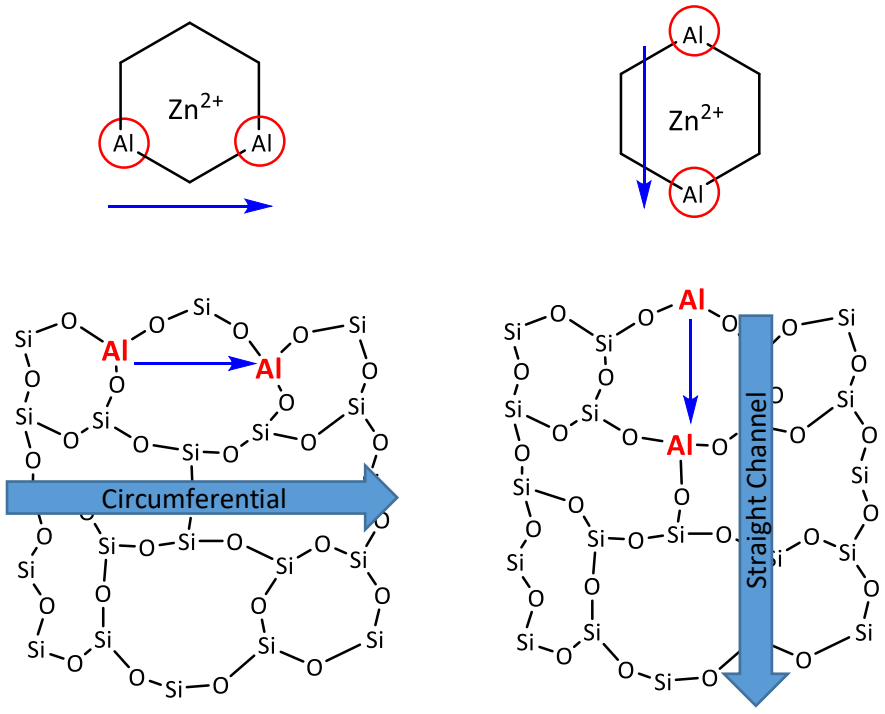

Figure 14: Representation of Al array direction within a zeolite framework: circumferential and straight channel directions.[2]

1.3.4.2 Zinc oxide clusters in zeolites

Zinc oxide clusters in zeolites have been shown to be catalytically active for propane aromatisation.[196, 197] Through *in situ* NMR spectroscopy studies, it has been observed that ZnO aggregates, alongside residual BAS, are active for propane aromatisation in a zinc impregnated

BEA sample. This is proposed to occur *via* dissociative adsorption of propane on the ZnO species within the pores of the zeolite *via* cleavage of a C–H bond.[196] ZnO clusters have been shown to promote ethane activation, but are unable to catalyse the aromatisation of ethane that takes place primarily over Lewis acidic Zn^{2+} or $[Zn–O–Zn]^{2+}$ sites.[198] However, systemic studies of zinc oxide and Zn^{2+} in Beta show that zinc oxide is unable to activate methane to form zinc methyl species.

Zinc sites are able to affect H/D exchange of CH_4/CD_4 in Zn/H–BEA with differing reactivity depending on the nature of the active site. Isolated Zn^{2+} cations show pronounced H/D exchange but ZnO clusters are also found to be active, with rate constants of 65×10^{-5} g mol^{-1} min^{-1} and 1.2×10^{-5} g mol^{-1} min^{-1}, respectively.[197] This reactivity, however, is limited to H/D exchange with no reaction observed for the alkylation of benzene with methane over these ZnO clusters. On the other hand, Zn^{2+} cations in BEA were able to activate methane to form the zinc methyl species which showed further reactivity with benzene to form substituted aromatics.[197] Similarly, Kazansky *et al.* have found that ZnO clusters in Zn/Na–Y are unable to perform heterolytic dissociative adsorption of methane.[199] The clusters in Zn/Na–Y can be reduced to form isolated Zn^{2+}, but this new site is also inactive for C-H cleavage of methane further indicating that the framework plays an important role in mediating the reaction.[199] Small perturbations of adsorbed methane have been observed on Zn/Y, where zinc has been introduced by zinc vapour deposition and methane exposure occurred at room temperature, but to date no methane activation has been observed.[200]

1.3.4.3 The role of Brønsted acid sites in C–H activation

Stepanov *et al.* have reported that residual BAS after zinc exchange play an interesting role in C–H activation. If BAS are present after zinc exchange on H-ZSM–5, CH_4 activation has been shown to be reversible under reduced pressure.[180] On the other hand, in a fully zinc-exchanged ZSM-5 the $Zn–CH_3$ fragments remain intact after exposure to vacuum.[201]

Conversely, Wu *et al.* found that no reformation of methane with evacuation on a bifunctional Zn/H–ZSM–5 zeolite prepared by impregnation methods.[202] This demonstrates that different methods of zinc introduction can have different reactivity or distribution of zinc species. Wu's sample prepared by impregnation had a variety of zinc species present whereas Stepanov's sample, which showed reversible reactivity, is proposed to have mainly Zn^{2+} present from zinc vapour deposition.

The synergic effect between BAS and zinc Lewis acid sites also supposedly impacts the temperature required for C–H activation. It has been observed that fully zinc-exchanged zeolites

require temperatures of 250 °C for activation to take place whereas partially exchanged systems are able to form zinc methyl species at room temperature indicating mechanistic differences caused by the presence of BAS.[180]

Deng *et al.* have carried out high field solid state NMR spectroscopy studies which show that a synergic effect between BAS and zinc species can promote H/D exchange. In this study, the spatial proximity of these sites is crucial, requiring a BAS–Zn distance <3.5 Å.[203] The enhanced activity of these zinc sites, according to Deng, is due to an increase in Brønsted acidity through the spatial proximity between the Zn^{2+} ions and the Brønsted acidic protons of the zeolite. The local electron density on the Zn^{2+} cation is increased (decreasing the electron density on the oxygen atoms around the BAS) leading to a weakening of the interaction between bridging oxygen atoms and acidic protons, overall increasing the acidity of the Zn-modified zeolites. However, a very recent paper by Stepanov *et al.* uses solid-state NMR and FTIR techniques to probe the strength of the Brønsted acidic protons with and without the presence of zinc in ZSM-5.[204] They find no evidence for BAS with enhanced acid strength in the presence of Zn^{2+} compared with the pure acid form.

1.3.4.4 Reactivity of methane with small molecules on zinc-modified zeolites

As mentioned in Section 1.3.4.1, the formation of zinc methoxy and zinc formate groups are observed when the zinc methyl species are exposed to dioxygen. Reactivity has been observed at ambient temperature, whilst additional heating of the sample results in the formation of higher oxygenates such as acetic acid.[180, 191] Further reactivity of zinc methyl species with molecules such as CO, CO_2 and H_2O has been explored by a number of groups and the chemical reactivity has been found to be very similar to that of organozinc compounds.[180, 191, 202, 205]

In situ NMR spectroscopy studies by Deng *et al.* investigated the reactivity of the zinc methyl groups on Zn/H–ZSM–5.[191] Proton donors such as water, methanol and HCl readily convert the zinc methyl species to methane at room temperature. Deng *et al.* found addition of oxygen to the methyl species results in formation of zinc methoxy and zinc formate groups at 300 °C, in agreement with the findings of Stepanov.[180, 191] However, small substoichiometric amounts of methanol are also observed in the NMR spectrum. The addition of CO and CO_2 to methane over zinc-exchanged zeolites has been studied in the context of the formation of acetic acid, demonstrated in Scheme 7. Acetic acid can be formed through two different pathways: CO reacting with surface zinc methoxy species or CO_2 reacting with zinc methyls.[206] The BAS play a

key role in the formation of acetic acid *via* proton transfer to the surface acetate species formed upon addition of CO_2.[202]

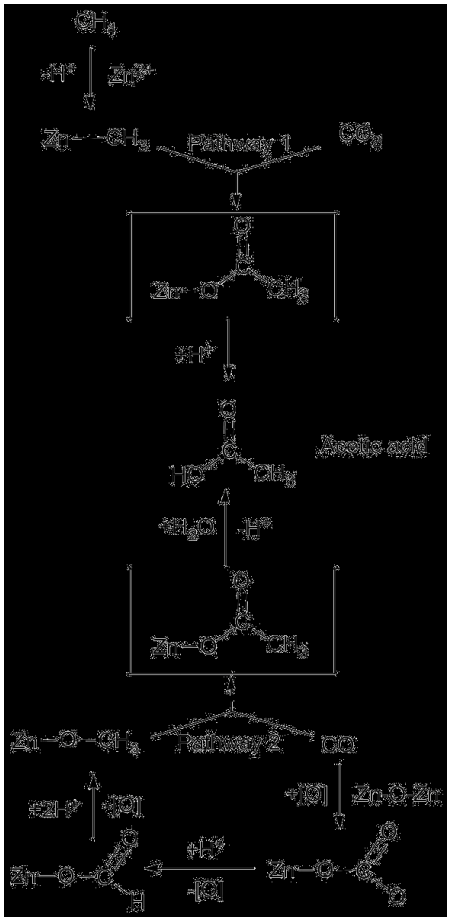

Scheme 7: Proposed reaction pathways for the formation of acetic acid from methane and carbon monoxide on Zn/ZSM-5. [190]

1.3.4.5 Differing reactivity between zinc and magnesium

Both Zn^{2+} and Mg^{2+} have similar ionic radii and charge,[207] hence, similar reactivity towards the C–H bond of methane could be expected. However it has been shown that magnesium exchanged ZSM–5 does not form $[Mg\text{-}CH_3]^+$ species under identical conditions to those used for zinc exchanged ZSM–5.[207] Furthermore, H_2 is also not readily chemisorbed on Mg/ZSM-5.[194] Kuroda *et al.* investigated these reactivity differences through IR spectroscopy studies, involving the adsorption of CH_4 and CO on Mg/ZSM-5 and Zn/ZSM-5, supported with DFT calculations.[207] Stronger perturbation of the adsorbed CH_4 molecule at room temperature was observed through interaction with Zn^{2+} compared with Mg^{2+}. Upon heating, the presence of a zinc methyl group was detected, but no change in the IR spectrum of Mg/ZSM-5 was observed. As the electrostatic force of Zn^{2+} is almost identical to that of Mg^{2+}, the authors suggest that the higher activation of the C–H bond observed for Zn^{2+} is due to an electron-transfer interaction

rather than based on electrostatics. Similarly, CO was used as a probe molecule and adsorption studies were undertaken. These studies determined that for Mg^{2+} (and group 2 ions in general), CO adsorption is predominantly governed by electrostatic interaction. However, zinc behaves as an electron acceptor for the CO molecule (as well as for the CH_4 molecule) and this electron–accepting nature is the key electronic feature for CH_4 heterolytic activation. The ability of Zn^{2+} to dissociate methane where Mg^{2+} is unable, can be ascribed to the greater electron accepting power of the monomeric Zn^{2+}, as supported by DFT calculations.[207] These conclusions are supported by Kazansky who undertook a study of methane adsorption on cationic forms of zeolties MOR, ZSM-5 and Y, in which the perturbation and polarization of the methane molecules were probed by IR spectroscopy.[208]

Overall, substantial research into the methane activation mechanism over Zn/ZSM-5 has been carried out using a variety of zinc introduction methods. Although no catalytic dMtM processes over Zn/zeolites have been reported, stoichiometric reactions of the $[Zn^{II}\text{-}CH_3]$ with small molecules such as CO and CO_2 resulting in acetic acid have been explored. The role of the BAS and Al distribution have been found to influence methane activation with lower activation temperatures required in the presence of BAS and certain Al configurations leading to more favourable heterolysis. However, the role of the zeolite framework on dMtM over Zn/Zeolites has yet to be explored and further fundamental understanding is required before development of a catalytic process will be possible.

1.4 Outlook and Areas for Future Research

The development of zeolite-based, dMtM catalysts that can compete with the existing two step syngas pathway, remains a major challenge though significant progress has been made in the last 20 years. Competing with the established syngas technology, which has been honed for decades through a combination of chemistry and chemical engineering, will require further substantial effort from industrial and academic communities. It should be stressed that the technology may not have to compete with the syngas route under certain scenarios; in the monetisation of associated natural gas or other waste methane sources, where it is simply too impractical and/or costly to build a syngas plant and a methanol plant.

At the present time, the single, major improvement that is required to help push dMtM forward as a technology is in preventing unwanted over oxidation to carbon oxides. For MDA reactions, the major challenge remains rapid catalyst deactivation due to the formation of carbonaceous deposits. These are major challenges as avoiding thermodynamic fate is no mean feat. However, zeolites are known to give reaction products that differ from thermodynamic predictions (e.g. toluene alkylation with methanol to p-xylene over ZSM-5)[209] and it stands that zeolites may be able to confer the desired reaction selectivities. Conceptually, this could be achieved with metal exchanged zeolite catalysts by exploiting the strategies below which either complement or build on some of the strategies recently suggested by others.[36, 140, 210, 211]

Confinement Zeolites are well known to be able to impart reaction selectivities that differ from those predicted by thermodynamics alone. In the case of dMtM it is unlikely that *product selectivity* will contribute to improving the selectivity of the reaction due to the similar size of the reactant and the product. On the other hand, exploiting confinement effects which can lower the transition state barrier to C–H activation would enable better activation kinetics and lower process operation temperature. To this end, confinement has very recently been experimentally shown to accelerate methane activation over copper oxide clusters in the MOR framework [212] whilst theoretical studies support this approach for further study.[111] Additionally, it is necessary for confinement effects not to accelerate the activation of the methanol product which could be mitigated by further strategies outlined below. Confinement effects have not been shown to affect the MDA reaction but, the 10 MR channels of ZSM-5 and MCM-22 have proved ideal for benzene product selectivity. Furthermore, the supercages of MCM-22 provide additional catalyst stability as higher levels of coke can be accommodated. Understanding and exploiting these framework effects further could lead to the formation of a highly active, stable Mo catalyst for MDA.

$1e^-$ vs $2e^-$ Processes The mechanism of methane oxidation to methanol by the vast majority of materials mentioned above operate *via* a radical based C–H bond activation process. For dMtM, these $1e^-$ processes are now well understood to result in low methanol selectivities due to the weaker C–H bond of methanol being kinetically more reactive and resulting in over oxidation. [211, 213] In the case of functionalisation by $2e^-$ processes, this need not be true. For example, where a sigma complex is formed prior to C–H bond cleavage (*e.g.* activation by Lewis acid and base or electrophilic activation by transition metals), the more electron rich C–H bond of methane favours coordination, and thus subsequent activation, over the relatively electron poor C–H bond of methanol. Therefore developing and exploring systems where methane complex formation precedes bond cleavage (such as methane activation by Lewis acid-base pairs over zinc exchanged ZSM–5) [189,214] should be a target for future endeavours. In the homogeneous Shilov system, which is capable of converting methane to methanol under remarkably mild conditions (120 °C, in water), the C–O bond forming reaction occurs by nucleophilic attack (a $2e^-$ process) of water at the carbon atom of a Pt(IV)–CH_3 group.[39] While thermodynamics exclude water as a viable oxidant, it highlights alternative mechanisms for C–O bond formation and shows that activation and functionalisation could potentially be separated from a cycle involving dioxygen. This would be akin to the Wacker process, the industrially practised method of acetaldehyde production from ethylene and dioxygen. The process is catalysed by Pd and Cu chloride salts in an acidic, aqueous solution and the C–O bond is in fact formed from water, not dioxygen.[215]

Theoretical studies Theoretical studies are making substantial contributions to the field of methane activation, providing insight into kinetic, mechanistic and thermodynamic considerations[140, 211, 216, 217]. Additionally, accurate modelling of long-range electrostatic interactions and dispersion in zeolite catalysis is now recognised as key to determining accurate theoretical activation energies.[218] There is substantial scope for theoretical studies to explore $2e^-$ based methane activation and functionalisation processes over metal-exchanged zeolites, and also to explore how the framework can confer optimised confinement effects. In MDA, modelling the reaction mechanism to discover the exact involvement of carbonaceous deposits in the formation of benzene could be critical to catalyst development.

In summary, there remains much to be achieved in methane activation research, but it is likely that zeolites incorporating transition metals will play a prominent role in bringing this long standing challenge to fruition.

Chapter 1: References

1. S. Raynes, M. A. Shah and R. A. Taylor, *Dalton Trans.*, 2019, **48**, 10364-10384.
2. A. Oda, T. Ohkubo, T. Yumura, H. Kobayashi and Y. Kuroda, *Phys. Chem. Chem. Phys.*, 2017, **19**, 25105-25114.
3. BP Energy Outlook, https://www.bp.com/en/global/corporate/media/press-releases/energy-outlook-2018.html, (accessed 9th November, 2018).
4. K. Aasberg-Petersen, I. Dybkjær, C. V. Ovesen, N. C. Schjødt, J. Sehested and S. G. Thomsen, *J. Nat. Gas Sci. Eng.*, 2011, **3**, 423-459.
5. K. Aasberg-Petersen, J. H. Bak Hansen, T. S. Christensen, I. Dybkjaer, P. S. Christensen, C. Stub Nielsen, S. E. L. Winter Madsen and J. R. Rostrup-Nielsen, *Appl. Catal., A*, 2001, **221**, 379-387.
6. S. C. Reyes, J. H. Sinfelt and J. S. Feeley, *Ind. Eng. Chem. Res.*, 2003, **42**, 1588-1597.
7. R. Reimert, F. Marschner, H.-J. Renner, W. Boll, E. Supp, M. Brejc, W. Liebner and G. Schaub, in *Ullmann's Encyclopedia of Industrial Chemistry*, Wiley-VCH Verlag GmbH & Co. KGaA, 2011, DOI: doi:10.1002/14356007.o12_o01.
8. S. A. Bhat and J. Sadhukhan, *AIChE J.*, 2009, **55**, 408-422.
9. J. Ott, V. Gronemann, F. Pontzen, E. Fiedler, G. Grossmann, D. B. Kersebohm, G. Weiss and C. Witte, in *Ullmann's Encyclopedia of Industrial Chemistry*, 15th October 2012, DOI: 10.1002/14356007.a16_465.pub3.
10. W. A. Bone and R. V. Wheeler, *J. Chem. Soc., Trans.*, 1902, **81**, 535-549.
11. C. Elvidge, M. Zhizhin, K. Baugh, F.-C. Hsu and T. Ghosh, *Energies*, 2016, **9**, 14.
12. BGR, *Energy Study 2013. Reserves, resources and availability of energy resources*, Hannover, 2013.
13. G. L. Foster, D. L. Royer and D. J. Lunt, *Nat. Commun.*, 2017, **8**, 14845.
14. P. G. Levi and J. M. Cullen, *Environ. Sci. Tech.*, 2018, **52**, 1725-1734.
15. OECD Environmental Outlook to 2030, (accessed 12th November, 2018).
16. IEA, World Energy Outlook 2017, (accessed 12th December, 19).
17. E. V. Kondratenko, T. Peppel, D. Seeburg, V. A. Kondratenko, N. Kalevaru, A. Martin and S. Wohlrab, *Catal. Sci. Technol.*, 2017, **7**, 366-381.
18. Siluria Technologies, http://siluria.com/Technology/Demonstration_Plant, (accessed 15th November 2018).
19. Siluria Technologies, http://siluria.com/Newsroom/Press_Releases, (accessed 2018).
20. L. Wang, L. Tao, M. Xie, G. Xu, J. Huang and Y. Xu, *Catal. Lett.*, 1993, **21**, 35-41.
21. S. Ma, X. Guo, L. Zhao, S. Scott and X. Bao, *J. Energy Chem.*, 2013, **22**, 1-20.
22. A. Galadima and O. Muraza, *Catal. Surv. Asia*, 2019, **23**, 149-170.
23. B. A. Arndtsen, R. G. Bergman, T. A. Mobley and T. H. Peterson, *Acc. Chem. Res.*, 1995, **28**, 154-162.
24. V. C. C. Wang, S. Maji, P. P. Y. Chen, H. K. Lee, S. S. F. Yu and S. I. Chan, *Chem. Rev.*, 2017, 8574–8621.
25. M. O. Ross and A. C. Rosenzweig, *J. Biol. Inorg. Chem.*, 2017, **22**, 307-319.
26. A. Dyer, *An introduction to zeolite molecular sieves*, 1998.
27. E. M. Flanigen, in *Stud. Surf. Sci. Catal.*, eds. H. van Bekkum, E. M. Flanigen and J. C. Jansen, Elsevier, 1991, vol. 58, pp. 13-34.
28. I. Z. Association, Zeolite Framework Types, http://izasc.fos.su.se/IZA-SC/ft.php).
29. R. M. Barrer, *J. Chem. Soc.*, 1948, DOI: 10.1039/JR9480002158, 2158-2163.
30. Y. Li, L. Li and J. Yu, *Chem*, 2017, **3**, 928-949.
31. V. Komvokis, L. X. L. Tan, M. Clough, S. S. Pan and B. Yilmaz, in *Zeolites in Sustainable Chemistry: Synthesis, Characterization and Catalytic Applications*, eds. F.-S. Xiao and X. Meng, Springer Berlin Heidelberg, Berlin, Heidelberg, 2016, DOI: 10.1007/978-3-662-47395-5_8, pp. 271-297.
32. S. M. Csicsery, *Zeolites*, 1984, **4**, 202-213.

33. N. K. Jensen, T. E. Rufford, G. Watson, D. K. Zhang, K. I. Chan and E. F. May, *J. Chem. Eng. Data*, 2012, **57**, 106-113.
34. D. Lance and S. H. Elworthy,FR352687, 1905.
35. T. E. Layng and R. Soukup, *Ind. Eng. Chem.*, 1928, **20**, 1052-1055.
36. M. Ravi, M. Ranocchiari and J. A. van Bokhoven, *Angew. Chem., Int. Ed.*, 2017, **56**, 16464-16483.
37. N. F. Gol'dshleger, M. B. Tyabin, A. E. Shilov and A. A. Shteinman, *Zh. Fiz. Khim.*, 1969, **18**, 2174-2175.
38. N. F. Gol'dshleger, V. V. Es'kova, A. E. Shilov and A. A. Shteinman, *Zh. Fiz. Khim.*, 1972, **46**, 1353-1354.
39. J. A. Labinger and J. E. Bercaw, *J. Organomet. Chem.*, 2015, **793**, 47-53.
40. M. Lersch and M. Tilset, *Chem. Rev.*, 2005, **105**, 2471-2526.
41. J. A. Labinger, *Chem. Rev.*, 2017, **117**, 8483–8496.
42. N. J. Gunsalus, A. Koppaka, S. H. Park, S. M. Bischof, B. G. Hashiguchi and R. A. Periana, *Chem. Rev.*, 2017, **117**, 8521-8573.
43. R. A. Periana, D. J. Taube, S. Gamble, H. Taube, T. Satoh and H. Fujii, *Science*, 1998, **280**, 560-564.
44. M. M. Konnick, S. M. Bischof, M. Yousufuddin, B. G. Hashiguchi, D. H. Ess and R. A. Periana, *J. Am. Chem. Soc.*, 2014, **136**, 10085-10094.
45. T. Zimmermann, M. Soorholtz, M. Bilke and F. Schüth, *J. Am. Chem. Soc.*, 2016, **138**, 12395-12400.
46. T. Zimmermann, M. Bilke, M. Soorholtz and F. Schüth, *ACS Catal.*, 2018, **8**, 9262-9268.
47. L. F. Albright, *Ind. Eng. Chem. Res.*, 2009, **48**, 1409-1413.
48. J. T. Grant, J. M. Venegas, W. P. McDermott and I. Hermans, *Chem. Rev.*, 2018, **118**, 2769-2815.
49. M. H. Mahyuddin, A. Staykov, Y. Shiota and K. Yoshizawa, *ACS Catal.*, 2016, **6**, 8321-8331.
50. N. D. Spencer and C. J. Pereira, *J. Catal.*, 1989, **116**, 399-406.
51. K. J. Zhen, M. M. Khan, C. H. Mak, K. B. Lewis and G. A. Somorjai, *J. Catal.*, 1985, **94**, 501-507.
52. S. Y. Chen and D. Willcox, *Ind. Eng. Chem. Res.*, 1993, **32**, 584-587.
53. N. D. Spencer, *J. Catal.*, 1988, **109**, 187-197.
54. O. Kiyoshi and H. Masaharu, *Chem. Lett.*, 1992, **21**, 2397-2400.
55. T. Weng and E. E. Wolf, *Appl. Catal. A*, 1993, **96**, 383-396.
56. C. A. G. Fajardo, D. Niznansky, Y. N'Guyen, C. Courson and A.-C. Roger, *Catal. Commun.*, 2008, **9**, 864-869.
57. V. A. Durante, D. W. Walker, S. M. Gussow and J. E. Lyons,US4918249A, 1990.
58. S. Han, E. A. Kaufman, D. J. Martenak, R. E. Palermo, J. A. Pearson and D. E. Walsh, *Catal. Lett.*, 1994, **29**, 27-32.
59. V. I. Sobolev, K. A. Dubkov, O. V. Panna and G. I. Panov, *Catal. Today*, 1995, **24**, 251-252.
60. A. Klerk, *Energ, Sci. Eng.*, 2015, **3**, 60-70.
61. P. Schwach, X. Pan and X. Bao, *Chem. Rev.*, 2017, **117**, 8497-8520.
62. J. J. Spivey and G. Hutchings, *Chem. Soc. Rev.*, 2014, **43**, 792-803.
63. V. R. Choudhary, A. K. Kinage and T. V. Choudhary, *Science*, 1997, **275**, 1286-1288.
64. B. M. Weckhuysen, D. Wang, M. P. Rosynek and J. H. Lunsford, *J. Catal.*, 1998, **175**, 347-351.
65. J. Yang, F. Deng, M. Zhang, Q. Luo and C. Ye, *J. Mol. Catal. A: Chem.*, 2003, **202**, 239-246.
66. Y. Shu, R. Ohnishi and M. Ichikawa, *Appl. Catal., A*, 2003, **252**, 315-329.
67. Y. Lai and G. Veser, *Environ. Prog. Sustan.*, 2016, **35**, 334-344.
68. P. L. Tan, C. T. Au and S. Y. Lai, *Catal. Lett.*, 2006, **112**, 239-245.

69. M. V. Luzgin, A. A. Gabrienko, V. A. Rogov, A. V. Toktarev, V. N. Parmon and A. G. Stepanov, *J. Phys. Chem. C*, 2010, **114**, 21555-21561.
70. I. Vollmer, B. van der Linden, S. Ould-Chikh, A. Aguilar-Tapia, I. Yarulina, E. Abou-Hamad, Y. G. Sneider, A. I. Olivos Suarez, J.-L. Hazemann, F. Kapteijn and J. Gascon, *Chem. Sci.*, 2018, **9**, 4801-4807.
71. Y. Xu, S. Liu, X. Guo, L. Wang and M. Xie, *Catal. Lett.*, 1994, **30**, 135-149.
72. I. Vollmer, E. Abou-Hamad, J. Gascon and F. Kapteijn, *Chem. Cat. Chem.*, 2020, **12**, 544**.**
73. D. Wang, J. H. Lunsford and M. P. Rosynek, *Top. Catal.*, 1996, **3**, 289-297.
74. H. Jiang, L. Wang, W. Cui and Y. Xu, *Catal. Lett.*, 1999, **57**, 95-102.
75. N. Kosinov, A. S. G. Wijpkema, E. Uslamin, R. Rohling, F. J. A. G. Coumans, B. Mezari, A. Parastaev, A. S. Poryvaev, M. V. Fedin, E. A. Pidko and E. J. M. Hensen, *Angew. Chem., Int. Ed.*, 2018, **57**, 1016-1020.
76. V. T. T. Ha, L. V. Tiep, P. Meriaudeau and C. Naccache, *J. Mol. Catal. A: Chem.*, 2002, **181**, 283-290.
77. N. K. Razdan, A. Kumar, B. L. Foley and A. Bhan, *J. Catal.*, 2020, **381**, 261-270.
78. M. Agote-Arán, A. B. Kroner, H. U. Islam, W. A. Sławiński, D. S. Wragg, I. Lezcano-González and A. M. Beale, *Chem. Cat. Chem.*, 2019, **11**, 473-480.
79. S. W. T. Price, D. J. Martin, A. D. Parsons, W. A. Sławiński, A. Vamvakeros, S. J. Keylock, A. M. Beale and J. F. W. Mosselmans, *Science Advances*, 2017, **3**.
80. R. W. Borry, Y. H. Kim, A. Huffsmith, J. A. Reimer and E. Iglesia, *J. Phys. Chem. B*, 1999, **103**, 5787-5796.
81. W. Ding, S. Li, G. D Meitzner and E. Iglesia, *J. Phys. Chem. B*, 2001, **105**, 506-513.
82. Y.-H. Kim, R. W. Borry and E. Iglesia, *Micro. Meso. Mater.*, 2000, **35-36**, 495-509.
83. F. Solymosi, J. Cserényi, A. Szöke, T. Bánsági and A. Oszkó, *J. Catal.*, 1997, **165**, 150-161.
84. Y. Xu, W. Liu, S.-T. Wong, L. Wang and X. Guo, *Catal. Lett.*, 1996, **40**, 207-214.
85. C.-L. Zhang, S. Li, Y. Yuan, W.-X. Zhang, T.-H. Wu and L.-W. LIn, *Catal. Lett.*, 1998, **56**, 207-213.
86. S. Liu, L. Wang, R. Ohnishi and M. Ichikawa, *J. Catal.*, 1999, **181**, 175-188.
87. J. Bai, S. Liu, S. Xie, L. Xu and L. Lin, *Catal. Lett.*, 2003, **90**, 123-130.
88. J. Bai, S. Liu, S. Xie, L. Xu and L. Lin, *React. Kinet. Catal. Lett.*, 2004, **82**, 279-286.
89. H. Liu, W. Shen, X. Bao and Y. Xu, *Appl. Catal., A*, 2005, **295**, 79-88.
90. H. Liu, L. Su, H. Wang, W. Shen, X. Bao and Y. Xu, *Appl. Catal., A*, 2002, **236**, 263-280.
91. S. Yuan, J. Li, Z. Hao, Z. Feng, Q. Xin, P. Ying and C. Li, *Catal. Lett.*, 1999, **63**, 73-77.
92. E. V. Matus, I. Z. Ismagilov, O. B. Sukhova, V. I. Zaikovskii, L. T. Tsikoza, Z. R. Ismagilov and J. A. Moulijn, *Ind. Eng. Chem. Res.*, 2007, **46**, 4063-4074.
93. Y. Song, Y. Xu, Y. Suzuki, H. Nakagome and Z.-G. Zhang, *Appl. Catal., A*, 2014, **482**, 387-396.
94. I. Lezcano-González, R. Oord, M. Rovezzi, P. Glatzel, S. W. Botchway, B. M. Weckhuysen and A. M. Beale, *Angew. Chem., Int. Ed.*, 2016, **55**, 5215-5219.
95. N. Kosinov, F. J. A. G. Coumans, G. Li, E. Uslamin, B. Mezari, A. S. G. Wijpkema, E. A. Pidko and E. J. M. Hensen, *J. Catal.*, 2017, **346**, 125-133.
96. Y. Xu, J. Lu, J. Wang, Y. Suzuki and Z.-G. Zhang, *Chem. Eng. J.*, 2011, **168**, 390-402.
97. A. C. C. Rodrigues and J. L. F. Monteiro, *Catal. Commun.*, 2008, **9**, 1060-1065.
98. M. R. Toosi, B. Sabour, T. Hamuleh and M. H. Peyrovi, *React. Kinet. Mech. Catal*, 2010, **101**, 221-226.
99. W. Vermeiren and J.-P. Gilson, *Top. Catal.*, 2009, **52**, 1131-1161.
100. R. Millini and G. Bellussi, in *Zeolites in Catalysis: Properties and Applications*, The Royal Society of Chemistry, 2017, DOI: 10.1039/9781788010610-00001, pp. 1-36.
101. R. Gounder and E. Iglesia, *Chem. Comm.*, 2013, **49**, 3491-3509.
102. A. Corma, *J. Catal.*, 2003, **216,** 291-312.

103. A. Bhan, A. D. Allian, G. J. Sunley, D. J. Law and E. Iglesia, *J. Am. Chem. Soc.*, 2007, **129**, 4919-4924.
104. B. Li, J. Xu, B. Han, X. Wang, G. Qi, Z. Zhang, C. Wang and F. Deng, *J. Phys. Chem. C*, 2013, **117**, 5840-5847.
105. G. I. Panov, V. I. Sobolev and A. S. Kharitonov, *J. Mol. Catal.*, 1990, **61**, 85-97.
106. G. I. Panov, G. A. Sheveleva, A. S. Kharitonov, V. N. Romannikov and L. A. Vostrikova, *Appl. Catal., A*, 1992, **82**, 31-36.
107. V. I. Sobolev, A. S. Kharitonov, Y. A. Paukshtis and G. I. Panov, *J. Mol. Catal.*, 1993, **84**, 117-124.
108. G. I. Panov, V. I. Sobolev, K. A. Dubkov, V. N. Parmon, N. S. Ovanesyan, A. E. Shilov and A. A. Shteinman, *React. Kinet. Catal. Lett.*, 1997, **61**, 251-258.
109. E. V. Starokon, M. V. Parfenov, L. V. Pirutko, S. I. Abornev and G. I. Panov, *J. Phys. Chem. C*, 2011, **115**, 2155-2161.
110. B. E. R. Snyder, P. Vanelderen, M. L. Bols, S. D. Hallaert, L. H. Böttger, L. Ungur, K. Pierloot, R. A. Schoonheydt, B. F. Sels and E. I. Solomon, *Nature*, 2016, **536**, 317.
111. F. Göltl, C. Michel, P. C. Andrikopoulos, A. M. Love, J. Hafner, I. Hermans and P. Sautet, *ACS Catal.*, 2016, **6**, 8404-8409.
112. E. V. Starokon, M. V. Parfenov, S. S. Arzumanov, L. V. Pirutko, A. G. Stepanov and G. I. Panov, *J. Catal.*, 2013, **300**, 47-54.
113. Y. K. Chow, N. F. Dummer, J. H. Carter, R. J. Meyer, R. D. Armstrong, C. Williams, G. Shaw, S. Yacob, M. M. Bhasin, D. J. Willock, S. H. Taylor and G. J. Hutchings, *Chem. Phys. Chem*, 2018, **19**, 402-411.
114. J. Valyon, W. S. Millman and W. K. Hall, *Catal. Lett.*, 1994, **24**, 215-225.
115. J. Leglise, J. O. Petunchi and W. K. Hall, *J. Catal.*, 1984, **86**, 392-399.
116. P. C. Andrikopoulos, Z. Sobalik, J. Novakova, P. Sazama and S. Sklenak, *Chem. Phys. Chem*, 2013, **14**, 520-531.
117. C. M. Fu, V. N. Korchak and W. K. Hall, *J. Catal.*, 1981, **68**, 166-171.
118. M. L. Bols, S. D. Hallaert, B. E. R. Snyder, J. Devos, D. Plessers, H. M. Rhoda, M. Dusselier, R. A. Schoonheydt, K. Pierloot, E. I. Solomon and B. F. Sels, *J. Am. Chem. Soc.*, 2018, **140**, 12021-12032.
119. B. Michalkiewicz, *Appl. Catal., A*, 2004, **277**, 147-153.
120. C. Hammond, M. M. Forde, M. H. Ab Rahim, A. Thetford, Q. He, R. L. Jenkins, N. Dimitratos, J. A. Lopez-Sanchez, N. F. Dummer, D. M. Murphy, A. F. Carley, S. H. Taylor, D. J. Willock, E. E. Stangland, J. Kang, H. Hagen, C. J. Kiely and G. J. Hutchings, *Angew. Chem. Int. Ed.*, 2012, **51**, 5129-5133.
121. C. Hammond, R. L. Jenkins, N. Dimitratos, J. A. Lopez-Sanchez, M. H. ab Rahim, M. M. Forde, A. Thetford, D. M. Murphy, H. Hagen, E. E. Stangland, J. M. Moulijn, S. H. Taylor, D. J. Willock and G. J. Hutchings, *Chem. Eur. J*, 2012, **18**, 15735-15745.
122. C. Hammond, N. Dimitratos, R. L. Jenkins, J. A. Lopez-Sanchez, S. A. Kondrat, M. Hasbi ab Rahim, M. M. Forde, A. Thetford, S. H. Taylor, H. Hagen, E. E. Stangland, J. H. Kang, J. M. Moulijn, D. J. Willock and G. J. Hutchings, *ACS Catal.*, 2013, **3**, 689-699.
123. C. Hammond, N. Dimitratos, J. A. Lopez-Sanchez, R. L. Jenkins, G. Whiting, S. A. Kondrat, M. H. ab Rahim, M. M. Forde, A. Thetford, H. Hagen, E. E. Stangland, J. M. Moulijn, S. H. Taylor, D. J. Willock and G. J. Hutchings, *ACS Catal.*, 2013, **3**, 1835-1844.
124. J. Xu, R. D. Armstrong, G. Shaw, N. F. Dummer, S. J. Freakley, S. H. Taylor and G. J. Hutchings, *Catal.*, 2016, **270**, 93-100.
125. M. H. Groothaert, P. J. Smeets, B. F. Sels, P. A. Jacobs and R. A. Schoonheydt, *J. Am. Chem. Soc.*, 2005, **127**, 1394-1395.
126. M. B. Park, S. H. Ahn, A. Mansouri, M. Ranocchiari and J. A. van Bokhoven, *Chem. Cat. Chem*, 2017, **9**, 3705-3713.
127. P. J. Smeets, M. H. Groothaert and R. A. Schoonheydt, *Catal.*, 2005, **110**, 303-309.

128. M. J. Wulfers, S. Teketel, B. Ipek and R. F. Lobo, *Chem Commun*, 2015, **51**, 4447-4450.
129. M. H. Groothaert, J. A. van Bokhoven, A. A. Battiston, B. M. Weckhuysen and R. A. Schoonheydt, *J. Am. Chem. Soc.*, 2003, **125**, 7629-7640.
130. M. H. Groothaert, K. Lievens, J. A. van Bokhoven, A. A. Battiston, B. M. Weckhuysen, K. Pierloot and R. A. Schoonheydt, *Chem. Phys. Chem.*, 2003, **4**, 626-630.
131. M. A. C. Markovits, A. Jentys, M. Tromp, M. Sanchez-Sanchez and J. A. Lercher, *Top. Catal.*, 2016, **59**, 1554-1563.
132. J. S. Woertink, P. J. Smeets, M. H. Groothaert, M. A. Vance, B. F. Sels, R. A. Schoonheydt and E. I. Solomon, *Proc. Natl. Acad. Sci.*, 2009, **106**, 18908-18913.
133. R. S. Czernuszewicz, J. E. Sheats and T. G. Spiro, *Inorg. Chem.*, 1987, **26**, 2063-2067.
134. M. H. Groothaert, K. Lievens, H. Leeman, B. M. Weckhuysen and R. A. Schoonheydt, *J. Catal.*, 2003, **220**, 500-512.
135. P. J. Smeets, R. G. Hadt, J. S. Woertink, P. Vanelderen, R. A. Schoonheydt, B. F. Sels and E. I. Solomon, *J. Am. Chem. Soc.*, 2010, **132**, 14736-14738.
136. M. L. Tsai, R. G. Hadt, P. Vanelderen, B. F. Sels, R. A. Schoonheydt and E. I. Solomon, *J. Am. Chem. Soc.*, 2014, **136**, 3522-3529.
137. S. Grundner, M. A. C. Markovits, G. Li, M. Tromp, E. A. Pidko, E. J. M. Hensen, A. Jentys, M. Sanchez-Sanchez and J. A. Lercher, *Nat. Commun.*, 2015, **6**, 7546.
138. G. Li, P. Vassilev, M. Sanchez-Sanchez, J. A. Lercher, E. J. M. Hensen and E. A. Pidko, *J Catal*, 2016, **338**, 305-312.
139. D. Palagin, A. J. Knorpp, A. B. Pinar, M. Ranocchiari and J. A. van Bokhoven, *Nanoscale*, 2017, **9**, 1144-1153.
140. J. N. Jocz, A. J. Medford and C. Sievers, *Chem. Cat. Chem.*, 2019, **11**, 593-600.
141. C. Paolucci, A. A. Parekh, I. Khurana, J. R. Di Iorio, H. Li, J. D. Albarracin Caballero, A. J. Shih, T. Anggara, W. N. Delgass, J. T. Miller, F. H. Ribeiro, R. Gounder and W. F. Schneider, *J. Am. Chem. Soc.*, 2016, **138**, 6028-6048.
142. A. R. Kulkarni, Z.-J. Zhao, S. Siahrostami, J. K. Nørskov and F. Studt, *ACS Catal.*, 2016, **6**, 6531-6536.
143. F. Giordanino, P. N. R. Vennestrøm, L. F. Lundegaard, F. N. Stappen, S. Mossin, P. Beato, S. Bordiga and C. Lamberti, *Dalton Trans.*, 2013, **42**, 12741-12761.
144. E. Borfecchia, K. A. Lomachenko, F. Giordanino, H. Falsig, P. Beato, A. V. Soldatov, S. Bordiga and C. Lamberti, *Chem. Sci.*, 2015, **6**, 548-563.
145. K. Narsimhan, K. Iyoki, K. Dinh and Y. Román-Leshkov, *ACS Cent. Sci.*, 2016, **2**, 424-429.
146. P. Vanelderen, J. Vancauwenbergh, B. F. Sels and R. A. Schoonheydt, *Coordin. Chem. Rev.*, 2013, **257**, 483-494.
147. P. Tomkins, M. Ranocchiari and J. A. van Bokhoven, *Acc. Chem. Res.*, 2017, **50**, 418-425.
148. Z.-J. Zhao, A. Kulkarni, L. Vilella, J. K. Nørskov and F. Studt, *ACS Catal.*, 2016, **6**, 3760-3766.
149. E. M. C. Alayon, M. Nachtegaal, A. Bodi and J. A. van Bokhoven, *ACS Catal.*, 2014, **4**, 16-22.
150. R. Oord, J. E. Schmidt and B. M. Weckhuysen, *Catal. Sci. Technol.*, 2018, **8**, 1028-1038.
151. M. H. Mahyuddin, T. Tanaka, Y. Shiota, A. Staykov and K. Yoshizawa, *ACS Catal.*, 2018, **8**, 1500-1509.
152. P. Tomkins, A. Mansouri, S. E. Bozbag, F. Krumeich, B. Park Min, E. M. C. Alayon, M. Ranocchiari and J. A. van Bokhoven, *Angew. Chem., Int. Ed.*, 2016, **55**, 5467-5471.
153. T. Sheppard, C. D. Hamill, A. Goguet, D. W. Rooney and J. M. Thompson, *Chem. Commun.*, 2014, **50**, 11053-11055.
154. A. Oda, H. Torigoe, A. Itadani, T. Ohkubo, T. Yumura, H. Kobayashi and Y. Kuroda, *J. Phys. Chem. C*, 2013, **117**, 19525-19534.
155. V. L. Sushkevich, D. Palagin and J. A. v. Bokhoven, *Angew. Chem., Int. Ed.*, 2018, **57**, 8906-8910.

156. P. Vanelderen, B. E. R. Snyder, M.-L. Tsai, R. G. Hadt, J. Vancauwenbergh, O. Coussens, R. A. Schoonheydt, B. F. Sels and E. I. Solomon, *J. Am. Chem. Soc.*, 2015, **137**, 6383-6392.
157. B. E. R. Snyder, P. Vanelderen, R. A. Schoonheydt, B. F. Sels and E. I. Solomon, *J. Am. Chem. Soc.*, 2018, **140**, 9236-9243.
158. E. G. Derouane, *J. Catal.*, 1986, **100**, 541-544.
159. P. Cheung, A. Bhan, G. J. Sunley and E. Iglesia, *Angew. Chem. Int. Ed.*, 2006, **45**, 1617-1620.
160. A. J. Jones, S. I. Zones and E. Iglesia, *J. Phys. Chem. C*, 2014, **118**, 17787-17800.
161. M. L. Sarazen, E. Doskocil and E. Iglesia, *ACS Catal.*, 2016, **6**, 7059-7070.
162. E. M. C. Alayon, M. Nachtegaal, M. Ranocchiari and J. A. van Bokhoven, *CHIMIA Int. J. Chem.*, 2012, **66**, 668-674.
163. M. A. Newton, A. J. Knorpp, A. B. Pinar, V. L. Sushkevich, D. Palagin and J. A. van Bokhoven, *J. Am. Chem. Soc.*, 2018, DOI: 10.1021/jacs.8b05139, 10090–10093.
164. S. E. Bozbag, E. M. C. Alayon, J. Pecháček, M. Nachtegaal, M. Ranocchiari and J. A. van Bokhoven, *Catal. Sci Tech*, 2016, **6**, 5011-5022.
165. D. K. Pappas, A. Martini, M. Dyballa, K. Kvande, S. Teketel, K. A. Lomachenko, R. Baran, P. Glatzel, B. Arstad, G. Berlier, C. Lamberti, S. Bordiga, U. Olsbye, S. Svelle, P. Beato and E. Borfecchia, *J. Am. Chem. Soc.*, 2018, DOI: 10.1021/jacs.8b08071, 15270–15278.
166. B. Ipek and R. F. Lobo, *Chem. Commun.*, 2016, **52**, 13401-13404.
167. M. Dusselier and M. E. Davis, *Chem. Rev.*, 2018, 5265–5329.
168. N. V. Beznis, B. M. Weckhuysen and J. H. Bitter, *Catal. Lett.*, 2010, **136**, 52-56.
169. N. V. Beznis, A. N. C. van Laak, B. M. Weckhuysen and J. H. Bitter, *Micro. Meso. Mat.*, 2011, **138**, 176-183.
170. Y. K. Krisnandi, B. A. P. Putra, M. Bahtiar, Zahara, I. Abdullah and R. F. Howe, *Proc. Chem.*, 2015, **14**, 508-515.
171. Y. K. Krisnandi, B. A. Samodro, R. Sihombing and R. F. Howe, *Indones. J. Chem.*, 2015, **15**, 263-268.
172. M. F. Fellah and I. Onal, *J. Phys. Chem. C*, 2010, **114**, 3042-3051.
173. J. Shan, W. Huang, L. Nguyen, Y. Yu, S. Zhang, Y. Li, A. I. Frenkel and F. Tao, *Langmuir*, 2014, **30**, 8558-8569.
174. A. A. Arvidsson, V. P. Zhdanov, P.-A. Carlsson, H. Gronbeck and A. Hellman, *Catal. Sci. Technol.*, 2017, **7**, 1470-1477.
175. M. H. Mahyuddin and K. Yoshizawa, *Catal. Sci. Technol.*, 2018, DOI: 10.1039/C8CY01441H, 5875-5885.
176. D. Radu, P. Glatzel, A. Gloter, O. Stephan, B. M. Weckhuysen and F. M. F. de Groot, *J. Phys. Chem. C*, 2008, **112**, 12409-12416.
177. V. B. Kazansky and A. I. Serykh, *Phys. Chem. Chem. Phys.*, 2004, **6**, 3760-3764.
178. S. M. T. Almutairi, B. Mezari, P. C. M. M. Magusin, E. A. Pidko and E. J. M. Hensen, *ACS Catal.*, 2012, **2**, 71-83.
179. I. Pinilla-Herrero, E. Borfecchia, J. Holzinger, U. V. Mentzel, F. Joensen, K. A. Lomachenko, S. Bordiga, C. Lamberti, G. Berlier, U. Olsbye, S. Svelle, J. Skibsted and P. Beato, *J. Catal.*, 2018, **362**, 146-163.
180. A. A. Gabrienko, S. S. Arzumanov, M. V. Luzgin, A. G. Stepanov and V. N. Parmon, *J. Phys. Chem. C*, 2015, **119**, 24910-24918.
181. E. Morra, G. Berlier, E. Borfecchia, S. Bordiga, P. Beato and M. Chiesa, *J. Phys. Chem. C*, 2017, **121**, 14238-14245.
182. I. Resa, E. Carmona, E. Gutierrez-Puebla and A. Monge, *Science*, 2004, **305**, 1136-1138.
183. G. Parkin, *Science*, 2004, **305**, 1117-1118.
184. T. Li, S. Schulz and P. W. Roesky, *Chem. Soc. Rev.*, 2012, **41**, 3759-3771.
185. A. Oda, T. Ohkubo, T. Yumura, H. Kobayashi and Y. Kuroda, *Dalton Trans.*, 2015, **44**, 10038-10047.

186. A. Dyer and T. I. Emms, *J. Mater. Chem.*, 2005, **15**, 5012-5021.
187. Y. G. Kolyagin, I. I. Ivanova, V. V. Ordomsky, A. Gedeon and Y. A. Pirogov, *J. Phys. Chem. C*, 2008, **112**, 20065-20069.
188. H. Elmar, *Z. Anorg. Allg. Chem.*, 2000, **626**, 2223-2227.
189. M. V. Luzgin, D. Freude, J. Haase and A. G. Stepanov, *J. Phys. Chem. C*, 2015, **119**, 14255-14261.
190. J. Xu, A. Zheng, X. Wang, G. Qi, J. Su, J. Du, Z. Gan, J. Wu, W. Wang and F. Deng, *Chem. Sci.*, 2012, **3**, 2932-2940.
191. J. F. Wu, W. D. Wang, J. Xu, F. Deng and W. Wang, *Chem. - Eur. J.*, 2010, **16**, 14016-14025.
192. A. Oda, T. Ohkubo, T. Yumura, H. Kobayashi and Y. Kuroda, *Inorg. Chem.*, 2019, **58**, 327-338.
193. A. Oda, T. Ohkubo, T. Yumura, H. Kobayashi and Y. Kuroda, *Angew. Chem., Int. Ed.*, 2017, **56**, 9715-9718.
194. A. Oda, H. Torigoe, A. Itadani, T. Ohkubo, T. Yumura, H. Kobayashi and Y. Kuroda, *Angew. Chem. Int. Ed.*, 2012, **51**, 7719-7723.
195. E. A. Pidko and R. A. van Santen, *J. Phys. Chem. C*, 2007, **111**, 2643-2655.
196. A. A. Gabrienko, S. S. Arzumanov, D. Freude and A. G. Stepanov, *J. Phys. Chem. C*, 2010, **114**, 12681-12688.
197. A. A. Gabrienko, S. S. Arzumanov, A. V. Toktarev, I. G. Danilova, I. P. Prosvirin, V. V. Kriventsov, V. I. Zaikovskii, D. Freude and A. G. Stepanov, *ACS Catal.*, 2017, **7**, 1818-1830.
198. A. Mehdad and R. F. Lobo, *Catal. Sci. Technol.*, 2017, **7**, 3562-3572.
199. V. B. Kazansky, V. Yu. Borovkov, A. I. Serykh, R. A. van Santen and P. J. Stobbelaar, *Phys. Chem. Chem. Phys.*, 1999, **1**, 2881-2886.
200. V. B. Kazansky, A. I. Serykh and E. A. Pidko, *J. Catal.*, 2004, **225**, 369-373.
201. A. G. Stepanov, S. S. Arzumanov, A. A. Gabrienko, V. N. Parmon, I. I. Ivanova and D. Freude, *Chem. Phys. Chem.*, 2008, **9**, 2559-2563.
202. J.-F. Wu, S.-M. Yu, W. D. Wang, Y.-X. Fan, S. Bai, C.-W. Zhang, Q. Gao, J. Huang and W. Wang, *J. Am. Chem. Soc.*, 2013, **135**, 13567-13573.
203. G. Qi, Q. Wang, J. Xu, J. Trébosc, O. Lafon, C. Wang, J.-P. Amoureux and F. Deng, *Angew. Chem. Int. Ed.*, 2016, **55**, 15826-15830.
204. A. A. Gabrienko, I. G. Danilova, S. S. Arzumanov, D. Freude and A. G. Stepanov, *ChemCatChem*, 2020, **12,** 478.
205. Y. Lin, S. Qi, L. Benedict, Z. Junlin, K. Dejing, M. Claire, T. Chiu and T. Edman, *Angew. Chem. Int. Ed.*, 2017, **56**, 10711-10716.
206. X. Wang, G. Qi, J. Xu, B. Li, C. Wang and F. Deng, *Angew. Chem., Int. Ed.*, 2012, **51**, 3850-3853.
207. A. Oda, H. Torigoe, A. Itadani, T. Ohkubo, T. Yumura, H. Kobayashi and Y. Kuroda, *J. Phys. Chem. C*, 2014, **118**, 15234-15241.
208. V. B. Kazansky, *Kinetics and Catalysis*, 2014, **55**, 737-747.
209. J. P. Breen, R. Burch, M. Kulkarni, D. McLaughlin, P. J. Collier and S. E. Golunski, *Appl. Catal., A*, 2007, **316**, 53-60.
210. K. T. Dinh, M. M. Sullivan, P. Serna, R. J. Meyer, M. Dincă and Y. Román-Leshkov, *ACS Catal.*, 2018, **8**, 8306-8313.
211. A. A. Latimer, A. Kakekhani, A. R. Kulkarni and J. K. Nørskov, *ACS Catal.*, 2018, **8**, 6894-6907.
212. B. E. R. Snyder, M. L. Bols, R. A. Schoonheydt, B. F. Sels and E. I. Solomon, *Chem. Rev.*, 2018, **118**, 2718-2768.
213. J. A. Labinger, *J. Mol. Catal. A: Chem.*, 2004, **220**, 27-35.
214. S. S. Arzumanov, A. A. Gabrienko, D. Freude and A. G. Stepanov, *Catal. Sci. Technol.*, 2016, **6**, 6381-6388.
215. J. A. Keith and P. M. Henry, *Angew. Chem., Int. Ed.*, 2009, **48**, 9038-9049.

216. A. A. Latimer, A. R. Kulkarni, H. Aljama, J. H. Montoya, J. S. Yoo, C. Tsai, F. Abild-Pedersen, F. Studt and J. K. Norskov, *Nat. Mater.*, 2017, **16**, 225-229.
217. M. H. Mahyuddin, Y. Shiota, A. Staykov and K. Yoshizawa, *Acc. Chem. Res.*, 2018, **51**, 2382-2390.
218. E. Mansoor, J. Van der Mynsbrugge, M. Head-Gordon and A. T. Bell, *Catal.*, 2018, **312**, 51-65.

Chapter 2: Project aims

Chapter 2: Project Aims

Despite many recent advances in alkane activation and functionalisation using metal-functionalised zeolites, there are still significant gaps in the fundamental understanding of methane activation mechanism and the nature of the active metal site.[1-5] In order to develop catalytic processes such as the direct conversion of methane to methanol or methane dehydroaromatisation to form benzene, a deeper understanding of the role of the zeolite framework and nature and location of the extraframework metal is required.

As well as understanding the role of the zeolite framework, a greater insight of the mechanism of methane activation over metal-modified zeolites is needed. As described in Section 1.3.2.2, methane activation over copper-functionalised zeolites occurs over multiple active sites *via* a radical abstraction mechanism which has little selectivity.[6-10] Whilst confinement effects have been found to promote the partial oxidation of methane in copper systems,[11-14] a major disadvantage remains the necessity of multiple steps over a variable temperature range.[10, 15, 16] Conversely, zinc exchanged zeolites are able to activate methane without an initial high temperature oxidation step increasing their industrial viability, although no catalytic processes have been reported with zinc to date.[17-20] The mechanism of methane activation over zinc-exchanged zeolites has not been studied to the same extent as iron and copper zeolites, but heterolytic cleavage of the C-H bond in methane compared with a radical mechanism could promote great selectivity.[18-22] Therefore, methane activation over zinc-modified zeolites has been investigated throughout the course of this project and three main questions have been addressed.

1) ***What is the role of the zeolite framework on methane activation over zinc-modified zeolites?***

Whilst methane activation and oxidation has been previously explored over zinc-modified ZSM-5,[18-25] the effect of the zeolite framework on the activation and subsequent functionalisation steps has not yet been investigated. To explore the effect of framework on the C-H activation of methane, three zeolites with intrinsically different micropore topologies, ZSM-5, FER and MOR were identified. We chose to introduce zinc by zinc vapour deposition as this method has been known to result in the full exchange of BAS sites, whilst primarily introducing Zn^{2+} cations.[18-21, 23, 26, 27] We aimed to investigate the effect of the zeolite framework on the initial methane activation and subsequent reactivity under oxidative conditions.

The reactivity of methane in a zinc-modified zeolite can also be dependent on a specific Al array within zeolite as determined by Kuroda *et al.* who suggest that heterolytic cleavage of H_2 was more favourable on a circumferentially-arrayed Al-Al site in Zn/ZSM-5.[28] It has also been suggested in the literature that distant Al pairs are required for methane activation as when fewer Al atoms are present, the Lewis acidity of the zinc sites is increased as the positive charge is not fully compensated. [18, 23, 28] Collaborators, Julien Devos and Michiel Dusselier at KU Leuven, Belgium, were able to synthesis a series of CHA samples with different levels of Al pairing.[29] Hence, using these samples, we planned to explore the role of Al paring on methane activation after zinc vapour deposition within the CHA framework.

The Si/Al ratio of the zeolite framework is also likely to affect the ability of the zinc-modified zeolite to break the C-H bond of methane as this affects the level of zinc exchange as well as the Al distribution. Therefore, methane activation over zeolites with different Si/Al ratio will also be studied.

2) ***What is the nature of the zinc active site for methane activation over zinc-modified zeolites?***

Whilst the mechanism of methane activation over Zn/zeolites has been debated since the initial findings of Kazansky *et al.* in 2004,[18, 23] it has been shown that methane activation over Zn^{2+} involves the heterolytic cleavage of methane, forming a [Zn^{II}-CH_3] species alongside a new BAS.[18-23, 25, 30] However, the nature of the zinc active site in zinc vapour depositions samples has not been thoroughly explored. XAS analysis can be a powerful tool to gaining insight into the coordination environment and oxidation state of the zinc site.[17, 31-33] Therefore, we aim to compare zinc vapour depositions samples with dehydrated ion exchange samples to identify if the active species for methane activation is dependent on the method of zinc introduction.

3) ***Does the method of zinc introduction or the zeolite topology affect the activity of the zinc catalyst for methane dehydroaromatisation reactions (MDA)?***

Previous literature studies have demonstrated that Zn/ZSM-5 catalysts have not performed overall as well as Mo/H-ZSM-5 for the MDA reaction in terms of methane conversion levels but under certain conditions, zinc catalysts have shown greater stability and higher activity that molybdenum catalysts.[34, 35] However, once again the role of zeolite framework or different methods of zinc introduction have not been thoroughly explored for the MDA reaction. Consequently, we plan to explore different methods of zinc introduction

(impregnation, ion exchange and zinc vapour deposition) on a number of different zeolite frameworks to explore the effect on the MDA reaction.

1. S. Raynes, M. A. Shah and R. A. Taylor, *Dalton Trans.*, 2019, **48**, 10364-10384.
2. M. H. Mahyuddin, A. Staykov, Y. Shiota and K. Yoshizawa, *ACS Catal.*, 2016, **6**, 8321-8331.
3. M. H. Mahyuddin, Y. Shiota and K. Yoshizawa, *Catal. Sci. Technol.*, 2019, **9**, 1744-1768.
4. S. Ma, X. Guo, L. Zhao, S. Scott and X. Bao, *J. Ener. Chem.*, 2013, **22**, 1-20.
5. N. Kosinov, A. S. G. Wijpkema, E. Uslamin, R. Rohling, F. J. A. G. Coumans, B. Mezari, A. Parastaev, A. S. Poryvaev, M. V. Fedin, E. A. Pidko and E. J. M. Hensen, *Angew. Chem. Int. Ed.*, 2018, **57**, 1016-1020.
6. A. R. Kulkarni, Z.-J. Zhao, S. Siahrostami, J. K. Nørskov and F. Studt, *ACS Catal.*, 2016, **6**, 6531-6536.
7. G. Li, P. Vassilev, M. Sanchez-Sanchez, J. A. Lercher, E. J. M. Hensen and E. A. Pidko, *J Catal*, 2016, **338**, 305-312.
8. J. S. Woertink, P. J. Smeets, M. H. Groothaert, M. A. Vance, B. F. Sels, R. A. Schoonheydt and E. I. Solomon, *Proc. Natl. Acad. Sci.*, 2009, **106**, 18908-18913.
9. Z.-J. Zhao, A. Kulkarni, L. Vilella, J. K. Nørskov and F. Studt, *ACS Catal.*, 2016, **6**, 3760-3766.
10. P. Vanelderen, J. Vancauwenbergh, B. F. Sels and R. A. Schoonheydt, *Coordin. Chem. Rev.*, 2013, **257**, 483-494.
11. E. G. Derouane, *J. Catal.*, 1986, **100**, 541-544.
12. R. Gounder and E. Iglesia, *Chem. Comm.*, 2013, **49**, 3491-3509.
13. A. J. Jones, S. I. Zones and E. Iglesia, *J. Phys. Chem. C*, 2014, **118**, 17787-17800.
14. M. L. Sarazen, E. Doskocil and E. Iglesia, *ACS Catal.*, 2016, **6**, 7059-7070.
15. M. H. Groothaert, P. J. Smeets, B. F. Sels, P. A. Jacobs and R. A. Schoonheydt, *J. Am. Chem. Soc.*, 2005, **127**, 1394-1395.
16. K. Narsimhan, K. Iyoki, K. Dinh and Y. Román-Leshkov, *ACS Cent. Sci*, 2016, **2**, 424-429.
17. S. M. T. Almutairi, B. Mezari, P. C. M. M. Magusin, E. A. Pidko and E. J. M. Hensen, *ACS Catal.*, 2012, **2**, 71-83.
18. V. B. Kazansky and A. I. Serykh, *Phys. Chem. Chem. Phys.*, 2004, **6**, 3760-3764.
19. A. A. Gabrienko, S. S. Arzumanov, M. V. Luzgin, A. G. Stepanov and V. N. Parmon, *J. Phys. Chem. C*, 2015, **119**, 24910-24918.
20. A. A. Gabrienko, S. S. Arzumanov, A. V. Toktarev, I. G. Danilova, I. P. Prosvirin, V. V. Kriventsov, V. I. Zaikovskii, D. Freude and A. G. Stepanov, *ACS Catal.*, 2017, **7**, 1818-1830.
21. M. V. Luzgin, D. Freude, J. Haase and A. G. Stepanov, *J. Phys. Chem. C*, 2015, **119**, 14255-14261.
22. Y. G. Kolyagin, I. I. Ivanova and Y. A. Pirogov, *Solid State Nucl. Magn. Reson.*, 2009, **35**, 104-112.
23. V. B. Kazansky, A. I. Serykh and E. A. Pidko, *J. Catal.*, 2004, **225**, 369-373.
24. A. Oda, H. Torigoe, A. Itadani, T. Ohkubo, T. Yumura, H. Kobayashi and Y. Kuroda, *J. Phys. Chem. C*, 2014, **118**, 15234-15241.
25. A. Oda, H. Torigoe, A. Itadani, T. Ohkubo, T. Yumura, H. Kobayashi and Y. Kuroda, *J. Phys. Chem. C*, 2013, **117**, 19525-19534.
26. Y. G. Kolyagin, I. I. Ivanova, V. V. Ordomsky, A. Gedeon and Y. A. Pirogov, *J. Phys. Chem. C*, 2008, **112**, 20065-20069.
27. V. B. Kazansky, *Kinet. Catal.*, 2014, **55**, 737-747.
28. A. Oda, T. Ohkubo, T. Yumura, H. Kobayashi and Y. Kuroda, *Phys. Chem. Chem. Phys.*, 2017, **19**, 25105-25114.

29. J. Devos, M. L. Bols, D. Plessers, C. V. Goethem, J. W. Seo, S.-J. Hwang, B. F. Sels and M. Dusselier, *Chem. Mater.*, 2020, **32**, 273-285.
30. S. C. Albarracín-Suazo, Y. J. Pagán-Torres and M. C. Curet-Arana, *J. Phys. Chem. C*, 2019, **123**, 16164-16171.
31. M. Juneau, R. Liu, Y. Peng, A. Malge, Z. Ma and M. D. Porosoff, *ChemCatChem*, 2020.
32. C. Hennig, F. Thiel, K. H. Hallmeiér, R. Szargan, A. Hagen and F. Roessner, *Spectro. Chim. Acta. A*, 1993, **49**, 1495-1497.
33. K. Wang, M. Dong, X. Niu, J. Li, Z. Qin, W. Fan and J. Wang, *Catal. Sci. Technol.*, 2018, **8**, 5646-5656.
34. L. Wang, L. Tao, M. Xie, G. Xu, J. Huang and Y. Xu, *Catal. Lett.*, 1993, **21**, 35-41.
35. B. S. Liu, Y. Zhang, J. F. Liu, M. Tian, F. M. Zhang, C. T. Au and A. S. C. Cheung, *J. Phys. Chem. C*, 2011, **115**, 16954-16962.

Chapter 3: Experimental Methods and Characterisation

Chapter 3: Experimental Methods and Characterisation Techniques

3.1 Experimental methods

3.1.1 Chemical Vapour Deposition (CVD) of zinc metal

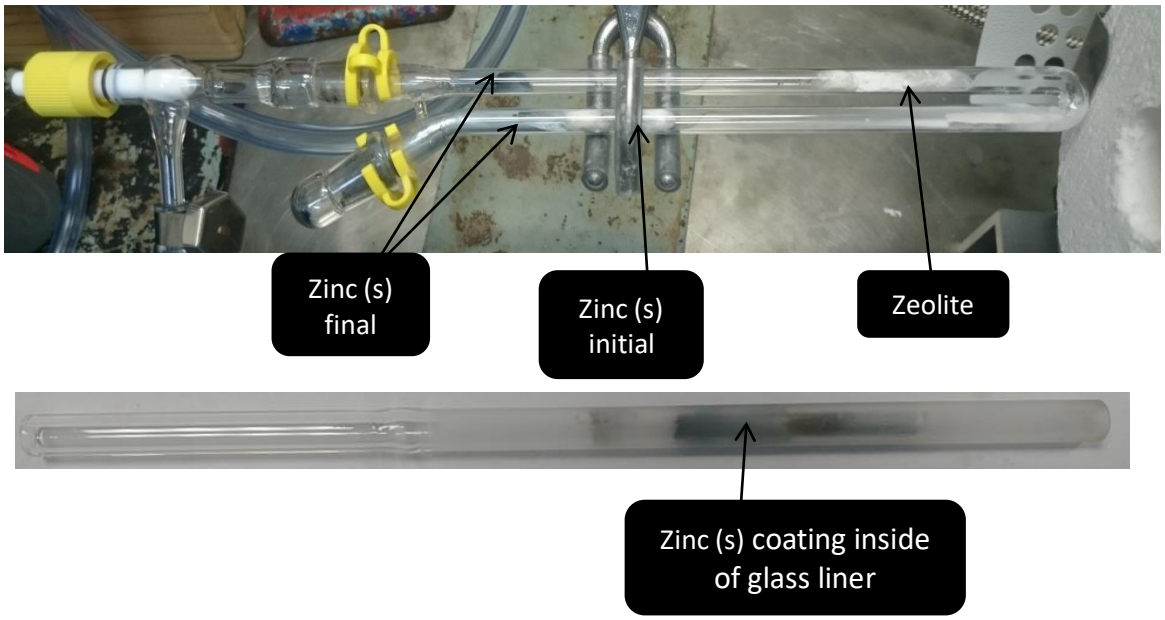

Figure 1: U-shaped quartz tube with liner specifically designed for CVD with zinc metal

Vapour deposition of zinc metal was carried out in the custom quartz u-tube shown in Figure 1. The zinc powder and dehydrated zeolite were loaded into separate sides of the u-tube, each powder held between glass wool plugs (Zn/Al = 100, typical ratios for H-ZSM-5 (15) Clar. for a vapour deposition reaction used 100 mg zeolite and 600 mg Zn powder). A close-fitting borosilicate glass insert was placed on the zeolite side of the u-tube, positioned in the areas where zinc vapour condensation occurs at cold spots (at the edge of the furnace and outside of the furnace). The loading of the u-tube was performed in an Ar filled glove box. Once loaded, the u -tube was sealed, removed from the glove box and attached to a Schlenk line and the zeolite and zinc powder were placed under vacuum (< 10^{-2} mbar). The u-tube was sealed, then inserted into a Carbolite tube furnace, ensuring both the zinc powder and zeolite were positioned in the isothermal zone of the furnace. The vapour deposition conditions were based on experimental conditions reported by Stepanov *et al*.[1] The furnace was heated to 500 °C at 5 °C min^{-1} and held for 1 h under static vacuum. Excess unreacted zinc vapour was further removed by continued heating at 500 °C for 2 h under dynamic vacuum. On the zeolite side of the u-tube, the zinc vapour condensed on the inside of the close-fitting borosilicate glass. The insert could then be removed, allowing the zeolite powder to be removed without

contamination from the condensed zinc metal. Initially, glass wool plugs were used to hold the zeolite and zinc powders in position in the u-tube, however, this resulted in erroneous elemental analysis due to the sodium content of the glass wool. Therefore, the glass wool plugs were swapped to quartz wool plugs to remove any chance of Na contamination.

It should be noted that most vapour depositions reactions were carried out using 100 mg of zeolite. Scale up reactions (> 200 mg) were attempted but methane activation results were found to be inconsistent.

3.2 Characterisation techniques

3.2.1 Nuclear Magnetic Resonance (NMR) Spectroscopy

Nuclear magnetic resonance spectroscopy is a powerful spectroscopic method for investigating the chemical structure of compounds. Radio waves are used to promote transitions between nuclear energy levels to probe the intrinsic spin properties of atomic nuclei, which in turn provide information about local structure and material composition.

Nuclear spin is an intrinsic property of atomic nuclei, which results in a magnetic moment, μ, (Equation 1) which is fundamental to NMR spectroscopy. When an atom with nuclear spin is placed into an external magnetic field (B_0), the spin can align with or against the field and $(2I + 1)$ orientations relative to the direction of the magnetic field can occur, where I is the spin quantum number, $I = \frac{n}{2}$ (n = 1, 2, 3, 4…). Each orientation has a different energy in the magnetic field and the transitions between these energy states are utilised in NMR. For example, for nuclei with spin 1/2 such as ^{1}H, there are two possible orientations for the nuclear spins to align with the magnetic field, separated by ΔE (Figure 2). The number of nuclei in each spin state is determined by the Boltzmann distribution.[2]

$$\mu = \gamma I$$

Equation 1: Magnetic moment relationship with γ (gyromagnetic ratio) and I (spin quantum number)

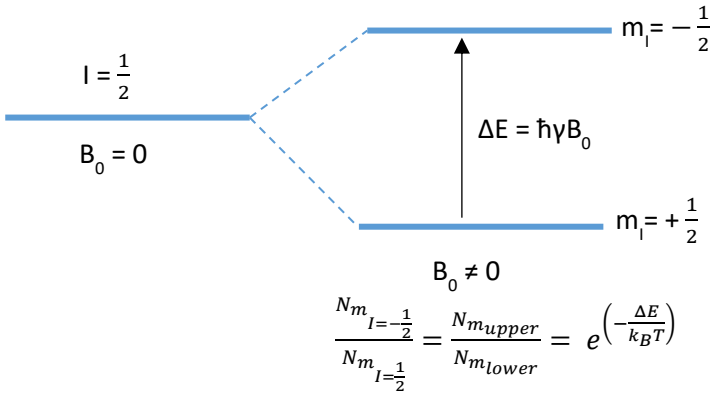

Figure 2: Nuclear spin energy diagram for splitting of I = ½ and population of levels given by Boltzmann distribution where T is temperature and k_B is the Boltzmann constant.

To obtain an NMR spectrum, a strong magnetic field is applied, lifting the degeneracy in energy levels. Short pulses of radio waves result in transitions, which promote parallel nuclear spins to an anti-parallel state resulting in a resonance which is dependent on the surroundings of the nuclei. The time taken for the nuclei to relax and return to their ground state is detected and a free induction decay (FID) is obtained. This response is dependent on the energy (ΔE), which is modified by the local environment of the spins. Shielding of the nucleus by the

surrounding electrons (chemical shift anisotropy) and dipolar coupling between nuclei (through-space interaction between two nuclear spins) are the major factors affecting the energy of spin-1/2 nuclei. Finally, a Fourier transform is carried out that relates the time-domain response to a frequency-domain spectrum which shows peaks corresponding to transitions between different nuclear energy levels.

3.2.1.1 Solid State NMR Spectroscopy

Dipolar coupling and shielding are both anisotropic interactions – that is their value has an orientation dependence. In a solution, rapid molecular tumbling averages out these interactions resulting in a sharp line in the spectrum at the isotropic chemical shift. In a powder all orientations exist and the superposition of the lines from each orientation results in very broad lines for a solid sample. To overcome the broadening, a technique called magic-angle spinning (MAS) is used for solid samples. This involves rapid sample spinning about an axis inclined at 54.7° to the external magnetic field. If the spin rate exceeds the magnitude of the anisotropic interaction a line will be observed at the isotropic chemical shift. If the spin rate is too slow, a line (centreband) will be observed at the isotropic chemical shift, but it will be accompanied by several spinning sidebands. These are separated from the centreband by an amount equal to the sample spin rate. Nuclei with a spin quantum number greater than a half, such as ^{27}Al, have a non-spherical charge distribution. This results in a quadrupole moment that can interact with the electric field gradient of the nucleus leading to a quadrupolar interaction which can change the energy levels. This can lead to line broadening that cannot be fully removed by magic-angle spinning.[3]

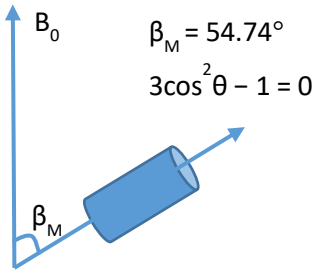

Figure 3: Magic angle spinning in solid state NMR.

3.2.1.2 ^{13}C NMR Spectroscopy

The formation of the [Zn^{II}-CH_3] species after methane activation over zinc exchanged zeolites can be monitored through ^{13}C NMR spectroscopy.[1, 4-10] As methane activation and functionalisation has been the main aim of this thesis, ^{13}C NMR has been utilised throughout for both qualitative and quantitative analysis.

Carbon spectra can be recorded using either direct-excitation or by a technique called cross polarisation (CP). The former offers a relatively straightforward approach to quantification but at the expense of measurement time. The later yields higher signal-to-noise spectra but at the expense of quantification. Furthermore, due to the nature of CP experiments, rigid species are favoured hence, direct excitation experiments can be used to observe species such as physisorbed methane. CP experiments involving the transfer of polarisation from the more abundant ^{1}H to less abundant ^{13}C nuclei were carried out. For CP experiments to take place, dipolar coupling must be present between ^{1}H and ^{13}C but also between the protons themselves. During the CP experiment, both spin-types are 'spin-locked' after the initial 90° pulse and the energy splitting for ^{1}H and ^{13}C is matched (Hartmann-Hahn matching) so polarisation can be exchanged (Figure 4). Experiments were run on a Varian VNMRS at 100.57 MHz or Bruker Avance III HD spectrometer at 100.62 MHz. When using carbon labelled methane, spectra were obtained using cross-polarisation with 2 ms contact time, 1 s recycle delay and 10,000 repetitions at a spin rate of 10 kHz. When using unlabelled methane, the number of scans was increased to 60,000 repetitions. Direct-excitation ^{13}C spectra were obtained using a 10 s recycle delay and 720 repetitions at a spin rate of 10 kHz. Spectral referencing was with respect to an external sample of neat tetramethylsilane (TMS) carried out by setting the high-frequency signal from adamantane to 38.5 ppm.

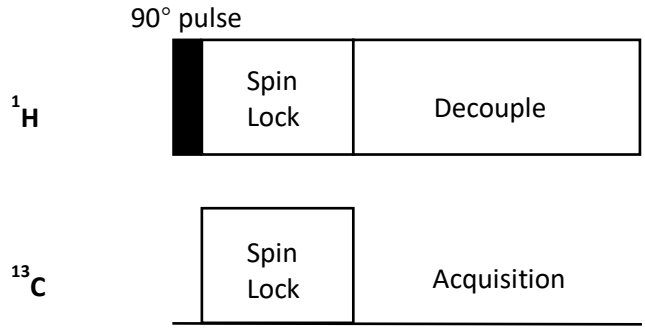

Figure 4: CP experiment consisting of a 90° pulse, spin lock and decoupling

Two-dimensional NMR techniques have been used to supplement the information gained from the direct-excitation and CP ^{13}C spectra. ^{1}H-^{13}C heteronuclear correlation experiments (HETCOR) have been carried out when spectral components have been overlapping to determine whether discrete $[Zn^{II}$-$^{13}CH_3]$ environments are present within the sample. ^{1}H-^{13}C HETCOR MAS NMR spectra were obtained using the pulse sequence shown in Figure 5 on the Bruker Avance III HD spectrometer with a 200 µs contact time, 1 s recycle delay and 128 repetitions with 256 increments. The pulse sequence consists of a 90° pulse on the protons

followed by an incremented proton evolution period. This is followed by cross polarisation to the ^{13}C nuclei and ^{13}C detection with dipolar decoupling of the protons (Figure 5).[11]

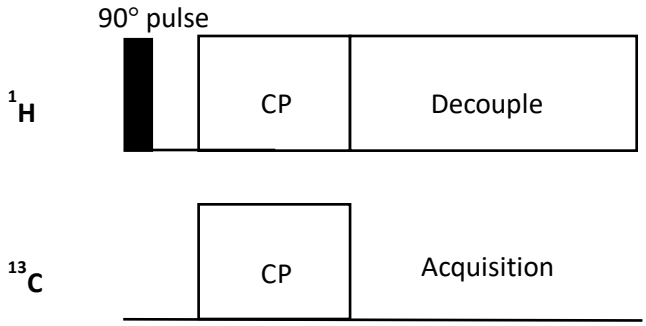

Figure 5: Pulse sequence for ^{1}H-^{13}C HETCOR experiments

Exchange spectroscopy (EXSY) experiments were carried out to determine whether multiple [Zn^{II}-CH_3] sites could chemically exchange or transfer magnetisation. This experiment is analogous to the solution state EXSY experiment except that instead of an initial 90° pulse, a CP sequence is used.[12] EXSY spectra were obtained with a mixing time of 200 ms, 1 s recycle delay and contact time of 2 ms with 128 increments repeated 16 times on the Bruker Avance III HD spectrometer. The pulse sequence is shown in Figure 6.

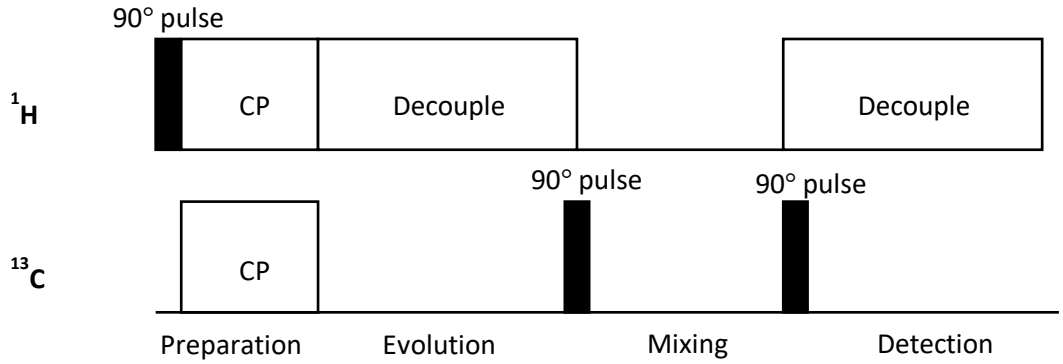

Figure 6: EXSY experiment sequence

3.2.1.3 ^{29}Si NMR Spectroscopy

As the ^{29}Si chemical shift in zeolites is related to the number and type of tetrahedrally bound atoms, ^{29}Si NMR can give direct information about the structure, co-ordination and neighbouring environments of the Si tetrahedra which form the basis of the zeolite framework.[13, 14] As the second co-ordination sphere of the Si changes, the chemical shift reflects this change (Figure 7).[15] However, these shifts do contain considerable overlap so deconvolution of the NMR spectra is often required to further understand the Si structure.

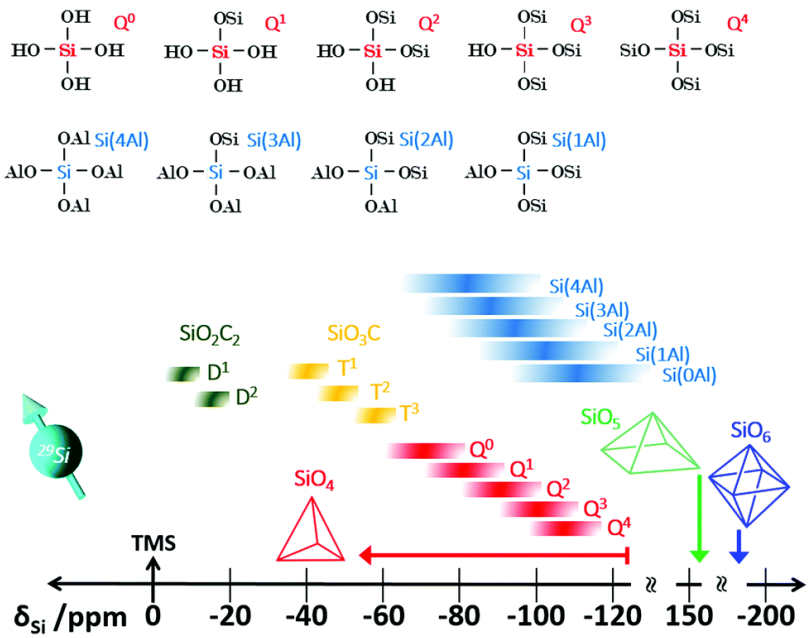

Figure 7: ^{29}Si MAS NMR spectroscopic chemical shift scale[15] Adapted from ref 15. Copyright 2018 Royal Society of Chemistry

As with ^{13}C NMR, both direct-excitation and ^{1}H-^{29}Si CP spectra are used in conjunction to gain information about the zeolite structure. Direct excitation spectra show all Si environments, whereas CP experiments enhance the signal strength of sites associated with proximal protons, nominally defect sites in zeolites. This is illustrated in Figure 8 where the direct and CP ^{29}Si spectra of partially dealuminated MOR are shown. The Q^3 sites formed through the dealumination process are clearly observed in the CP spectrum giving rise to the peak at −103 ppm.

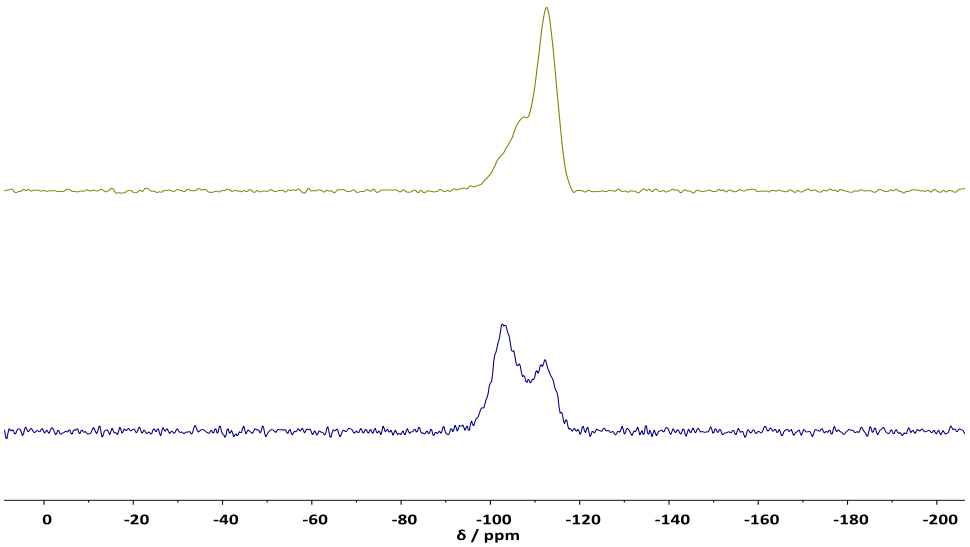

Figure 8: Comparing direct and CP ^{29}Si spectra of dealuminated MOR. (^{29}SI – 79.44 MHz, 8 kHz spin rate)

For this thesis, ^{29}Si NMR spectroscopy has been used to determine whether the harsh conditions of zinc vapour deposition have damaged the zeolite framework and also to complement ^{27}Al NMR spectroscopy in the studies of dealumination reactions on MOR. All ^{29}Si NMR spectra were acquired with a Varian VNMRS spectrometer operating with a ^{29}Si resonance frequency of 79.44 MHz. Spectra were obtained using direct excitation with a recycle delay of 30-60 s over 720 scans and a spin rate of 8 kHz. Silanol defect sites were detected using a cross-polarisation pulse sequence with a 5 ms contact time and 1 s recycle delay over 1800 scans. Spectra were referenced to an external standard of TMS by setting the high frequency signal from tetrakis(tetramethylsilyl) silane to −9.9 ppm.

3.2.1.4 ^{27}Al NMR spectroscopy

Although determining the location of aluminium in the zeolite framework is far from trivial, ^{27}Al NMR spectroscopy can be used to determine the co-ordination of the Al present in the zeolite.[16] Al is a spin 5/2 nucleus and is greatly affected by quadrupolar interactions, which leads to dehydrated zeolite samples showing extremely broad line shapes. However, the chemical shift of hydrated zeolite samples can provide significant information on the Al co-ordination environment. Framework Al (Al_{tet}) typically has a tetrahedral coordination resulting in a chemical shift of around 55 ppm whilst octahedral Al (Al_{oct}) has a chemical shift at 0 ppm.[5, 17, 18] This is particularly useful when dealumination is carried out on a zeolite framework as this process can be monitored by the increase of octahedral Al species in the NMR spectrum.

All ^{27}Al solid state NMR spectra were acquired with a Varian VNMRS spectrometer operating with a ^{27}Al resonance frequency of 104.198 MHz. All ^{27}Al spectra obtained were measured using direct excitation with a pulse duration of 1.0 µs (pulse angle ~ 30^{o}), recycle time of 0.2 sec, 7000 repetitions and a spin-rate of 14 kHz. Spectral referencing was with respect to an external sample of 1M aq. $Al(NO_3)_3$ solution.

While determining Al co-ordination is very useful, ^{27}Al NMR spectroscopy can also be used to provide important information about the zinc vapour deposition process used in this thesis. The zinc vapour reacts with Brønsted acid sites (BAS) during the CVD process. These BAS are in close proximity to Al atoms within the zeolite framework and this proximity can be probed using a Rotational Echo Adiabatic Passage Double Resonance (REAPDOR) experiment. The ^{1}H-^{27}Al REAPDOR experiment probes the aluminium-proton separation by reintroducing the dipolar coupling that is removed by magic angle spinning, thus enabling the determination of which signals in the ^{1}H spectrum are closely associated with ^{27}Al nuclei.[19] If after vapour deposition, the BAS signal can no longer be observed, full zinc exchange of the protons has taken place

(Figure 9). ^{1}H-^{27}Al REAPDOR spectroscopic experiments were carried out on the Bruker Avance III HD spectrometer. Spectra were obtained using a 1.9 mm rotor, a spin rate of 40 kHz, 2 s recycle delay and 512 repetitions at room temperature. The 1.9 mm rotor was chosen to achieve the high spin rate of 40 kHz to achieve high resolution proton spectra.

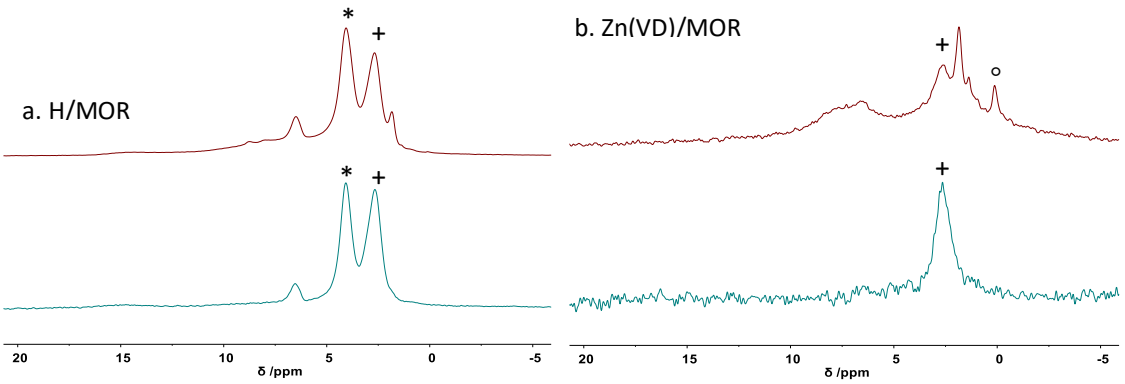

Figure 9: ^{1}H MAS NMR (red) and ^{1}H-^{27}Al REAPDOR difference spectra (green) for MOR * Signal at 4 ppm related to BAS disappeared upon zinc vapour deposition, + signal at 2.5 ppm associated with extraframework Al, o peak at 0 ppm due to adventitious silicon vacuum grease. (^{27}Al – 104.20 MHz, 14 kHz spin rate)

The REAPDOR experiment combines both rotational-echo, double resonance (REDOR) NMR, which can detect heteronuclear dipolar interactions between spin pairs, with transfer of populations double resonance (TRAPOR) NMR, where heteronuclear dipolar interactions between S=1/2 and I>1/2 spin pairs can be measured using adiabatic passages. REDOR experiments cannot be applied to quadrupolar nuclei and TRAPDOR experiments can be limited, especially for weak interactions. The REAPDOR pulse sequence consists of a combination of 180° pulses and a single adiabatic-passage pulse to allow dipolar evolution to occur for as long as the 180° pulse train is applied.

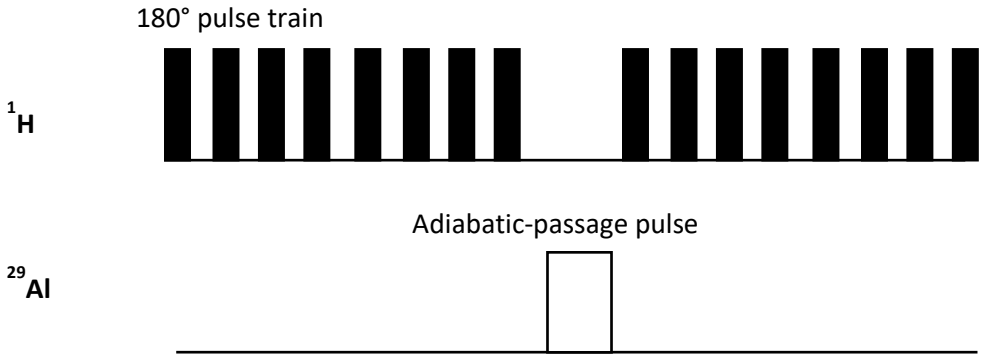

3.2.1.5 ^{133}Cs NMR spectroscopy

^{133}Cs NMR can be used to investigate the topological environments within zeolite frameworks. For example, for MOR, two distinct signals are observed in the ^{133}Cs NMR spectrum

of fully dehydrated Cs-exchanged MOR corresponding to the 12 MR and 8MR side pockets.[20, 21] For this thesis, Cs NMR has been used to determine the effect of selective dealumination on the different sites within MOR. Fully dehydrating the Cs-exchanged MOR sample is crucial to obtaining a defined Cs NMR spectrum.

All ^{133}Cs solid state NMR spectra were acquired with a Varian VNMRS spectrometer operating with a ^{133}Cs resonance frequency of 52.45 MHz. All ^{133}Cs spectra obtained were measured using direct excitation with a recycle time of 0.5 sec, 7200 repetitions and a spin-rate of 14 kHz. Spectral referencing was with respect to an external sample of 1M aq. $CsNO_3$ solution.

3.2.1.6 Solution state NMR Spectroscopy

Solution state ^{1}H NMR spectra were acquired on a Bruker Avance-400 operating at a proton frequency of 400 MHz. Solutions were prepared using acetone-d_6 (99.9% D) with an internal standard of TMS.

3.2.2 X-Ray Diffraction (XRD)

X-Ray powder diffraction is an analytical technique used for the characterisation of crystalline materials. Harsh processes like dealumination can affect the crystallinity of the zeolite sample, hence, XRD is used to assess the impact of these processes throughout this thesis. X-rays are a form of electromagnetic radiation with a wavelength of around 1 Å.[22, 23] This wavelength is comparable to the interatomic spacing of a crystal lattice; hence, X-rays can be used to study the atomic structure of crystalline materials. The crystal structure is composed of a regular array of identical lattice points of which the smallest possible repeating unit is considered the unit cell. These lattice points can be connected by two-dimensional lattice planes labelled using Miller indices, (hkl) notation. The three-dimensional unit cell can be described using one of seven crystal systems ranging from the highest symmetry cubic system (all lattice parameter lengths identical, 90° angles) to the triclinic system (no relationship between lengths or angles).X-Rays are scattered by the electron shells of individual atoms in a crystalline solid. Diffraction is observed as the scattered X-ray waves undergo interference. The relationship between the separation of the planes and construction is described by Bragg's law, where d is the lattice spacing between planes, θ is the angle of incidence to the plane and λ is the wavelength of the x-rays.

$$n\lambda = 2d_{hkl}\sin(\theta)$$

Equation 2: Bragg's law

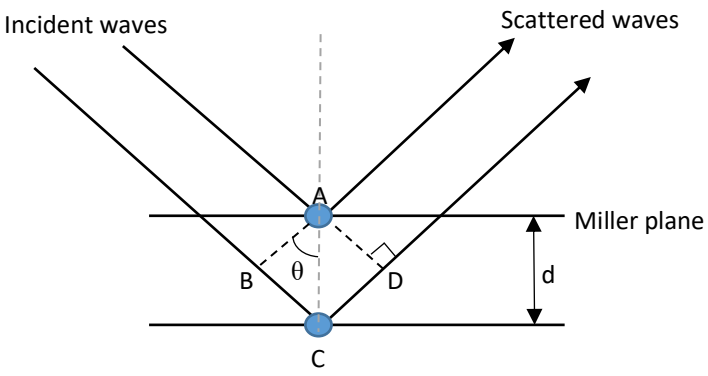

Figure 10: Simplified diagram demonstrating Bragg's law

Constructive interference is observed when the distance travelled by a wave is an integer multiple of the wavelength, i.e. when BC+CD = n λ (Figure 10). When n is a non-integer, destructive interference is seen. The scattering of an X-ray will therefore give rise to a large number of reflections which are dependent on lattice parameters, Miller indices and X-ray wavelength. The scattering power of the reflections is dependent on the number of electrons within the structure, indicated by f, the scattering factor. Atoms with a higher atomic number i.e. with more electrons scatter more intensely. The intensity of each reflection is related to the structure factor Fhkl:

$$F_{hkl} = \sum_i f_i \, e^{2\pi i\left(hx_i + ky_i + lz_i\right)}$$

Equation 3: Relationship between structure factor, Miller indices (hkl), fractional coordinates for each atom (x_i, y_i, z_i) and intensity of reflections

Most X-rays are generated using a high vacuum tube where a beam of electrons, generated by an applied voltage, is focused on a metal plate usually made from copper or molybdenum. These high velocity electrons can cause expulsion of core electrons from the atoms of the metal plate. The vacancy created is filled by an electron from a higher orbital, dropping in energy and emitting radiation in the X-ray region. For diffraction experiments, a single X-ray wavelength is required, hence, filters or monochromaters are often used.

For microporous materials such as zeolites, powder diffraction is commonly used to analyse samples due to the small crystal size.[24, 25] These experiments involve the rotation of the sample continuously to analyse and average a variety of crystal orientations. The detector scans around the sample along the circumference of a circle, cutting the diffraction cones produced from the sample. This is reported as a function of the detector angle, 2θ.

For all zeolite samples included in this report, the powder XRD patterns were recorded over a 2θ range of 5° to 70° with a step size of 0.02° on a Bruker D8 Advance diffractometer with

Cu K_α radiation (λ = 1.541 84 Å). Samples were ground and sieved to 60 mesh and adhered to a Si (9 1 1) sample holder using petroleum jelly.

3.2.3 Surface Area Analysis

As zeolites are microporous materials, gas adsorption can be used to characterise zeolite porosity, surface area and gas uptake. The high surface area of zeolites is an important characteristic for catalysis, hence, gas adsorption is a useful analytical tool. Adsorption involves the adhesion of molecules (gas or liquid) to the surface of a solid and two processes can take place – chemisorption or physisorption. Chemisorption results in the formation of chemical bonds whilst physisorption refers to the adsorbate being brought into contact with the surface of the material due to weak van der Waals interactions. Characterisation of the surface area of zeolites is primarily measured through the physisorption of probe molecules such as N_2 or Ar.

Langmuir and Brunauer Emmett Teller (BET) theories are used as models to describe adsorption. Typically gas adsorption isotherms are collected where the amount of gas adsorbed by a material (mmol/g) is plotted against the equilibrium relative pressure (p/p^0 where p^0 is the saturation vapour pressure of the adsorbate). The shape of the isotherm indicates how the adsorption process is occurring and these are classified into eight groups (Figure 11).[26]

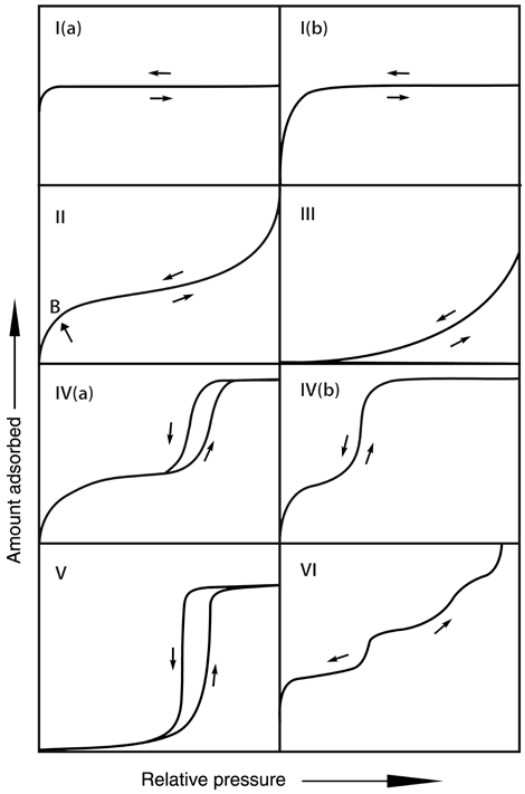

Figure 11: Classification of physiorption isotherms[26]. Adapted from ref 26. Copyright 1997 De Gruyter.

Type I isotherms are typical for microporous solids with relatively small external surfaces where the micropores are quickly saturated. Materials with mainly narrow micropores (< 1 nm) give Type I(a) isotherms whereas Type I(b) isotherms result from materials with a broader range of pore sizes (up to 2.5 nm). Type II isotherms are characteristic for nonporous or macroporous materials where unrestricted monolayer-multilayer formation adsorption can occur (completion of monolayer coverage at point B). Type III isotherms are also given by nonporous or macroporous materials, but where the monolayer formation cannot be identified. Adsorbate-adsorbate interactions are more favourable than adsorbate-adsorbent interactions so clusters are formed around favourable sites. Type IV isotherms apply to mesoporous materials where the adsorption behaviour has a similar shape to Type II isotherms until pore condensation occurs. This is where a gas condenses to a liquid-like phase at $p<p^0$ in the pore system. In Type IV(a) isotherms, capillary condensation results in hysteresis, typically for pores larger than 4 nm. Smaller mesopores result in Type IV(b) isotherms. Type V isotherms are very similar to Type III isotherms in a low p/p^0 range but at higher relative pressures, pore filling results in restricted adsorption. Finally, Type VI isotherm represent a build-up of individual layers on a uniform nonporous surface. Zeolites typically present behaviour in line with Type IV(a) isotherms (Figure 12).[26]

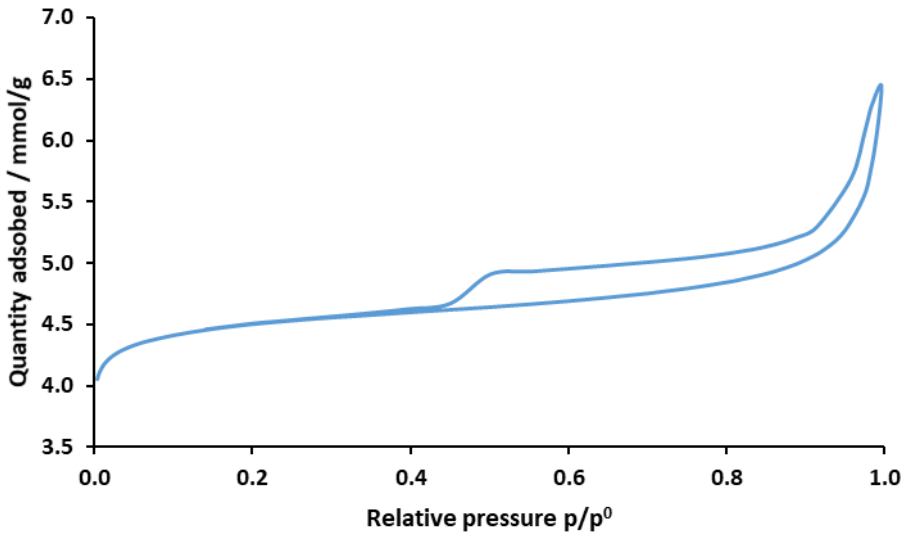

Figure 12: N_2 adsorption isotherm for NH_4-FER (10) which shows a clear Type IV(a) isotherm, common to all materials analysed in this thesis.

The Langmuir model only applies to monolayer formation, whereas BET theory can be applied to materials that form multilayers. Conflicting opinions exist about the best method to use for the calculation of zeolites' surface area as neither Langmuir or BET theories fully describe N_2 adsorption on zeolites,[27] however, BET theory is widely used and values can be compared if

calculated in similar pressure ranges. In microporous materials like zeolites, it is particularly difficult to distinguish between monolayer formation and pore filling, which in some cases can occur at very low pressures. However, using the BET equation (Equation 4) the BET model can be used to analyse the surface area of microporous materials. Note if the adsorbent conforms to BET theory and the pressure range chosen for the material is correct, the constant C must be positive and a straight line with gradient $\frac{C-1}{V_m C}$ and intercept $\frac{1}{V_m C}$ should be observed.

$$\frac{P}{V_a(P^0 - P)} = \frac{1}{V_m C} + \frac{C-1}{V_m C}\left[\frac{P}{P^0}\right]$$

Equation 4: Linear form of BET equation where V_a is the volume adsorbed, V_m is the capacity of the monolayer, and C is the BET constant related to the enthalpy of adsorption of the gas in the material

For this thesis, the surface areas and pore volumes of the zeolite samples were measured by means of nitrogen adsorption at 77 K on a Micromeritics ASAP 2020 gas adsorption analyser in a pressure range of P/P_0 = 0.005–0.15. Before the nitrogen adsorption, samples were degassed at 350 °C (623 K) for 4 hours. The total surface area was calculated via the Brunauer–Emmett–Teller (BET) equation. To confirm our pressure was within the correct range for our zeolite materials, BET measurements were carried out on NH_4-FER purchased from Alfa Aesar. We recorded a BET value of 404.1 ± 0.5 m^2/g compared with the supplier value of 400 m^2/g indicating our measurements were within the correct range. All BET measurements were carried out by Samuel Raynes at Durham University.

3.2.4 Elemental Analysis

Measuring the extraframework metal content, Si/Al ratio and coke formation of zeolites materials is fundamental to understanding these materials as catalysts.[28] Three different analytical methods have been used to probe these factors. ICP-OES and WD-XRF elemental analyses was carried out by Dr Emily Unsworth and Dr Kamal Badreshany, respectively, at Durham University.

3.2.4.1 Inductively coupled plasma optical emission spectrometry (ICP-OES)

ICP-OES is able to detect trace-levels of elements using emission spectra to identify and quantify the elements present in a material. This method requires the samples to be in solution form so solid zeolite catalysts are pretreated, often with HF acid. One key advantage to ICP-OES is very small amounts of sample are needed for quantitative analysis of metal content.

Two different acid digestion processes were used before ICP-OES analysis was carried out on the samples. Traditionally, zeolites are digested using concentrated HF solution, which is

subsequently evaporated. During this process SiF_4 is formed and lost by evaporation so Si content is unable to be determined using this method. Once evaporated, the samples are made-up to a given volume in nitric acid and the analysed by ICP-OES. Alternatively, samples can be prepared for ICP-OES by digestion using Inorganic Ventures' UniSolv Acid Dissolution reagents.[29] UA-1, the HF solution, is added to the zeolite alongside nitric acid. This is followed by addition of a stabilising reagent, UNS-1 before dilution and analysis by ICP-OES. Using this alternative method allows analysis of Si content alongside other metal content.

ICP-OES uses argon plasma to excite the sample resulting in an emission spectrum that is characteristic of the elemental composition of the material.[30] The plasma is generated using a quartz torch supplied with argon gas. A high frequency electric current is applied to a coil at the tip of the torch which ionises the argon gas generating a stable plasma at 5000 – 7000 K. The sample is introduced to the plasma through a tube in the centre of the torch where the molecules break down and give off radiation at the characteristic wavelengths of the elements present. After the light is separated into different wavelengths, the light intensity is measured and compared to a previously measured intensities of known concentrations. All ICP-OES measurements were carried out on a Jobin Yvon Horiba Ultima 2 instrument with a radial torch and sequential monochromater.

3.2.4.2 Wavelength Dispersive X-Ray Fluorescence (WDXRF)

Preparation of the zeolite sample for ICP-OES analysis can be a lengthy process due to the HF acid digestion required and using these traditional digestion methods, Si content cannot be measured. XRF is an alternative method where the interaction of X-rays with the sample is used to determine elemental composition.

When the sample is exposed to the X-rays, some of the atoms are ionised through the ejection of one or more electrons resulting in a high energy, unstable configuration.[31] An electron from a higher energy, outer orbital fills the hole and excess energy is emitted in the form of a fluorescent X-ray. The energy of the emission is characteristic of the element and as a number of transitions are possible for most atoms, a characteristic fingerprint for each element is observed in the XRF spectrum. Wavelength dispersive XRF is distinguished by the addition of crystals that disperse the fluorescent radiation into multiple wavelengths, corresponding to each element. This allows higher sensitivity and resolution, particularly of lighter elements.[32]

For WDXRF analysis, samples were fused in beads with Lithium Borate flux in a Claisse La Neo Fluxer. The fused beads were analysed on a Panalytical Zeitium WD-XRF with a 4 kW

rhodium anode tube. The samples were analysed using Panalytical's proprietary 'Wroxi' calibration and corrections were made for the variable weight of each sample.

3.2.4.3 CHN analysis

Measuring the carbon, hydrogen and nitrogen content of a zeolite sample is important both in synthesis and catalysis. Successful calcination and removal of organic SDAs can be determined from CHN analysis. In catalysis, the level of coke present in the samples can be analysed. CHN microanalysis was carried out on an Exeter Analytical Inc. E-440 elemental analyser using a dynamic flash combustion method. A very small mass of sample (2-3 mg) is placed in a tin container and purged with a helium flow.[33] The sample holder is dropped into the reactor chamber at high temperatures (900 – 1000 °C) where excess oxygen is added to the helium stream. The sample is oxidised into CO, CO_2, H_2O and NO_x and subsequent complete oxidation is achieved using a tungsten trioxide catalyst. The gaseous stream, which still contains excess oxygen, is passed over a silica tube packed with copper granules at 500 °C. This removes the excess oxygen and reduces the NO_x to N_2. Finally, the sample is transferred to a chromatographic column equipped with a thermal conductivity detector, which separates the components and calculates the C, H and N levels in the sample from CO_2, H_2O and N_2 respectively.

3.2.5 Electron microscopy

Scanning electron microscopy (SEM) and transmission electron microscopy (TEM) are used to determine crystal size, morphology and presence of metal clusters in zeolite catalysts.[34-36] Both techniques are powerful tools in catalysis as changes in the morphology of the materials after high temperature treatment or formation of metal clusters can be observed.

3.2.5.1 Scanning electron microscopy (SEM)

For this project, SEM has mainly been used to monitor if changes in zeolite morphology occur after treatment with zinc vapour or high temperature catalysis experiments. An image is produced by scanning the surface of the sample with a focussed beam of electrons at 5-15 keV.[37] This results in a number of signals including the production of secondary electrons (SE), reflected/back-scattered electrons (BSE) and X-ray emission (Figure 13).

An inelastic collision of high energy electrons with the material can result in the ionisation of valence electrons resulting in the formation secondary electrons (SE). These SE are detected and converted to photons by a scintillator resulting in a topographical map of the material. The BSE, which are a result of elastic scattering, alongside the X-rays produced can be used for analytical SEM to gain further understanding of elemental composition. SEM was

performed on a FEI Helios Nanolab SEM operated at 5 kV on samples which had been coated with 20 nm gold using a Cressington sputter coater 108 Auto.

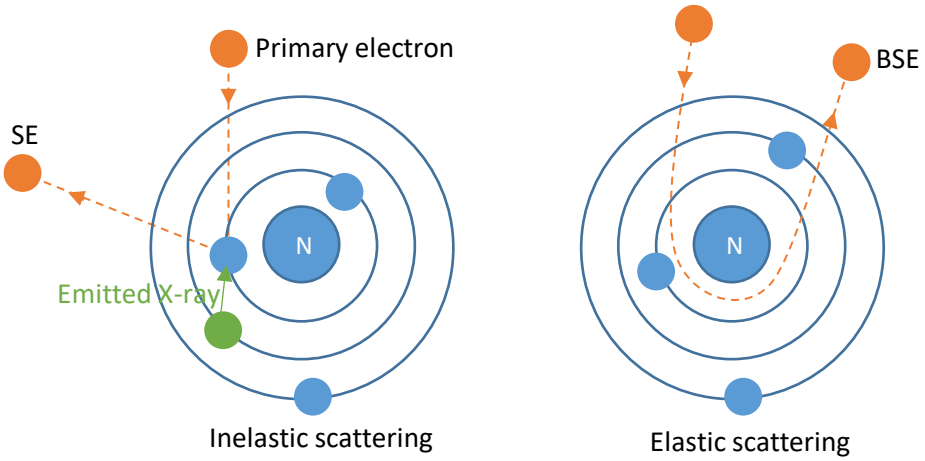

Figure 13: Different signals produced from SEM. Left: production of secondary electrons used primarily for imaging and X-Ray emission which can be used for elemental analysis. Right: formation of back scattered electrons from elastic scattering.

3.2.5.2 Transmission electron microscopy (TEM)

As TEM can produce a higher resolution image than SEM, it can be used to determine whether metal clusters have formed in or on the surface of the zeolite. The image is produced by transmitted electrons rather than reflected electrons in TEM. A high voltage electricity supply powers the cathode which generates the beam of electrons which travel through a vacuum down the microscope.[38] An electromagnetic coil (first lens) concentrates the electrons into a more powerful beam before a second lens focuses the beam onto the sample. After passing through the sample, a third lens magnifies the image which is formed by the transmitted electrons hitting the fluorescent screen at the base of the microscope. TEM was performed on a JEOL 2100F TEMA FEI Helios Nanolab SEM operated at 200 KeV. The zeolite sample was deposited on a holey carbon film on 300 mesh copper grid.

3.2.6 X-Ray absorption spectroscopy (XAS)

X-Ray absorption spectroscopy experiments were carried out at the Diamond Light Source synchrotron facility to study the nature of zinc after ion exchange and vapour deposition into zeolites. This in turn allowed investigation of the zinc site active for breaking the C-H bond of methane.

X-Ray absorption near edge structure (XANES) analysis is sensitive to the local bonding environment and can be used to determine catalytically active sites in zeolites.[39-44] The fundamental principle of XANES is the absorption of an X-ray photon into a core level of the

sample which is followed by photoelectron emission.[45] This results in either fluorescence or the emission of an Auger electron (Figure 14). In XANES measurements, the initial photoelectron is measured alongside the fluorescence photon or Auger electron. As the initial X-ray photon is absorbed, an absorption edge is observed in the XAS spectrum which corresponds to a specific core electron. For this thesis, all transmission measurements were carried out on the K-edge, corresponding to the 1s electrons of Zn.

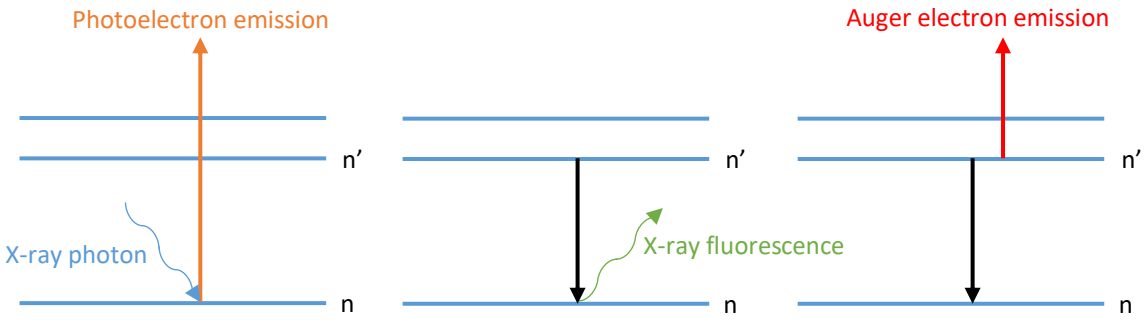

Figure 14: Fundamental principles of XANES involving the absorption of an X-ray photon resulting in photoelectron emission followed by either X-Ray fluorescence or Auger electron emission.

The spectra are often complex consisting of pre-edge features, which correspond to weak transitions below the absorption edge. The XANES spectrum is normally considered to be within 50 eV of the absorption edge whilst the Extended X-Ray Absorption Fine Structure (EXAFS) corresponds to the oscillating region spanning from 50 eV to 1000 eV above the edge. XANES spectra are sensitive to the co-ordination environment of the absorbing atom and can be used to determine the average oxidation state of the element in the sample, hence, providing key information about the active site in our zeolite catalysts.

As for all absorption techniques, the Beer-Lambert law can be applied to XAS measurements. Traditionally, absorbance is defined as a function of concentration for solution samples (Equation 5, (1)). As this cannot be defined for a solid, for XANES measurements on solids samples, the absorbance can be related to the absorption coefficient, μ and the thickness of the sample (Equation 5, (2)).

$$A = \log\left(\frac{I_0}{I_t}\right) = \varepsilon c l \qquad (1) \quad A = \ln\left(\frac{I_0}{I_t}\right) = \mu t \qquad (2)$$

Equation 5: (1) Beer-Lambert law for solutions where I_0 is the intensity of incident rays, I_t is the transmitted intensity, ε is the molar absorption coefficient, c is molar concentration and l is the optical path length. (2) Beer-Lambert law for solids where μ is the absorption coefficient and t is sample thickness used for XAS analysis.

Analysis of the EXAFS region of the XAS spectra can provide further information on the atom's local environment.[45] Wave interactions between the ejected photoelectron and

surrounding electrons result in oscillations in the EXAFS. The oscillations are characteristic of the surrounding environment as different distances and back scattering paths, resulting in different wave interactions, will be observed from different elements. These oscillations can be described by fluctuations in the absorption coefficient, described by Equation 6. EXAFS fitting and analysis was carried out by Dr. Simon Beaumont at Durham University.

$$\chi(E) = \frac{\mu(E) - \mu_0}{\mu_0}$$

Equation 6: EXAFS, $\chi(E)$, can be defined as the normalised oscillatory part of the absorption coefficient, $\mu_0$is defined as the smooth varying portion of μ past the edge.

The Zn/zeolite and Zn/CH_4/zeolite samples were mixed with cellulose binder in a glovebox, pressed into pellets and placed into an airtight cell (approximately 25 mg of zeolite mixed with 15 mg of cellulose). The XANES and EXAFS spectra of the Zn–K edge for the studied samples were obtained at the B18 beamline, Diamond Light Source. An electron beam energy of 3 keV and average stored current of 300 mA was used as the source of radiation. The X-ray energy was monitored with a channel cut Si(111) monochromator. All spectra were recorded under transmission mode with steps of 0.3 eV.

3.2.7 Further Analysis of Carbonaceous Deposits

Carbonaceous deposits formed in the reaction of methane to benzene was further analysed using Ultra Violet-Raman analysis, temperature programmed oxidation with mass spectrometry (TPO-MS) and atmospheric solid analysis probe – mass spectrometry (ASAP-MS).

UV-Raman was conducted on a Renishaw inVia Spectrometer equipped with a 266 nm laser line. A few mg of the powder sample was placed on an aluminium plate and pressed into a flat disc using a glass slide. The sample disc was focussed under white light prior to the UV-Raman measurement. The measurement was conducted at between 5 – 10% laser power to avoid damaging the carbonaceous deposits. The signal was accumulated for 30 minutes at a resolution of 4 cm^{-1}. Raman signal was recorded from two different regions of the sample disc to ensure the same species of carbonaceous deposit was present throughout the sample. UV – Raman anlaysis was carried out by Dr. Abdul Adedigba.

TPO-MS was carried out in a 10% oxygen stream using a Perkin Elmer Pyris 1 TGA connected to a Hiden HPR 20 mass spectrometer. The temperature was ramped from room temperature to 800 °C at 10 °C min^{-1} with a one hour hold at 150 °C to remove any water. TPO-MS analysis was carried out by Mr William Carswell.

ASAP-MS was carried out on spent zeolite catalysts (solid samples or as extracted coke in DCM) using an LCT Premier XE mass spectrometer. A melting point tube was dipped into the sample and analysis was carried out isothermally at 350 °C. Any volatile products were vaporised and atmospheric pressure chemical ionisation occurred.

3.3 Chapter 3 References

1. A. A. Gabrienko, S. S. Arzumanov, M. V. Luzgin, A. G. Stepanov and V. N. Parmon, *J. Phys. Chem. C*, 2015, **119**, 24910-24918.
2. M. T. Weller and N. A. Young, in *Characterisation methods in Inorganic Chemsitry*, 2017, ch. 3, pp. 66-112.
3. M. J. Duer, in *Solid-State NMR Spectroscopy Principles and Applications*, DOI: 10.1002/9780470999394.ch1, ch. 1, pp. 1-72.
4. A. A. Gabrienko, S. S. Arzumanov, A. V. Toktarev, I. G. Danilova, I. P. Prosvirin, V. V. Kriventsov, V. I. Zaikovskii, D. Freude and A. G. Stepanov, *ACS Catal.*, 2017, **7**, 1818-1830.
5. J. Xu, Q. Wang, S. Li and F. Deng, in *Solid-State NMR in Zeolite Catalysis*, Springer Singapore, Singapore, 2019, DOI: 10.1007/978-981-13-6967-4_3, pp. 93-132.
6. G. Qi, Q. Wang, J. Xu, J. Trébosc, O. Lafon, C. Wang, J.-P. Amoureux and F. Deng, *Angew. Chem. Int. Ed.*, 2016, **55**, 15826-15830.
7. G. Qi, J. Xu, J. Su, J. Chen, X. Wang and F. Deng, *J. Am. Chem. Soc.*, 2013, **135**, 6762-6765.
8. M. A. Shah, S. Raynes, D. C. Apperley and R. A. Taylor, *Chem. Phys. Chem*, 2020, **21**, 673-679.
9. Y. G. Kolyagin, I. I. Ivanova, V. V. Ordomsky, A. Gedeon and Y. A. Pirogov, *J. Phys. Chem. C*, 2008, **112**, 20065-20069.
10. Y. G. Kolyagin, I. I. Ivanova and Y. A. Pirogov, *Solid State Nucl. Magn. Reson.*, 2009, **35**, 104-112.
11. K. Schmidt-Rohr, J. Clauss and H. W. Spiess, *Macromolecules*, 1992, **25**, 3273-3277.
12. N. M. Szeverenyi, M. J. Sullivan and G. E. Maciel, *J. Magn. Reson*, 1982, **47**, 462-475.
13. G. Engelhardt, in *Stud. Surf. Sci. Catal.*, eds. J. Klinowski and P. J. Barrie, Elsevier, 1989, vol. 52, pp. 151-162.
14. H. Koller and M. Weiß, in *Solid State NMR*, ed. J. C. C. Chan, Springer Berlin Heidelberg, Berlin, Heidelberg, 2012, DOI: 10.1007/128_2011_123, pp. 189-227.
15. G. Paul, C. Bisio, I. Braschi, M. Cossi, G. Gatti, E. Gianotti and L. Marchese, *Chem. Soc. Rev.*, 2018, **47**, 5684-5739.
16. J. B.Nagy and E. G. Derouane, in *Perspectives in Molecular Sieve Science*, American Chemical Society, 1988, vol. 368, ch. 1, pp. 2-32.
17. A. A. C. Reule, J. A. Sawada and N. Semagina, *J. Catal.*, 2017, **349**, 98-109.
18. M. Ravi, V. L. Sushkevich and J. A. van Bokhoven, *J. Phys. Chem. C*, 2019, **123**, 15139-15144.
19. T. Gullion, *Chem. Phys. Lett.*, 1995, **246**, 325-330.
20. P. J. Chu, B. C. Gerstein, J. Nunan and K. Klier, *J. Phys. Chem.*, 1987, **91**, 3588-3592.
21. P. Norby, F. I. Poshni, A. F. Gualtieri, J. C. Hanson and C. P. Grey, *J. Phys. Chem. B*, 1998, **102**, 839-856.
22. Barbara L. Dutrow and C. M. Clark, X-ray Powder Diffraction (XRD), https://serc.carleton.edu/research_education/geochemsheets/techniques/XRD.html, (accessed 30th August, 2019).
23. M. T. Weller and N. A. Young, in *Characterisation Methods in Inorganic Chemistry*, Oxford University Press, USA, 2017, ch. 2, pp. 20-38.
24. M. M. J. Treacy and J. B. Higgins, in *Collection of Simulated XRD Powder Patterns for Zeolties*, 2007, DOI: https://doi.org/10.1016/B978-0-444-53067-7.X5470-7, ch. 2, pp. 18-475.
25. H. van Koningsveld and J. M. Bennett, in *Structures and Structure Determination*, eds. C. Baerlocher, J. M. Bennett, W. Depmeier, A. N. Fitch, H. Jobic, H. van Koningsveld, W. M. Meier, A. Pfenninger and O. Terasaki, Springer Berlin Heidelberg, Berlin, Heidelberg, 1999, DOI: 10.1007/3-540-69749-7_1, pp. 1-29.
26. M. Thommes, *Pure Appl. Chem.*, 2016, **38**, 25.

27. R. Cid, R. Arriagada and F. Orellana, *Journal of Catalysis*, 1983, **80**, 228-230.
28. H. Kosslick and R. Fricke, in *Characterization II*, eds. H. G. Karge and J. Weitkamp, Springer Berlin Heidelberg, Berlin, Heidelberg, 2007, DOI: 10.1007/3829_001, pp. 1-66.
29. P. Gaines, Elemental Analysis of Zeolites, https://www.inorganicventures.com/guides-and-papers/elemental-analysis-of-zeolites, (accessed Jan, 2019).
30. R. D. Koons, *J. Am. Chem. Soc.*, 2003, **125**, 16154-16154.
31. F. Scholze, in *Handbook of Practical X-Ray Fluorescence Analysis*, 2006, pp. 199-308.
32. R. L. Jenkins, in *X-Ray Fluorescence Spectrometry*, 2012, DOI: 10.1002/9781118521014.ch7, pp. 111-121.
33. A. M. Committee, *The Royal Society of Chemistry Analytical Methods Committee* 2008.
34. M. Pan, *Micron*, 1996, **27**, 219-238.
35. A. Mayoral, Y. Sakamoto and I. Diaz, in *Advanced Transmission Electron Microscopy: Applications to Nanomaterials*, eds. F. L. Deepak, A. Mayoral and R. Arenal, Springer International Publishing, Cham, 2015, DOI: 10.1007/978-3-319-15177-9_4, pp. 93-138.
36. W. Wan, J. Su, X. D. Zou and T. Willhammar, *Inorganic Chemistry Frontiers*, 2018, **5**, 2836-2855.
37. A. Ul-Hamid, in *A Beginners' Guide to Scanning Electron Microscopy*, 2018, ch. 2, pp. 15-76.
38. R. F. Egerton, in *Physical Principles of Electron Microscopy*, 2005, ch. 3, pp. 57-92.
39. J. A. van Bokhoven and C. Lamberti, in *XAFS Techniques for Catalysts, Nanomaterials, and Surfaces*, eds. Y. Iwasawa, K. Asakura and M. Tada, Springer International Publishing, Cham, 2017, DOI: 10.1007/978-3-319-43866-5_20, pp. 299-316.
40. D. E. Doronkin, M. Casapu, T. Günter, O. Müller, R. Frahm and J.-D. Grunwaldt, *J. Phys. Chem. C*, 2014, **118**, 10204-10212.
41. G. T. Palomino, S. Bordiga, A. Zecchina, G. L. Marra and C. Lamberti, *J. Phys. Chem. B*, 2000, **104**, 8641-8651.
42. S. M. T. Almutairi, B. Mezari, P. C. M. M. Magusin, E. A. Pidko and E. J. M. Hensen, *ACS Catal.*, 2012, **2**, 71-83.
43. A. Oda, T. Ohkubo, T. Yumura, H. Kobayashi and Y. Kuroda, *Dalton Trans.*, 2015, **44**, 10038-10047.
44. C. Hennig, F. Thiel, K. H. Hallmeiér, R. Szargan, A. Hagen and F. Roessner, *Spectro. Chimi. Acta. A,* 1993, **49**, 1495-1497.
45. Y. Joly and S. Grenier, in *X-Ray Absorption and X-Ray Emission Spectroscopy*, DOI: 10.1002/9781118844243.ch4, pp. 73-97.

Chapter 4: Framework Effects on Activation and Functionalisation of Methane in Zinc-Exchanged Zeolites

Includes published work, M. A. Shah, S. Raynes, D. C. Apperley and R. A. Taylor, *ChemPhysChem*, 2020, **21**, 673-679 with permission from all authors. The paper can be found in Appendix 8.

Chapter 4: Framework Effects on Activation and Functionalisation of Methane in Zinc-Exchanged Zeolites[1]

4.1 Introduction

In 2004, Kazansky *et al.* reported the heterolytic bond dissociation of CH_4 over zinc-modified ZSM-5.[2, 3] A major advantage of these zinc-based systems, compared to copper or iron exchanged zeolites, is the ability to form active species without an initial high temperature oxidation step as required for iron and copper modified zeolites.[4] Whilst framework bound Zn^{2+} cations are believed to be responsible for C-H activation within zeolite frameworks,[2, 5-7] the nature of the zinc species formed is dependent on the method of zinc introduction.[8] Incipient wetness impregnation (IWI) and ion exchange using a decomposable zinc salt are two commonly practiced methods. Whereas ion exchange methods introduce predominantly Zn^{2+} cations,[9] IWI can result in the formation of a variety of species including $[Zn\text{-}O\text{-}Zn]^{2+}$ [8] or ZnO clusters[10, 11] alongside partially hydrolysed $[Zn\text{-}OH]^{+}$ extraframework ions,[12] which complicates understanding and studying the active species responsible for C-H activation by zinc.[13, 14]

Chemical vapour deposition (CVD) methods can also be used to introduce zinc into zeolites. Vapour deposition with zinc metal leads to a redox reaction involving the exchange of Brønsted acid sites (BAS) for Zn^{2+} cations and the evolution of H_2 gas.[2, 5, 6, 15]

$$Zn_{(s)} + 2H^{+}{}_{(s)} \rightarrow Zn^{2+}{}_{(s)} + H_{2\,(g)}$$

Equation 1: Reaction of zinc metal with Brønsted acid sites (BAS) under vapour deposition conditions to form extraframework Zn^{2+} cations and H_2 gas

Under certain CVD conditions, additional zinc species have been detected (Zn^{+},[16] $[Zn_2]^{2+}$ [17]) but these have not been reported to react with methane. The level of zinc exchange can also vary with the method of zinc introduction. Whilst CVD often results in complete exchange of BAS, IWI and ion exchange techniques often result in lower zinc exchange levels at extraframework positions.[2, 18, 19] Reduced zinc loading, particularly in high silica zeolites, is often attributed to the difficulty of stabilising the formal 2+ charge associated with Zn^{2+} cations by remote $[AlO_4]^{-}$ pairs.[20]

As evidenced by DRIFTS and MAS NMR studies, methane activation at Zn^{2+} exchanged ZSM-5 zeolites is generally accepted to result in heterolytic cleavage of the C-H bond in methane, leading to the formation of a [Zn^{II}-CH_3] species and a new BAS (Scheme 1). [2, 5-7]

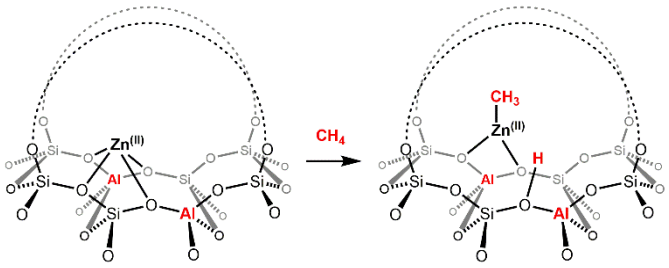

Scheme 1: C–H activation step for dissociative adsorption of methane over Zn^{2+} forming a [Zn^{II}-CH_3] species and a BAS

Spectroscopic and theoretical studies have shown that the process of C-H activation proceeds through initial complexation of methane to the Lewis acidic Zn^{2+} species, with a CH_4 δ(C-H) orbital donating electron density into the Zn-4s orbital (methane sigma complex), after which the framework oxygen atom acts as a Lewis base, leading to C-H bond cleavage.[2, 5, 9, 21] The resulting [Zn^{II}-CH_3] species has a distinctive ^{13}C MAS NMR chemical shift of −19 ppm, characteristic of methyl groups in organozinc compounds.[15, 22]

Reactivity of the resulting zinc methyl fragment with other small molecules has been explored by a number of groups, in the context of stoichiometric reactions as well as potential catalytic applications. Addition of dioxygen to [Zn^{II}-CH_3]/ZSM-5 at elevated temperature has been shown to result in the formation of zinc methoxy and zinc formate species, as monitored through NMR spectroscopic studies. [6, 14] Reactivity with O_2 has also been observed at ambient temperature, forming a zinc methoxy species, which was able to form methanol upon extraction with H_2O.[6, 23] It has also been shown that the chemical reactivity of [Zn^{II}-CH_3] within ZSM-5, with molecules such as CO, CO_2 and H_2O, has been found to be very similar to that of organozinc compounds.[6, 14, 24]

Whilst methane activation and oxidation has been explored over zinc-modified ZSM-5, the effect of the zeolite framework on the activation and subsequent functionalisation steps has not yet been investigated. To this end we have conducted a series of studies exploring the C-H activation of methane in three different zinc-modified frameworks, MFI, MOR and FER, which have intrinsically different micropore topologies. We report that selective methane activation occurs over ZSM-5, FER and MOR zeolites that have been modified by zinc vapour at elevated temperature. Solid state NMR spectroscopic studies have shown that two distinct [Zn^{II}-CH_3] species are formed in MOR, due to the very different topological environments within the MOR Framework. Additionally we show that the zeolite framework can influence the observed

product(s) when [Zn^{II}-CH_3] reacts with O_2 or air. Uniquely, methanol is the sole observable carbon containing product when the [Zn^{II}-CH_3] species is exposed to air for Zn(VD)/MOR. These results point at the ability of the framework topology to effect the outcome of the reaction in methane oxidation as mediated by zinc-exchanged zeolites.

4.2 Results and Discussion

4.2.1 The effect of zeolite framework on CH_4 activation

The three zeolite frameworks, MFI, FER and MOR, investigated for CH_4 activation vary significantly in zeolite micropore topology. The frameworks range from 3D to 1D channel systems with varying ring sizes and channel diameters, as given in Table 1.

Table 1: Zeolite topology including ring sizes and channel system for MFI, FER and MOR type zeolites. Images from IZA website.

	MFI	**FER**	**MOR**
	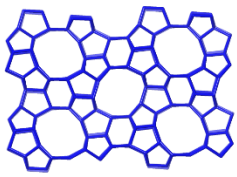	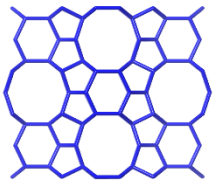	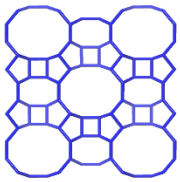
Channel system	3D	2D	1D[1]
Ring sizes (nMR)	10, 6, 5, 4	10, 8, 6, 5	12, 8, 5, 4
Channel diameter (nMR : Å)	10: 5.1 x 5.5 10: 5.3 x 5.6	10: 4.2 x 5.4 8: 3.5 x 4.8[2]	12: 6.5 x 7.0 8: 2.6 x 5.7 Side pocket: 3.4 x 4.8

Zinc-exchanged zeolites of three differing frameworks, H-ZSM-5, NH_4-FER and H-MOR, were prepared by chemical vapour deposition (CVD) with an excess of zinc metal (100:1 Zn:Al) in a custom designed u-shaped quartz tube (Section 3.1.1). CVD was carried out at 500 °C under reduced pressure (less than 10^{-2} mbar). This was followed by methane activation at 250 °C, based on conditions reported previously by Stepanov *et al*.[6] Particular care was taken to prevent aerial oxidation, especially after CH_4 exposure, hence, all the samples was transferred to a glovebox and packed into an NMR rotor in an inert environment (Ar). An additional sample prepared by aqueous ion exchange (IE) was also prepared to provide a comparison to the CVD samples.

[1] Although MOR has a 2D channel system, the 8 MR channel can only accommodate He due to small size (2.6 Å kinetic diameter), therefore MOR will be treated as a 1D channel system
[2] 8 MR of FER run horizontally through the image shown.

CVD methods introduce predominantly Zn^{2+} cations to high exchange levels.[2, 5, 7] Under certain CVD conditions, additional zinc species have been detected (Zn^{+},[16] $[Zn_2]^{2+}$ [17]), but these have not been reported to react with methane. To investigate the level of exchange of the BAS for zinc cations after CVD treatment with zinc metal vapour, ^{1}H NMR and ^{1}H-^{27}Al REAPDOR NMR spectroscopic experiments were conducted on the parent zeolites and the products of the CVD reaction. The ^{1}H-^{27}Al REAPDOR experiment probes the aluminium-proton separation by reintroducing the dipolar coupling that is removed by magic angle spinning, thus enabling the determination of which signals in the ^{1}H spectrum are closely associated with ^{27}Al.[25] For the parent zeolites, the signal at 4.0 ppm corresponding to BAS or 6.6 ppm corresponding to $[NH_4]^{+}$ (in the case of FER), is clearly associated with Al as determined by the appearance in the ^{1}H-^{27}Al REAPDOR difference spectrum (MOR: Figure 1a; ZSM-5: Figure 1c; FER: Figure 1e). Upon exposure to zinc vapour, this peak either disappears indicative of full exchange with Zn^{2+} (MOR: Figure 1b, FER: Figure 1f) or decreases drastically (ZSM-5) (Figure 1d).

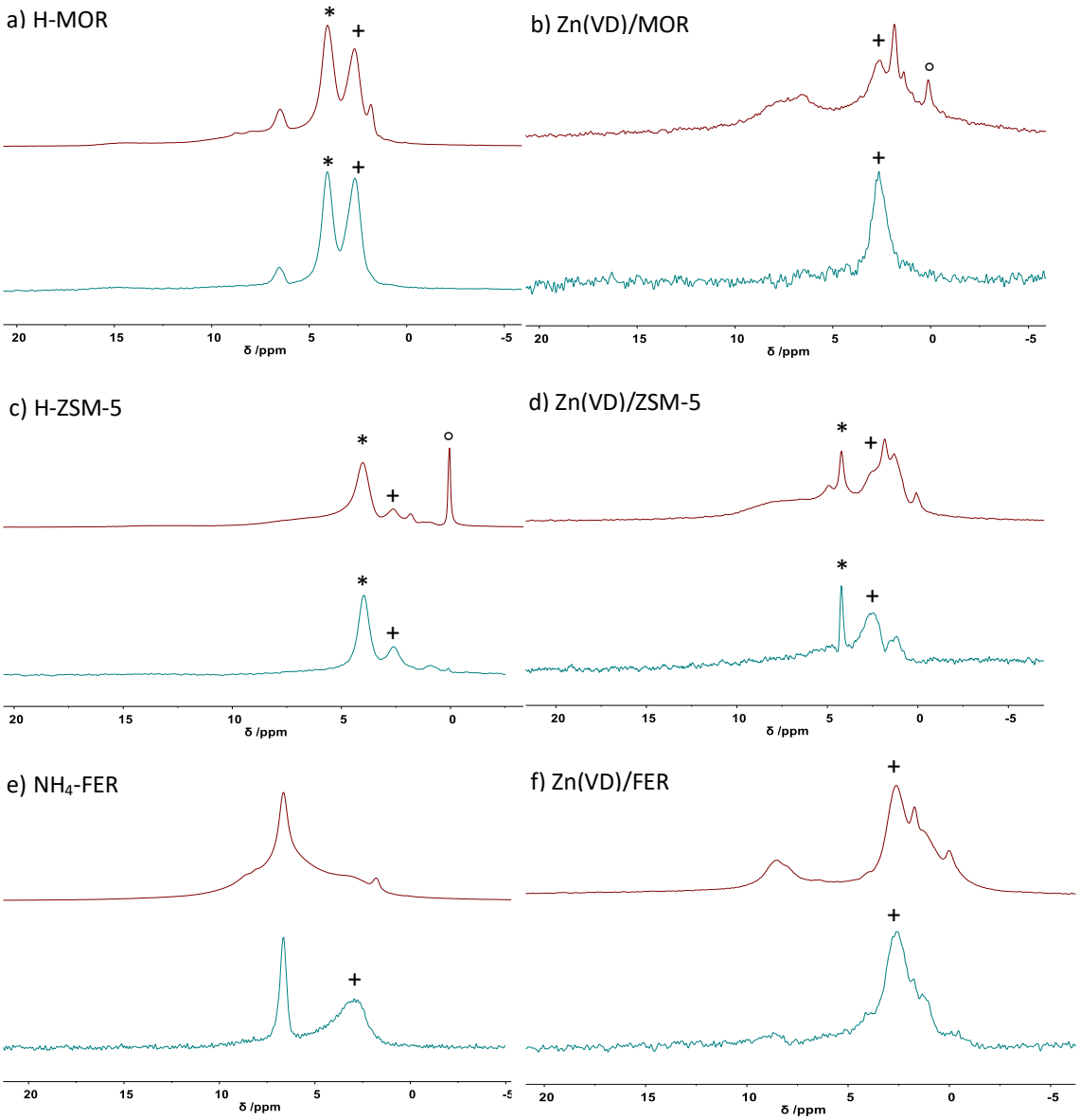

Figure 1: ^{1}H MAS NMR (red) and ^{1}H-^{27}Al REAPDOR difference spectra (green) for MOR, ZSM-5 and FER frameworks * Signal at 4 ppm related to BAS (MOR and ZSM-5) disappears upon vapour deposition of zinc metal. For FER signal due to NH_4^+ (6.6 ppm) disappears upon vapour deposition. $^+$Signal at 2.5 ppm associated with extraframework Al. ^{o} Peak at 0 ppm due to adventitious silicon vacuum grease. (^{1}H – 399.48 MHz, 40 kHz spin rate)

Elemental analysis (Table 2) was also used to determine the extent of zinc exchange after CVD and ion exchange. The Zn/Al ratios were found to be over the theoretical maximum exchange value of 0.5 for all CVD samples but values greater than 0.5 have previously been observed and attributed to excess Zn(0) present within the sample.[18] The higher than expected Zn/Al ratio will be discussed further in Chapter 6. Brunauer–Emmett–Teller (BET) measurements were carried out in order to confirm that the zinc introduction methods did not cause pore blockage of the zeolites, particularly for MOR, which has a unidirectional pore system. A small reduction in surface area is observed due to the presence of extraframework zinc (Table 1), similar to the results of Pidko *et al.*.[18]

Table 2: Elemental analysis, BET measurements and C-H activation results for zinc-exchanged zeolites.

Sample (given Si/Al)	Measured Si/Al*	Zn/Al#	BET / m^2/g	Successful C-H activation
H-ZSM-5 (15)	12.5	-	435.0 ± 0.2	N
NH_4-ZSM-5 (12.5)	11.6	-	447.3 ± 0.4	N
H-MOR (10)	7.9	-	542.2 ± 1.6	N
NH_4-FER (10)	11.2	-	404.1 ± 0.5	N
Zn(VD)/ZSM-5	12.5	0.78	303.7 ± 0.4	-
Zn(VD)/CH_4/ZSM-5	12.5	0.73		Y
Zn(VD)//FER	11.2	0.69	305.5 ± 0.3	-
Zn(VD)//CH_4/FER	11.2	0.77		Y
Zn(VD)//MOR	7.9	0.74	421.9 ± 0.6	-
Zn(VD)//CH_4/MOR	7.9	0.75		Y
Zn(IE)//H-ZSM-5	11.6	0.45	377.3 ± 0.3	Y

***determined by WDXRF, # determined by ICP-OES**

The materials have been additionally analysed by powder X-ray diffraction (pXRD) to determine the effect of CVD on the zeolite structure. Figure 2 compares the pXRD patterns of the parent zeolites with the pXRD patterns after vapour deposition confirming that after CVD of zinc metal the framework remains intact. Furthermore, no additional reflections corresponding to zinc metal were observed in the pXRD patterns.

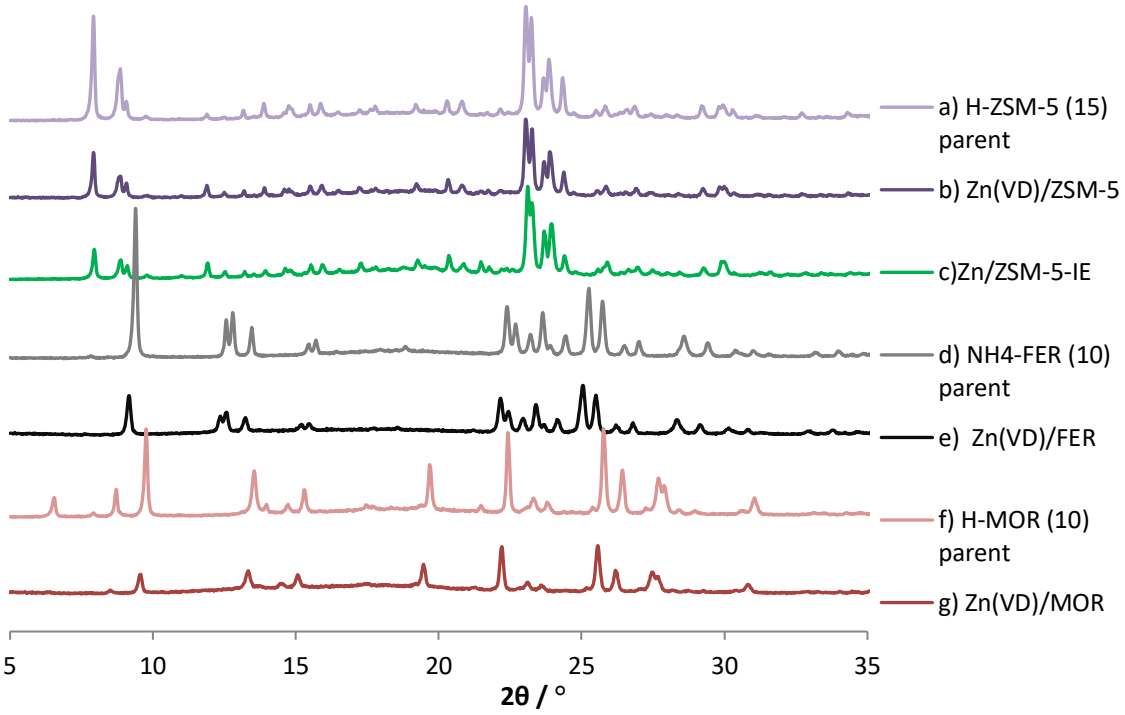

Figure 2: pXRD patterns for ZSM-5 (purple), FER (black) and MOR (red). Note parent zeolite pXRD patterns collected as packed samples whilst Zn/zeolite samples collected with sample adhered to Si wafer using petroleum jelly.

^{27}Al NMR and ^{1}H-^{29}Si CP NMR spectroscopy**,** demonstrated in Figure 3, can be used to assess the state of the framework post reaction with zinc vapour. Framework Al (Al_{tet}) typically has a tetrahedral coordination resulting in a chemical shift of around 55 ppm, whilst octahedral Al (Al_{oct}) has a chemical shift at 0 ppm.[26] No additional extra framework Al was observed after zinc CVD as determined through ^{27}Al MAS NMR spectroscopy as no increase is observed in the signal at 0 ppm. Analysis by ^{1}H-^{29}Si CP NMR spectroscopy established that no additional defects arose within the zeolites, as no increase is observed in signals associated with Q^3 and Q^4 Si environments, after exposure to zinc metal vapour. Direct ^{29}Si spectra can be found in Appendix 1.

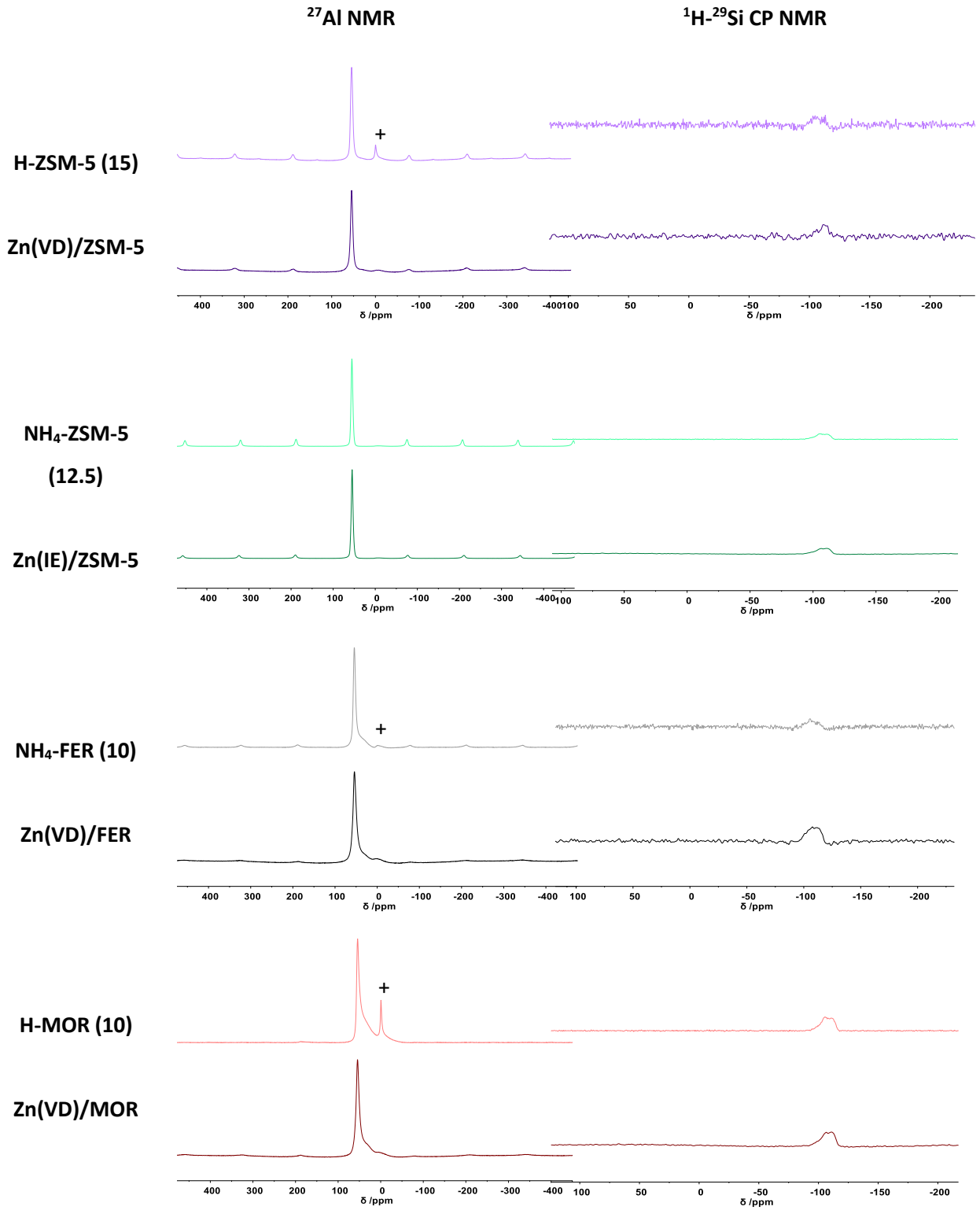

Figure 3: ^{27}Al NMR and ^{1}H-^{29}Si CP NMR spectra for parent zeolites and Zn/Zeolites. $^{+}$Associated with extraframework Al. (^{27}Al – 104.20 MHz, 14 kHz spin rate and ^{29}Si – 79.44 MHz, 8 kHz spin rate)

Scanning electron microscopy (SEM) and transmission electron microscopy (TEM) are powerful tools in investigating zeolite morphology. These imaging techniques were used to determine if large zinc clusters were formed during the vapour deposition process (Figure 4). The H-ZSM-5 (15) material exhibits predominantly coffin-shaped morphology with addition needle-like crystals. Post zinc vapour deposition, no change is observed in the morphology and no additional zinc clusters can be observed. The NH_4-ZSM-5 (12.5) has a slightly different morphology to the H-ZSM-5 (15) consisting mainly of larger coffin-like crystals with no needle-like crystals observed. This is reflected in the Zn(IE)/ZSM-5 sample, which again shows no obvious zinc clusters. Both the FER and MOR samples consist of smaller scale-like crystals sitting on the surface of bulkier crystals. No change in morphology is observed after zinc vapour deposition for Zn(VD)/FER and Zn(VD)/MOR.

The TEM images compare two Zn/ZSM-5 samples where the zinc has been introduced by vapour deposition and through ion exchange methods. Both samples are very similar, and no zinc clusters are observed.

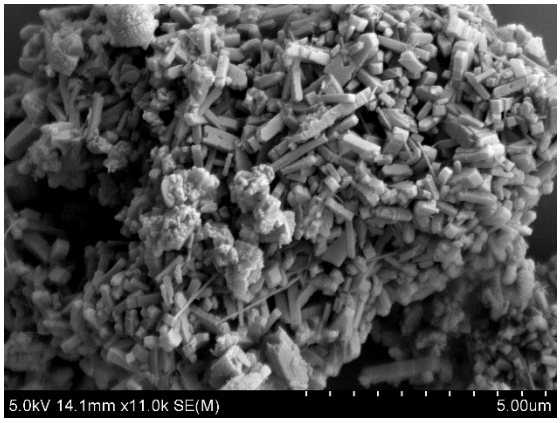

H-ZSM-5

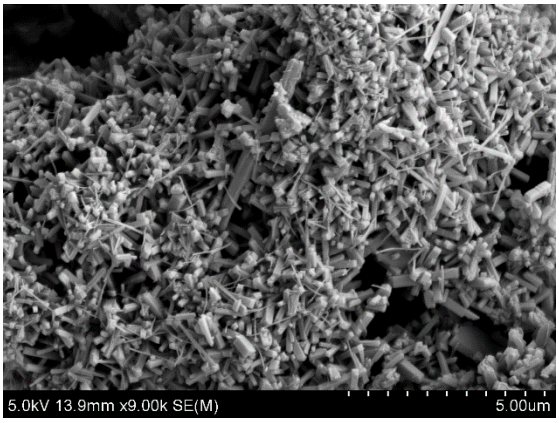

Zn(VD)/ZSM-5

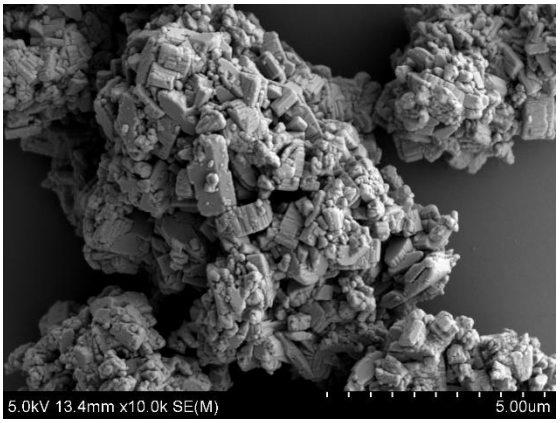

Zn(IE)/ZSM-5

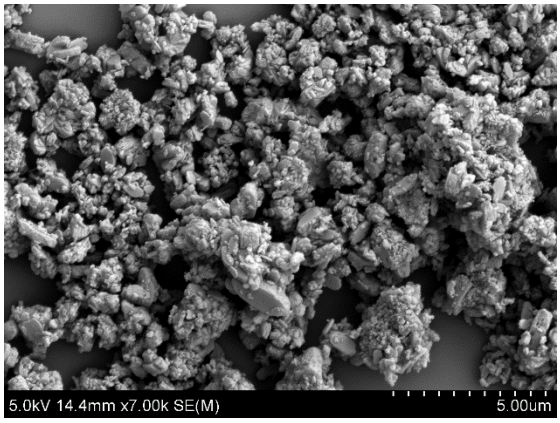

NH_4-FER

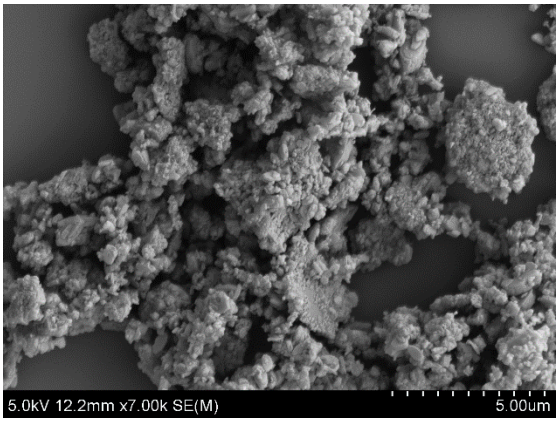

Zn(VD)/FER

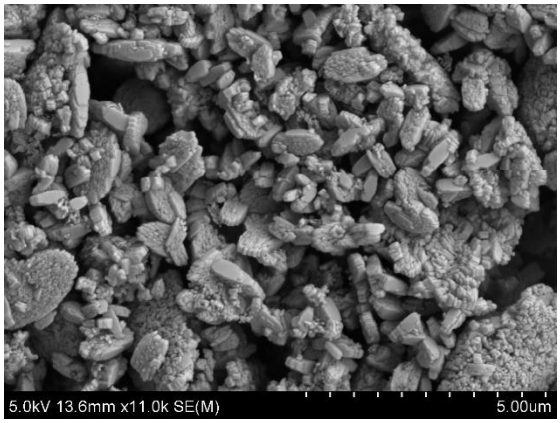

H-MOR

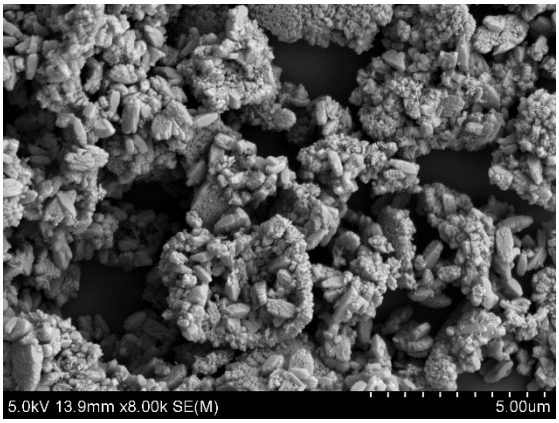

Zn(VD)/MOR

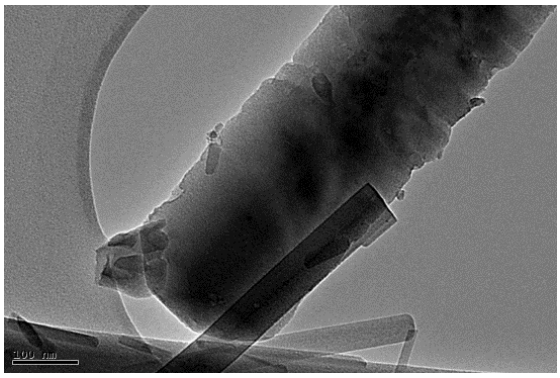

TEM: Zn(VD)/ZSM-5

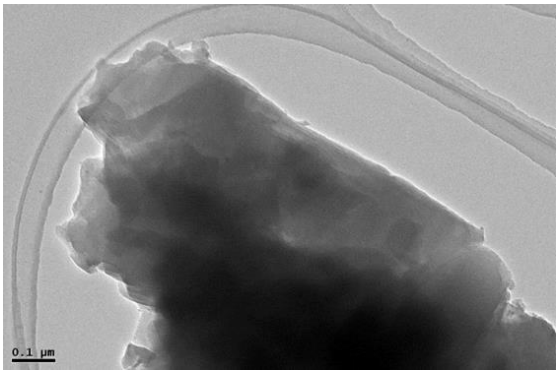

Zn(IE)/ZSM-5

Figure 4: SEM and TEM images of parent zeolites compared with zeolites post zinc vapour deposition. No large zinc clusters are formed during the vapour deposition reaction.

Having demonstrated successful exchange of BAS for Zn^{2+} cations of ZSM-5, FER and MOR, without framework damage or pore blockage, the materials were studied for the capacity to effect C-H activation of methane, following similar conditions to those reported by Stepanov.[6] To confirm the parent zeolites had no capacity to activate methane without the presence of zinc, all parent zeolite samples were dehydrated and exposed to a flow of unlabelled methane for 15 minutes at 250 °C. No signals were observed in the ^{13}C NMR spectrum for any of the parent samples.

The Zn(VD)/CH_4/zeolite samples were then prepared with reaction with zinc vapour at 500 °C, subsequent cooling to 250 °C, and exposed to $^{13}CH_4$ and sealed for 15 minutes. When the Zn(VD)/CH_4/ZSM-5 CVD sample was analysed by ^{13}C CP MAS NMR spectroscopy a signal at −19 ppm (Figure 5a) was observed, characteristic of the [Zn^{II}-CH_3] fragment, in line with previous reports.[2, 5-7] When the Zn(VD)/CH_4/FER was likewise analysed, a signal at -20 ppm was also observed (Figure 5c), indicating the successful activation of methane to form the [Zn^{II}-CH_3] fragment. Most excitingly, after exposure to $^{13}CH_4$ analysis of the Zn(VD)/CH_4/MOR sample showed the presence of two signals at −15 ppm and −20 ppm (Figure 5d). Neither FER or MOR frameworks, modified with zinc, have been previously reported to activate methane. Zn(IE)/CH_4/ZSM-5, prepared by aqueous ion exchange of Zn^{2+} ions, also is able to activate methane, as demonstrated by the ^{13}C NMR signal observed at −19 ppm (Figure 5b), in line with observations reported by other groups.[9, 27, 28] It should be noted that the conditions required to observe C-H activation of methane with the IE sample (Zn(IE)/CH_4/ZSM-5) were based on those reported in the literature, but are substantially different to those required using samples prepared by CVD with zinc vapour.[27] The IE sample requires a higher activation temperature of 600 °C hence, prior to methane exposure, the Zn(IE)/ZSM-5 is heated to 600 °C for 4 h. Futhermore, the IE sample requires longer exposure to the methane gas and is held at 250 °C, under a methane atmosphere, for 2 h compared with 15 min exposure time used for the vapour deposition samples.

^1H NMR and ^1H-^{27}Al REAPDOR NMR spectroscopic experiments were conducted on the samples post zinc vapour deposition and methane exposure. After exposure to methane at 250 °C, a peak at 0 ppm is observed coresponding to a [Zn^{II}-CH_3] species in the ^1H NMR spectrum. For all three zeolite frameworks, there is some Al association seen in the REAPDOR difference spectrum for this species. Spectra can be found in Appendix 1.1.

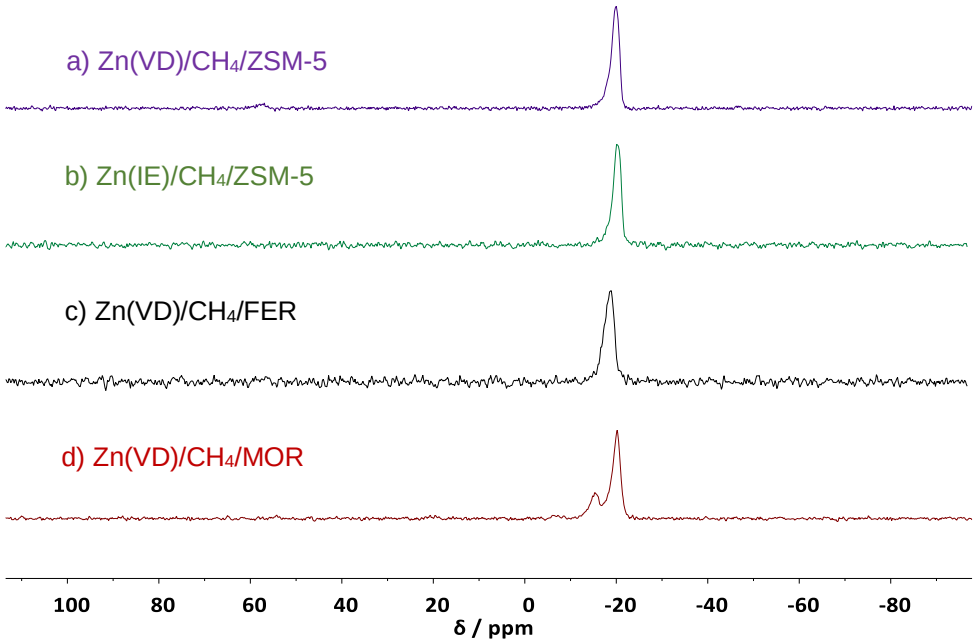

Figure 5: ^{13}C CP MAS NMR spectra of (a) $Zn/CH_4/ZSM\text{-}5$, (b) $Zn/CH_4/ZSM\text{-}5\text{-}IE$, (c) $Zn/CH_4/FER$ and (d) $Zn/CH_4/MOR$. A characteristic signal for the $[Zn^{II}\text{-}CH_3]$ species is observed at a chemical shift of around -19 ppm in all spectra. (^{13}C – 100 . 57 MHz, 10 kHz spin rate)

Quantifying the number of zinc active sites is an important part of understanding zeolite framework effects, hence, an NMR-based method was developed that would determine the percentage of zinc sites that resulted in the formation of the $[Zn^{II}\text{-}CH_3]$ species (Table 3). Previous quantification methods have utilised hydrogen physisorption,[2] but using hexamethylbenzene (HMB) as a standard, the number of zinc active sites could be calculated without use of hydrogen. Acquisition of direct excitation ^{13}C NMR spectra coupled with elemental analysis was used to quantify two separate reactions. Details of the quantification calculations can be found in Appendix 2. It was found that on average 5.7% of the zinc sites in $Zn(VD)/CH_4/ZSM\text{-}5$ formed $[Zn^{II}\text{-}CH_3]$. This is in line with values reported in the literature by Kuroda *et al.* who found that 5-10% of sites are active.[27] The average number of active zinc sites in $Z(VD)n/CH_4/FER$ and $Zn(VD)/CH_4/MOR$ were found to be substantially fewer, 0.5% and 1.2%, respectively. This is potentially due to the differences in topology between the three frameworks, highlighted above. Different channel sizes and dimensions could affect the accessibility and reactivity of the extraframework zinc. Other factors such as Al distribution could also play a role in this finding, where for ZSM-5 in particular, the circumferentially-arrayed Al-Al site is the most active.[8, 29]

The Zn(IE)/H-ZSM-5 material was also found to have fewer active sites (0.9%) than Zn(VD)/ZSM-5. Although high Zn exchange levels were achieved with the ion exchange (90%), Kuroda suggests that the hardest sites to exchange are likely to be the most active.[27] Therefore,

the lower activity from the ion-exchanged sample could be due to the inability to exchange the final 10% of sites.

Table 3: Elemental analysis and percentage zinc active sites determined using NMR spectroscopic quantification for the three zeolite frameworks.

Sample	Measured Si/Al*	Zn/Al#	Percentage Zn active sites ‡		
					Average
Zn(VD)/CH_4/ZSM-5	12.5	0.73	7.3%	4.2%	5.7%
Zn(VD)/CH_4/FER	11.2	0.77	0.5%	0.5%	0.5%
Zn(VD)/CH_4/MOR	7.9	0.75	1.0%	1.5%	1.2%
Zn(IE)/H-ZSM-5	11.6	0.45		0.9%	

***determined by WDXRF, # determined by ICP-OES, ‡NMR quantification with hexamethylbenzene (HMB) as a standard. Percentage of zinc sites that result in [Zn^{II}-CH_3]species. Details on quantification can be found in Appendix 2**

Interestingly, alongside the [Zn^{II}-CH_3] ^{13}C NMR spectroscopic signal observed at −20 ppm in Zn(VD)/CH_4/MOR, an unexpected second signal was observed at −15 ppm, also in the range expected for a [Zn^{II}-CH_3] species (Figure 6).[15, 22] Deconvolution of the direct ^{13}C NMR spectrum showed the two species are formed in a 1:3 ratio.

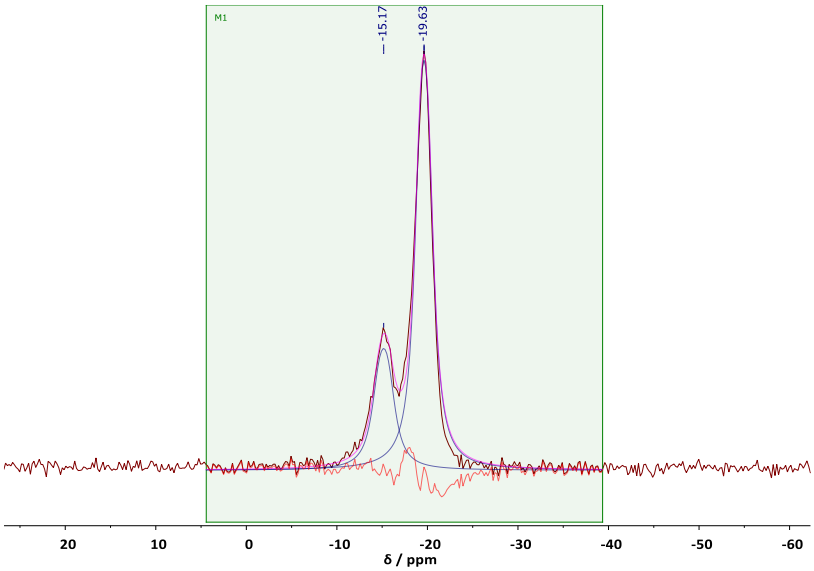

Shift ppm	Height	Width	Area
−15.2	158	259	2906
−19.6	530	219	8268

Figure 6: ^{13}C NMR spectrum and deconvolution data calculated using MNova of the 2 peaks observed for Zn(VD)/CH_4/MOR, which result in a 1:3 ratio. (^{13}C – 100 . 57 MHz, 10 kHz spin rate)

MOR is a 1D zeolite framework containing 12 MR channels and 8 MR side pockets, both of which are accessible to methane gas (Figure 7a). We hypothesised that the two peaks observed in the ^{13}C NMR spectrum of Zn(VD)/CH_4/MOR correspond to two [Zn^{II}-CH_3] species contained within these two different framework environments.

Further NMR spectroscopic experiments were carried out to investigate the two signals observed for Zn(VD)/CH_4/MOR. Through a ^{1}H-^{13}C heteronuclear correlation (HETCOR) MAS NMR experiment (spectrum shown in Figure 7b) it can be seen that there are two discrete [Zn^{II}-$^{13}CH_3$] environments within Zn(VD)/CH_4/MOR. Due to the use of 99% labelled ^{13}C CH_4, the ^{1}H signal shows coupling to the ^{13}C nucleus giving a doublet and each environment has a different J-coupling constant: 125 Hz for the main species and 140 Hz for the minor species. Coupling constants are known to depend on confinement, where tighter confinement gives larger coupling constants.[30] Therefore, the signals are likely to correspond to strong confinement of [Zn^{II}-CH_3] species in the 8 MR side pockets (140 Hz) compared with [Zn^{II}-CH_3] in the 12 MR main channel (125 Hz).

To confirm that the two [Zn^{II}-CH_3] sites could not chemically exchange or transfer magnetisation an EXSY experiment was conducted. The absence of any off-diagonal peaks in Figure 7c indicates no transfer between sites after 200 ms of mixing. This strongly suggests the presence of at least two well separated [Zn^{II}-CH_3] environments within Zn(VD)/CH_4/MOR.

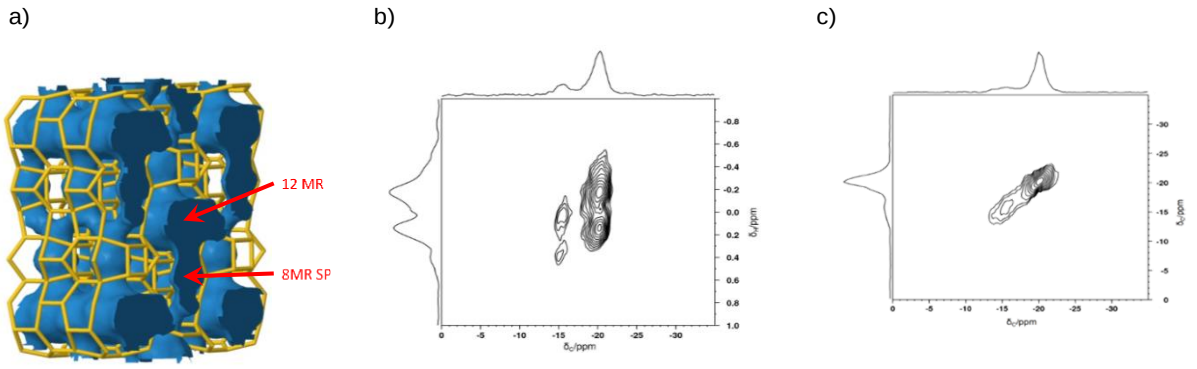

Figure 7 (a) Framework representation of MOR framework taken from IZA database highlighting the 12 MR channel and 8 MR SP. (b) ^{1}H-^{13}C heteronuclear correlation (HETCOR) MAS NMR spectrum for Zn(VD)/CH_4MOR indicating two distinct [Zn^{II}-CH_3] environments. (c) EXSY experiment of Zn(VD)/CH_4MOR highlighting lack of chemical exchange or transfer of magnetisation between the two [Zn^{II}-CH_3] sites. (^{13}C – 100 . 57 MHz, 10 kHz spin rate)

The distinct topological environments of the 12 MR and the 8 MR SP within MOR have previously been observed to give rise to two distinct chemical environments, as determined by ^{23}Na and ^{133}Cs MAS NMR spectroscopy studies.[31, 32] Gerstein *et al.* observed two signals in the ^{133}Cs NMR spectrum of fully dehydrated Cs-exchanged mordenite. The peaks are observed in a

1:3 ratio that the authors assigned to the 12 MR main channel and 8 MR side pocket within the MOR framework.[32] Two-dimensional triple-quantum (2D-3Q) ^{23}Na MAS NMR spectroscopy of sodium cations in dehydrated Na/MOR also shows two clear signals assigned to Na cations within the 12 MR channels and Na cations located in the 8 MR side pockets of the mordenite channels.[31] Overall, based on NMR spectroscopy studies, the two peaks observed for the [Zn^{II}-CH_3] species in MOR correspond to two distinct chemical environments likely associated with the 8MR side pocket and 12 MR channels within the zeolite framework. Further experiments to explore the two peaks observed for MOR after CH_4 activation were conducted and the results are discussed in Chapter 5.

4.2.2 Effect of Si/Al ratio on CH_4 activation

The Si/Al ratios of the three frameworks used to study the effect of zeolite topology on methane activation were chosen to have a small range (Si/Al: 8-12.5) so the results between zeolite frameworks could be compared. In theory, two closely situated framework Al atoms are required to counter balance a Zn^{2+} extra framework cation hence, varying the Si/Al ratio should have a considerable impact on methane activation. Although the specific locations of BAS and framework Al atoms cannot be easily characterised, in zeolite catalysis, it has been well established that the location of the counter cation can influence reactions that occur at that extraframework site (the side pockets of MOR have been studied extensively in relation to carbonylation chemistry).[29, 33-36] Furthermore, reactivity can be dependent on a specific Al array within the zeolite. As mentioned in Section 1.3.4.1, Kuroda determined that in Zn/MFI, heterolytic cleavage of H_2 was more favourable on a circumferentially-arrayed Al-Al site.[29]

A small study was undertaken to investigate how Si/Al effects methane activation on Zn/zeolites comparing a high Al zeolite (H-Y (2.55)) and low Al zeolite (H-ZSM-5 (45)). Although higher activation would perhaps be expected in samples with more Al with a higher chance of Al pairing as more zinc can theoretically be incorporated previous studies by Kazansky *et al.* suggest otherwise. Zinc vapour deposition on high silica H-ZSM-5 (Si/Al of 41) followed by hydrogen adsorption was carried out by Kazansky.[2] Although no methane activation was carried out, unexpectedly high activity was found for heterolytic dissociative adsorption of H_2 at moderate temperatures. Kazansky reasons that when fewer Al atoms are present, there is the potential for more of the Zn sites to be active as the 2+ charge is only partially compensated for which can lead to greater Lewis acidity.[2, 3, 29] Kazansky has also previously compared Zn(VD)/ZSM-5 (25) with Zn(VD)/Y (2.5) prepared by zinc vapour deposition, exposed to methane at room temperature and monitored with DRIFTS.[3] They found a much stronger perturbation of adsorbed methane to occur from the higher silica Zn(VD)/ZSM-5 than Zn(VD)/Y, supporting that

partial compensation of positive charge of Zn^{2+} from distantly separated Zn^{2+} ions results in more active sites. As methane activation was not studied by Kazansky on either the high silica H-ZSM-5 or the high Al H-Y, this was explored further.

Zinc vapour deposition and methane activation was carried out on both H-Y (2.55) and H-ZSM-5 (45). The Zn/Al ratio of 0.19 for the Zn(VD)/CH_4/Y (2.55) sample is considerably lower that the Zn/Al ratio of 0.73 of the Zn(VD)/CH_4/ZSM-5 (45) sample. Multiple attempts of zinc vapour deposition on the H-Y (2.55) resulted in similarly low Zn/Al ratios. The ^{27}Al NMR spectrum of the H-Y (2.55) parent (Appendix 1) indicates the presence of significant five and six coordinate Al species and the ^{29}Si CP NMR spectrum shows that some defects are present in the parent zeolite. The presence of five and six coordinate Al could explain why less than 100% zinc exchange was achieved in Zn(VD)/CH_4/Y.

Included in Figure 8 is a spectrum corresponding to unlabelled methane activation on Zn(VD)/ZSM-5 (15) for comparison. A peak at around −20 ppm corresponding to successful methane activation (formation of [Zn^{II}-CH_3]) can be observed in the ^{13}C NMR spectra for both zeolites (note the low intensity is partially due to the use of unlabelled methane). pXRD patterns (Appendix 1.2) show no change post zinc vapour deposition on ZSM-5 (45) and Y (2.55) Further NMR spectra (^{27}Al and ^{29}Si) of Zn/Y (2.55) and Zn(VD)/ZSM-5 (45) can be found in Appendix 1.2 demonstrating no additional extraframework Al or additional zeolite defects are produced after zinc vapour deposition.

Table 4: Elemental analysis and C-H activation results for ZSM-5 (45) and Y (2.55)

Sample (given Si/Al)	Measured Si/Al	Zn/Al	Successful C-H activation
Zn(VD)/CH_4/Y (2.55)	3.50	0.19	Y
Zn(VD)/CH_4/ZSM-5 (45)	52.20	0.73	Y

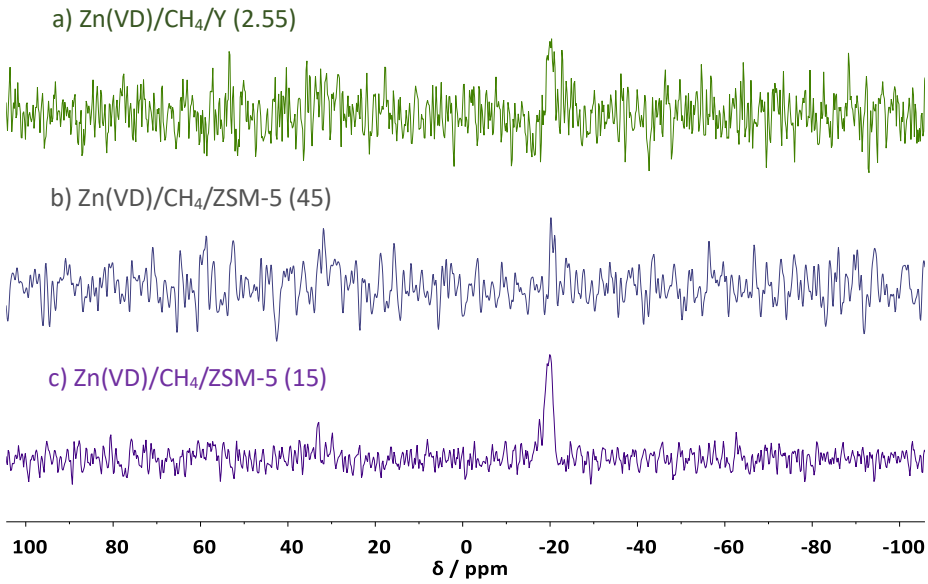

Figure 8: ^{13}C CP MAS NMR spectra of (a) Zn(VD)/CH_4/Y (2.55), (b) Zn(VD)/CH_4/ZSM-5 (45) and (c) Zn(VD)/CH_4/ZSM-5 (15). A characteristic signal for the [Zn^{II}-CH_3] species is observed at a chemical shift of −20 ppm in all spectra. Note low intensity due to use of unlabelled methane. (^{13}C – 100 . 57 MHz, 10 kHz spin rate)

Whilst no quantitative analysis was carried out, it is clear that both Zn(VD)/Y (2.55) and Zn(VD)/ZSM-5 (45) are able to activate methane to a similar degree and this is significantly lower than that achieved by H-ZSM-5 (15). This result is quite surprising considering the variation in Si/Al ratio between the samples, but as established in the first part of this chapter, zeolite topology can have a significant effect on methane activation. It should be noted that the Zn/Al ratios are considerably different for both samples, and this could also have an impact on the methane activation. As the high silica ZSM-5 sample is unlikely to contain many Al pairs, the high Zn exchange levels alongside the methane activation results reinforce Kazansky's ideas that distant Al pairs are required for methane activation post zinc vapour deposition. To gain further insight into the effect of Si/Al ratio on methane activation in Zn/zeolites, quantitative analysis calculating the number of active zinc sites should be conducted on Zn(VD)/ZSM-5 with different Si/Al ratios.

4.2.3 Reactivity of [Zn^{II}-CH_3] under oxidative conditions

Having determined that zinc-modified ZSM-5, FER and MOR are able to activate methane to form well defined [Zn^{II}-CH_3] species, we subsequently explored the reactivity of these species under oxidative conditions. After confirming the formation of the [Zn^{II}-CH_3] species using ^{13}C NMR spectroscopy, the samples were exposed to differing oxidative conditions. Upon exposure to 20% O_2 in Ar at room temperature for 20 minutes, the three zeolites

Zn(VD)/CH_4/O_2/ZSM-5, Zn(VD)/CH_4/O_2/FER and Zn(VD)/CH_4/O_2/MOR, showed clear differences in reactivity however the [Zn^{II}-CH_3] signal is still observed in all spectra in Figure 5 after exposure to 20% O_2/Ar. Two new signals appear in the ^{13}C CP MAS NMR spectrum of Zn(VD)/CH_4/O_2/ZSM-5 (Figure 9a). These correspond to a zinc methoxy species (54 ppm) and a zinc formate species (173 ppm), which is in line with previous findings on the exposure of [Zn^{II}-CH_3]/ZSM-5 to O_2.[6, 14] Conversely, the FER sample shows the presence of a zinc formate peak only (Figure 9b), while the MOR sample exhibits no reactivity towards dioxygen at room temperature after 20 minutes exposure (Figure 9c). This indicates that the framework environment plays a key role in the reactivity of [Zn^{II}-CH_3] with O_2 at room temperature, with the MFI framework giving rise to more detectable products than either FER or MOR.

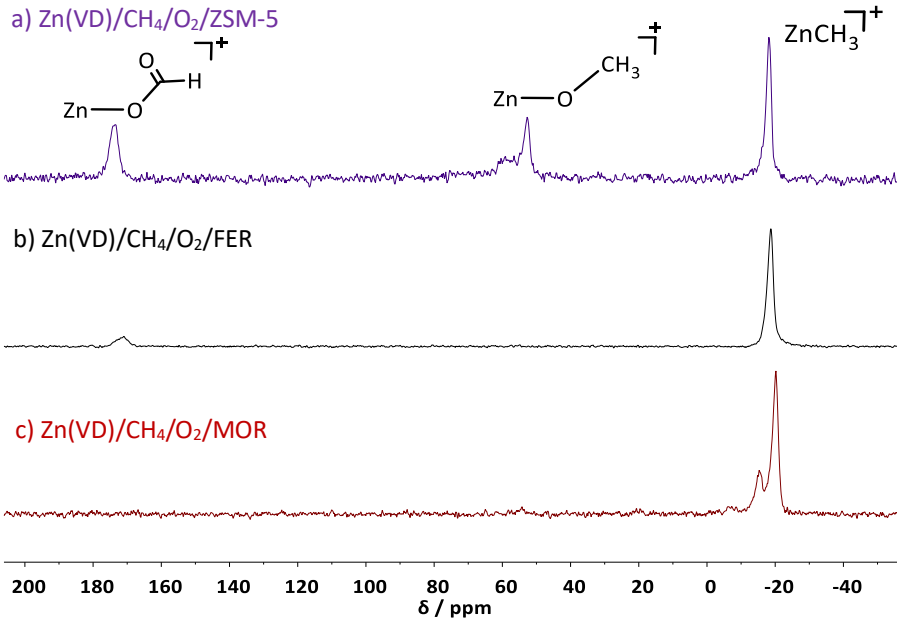

Figure 9: ^{13}C CP MAS NMR spectrum of Zn(VD)/CH_4/O_2/ZSM-5 (a), Zn(VD)/CH_4/O_2/FER (b) and Zn(VD)/CH_4/O_2 MOR (c) after exposure to 20% O_2 in Ar at room temperature. Signals corresponding to a zinc methoxy species (54 ppm) and zinc formate species (173 ppm) are observed for ZSM-5 and FER. (^{13}C – 100 . 57 MHz, 10 kHz spin rate)

Contrary to the reaction at room temperature, the Zn(VD)/CH_4/ZSM-5, Zn(VD)/CH_4/FER and Zn(VD)/CH_4/MOR show similar reactivity when the [Zn^{II}-CH_3] species is exposed to O_2 (20% in Ar) at 200 °C for 15 min, forming zinc methoxy and zinc formate species with similar spectral intensities (Figure 10). After a further 12 hours at room temperature the zinc methoxy and zinc formate species in ZSM-5 are still present at comparable intensity indicating further reaction at room temperature is not substantial (Figure 10b) and that the zinc methoxy and zinc formate species are stable at room temperature. The [Zn^{II}-CH_3] species once again does not react fully and can be seen in all spectra.

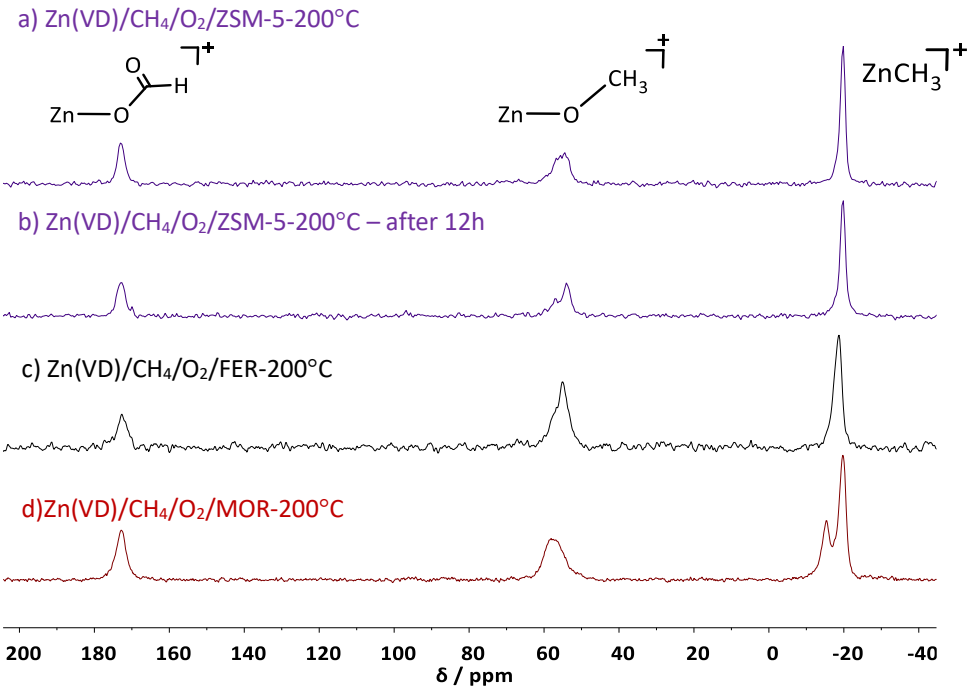

Figure 10: ^{13}C CP MAS NMR spectrum of Zn(VD)/CH_4/O_2/ZSM—200°C (a), Zn(VD)/CH_4/O_2/ZSM-5—200°C after 12 h (b), Zn(VD)/CH_4/O_2 FER—200°C (c) and Zn(VD)/CH_4/O_2/MOR—200°C (d) after exposure to 20% O_2 in Ar at 200 °C for 15 min. Peaks corresponding to a zinc methoxy species (54 ppm) and zinc formate species (173 ppm) observed in all spectra. (^{13}C – 100 . 57 MHz, 10 kHz spin rate)

It should also be noted that the two signals discussed previously for the [Zn^{II}-CH_3] species in MOR are both present after each reaction with O_2. However, as the data in Figure 10 shows, the species corresponding to the −20 ppm peak appears to be more reactive. The intensity ratio for the −15 ppm and −20 ppm peaks changes from approximately 0.5:1 for the Zn(VD)/CH_4/MOR to 0.8:1 for the oxygen-exposed sample, Zn/CH_4/O_2/MOR. The spectra in Figure 11 are plotted on equivalent vertical scales after taking into account the differing number of repetitions (800 vs 4000) and the change in relaxation behaviour involved in exposure to oxygen. The differences in loss of signal intensity indicates that they undergo different rates of reaction. As mentioned

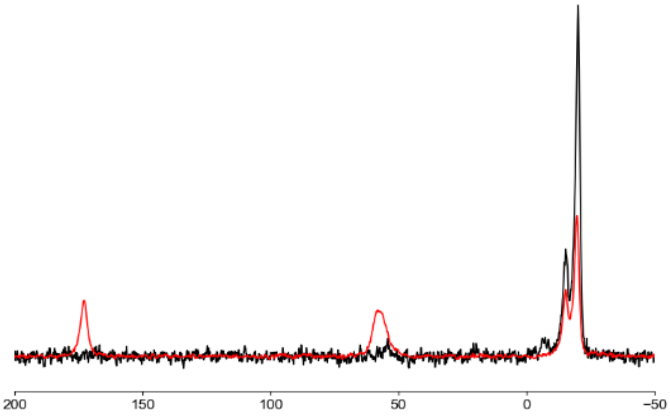

Figure 11: ^{13}C CP MAS spectra from Zn(VD)/CH_4/MOR before (black) and after (red) exposure to 20% O_2 in Ar at 200 °C. (^{13}C – 100 . 57 MHz, 10 kHz spin rate)

above, the signal at –15 ppm is assigned to the [Zn^{II}-CH_3] fragment in the 8 MR SP while the signal at –20 ppm is assigned to the [Zn^{II}-CH_3] fragment in the 12 MR main channel. Our observations for the [Zn^{II}-CH_3]/MOR system indicate that confinement hinders reactivity with the [Zn^{II}-CH_3] species in the 8 MR SP, leading to lower reactivity in the presence of O_2.

The reactivity of the [Zn^{II}-CH_3] species was further tested by exposure to air. After zinc vapour deposition and exposure to $^{13}CH_4$, Zn(VD)/CH_4/ZSM-5, Zn(VD)/CH_4/FER and Zn(VD)/CH_4/MOR were left open to the atmosphere overnight by removal of the NMR rotor cap. The three samples exhibited varying reactivity under these conditions. For both the Zn(VD)/CH_4/air/ZSM-5 and Zn(VD)/CH_4/air/FER (Figure 12a and Figure 12b respectively), the signal corresponding to [Zn^{II}-CH_3] is absent and, free MeOH (50 ppm)[14] and zinc formate species have been formed. We note that the Zn(VD)/CH_4/air/FER spectrum has a higher signal to noise ratio. Zn(VD)/CH_4/air/MOR proves to be the most interesting sample as it is the only framework that still gives a signal from the [Zn^{II}-CH_3] species after overnight exposure to the atmosphere. Even after 36 h, there is a signal present from residual [Zn^{II}-CH_3] species. The MOR framework is also unique in the fact that predominantly methanol is formed, while trace amounts of zinc formate are observed. The reduced signal intensity of Zn(VD)/CH_4/air/FER and Zn(VD)/CH_4/air/MOR after 36 h is likely due to loss of the methanol or protonlysis of the [Zn^{II}-CH_3] species by water to form methane.[14] Furthermore, we also propose that the complete loss of the signal associated with [Zn^{II}-CH_3] in the air exposure experiments compared to O_2/Ar (Figure 10) is due to the differences in experimental conditions of O_2/Ar exposure (sample sealed under O_2/Ar in a capped rotor, *i.e.* limited O_2) vs air exposure (sample in an uncapped rotor).

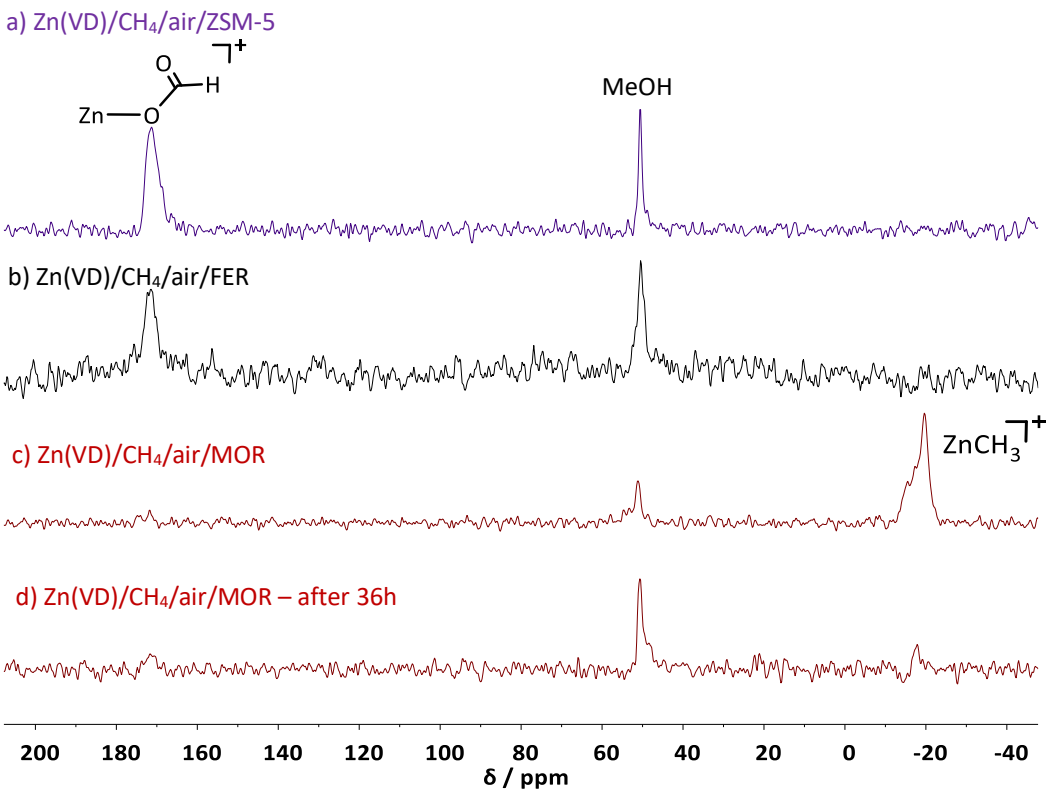

Figure 12: ^{13}C CP MAS NMR spectrum of Zn(VD)/CH_4/air/ZSM-5 (a), Zn(VD)/CH_4/air/FER (b), Zn(VD)/CH_4/air/MOR (c) after exposure to air overnight at room temperature. (d) shows reactivity for Zn(VD)/CH4/air/MOR after 36h. Signals corresponding to free methanol (50 ppm) and formate species (173 ppm) observed. (^{13}C – 100 . 57 MHz, 10 kHz spin rate)

While it is unclear why the differing frameworks display disparate reactivity under different oxidative conditions, these findings highlight that the framework plays a crucial role in the reactivity of the [Zn^{II}-CH_3] species. The MFI framework seems to be the most reactive environment for the [Zn^{II}-CH_3] species under oxidative conditions. The three dimensional 10 MR channels of ZSM-5 could allow higher accessibility to the [Zn^{II}-CH_3] species compared to the smaller two dimensional channel system of FER. The MOR framework contains larger 12 MR rings, but as established above, the [Zn^{II}-CH_3] species confined in the 8 MR SP are potentially less accessible as their reactivity with O_2 is hindered. Other factors such as distribution of Al pairs could also greatly affect reactivity of the [Zn^{II}-CH_3] species. The selectivity of products under oxidative conditions also varied between frameworks and Zn(VD)/CH_4/air/MOR seemed to show the highest selectivity for methanol. Zeolite shape, size and dimensions could play a large part in this selectivity. Confinement of active copper species in the 8 MR SP of Cu/MOR have been shown to give high selectivity of methanol alongside producing the highest yield of methanol.[37] Similar effects could similarly increase the selectivity of Zn(VD)/MOR.

4.2.4 The Role of Al pairing on methane activation over Zn/CHA

The activation of methane over Zn/zeolites and subsequent reactivity under oxidative conditions has been explored over four different zeolite frameworks, ZSM-5, MOR, FER and Y, thus far in this chapter. The different zeolite frameworks produce a different number of zinc active sites and demonstrate dissimilar reactivity under oxidative conditions, highlighting that zeolite framework plays a crucial role in the activation of methane. Whilst Al pairing has not been studied explicitly, the brief study into the effect of Si/Al ratio using Zn(VD)/CH_4/Y (2.55) and Zn(VD)/CH_4/ZSM-5 (45), where similar levels of methane activation were observed despite the drastic difference in Si/Al ratio, reinforced Kazansky's ideas that distant Al pairs are required for methane activation post zinc vapour deposition. The authors believe that when fewer Al atoms are present, more of the Zn sites are likely to be active as the 2+ charge is only partially compensated for which can lead to greater Lewis acidity.[2, 3, 29] To explore the role of Al pairing in methane activation further, collaborative work with Julien Devos and Michiel Dusselier at KU Leuven, Belgium was conducted.

It is fairly well known that the properties of counter cations in zeolites significantly depend on the position and concentration of Al atoms present throughout the zeolite framework.[29, 33-36, 38] Therefore, understanding the relationship between the Al distribution of the zeolite and the counteraction remains crucial for catalytic performance. However, due to the uncertainty related to the Al distribution and the difficultly in precisely controlling the location of the Al, this remains a major challenge.[29, 39-43] However, Di Iorio and Gounder have established synthetic control of the Al distribution in CHA by tailoring the CHA synthesis method.[39, 44, 45] To probe the Al arrangements, a Co^{2+} titration method can be used where only two tetrahedral Al close enough to exchange the divalent cations will do so.[43, 46] Therefore, where Co^{2+} is exchanged, the Al are thought to be in close proximity in a paired configuration. A series of CHA samples, where the Al pairing was analysed by this Co^{2+} titration method, was prepared by collaborators[47] to investigate whether Al pairing had an impact on methane activation.

CHA has a 3D structure shown in Figure 13, consisting of double six rings comprising of an 8 MR channel with dimensions of 3.8 x 3.8 Å (substantially smaller than any other zeolite framework considered so far). Computation studies have shown 25 distinct symmetry combinations within the CHA unit cell containing two Al atoms. The most stable combination for divalent cations (Cu^{2+}, Fe^{2+} and Co^{2+}) has been shown to be a square planar coordination on two opposite Al tetrahedral.[48-52] Recently, substantial interest in methane activation on Cu/CHA has been explored resulting in competitive quantities of methanol per copper atom compared with

Cu/ZSM-5 and Cu/MOR.[37, 53-58] However, methane activation over Zn(VD)/CHA has not yet been reported.

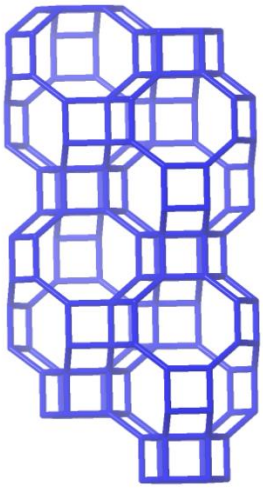

Figure 13: CHA structure consisting of double six rings with a 3D channel system. Image taken from IZA website.

Four CHA samples with different levels of Al pairing were tested for methane activation after reaction with zinc vapour. Initially, a sample prepared by a standard CHA synthesis method (STD) was reacted with zinc vapour and exposed to $^{13}CH_4$. The Al paring of this sample was not controlled and 'random' Al pairing would be expected. As observed for the other zeolite frameworks, a [Zn^{II}-CH_3] species is formed, identified through ^{13}C NMR spectroscopy (Figure 14A). Three further CHA samples were tested where the level of Al pairing was controlled through careful synthesis conditions.[47] A sample with high, low and no Al pairs underwent zinc vapour deposition and reaction with $^{13}CH_4$. All three CHA samples, High, Low and None, reacted with the methane to form a [Zn^{II}-CH_3] species (Figure 14B, C and D respectively).

Thorough analysis of the CHA samples was carried out using ^{27}Al NMR spectroscopy, ^{29}Si NMR spectroscopy, elemental analysis and pXRD. Zn/Al ratios of the CHA samples are reported in Table 5 where Zn/Al values greater than 1 are observed for all samples. This is substantially higher than the theoretical maximum of 0.5 as well as the Zn/Al values for other zeolite frameworks prepared by Zn^0 vapour deposition reported earlier in this chapter. To determine the cause of this high Zn/Al ratio, further analysis was carried out to examine whether the CHA framework was particularly defective or if multinuclear zinc clusters were perhaps forming. The ^{27}Al NMR spectra (Appendix 3, Figure 8) show some octahedral Al is present in the parent CHA samples. This small signal at 0 ppm disappears on reaction with zinc vapour, highlighting that this octahedral Al is likely to be attached to the zeolite framework.[59] However, the ^{29}Si CP NMR spectra (Appendix 3, Figure 9) demonstrate that CHA frameworks do contain some defect sites.

Upon exposure to zinc vapour, the signal in the ^{29}Si CP NMR decreases significantly indicating that either the silanol nests present in the CHA parent samples are healing or zinc is being incorporated to these nests.[60] Based on the very high Zn/Al ratios present, it is more likely that the zinc is entering the defect sites. Direct excitation ^{29}Si NMR spectra can be found in Appendix 3, Figure 10, the spectra show broadening after reaction with zinc vapour reinforcing the inclusion of zinc into the framework. Lastly, pXRD analysis of all samples was carried out by our collaborators. They found that the samples remained crystalline after the zinc vapour deposition reaction and no extra peaks due to zinc metal were observed (Appendix 3, Figure 11). Based on these analysis methods, it is hard to justify why the Zn/Al ratio is considerably higher for all the CHA samples. Some aspect of this is likely due to zinc incorporation into the silanol nests as well as the presence of excess Zn(0) which has not been fully removed.[18] TEM images to look for zinc clusters alongside additional XAS analysis could provide insight into these high Zn/Al ratios.

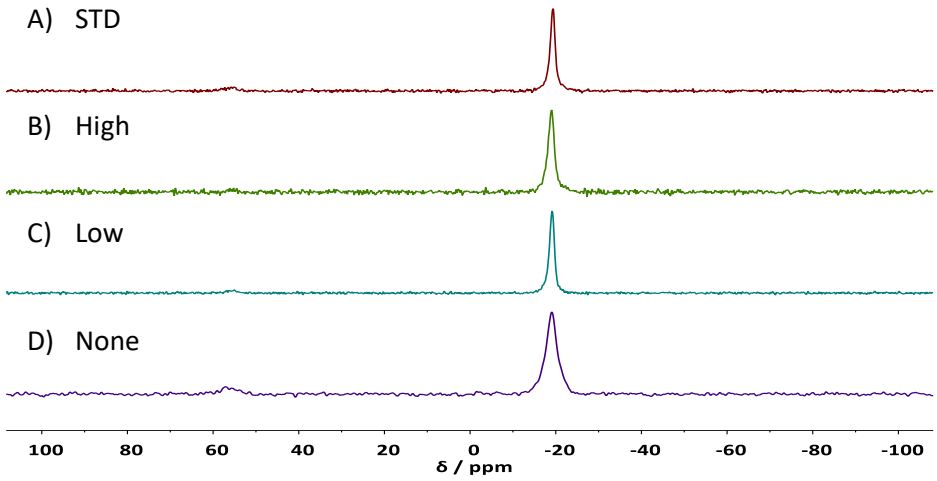

Figure 14: ^{13}C CP NMR spectra for CHA samples with different Al distributions. STD is prepared by standard synthesis methods whilst High, Low and None CHA samples have been prepared by controlling the Al distribution. All samples show only a [Zn^{II}-CH_3] species at −20 ppm in the ^{13}C NMR spectra after zinc vapour deposition and exposure to $^{13}CH_4$ under standard conditions. (^{13}C – 100 . 57 MHz, 10 kHz spin rate)

Table 5: Elemental analysis and percentage zinc active sites determined using NMR quantification for the CHA samples with varying Al distributions. All samples show similar activity and higher than expected Zn/Al ratios.

Sample	Measured Si/Al*	Zn/Al*	Percentage Zn active sites		
					Average
STD	36.3	1.66	3.9	4.3	4.1
High	34.0	1.14	3.5	2.8	3.2
Low	41.6	1.53	3.0	4.1	3.6
None	42.6	1.80	2.7	3.8	3.3

***Average value from two reactions measured by ICP-OES using IV solutions**

Similar NMR spectroscopic quantification using HMB was carried out to determine the percentage of zinc sites which are able to form [Zn^{II}-CH_3] species. To check no matrix effects were caused by the CHA framework, a sample of STD CHA after zinc vapour deposition and exposure to $^{13}CH_4$ was mixed with HMB direct ^{13}C NMR spectrum were acquired (Appendix 3, Table 4). No matrix effects were observed and the number of active zinc sites were calculated using the Zn/Al ratios and the ^{13}C NMR direct spectra shown in Appendix 3, Table 4. Curiously, the percentage of active zinc sites was found to 3-4% for all CHA samples, regardless of Al pairing. The CHA framework shows a higher number of active sites than both Zn/MOR and Zn/FER but still has lower activity than Zn/ZSM-5. Nevertheless, it can be concluded that for CHA, Al pairing has no bearing on the reaction with zinc vapour and subsequent methane activation, unlike Kuroda's suggestions for ZSM-5.[29]

As Al pairing did not seem to affect the number of zinc active sites present in the CHA samples, we decided to investigate whether the Si/Al ratio of the CHA samples has an impact on methane activation. Two additional samples were synthesised by collaborators at KU Leuven, a low silica CHA – CHA (12) and a high silica CHA – CHA (62) to explore the influence of Si/Al ratio. Once again zinc vapour deposition was carried out under standard vapour deposition conditions and both CHA (12) and CHA (62) formed the [Zn^{II}-CH_3] species (Figure 15A and B). The percentage of zinc sites was quantified for both samples and surprisingly the CHA (62) showed remarkably high activity (20% of the zinc sites were active for forming the [Zn^{II}-CH_3] species). As this result was so remarkably different to any other Zn/zeolite, another sample with Si/Al of 62 was prepared by Julien (CHA (62)A). This sample also formed the [Zn^{II}-CH_3] species (Figure 15C) and demonstrated unusually high activity (Table 6). The Zn/Al ratio of both the high silica CHA samples was also inexplicably high (Zn/Al = 3). Further analysis was carried out in an attempt to explain the activity and high Zn/Al ratios found for the Si/Al 62 CHA samples.

The pXRD pattern (Appendix 3, Figure 11) of CHA (62) only shows peaks corresponding to CHA, no extra reflections were observed. Whilst both CHA (62) and CHA (62)A parent samples contain octahedral Al, this once again disappears on reaction with zinc vapour, indicating that it is framework attached. The ^{29}Si CP NMR show that CHA (12), CHA (62) and CHA (62)A contain framework defects but the signals lose intensity after the reaction with zinc vapour supporting the conclusion that some zinc is incorporated into the zeolite framework. However, unlike the other CHA samples, some framework defects are still present after the reaction with zinc vapour for CHA (62) and CHA (62)A. Analysis by pXRD and NMR spectroscopy was unable to lead us to any conclusions to why the Zn/Al ratios were significantly higher for the high silica CHA samples. Therefore, TEM analysis of CHA(62) was carried out in an attempt to observe in zinc clusters

were forming in the high Si CHA samples. No zinc clusters were observed i(Figure 16) and the parent CHA sample looked very similar to CHA(62) post zinc vapour depositions under the microscope. Unfortunately, without further analysis, perhaps using UV-vis spectroscopy or XAS the Zn/Al ratio of 3 observed for CHA(62) and CHA (62)A is hard to explain.

A Na ion-exchanged CHA (12) was prepared to investigate to what extent the CHA framework was reacting with the zinc vapour. No BAS sites were present so in theory, no zinc should be exchanged into the CHA. However, the Zn/Al ratio of NaCHA (12) after the reaction with zinc vapour is 0.58, indicating that a significant amount of zinc is present after vapour deposition. This supports the evidence presented through the ^{29}Si CP NMR spectroscopic investigations which suggested that the zinc vapour is reacting with defect sites present in the CHA parent frameworks. This explains why a Zn/Al ratio of ~1 is observed for most of the CHA samples and it is likely that a similar mechanism of activation is present in Zn/CHA as with Zn/ZSM-5, for all CHA samples except the CHA(62). The higher Zn/Al ratio of 3 observed for CHA(62) perhaps indicates a different zinc species is introduced upon zinc vapour deposition.

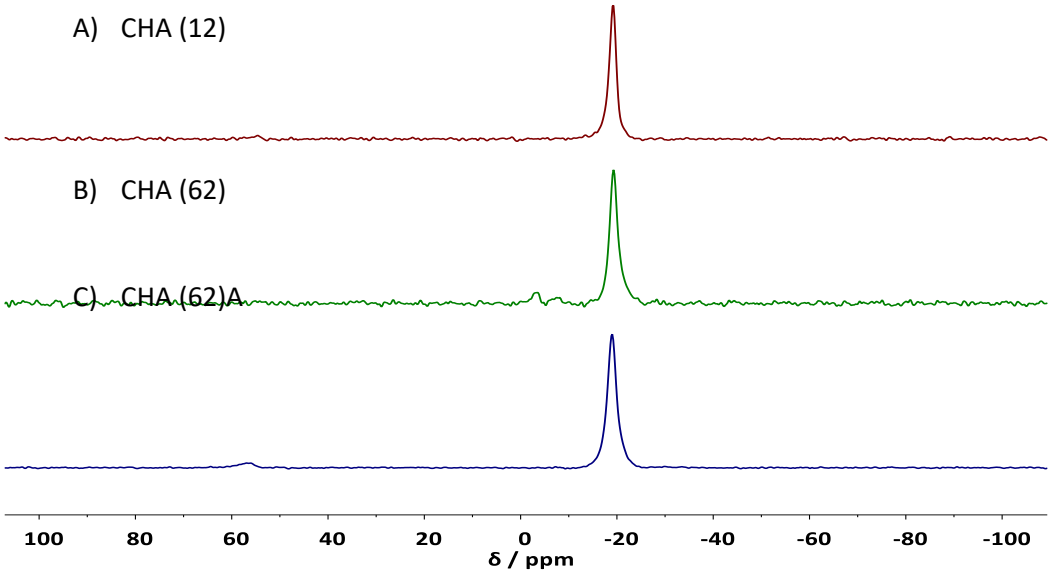

Figure 15: ^{13}C CP NMR spectra for CHA samples with different Si/Al ratios (Si/Al=12 and Si/Al = 62). All three samples show only a [Zn^{II}-CH_3] species at −20 ppm in the ^{13}C NMR spectra after zinc vapour deposition and exposure to $^{13}CH_4$ under standard conditions. (^{13}C – 100 . 57 MHz, 10 kHz spin rate)

Table 6: Elemental analysis and percentage zinc active sites determined using NMR quantification for the CHA samples with varying Si/Al ratios.

Sample	Measured Si/Al*	Zn/Al*	Na/Al	Percentage Zn active sites		
						Average
CHA (12)	12.7	1.34	0.00	6.7	4.4	5.6
CHA (62)	50.3	3.13	0.00	22.0	16.8	19.4
CHA (62)A	69.9	2.93	0.00	32.2	13.9	23.1
NaCHA (12)	15.4	0.58	0.65		-	

***Average value from two reactions for all samples except NaCHA (12) measured by ICP-OES using IV solutions**

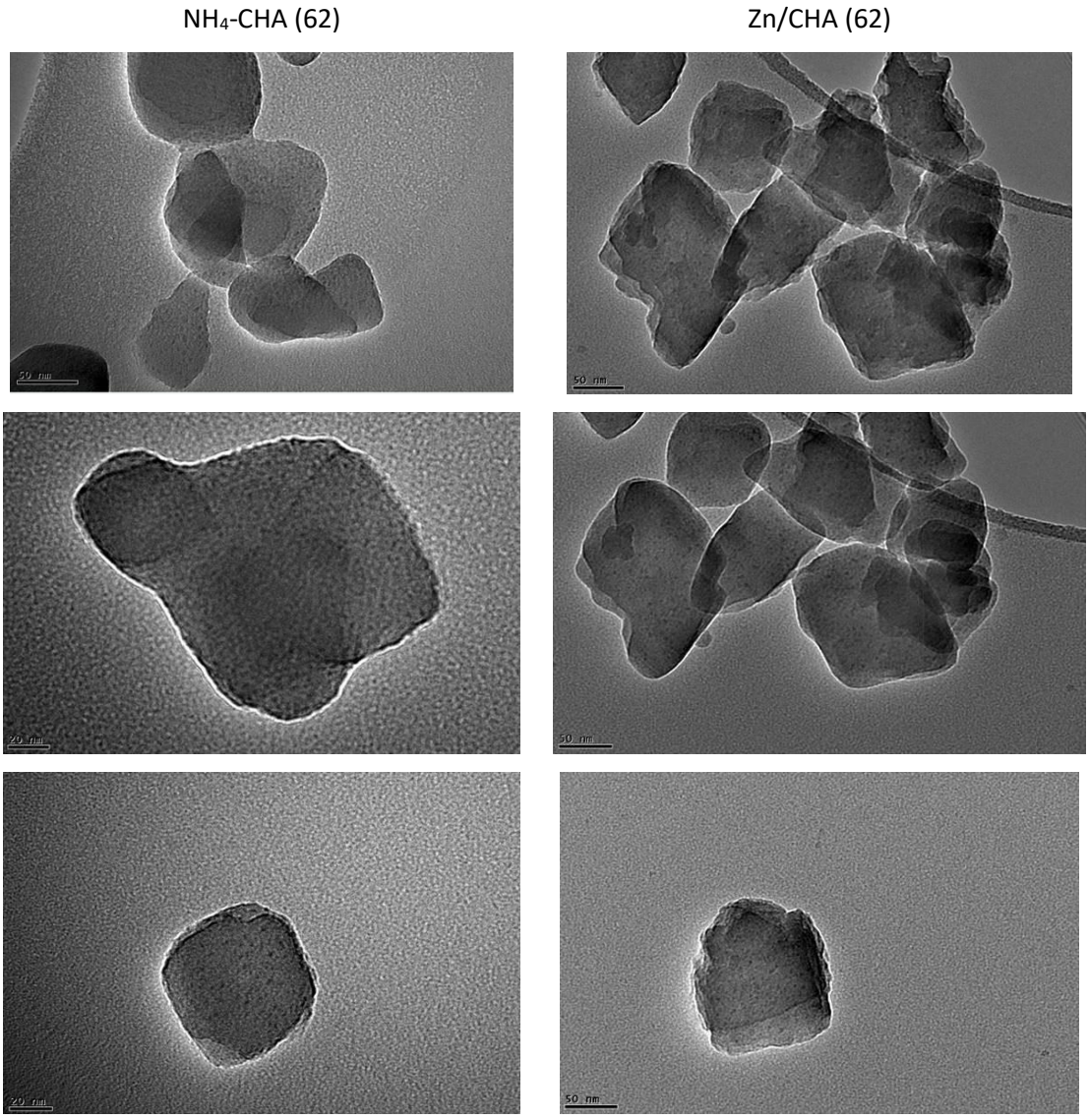

Figure 16: TEM images of the parent CHA NH4-CHA (62) sample (left) compared with the CHA (62) sample after zinc vapour deposition (right). No obvious zinc clusters were observed.

The remarkably high activity of high silica CHA samples, synthesised by collaborators, towards methane currently remains unexplained. To test whether the [Zn^{II}-CH_3] species formed by CHA(62)A reacts similarly to Zn(VD)/CH_4/air/ZSM-5 when exposed to air, the rotor cap was removed after the vapour deposition and $^{13}CH_4$ reaction was carried out. After exposure to air for 12 h, some physisorbed methanol and zinc formate species are observed (**Error! Reference source not found.**B) by ^{13}C CP NMR spectroscopy. A small amount of physisorbed methane (−6 ppm) and MeOH can be observed in the direct ^{13}C NMR spectrum (**Error! Reference source not found.**C). However, similar to Zn(VD)/CH_4/air/MOR, a substantial peak corresponding to the [Zn^{II}-CH_3] species remains after air exposure for 12 h. This could indicate that the [Zn^{II}-CH_3] species is particularly stable in the small cages of CHA or that diffusion of the products is perhaps difficult. After 24 h of air exposure (the rotor cap was removed for a further 12 h), no trace of the [Zn^{II}-CH_3] species is observed in the ^{13}C CP NMR spectrum (**Error! Reference source not found.**D). A substantial amount of physisorbed MeOH is detected in both the CP and direct ^{13}C NMR spectra and a small amount of zinc formate due to over oxidation. Therefore, the CHA(62)A produces the same products, methanol and zinc formate species, as other Zn/zeolites upon reaction with zinc vapour and methane followed by exposure to air. Although, the [Zn^{II}-CH_3] species is still observed after 12 h exposure to air, somewhat similar to Zn(VD)/CH_4/air/MOR.

Investigating the role of Al distribution in CHA on methane activation led to some interesting conclusions. Overall, the level of Al pairing did not seem to impact the percentage of zinc active sites produced, but Si/Al ratio seems to have a significant impact on the number of active sites. Zn/Al ratios were found to be higher than expected, partially due to the reaction of zinc vapour with defect sites present in the CHA parents as determined by ^{29}Si CP NMR spectroscopy. However, the Zn/Al ratio of 3 for CHA(62) remains inexplicable without further analysis. This CHA(62) shows remarkable activity and potentially contains a different zinc active site. However, all samples reacted as expected with methane producing a [Zn^{II}-CH_3] species and subsequent exposure to air for CHA(62) resulted in physiorbed MeOH and zinc formate species.

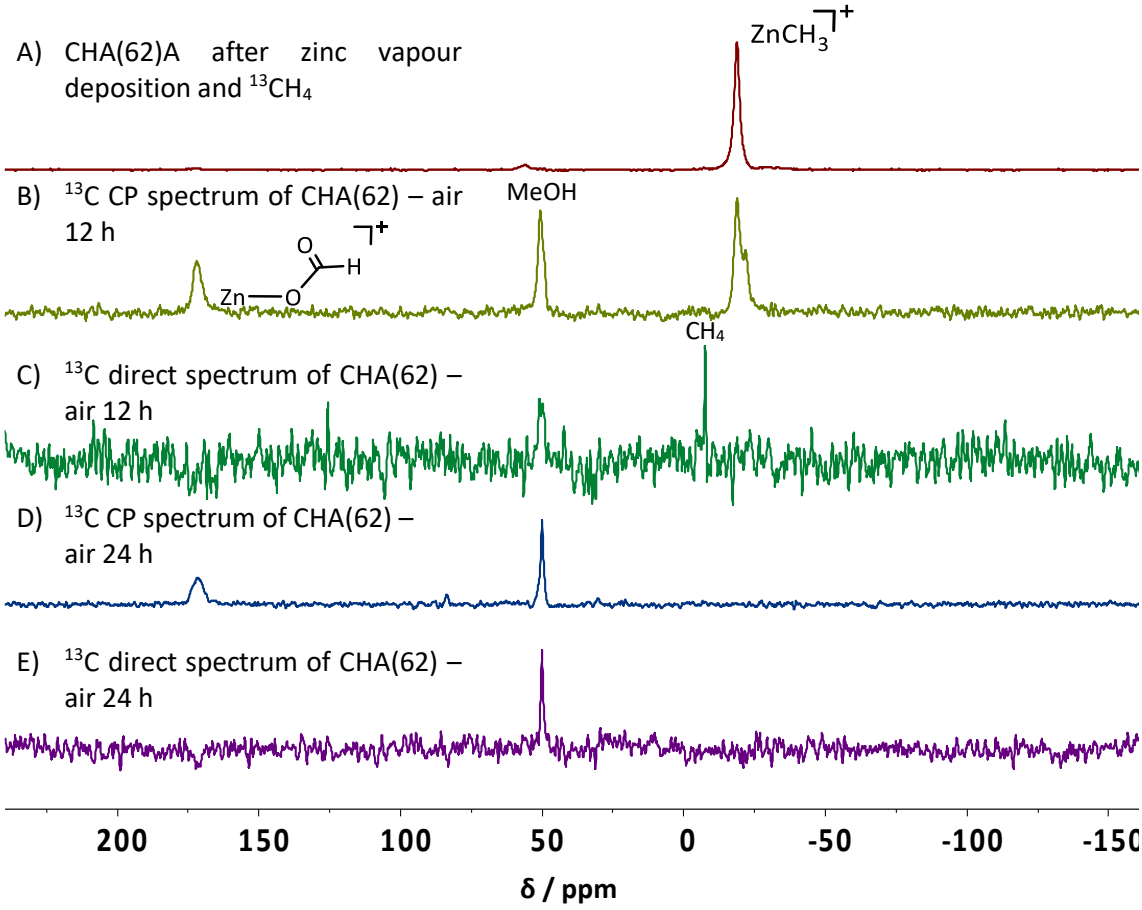

Figure 17: ^{13}C NMR spectra of CHA(62) after exposure to air for 12 h and 24 h. Both direct and CP ^{13}C spectra are shown. Signals corresponding to free methanol (50 ppm) and formate species (173 ppm) observed after air exposure. (^{13}C – 100 . 57 MHz, 10 kHz spin rate)

4.3 Conclusions

Using CVD with an excess of zinc metal, zinc-modified zeolites of three frameworks (ZSM-5, FER and MOR) were prepared with high levels of zinc exchange. After CVD, the materials retained high surface areas, good crystallinity and no additional defects were observed. Upon exposure to $^{13}CH_4$, C-H activation was observed to occur for all three frameworks, as determined by a characteristic signal resulting from [Zn^{II}-CH_3] in ^{13}C MAS NMR spectroscopic studies. Using HMB as an internal standard, the percentage of zinc atoms that resulted in the formation of the [Zn^{II}-CH_3] species was determined; the order was found to be Zn(VD)/CH_4/ZSM-5 (5.7%), Zn(VD)/CH_4/MOR (1.2%) and Zn(VD)/CH_4/FER (0.5%). At this stage it is unclear why the ZSM-5 framework results in a substantially greater number of active Zn sites than either MOR or FER, but this is potentially due to the difference in topology between the three frameworks or difference in Al distribution for example.

A small study was undertaken into the effect of Si/Al on methane activation using high Al Y (2.55) and low Al ZSM-5 (45). Both zeolite samples were able to activate methane to a similar degree indicating that Al pairs are not necessarily required for methane activation post zinc vapour deposition, although, no quantitative analysis was performed.

The activation of methane over Zn(VD)/MOR proved to be particularly interesting as two signals were observed in the ^{13}C NMR spectrum after exposure to $^{13}CH_4$. Further NMR spectroscopy experiments determined that these two signals belonged to two distinct chemical environments, which were unable to chemically exchange and had different J-coupling constants. This fitted with our hypothesis that the two signals are associated with [Zn^{II}-CH_3] species present in the 12 MR channels and the 8 MR side pockets of the MOR framework. Additionally, the two species undergo different rates of reaction upon exposure to O_2.

After establishing stoichiometric methane activation, the reactivity of the [Zn^{II}-CH_3] species under oxidative conditions was explored. As expected, zinc methoxy and zinc formate species were formed by all three frameworks after exposure to O_2 at elevated temperatures. However, the three frameworks demonstrated dissimilar reactivity under different oxidative conditions highlighting that the framework plays a key role in the reactivity of the [Zn^{II}-CH_3] species. ZSM-5 framework was found to be the most reactive environment for the [Zn^{II}-CH_3] species whilst Zn(VD)/CH_4/air/MOR seemed selective for methanol.

To further explore the role of Al pairing on methane activation in zinc zeolites, three CHA samples with different levels of pairing (high, low and none) were synthesised by collaborators. Interestingly, the three samples produced similar percentages of active zinc sites

(3-4%) in line with the 4% produced by the standard CHA sample. Whilst Al paring did not impact methane activation levels, Si/Al ratio had a significant impact on the number of zinc active sites produced as in CHA(62), 20% of the zinc sites were able to form the [Zn^{II}-CH_3] species. Zn/Al ratios were higher than expected, likely due to the reaction of zinc vapour with defect sites present in the parents, evidenced by ^{29}Si CP NMR spectroscopy. However, a Zn/Al ratio of 3 for CHA(62) alongside its remarkable activity remains inexplicable, perhaps indicating a different zinc species is present in high silica CHA.

4.4 Experimental

H–MOR (Si/Al = 10), H–ZSM–5 (15) and H-ZSM-5 (45) were kindly provided by Clariant. NH_4–ZSM-5 (12.5) was kindly provided by Johnson Matthey. NH_4–FER (10) and H-Y (2.55) were purchased from Alfa Aesar. All CHA samples were synthesised by Julien Devos at KU Leuven, all CHA experiments were in collaboration with Michiel Dusselier, KU Leuven. Zinc powder (Goodfellow, 99.9%, max particle size 150 µm) was used as purchased. Zinc nitrate hexahydrate (99%) was used as purchased from Alfa Aesar. Methane-^{13}C (99% ^{13}C) was purchased from Sigma-Aldrich. CH_4 (99.995%), O_2 (99.5%), N_2 (oxygen free) and Ar (99.998%) cylinders were purchased from BOC. Zinc powder was stored and used in a PureLab HE glove box under an argon atmosphere.

The ion exchanged ZSM–5 (Zn(IE)/ZSM-5) was prepared by treating NH_4–ZSM–5 (12.5) with an aqueous solution $Zn(NO_3)_2$ based on a method reported by Kuroda *et al.*.[27] Zinc ion exchanges were carried out using 2.5 g of zeolite in a centrifuge tube in contact with 50 ml of 0.3M $Zn(NO_3)_2$ solution for 1 h with constant agitation from a mechanical tube roller. The tube was centrifuged at 4500 rpm for 5.5 min and the resulting supernatant decanted. The zeolite was then re-dispersed into the zinc nitrate solution and this process was repeated 10 times. The sample was then washed with 50 ml of deionised water 8 times and dried at 80 °C overnight. The resulting sample is referred to Zn(IE)/ZSM–5.

The vapour deposition samples were prepared by an exchange reaction between metallic zinc vapour and the H-form/NH_4-form of the zeolite. This was carried out in a custom quartz u-tube which ensured the separation of the zinc powder and zeolite. All parent zeolites were pre-treated in the same way to dehydrate the sample before exposure to zinc vapour. The parent zeolite was placed into a quartz tube under vacuum (pressure < 10^{-2} mbar) and heated to 150 °C for 1 h followed by 5 h at 550 °C in a tube furnace. A 5 °C min^{-1} ramp rate was used for all furnace program steps. After dehydration, the zeolites were stored in the glovebox. The zinc vapour deposition conditions were based on a method reported by Stepanov *et al*..[6] To achieve maximum ion exchange, a 100-fold excess of zinc (Zn/Al =100) was used for the vapour deposition. The quartz u-tube and liner used for the reaction are shown in Chapter 3.1.1. The u-tube was loaded with zinc metal and zeolite in the glovebox, ensuring the powders were well separated on either sides of the tube. The u-tube was then attached to a Schlenk line and placed under vacuum (pressure <10^{-2} mbar). To expose the zeolite sample to zinc vapour, the u-tube was sealed and placed in a tube furnace where it was heated to 500 °C at 5 °C min^{-1} and held for 1 h under static vacuum. Excess unreacted zinc vapour was further removed by continued

heating at 500 °C for 2 h under dynamic vacuum. These samples are referred to as Zn(VD)/zeolite.

Where methane activation took place, the u-tube containing the zinc modified zeolite was cooled to 250 °C in the furnace. The u-tube was filled with 1 atm of $^{13}CH_4$, sealed and held at 250 °C for 15 min. After cooling, the sealed tube was taken into the argon glovebox. These samples, labelled Zn(VD)/CH_4/zeolite, were packed into a solid state NMR rotor in the glovebox. NMR experiments were typically conducted immediately after C-H activation.

The ion exchanged sample, Zn(IE)/ZSM-5, was activated based on a method by Kuroda *et al.*.[27] The zeolite was heated to 600 °C for 4 h at 5 °C min^{-1} ramp rate under vacuum. This was cooled to 250 °C after which the tube was sealed under 1 atm of $^{13}CH_4$ and held at 250 °C for 2 h. After cooling, the sealed tube was taken into the argon glovebox. The sample, labelled Zn(IE)/CH_4/ZSM–5, was packed into a solid state NMR rotor in the glovebox. NMR experiments were typically conducted immediately after C-H activation.

The [Zn^{II}-CH_3] species in Zn(VD)/CH_4/ZSM–5, Zn(VD)/CH_4/MOR Zn(VD)/CH_4/FER and CHA(62)A were tested for reactivity with O_2 and air. After exposure to zinc vapour and $^{13}CH_4$ using the conditions above, a solid state NMR rotor was packed in the glove box and a ^{13}C NMR spectrum was taken to confirm the presence of the [Zn^{II}-CH_3] species and check no other signals were observed. The rotor containing Zn/CH_4/zeolite was subsequently placed in a Schlenk flask under a flow of O_2/Ar, after removing the rotor cap. This was exposed to a mixture of 20% O_2 in Ar flowing at room temperature for 15 min. When testing reactivity at 200 °C, the flask was sealed under the atmosphere of the O_2/Ar mixture, and the samples were heated at 200 °C for 15 min. After cooling to room temperature, the rotor was then re-capped under a nitrogen flow. Reactivity with air was tested by removing the rotor cap of samples Zn/CH_4/zeolite and leaving the samples exposed to air overnight.

4.5 Chapter 4 References

1. M. A. Shah, S. Raynes, D. C. Apperley and R. A. Taylor, *Chem. Phys. Chem.*, 2020, **21**, 673-679.
2. V. B. Kazansky and A. I. Serykh, *Phys. Chem. Chem. Phys.*, 2004, **6**, 3760-3764.
3. V. B. Kazansky, A. I. Serykh and E. A. Pidko, *J. Catal.*, 2004, **225**, 369-373.
4. B. E. R. Snyder, M. L. Bols, R. A. Schoonheydt, B. F. Sels and E. I. Solomon, *Chem. Rev.*, 2018, **118**, 2718-2768.
5. M. V. Luzgin, D. Freude, J. Haase and A. G. Stepanov, *J. Phys. Chem. C*, 2015, **119**, 14255-14261.
6. A. A. Gabrienko, S. S. Arzumanov, M. V. Luzgin, A. G. Stepanov and V. N. Parmon, *J. Phys. Chem. C*, 2015, **119**, 24910-24918.
7. Y. G. Kolyagin, I. I. Ivanova and Y. A. Pirogov, *Solid State Nucl. Magn. Reson.*, 2009, **35**, 104-112.
8. E. A. Pidko and R. A. van Santen, *J. Phys. Chem. C*, 2007, **111**, 2643-2655.
9. A. Oda, H. Torigoe, A. Itadani, T. Ohkubo, T. Yumura, H. Kobayashi and Y. Kuroda, *J. Phys. Chem. C*, 2013, **117**, 19525-19534.
10. J. Chen, Z. Feng, P. Ying and C. Li, *J. Phys. Chem. B*, 2004, **108**, 12669-12676.
11. A. A. Gabrienko, S. S. Arzumanov, D. Freude and A. G. Stepanov, *J. Phys. Chem. C*, 2010, **114**, 12681-12688.
12. I. Pinilla-Herrero, E. Borfecchia, J. Holzinger, U. V. Mentzel, F. Joensen, K. A. Lomachenko, S. Bordiga, C. Lamberti, G. Berlier, U. Olsbye, S. Svelle, J. Skibsted and P. Beato, *J. Catal.*, 2018, **362**, 146-163.
13. A. Mehdad and R. F. Lobo, *Catal. Sci. Technol.*, 2017, **7**, 3562-3572
14. J. F. Wu, W. D. Wang, J. Xu, F. Deng and W. Wang, *Chem. - Eur. J.*, 2010, **16**, 14016-14025.
15. Y. G. Kolyagin, I. I. Ivanova, V. V. Ordomsky, A. Gedeon and Y. A. Pirogov, *J. Phys. Chem. C*, 2008, **112**, 20065-20069.
16. E. Morra, G. Berlier, E. Borfecchia, S. Bordiga, P. Beato and M. Chiesa, *J. Phys. Chem. C*, 2017, **121**, 14238-14245.
17. A. Oda, T. Ohkubo, T. Yumura, H. Kobayashi and Y. Kuroda, *Dalton Trans.*, 2015, **44**, 10038-10047.
18. S. M. T. Almutairi, B. Mezari, P. C. M. M. Magusin, E. A. Pidko and E. J. M. Hensen, *ACS Catal.*, 2012, **2**, 71-83.
19. V. B. Kazansky, V. Y. Borovkov, A. I. Serikh, R. A. Van Santen and B. G. Anderson, *Catal. Lett.*, 2000, **66**, 39-47.
20. A. Dyer and T. I. Emms, *J. Mater. Chem.*, 2005, **15**, 5012-5021.
21. S. C. Albarracín-Suazo, Y. J. Pagán-Torres and M. C. Curet-Arana, *J. Phys. Chem. C*, 2019, **123**, 16164-16171.
22. H. Elmar, *Z. Anorg. Allg. Chem.*, 2000, **626**, 2223-2227.
23. A. Oda, T. Ohkubo, T. Yumura, H. Kobayashi and Y. Kuroda, *Inorg. Chem.*, 2019, **58**, 327-338.
24. Y. Lin, S. Qi, L. Benedict, Z. Junlin, K. Dejing, M. Claire, T. Chiu and T. Edman, *Angew. Chem. Int. Ed.*, 2017, **56**, 10711-10716.
25. T. Gullion, *Chem. Phys. Lett.*, 1995, **246**, 325-330.
26. A. A. C. Reule, J. A. Sawada and N. Semagina, *J. Catal.*, 2017, **349**, 98-109.
27. A. Oda, H. Torigoe, A. Itadani, T. Ohkubo, T. Yumura, H. Kobayashi and Y. Kuroda, *J. Phys. Chem. C*, 2014, **118**, 15234-15241.
28. A. A. Gabrienko, S. S. Arzumanov, A. V. Toktarev, I. G. Danilova, I. P. Prosvirin, V. V. Kriventsov, V. I. Zaikovskii, D. Freude and A. G. Stepanov, *ACS Catal.*, 2017, **7**, 1818-1830.
29. A. Oda, T. Ohkubo, T. Yumura, H. Kobayashi and Y. Kuroda, *Phys. Chem. Chem. Phys.*, 2017, **19**, 25105-25114.

30. J. Geertsen, J. Oddershede, W. T. Raynes and G. E. Scuseria, *J. Magn. Reson*, 1991, **93**, 458-471.
31. M. Hunger, P. Sarv and A. Samoson, *Solid State Nucl. Magn. Reson.*, 1997, **9**, 115-120.
32. P. J. Chu, B. C. Gerstein, J. Nunan and K. Klier, *J. Phys. Chem.*, 1987, **91**, 3588-3592.
33. A. Bhan, A. D. Allian, G. J. Sunley, D. J. Law and E. Iglesia, *J. Am. Chem. Soc.*, 2007, **129**, 4919-4924.
34. M. Boronat, C. Martinez-Sanchez, D. Law and A. Corma, *J. Am. Chem. Soc.*, 2008, **130**, 16316-16323.
35. R. Gounder and E. Iglesia, *J. Am. Chem. Soc.*, 2009, **131**, 1958-1971.
36. A. Janda and A. T. Bell, *J. Am. Chem. Soc.*, 2013, **135**, 19193-19207.
37. D. K. Pappas, A. Martini, M. Dyballa, K. Kvande, S. Teketel, K. A. Lomachenko, R. Baran, P. Glatzel, B. Arstad, G. Berlier, C. Lamberti, S. Bordiga, U. Olsbye, S. Svelle, P. Beato and E. Borfecchia, *J. Am. Chem. Soc.*, 2018, DOI: 10.1021/jacs.8b08071, 15270–15278.
38. N. Katada, K. Suzuki, T. Noda, G. Sastre and M. Niwa, *J. Phys. Chem. C*, 2009, **113**, 19208-19217.
39. J. R. Di Iorio and R. Gounder, *Chem. Mater.*, 2016, **28**, 2236-2247.
40. P. Sazama, J. Dědeček, V. Gábová, B. Wichterlová, G. Spoto and S. Bordiga, *J. Catal.*, 2008, **254**, 180-189.
41. A. B. Pinar, C. Márquez-Álvarez, M. Grande-Casas and J. Pérez-Pariente, *J. Catal.*, 2009, **263**, 258-265.
42. Y. Román-Leshkov, M. Moliner and M. E. Davis, *J. Phys. Chem. C*, 2011, **115**, 1096-1102.
43. J. Dědeček, Z. Sobalík and B. Wichterlová, *Catal. Rev.*, 2012, **54**, 135-223.
44. B. C. Knott, C. T. Nimlos, D. J. Robichaud, M. R. Nimlos, S. Kim and R. Gounder, *ACS Catal.*, 2018, **8**, 770-784.
45. J. R. Di Iorio, C. T. Nimlos and R. Gounder, *ACS Catal.*, 2017, **7**, 6663-6674.
46. J. Dědeček, E. Tabor and S. Sklenak, *Chem. Sus. Chem.*, 2019, **12**, 556-576.
47. J. Devos, M. L. Bols, D. Plessers, C. V. Goethem, J. W. Seo, S.-J. Hwang, B. F. Sels and M. Dusselier, *Chem. Mater.*, 2020, **32**, 273-285.
48. K. Mlekodaj, J. Dedecek, V. Pashkova, E. Tabor, P. Klein, M. Urbanova, R. Karcz, P. Sazama, S. R. Whittleton, H. M. Thomas, A. V. Fishchuk and S. Sklenak, *J. Phys. Chem. C*, 2019, **123**, 7968-7987.
49. S. Li, H. Li, R. Gounder, A. Debellis, I. B. Müller, S. Prasad, A. Moini and W. F. Schneider, *J. Phys. Chem. C*, 2018, **122**, 23564-23573.
50. D. W. Fickel and R. F. Lobo, *J. Phys. Chem. C*, 2010, **114**, 1633-1640.
51. M. L. Bols, S. D. Hallaert, B. E. R. Snyder, J. Devos, D. Plessers, H. M. Rhoda, M. Dusselier, R. A. Schoonheydt, K. Pierloot, E. I. Solomon and B. F. Sels, *J. Am. Chem. Soc.*, 2018, **140**, 12021-12032.
52. S. D. Hallaert, M. L. Bols, P. Vanelderen, R. A. Schoonheydt, B. F. Sels and K. Pierloot, *Inorg. Chem.*, 2017, **56**, 10681-10690.
53. M. J. Wulfers, S. Teketel, B. Ipek and R. F. Lobo, *Chem. Comm.*, 2015, **51**, 4447-4450.
54. B. Ipek and R. F. Lobo, *Chem Commun*, 2016, **52**, 13401-13404.
55. R. Oord, J. E. Schmidt and B. M. Weckhuysen, *Catal. Sci. Technol.*, 2018, **8**, 1028-1038.
56. C. Paolucci, A. A. Parekh, I. Khurana, J. R. Di Iorio, H. Li, J. D. Albarracin Caballero, A. J. Shih, T. Anggara, W. N. Delgass, J. T. Miller, F. H. Ribeiro, R. Gounder and W. F. Schneider, *J. Am. Chem. Soc.*, 2016, **138**, 6028-6048.
57. A. R. Kulkarni, Z.-J. Zhao, S. Siahrostami, J. K. Nørskov and F. Studt, *ACS Catal.*, 2016, **6**, 6531-6536.
58. K. Narsimhan, K. Iyoki, K. Dinh and Y. Román-Leshkov, *ACS Cent. Sci.*, 2016, **2**, 424-429.
59. M. Ravi, V. L. Sushkevich and J. A. van Bokhoven, *J. Phys. Chem. C*, 2019, **123**, 15139-15144.
60. H. K. Beyer, G. Pál-Borbély and M. Keindl, *Micro. Meso. Mater.*, 1999, **31**, 333-341.

Chapter 5: Selective dealumination of MOR and subsequent effect on C-H activation

Chapter 5: Selective dealumination of MOR and subsequent effect on C-H activation

5.1 Introduction

Regardless of their widespread use in industry, dealuminated zeolites and the dealumination process itself, are poorly understood despite substantial effort from groups across the community.[1-5] Dealumination causes a reduction in the framework charge and therefore results in the loss of extraframework cation capacity. The aluminium removed from the framework may form extraframework alumina, which can cause pore blockage and its Lewis acidic nature can promote other reaction pathways in catalysts. However, in certain cases, dealumination can be used to provide desirable benefits. For example, the activity of zeolites as acid-catalysts in industrial reactions can be improved through steam treatment due to the formation of mesopores.[1-4] Additionally, the dealumination of zeolite Y to form ultra-stable Y (USY) for hydrocarbon cracking has been found to improve thermal and hydrothermal stability of the material.[5]

The MOR framework is a one dimensional framework that consists of 12 MR channels, 8 MR channels and 8 MR side pockets (Figure 1). This framework is particularly susceptible to dealumination due to the presence of 4 MRs as the extend of dealumination can be correlated with the number of 4 MRs present in a zeolite: beta>MOR>ZSM-5>FER.[6] This is likely due to the highly strained Al environment present in 4 MRs which leads to distortion of the ideal tetrahedral shape. Additional spectroscopic evidence from van Geem *et al.* demonstrates that steaming removes Al from the 4 MR only.[7] In this study, two processes for the selective dealumination of MOR were investigated, dealumination *via* steaming or using nitric acid where both methods are likely to result in the removal of tetrahedral Al from the 4 MRs of MOR.

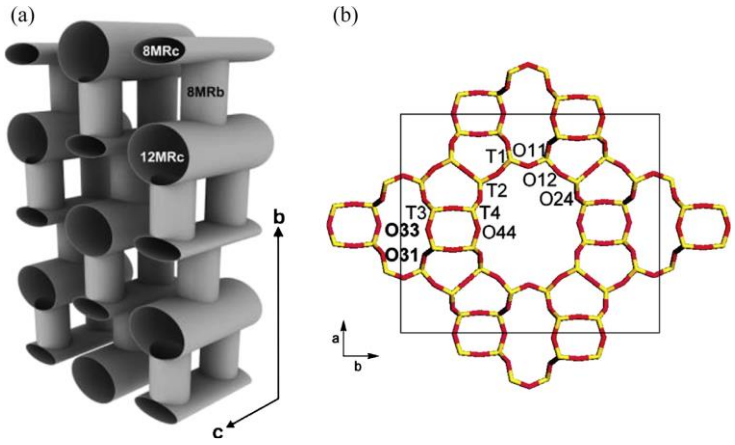

Figure 1: Four different crystallographic tetrahedral sites in MOR: T_1 and T_2 are located in the 12 MR whilst T_3 and T_4 are located in the 8 MR side pockets. Adapted from ref 12. Copyright 2017 Elsevier.

The mechanism of dealumination with acid has been explored using ^{27}Al and ^{29}Si NMR spectroscopies complemented with computational studies.[8-10] The formation of extraframework Al can be monitored through ^{27}Al NMR spectroscopy whilst the formation of SiOH groups can be detected and quantified through ^{29}Si NMR spectroscopy. Raybaud *et al.* determined through DFT calculations that dealumination is initiated through water adsorption in anti-position to the BAS.[9] This results in a pentahedral/distorted tetrahedral Al atom from which the Al-O bonds can be hydrolysed. Typically, the ratio of BAS in MOR is approximately 50:50 between the 8 MR channels and 12 MR channels for a wide range of Si/Al ratios and MOR consists of four different crystallographic tetrahedral sites – T-sites (Figure 1).[10-14] de Jong *et al.* have thoroughly investigated the mechanism of dealumination on MOR using experimentally validated Monte Carlo simulations.[10] They suggest that Dempsey's rule,[15] which states that the number of Al-O-Si-O-Al linkages assumes a minimum for a given Si/Al ratio, is valid for all of the building units of MOR except the 4 MRs as the presence of Al stabilises these 4 MRs.[10] They conclude from simulations and ^{29}Si NMR experiments that the dealumination mechanism in MOR is a multiple-step process where Al is removed from the zeolite framework and stacking faults simultaneously, forming SiOH nests. Migrating Si atoms are able to heal some of the SiOH nests produced until the final structure of dealuminated MOR shows micropores and mesopores. Argon physisorption experiments combing again with Monte Carlo simulations indicated that Al-rich 4 MR are mainly dissolved alongside some of the internal surfaces of the main channels resulting in large pores after the dealumination.

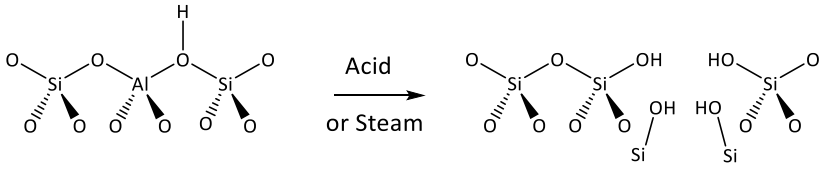

Figure 2: Formation of silanol nests after dealumination of zeolite with acid or steam treatment

Dealumination of MOR through steam treatment results in the extraction of Al that is subsequently deposited on the channels and outer surface of the zeolite as alumina.[8, 16-18] This extraframework aluminium can be removed by acid washing the zeolite using mineral acids such as HCl or organic acids such as oxalic acid.[6, 11, 16, 19-21] Whist dealumination preferentially occurs at the T_3 and T_4 sites due to the strained environment in the 4 MRs, it has been shown that the Al sites in the 8 MR can be protected from dealumination through partial exchange of a univalent metal such as Na^+. The cation is preferentially exchanged into the 8 MR side pocket leading to dealumination of Al in the 12 MR channels only.[8, 11, 22, 23] Once the Al in the 8 MR SP is protected with the Na^+ cation, the Al-O cannot be hydrolysed as the initial water molecule cannot be adsorbed as no BAS is present, [9] hence, no dealumination will occur where Na^+ is exchanged.

As determined in Chapter 4, methane activation over Zn(VD)/MOR results in the formation of two distinct [Zn^{II}-CH_3] species which can be observed as two signals in the ^{13}C NMR spectrum. The signal at –15 ppm is assigned to the [Zn^{II}-CH_3] fragment in the 8MR SP while the signal at –20 ppm is assigned to the [Zn^{II}-CH_3] fragment in the 12MR main channel. In this chapter, the effect of the selective dealumination of MOR on methane activation is explored. NMR experiments have been used in conjunction with pXRD, elemental, SEM and BET analysis to determine the selectivity and extent of dealumination in MOR. ^{13}C NMR spectroscopic studies have been utilised to monitor changes in the methane activation after the dealumination treatment using nitric acid or steam.

5.2 Results and Discussion

5.2.1 Selective dealumination of MOR

In this study, two processes for the selective dealumination of MOR were investigated; dealumination *via* steaming or using nitric acid. Both of these methods should primarily remove Al from the T_3 and T_4 sites located in the 4 MR as this is the most strained Al environment in the MOR framework. [6, 7] Protecting the 4 MR by exchanging a 1+ cation into the 8 MR side pockets should result in dealumination from the 12MR channels of MOR. These three dealumination methods were carried out on H-MOR (10), supplied by Clariant, and the extent of dealumination monitored through elemental analysis and Al NMR.

^{27}Al MAS NMR spectroscopy was used to determine the effect of dealumination and acid washing. Framework Al (Al_{tet}) typically has a tetrahedral coordination environment resulting in a chemical shift of around 55 ppm whilst octahedral Al (Al_{oct}) has a chemical shift at 0 ppm.[24] The commercial H-MOR (10) parent sample, provided by Clariant, shows two resonances in its ^{27}Al NMR spectrum, with a broad shoulder corresponding to the tetrahedral signal (Figure 3). This suggests the presence of heterogeneity within the Al sites potentially including five co-ordinate or distorted tetrahedral species.[25] In the parent sample, the octahedrally co-ordinated species may be framework-associated and not extraframework aluminium. van Bokhoven *et al.* have demonstrated that for MOR, ion exchange from the protic to ammonium form of the zeolite results in an increase in the tetrahedrally coordinated aluminium, clearly indicating the octahedral species is linked to the zeolite framework.[25] Calcination of the ammonium form of the MOR results in the return of the octahedrally co-ordinated species, observed by ^{27}Al NMR spectroscopy, indicating the reversibility of coordination. For Beta, SSZ-33 and SSZ-35 frameworks, aluminium species which demonstrate a sharp signal at around 0 ppm are able to reinsert back into the zeolite framework.[26, 27] A broader feature at 0 ppm is often observed from extraframework octahedral aluminium which is unable to reinsert into the zeolite framework.

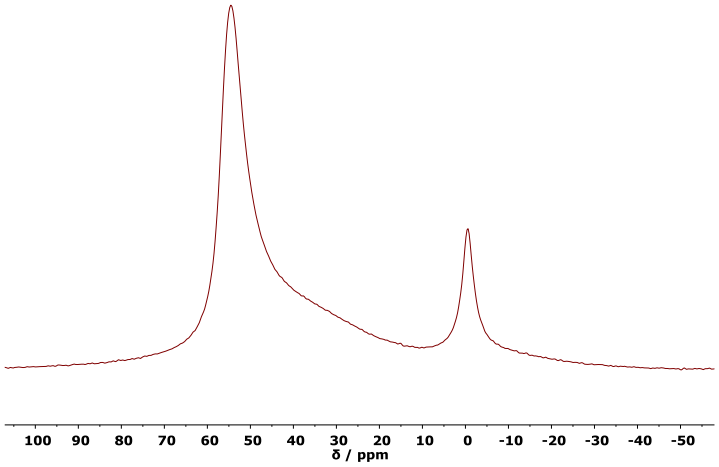

Figure 3: ^{27}Al NMR of H-MOR (10) parent material supplied by Clariant. (^{27}Al – 104.20 MHz, 14 kHz spin rate)

Whilst there is some uncertainty over the state of octahedral framework Al in zeolites, two differing species have been proposed for zeolites Beta and Y (Figure 4) through extensive ^{27}Al NMR spectroscopic studies, probe molecule absorption and XANES. Originally, Montouillout *et al.* suggested that tetrahedral framework Al coordinated to a water molecule and hydronium cation forming octahedral framework Al (Figure 4B).[28] However, further studies suggest that the bond between the framework Al and bridging hydroxyl is hydrolysed resulting in 3-coordinate Al, which subsequently binds to three water molecules (Figure 4A).[29, 30] XANES studies on beta and MOR zeolites support this hypothesis as upon dehydration to temperatures higher that 675 K, a unique pre-edge feature in the Al-edge XANES is observed, indicative of three-fold coordinated aluminium oxide species.[31] The amount of three-coordinate Al formed increases as a function of temperature; 5-10% at 985 K in MOR.[32] The species remain stable upon cooling to room temperature and upon rehydration of the materials, 6-coordinate Al forms. van Bokhoven *et al.* carried out a further comparison of 3-coordinate Al in steamed and unsteamed Beta.[31] The steamed sample was found to contain more three-coordinate Al likely due to the creation of defect sites during the steaming process.

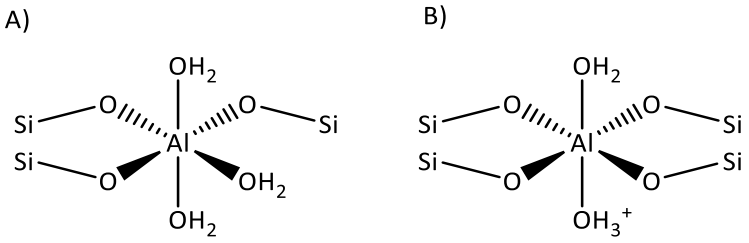

Figure 4: Differing species proposed for framework associated octahedral Al. (^{27}Al – 104.20 MHz, 14 kHz spin rate)

The parent zeolite, H-MOR (10), was treated with steam (H-MOR-deAL) or nitric acid (H-MOR-nitric) to remove Al from the zeolite framework. Additionally, after partial exchange with Na^+ (Na/Al = 0.4) to protect the aluminium in the 4MRs, similar steam treatment was carried out (Na/H-MOR-deAl). To remove the extraframework Al debris, all of the steamed samples were acid washed. Initially, one wash with 1M HCl at 80 °C was carried out and whilst some extraframework Al was removed, a significant signal remained at 0 ppm in the ^{27}Al NMR spectrum (Figure 5). A second wash with oxalic acid was carried out to try to remove the remaining Al debris and significant five and six co-ordinate Al was removed.

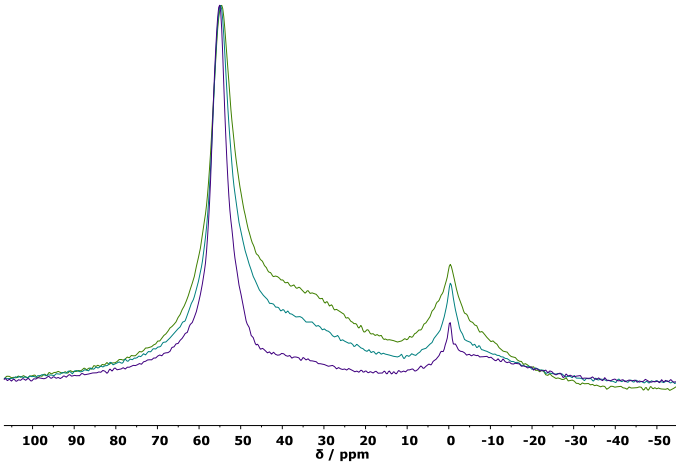

Figure 5: Stacked plot of ^{27}Al NMR demonstrating effect of acid washing on H-MOR dealuminated with steam. Green: H-MOR-deAl no washes, blue: H-MOR-deAl after one HCl wash and purple: H-MOR-deAl after one HCl wash and one oxalic acid wash. (^{27}Al – 104.20 MHz, 14 kHz spin rate)

Dealumination, particularly the harsh conditions of the steam treatment at 500 °C for 4 h, can damage the zeolite framework. Furthermore, the extraframework Al that is formed can block pore sites and channels if not removed by acid washing. Numerous techniques must be used in conjunction to establish structural stability and lack of pore blockage.

Elemental analysis was performed to determine how much Al was removed from the samples after steaming and treatment with nitric acid. This was measured after the acid washing on the steamed samples was carried out. To determine the quantity of tetrahedral Al in each sample, the ratio of tetrahedral to octahedral Al was determined from integration of the two signals in the ^{27}Al NMR spectra (Figure 6). The Si/Al_{tet} increases significantly for both steamed samples whilst a smaller change is observed after treatment with nitric acid (Table 1). The higher dealumination from steaming compared with the nitric acid treatment is likely due to the higher temperatures (500 °C compared to 85 °C) and longer treatment time (4 h compared to 1 h).

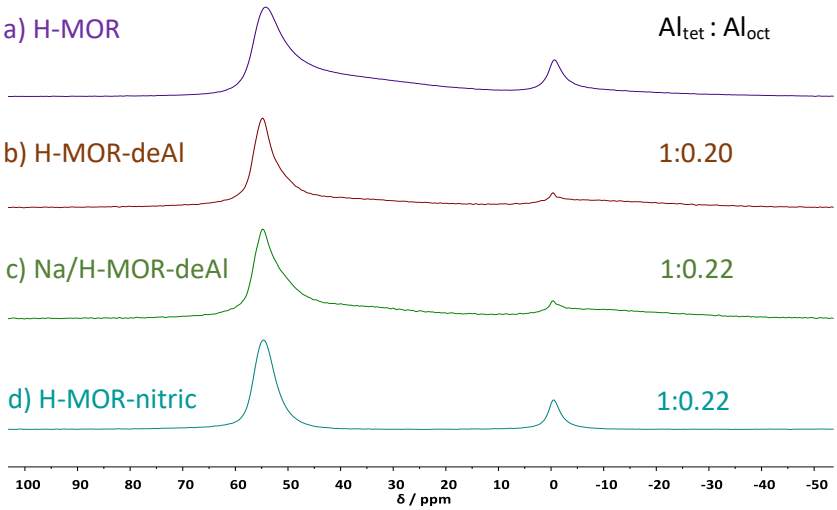

Figure 6: ^{27}Al NMR and Al_{tet} : Al_{oct} ratios for a) H-MOR parent, b) H-MOR-deAl, c)Na/H-MOR-deAl and d)H-MOR nitric. Spectra shown for steamed samples are post acid washing. (^{27}Al – 104.20 MHz, 14 kHz spin rate)

Table 1: Elemental analysis and BET measurements after dealumination with steaming, nitric acid and subsequent healing with TEOS was carried out on H-MOR.

Sample	Si/Al_{tet}	BET / m^2/g
H-MOR	8.51	542 ± 2
H-MOR-deAl	22.48	463 ± 3
Na/H-MOR-deAl	30.45	490 ± 3
H-MOR-nitric	15.37	495 ± 3
H-MOR-TEOS	9.43	469 ± 3

BET analysis was carried out on all samples post dealumination and an increase in BET surface area is expected as the side pockets of MOR begin to open as Al is removed.[12, 33] Unfortunately, a small decrease in BET surface area is observed for all the dealuminated samples (Table 1), which implies Al debris is likely to still be present. This is supported by the ^{27}Al NMR spectroscopy (Figure 6) as a signal at 0 ppm corresponding to octahedral Al is present in all dealumination samples even after acid washing. As MOR is a 1D framework, even a small amount of Al debris could cause significant pore blockage which would affect the BET surface area.

Removing too much Al from the zeolite can result in framework collapse[12] hence it is important to check the integrity of the zeolite framework after dealumination has taken place. The pXRD patterns shown in Figure 7 demonstrate that the framework remains intact after Al removal using both steaming and nitric acid. This is reinforced through the SEM images in Figure

8 which demonstrate that no change in zeolite morphology or crystal size is observed after the harsh treatments of Al removal.

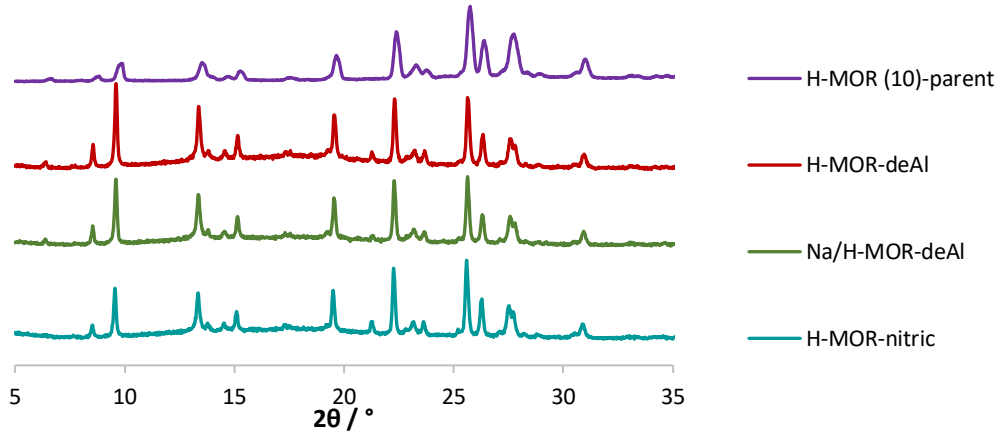

Figure 7: pXRD patterns post dealumination for MOR samples demonstrate the framework remains intact after removal of Al. Note H-MOR (10) parent pXRD pattern was collected as a packed sample whilst deAl samples were collected with the sample adhered to Si wafer using petroleum jelly.

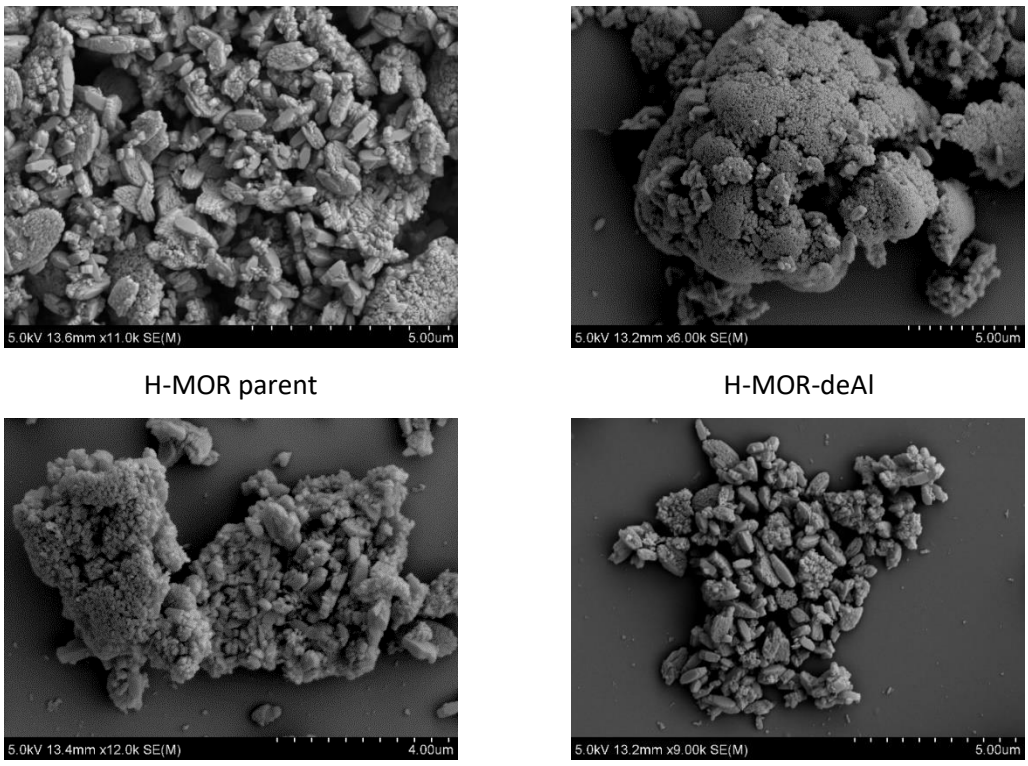

Figure 8: SEM images of MOR post dealumination treatments. No obvious change in morphology is observed post Al removal.

Whilst the above techniques provide proof that successful dealumination has occurred without framework damage and minimal pore blockage, no information is provided about the selectivity of the dealumination process. Diffuse reflectance infra-red (IR) spectroscopy can monitor the O-H stretches of BAS sites in MOR; a band at 3610 cm^{-1} is observed for BAS in the 12MR channels and 3590 cm^{-1} for BAS in the 8MR SPs.[11, 23] After selective dealumination, the IR spectrum can be measured and no BAS sites will be present where Al has been removed, hence, IR is commonly used for interpreting the selectivity of dealumination.[11, 12, 23] As access to high vacuum IR was not possible, ^{133}Cs NMR spectroscopy was used to interpret the selectivity of the dealumination reactions. ^{133}Cs NMR spectroscopy is mostly used for analysing the binding of Cs complexes [34, 35] but can be used to determine environment in Cs exchanged zeolites.[36, 37] ^{133}Cs is 100% abundant and although has a spin of 7/2, the quadrupolar moment is very small (an order of magnitude lower than Al).[38] Two signals have been observed in the ^{133}Cs NMR spectrum of fully dehydrated Cs-exchanged mordenite which was assigned to Cs located in the the 12 MR main channel and 8 MR side pocket within the MOR framework.[36] As preferential dealumination of one site occurs, the ratio between signals in the ^{133}Cs NMR spectrum should change.

The level of Cs ion exchange in the Cs/MOR samples is reported in Table 2 and if full Cs exchange was achieved, the Cs/Al_{tet} ratio would be 1. Full Cs exchange has been found to be difficult in a variety of zeolite frameworks (A, X, Y, ZSM-5) in the literature with exchange values ranging from 60-83%.[37, 39-47] The lower exchange levels observed for this H-MOR parent could be due to the presence of Al debris or lower exchange may just be an inherent property of this H-MOR parent, perhaps due to stacking faults.[10] 100% Cs ion exchange is ideal for full interpretation of the selectivity of dealumination as without all the sites being exchanged, the ratio determined from the two peaks in the ^{133}Cs NMR does not accurately represent all of the Al sites present in the zeolite. Despite not achieving full exchange on all the Cs/MOR dealuminated samples, ^{133}Cs NMR spectroscopy was carried out and the ratio of the signals in the NMR spectra was analysed.

Table 2: Cs/Al_{tet} ion exchange levels of MOR delaluminated samples, the ratio of signals observed in ^{133}Cs NMR spectrum and normalised absolute intensity in ^{133}Cs NMR spectrum

Sample	Cs/Al_{tet}	Ratio of the signals observed in ^{133}Cs NMR	Normalised Absolute Intensity in ^{133}Cs NMR spectrum
Cs/MOR	0.75	1 : 1	38
Cs/MOR-deAl	1.14	0.71 : 1	13
Cs/Na/MOR-deAl	1.03	0.72 : 1	18
Cs/MOR-nitric	0.74	0.71 : 1	34
Cs/MOR-TEOS[1]	0.66	0.76 : 1	23

As mentioned above, to observe the different sites of MOR using ^{133}Cs NMR spectroscopy, the Cs exchanged samples require full dehydration as even small amounts of moisture can cause the signals to combine and shift,[36] demonstrated by the Cs/MOR – nitric sample in Figure 9. The spectrum of the dehydrated sample shows two distinct signals, but the spectrum of the same sample, which had been left in the NMR rotor overnight, is quite different.

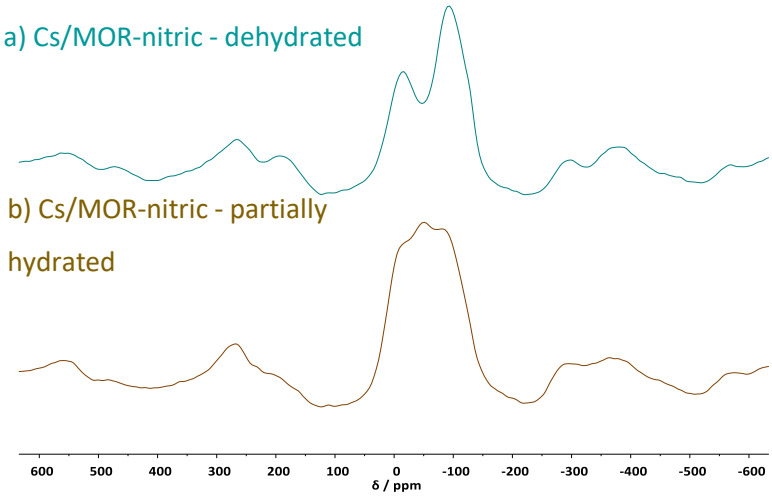

Figure 9: Comparison of dehydrated and partially hydrated ^{133}Cs NMR spectra of Cs/MOR-nitric. (^{133}Cs – 52.45 MHz, 14 kHz spin rate)

To try to determine the selectivity of the dealumination carried out on MOR ^{133}Cs NMR spectra of all dehydrated samples were analysed. The spectra, shown in Figure 10, are relatively complicated with significant spinning side bands and a rolling baseline which can complicate the deconvolution of the NMR spectra. Furthermore, three bands can be observed for most of the

[1] Tetraethyl orthosilicate (TEOS) was used to heal defects in the H-MOR-nitric sample, this is explained further in section 5.2.2

samples, not two clear bands corresponding to Cs in the 8 MR side pockets and to Cs in the 12 MR channels. The signal at −15 ppm was assigned to the 8 MR side pocket whilst the two right-hand bands were assigned to the two T sites found in the 12 MR channels of MOR based on the results from Gerstein *et al.*.[36] IR studies of the BAS sites in MOR have shown three different OH types exist in MOR, 2 are present in the 12 MR channels and the other is present in the 8 MR SP.[14, 48] This could correlate to the three peaks observed in the ^{133}Cs NMR spectra of the dealuminated MOR samples.

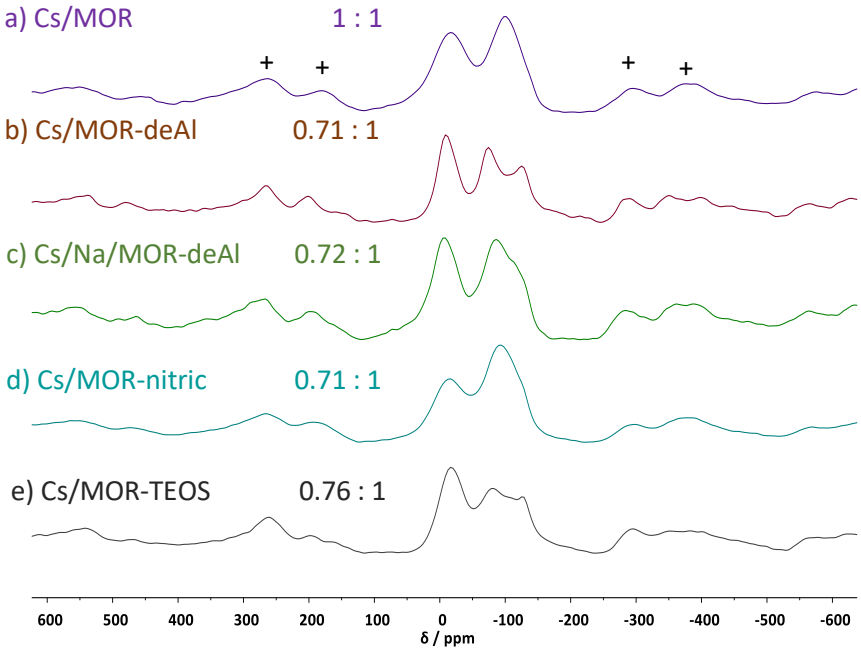

Figure 10: ^{133}Cs NMR spectra and associated ratios for Cs exchanged dealuminated MOR samples. Spinning sidebands denoted with +.

To calculate the ratio between the signals, deconvolution and fitting of the spectra was carried out. The comparison of the fitted spectra with the ^{133}Cs spectra shown above can be found in Appendix 4, Figure 12.This fit was mainly calculated from the shielding anisotropy rather than from the quadrupolar moment as this was found to contribute more significantly. As seen in Table 2, all dealuminated samples show a decrease in the signal corresponding to Cs in the 8 MR side pockets, compared with the parent sample, indicating that removal of Al from the 8 MRs occurred using both steaming and nitric acid methods. However, a few flaws in this analysis method must be addressed. Firstly, as mentioned above, 100% Cs exchange was not reached for all samples and this could drastically impact the ratios observed in the ^{133}Cs NMR spectra. The Al sites which remain associated with a BAS would not be observed by ^{133}Cs NMR

spectroscopy and currently, we are unsure about the location of these Al sites. Therefore, the ratio determined from ^{133}Cs NMR spectroscopy does not characterise all of the Al sites present in the zeolite. Furthermore, as more Al is removed from the framework, less Cs is present in the sample and hence less NMR signal is obtained (Table 2). These two factors combined with the need for complete dehydration of the exchanged samples and the complex deconvolution carried out leads to errors in this analysis method.

5.2.2 Effect of selective dealumination of MOR on methane activation

Although selectivity of the two dealumination process could not be accurately determined, the samples were exposed to zinc vapour in preparation for methane activation to investigate if any affect could be observed. In Chapter 4, it was established that the two signals observed in the ^{13}C NMR spectrum of MOR correspond to the [Zn^{II}-CH_3] fragment in the 8MR SP (–15 ppm) and the [Zn^{II}-CH_3] fragment in the 12MR main channel (–20 ppm). As Al has been removed from either 12 MR or 8 MR SPs during the dealumination reactions, the ratio between the two signals in the ^{13}C NMR spectra, corresponding to the [Zn^{II}-CH_3] fragments, should change.

As Al has been removed from the framework and the CVD process uses high temperature (500 °C) under vacuum (< 10^{-2} mbar), it was important to check the dealuminated samples framework could survive the CVD reaction. The steamed samples showed little change in their pXRD patterns after zinc vapour deposition, but the H/MOR-nitric sample shows some loss in crystallinity (Figure 11). Tetraethyl orthosilicate, TEOS, has been used to stabilise double four rings through Si enrichment in germanosilicate zeolites post synthesis which are particularly prone to collapse under hydrolytic conditions.[49, 50] This stabilisation process was carried out on H-MOR-nitric to try to heal some of the silanol nests through addition of Si. Successful healing occurred as the Si/Al ratio decreased from 15.37 to 9.43 post healing (Table 3). The pXRD pattern post treatment with TEOS and exposure to zinc vapour shows no framework damage (Figure 11, Zn(VD)/MOR - TEOS).

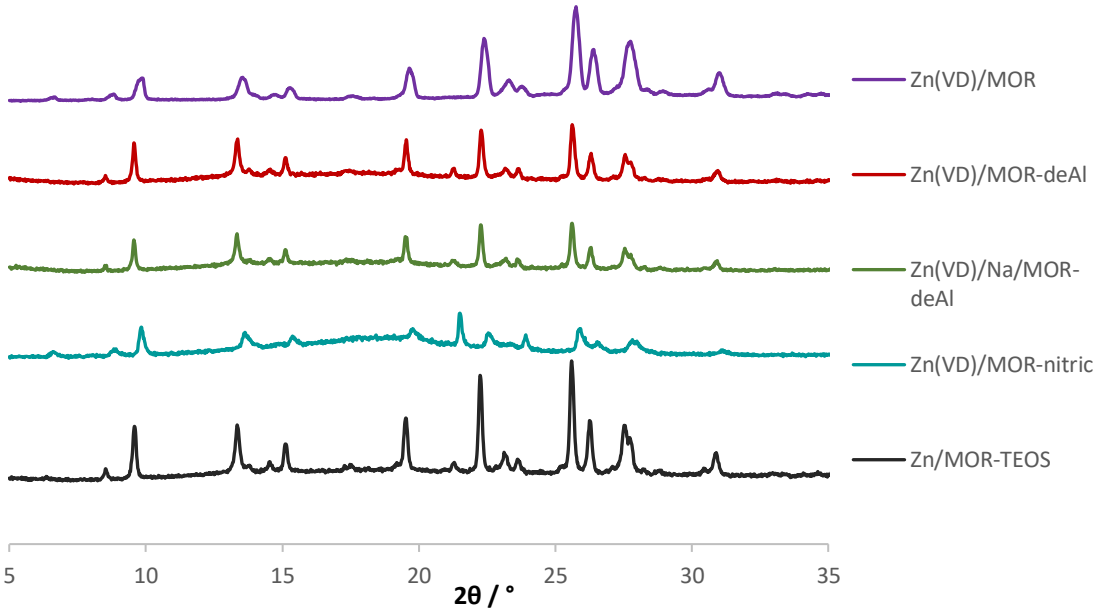

Figure 11: pXRD patterns post zinc vapour deposition for dealuminated MOR sample compared with the pXRD pattern of the zinc vapour deposition on H-MOR (10) parent zeolite.

Table 3: Elemental analysis of dealuminated samples post zinc vapour deposition.

Sample	Si/Al_{tet}	Si/Al_{tet} post zinc	Zn/Al_{tet}
Zn(VD)/MOR	8.51	8.64	0.67
Zn(VD)/MOR-deAl	22.48	30.87	1.09
Zn(VD)/Na/MOR-deAl	30.45	31.50	1.30
Zn(VD)/MOR-nitric	15.37	13.65	0.69
Zn(VD)/MOR-TEOS	9.43	18.04	0.79

Elemental analysis was carried out to investigate if the Si/Al_{tet} ratio changed post Zn vapour deposition and to determine the level of zinc exchange. Whilst for most samples, the Si/Al_{tet} ratio did not change significantly, the Zn(VD)/MOR-deAl and Zn(VD)/MOR-TEOS sample showed an increase Si/Al_{tet} ratio (Table 3). This could be due to contamination from the quartz wool used to hold the zeolite sample in place during the CVD process. This is supported by the fact that no further framework damage has occurred, as indicted by the ^{27}Al NMR spectroscopic analysis post zinc deposition, which shows no signal at 0 ppm for all samples (Figure 12). The zinc CVD process seems to remove any octahedral Al present after the dealumination process that could impact the Si/Al_{tet} ratios. This could be due to the fact that BAS are removed as the vapour deposition reaction is carried out, indicating that the octahedral species observed in the

^{27}Al NMR spectra of the MOR samples before the reaction with zinc, is linked to the zeolite framework.[25]

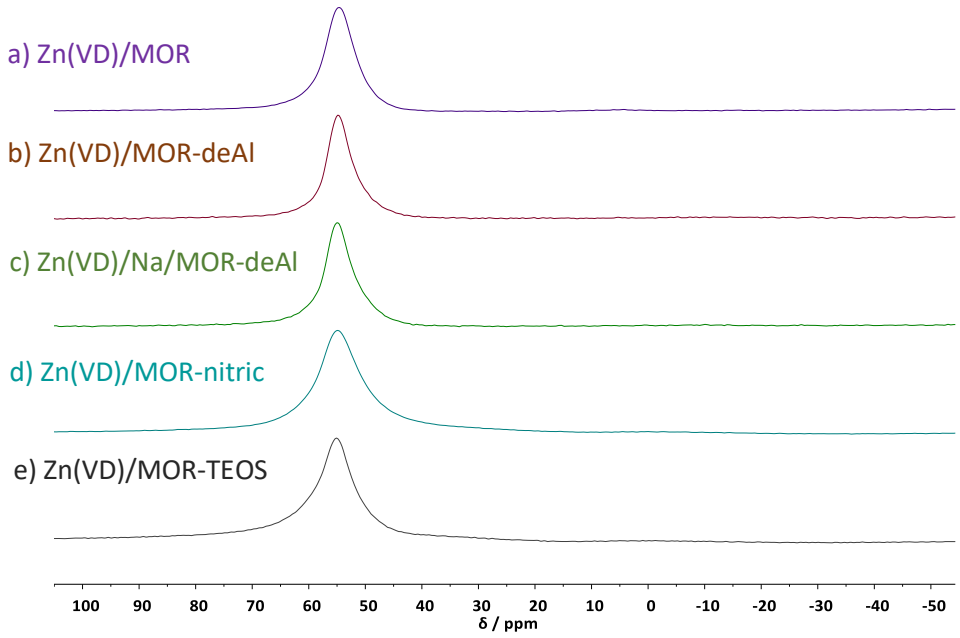

Figure 12: ^{27}Al NMR post zinc vapour deposition for dealuminated MOR samples. (^{27}Al – 104.20 MHz, 14 kHz spin rate)

As found Chapter 4, Zn/Al ratios were found to be over the theoretical maximum exchange value of 0.5 for the parent MOR sample and this is potentially due to excess Zn^0 present within the sample (Table 3).[51] However, the Zn/Al_{tet} ratio for the steamed samples is significantly higher (Zn/Al_{tet}: 1.09 and 1.30) and it seems unlikely that this increase is only due to the presence of excess Zn^0. Beyer *et al.* have shown evidence of zinc metal reacting with the silanol nests of dealuminated MOR by monitoring the silanol stretching frequency using FTIR spectroscopy.[52] If zinc vapour is reacting with the silanol nests formed through the dealumination process, ^{29}Si CP NMR spectroscopic measurement can be used to monitor this process. As the Q^3 defect sites formed by dealumination react with the zinc vapour, a decrease in the Q^3 signal observed at −102 ppm will occur (Scheme 1). The ^{1}H-^{29}Si CP spectra for the dealuminated samples before and after reaction with zinc vapour are shown in Figure 13 and a clear decrease in the Q^3 defect sites is observed after exposure to zinc vapour. Whilst this could be due to the silanol nests healing at 500 °C, the higher Zn/Al_{tet} values in the dealuminated samples indicate this is likely due to incorporation of Zn metal into silanol nests. Corresponding direct excitation spectra can be found in Appendix 4.

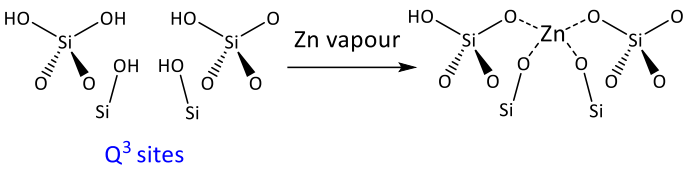

Scheme 1: Reaction of zinc vapour with silanol nests (Q^3 sites) which have been formed through the removal of Al.

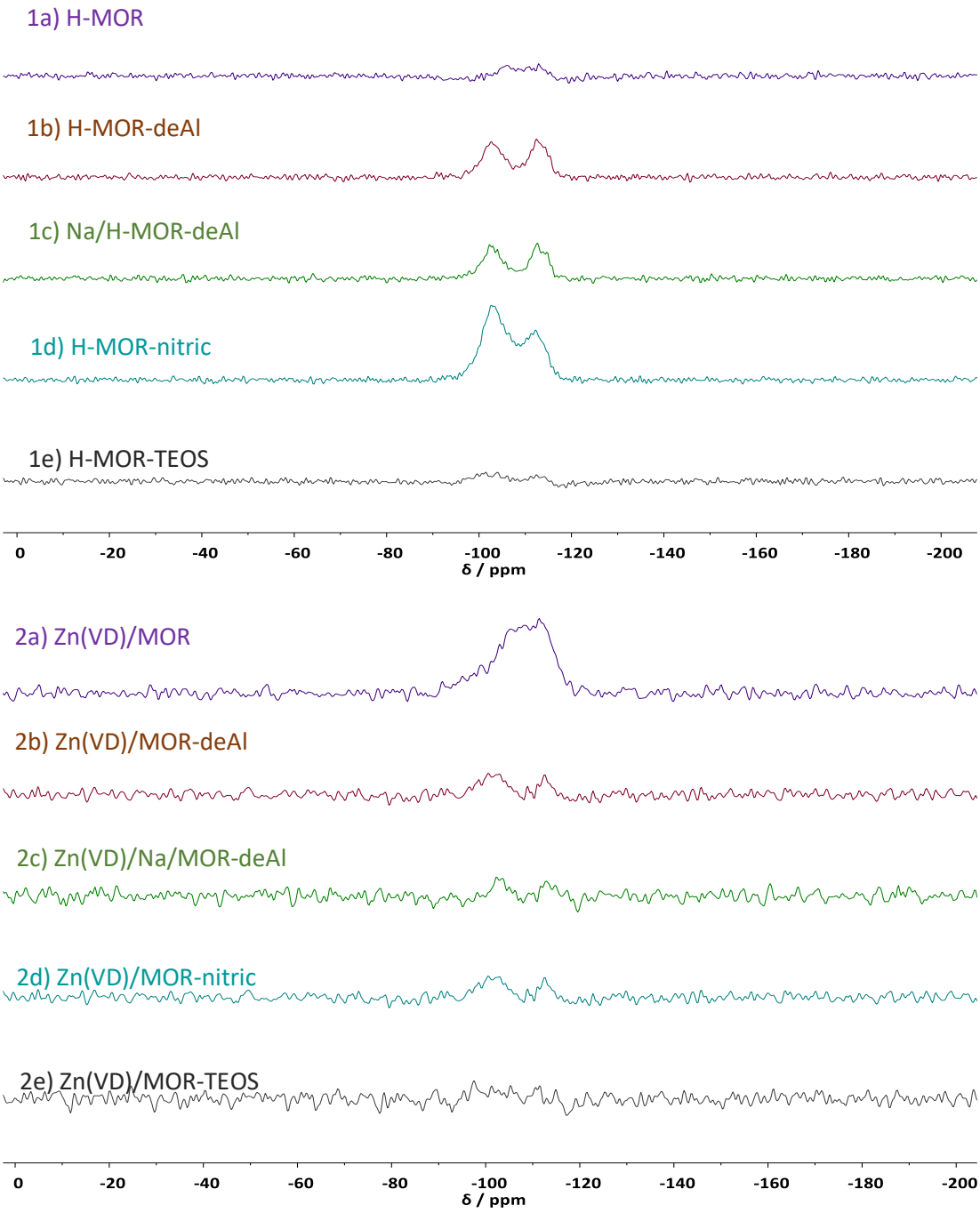

Figure 13: ^{1}H-^{29}Si CP spectra for the MOR dealuminated samples before (1a-e) and after reaction with zinc vapour (2a-e). (^{29}Si – 79.44 MHz, 8 kHz spin rate)

The zinc-exchanged, dealuminated and TEOS healed samples were subsequently exposed to $^{13}CH_4$ and their reactivity was compared with the Zn(VD)/CH_4/MOR sample, which had not had any dealumination treatments. Two signals corresponding to the 8 MRs and 12 MRs were observed for all samples, but the ratio between the two signals changed significantly depending on the dealumination method (Figure 14). The most substantial change was observed for Zn(VD)/CH_4/MOR – nitric, the sample dealuminated with nitric acid. The nitric acid dealumination method is reported to remove Al from the 8 MR side pockets of Zn-MOR – nitric and this is reflected in the ^{13}C NMR spectrum where a substantial decrease is observed in the signal at −15 ppm that was assigned to the [Zn^{II}-CH_3] species located in the 8 MR SP (Section 4.2.1). Both Zn(VD)/MOR-deAl and Zn(VD)/Na-MOR-deAl samples show a relative decrease in signal corresponding to the [Zn^{II}-CH_3] species located in the 12 MRs. This is surprising as the unprotected sample was expected to dealuminate in the weaker 8 MR sites whereas the Na^+ protected sample was expected to dealuminate in the 12 MRs. This could be due to the harsh steaming conditions used which were able to remove Al from both the 8 and 12 MR sites. However, this could be due to the migration of Na^+ at elevated temperatures, which is discussed further in Section 5.2.3.1.[43, 53]

The most unusual result of methane activation is from the Zn(VD)/MOR-TEOS healed sample, shown in Figure 14e, where the ratio is drastically different to the nitric acid dealuminated sample that was found to have a much higher concentration of [Zn^{II}-CH_3] species located in the 12 MRs. The Zn(VD)/MOR-TEOS sample however showed [Zn^{II}-CH_3] species located in both the 8 MRs and the 12 MRs in a 0.54:1 ratio. The healing process involved introducing Si into the nests formed during the removal of Al and this involved heating Zn(VD)/MOR-nitric in an autoclave under hydrothermal conditions at 180 °C for 24 h. These healing conditions are somewhat similar to zeolite synthesis conditions and we hypothesise that during this process, Al could migrate and redistribute throughout the MOR framework. Redistributing Al across the zeolite would change the location of [Zn^{II}-CH_3] species throughout the zeolite.

Although the selectivity of dealumination could not be determined using techniques such as ^{133}Cs NMR spectroscopy, the reaction of Zn vapour and $^{13}CH_4$ with the dealuminated MOR samples has shown clear differences between the varying dealumination methods, in particular the Zn(VD)/CH_4/MOR – nitric sample which shows a significant decrease in the signal at −15 ppm corresponding to the [Zn^{II}-CH_3] species located in the 8 MR SP.

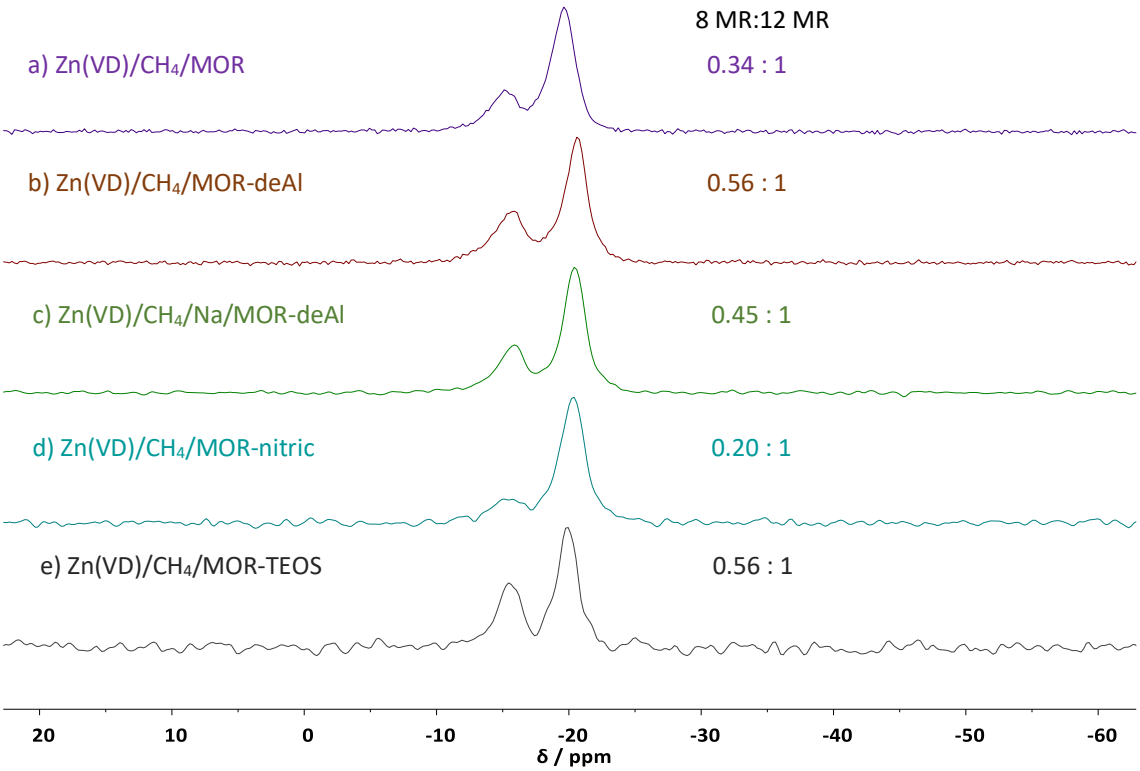

Figure 14: ^{13}C NMR of dealuminated MOR samples after treatment with Zn vapour. The ratio between the [Zn^{II}-CH_3] species present in the 8 MR : 12 MR has been calculated for all samples. (^{13}C – 100.57 MHz, 10 kHz spin rate)

5.2.3 Other methods to explore selectivity of methane activation in MOR

5.2.3.1 Partial Na^+ exchange into MOR and subsequent effect of CH_4 activation

As mentioned above, Na^+ is reported to preferentially exchange into the 8 MR sidepockets of MOR. [8, 11, 22, 23] We hypothesise that if acid sites in the 8MR SP of MOR were titrated with Na^+, only the remaining acid sites in the 12 MR channels would react with Zn vapour and result in [Zn^{II}-CH_3] species in the 12 MRs.

Partial sodium ion exchange was carried out on NH_4-MOR (10), with the target of 25% and 50% Na^+ exchange to compare the effect of increasing Na^+ content on CH_4 activation. The ammonium parent was used as Na^+ ion exchange was found to be higher than with the H-MOR (10) parent. The exchange levels were slightly higher than expected (Table 4) but the NH_4-MOR parent sample and the Na/NH_4-MOR partially exchanged samples were tested for methane activation after exposure to zinc vapour deposition.

Table 4: Na^+ ion exchange levels and $[Zn^{II}\text{-}CH_3]$ ratios in ^{13}C NMR spectra for $^{13}CH_4$ activation on partially exchanged Na/MOR after zinc vapour deposition.

Sample	Na^+ Ion Exchange Level	Ratio of −15 : −20 ppm signals in ^{13}C NMR
Zn(VD)/CH_4/MOR parent	0 %	0.52 : 1
Na/Zn(VD)/CH_4/MOR	37 %	0.67 : 1
Na/Zn(VD)/CH_4/MOR	58 %	0.45 : 1

Two signals were observed in the ^{13}C NMR spectra for all three samples, but the ratios between the signals were not as expected (Figure 15). As Na^+ content increased, it was expected that the signal at −15 ppm corresponding to the $[Zn^{II}\text{-}CH_3]$ fragment in the 8MR SP would decrease. Upon deconvolution of the two signals (Appendix 4), it was observed that the ratios showed no consistent trend as the Na^+ content increased. It should be noted that slight air contamination must have occurred as zinc methoxy and zinc formate species can be observed in the NMR spectra.

The zinc vapour deposition is carried out at high temperature (500 °C) and it is likely that at these temperature cations are mobile.[43] Rearrangement of cations is likely taking place at these temperatures hence, upon exposure to $^{13}CH_4$, a trend in ratios is not observed in the ^{13}C NMR spectra.

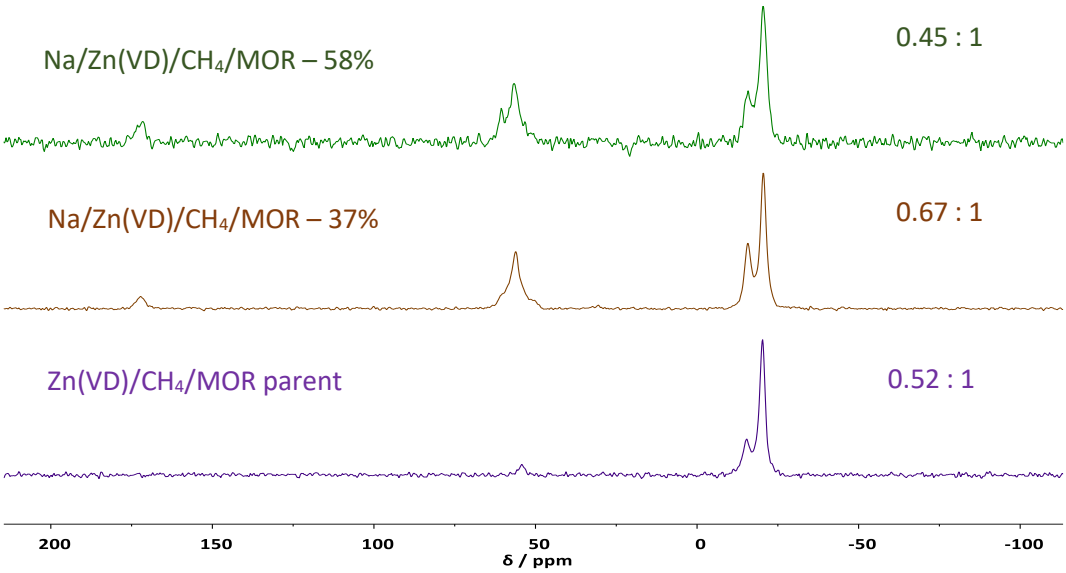

Figure 15: ^{13}C NMR on partially exchanged Na/MOR after zinc vapour deposition and exposure to methane. Ratios between the two signals show no trend with increasing Na^+ concentration. N.B contamination from O_2 has resulted in formation of zinc methoxy and zinc formate species for the partially exchanged samples. (^{13}C – 100.57 MHz, 10 kHz spin rate)

5.2.3.2 Pyridine adsorption into MOR

Pyridine adsorption/desorption coupled with IR spectroscopy is commonly used to measure the total number of acidic sites in a zeolite catalyst.[54] The strength and type of bond between the pyridine molecule and surface acid affects the frequency of the vibration mode of the pyridine molecule (vCCN: 1700 – 1400 cm^{-1}).[55] For MOR, temperature programmed desorption (TPD) of ammonia followed by 'poisoning' from pyridine can give quantitative analysis on the number of acid sites in the 8 MR SP compared with the 12 MR.[56] This is because the kinetic diameter of pyridine (Figure 16) is much larger than the 8 MR channels and so only acid sites in the 12 MR channels are affected by pyridine adsorption.

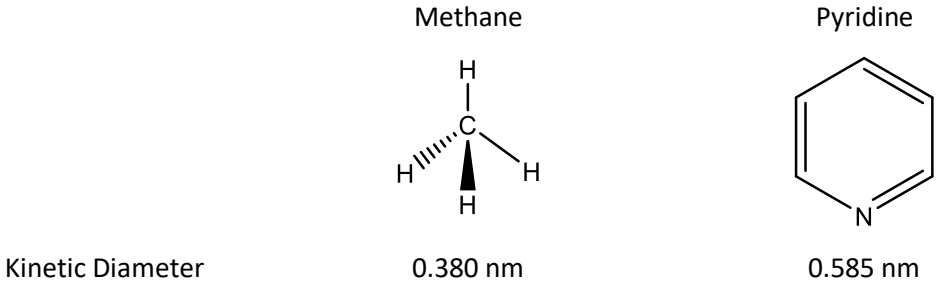

Figure 16: Kinetic diameter and structure of methane and pyridine[56]

This property of pyridine was exploited in the following reactions. As established in Chapter 4, two signals observed in the ^{13}C NMR spectrum of Zn(VD)/CH_4/MOR correspond to the [Zn^{II}-CH_3] fragment in the 8 MR SP (–15 ppm) and the [Zn^{II}-CH_3] fragment in the 12 MR main channel (–20 ppm). If pyridine was added post methane activation, the signal corresponding to [Zn^{II}-CH_3] species in the 8 MR SP at −15 ppm in the ^{13}C NMR spectrum should not be affected as pyridine cannot access these sites. However, it was hypothesised that the signal corresponding to [Zn^{II}-CH_3] species in the 12 MR channels (at −20 ppm) may exhibit a chemical shift change as the pyridine binds to the zinc. The zinc is co-ordinately unsaturated[57] and sufficiently Lewis acidic that the pyridine could bind in the 12 MR channels causing a shift in the NMR spectrum due to a change in the environment surrounding the [Zn^{II}-CH_3] species.

This hypothesis was tested by adding pyridine vapour post methane activation to a sample of Zn(VD)/MOR. The reaction was initially carried out using unlabelled methane (Figure 17) and two signals relating to pyridine are observed at 149 ppm and 127 ppm. An unknown third signal in the alkyl region at 30 ppm is also observed. To determine if any shift in signal from the [Zn^{II}-CH_3] in the 12 MR channels is observed, the reaction was repeated with ^{13}C labelled methane. Unfortunately, no change in the chemical shift was observed and similar pyridine signals were present. Whilst pyridine is able to fit into the 12 MR channels of MOR (0.65 nm x

0.70 nm), it is substantially larger than methane and access to the zinc in [Zn^{II}-CH_3] sites may be difficult, particularly when the zinc is sitting at the mouth of the 8 MR SP (Figure 18).

Although no chemical shift change was observed, the ratio between the −15 ppm and −20 ppm signals changed from 0.43 : 1 to 0.96 : 1 when using $^{13}CH_4$. This is likely due to the oxygen contamination confirmed by the presence of methoxy and formate species visible in the NMR spectrum in Figure 17a. As established in Chapter 4, the [Zn^{II}-CH_3]species in the 12 MR channels reacts faster in an oxidative environment leading to the change in ratios between these signals.

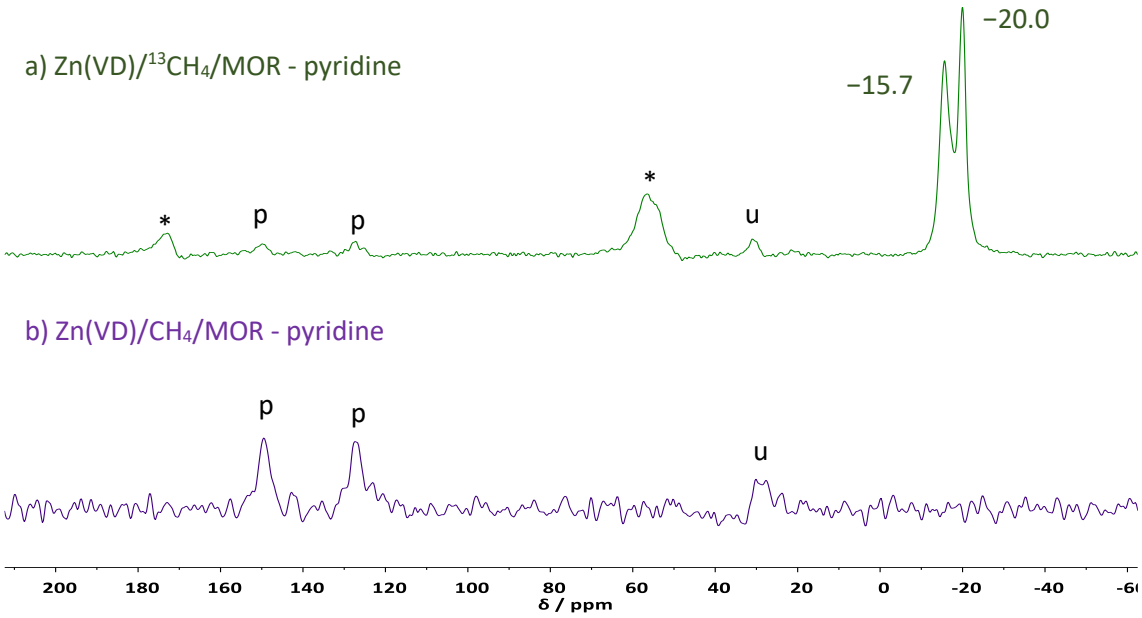

Figure 17: ^{13}C NMR spectra for pyridine absorption studies on MOR: a) labelled methane reaction followed by pyridine absorption, b) unlabelled methane reaction followed by pyridine adsorption. Signals labelled with * are from oxygen contamination. Signals labelled with p are from pyridine. Unknown alkyl species are labelled with u.

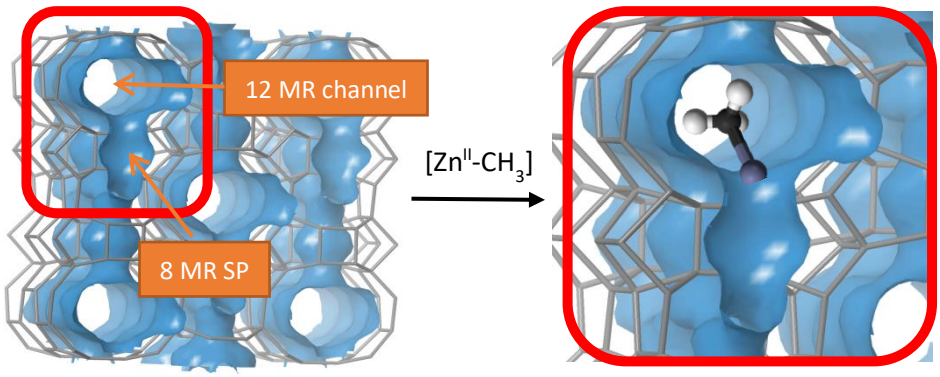

Figure 18: Illustrative representation of [Zn^{II}-CH_3] species in the 12 MR channels of MOR where the zinc would be hard to access by the pyridine probe molecule.

5.3 Conclusions

As described in Chapter 4, methane activation over MOR treated with Zn vapour gives rise to two signals in the ^{13}C NMR spectrum which have been assigned to [Zn^{II}-CH_3] species in the 8MR SP and 12 MR channel on the basis of a suite of NMR experiments. In order to further confirm this assignment, a series of dealumination reactions were carried out. The parent zeolite, H-MOR (Clariant), was treated with steam and nitric acid in an attempt to remove Al selectively. Protection of the 8 MRs using partial exchange of a 1+ cation, Na^+, was attempted to achieve selective dealumination of the 12 MRs. Both methods of dealumination result in different degrees of framework aluminium removal but crucially for both processes, no framework damage was observed by either dealumination method. Using BET analysis in conjunction with ^{27}Al NMR, it was determined that Al debris was likely to still be present in the samples, even after acid washing the steamed samples, which could potentially hindered the vapour deposition reaction. After Cs cation exchange, ^{133}Cs NMR spectroscopy experiments were conducted to investigate the selectivity of the dealumination processes but despite multiple exchange methods full Cs exchange was not achieved on all samples. Furthermore, the lower Cs content from the dealuminated samples, combined with the complex deconvolution required to analyse the NMR data, lead to difficulty interpreting the selectivity of the dealumination process using ^{133}Cs NMR spectroscopy. Additional analysis should be carried out on the dealuminated samples using high vacuum IR spectroscopy to monitor the O-H stretches of BAS in MOR to reach conclusions regarding the selectivity of the dealumination methods.

Although the selectivity of the dealumination could not be analysed definitively, zinc vapour deposition and methane activation were carried out to probe the effects of Al removal. As the zinc vapour deposition uses harsh conditions of high vacuum and high temperature, thorough analysis of the dealuminated samples was carried out post exposure to the zinc vapour. Whilst the sample dealuminated by steam retained crystallinity after the zinc vapour treatment, the H-MOR-nitric sample showed loss in crystallinity after exposure to zinc vapour. To rectify this, healing of the silanol nests formed within H-MOR-nitric upon Al removal was attempted using TEOS. An increase in Si/Al in H-MOR-TEOS, and no sign of framework damage post exposure to zinc vapour, led to the conclusion that successful healing had occurred.

Post exposure to zinc vapour, all dealuminated MOR samples showed high Zn/Al_{tet} ratio, with values greater than 1 for the steamed samples. Using ^{1}H-^{29}Si CP NMR experiments, it was noted that as the samples reacted with zinc vapour, the signal from the Q^3 defect sites formed through the dealumination decreased significantly. Whilst this could be a result of silanol nests

healing at high temperautres, the high Zn/Al ratio implies this is due to the zinc inserting into the silanol nests and supports a similar findings by Beyer *et al.*. [52]

After exposure to $^{13}CH_4$, the dealuminated and healed samples all showed 2 signals in the ^{13}C NMR spectra corresponding to [Zn^{II}-CH_3] species in the 8 MR side pockets and 12 MR channels, as established previously. The ratio between the two signals differed substantially between the samples indicating some selectivity in dealumination had occurred. Zn(VD)/CH_4/MOR-nitric showed a substantial decrease in the signal corresponding to the [Zn^{II}-CH_3] species located in the 8 MRs as expected from the reported selective dealumination of the 8 MR SP by nitric acid.[8, 9] The TEOS healed sample, Zn(VD)/CH_4/MOR-TEOS, however showed [Zn^{II}-CH_3] species located in both the 8 MRs and the 12 MRs in a 0.54:1 ratio. This indicated that during the healing process, which occurred under hydrothermal conditions, the Al was able to redistribute throughout the MOR framework. Both steamed samples showed a relative decrease in signal intensity corresponding to the [Zn^{II}-CH_3] species located in the 12 MRs suggesting the harsh steaming conditions were able to remove Al from all sites in MOR. Although the selectivity of the different dealumination methods was not inherently established by ^{133}Cs NMR spectroscopy, clear differences were observed post reaction with zinc vapour and methane which support the NMR based assignment established in Chapter 4.

As established above, dealumination of MOR required multiple steps and harsh conditions that have the potential to damage the zeolite framework. The process is also difficult to control and selectivity hard to measure, hence, two alternative methods were investigated to help confirm the assignment of [Zn^{II}-CH_3] species in the 8 MR side pockets and 12 MR channels of MOR. The first method involved titrating different levels of Na^+ into the 8 MR side pockets of H-MOR before reaction with zinc vapour and exposure to methane. Unfortunately, no trend was observed between the Na ion exchange level and the ratio of [Zn^{II}-CH_3] species in the 8 MR side pockets and 12 MR channels observed by ^{13}C NMR spectroscopy. This believed to be due to the fact that the zinc vapour deposition is carried out at high temperature (500 °C) and at these temperatures, cations are mobile and able to redistribute. The second method attempted to exploit the physical properties of pyridine as it is unable to fit into the 8 MR side pockets of MOR. The [Zn^{II}-CH_3] species formed upon methane activation is co-coordinatively unsaturated, hence, it was hypothesised that pyridine could bind to the [Zn^{II}-CH_3] species in the 12 MRs only and cause a shift in the ^{13}C NMR spectrum. However, no pyridine binding was observed, potentially due to the steric restrictions of the 12 MR channels resulting in difficult accessing the [Zn^{II}-CH_3] species. Nevertheless, this idea could be adapted by activating bigger alkyl molecules which only fit in the 12 MR of MOR instead of methane.

Overall, selective dealumination was successfully carried out on H-MOR using two different methods. This resulted in substantial differences in the ratio between the signals corresponding to [Zn^{II}-CH_3] species in the 8 MR channels and the 12 MR side pockets observed in the ^{13}C NMR spectrum after zinc vapour deposition and methane activation, supporting the assignment made by NMR experiments. As established in Chapter 4, these two species have different reaction rates in oxidative conditions and selective dealumination could be used to help exploit this effect.

5.4 Experimental

H–MOR (Si/Al = 10) and NH_4–MOR (Si/Al = 10), were kindly provided by Clariant. Zinc powder (Goodfellow, 99.9%, max particle size 150 µm), sodium nitrate (ACS, Alfa Aesar, 99.0%), caesium nitrate (Alfa Aesar, 99.8%), oxalic acid (Sigma Aldrich, 98%), nitric acid (70%), TEOS (Fisher, 98%), pyridine (ACROS Organics, extra dry over molecular sieves, 99.5%) were used as purchased. Methane-^{13}C (99% ^{13}C) was purchased from Sigma-Aldrich. Methane (99.995%) was purchased from BOC. Zinc powder was stored and used in an INERT technologies glove box under an argon atmosphere.

Selective dealumination of aluminium within the 12MR channels of MOR was attempted through partial exchange with sodium cations followed by steam treatment of the zeolite following a patent.[11] Two samples were compared, H-MOR and Na/H-MOR. Na/H-MOR was prepared through an aqueous ion exchange where 1 g of zeolite was placed in a centrifuge tube in contact with 0.3 M $NaNO_3$ solution for 1 h with constant agitation from a mechanical tube roller. The tube was centrifuged at 4500 rpm for 5.5 min and the resulting supernatant decanted. The sample was then washed with 50 ml of deionised water 3 times and dried at 80 °C overnight. Steaming was carried out on 1 g of zeolite placed in a quartz furnace tube, secured between quartz wool. Under a nitrogen flow of 80 ml min^{-1}, the zeolite was heated using a ramp rate of 5 °C min^{-1} for the following heating program: held at 90 °C for 30 min, 110 °C for 30 min, 500 °C for 4 h. At 500 °C, a flow of water at 1 ml min^{-1} was introduced into the top of the quartz tube through a needle. After 4 h, the water flow was stopped and the sample was allowed to cool for 12 h under the nitrogen flow. To remove extraframework Al, the zeolite was treated with an aqueous solution of HCl (20 ml, 1M) at 80 °C for 1 h and then washed with deionised water (3 x 50 ml in centrifuge tube). After characterisation by ^{27}Al NMR spectroscopy, a portion of the zeolite was subsequently treated with oxalic acid solution (oxalic acid/Al=4) at 70 °C for 4 h, washed with water and dried overnight at 80 °C using a method reported in the literature.[19] The

sample was calcined (550 °C, 6 h) to remove any residual organic components. These samples are referred to as H-MOR-deAl or Na/H-MOR-deAl.

Selective dealumination of aluminium within the 8 MR side pockets of MOR was carried out using nitric acid following a literature procedure.[12] H-MOR, 1 g, was stirred with 20 mL of HNO_3 solution (0.55 M) at 85 °C for 1 h in a round bottom flask fitted with a condenser. The sample, H-MOR-nitric, was then washed with deionised water until the supernatant was near neutral (pH 8) and dried overnight at 80 °C. Healing of the defect sites was carried out using TEOS in an ethanol solution (1 mmol of TEOS per 0.5 g of zeolite) adapted from literature procedures.[49, 50] After nitric acid dealumination, 0.5 g of H-MOR-nitric was treated with 20 mL of TEOS solution in ethanol. The mixture was stirred for 0.5 h at room temperature and subsequently transferred to a Teflon-lined autoclave (25 ml capacity) and heated at 180 °C for 24 h. After treatment, the zeolite was transferred to a centrifuge tube and washed with deionised water (5 x 50 ml). The sample was then dried at 80 °C overnight and calcined in a muffle furnace (150 °C 1 h, 550 °C 5 h). The healing process was repeated twice and the sample referred to as H-MOR-TEOS.

Caesium exchange was carried out initially by treating the samples with $CsNO_3$ based on ion exchange conditions reported by Kuroda *et al.*.[58] The sample was placed in a centrifuge tube in contact with 50 ml of 0.3M $CsNO_3$ solution for 1 h with constant agitation from a mechanical tube roller. The tube was centrifuged at 4500 rpm for 5.5 min and the resulting supernatant decanted. The zeolite was then re-dispersed into a fresh portion of the $CsNO_3$ solution and this process was repeated 10 times. The sample was then washed with 50 ml of deionised water 8 times and dried at 80 °C overnight. Full Cs exchange was not achieved using this method so the samples were subsequently treated with 1M $CsNO_3$ at 80 °C overnight. The samples were washed with deionised water and the process repeated three times before drying at 80 °C overnight. Before ^{133}Cs NMR experiments were conducted , the samples were dehydrated under vacuum; the samples were placed into a quartz tube under vacuum (pressure < 10^{-2} mbar) and heated to 150 °C for 1 h followed by 5 h at 550 °C in a tube furnace (ramp rate of 5 °C min^{-1}). After cooling, the tube was transferred into the glove box and the sample packed into a NMR rotor.

The vapour deposition samples were prepared by an exchange reaction between metallic zinc vapour and the H-form of the zeolite as reported previously.[59] The zeolite was placed into a quartz u-tube under vacuum (pressure < 10^{-2} mbar) and heated to 150 °C for 1 h followed by 5 h at 550 °C in a tube furnace. A 5 °C min^{-1} ramp rate was used for all furnace

program steps. A 100-fold excess of zinc (Zn/Al =100) was used for the zinc metal vapour deposition. To expose the zeolite sample to zinc vapour, the u-tube was sealed and placed in a tube furnace where it was heated to 500 °C at 5 °C min^{-1} and held for 1 h under static vacuum. Excess unreacted zinc vapour was further removed by continued heating at 500 °C for 2 h under dynamic vacuum. For methane activation, the u-tube containing the zinc modified zeolite was cooled to 250 °C in the furnace. The u-tube was filled with 1 atm of $^{13}CH_4$, sealed and held at 250 °C for 15 min. After cooling, the sealed tube was taken into the argon glovebox. The sample was packed into a solid state NMR rotor in the glovebox. NMR experiments were typically conducted immediately after C-H activation.

Partial sodium exchange was carried out by treating NH_4-MOR (10) with $NaNO_3$ with a Na:Al ratio of 200:1. The sample was placed in a centrifuge tube in contact with 50 ml $NaNO_3$ solution for 1 h with constant agitation from a mechanical tube roller. The tube was centrifuged at 4500 rpm for 5.5 min and the resulting supernatant decanted. To obtain the 58% Na exchanged sample, NH_4-MOR (10) underwent the exchange process for a second time.. The samples were washed with 50 ml of deionised water 3 times and dried at 80 °C overnight. Zinc vapour deposition and methane activation was carried out as above.

Pyridine absorption was carried out on a sample of Zn(VD)/CH_4/MOR and Zn(VD)/$^{13}CH_4$/MOR. Both Zn(VD)/CH_4/MOR and Zn(VD)/$^{13}CH_4$/MOR were prepared as above and stored in a glovebox before transfer into the apparatus shown in Figure 19. After removal from the glove box, the tube was placed onto a Schlenk line and 200 μL of pyridine was added under a flow of N_2. The pyridine was frozen with liquid N_2 and the tube put under static vacuum (10^{-2} mbar). To expose the zeolite sample to the pyridine, the frozen pyridine was gently warmed using a 20 °C water bath for 30 min. Excess pyridine was removed by placing the tube under dynamic vacuum for 1.5 h. The sample was taken into the glovebox, packed into a rotor and ^{13}C NMR experiments were conducted.

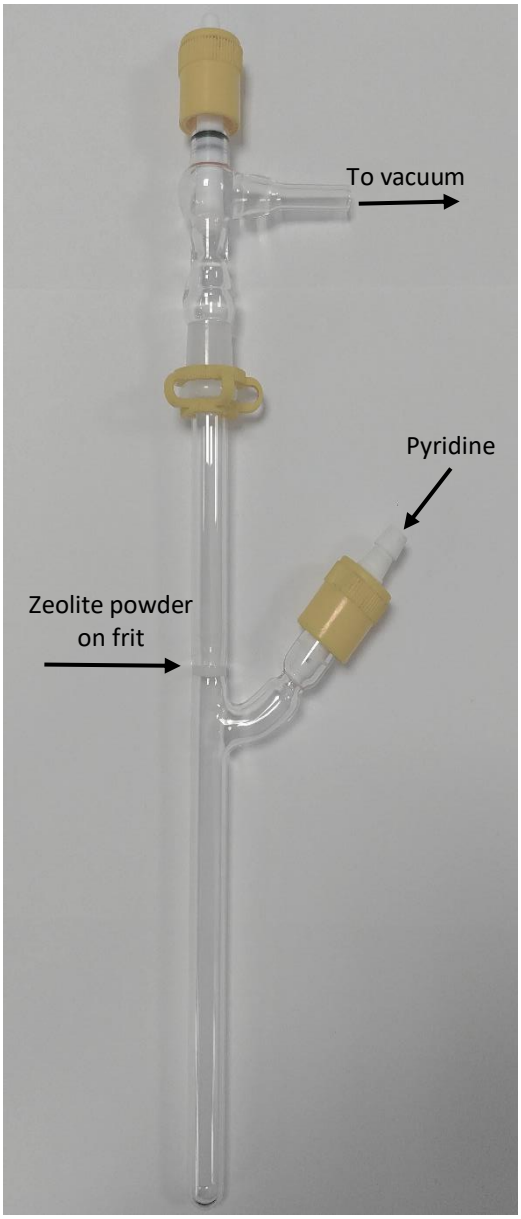

Figure 19: Apparatus for Pyridine absorption: glass tube with frit to place zeolite, bleed tap to introduce pyridine and Young's tap to prevent contamination with air.

5.5 Chapter 5 References

1. G. Agostini, C. Lamberti, L. Palin, M. Milanesio, N. Danilina, B. Xu, M. Janousch and J. A. van Bokhoven, *J. Am. Chem. Soc.*, 2010, **132**, 667-678.
2. R. Bai, Y. Song, Y. Li and J. Yu, *Trends Chem.*, 2019, **1**, 601-611.
3. A. Corma, *Chem. Rev.*, 1997, **97**, 2373-2420.
4. J. Zhu, X. Meng and F. Xiao, *Front. Chem. Sci. Eng.*, 2013, **7**, 233-248.
5. X. Li, K. Qiao, L. He, X. Liu, Z. Yan, W. Xing, L. Qin, B. Dai and Z. Zhang, *App. Pet. Res.*, 2014, **4**, 343-349.
6. M. Müller, G. Harvey and R. Prins, *Micro. Meso. Mater.*, 2000, **34**, 135-147.
7. P. C. Van Geem, K. F. M. G. J. Scholle, G. P. M. Van der Velden and W. S. Veeman, *J. Phys. Chem.*, 1988, **92**, 1585-1589.
8. P. Bodart, J. B. Nagy, G. Debras, Z. Gabelica and P. A. Jacobs, *J. Phys. Chem.*, 1986, **90**, 5183-5190.
9. M.-C. Silaghi, C. Chizallet, J. Sauer and P. Raybaud, *J. Catal.*, 2016, **339**, 242-255.
10. S. Ban, A. N. C. van Laak, J. Landers, A. V. Neimark, P. E. de Jongh, K. P. de Jong and T. J. H. Vlugt, *J. Phys. Chem. C*, 2010, **114**, 2056-2065.
11. G. G. Armitage and J. G. Sunley,US 8,956,588 B2, 2015.
12. A. A. C. Reule, J. A. Sawada and N. Semagina, *J. Catal.*, 2017, **349**, 98-109.
13. D. B. Lukyanov, T. Vazhnova, N. Cherkasov, J. L. Casci and J. J. Birtill, *J. Phys. Chem. C*, 2014, **118**, 23918-23929.
14. N. Cherkasov, T. Vazhnova and D. B. Lukyanov, *Vib. Spectrosc.*, 2016, **83**, 170-179.
15. E. Dempsey, G. H. Kuehl and D. H. Olson, *J. Phys. Chem.*, 1969, **73**, 387-390.
16. A. W. O'Donovan, C. T. O'Connor and K. R. Koch, *Micro. Mat.*, 1995, **5**, 185-202.
17. M. Boveri, C. Márquez-Álvarez, M. Á. Laborde and E. Sastre, *Catal. Today*, 2006, **114**, 217-225.
18. G. J. Hutchings, A. Burrows, C. Rhodes, C. J. Kiely and R. McClung, *J. Chem. Soc., Faraday Trans.*, 1997, **93**, 3593-3598.
19. M. Abdolrahmani, K. Chen and J. L. White, *J. Phys. Chem. C*, 2018, **122**, 15520-15528.
20. A. Corma, V. Fornés and F. Rey, *App. Catal.*, 1990, **59**, 267-274.
21. Y. Fan, X. Bao, X. Lin, G. Shi and H. Liu, *J. Phys. Chem. B*, 2006, **110**, 15411-15416.
22. J. Nagano, T. Eguchi, T. Asanuma, H. Masui, H. Nakayama, N. Nakamura and E. G. Derouane, *Micro. Meso. Mater.*, 1999, **33**, 249-256.
23. H. Xue, X. Huang, E. Zhan, M. Ma and W. Shen, *Catal. Commun.*, 2013, **37**, 75-79.
24. J. Xu, Q. Wang, S. Li and F. Deng, in *Solid-State NMR in Zeolite Catalysis*, Springer Singapore, Singapore, 2019, DOI: 10.1007/978-981-13-6967-4_3, pp. 93-132.
25. M. Ravi, V. L. Sushkevich and J. A. van Bokhoven, *J. Phys. Chem. C*, 2019, **123**, 15139-15144.
26. M. Haouas, A. Kogelbauer and R. Prins, *Catal. Lett.*, 2000, **70**, 61-65.
27. B. Gil, S. I. Zones, S.-J. Hwang, M. Bejblová and J. Čejka, *J. Phys. Chem. C*, 2008, **112**, 2997-3007.
28. V. Montouillout, S. Aiello, F. Fayon and C. Fernandez, in *Stud. Surf. Sci. Catal.*, eds. R. Aiello, G. Giordano and F. Testa, Elsevier, 2002, vol. 142, pp. 383-390.
29. A. Omegna, J. A. van Bokhoven and R. Prins, *J. Phys. Chem. B*, 2003, **107**, 8854-8860.
30. Z. Zhao, S. Xu, M. Y. Hu, X. Bao, C. H. F. Peden and J. Hu, *J. Phys. Chem. C*, 2015, **119**, 1410-1417.
31. J. A. van Bokhoven, A. M. J. van der Eerden and D. C. Koningsberger, *J. Am. Chem. Soc.*, 2003, **125**, 7435-7442.
32. L. A. Bugaev, J. A. van Bokhoven, A. P. Sokolenko, Y. V. Latokha and L. A. Avakyan, *J. Phys. Chem. B*, 2005, **109**, 10771-10778.
33. N. Viswanadham and M. Kumar, *Micro. Meso. Mater.*, 2006, **92**, 31-37.
34. W. Xu, H. Zhang, S. Dong and J. Hao, *Langmuir*, 2014, **30**, 11567-11573.

35. J. Goodman, J. J. Neil and J. J. H. Ackerman, *NMR Biomed.*, 2005, **18**, 125-134.
36. P. J. Chu, B. C. Gerstein, J. Nunan and K. Klier, *J. Phys. Chem.*, 1987, **91**, 3588-3592.
37. P. Norby, F. I. Poshni, A. F. Gualtieri, J. C. Hanson and C. P. Grey, *J. Phys. Chem. B*, 1998, **102**, 839-856.
38. D. C. Apperley, R. K. Harris and P. Hodgkinson, in *Solid State NMR Basic principles and practice*, 2012, ch. 6.
39. H. Koller, B. Burger, A. M. Schneider, G. Engelhardt and J. Weitkamp, *Micro. Mater.*, 1995, **5**, 219-232.
40. H. Liu and C. P. Grey, *Micro. Meso. Mater.*, 2002, **53**, 109-120.
41. M. Hunger, U. Schenk, B. Burger and J. Weitkamp, *Angew. Chem. Int. Ed.*, 1997, **36**, 2504-2506.
42. D. K. Murray, J. W. Chang and J. F. Haw, *J. Am. Chem. Soc.*, 1993, **115**, 4732-4741.
43. M. Hunger, U. Schenk and A. Buchholz, *J. Phys. Chem. B*, 2000, **104**, 12230-12236.
44. K. Yoshida, K. Toyoura, K. Matsunaga, A. Nakahira, H. Kurata, Y. H. Ikuhara and Y. Sasaki, *Scientific Reports*, 2013, **3**, 2457.
45. T. Sooknoi, T. Danuthai, L. L. Lobban, R. G. Mallinson and D. E. Resasco, *J. Catal.*, 2008, **258**, 199-209.
46. T. Tokuhiro, M. Mattingly, L. E. Iton and M. K. Ahn, *J. Phys. Chem.*, 1989, **93**, 5584-5587.
47. F. Yagi, N. Kanuka, H. Tsuji, S. Nakata, H. Kita and H. Hattori, *Micro. Mater.*, 1997, **9**, 229-235.
48. O. Marie, P. Massiani and F. Thibault-Starzyk, *J. Phys. Chem. B*, 2004, **108**, 5073-5081.
49. H. Xu, J.-g. Jiang, B. Yang, L. Zhang, M. He and P. Wu, *Angew. Chem., Int. Ed.*, 2014, **53**, 1355-1359.
50. M. V. Shamzhy, P. Eliašová, D. Vitvarová, M. V. Opanasenko, D. S. Firth and R. E. Morris, *Chem. Eur. J.*, 2016, **22**, 17377-17386.
51. S. M. T. Almutairi, B. Mezari, P. C. M. M. Magusin, E. A. Pidko and E. J. M. Hensen, *ACS Catal.*, 2012, **2**, 71-83.
52. H. K. Beyer, G. Pál-Borbély and M. Keindl, *Micro. Meso. Mater.*, 1999, **31**, 333-341.
53. L. Benco, T. Bucko, J. Hafner and H. Toulhoat, *J. Phys. Chem. B*, 2005, **109**, 20361-20369.
54. M. I. Zaki, M. A. Hasan, F. A. Al-Sagheer and L. Pasupulety, *Colloid Surface A*, 2001, **190**, 261-274.
55. S. Bordiga, C. Lamberti, F. Bonino, A. Travert and F. Thibault-Starzyk, *Chem. Soc. Rev.*, 2015, **44**, 7262-7341.
56. H. Xue, X. Huang, E. Ditzel, E. Zhan, M. Ma and W. Shen, *Ind. Eng. Chem. Res.*, 2013, **52**, 11510-11515.
57. A. Oda, T. Ohkubo, T. Yumura, H. Kobayashi and Y. Kuroda, *Phys. Chem. Chem. Phys.*, 2017, **19**, 25105-25114.
58. A. Oda, H. Torigoe, A. Itadani, T. Ohkubo, T. Yumura, H. Kobayashi and Y. Kuroda, *J. Phys. Chem. C*, 2014, **118**, 15234-15241.
59. M. A. Shah, S. Raynes, D. C. Apperley and R. A. Taylor, *Chem. Phys. Chem*, 2020, **21**, 673-679.

Chapter 6: The nature of the zinc active site for methane activation

Chapter 6: The nature of the zinc active site for methane activation

6.1 Introduction

The mechanism of methane activation over Zn/zeolites has been debated since the initial findings of Kazansky *et al.* in 2004.[1, 2] However, spectroscopic evidence, including DRIFTS and NMR spectroscopy, has shown that methane activation over Zn^{2+} involves the heterolytic cleavage of methane, forming a [Zn^{II}-CH_3] species alongside a new BAS.[1-7] To date, zinc oxide has been not been shown to form the [Zn^{II}-CH_3] species, but H/D exchange has been reported for ZnO/H-ZSM-5,[2, 8] and ZnO clusters have been found to be catalytically active for the aromatisation of propane.[8, 9]

Ion exchange methods predominately introduce Zn^{2+} into extraframework positions.[6, 10-13] Similarly, Zn^{2+} can be introduced into the zeolite by chemical vapour deposition of Zn^0. This results in a redox reaction where BAS sites of the zeolite are exchanged for Zn^{2+} cations with concomitant formation of H_2, shown in Equation 1.[1-4, 14, 15] CVD of zinc metal, in the presence of excess zinc, normally results in full exchange of BAS sites to Zn^{2+}, but elemental analysis can result in Zn/Al values higher than the theoretical maximum of 0.5, indicating that the reaction shown in Equation 1 may not be the only process occurring.[10, 16, 17] Pidko *et al.* observed Zn/Al ratio of 0.57 and suggest this is due to excess unreacted Zn^0 present in the materials.[12] Beyer *et al.* demonstrated that zinc metal can react with silanol nests of dealuminated MOR,[13] this is supported by the ^{1}H-^{29}Si CP NMR spectra presented in Chapter 5. However, many groups do not report Zn/Al ratios as they measure the level of zinc exchange through other analytical methods. For example, Stepanov *et al.* has often analysed the residual quantity of bridged OH groups using ^{1}H NMR spectroscopy with methane or TMS as an internal standard.[3, 4, 8, 18] Kazansky *et al.* measured the released H_2 volumetrically to determine zinc exchange level.[1, 2]

$$Zn_{(s)} + 2H^+_{(s)} \rightarrow Zn^{2+}_{(s)} + H_{2\,(g)}$$

Equation 1: Reaction of zinc metal with Brønsted acid sites (BAS) under vapour deposition conditions to form extraframework Zn^{2+} cations and H_2 gas

In 2015, Kuroda *et al.* reported the formation of a low valent zinc dimer, [Zn^{I}-Zn^{I}], in ZSM-5 which was characterised by XAS analysis,DR-UV-vis and electron spin resonance (ESR) spectroscopy alongside DFT calculations.[19] The authors found that in the presence of low levels of Zn vapour, Zn^{2+} is exchanged into ZSM-5 as expected. As the Zn^0 loading in the reaction was increased, less monomeric Zn^{2+} was observed as the intensity of the XANES bands at 9663.7 and 9669.7 eV weakened. A new band was observed in the XANES spectrum at 9660.7 eV that

increased in intensity with zinc loading, implying a new zinc species was formed at higher zinc levels. Analysis of EXAFS data led the authors to assign this signal to the formation of a [Zn^{+}-Zn^{+}] species, formed from the reaction between Zn^{2+} and Zn^{0}. DFT calculations of the UV-Vis spectra support the formation of this dimeric zinc-ion species in ZSM-5 samples with a Si/Al ratio of 12 or less. The authors suggest that formation of the dimer species may be difficult in zeolite samples with a higher Si/Al due to the increase in Al-Al distance. Upon irradiation of UV-light, photolytic cleavage of the [Zn^{I}-Zn^{I}] species occurred, resulting in two paramagnetic Zn^{+} ions which were detected through ESR. These Zn^{+} ions were able to be recombined by heating the UV-irradiated sample. This mechanism of reversible bond cleavage led the authors to believe that ZSM-5 was able to stabilise both the diamagnetic [Zn^{I}-Zn^{I}] dimer and two paramagnetic Zn^{+} ions with an energy barrier between both species. A scheme summarising the species formed is shown in Scheme 1. The proposed scheme has been supported by additional work by Chiesa *et al.* where Zn^{+} cations are detected by EPR spectroscopy upon UV irradiation of Zn/ZSM-5, where the zinc has been introduced by vapour deposition.[20] The Zn^{+} species are found to have preferential interaction with Al^{3+} cations through hyperfine sublevel correlation spectroscopy.

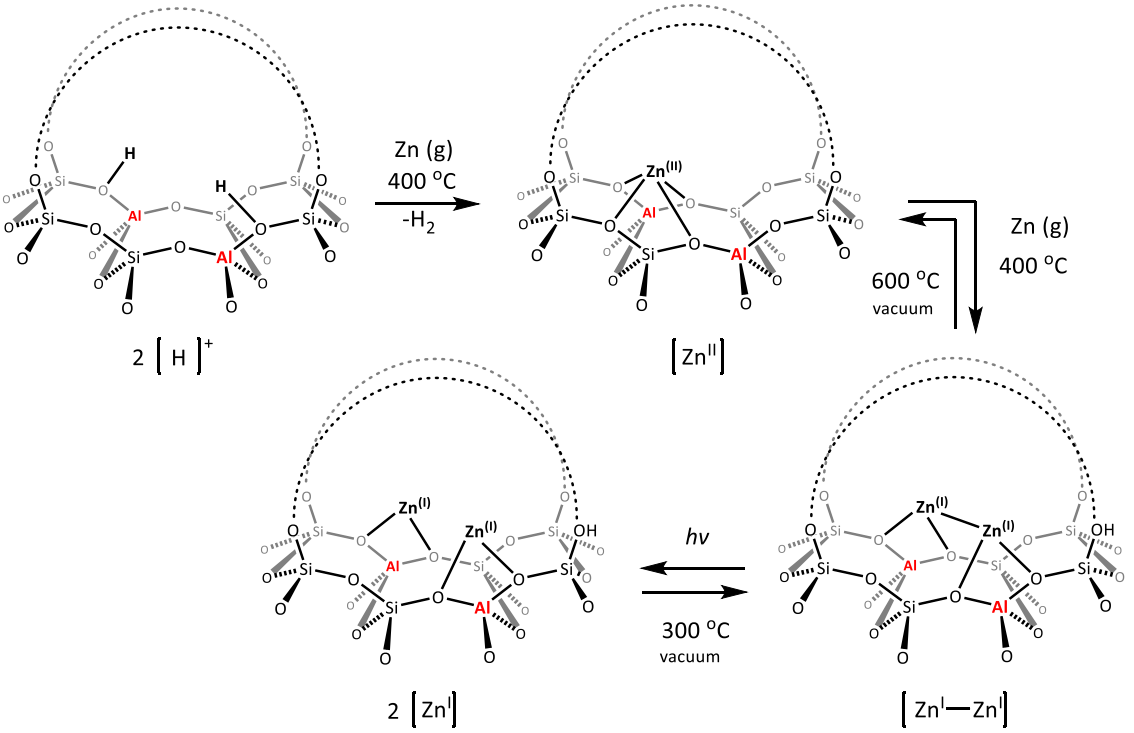

Scheme 1: Formation of a [Zn^{I}-Zn^{I}] dimer when zinc vapour deposition is carried out in the presence of excess zinc. The formation of the dimer is reversible at high temperature.

In the wider literature beyond zeolite systems, the first [Zn^{I}-Zn^{I}] bonded species was synthesised by Carmona *et al.* as decamethyldizincocene, $Zn_2(\eta^5\text{-}C_5Me_5)_2$.[21] Since this initial finding in 2004, several studies have been carried out to understand the nature of the Zn-Zn

bond and its reactivity. However, many complexes containing [Zn^{I}-Zn^{I}] species decompose easily and disproportionate to form Zn^{2+} and Zn^{0} between 25 – 300 °C.[22-27] On the other hand, the [Zn^{I}-Zn^{I}] species formed by Kuroda *et al.* is thermally stable as disproportionation only occurs at 600 °C under vacuum, indicating the zeolite framework provides stabilisation for the Zn-Zn bond. This is supported by DFT calculations on Zn/FER by Benco, which suggest that the [Zn^{I}-Zn^{I}] species is strongly stabilised by the 8MR and 10MR of the zeolite framework.[28] Benco also suggests that the [Zn^{I}-Zn^{I}] dimer is likely to be highly reactive due to the presence of two extra electrons which are shared by both Zn^{+} cations in a covalent bond (analogous to H_2).

In this chapter, we explore the high Zn/Al ratios present in Zn(VD)/ZSM-5 and Zn(VD)/MOR vapour deposition samples through XAS analysis. We hypothesise that the [Zn^{I}-Zn^{I}] species is the active species in zinc vapour deposition samples that activate methane, despite the lack of reactivity of $Zn_2(\eta^5\text{-}C_5Me_5)_2$ towards H_2, CO or CO_2.[23] This is supported experimentally by the addition of zinc through vapour deposition into partially exchanged Zn/Na zeolites, a process that increases the activity of these samples towards methane.

6.2 Results and Discussion

6.2.1 XAS analysis of the zinc active site for methane activation

Zinc vapour deposition samples (Zn(VD)/ZSM-5 and Zn(VD)/MOR) in Chapter 4 were reported to have Zn/Al ratios that were higher than the theoretical maximum of 0.5. Additionally, ^{29}Si CP NMR spectra of the parent zeolites, NH_4-ZSM-5 (12.5) and H-MOR (10), (Chapter 4, Figure 3), indicated that very few defects were present. Therefore, the increased zinc content was unlikely to be due to incorporation of zinc into silanol nests as reported by Beyer *et al.*.[16] We hypothesised that if the elevated zinc content was due to excess Zn^{0}, as suggested by Pidko *et al.*,[12] longer time at elevated temperature under vaccuum could remove this excess zinc.

To investigate this theory, Zn(VD)/ZSM-5 and Zn(VD)/MOR were synthesised under standard zinc vapour deposition conditions at 500 °C (as reported in Chapter 3). The samples were further heated to 550 °C for 2 h and 600 °C for 4 h under dynamic vacuum before being exposed to CH_4 at 250 °C. Both samples, Zn(VD)/CH_4/ZSM-5–600 °C and Zn(VD)/CH_4/MOR–600 °C, showed a small decrease in Zn/Al after this treatement (Table 1), but, the Zn/Al ratio was still higher than the theoretical value of 0.5 expected. Futhermore, after treating the Zn/zeolites under these conditions, no methane activation was observed. Both standard vapour deposition methane activation conditions (250 °C, 15 min) and ion exchange activation conditions (250 °C, 2 h) using both labelled and unlabelled methane were attempted on Zn(VD)/CH_4/ZSM-5–600 °C

and Zn(VD)/CH_4/MOR–600 °C, but no [Zn^{II}-CH_3] species was observed in the ^{13}C NMR spectra for the samples treated at higher temperature.

Table 1: Elemental analysis of Zn(VD)/ZSM-5 and Zn(VD)/MOR vapour deposition samples before and after exposure to methane. Analysis of Zn(VD)/ZSM-5 and Zn(VD)/MOR treated at 600 °C in an attempt to remove excess zinc. Zn(IE)/ZSM-5 included for comparison.

Sample (given Si/Al)	Measured Si/Al[1]	Zn/Al[2]	Successful C-H activation[3]
Zn(VD)/ZSM-5	12.5	0.78	-
Zn(VD)/CH_4/ZSM-5	12.5	0.73	Y
Zn(VD)/CH_4/ZSM-5–600°C	12.5	0.70	N
Zn(VD)/MOR	7.9	0.74	-
Zn(VD)/CH_4/MOR	7.9	0.75	Y
Zn(VD)/CH_4/MOR–600°C	7.9	0.60	N
Zn(IE)/ZSM-5 – IE	11.6	0.45	Y

[1]determined by WDXRF, [2]determined by ICP-OES, [3] For successful C-H activation, a [Zn^{II}-CH_3] species was observed in the ^{13}C NMR spectrum

The lack of methane activation from Zn(VD)/CH_4/ZSM-5–600 °C and Zn(VD)/CH_4/MOR–600 °C indicates that the zinc active species in vapour deposition samples is lost upon treatment at 600 °C. Conversly, Zn(IE)/ZSM-5 requires higher activation temperatures and longer methane exposure time than VD samples.The Zn(IE)/ZSM-5 sample does not activate methane undergoing the same thermal treatment as VD samples, but requires heating to 600 °C. This could indicate that the active species in Zn(IE)/ZSM-5 is not actually formed until higher temperatures are used. To obtain further information on the nature of Zn sites in both vapour deposition and ion exchanged samples before and after exposure to CH_4, Zn K-edge XAS was carried out. The position of the absorption edge in the XANES spectra is dependent on the oxidation state of the Zn, for example oxidation from Zn^0 to Zn^{2+} results in a shift to higher energies (9659 to 9662 eV).[10, 29-31] Hence, XAS can probe the coordiantion environment and oxidation state and therefore the nautre of the zinc active site for methane activation.

Figure 2 compares the XANES spectra for Zn/MOR and Zn/ZSM-5 samples that have been prepared by vapour deposition, ion exchange or treated at 600 °C after vapour deposition. All samples were analysed under inert conditions by careful handling under Ar. The dehydrated Zn(IE)/ZSM-5 sample produces a characteristic XANES spectrum with two post-edge features with energies indicitive of the 1s to 4p transitions for monomeric Zn^{2+} (9665 eV and 9670 eV).[10-12, 19, 32] The shape of the spectrum is indicitive of tetrahedral Zn complexes, which is expected

for extraframework Zn-sites present in a zeolite where the coordiation geometry is likely to be distorted tetrahedral.[10, 33] The spectrum is also substantially different in shape to a characteristic ZnO XANES spectrum shown in Figure 1b (results from Pidko *et al.*).[10, 11, 19] Therefore, it can be concluded that the XANES spectrum of Zn(IE)/ZSM-5 demonstrates clearly the presence of extraframework Zn^{2+} cations in ZSM-5.

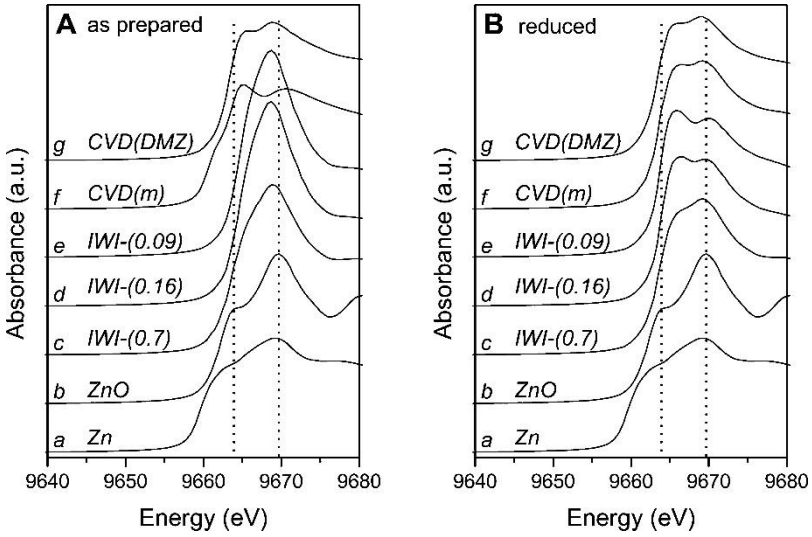

Figure 1: XANES spectra of (a) Zn foil and (b) ZnO reference materials as well as those of (A) as prepared and (B) reduced in H2 at 550 °C Zn/ZSM-5 catalysts: (c–e) Zn-ZSM-5(20)-IWI and (f–g) Zn-ZSM-5(20)-CVD. Adapted with permission from ref 10. Copyright ACS 2011.

The zinc vapour deposition samples, Zn(VD)/ZSM-5 and Zn(VD)/MOR, produce XAS spectra that are quite different to both Zn(IE)/ZSM-5 (containing Zn^{2+}) and zinc foil representing Zn metal (Figure 2A). Pidko *et al.* observe similar shaped XANES spectra from a Zn-CVD-ZSM-5 sample.[10] They suggest the distinct shoulder at low energies is indicative of the presence of substantial metallic zinc as they observed that the shoulder disappeared on high temperature treatment.[10] However, Kuroda *et al.* ascribe the the absoprtion band at 9661 eV to the [Zn^{I}-Zn^{I}] dimer species.[19] Due to the small concentration of Zn^0 or the [Zn^{I}-Zn^{I}] present, it is difficult to distinguish between the two species. Therefore, we hypothesise that in the zinc vapour deposition samples, Zn(VD)/ZSM-5 and Zn(VD)/MOR, both the Zn^0 and [Zn^{I}-Zn^{I}] could present alongside the Zn^{2+} observed. Chiesa *et al.* have presented XANES spectra of Zn(VD)/ZSM-5 where the zinc has been introduced by vapour deposition.[20] However, before XAS analysis, the sample was exposed to the atmosphere. The Zn(VD)/ZSM-5 spectrum consequently looked very similar to their hydrated IE sample. This indicates that the species of interest are only observed when the samples are treated in a N_2/Ar environment without any exposure to air.

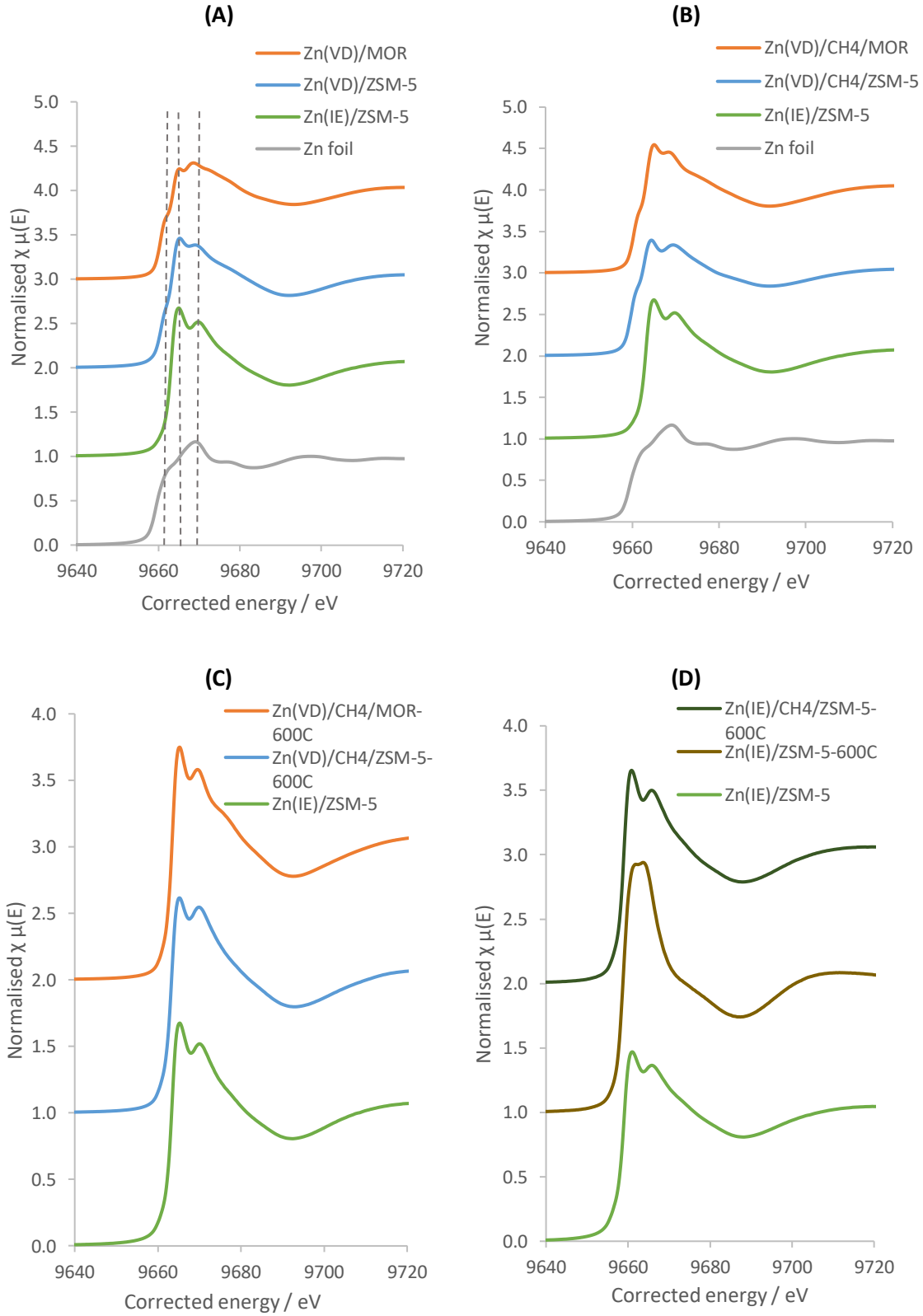

Figure 2: Normalised XANES spectra for Zn/ZSM-5 and Zn-MOR samples. Energy scale corrected with reference to a zinc foil measured concurrently to the sample. (A) Comparison of vapour deposition samples with Zn(IE)/ZSM-5 and zinc foil. (B) Comparison of vapour deposition, methane activated samples with Zn(IE)/ZSM-5 and zinc foil. (C) Comparison of vapour deposition samples treated at 600 °C with Zn(IE)/ZSM-5. (D) Comparison of dehydrated Zn(IE)/ZSM-5-IE with activated Zn(IE)/ZSM-5– 600 °C and methane exposed Zn(IE)/CH_4/ZSM-5–600 °C.

Despite a number of studies utilising XAS analysis to probe the state of zinc-exchanged into zeolites, there has not been a published study of XAS analysis of methane-activated zinc samples. Upon exposure of the Zn/zeolite to methane, ^{13}C NMR spectroscopy shows that a [Zn^{II}-CH_3] species is formed, changing the environment around the zinc active species. We hypothesised that this change in zinc environment could be detected through XAS analysis. The XANES spectra of Zn(VD)/CH_4/ZSM-5 and Zn(VD)/CH_4/MOR are shown in Figure 2B. Slight changes in the spectra are observed when comparing the zinc vapour deposition samples before and after methane exposure. A shoulder is observed at slightly lower energy in the spectra of Zn(VD)/CH_4/ZSM-5 and Zn(VD)/CH_4/MOR. To highlight this change, the XANES spectra of Zn(VD)/ZSM-5 and Zn(VD)/CH_4/ZSM-5 are shown in Figure 3. We hypothesis that the shoulder at 9659 eV in the XANES spectra of Zn(VD)/CH_4/ZSM-5 is due to a low valent zinc species – Zn^0 that is formed upon the reaction of the [Zn^{I}-Zn^{I}] dimer with methane. This is discussed further in section 6.2.2. Without further detailed analysis of the XANES spectra, supported by modelling calculations, we cannot accurately assign the shoulder observed, however, the presence of Zn^0 after the reaction of the dimer with methane supports our current hypothesis about the reaction occurring in vapour deposition samples.

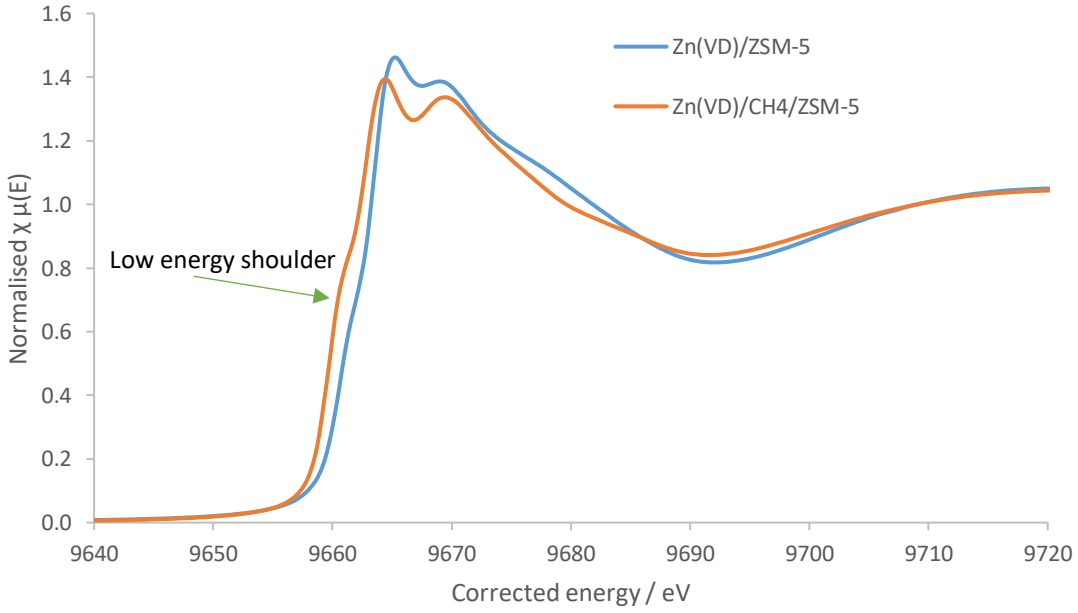

Figure 3: XANES spectra of Zn(VD)/ZSM-5 and Zn(VD)/CH_4/ZSM-5 highlighting the shoulder observed at 9659 eV which could correspond to a low valent Zn^0 species.

Upon heating Zn(VD)/ZSM-5 and Zn(VD)/MOR vapour deposition samples to 600 °C to try to remove any excess Zn^0, the XANES spectra change significantly (Figure 2C). The spectra of the Zn(VD)/CH_4/ZSM-5–600°C and Zn/CH_4/MOR–600 °C samples are very similar to the Zn(IE)/ZSM-5 sample (Figure 2C). The low energy shoulder has disappeared upon heating at

higher temperatures, in line with the observations of Pidko *et al.,*[10] and the samples show characteristic Zn^{2+} XANES spectra. As these samples were unable to produce the [Zn^{II}-CH_3] species, we believe that the zinc active species is no longer present after this high temperature treatment. This corroborates the results from Kuroda *et al.* where the Zn-Zn bond in [Zn^{I}-Zn^{I}] dimer species is cleaved at 600 °C under vacuum.[19] Therefore, we suggest that the zinc species that activates methane in zinc vapour depositions samples is a [Zn^{I}-Zn^{I}] dimer. Further experimental work to support this hypothesis is presented in Section 6.2.2.

Whilst the active site in zinc vapour deposition species is no longer present at 600 °C, Zn(IE)/ZSM-5 requires a temperature of 600 °C to be able to affect methane activation. To investigate this phenomenon, three ion exchanged ZSM-5 samples were compared: Zn(IE)/ZSM-5 which had only been dehydrated at 550 °C, Zn(IE)/ZSM-5-600°C which had been treated under zinc ion exchange activation conditions (600 °C, 4h) and Zn(IE)/CH_4/ZSM-5, activated and exposed to methane. The XANES spectra of these three samples are shown in Figure 2D. The Zn(IE)/ZSM-5 and the Zn(IE)/CH_4/ZSM-5 spectra are very similar and neither spectra contain a shoulder at lower energies corresponding to the [Zn^{I}-Zn^{I}] dimer. This suggests that methane activation over Zn(IE)/ZSM-5 occurs over Zn^{2+} cations, potentially a different mechanism to the vapour depositions samples. Unfortunately, the spectrum corresponding to Zn(IE)/ZSM-5–600°C sample shows signs of hydration as two distinct peaks are no longer observed at 9665 and 9669 eV , corresponding to hydrated spectra of Zn^{2+}/ZSM-5 in the literature.[10-12, 19, 32, 34] As this was an intermediate to the other two samples it must be assumed this is the result of unintended air exposure, but from the other two IE samples it is clear that the IE samples clearly do not show the same spectral trends as those derived by Zn vapour deposition.

Initial analysis by Dr Simon Beaumont, Durham University, of the corresponding EXAFS data is given in Figure 4 which compares the spectra of the real part of χ(R) of the EXAFS region for Zn/MOR and Zn/ZSM-5 samples that have been prepared by vapour deposition, ion exchange or treated at 600 °C after vapour deposition. The corresponding structural analysis can be found in Table 2 where two different fitting models were tested for all samples.

Figure 4A compares the spectra of Zn(VD)/MOR, Zn(VD)/ZSM-5 with Zn/ZSM-5 (IE). A feature just below 2 Å is observed for Zn(VD)/MOR and Zn(VD)/ZSM-5, but this feature is not present in Zn(IE)/ZSM-5. Upon exposure to methane, Zn(VD)/CH_4/MOR and Zn(VD)/CH_4/ZSM-5 also display this feature. Preliminary fitting analysis indicates that this feature is consitenet with a [Zn^{I}-Zn^{I}] dimer (Table 2, Figure 5). When the Zn(VD)/MOR, Zn(VD)/ZSM-5 and subsequent methane activated Zn(VD)/CH_4/MOR and Zn(VD)/CH_4/ZSM-5 were fitted using only Zn-O, the R-

factor (which establishes the agreement of the fit with the experimental data) was considerably high. If the [Zn^{I}-Zn^{I}] dimer is included in the fit, the R-factor decreases by a factor of ~ five. However, for Zn(IE)/ZSM-5, no fit was possible when including the [Zn^{I}-Zn^{I}] dimer, reinforcing the conclusions from the XANES spectra above. It is clear from Figure 5 that the feature observed in the Zn(VD)/MOR, Zn(VD)/ZSM-5, Zn(VD)/CH_4/MOR and Zn(VD)/CH_4/ZSM-5 samples is well fitted by the inclusion of the [Zn^{I}-Zn^{I}] dimer. It should be noted that the bond length used for the [Zn^{I}-Zn^{I}] dimer when fitting (2.32 Å) is shorter than twice the metallic radius of Zn (1.37 Å). This value was utilised as it has been derived from DFT calculations by Kuroda *et al.* [19] and Benco,[28] and in line with results for related compounds (decamethyldizincocene).[21, 23] If a longer bond length is used, the fit is significantly worse. This in turn suggests that metallic Zn-Zn contributions are not detectable and thus the samples are unlikely to contain Zn^0 clusters.

Whilst the value for the co-ordination number (CN) for the [Zn^{I}-Zn^{I}] dimer contains substantial error, likely due to the small percentage of [Zn^{I}-Zn^{I}] dimers formed, two conclusions can be drawn. A higher concentration of [Zn^{I}-Zn^{I}] dimers are formed in Zn(VD)/ZSM-5 than in Zn(VD)/MOR. If this [Zn^{I}-Zn^{I}] dimer is the species active for reactivity with methane, it supports why the percentage of active zinc sites in Zn(VD)/ZSM-5 are higher than for Zn(VD)/MOR (5.7% compared with 1.2%). Furthermore, no dimers are present in Zn(IE)/ZSM-5, perhaps explaining the different activation conditions required.

Figure 4B compares Zn(VD)/CH_4/MOR–600°C and Zn(VD)/CH_4/ZSM-5-600 °C with Zn(IE)/ZSM-5. The spectra look very similar and no feature near 2 Å is observed. Additionally, when attempting to fit the 600 °C treated spectra, no fit was possible when including the [Zn^{I}-Zn^{I}] species. This highlights the similarities seen in the XANES spectra above between Zn(VD)/CH_4/MOR–600°C and Zn(VD)/CH_4/ZSM-5-600 °C with Zn(IE)/ZSM-5. The absence of the dimer supports why no [Zn^{II}-CH_3] species was formed after the 600 °C treatment.

To futher analyse the active site present in Zn(IE)/ZSM-5, the EXAFS spectra of Zn(IE)/ZSM-5, Zn(IE)/ZSM-5-600°C and Zn(IE)/CH_4/ZSM-5 were compared in Figure 4C. The spectra look similar and no feature corresponding to the [Zn^{I}-Zn^{I}] species is observed. The fit using only Zn-O is acceptable for all three samples and when considering the [Zn^{I}-Zn^{I}] species for Zn(IE)/CH_4/ZSM-5 a co-ordination of 0.01 ± 0.03 is calculated, hence, the dimer is not present. This emphasises that a different active site for methane activation is likely on zinc ion-exchanged samples. It should be noted that for the Zn(IE)/ZSM-5–600 °C sample, a significantly higher co-ordination number of 7 ± 0.5 is calculated compared with the co-ordination of 4 or 5 for the other samples. Zinc introduced through vapour deposition or ion exchange is expected to have

a co-ordination of 4 or 5 as the zinc takes a distorted tetrahedral geometry.[10, 19] The XANES spectrum of Zn(IE)/ZSM-5–600 °C indicated that the species may have been inadvertently hydrated through air exposure and the higher co-ordination number supports this finding as hydrated Zn^{2+} would form an octahedral coordination environment.[11]

The presence of the the [Zn^{I}-Zn^{I}] species post methane activation (in Zn(VD)/CH_4/ZSM-5 and Zn(VD)/CH_4/MOR) could be construed as evidence that the dimer is not the active species in the vapour deposition samples. However, based on the Zn/Al ratios presented in Table 1 and that less than 6% of zinc present forms the [Zn^{II}-CH_3] species (determined by NMR spectroscopy), not all the [Zn^{I}-Zn^{I}] species present in the zeolite are activated. The Zn(VD)/CH_4/ZSM-5 – 600 °C sample has a Zn/Al ratio of 0.7, higher than the theoretical maximum of 0.5, but XAS analysis has established that only Zn^{2+} cations are present. Under the conditions the sample was prepared (600 °C, 4 h under vacuum) all excess Zn^0 should be removed. Hence, it is difficult to explain the higher than expected Zn/Al ratio. Although the ^{29}Si CP NMR spectrum of the H-ZSM-5 (15) parent material does not indicate that many defects are present (Chapter 4, Figure 3), no zeolite is completely defect free and some of the Zn vapour could be reacting with silanol nests and inserting into the zeolite framework. However, based on the Zn/Al ratio of Zn(VD)/CH_4/ZSM-5–600°C, we can assume that 0.70 is the maximum amount of Zn^{2+} species present in Zn(VD)/ZSM-5 (Zn/Al 0.78). Assuming no further reactions with the zeolite framework, the any additional zinc can be assumed to be present as a [Zn^{I}-Zn^{I}] dimer. Based on this calculation[1], 21% of the zinc in Zn(VD)/ZSM-5 is present as the [Zn^{I}-Zn^{I}] dimer species. Through NMR quantification, only 6% of these sites were found to be active, hence, the [Zn^{I}-Zn^{I}] species can still be observed in Zn(VD)/CH_4/ZSM-5 and Zn(VD)/CH_4/MOR whilst also functioning as the active species.

[1]The Zn/Al ratio of Zn(VD)/ZSM-5 is 0.78 whilst the Zn/Al ratio of Zn(VD)/CH_4/ZSM-5–600°C is 0.70, therefore the excess zinc removed by vacuum is a Zn/Al ratio 0.08. This Zn/Al ratio of 0.08 can be assigned to half the zinc that is present as the [Zn^{I}-Zn^{I}] dimer, *i.e.* Zn^{+} which is removed upon the 600 °C treatment under vacuum. The total zinc remaining (0.70) consists of Zn^{2+} and the remainder of the Zn^{+} that formed part of the dimer (0.08). Therefore, the zinc that is present as Zn^{2+} is equal to 0.70 – 0.08 = 0.62. This translates to 79% of the zinc is present as a Zn^{2+}, whilst the remaining 21% is present as the [Zn^{I}-Zn^{I}] dimer.

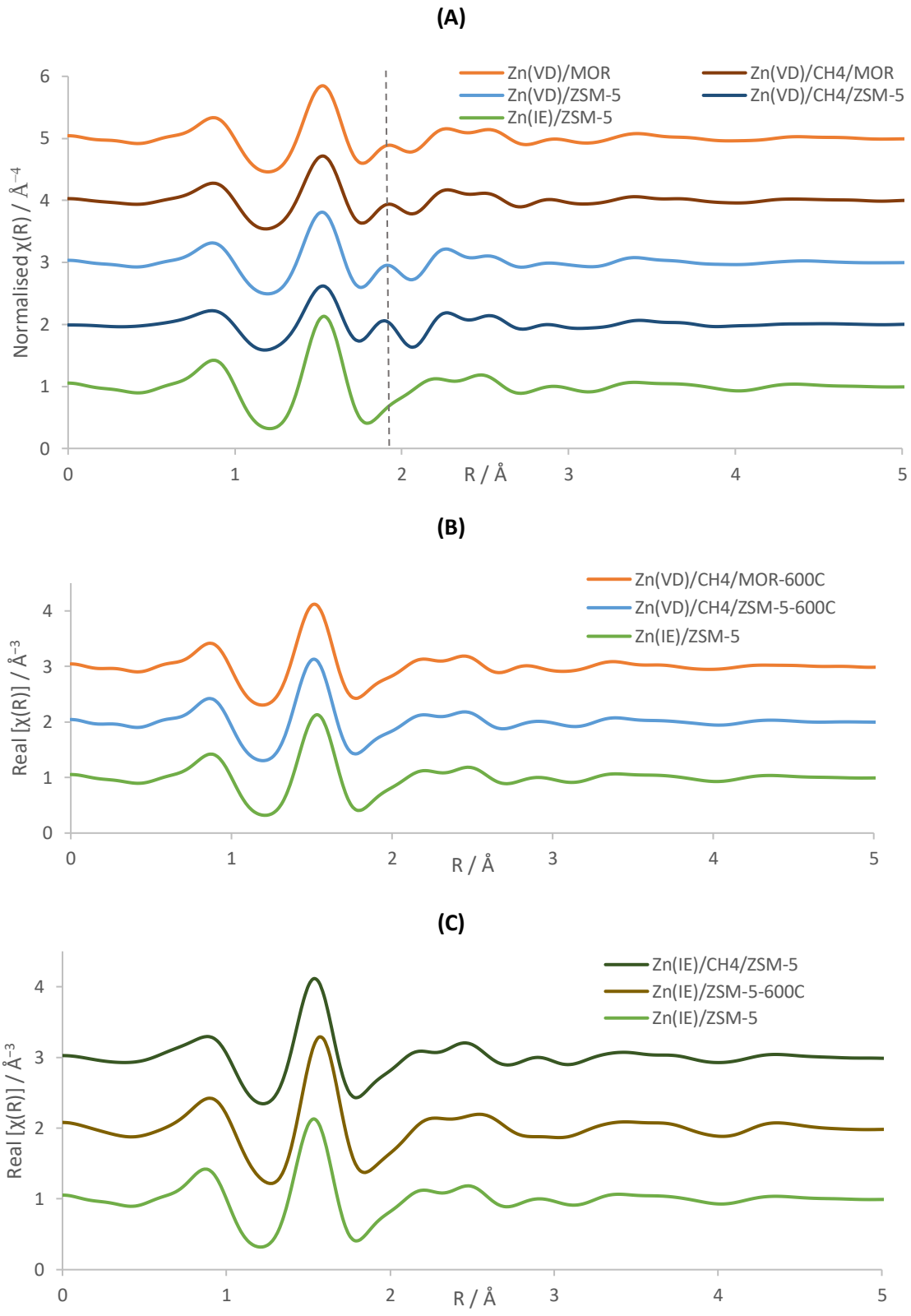

Figure 4: Real component of EXAFS R-space spectra for Zn/ZSM-5 and Zn/MOR samples. (A) Comparison of vapour deposition samples before and after methane exposure with Zn(IE)/ZSM-5. The peak associated with the [Zn^{I}-Zn^{I}] dimer is highlighted with a dashed line. (B) Comparison of Zn(VD)/CH_4/MOR–600°C and Zn(VD)/CH_4/ZSM-5–600°C with Zn(IE)/ZSM-5. (C) Comparison of dehydrated Zn(IE)/ZSM-5 with activated Zn(IE)/ZSM-5-600°C and methane exposed Zn(IE)/CH_4/ZSM-5-600°C.

Table 2: EXAFS structural analysis where CN refers to co-ordination number and the R-factor corresponds to the agreement between the model and the experimental EXAFS data. Two fitting models were tested on all samples, one fit addressed only the presence of O in the Zn first co-ordination sphere whilst the second investigated the presence of both O and a second Zn species. R-factors highlighted in red are considered high. No acceptable fit was reported where any attempt to include the second zinc gave a negative CN or an impractical bond length. The CN highlighted in purple indicates a CN of 0.01 where the fit is so small that the [Zn^{I}-Zn^{I}] dimer can be considered non-existent.

Sample	Attempted fit with only Zn-O		Attempted fit with Zn-O and [Zn^{I}-Zn^{I}]		
	CN (Zn-O)	R-factor	CN (Zn-O)	CN [Zn^{+} - Zn^{+}]	R-factor
Zn(VD)/ZSM-5	3.7 ± 0.7	0.081	4.00 ± 0.48	0.28 ± 0.22	0.014
Zn(VD)/CH_4/ZSM-5	3.3 ± 1.1	0.190	3.79 ± 0.62	0.44 ± 0.21	0.013
Zn(VD)/CH_4/ZSM-5–600 °C	4.9 ± 0.5	0.018	No acceptable / physical fit		
Zn(VD)/MOR	3.2 ± 0.4	0.036	3.52 ± 0.41	0.05 ± 0.05	0.007
Zn(VD)/CH_4/MOR	3.3 ± 0.6	0.072	3.64 ± 0.58	0.20 ± 0.20	0.022
Zn(VD)/CH_4/MOR–600°C	4.9 ± 0.6	0.021	No acceptable / physical fit		
Zn(IE)/ZSM-5- IE	3.8 ± 0.4	0.019	No acceptable / physical fit		
Zn(IE)/ZSM-5-600°C	7.0 ± 0.5	0.010	No acceptable / physical fit		
Zn(IE)/CH_4/ZSM-5	4.8 ± 0.4	0.014	3.23 ± 0.49	0.01 ± 0.03	0.014

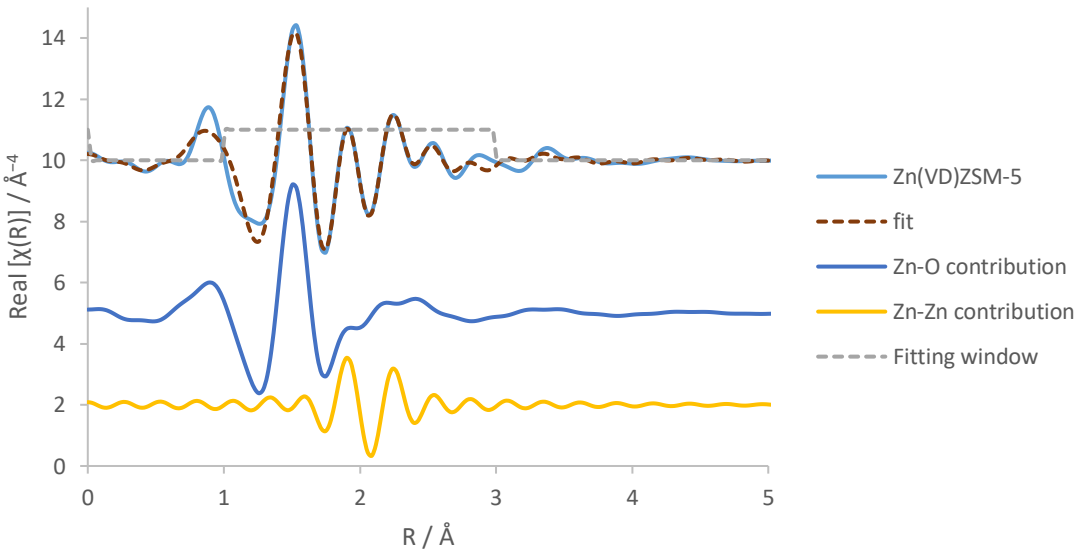

Figure 5: Example of fitting conditions for the real part of the EXAFS R-space spectrum of Zn/ZSM-5 sample with both Zn-O contribution and Zn-Zn contribution on Zn(VD)/ZSM-5. The feature just below 2 Å is from the [Zn^{I}-Zn^{I}].

6.2.2 Addition of zinc vapour to partially exchanged Zn/Na zeolites

To further investigate the hypothesis that the [Zn^{I}-Zn^{I}] dimer was the active species in zinc vapour deposition samples, additional methane activation experiments were carried out on Na-ZSM-5 (12.5) (produced from NH_4-ZSM-5 (12.5), Na/Al = 0.95) and Na-MOR (7). As the Na-MOR (7) parent has not been previously used for methane activation, ^{27}Al and ^{29}Si NMR spectra were taken. The spectra, which can be found in Appendix 5, indicate that no extraframework Al is present and the ^{29}Si CP NMR spectrum of Na-MOR contains very few defects.

Two zinc ion-exchanged samples were prepared from each parent, an almost fully exchanged Zn(IE)/ZSM-5 (90% zinc exchange level) and Zn(IE)/MOR (92% zinc exchange level) and a partially exchanged Zn(IE)/Na-ZSM-5 (54% zinc exchange level) and Zn(IE)/Na-MOR (58% zinc exchange level). Methane activation was carried out using $^{13}CH_4$ under ion exchange activation conditions (600 °C for 4 h, $^{13}CH_4$ sealed at 250 °C for 2 h). Both Zn(IE)/ZSM-5 and Zn(IE)/MOR were able to activate methane with 0.9% and 1.5% respectively of zinc present active for forming the [Zn^{II}-CH_3] species observed by ^{13}C NMR spectroscopy (Table 3). Direct ^{13}C NMR spectra used for NMR quantification can be found in Appendix 5. This is the first methane activation observed on zinc ion exchanged MOR. It should be noted that two peaks are observed in the ^{13}C CP NMR spectrum (Figure 6D), as previously detected from Zn(VD)/CH_4/MOR vapour deposition samples. The two peaks correspond to [Zn^{II}-CH_3] species present in the 12 MR and the 8 MR SP of MOR, as discussed in Chapter 4. No methane activation was observed on the partially exchanged samples Zn(IE)/Na-ZSM-5 and Zn(IE)/Na-MOR (Fig 2B and E, respectively). Kuroda *et al.* suggest that the zinc sites, which are able to activate methane are the sites which are hardest to ion exchange due to distant Al pairs.[35] These sites are the most active due to the incomplete charge balance on the Zn^{2+}, which can lead to greater Lewis acidity.[1, 2, 36] Therefore, it is likely that the partially zinc-exchanged Zn(IE)/Na-zeolites do not yet contain these active zinc sites and are consequently unable to activate methane.

To test our hypothesis that the [Zn^{I}-Zn^{I}] dimer is the active zinc species for methane activation, a vapour deposition was carried out on the partially exchanged samples, Zn(IE)/Na-ZSM-5 and Zn(IE)/Na-MOR. Zinc vapour deposition with an acidic zeolite normally occurs *via* a redox reaction involving the exchange of BAS for Zn^{2+} cations and the evolution of H_2 gas.[1-4, 14] No BAS sites are present in the Zn(IE)/Na-ZSM-5 and the Zn(IE)/Na-MOR samples hence, a traditional vapour deposition reaction cannot take place. However, the Zn/Al ratios reported in Table 3 demonstrate that after exposure to zinc vapour, the Zn/Al ratio increases significantly for both Zn(IE)/Na-ZSM-5 and the Zn(IE)/Na-MOR. Furthermore, the Zn(VD)/Zn(IE)/Na-ZSM-5 and the Zn(VD)/Zn(IE)/Na-MOR are now able to activate methane (Figure 6C and F), with 3% and

1.3% respectively of zinc present active for forming the [Zn^{II}-CH_3] species. This indicates that zinc was able to be added to the zeolite without the presence of BAS.

The Zn(VD)/Zn(IE)/Na-ZSM-5 spectrum displays a shoulder at −22 ppm (Figure 6C), a feature that has not been observed for methane activation on Zn(VD)/ZSM-5 previously. We hypothesise that this is due to different [Zn^{II}-CH_3] environments within the zeolite due to the presence of Na^+ cations, but without further analysis, this cannot be confirmed. The vapour deposition reaction and $^{13}CH_4$ exposure on Zn(IE)/Na-ZSM-5 was repeated (Appendix 5) and the shoulder was observed again. The two peaks observed for Zn(VD)/MOR have been assigned to [Zn^{II}-CH_3] species present in the 12 MR and the 8 MR SP of MOR, as discussed in Chapter 4. However, ZSM-5 does not contain two distinct pore systems, but is made up of two 10 MR channels of similar dimensions (5.1 x 5.5 Å and 5.3 x 5.6 Å), hence the shoulder observed is unlikely to relate to the zeolite pore structure. As the shoulder is not observed in the ^{13}C NMR spectrum of Zn(IE)/ZSM-5 (Figure 6A) or on previously reported zinc vapour depositions samples Zn(VD)/ZSM-5 (Chapter 4), we believe the shoulder is likely due to the presence of the Na. IR spectroscopic analysis of the Zn(VD)/Zn(IE)/Na-ZSM-5 sample could confirm that [Zn^{II}-CH_3] species in two different environments are present. A ^{13}C– ^{23}Na 2D NMR correlation experiment could be carried out, similar to the 1H-^{27}Al REAPDOR experiments presented in Chapter 4 to determine if the shoulder at −22 ppm corresponds to [Zn^{II}-CH_3] species near Na^+ cations.

The Na/Al ratios reported in Table 3 are higher than expected for the Zn(IE)/ZSM-5 and Zn(IE)/MOR samples. After thorough investigation, we determined that Na was leaching into the zeolite samples from the glass wool plugs that hold the zeolite in the u-tube during the vapour deposition reaction. This led to inaccuracies in the Na/Al ratios from the ICP-OES analysis, particularly noticeable for the Zn(IE)/ZSM-5 and Zn(IE)/MOR samples. All further experiments were carried out with quartz wool to minimise this effect. Conversely, the Na/Al ratios were lower than expected for the partially zinc exchanged Zn(IE)/Na-ZSM-5 and Zn(IE)/Na-MOR samples. For the Zn(IE)/Na-ZSM-5, 54% of the sites are zinc ion exchanged, which should mean that 46% remain counter balanced by Na ions but the Na/Al ratio recorded is only 0.35, 11% of the sites are unaccounted for. The exact cause of the lower Na/Al ratio in the Zn(IE)/Na-ZSM-5 and Zn(IE)/Na-MOR samples remains unclear, but repeat experiments with different Na parent zeolites should be carried out to try to determine whether this is an inaccuracy with the ICP-OES measurements or if the remainder of the sites are no longer Na exchanged. However, this was beyond the scope of the experiments carried out to determine whether the [Zn^{I}-Zn^{I}] dimer is the active zinc species for methane activation.

Table 3: Methane activation results for Zn(IE)/ZSM-5 (12.5) and Zn(IE)/MOR (7) samples, partially zinc exchanged Zn(IE)/Na-ZSM-5 and Zn(IE)/Na-MOR and subsequent vapour depositions samples. Percentage zinc active sites determined using NMR quantification with HMB as a standard can be found below. Elemental analysis for all samples, including the vapour deposition carried out on Na-MOR (7), and BET data are also reported.

Sample	C-H activation	Measured Si/Al	Zn/Al	Na/Al[2]	Percentage of active [Zn^{II}-CH_3]	BET / m^2/g
Zn(IE)/ZSM-5	Y	13.1	0.45	0.20	0.9%	346.8 ± 0.6
Zn(IE)/Na-ZSM-5	N	14.1	0.27	0.35	-	320.6 ± 1.7
Zn(VD)/Zn(IE)/Na-ZSM-5	Y	14.9	0.71	0.32	3.0%	282.4 ± 1.6
Zn(IE)/MOR	Y	6.60	0.46	0.22	1.5%	336.7 ± 3.4
Zn(IE)/Na-MOR	N	6.73	0.29	0.34	-	322.2 ± 2.5
Zn(VD)/Zn(IE)/Na MOR	Y	6.25	0.63	0.32	1.3%	-
Na-MOR - VD	N	6.6	0.03	0.90	-	-

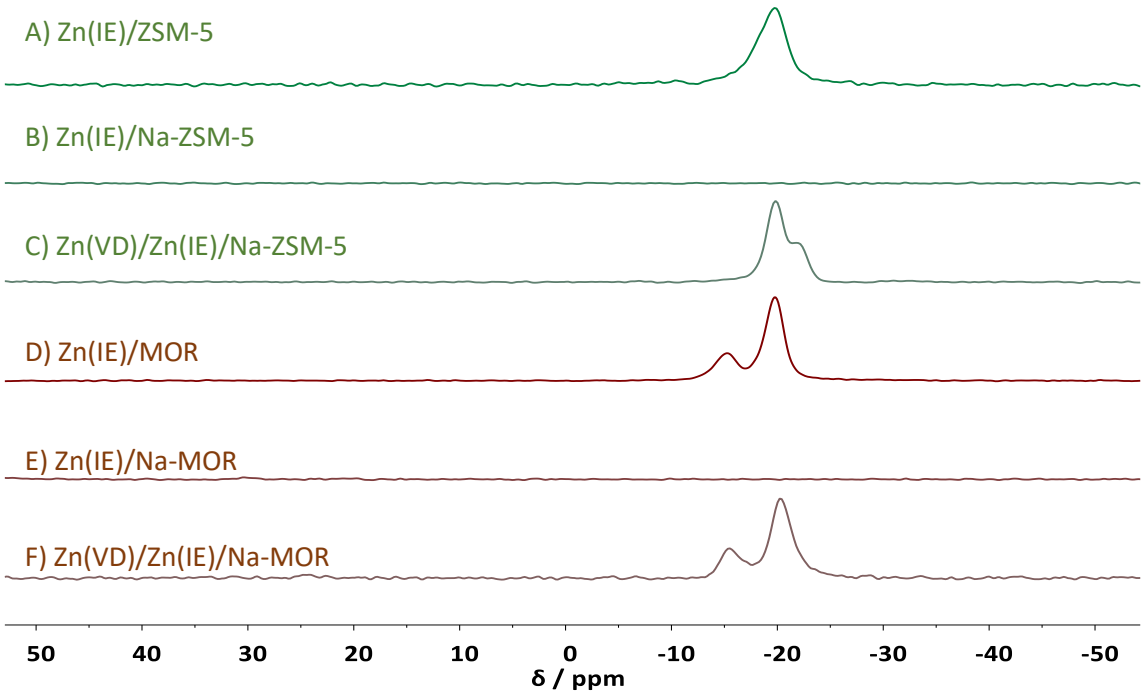

Figure 6: ^{13}C CP NMR spectra of Zn(IE)/ZSM-5 (12.5) and Zn(IE)/MOR (7) samples, partially zinc exchanged Zn(IE)/Na-ZSM-5 and Zn(IE)/Na-MOR and subsequent vapour depositions samples. The characteristic [Zn^{II}-CH_3] can be observed for the 90% ion exchanged samples as well as the vapour deposition samples. Both Zn(IE)/MOR and Zn(VD)/Zn(IE)/Na-MOR show two signals, as observed previously for Zn(VD)/CH_4/MOR, corresponding to [Zn^{II}-CH_3] species in the 12 MR and 8 MR side pockets of MOR. (^{13}C – 100.57 MHz, 10 kHz spin rate)

[2] Na/Al level were higher than expected for Zn/ZSM-5 and Zn/MOR samples likely due to contamination from the glass wool plugs used to hold the zeolite powder during the VD reaction.

To confirm that Na-zeolites cannot react with zinc vapour, a vapour deposition reaction was carried out on the Na-MOR (7) parent. No zinc was exchanged into Na-MOR and no methane activation was observed. No extra reflections corresponding to zinc metal can be observed in the pXRD patterns, which is particularly important for both Zn(VD)/Zn(IE)/Na-ZSM-5 or Zn(VD)/Zn(IE)//Na-MOR samples (Figure 7). Furthermore, no significant change in crystallinity is observed after the samples have been treated under methane activation conditions. BET analysis of ZSM-5 samples indicated that upon zinc vapour deposition, a small decrease in surface area is observed (Table 3). This is expected as the Zn/Al ratio increases from 0.27 to 0.76 as more zinc is incorporated into the zeolite micropore. Unfortunately, attempts to measure the BET surface area of Zn(VD)/Zn(IE)/Na-MOR were unsuccessful, as two different samples were unable to equilibrate at the low pressure range in a reasonable analysis window. We suggest that as MOR is a 1D zeolite, even a small amount of pore blockage could result in difficulty in measuring the BET surface area. The Zn(VD)/Zn(IE)/Na MOR is still able to perform methane activation to a similar degree to Zn(VD)/Zn(IE)/Na-ZSM-5.

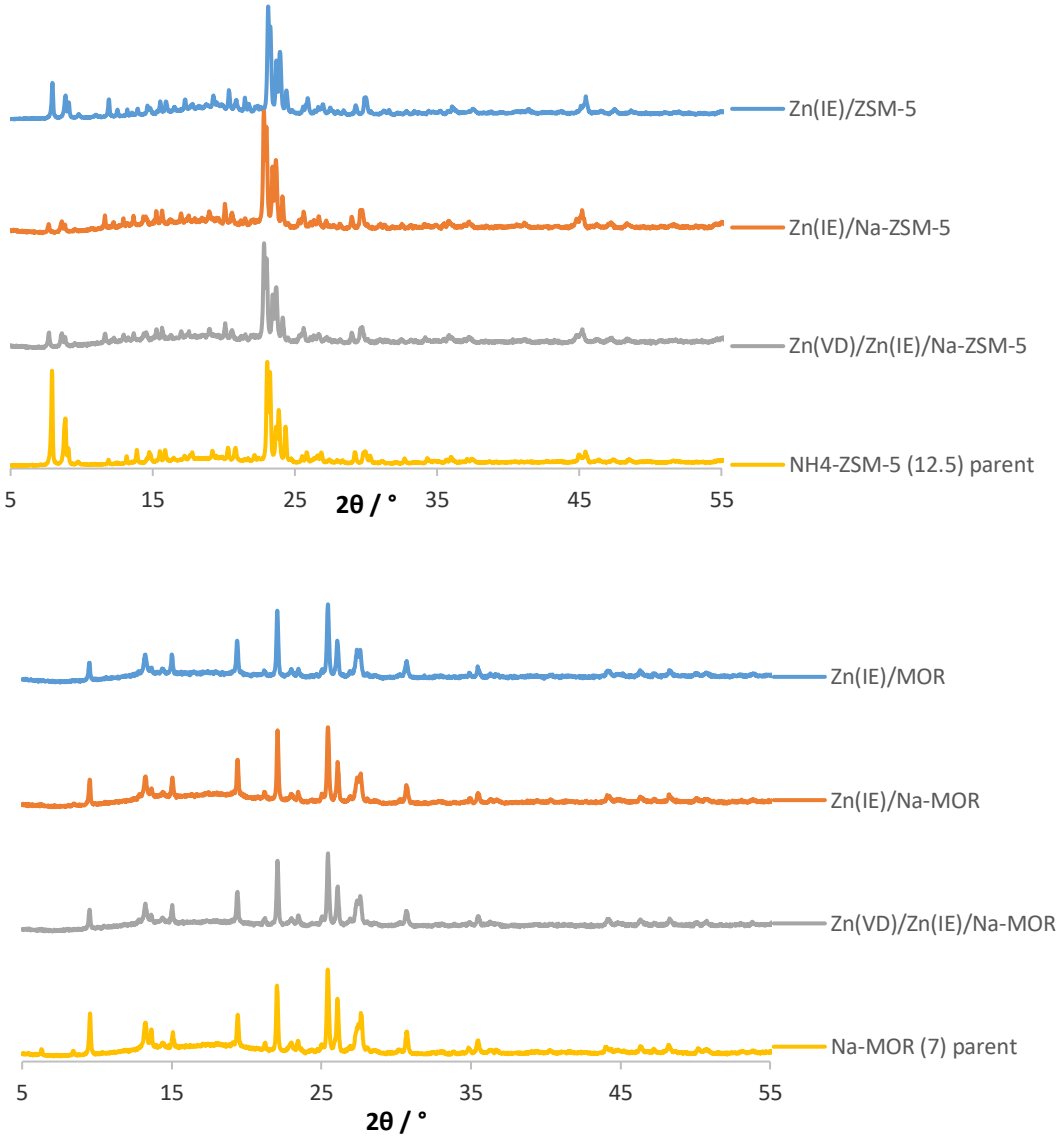

Figure 7: pXRD patterns for ZSM-5 and MOR comparing the fully ion exchanged samples Zn(IE)/ZSM-5, Zn(IE)/MOR, with the partially exchanged IE samples, Zn(IE)/Na-ZSM-5 and Zn(IE)/Na-MOR, with and without the vapour deposition reaction. All pXRD patterns are measured after methane activation has taken place. No extra peaks are observed for zinc metal in any sample. No loss in crystallinity is observed for any sample.

Based on the study above, especially the Zn/Al ratios and methane activation results of Zn(VD)/Zn(IE)/Na-ZSM-5 and Zn(VD)/Zn(IE)/Na-MOR, we suggest that zinc vapour is reacting with Zn^{2+} to form the $[Zn^{I}\text{-}Zn^{I}]$ dimer as shown in Equation 2. This supports the results of Kuroda *et al.* who suggest that in the presence of excess zinc, the $[Zn^{I}\text{-}Zn^{I}]$ dimer is formed.[19] As the Zn(IE)/Na-ZSM-5 and Zn(IE)/Na-MOR partially exchanged samples are unable to activate methane, we believe that the $[Zn^{I}\text{-}Zn^{I}]$ dimer is the active site in zinc vapour deposition reactions, supporting the XAS analysis presented earlier in the chapter.

$$Zn^{2+}\ (s) + Zn^{0}\ (g) \rightarrow [Zn^{+} - Zn^{+}]\ (s)$$

Equation 2: Reaction of zinc vapour with Zn^{2+} in Zn/Na-ZSM-5 – VD and Zn/Na-MOR – VD to from the [Zn^{I}-Zn^{I}] dimer.

The accepted methane activation reaction thus far over isolated Zn^{2+} cations involves the formation of [Zn^{II}-CH_3] species and a new BAS.[1-7] If the [Zn^{I}-Zn^{I}] dimer is the active species in the vapour deposition samples, there remain some questions as to the reactions products. As per methane activation at isolated Zn^{2+} sites, the diamagnetic [Zn^{II}-CH_3] species is the sole detectable product determined from ^{13}C NMR spectroscopy. As such, a redox reaction must have occurred, however the fate of the second zinc atom of the dimer remains unclear at this stage. A potential reaction scheme involving the formation of Zn^0 alongside the [Zn^{II}-CH_3] species and new BAS is presented in Scheme 2. Whilst atomic Zn^0 is generally considered to be unstable, Kuroda *et al.* report the formation of a stable Zn^0 species through the reaction of H_2 with Zn^{2+}/ZSM-5 (Si/Al 12) at 300 °C.[37] The zinc was introduced by ion exchange with 95% zinc exchange levels achieved. Using IR spectroscopy to monitor the reaction between H_2 and Zn/ZSM-5, heterolytic bond cleavage of H_2 was observed where [Zn^{II}-H] species and a new BAS were formed. At temperatures higher than 150 °C, the amount of the [Zn^{II}-H] species decreased despite the authors observing an increase in OH species, leading them to suggest the formation of a stable Zn^0 species. DR-UV-vis analysis and XANES data, supported by DFT calculations, provided evidence of this stable Zn^0 species. The modelling suggested that the species is stabilised through simultaneous interaction with two H^+ ions at BAS of the zeolite. Furthermore, the Zn^0 species reverts back to Zn^{2+}, and liberating H_2, upon heating the sample under vacuum.

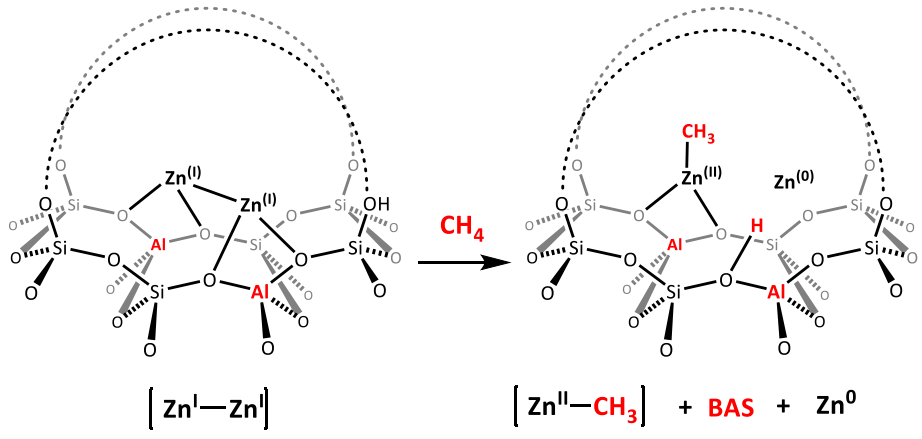

Scheme 2: Proposed reaction scheme for methane activation over [Zn^{I}-Zn^{I}] dimer forming a [Zn^{II}-CH_3], a new BAS and Zn^0.

Based on these finding by Kuroda *et al.* we believe reaction shown in Scheme 2 is plausible. As Zn^0 would not be detected by ^{13}C NMR spectroscopy or IR spectroscopy and is unlikely to be visible in TEM images, current analysis of zinc vapour deposition samples in the

literature have not considered the presence Zn^0 alongside the $[Zn^{II}\text{-}CH_3]$ species and BAS. Whilst XAS analysis of zinc CVD samples has been performed, the shoulder at low energies (9661 eV) has been assigned to Zn^0.[10] There is little difference in energy between Zn^0 (9659 eV) and the dimer (9661 eV), hence the dimer could easily have been mistaken for excess Zn^0. Furthermore, no previous XAS studies have been carried out on methane activated samples or on vapour deposition samples treated at high temperatures (600 °C). The comparison of the XANES spectra of Zn(VD)/CH_4/ZSM-5 compared with Zn(VD)/ZSM-5 (Figure 3) highlights an increase in a shoulder at low energies perhaps corresponding to the presence of Zn^0. Further detailed analysis of XANES spectra of Zn(VD)/CH_4/ZSM-5 and Zn(VD)/CH_4/MOR accompanied by DFT modelling could confirm this hypothesis.

We have suggested the formation of a $[Zn^{I}\text{-}Zn^{I}]$ dimer in Zn/zeolites where the zinc has been introduced by zinc vapour deposition and the Zn/Al ratios are higher than the theoretical 0.5. However, the results of zinc vapour deposition and methane activation over high silica CHA, CHA(62) presented in Chapter 4 do not fit this hypothesis. The high Zn/Al ratio of 3 compared with 0.78 for Zn(VD)/ZSM-5 and the unprecedented percentage of active zinc sites of 21.3% indicates that perhaps a different zinc species is introduced in CHA(62). Until further analysis, such as XAS or EPR, of this high silica CHA is carried out, the nature of the active site in this sample remains unknown. Whilst some of the zinc vapour may be reacting with defect sites in the CHA, the significantly higher Zn/Al ratio of 3 suggests the presence of a zinc complex perhaps containing three zinc atoms. Mixed valence zinc complexes, $[Cp_2Zn_n]$ (n=3–5; Cp=$\eta^5\text{-}C_5H_5^-$), have been predicted through computational studies where the structure of the complexes consists of linear chains of zinc atoms capped by the Cp ligand.[38] However, practically the species are thermodynamically unstable due to loss of the zinc metal.[38] Nevertheless, in 2015, a surprisingly stable anionic cluster complex, $[Zn^{I}_8(HL)_4(L)_8]^{12-}$ (L=tetrazole dianion), containing a cubic core of eight Zn atoms, formally in the +1 oxidation state, was synthesised by Li *et al.*.[39] A triangular cluster complex $[Zn_3Cp^*_3]^+$ was also reported by Fischer *et al.* in 2015.[40] The bonding was described by the authors as σ-aromatic, *i.e.* the bonding electrons were found to be delocalised over the three metal centre where formally two of the zinc atoms are in the +1 oxidation state whilst the other is in the +2 oxidation state. Similarly, Jones *et al.* synthesised a mixed valence tri-zinc complex, $[L^*Zn^{I}Zn^{0}Zn^{I}L^*]$ where L is a bulky amide ligand, shown in Figure 8.[41] Whilst a tri-zinc species has yet to be reported in a zeolite, the CHA double six rings could potentially stabilise a $[Zn^{I}\text{-}Zn^{0}\text{-}Zn^{I}]^{2+}$ species, comparable to the stabilisation of the $[Zn^{I}\text{-}Zn^{I}]$ dimer in Zn/FER as suggested by Benco,[28] leading to the high Zn/Al ratios observed in CHA(62). However, as

stated above, until further spectroscopy analysis is undertaken, the active species in CHA(62) remains unidentified.

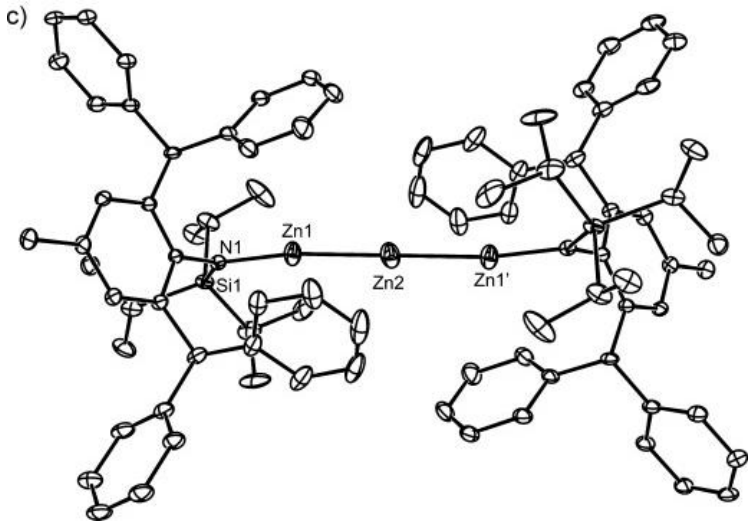

Figure 8: Molecular structures of [L*Zn^{I}Zn^{0}Zn^{I}L*] Zinc trimer species synthesised by Jones *et al.*[41] Adapted with permission from Ref 41. Copyright Wiley 2015.

6.3 Conclusions

In order to investigate the high Zn/Al ratios present in Zn(VD)/ZSM-5 and Zn(VD)/MOR, XAS analyses were performed. Standard vapour deposition reactions were carried out followed by longer high temperature treatment (Zn(VD)/CH_4/ZSM-5–600°C and Zn(VD)/CH_4/MOR–600°C) in an attempt to remove any excess Zn^0 present in the samples. Although the Zn/Al ratio decreased slightly (0.78 to 0.70 for Zn/ZSM-5), the Zn(VD)/CH_4/ZSM-5–600°C and Zn(VD)/CH_4/MOR–600°C samples were no longer active and able to form the [Zn^{II}-CH_3] species. XANES analysis showed that upon this high temperature treatment a low energy band observed in the standard vapour deposition samples, Zn(VD)/ZSM-5 and Zn(VD)/MOR, is no longer present. This low energy band is assigned to a [Zn^{I}-Zn^{I}] dimeric species, supported by previous work by Kuroda *et al.*,[19] which we hypothesise is the active site in zinc vapour deposition samples. Samples prepared by ion exchange do not show this band, indicating a different method active species for C-H activation, which is formed only under the specific pre-treatment conditions.

EXAFS analysis comparing the vapour deposition, ion exchanged and 600 °C treated samples for Zn(VD)/MOR and Zn(VD)/ZSM-5 was carried out by Dr Simon Beaumont at Durham Unviersity. A band associated with the [Zn^{I}-Zn^{I}] dimer is clearly observed in the real part of χ(R) of the EXAFS region for Zn(VD)/MOR, Zn(VD)/CH_4/MOR, Zn(VD)/ZSM-5 and Zn(VD)/CH_4/ZSM-5.

Structural analysis indcated that only these four samples can be fitted using a model containing both Zn-O and [Zn^{I}-Zn^{I}] in the first co-ordination sphere, whilst Zn(IE)/ZSM-5 and the Zn(VD)/CH_4/ZSM-5–600°C and Zn(VD)/CH_4/MOR–600 °C sample could only be fitted using Zn-O. Whilst the CN numbers have a high degree of error due to the small quantity of dimer species observed, it is clear that a higher concentration of [Zn^{I}-Zn^{I}] dimers are formed in Zn(VD)/ZSM-5 than in Zn(VD)/MOR, supporting the activation results presented in Chapter 4 where 5.7% of zinc sites are active in ZSM-5 compared with 1.2% which are active in Zn/MOR. XAS analysis indicates that the [Zn^{I}-Zn^{I}] species is still present in the samples Zn(VD)/CH_4/ZSM-5 and Zn(VD)/CH_4/MOR (after methane activation) which could be interpreted as evidence that the dimer is not the active species for C-H cleavage in theses samples. However, based on the measured Zn/Al ratios (0.73 for Zn/CH_4/ZSM-5) and the low percentage of zinc that is active (5.7% for Zn/ZSM-5), it is in accordance the XANES signal of [Zn^{I}-Zn^{I}] dimer does not disappear upon exposure to methane. Furthermore, this indicates that not all the [Zn^{I}-Zn^{I}] species present in the zeolite are active and therefore there is likely to be a local zeolite framework effect, which renders the dimer reactive towards methane. Whilst investigating the materials Zn(IE)/ZSM-5 and Zn(IE)/CH_4/ZSM-5 with XAS, only Zn^{2+} ions were observed highlighting that different active species could be present depending on the method of zinc introduction. Therefore, the XAS results presented in this chapter support the hypothesis that the [Zn^{I}-Zn^{I}] dimer could be the active site in zinc vapour deposition samples.

To explore the formation of the dimer experimentally, additional methane activation experiments were carried out on samples with varying degrees of Zn and Na exchange levels. No methane activation is observed on the Na parent zeolites, Na-ZSM-5 (12.5) and Na-MOR (7). Both Zn(IE)/ZSM-5 (90% zinc exchange level) and Zn(IE)/MOR (92% zinc exchange level) were able to active methane under standard ion exchange activation conditions where 0.9% and 1.5% respectively of zinc present was active for forming the [Zn^{II}-CH_3] species. Methane activation over Zn(IE)/MOR shows the characteristic two peaks observed initially observed in Chapter 4 for MOR corresponding to [Zn^{II}-CH_3] species present in the 12 MR as well as the 8 MR SP of MOR. Partially exchanged Zn(IE)/Na-ZSM-5 (54% zinc exchange level) or the Zn(IE)/Na-MOR (58% zinc exchange level) were unable to active methane under standard ion exchange activation conditions.

To test the hypothesis that the [Zn^{I}-Zn^{I}] dimer is the active zinc species for methane activation, a vapour deposition was carried out on the partially exchanged Zn(IE)/Na-ZSM-5 and Zn(IE)/Na-MOR samples. No BAS acid sites were present to allow a traditional vapour deposition reaction but Zn/Al ratios increased significantly after exposure of Zn(IE)/Na-ZSM-5 and the

Zn(IE)/Na-MOR to zinc vapour. Furthermore, the Zn(VD)/Zn(IE)/Na-ZSM-5 and Zn(VD)/Zn(IE)/Na-MOR were now able to activate methane with 3% and 1.3%, respectively, of zinc present active for forming the [Zn^{II}-CH_3] species. This indicates that zinc was able to be added to the zeolite without the presence of BAS, and the addition of this zinc increased the activity of the partially exchanged Zn(IE)/Na-ZSM-5 and Zn(IE)/Na-MOR. Furthermore, no zinc can be added to Na-MOR(7) through performing a zinc vapour deposition, which proves that Na cations do not react with Zn^0 under the given conditions.

Based on the ability of the Zn(VD)/Zn(IE)/Na-ZSM-5 and Zn(VD)/Zn(IE)/Na-MOR to activate methane after a zinc vapour deposition reaction, we suggest that zinc vapour is reacting with Zn^{2+} to form the [Zn^{I}-Zn^{I}] dimer in a redox type reaction, comparable to the results of Kuroda *et al.* who suggest that in the presence of excess zinc, the [Zn^{I}-Zn^{I}] dimer is formed.[19] As the Zn(IE)/Na-ZSM-5 and Zn(IE)/Na-MOR partially exchanged samples are unable to activate methane, the modification of the materials with Zn^0 to form the [Zn^{I}-Zn^{I}] dimer strongly suggests that the dimer is the active site for methane activation, supporting the XAS analysis presented earlier in the chapter. The suggested reaction stoichiometry of methane activation over the [Zn^{I}-Zn^{I}] dimer results in the formation of a [Zn^{II}-CH_3] species, a new BAS site and a Zn^0 species. Although atomic Zn^0 is generally considered to be unstable, Kuroda *et al.* report the formation of a stable Zn^0 species through the reaction of H_2 with Zn^{2+}/ZSM-5 at 300 °C.[37] However, further investigation to confirm the presence of the Zn^0 reaction product should be carried out through detailed analysis of the XANES spectra of Zn(VD)/CH_4/ZSM-5 and Zn(VD)/CH_4/MOR, accompanied by DFT modelling. Analysis of the reaction of the dimer species [Zn^{I}-Zn^{I}] with methane using DR-UV-vis could also provide useful information of the active species.

6.4 Experimental

H–MOR (Si/Al = 10), H–ZSM–5 (15) and Na-MOR (7) were kindly provided by Clariant. NH_4–ZSM-5 (12.5) was kindly provided by Johnson Matthey. Zinc powder (Goodfellow, 99.9%, max particle size 150 μm) was used as purchased. Zinc nitrate hexahydrate (99%) and sodium nitrate were used as purchased from Alfa Aesar. Methane-^{13}C (99% ^{13}C) was purchased from Sigma-Aldrich. CH_4 (99.995%) and Ar (99.998%) cylinders were purchased from BOC. Zinc powder was stored and used in a PureLab HE glove box under an argon atmosphere.

The vapour deposition samples were prepared by an exchange reaction between metallic zinc vapour and the H-form of the zeolite as reported previously.[17] The zeolite was placed into a quartz u-tube under vacuum (pressure < 10^{-2} mbar) and heated to 150 °C for 1 h followed by 5 h at 550 °C in a tube furnace. A 5 °C min^{-1} ramp rate was used for all furnace program steps. A 100-fold excess of zinc (Zn/Al =100) was used for the zinc metal vapour deposition. To expose the zeolite sample to zinc vapour, the u-tube was sealed and placed in a tube furnace where it was heated to 500 °C at 5 °C min^{-1} and held for 1 h under static vacuum. Excess unreacted zinc vapour was further removed by continued heating at 500 °C for 2 h under dynamic vacuum. For methane activation, the u-tube containing the zinc modified zeolite was cooled to 250 °C in the furnace. Methane was introduced into the tube and left flowing for 15 min. The tube was sealed and after cooling, was taken into the argon glovebox. Where ^{13}C labelled methane was used, the u-tube was filled with 1 atm of $^{13}CH_4$, sealed and held at 250 °C for 15 min.

The ion exchanged sample, Zn/ZSM-5-IE, was activated based on a method by Kuroda *et al*.[35] The zeolite was heated to 600 °C for 4 h at 5 °C min^{-1} ramp rate under vacuum. This was cooled to 250 °C after which methane was introduced and left flowing for 2 h. Where ^{13}C labelled methane was used, the u-tube was filled with 1 atm of $^{13}CH_4$, sealed and held at 250 °C for 2 h.

For Zn/CH_4/ZSM-5 - 600 °C and Zn/CH_4/MOR - 600 °C samples, a standard VD was carried out. After the excess zinc vapour was removed, the sample was heated to 550 °C for 2 h and 600 °C for 4 h in an attempt to remove Zn(0). Methane activation under vapour deposition conditions and ion exchange conditions was attempted on both samples. For XAS analysis, the Zn/zeolite and Zn/CH_4/zeolite samples were transported to B18, Diamond Light Source in a sealed Schlenk tube and immediately stored in a N_2 glovebox. The samples were mixed with cellulose binder in a glovebox, pressed into pellets and placed into an airtight cell with Kapton windows shown in Figure 9 (approximately 25 mg of zeolite mixed with 15 mg of cellulose).

Figure 9: Air tight cell used for XAS analysis at B18, Diamond Light Source

XANES spectra were aligned by calibration of the first zero crossing point of the second derivative of the Zn metal foil reference spectra in each case. XAFS data processing was performed using the Athena software from the Horae package.[42] EXAFS analysis was performed by Dr Simon Beaumont, Durham Unviersity, and EXAFS data processing was performed using IFEFFIT with the Horae package (Athena and Artemis).[42] The amplitude reduction factor, S_0^2 was derived from EXAFS data analysis of the Zn foil reference spectrum (for which the co-ordination numbers of the fcc metal are known). This was then fixed in the analysis of sample spectra. The parameters corresponding to the correction to the photoelectron energy origin, co-ordination numbers of Zn^{2+}-Zn^{2+} and/or Zn-O, bond lengths, and mean-squared relative deviation of atoms around absorbing atoms were then varied during fitting, and considered as the two possible models for contributions to first shell fits (adding a contribution from Zn(m)-Zn(m) did not improve any of the fits). All fits were performed using multiple k-weight fitting. Plots of the Real R-space component of the EXAFS spectrum are shown to highlight the differences seen in the data between samples, which are less obvious from the plots of magnitude R-Space EXAFS data.

Zn/MOR and Zn/ZSM-5 were prepared by treating NH_4–ZSM–5 (12.5) or Na-MOR (7) with an aqueous solution $Zn(NO_3)_2$ based on a method reported by Kuroda *et al.*.[35] Zinc ion exchanges were carried out using 2.5 g of zeolite in a centrifuge tube in contact with 50 ml of 0.3M $Zn(NO_3)_2$ solution for 1 h with constant agitation from a mechanical tube roller. The tube was centrifuged at 4500 rpm for 5.5 min and the resulting supernatant decanted. The zeolite was then re-dispersed into the zinc nitrate solution and this process was repeated 10 times. The sample was then washed with 50 ml of deionised water 8 times and dried at 80 °C overnight. Na-ZSM-5 was prepared using the same method but using a 0.3M $NaNO_3$ solution.

Partially exchanged Zn/Na-MOR and Zn/Na-ZSM-5 were prepared by treating Na–ZSM–5 (12.5) or Na-MOR (7) with 0.3M $Zn(NO_3)_2$ solution for 1 h with constant agitation from a mechanical tube roller. The tube was centrifuged at 4500 rpm for 5.5 min and the resulting supernatant decanted. The sample was then washed with 50 ml of deionised water 3 times and dried at 80 °C overnight.

Zn/MOR, Zn/ZSM-5, Zn/Na-MOR and Zn/Na-ZSM-5 were exposed to methane under IE activation conditions. The zeolite was heated to 600 °C for 4 h under vacuum and exposed to labelled methane for 15 min after the furnace had cooled to 250 °C. Zn/Na-MOR – VD and Zn/Na-ZSM-5 – VD were prepared by dehydrating Zn/Na-MOR and Zn/Na-ZSM-5 under standard vapour deposition conditions. A vapour deposition reaction was carried out as above and the samples were exposed to labelled methane using the standard procedure. The samples were packed into a solid state NMR rotor in the glovebox. NMR experiments were typically conducted immediately after C-H activation.

6.5 Chapter 6 References

1. V. B. Kazansky and A. I. Serykh, *Phys. Chem. Chem. Phys.*, 2004, **6**, 3760-3764.
2. V. B. Kazansky, A. I. Serykh and E. A. Pidko, *J. Catal.*, 2004, **225**, 369-373.
3. M. V. Luzgin, D. Freude, J. Haase and A. G. Stepanov, *J. Phys. Chem. C*, 2015, **119**, 14255-14261.
4. A. A. Gabrienko, S. S. Arzumanov, M. V. Luzgin, A. G. Stepanov and V. N. Parmon, *J. Phys. Chem. C*, 2015, **119**, 24910-24918.
5. Y. G. Kolyagin, I. I. Ivanova and Y. A. Pirogov, *Solid State Nucl. Magn. Reson.*, 2009, **35**, 104-112.
6. A. Oda, H. Torigoe, A. Itadani, T. Ohkubo, T. Yumura, H. Kobayashi and Y. Kuroda, *J. Phys. Chem. C*, 2013, **117**, 19525-19534.
7. S. C. Albarracín-Suazo, Y. J. Pagán-Torres and M. C. Curet-Arana, *J. Phys. Chem. C*, 2019, **123**, 16164-16171.
8. A. A. Gabrienko, S. S. Arzumanov, A. V. Toktarev, I. G. Danilova, I. P. Prosvirin, V. V. Kriventsov, V. I. Zaikovskii, D. Freude and A. G. Stepanov, *ACS Catal.*, 2017, **7**, 1818-1830.
9. A. A. Gabrienko, S. S. Arzumanov, D. Freude and A. G. Stepanov, *J. Phys. Chem. C*, 2010, **114**, 12681-12688.
10. S. M. T. Almutairi, B. Mezari, P. C. M. M. Magusin, E. A. Pidko and E. J. M. Hensen, *ACS Catal.*, 2012, **2**, 71-83.
11. I. Pinilla-Herrero, E. Borfecchia, J. Holzinger, U. V. Mentzel, F. Joensen, K. A. Lomachenko, S. Bordiga, C. Lamberti, G. Berlier, U. Olsbye, S. Svelle, J. Skibsted and P. Beato, *J. Catal.*, 2018, **362**, 146-163.
12. J. A. Biscardi, G. D. Meitzner and E. Iglesia, *J. Catal.*, 1998, **179**, 192-202.
13. V. B. Kazansky, V. Y. Borovkov, A. I. Serikh, R. A. Van Santen and B. G. Anderson, *Catal. Lett.*, 2000, **66**, 39-47.
14. Y. G. Kolyagin, I. I. Ivanova, V. V. Ordomsky, A. Gedeon and Y. A. Pirogov, *J. Phys. Chem. C*, 2008, **112**, 20065-20069.
15. V. B. Kazansky, *Kinetic Catal.*, 2014, **55**, 737-747.
16. H. K. Beyer, G. Pál-Borbély and M. Keindl, *Micro. Meso. Mater.*, 1999, **31**, 333-341.
17. M. A. Shah, S. Raynes, D. C. Apperley and R. A. Taylor, *ChemPhysChem*, 2020, **21**, 673-679.
18. S. S. Arzumanov, A. A. Gabrienko, D. Freude and A. G. Stepanov, *Catal. Sci. Technol.*, 2016, **6**, 6381-6388.
19. A. Oda, T. Ohkubo, T. Yumura, H. Kobayashi and Y. Kuroda, *Dalton Trans.*, 2015, **44**, 10038-10047.
20. E. Morra, G. Berlier, E. Borfecchia, S. Bordiga, P. Beato and M. Chiesa, *J. Phys. Chem. C*, 2017, **121**, 14238-14245.
21. I. Resa, E. Carmona, E. Gutierrez-Puebla and A. Monge, *Science*, 2004, **305**, 1136-1138.
22. G. Parkin, *Science*, 2004, **305**, 1117-1118.
23. T. Li, S. Schulz and P. W. Roesky, *Chem. Soc. Rev.*, 2012, **41**, 3759-3771.
24. A. Schnepf and H.-J. Himmel, *Angew. Chem. Int. Ed.*, 2005, **44**, 3006-3008.
25. A. Grirrane, I. Resa, A. Rodriguez, E. Carmona, E. Alvarez, E. Gutierrez-Puebla, A. Monge, A. Galindo, D. del Río and R. A. Andersen, *J. Am. Chem. Soc.*, 2007, **129**, 693-703.
26. E. Carmona and A. Galindo, *Angew. Chem. Int. Ed.*, 2008, **47**, 6526-6536.
27. C.-S. Cao, Y. Shi, H. Xu and B. Zhao, *Coord. Chem. Rev.*, 2018, **365**, 122-144.
28. L. Benco, *J. Phys. Chem. C*, 2016, **120**, 6031-6038.
29. M. Juneau, R. Liu, Y. Peng, A. Malge, Z. Ma and M. D. Porosoff, *Chem Cat Chem*, 2020.
30. C. Hennig, F. Thiel, K. H. Hallmeiér, R. Szargan, A. Hagen and F. Roessner, *Spectro. Chim. Acta A*, 1993, **49**, 1495-1497.
31. K. Wang, M. Dong, X. Niu, J. Li, Z. Qin, W. Fan and J. Wang, *Catal. Sci. Technol.*, 2018, **8**, 5646-5656.

32. J. Penzien, A. Abraham, J. A. van Bokhoven, A. Jentys, T. E. Müller, C. Sievers and J. A. Lercher, *J. Phys. Chem. B*, 2004, **108**, 4116-4126.
33. C. Hennig, K.-H. Hallmeier, G. Zahn, F. Tschwatschal and H. Hennig, *Inorg. Chem.*, 1999, **38**, 38-43.
34. J. Heemsoth, E. Tegeler, F. Roessner and A. Hagen, *Micro. Meso. Mater.*, 2001, **46**, 185-190.
35. A. Oda, H. Torigoe, A. Itadani, T. Ohkubo, T. Yumura, H. Kobayashi and Y. Kuroda, *J. Phys. Chem. C*, 2014, **118**, 15234-15241.
36. A. Oda, T. Ohkubo, T. Yumura, H. Kobayashi and Y. Kuroda, *Phys. Chem. Chem. Phys.*, 2017, **19**, 25105-25114.
37. O. Akira, T. Hiroe, I. Atsushi, O. Takahiro, Y. Takashi, K. Hisayoshi and K. Yasushige, *Angew. Chem., Int. Ed.*, 2012, **51**, 7719-7723.
38. A. Velazquez, I. Fernández, G. Frenking and G. Merino, *Organometal.*, 2007, **26**, 4731-4736.
39. P. Cui, H.-S. Hu, B. Zhao, J. T. Miller, P. Cheng and J. Li, *Nat. Commun.*, 2015, **6**, 6331.
40. K. Freitag, C. Gemel, P. Jerabek, I. M. Oppel, R. W. Seidel, G. Frenking, H. Banh, K. Dilchert and R. A. Fischer, *Angew. Chem., Int. Ed.*, 2015, **54**, 4370-4374.
41. J. Hicks, E. J. Underhill, C. E. Kefalidis, L. Maron and C. Jones, *Angew. Chem., Int. Ed.*, 2015, **54**, 10000-10004.
42. B. Ravela and M. Newvilleb, *J. Synchro. Rad.*, 2005, **12**, 537-541.

Chapter 7: Methane Dehydroaromatisation (MDA) over Zinc-Modified Zeolites

Chapter 7: Methane Dehydroaromatisation (MDA) over Zinc-Modified Zeolites

7.1 Introduction

Direct conversion of methane into aromatic products combines two great challenges: activation of one of the strongest C-H bonds of all hydrocarbons and selectively forming aromatic products. Due to the thermodynamic restraints of the MDA reaction, at the temperatures where benzene yields are significant (7.8 – 21.5 mol%), significant coke formation resulting in fast catalyst deactivation occurs.[1-4] Mo (impregnated zeolite) catalysts, in particular Mo/ZSM-5, remain the most investigated for MDA reactions as they have shown the best performance so far.[5, 6] Different metals[7, 8] and other supports[9] have not been as successful in catalysing the MDA reaction.

The mechanism for MDA reactions over Mo/zeolites remains highly debated though a two-step mechanism, which involves a bifunctional Mo/H-ZSM-5 catalyst has had some consensus.[6, 10-14] This involves the activation of methane over Mo sties to form C_2 intermediates which then form benzene and other aromatics over BASs of the zeolite. However, the Mo active site remains hard to characterise and the role of carbonaceous species in the reaction mechanism have not yet been fully established.[5, 15-17]

Initial work by Xu *et al.* in 1993 using zinc-modified zeolites for MDA reactions demonstrated that loading zinc onto the zeolite enhanced activity for MDA compared to the parent zeolite.[18] They achieved 3% methane conversion over Zn-impregnated H-ZSM-5 (12.5) with 100% benzene selectivity at 700 °C, 2 bar pressure and a gas hourly space velocity of (GHSV) 1440 ml g^{-1} h^{-1}. However, methane conversion over Zn/ZSM-5 is lower than Mo/H-ZSM-5, which is able to achieve 10-12% methane conversion with 60-70% benzene selectivity at 700 °C , nevertheless the zinc system still shows some promise.[5]

As for Mo/zeolite, different mechanisms for MDA over zinc catalysts have been reported. In 1993, Xu suggested the mechanism of MDA over Zn/H-ZSM-5 involves Zn^{2+} cations acting as a hydride acceptor forming [Zn^{II}-H].[18] They proposed these results in the formation of a carbenium ion which can react further to form benzene (Equation 1). A similar mechanism is suggested for the conversion of isobutene into aromatics over ZnO/H-ZSM-5.[19]

$$CH_4 + Zn^{2+} \rightarrow CH_3^+ + [Zn - H]^+$$

Equation 1: Carbenium ion mechanism for methane activation over Zn catalysts.

In 2008, Stepanov *et al.* also reported studies into the MDA mechanism with $^{13}CH_4$ over Zn-modified Beta (ZnO/H-BEA), a high silica zeolite, monitored with ^{13}C NMR spectroscopy and GC-MS.[20] They report the transfer of ^{13}C-labelled atoms from methane into aromatic products during the co-conversion of methane and propane over Zn-modified Beta at 550 °C. Enriched products include ^{13}C in both methyl groups and aromatic rings. The mechanism proposed involves the formation of a $[Zn\text{-}H]^-$ and $[ZnO\text{-}^{13}CH_3]^+$, shown in Scheme 1 **Error! Reference source not found.**. This is supported by Cheung *et al.* who confirmed the presence of two zinc species during MDA using Auger electron spectroscopy.[21] Two Auger signals were observed in the Zn LMM spectrum at 985.0 eV and 988.5 eV and the authors suggest that the signal at lower energy is likely due to the formation of $[ZnO\text{-}CH_3]^+$ species, whilst the higher energy signal could be due to the ZnO interaction with hydride ions.

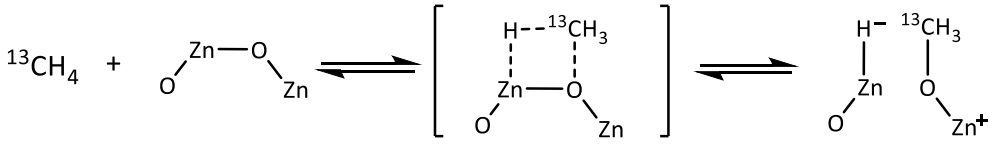

Scheme 1: First step in the mechanism of ^{13}C transfer from $^{13}CH_4$ during methane and propane co-conversion over Zn/H-BEA

However, since these early studies on methane activation over Zn/zeolites, numerous stoichiometric studies, analysed by NMR spectroscopy and DRIFTS, have concluded that methane activation over isolated zinc cations in ZSM-5 (Zn^{2+}/ZSM-5) occurs by heterolytic cleavage of the C-H bond in methane, leading to the formation of a $[Zn^{II}\text{-}CH_3]$ species and a new BAS.[22-26] This zinc methyl fragment is able to react with small molecules such as O_2, CO, CO_2 and H_2O to form oxygenated products.[24, 27]

As well as no consensus on the mechanism for MDA over Zn/zeolites, the active Zn species is also unclear. As for dMtM, numerous zinc species (Zn^{2+} ions, Zn dimers, Zn^+ ions, *etc.*) could be present and these depend on the method of zinc introduction.[28] Shekhawat *et al.* determined that anchored $[Zn(OH)]^+$ sites acting as strong Lewis acids were more reactive and stable than ZnO particles for MDA on a Zn-impregnated catalyst.[29] Through catalyst characterisation, they determined two Zn oxide species were present in ZSM-5: anchored, stable, reactive $[Zn(OH)]^+$ sites bound to BAS and unreactive ZnO, which were easily reduced to Zn^0 and subsequently lost due to the high volatility of Zn^0, located on external support surfaces.

The loading of this unreactive ZnO increased with higher Zn loading. Volter *et al.* suggest that some of this unreactive ZnO can be reduced to Zn^{2+} under reaction conditions and can form new active sites for the MDA reaction.[30] Conversely, Veser *et al.* suggest that metallic Zn is the active species for benzene formation as they observed strong initial CO_2 formation from ZnO/H-ZSM-5, implying that ZnO is reduced in the induction period before the catalyst shows aromatisation activity.[31] By comparing Zn/H-ZSM-5 where the zinc has been introduce by three different methods (wet ion exchange, wet impregnation and ZnO nanoparticles), Veser suggests that Zn^0 nanoclusters inside the zeolite micropores are the most active but are irreversibly lost from the catalyst under the high-temperature MDA reaction conditions. The authors find that Zn^{2+} is strongly anchored at ion exchange sites of the zeolite hence, is more stable, but shows little aromatisation activity.

Cheung *et al.* explore the reactivity of Zn-based/H-ZSM-5 catalyst from MDA reactions under atmospheric pressure and supersonic jet expansion.[21] Their results show that at atmospheric pressure, the activity of Zn/ZSM-5 is rather low (5.5% conversion with low benzene selectivity) compared with mixed metal catalysts (Zn/Ga, Ga/Mo or Zn/Mo). The addition of Zn or Ga however, does enhance the activity of Mo/H-ZSM-5 by increasing catalyst stability. Under supersonic jet expansion, the catalytic activity of Zn/H-ZSM-5 is found to be the highest as the dehydroaromatisation reaction of methane occurred more favourably over ZnO nanoparticles.

Whilst zinc catalysts have shown some promise for the MDA reaction, a challenge that should be highlighted is the difficulty to stabilise the catalyst due to the reducing reaction conditions and the high vapour pressure of zinc.[20, 30, 31] This often results in loss of the zinc active sites potentially hindering industrially applications. Veser suggests that alloying could perhaps offer stabilisation of the zinc and initial studies by Zheng *et al.* suggest that the addition of a second metal (Pt, Cu, Co, Fe) increase benzene selectivity and lower coke formation.[31-33]

Whilst direct activation of methane provides thermodynamic challenges, many groups have turned to the addition of co-reactants to decrease reaction temperatures and increase product yields. However, the addition of co-reactants can decrease benzene selectivity, for example, the selectivity of aromatics changes with the methane to propane molar ratio of the gas feed, (31.5% benzene selectivity decreases to 28% selectivity upon a higher ratio of propane to methane).[32] The addition of ethane,[34] propane,[32] n-pentane,[35] n-hexane[36] or light gasoline (C_5 + C_6)[37] to the methane feed over a Zn/H-ZSM-11 catalyst (a 2D zeolite with 10 MR pore structure) resulted in high aromatic yields (10-40 mol%) with over 30% methane conversion at temperatures around 500 °C, edging closer to an economically feasible reaction.

In this chapter, zinc modified zeolites prepared through impregnation, ion exchange and zinc vapour deposition, and were subsequently tested for methane aromatisation. MDA reactions were carried out in a quartz u-tube reactor at 800 °C under atmospheric pressure and a GHSV of 6000 ml g^{-1} h^{-1}. Liquid products were trapped in a dry-ice/acetone bath (−78 °C) and quantified using solution state NMR spectroscopy with an internal standard of TMS. Characterisation of the zinc catalysts and the carbonaceous deposits formed was carried out using pXRD, SEM, TPO-MS and UV-Raman spectroscopy. As established in Chapter 4, the zeolite framework can impact the number of active zinc sites present in the zeolite, hence, the effect of zeolite framework on the MDA reaction was explored. The XAS analysis in Chapter 6 indicated that different zinc species were present depending on the method of zinc introduction. The activity of the different species, Zn^{2+} in IE samples, ZnO in impregnated samples and the [Zn^{I}-Zn^{I}] dimer in zinc vapour deposition samples, towards the MDA reaction was investigated.

7.2 Results and Discussion

In order to investigate MDA reactions over zinc-modified catalysts, a quartz u-tube, shown in Figure 1, was designed with capability of air-sensitive catalyst packing. The u-tube could be taken into the glovebox where air-sensitive catalysts could be packed and the tube sealed at both ends. After packing the catalyst, the u-tube was placed in an upright clamshell furnace and the catalyst bed was positioned to be at the centre of the isothermal zone of the furnace. Liquid products were condensed using a −78 °C acetone/dry ice bath and measured against a TMS internal standard in acetone-d_6. Initially, reaction conditions similar to that of Shekhawat *et al.* were chosen in order to test the materials for the MDA reaction: 200 mg of catalyst, 700 °C, atmospheric pressure and GHSV of 6000 ml g^{-1} h^{-1}.[29]

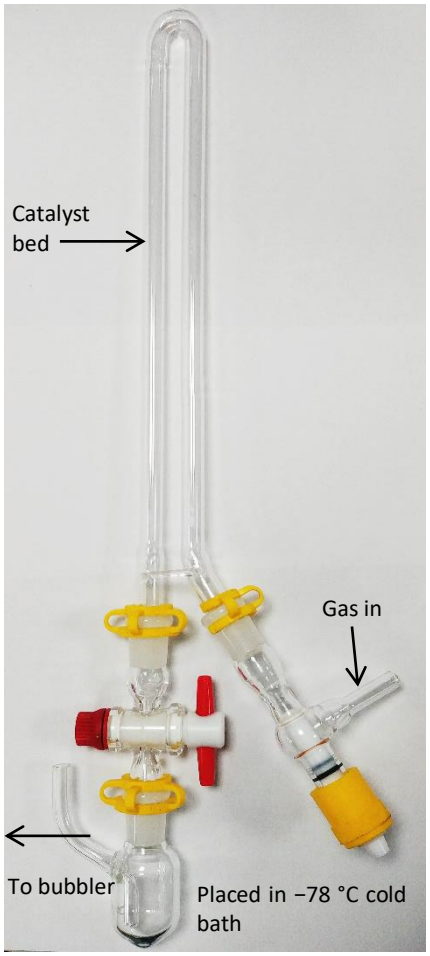

Figure 1: Quartz u-tube designed for MDA reactions with capability of air-sensitive catalyst packing. The catalyst bed was positioned to be in centre of the isothermal zone of an upright clamshell furnace. The condenser was placed in −78 °C cold bath to trap any liquid products.

Research into MDA catalysts has focussed mainly on ZSM-5 as this has shown great promise when using Mo,[5, 6, 10-14] hence, this was the first zeolite framework that was investigated. The parent zeolite, NH_4-ZSM-5 (12.5) was calcined and tested for MDA activity at 700 °C, atmospheric pressure and GHSV of 6000 ml g^{-1} h^{-1}, but no liquid products were observed. Zn(IMP)/ZSM-5 prepared by impregnation (3 wt% Zn) was subsequently tested under these reaction conditions, however, no liquid products were observed once again. At equilibrium, benzene formation is only significant at very high temperatures and solid carbon (C_s) is the favoured product. Consequently, the reaction temperature was increased to 800 °C and benzene was observed for the Zn(IMP)/ZSM-5 catalyst, established by a signal at 7.4 ppm[38] in the ^{1}H NMR spectrum shown in Figure 2. The parent zeolite H-ZSM-5 (12.5) was retested at 800 °C and once again, no liquid products were observed, highlighting that the presence of Zn was crucial in the catalysis of methane to benzene.

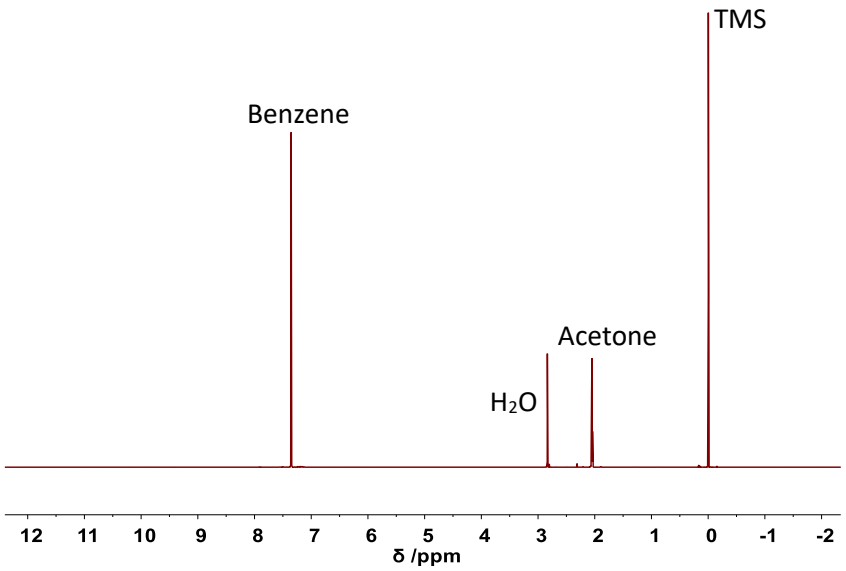

Figure 2: ^{1}H NMR spectrum of MDA reaction over Zn(IMP)/ZSM-5 catalyst showing formation of benzene at 800 °C. (^{1}H – 400 MHz)

Once it was established that Zn(IMP)/ZSM-5 was able to form benzene at 800 °C, the effect of different zinc species on the MDA reaction was investigated. It has been established in Chapter 6 through XAS analysis that zinc introduced to ZSM-5 by ion exchange predominantly contains Zn^{2+} cations whilst zinc introduced by CVD contains both Zn^{2+} and [Zn^{I}-Zn^{I}] dimer species.[39, 40] All three methods of zinc introduction were compared and the results are presented in Table 1, where the average result from two MDA reactions over each catalyst is shown. Additionally, after the introduction of zinc, the Zn(IE)/zeolites and Zn(IMP)/zeolites are calcined in air at 550 °C in a muffle furnace to remove any organic compounds, this results in the formation of ZnO species. Hence, the effect of inert calcination post impregnation and ion exchange on the MDA reaction was also studied and the samples Zn(IMP)/ZSM-5-inert and Zn(IE)/ZSM-5-inert were calcined at 550 °C under vacuum. For the Zn(VD)/ZSM-5, the reaction was carried out inertly and the MDA reactor was packed in the glovebox. To probe the effect of air on the active sites produced in the VD reaction and their subsequent reactivity, the sample was exposed to air before being packed into the reactor (sample Zn(VD)/ZSM-5-air).

It is clear that Zn(VD)/ZSM-5 is the most active for benzene formation after 4 h of exposure to CH_4 at 800 °C. Whilst having the highest activity, the Zn(VD)/ZSM-5 catalyst also produces similar levels of coke (1.4% C) compared with the Zn(IMP)/ZSM-5 or Zn(IE)/ZSM-5 catalysts (1.3% or 0.9%, respectively). The results also show that the active sites within the Zn(VD)/ZSM-5 sample are air-sensitive as once exposed to the atmosphere, the activity of the catalyst drastically decreases. This is similar to stoichiometric methane activation studies carried

out on Zn(VD)/ZSM-5 where no [Zn^{II}-CH_3] species were observed by ^{13}C NMR spectroscopy after zinc vapour deposition samples were exposed to the atmosphere. This indicates that the [Zn^{I}-Zn^{I}] dimer is highly air-sensitive and that this species is most likely to be active for the MDA reaction in the VD samples.

Table 1: Analysis of MDA reactions at 800 °C, 4 h reaction time, using Zn/ZSM-5 catalysts with Si/Al (12.5), where zinc was introduced by three different methods: impreg, IE and VD. Both inert (under vacuum) and non-inert (in air) calcinations were carried out on all methods. The values given in the table are an average of two seperarate MDA reactions carried out on each sample.

Sample	Zn/Al initial	Inert Calcination	Average Mass Benzene / mg	Average Mass Benzene normalised to initial Zn content / mg	Zn/Al final	Average %C
Zn(IMP)/ZSM-5	0.37	N	1.61	0.23	0.28	1.3
Zn(IMP)/ZSM-5-inert	0.37	Y	-	-	0.28	0.6
Zn(IE)/ZSM-5	0.45	N	1.19	0.54	0.34	0.9
Zn(IE)/ZSM-5-inert	0.45	Y	-	-	0.34	0.1
Zn(VD)/ZSM-5	0.65	Y	4.04	2.63	0.32	1.4
Zn(VD)/ZSM-5-air	0.65	Exposed to air post VD	0.04	0.03	0.26	0.01

The Zn(IMP)/ZSM-5 and Zn(IE)/ZSM-5 catalysts produce similar amounts of benzene as well as coking to similar degrees. Interestingly, the catalysts that were calcined under vacuum produced no detectable liquid products. This supports that a zinc oxide type species is likely to be the active zinc species in the Zn(IMP)/ZSM-5 and Zn(IE)/ZSM-5 catalysts. This is in line with conclusions from Shekhawat *et al.* who suggested that $[Zn(OH)]^{+}$ was likely the active site for these catalysts[29] as well as results from Veser *et al.* which suggest that ZnO, which is reduced under MDA reaction conditions, is the active species.[31]

An issue with MDA reactions, as has been established in the literature for Mo,[41] is the leaching of the metal active sites. This is due to the reducing conditions of the reaction and the elevated temperatures required. In the case of Mo, low valent, volatile Mo^{II} carbide species are formed under the reaction conditions.[5, 10, 41-44] In the case of zinc, volatile Zn^{0} species are formed under high temperature reducing atmosphere[20, 30, 31] and all of the Zn/ZSM-5 catalysts tested for the MDA reaction at 800 °C showed some level of zinc leaching as the Zn/Al ratios were lower

post reaction for all the catalysts. This was particularly significant for the Zn(VD)/ZSM-5 catalysts as the Zn/Al ratio halved over the course of the 4 h reaction. This is additionally evidenced by the pXRD patterns (shown in Figure 3) where the extra reflections present at 35.6° and 38.2° 2θ are highlighted. The reflections do not correlate with those present in the pXRD patterns of zinc metal or ZnO shown in Figure 3 nor are they reflections corresponding to $Zn(Al_2O_4)$ which has peaks at 31.2° and 37.0°.[45] Therefore it is unclear exactly what zinc species these reflections correspond to, however, we hypothesise that perhaps the reflections correspond to Zn/ZnO clusters formed under the reducing conditions of the MDA reaction.[46] However, despite the zinc leaching, all Zn/ZSM-5 catalysts retained their framework crystallinity after a reaction time of 4 h at 800 °C (Figure 3).

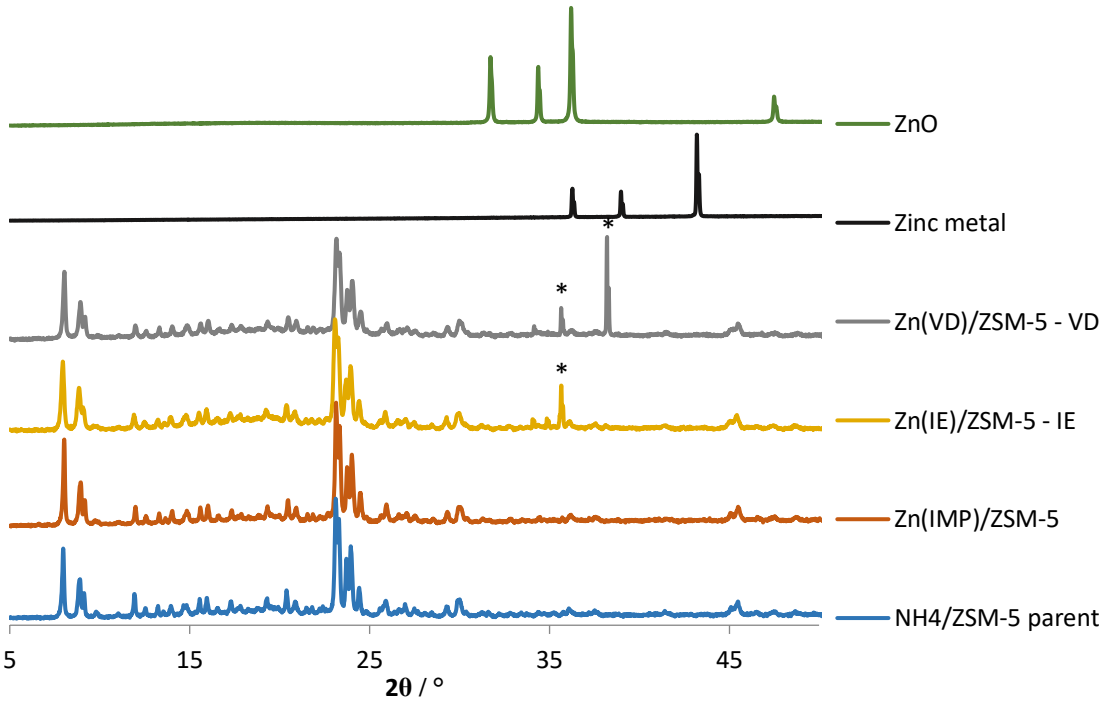

Figure 3: pXRD patterns for Zn/ZSM-5 catalysts post MDA reaction. All catalysts retained crystallinity under the harsh MDA reaction conditions. * Denotes extra reflections due to zinc leaching.

SEM images of the spent catalysts were taken to investigate if the high temperature, 800 °C treatment caused any changes in zeolite morphology or if large zinc particles could be observed after the MDA reaction. Figure 4 demonstrates that for all the catalysts, no change in morphology was observed. Whilst the high temperatures caused zinc leaching, demonstrated by the Zn/Al ratios determined elemental analysis, no obvious zinc clusters were observed using

SEM. Analysis by ^{27}Al NMR spectroscopy indicated that little extraframework Al was observed post the MDA reaction (Appendix 6) supporting that no zeolite framework damage occurred. This is very promising as one of the downfalls of Mo catalysts for this reaction is the formation of $Al_2(MoO_4)_3$ which results in the collapse of the zeolite framework.[41]

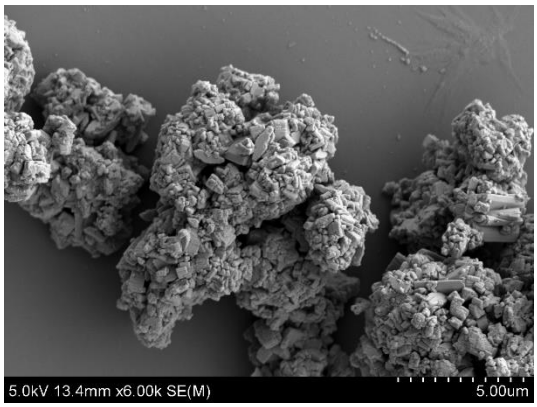

NH4-ZSM-5 (12.5) parent

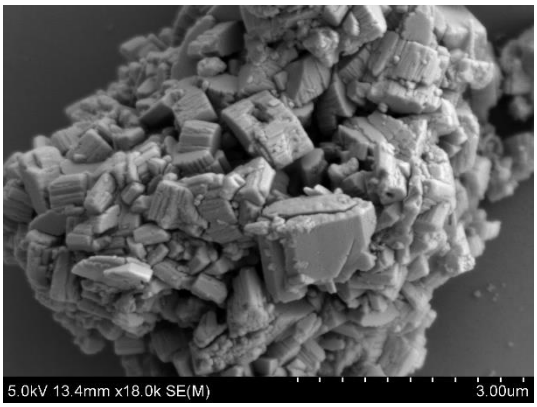

Zn(VD)/ZSM-5

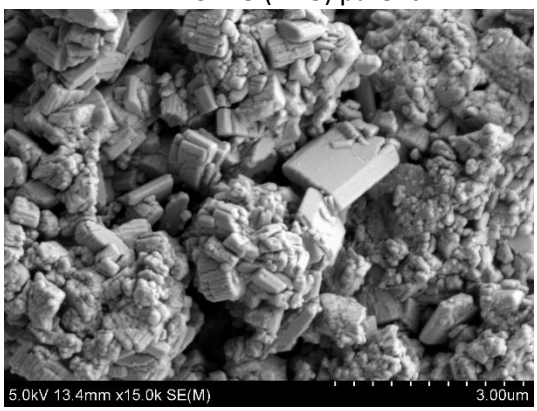

Zn(IE)/ZSM-5 before reaction

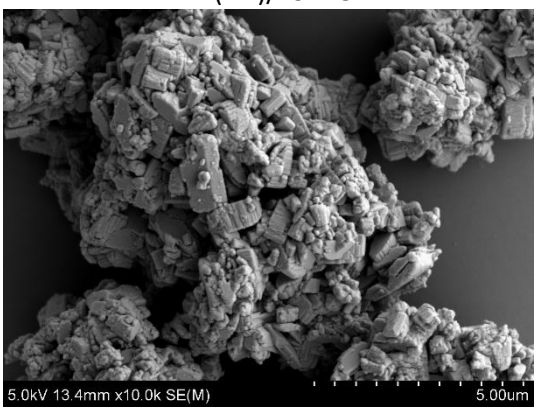

Zn(IE)/ZSM-5 post reaction

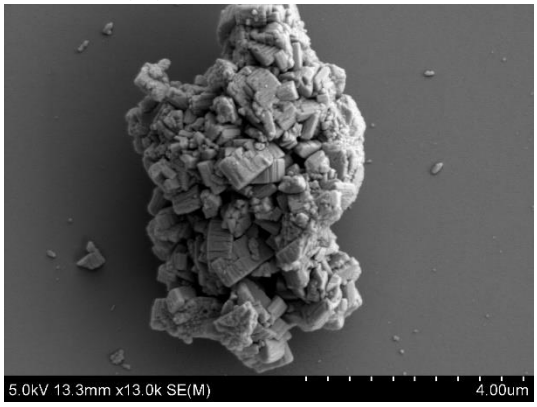

Zn(IMP)/ZSM-5 before reaction

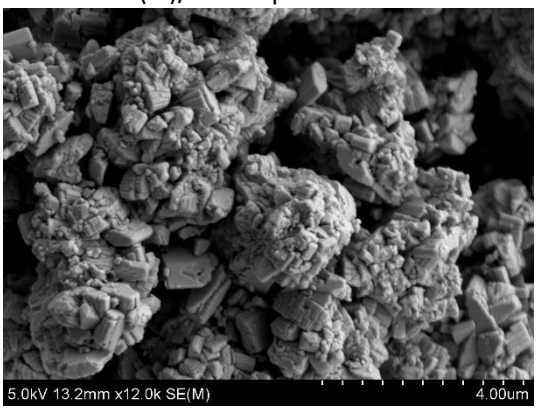

Zn(IMP)/ZSM-5 after reaction

Figure 4: SEM images for Zn/ZSM-5 catalysts before and after MDA reaction. The materials retain their morphology and no obvious zinc clusters were observed.

Three other zeolite frameworks (Beta (12.5), MOR (10) and FER (10)) were loaded with zinc and tested for the MDA reaction to explore the effect of zeolite framework on the MDA reaction. We have recently reported that Zn(VD)/ZSM-5, Zn(VD)/MOR and Zn/(VD)FER, have been shown to be active for stoichiometric methane activation.[47] Stepanov *et al.* have demonstrated methane activation over Zn(VD)/Beta (21),[48] but we were unable to observe stoichiometric methane activation over Zn(VD)/Beta (12.5). This could be due to the Al distribution of the material, which may be unable to support the [Zn^{I}-Zn^{I}] dimer active site, as a result of the synthesis method used to make the parent NH_4-Beta.

The Beta (12.5), MOR (10) and FER (10) frameworks were tested for the MDA reaction at 800 °C for 4 h and the results are compared to ZSM-5 (12.5) in Table 2. pXRD patterns (Appendix 6) confirm that all frameworks retained crystallinity during the MDA reaction but only zinc exchanged Beta was able to produce detectable liquid products. The mass of benzene produced by Zn(IE)/Beta and Zn(IMP)/Beta (0.56 and 0.57 mg respectively) is similar to Zn(IE)/ZSM-5 and Zn(IMP)/ZSM-5 (0.54 and 0.23 mg respectively) after a 4 h MDA reaction. However, the level of carbonaceous deposits formed in all Zn/Beta catalysts is substantially higher than for any other framework tested for the MDA reaction (Figure 6). Beta is a 3D zeolite consisting of 12 MR channels (6.6 x 6.7 Å and 5.6 x 5.6 Å), larger than the 10 MR channels of ZSM-5 (5.1 x 5.5 Å and 5.3 x 5.6 Å). The larger channels of Beta seem to promote the formation of significantly more carbonaceous deposits during the MDA reaction. Figure 5 highlights the maximum free sphere diameter of zeolites Beta (BEA) and ZSM-5 (MFI) calculated by Friedrichs *et al*.[49] The larger maximum sphere diameter for beta could partially explain why the high levels of coking are observed compared with ZSM-5 (20.3% compared with 1.4%).

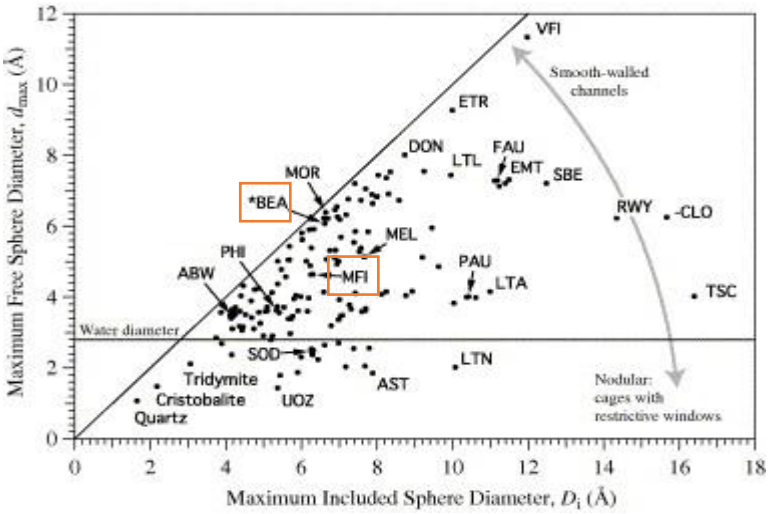

Figure 5: Plot comparing the maximum free sphere diameter against the maximum included sphere diameter.[49]

Adapted with permission from Ref 49. Copyright Elsevier 2006.

Interestingly, Zn(VD)/Beta does not perform as well as Zn(VD)/ZSM-5 (0.25 mg of benzene produced compared with 2.63 mg, respectively), and this catalyst produces the highest level of carbonaceous deposits. As mentioned above, Zn(VD)/Beta was unable to perform stoichiometric methane activation and this could link to the poor performance of Zn(VD)/Beta for the MDA reaction. If the [Zn^{I}-Zn^{I}] dimer, which we believe is the active site for stoichiometric methane activation on zinc vapour deposition samples, is also active for the MDA reaction, the high activity of Zn(VD)/ZSM-5 can be explained. We hypothesise that Zn(VD)/Beta is unable to support the dimer, hence, the catalyst shows poorer performance for the MDA reaction.

Unfortunately, Zn/MOR or Zn/FER catalysts were unable to produce detectable liquid products under these MDA conditions, although both frameworks showed catalyst coking and loss of zinc. Kong *et al.* have found that for other catalytic processes (toluene disproportionation, n-heptane cracking and benzene alkylation), the coking rate over H-Beta is substantially higher than that of H-MOR, but the deactivation rate of H-Beta is substantially lower.[50] This is because the 1D channel system of MOR is easily blocked and, in a similar manner, we believe that rapid channel blocking is the likely cause for lack of detectable levels of benzene detection formation in the MDA reaction for Zn/MOR. Although FER is a 2D catalyst with a 10 MR channel (4.2 x 5.4 Å), this channel is smaller than that of ZSM-5 and considering that benzene has a kinetic diameter of 5.85 Å, it is unlikely to be able to form in FER.[51]

Overall, Zn(VD)/ZSM-5 produced the highest mass of benzene with low formation of carbonaceous deposits and high catalyst stability. However, the methane to benzene conversion was still significantly lower than one percent[1] which is poorer conversion than reported in the literature. Cheung *et al.* reported 5.5% methane conversion over Zn(IMP)/H-ZSM-5 using 0.5 g of catalyst at atmospheric pressure with a GHSV of 1680 ml g^{-1} h^{-1}.[21] Veser *et al.* report lower conversions of 1.2% over Zn(IMP)/H-ZSM-5 at atmospheric pressure with a GHSV of 3750 ml g^{-1} h^{-1} [31] and both groups are able to produce benzene at 700 °C. Due to the vapour deposition process, our mass of catalyst was limited to 200 mg which partially explains the low methane conversion values. Furthermore, both groups had significantly lower GHSV compared with GHSV of 6000 ml g^{-1} $h^{-}1$ used in our reactor, leading to significantly higher residence time over the zinc catalysts, likely impacting the methane conversion observed. Both the mass of catalyst and GHSV could also explain why we did not observe benzene formation at 700 °C. Changing the

[1] Calculated from total moles of benzene produced compared with total moles of CH_4 flowed throughout 4 h reaction. For Zn(VD)/ZSM-5 the methane to benzene conversion was found to be: $\frac{5.2 \times 10^{-5}\ mol\ of\ benzene}{0.21\ mol\ of\ CH_4} \times 100 = 0.02\%$ over a 4 h reaction period.

GHSV was not yet attempted on our reactor, but could provide interesting future results for the MDA reaction, in particular over Zn(VD)/ZSM-5.

Table 2: Analysis of MDA reactions at 800 °C, 4 h reaction time, using Zn/zeolite catalysts with four different frameworks: ZSM/-5, Beta, FER and MOR, where zinc was introduced by three different methods: impreg, IE and VD.

	Sample	Si/Al	Zn/Al initial	Average Mass Benzene / mg	Average Mass Benzene normalised to initial Zn content / mg	Zn/Al final	%C
1	Zn(IMP)/ZSM-5	12.5	0.37	1.61	0.23	0.28	1.3
2	Zn(IE)/ZSM-5	12.5	0.45	1.19	0.54	0.34	0.9
3	Zn(VD)/ZSM-5	12.5	0.65	4.04	2.63	0.32	1.4
4	Zn(VD)/ZSM-5-air	12.5	0.65	0.04	0.03		0.01
5	Zn(IMP)/Beta	12.5	0.46	1.24	0.57	0.17	11.2
6	Zn(IE)/Beta	12.5	0.45	1.24	0.56	0.14	12.7
7	Zn(VD)/Beta	12.5	0.63	0.40	0.25	0.08	20.3
8	Zn(IMP)/MOR	10	0.36	-	-	0.25	4.5
9	Zn(IE)/MOR	10	0.32	-	-	0.28	4.1
10	Zn(VD)/MOR	10	0.70	-	-	0.25	4.6
11	Zn(IMP)/FER[2]	10	0.43	-	-	0.42	0.4
12	Zn(VD)/FER	10	0.77	-	-	0.36	1.4

[2] Zn introduced into FER by IE was not used for the MDA reaction because only low levels of Zn were able to be exchanged using this method (Zn/Al < 0.1)

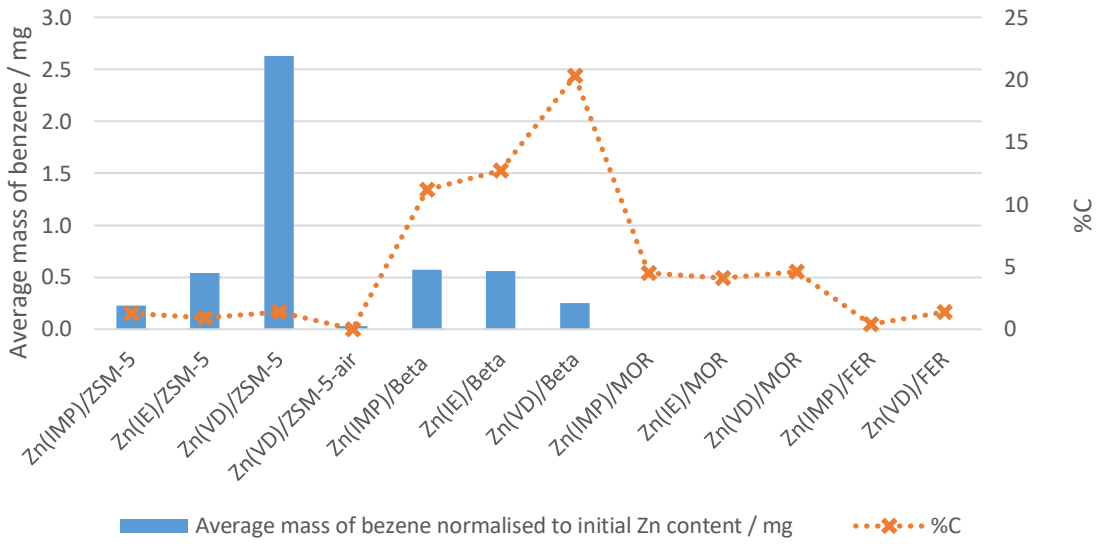

Figure 6: Average mass of benzene normalised to initial Zn content produced for each catalyst alongside %C for each Zn/zeolite catalyst. Conditions: 800 °C, atmospheric pressure, 200 mg of catalyst, 4 h reaction time and 20 ml min^{-1} CH_4.

In order to investigate catalyst lifetime, Zn(IMP)/ZSM-5 and Zn(VD)/ZSM-5 catalysts were tested for 10 h at 800 °C. The Zn(VD)/ZSM-5-10h catalyst performed substantially better than the Zn(IMP)/ZSM-5-10h catalyst producing five times more benzene, whilst producing similar levels of carbonaceous deposits (Table 3). It should be noted that the level of coke produced after the 10 h reaction by both catalysts (4%) is low compared with Mo-catalysts (16.5% over Mo/H-ZSM-5).[6, 52-54] However, methane to benzene conversion, calculated to be 0.1% for Zn(VD)/ZSM-5-10h, is still significantly lower than conversions reported for Mo/H-ZSM-5 (10 - 12%).[5, 6]

Table 3: Analysis of MDA reactions at 800 °C, 10 h reaction time, using Zn/ZSM-5 – impreg and Zn/ZSM-5 – VD. Table shows average results from two MDA reactions carried out on each catalyst.

Sample	Si/Al	Zn/Al initial	Average Mass Benzene / mg	Average Mass Benzene normalised to initial Zn content / mg	Zn/Al final	%C
Zn(IMP)/ZSM-5–10h	12.5	0.37	3.31	1.22	0.16	3.57
Zn(VD)/ZSM-5–10h	12.5	0.65	10.42	6.77	0.08	3.75

However, the Zn/Al ratio after the MDA reaction was run for 10 h indicated that both catalysts had lost a substantial amount of zinc, which is problematic for future applications. Furthermore, pXRD analysis (Figure 7) demonstrated that both catalysts lost crystallinity and reflections corresponding to a Zn/ZnO type species were observed at 34.1°, 35.6° and 38.2° 2θ. The reflections at 35.6° and 38.2° 2θ were observed for Zn(VD)/ZSM-5 after the MDA reaction run for 4 h. The reflection at 34.1° can be assigned to a ZnO type species as a similar reflection (34.3°) is observed in the pXRD pattern of ZnO shown in Figure 7. The other reflections were assigned to a Zn/ZnO-type species as above.[46]

This destruction of the zeolite framework was also supported by the ^{27}Al NMR spectra, shown in Figure 8, where significant extraframework Al was observed (signal at 0 ppm) after the 10 h reaction. The signal/noise ratio decreased drastically when compared with the parent zeolite indicating Al had also likely been lost from the catalysts. Therefore, whilst promising benzene yields were obtained with low zeolite coking, the collapse of the catalyst after 10 h indicates that until the catalyst can be stabilised under these reaction conditions, Zn(VD)/ZSM-5 is unlikely to be viable for industrial MDA reactions. The stability of the zinc catalyst has been questioned in the literature and suggestions such as alloying with a second metal to offer additional stabilisation of the zinc species have been made. [20, 30-33]

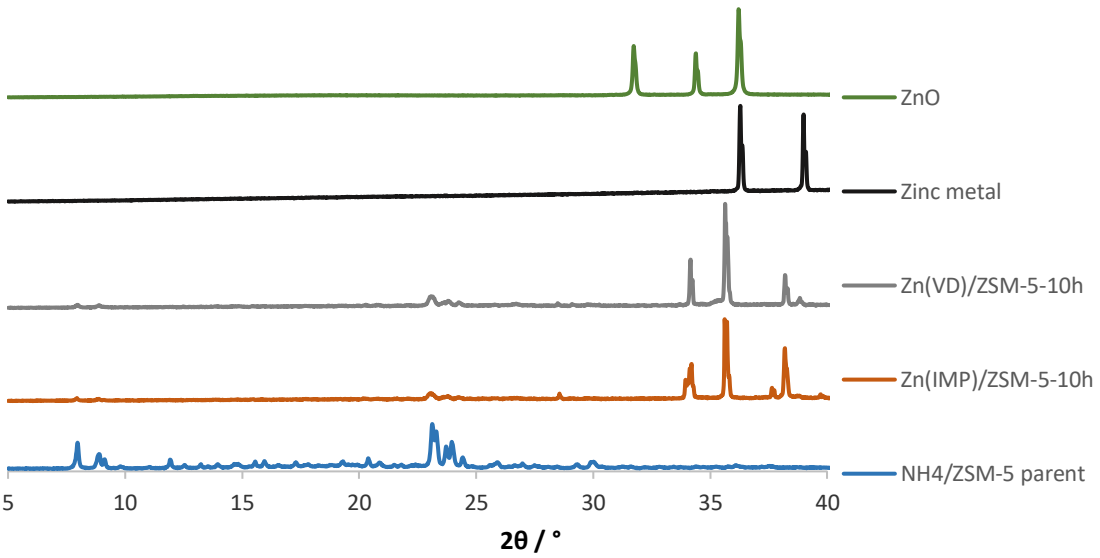

Figure 7: pXRD patterns for Zn(VD)/ZSM-5-10h and Zn(IMP)/ZSM-5-10h post MDA reaction at 800 °C for 10h. Clear loss in crystallinity is observed alongside the formation of Zn/ZnO type species.

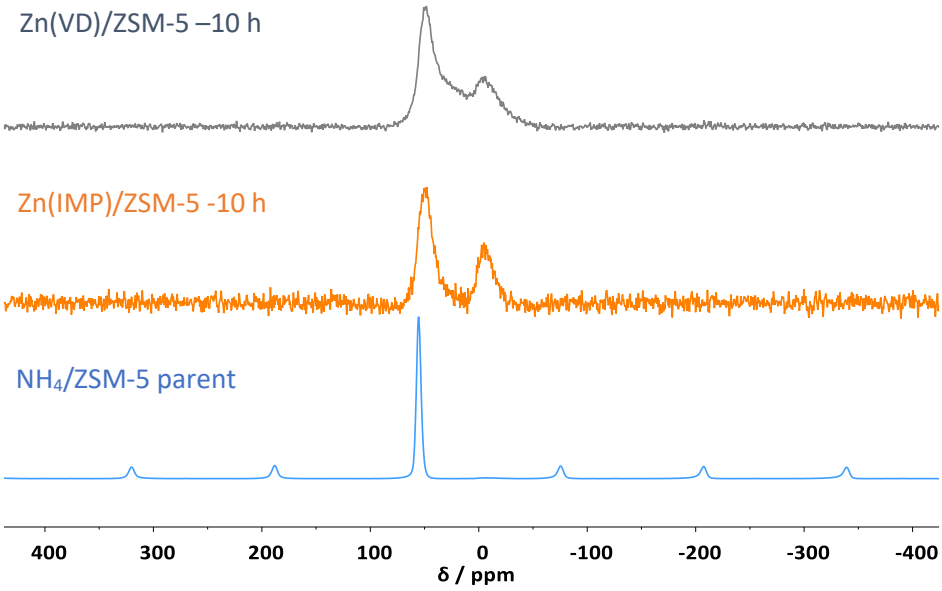

Figure 8: ^{27}Al NMR spectra for Zn(VD)/ZSM-5-10h and Zn(IMP)/ZSM-5-10h post 10 h MDA reaction compared with parent zeolite. Extraframework Al (signal at 0 ppm) alongside a decrease in signal/noise is observed after the reaction. (^{271}H – 104.20 MHz, 14 kHz spin rate)

7.2.1 Analysis of carbonaceous deposits in Zn/ZSM-5 catalyst

The greatest challenge for Mo/ZSM-5 as the catalyst for MDA reactions, is the limited catalyst lifetime due to coke deposition which results in pore blockage.[2, 3, 6, 55, 56] For this particular catalyst, three types of coke have been observed and catalyst deactivation is likely caused by the spread of pre-graphitic type carbon.[6] Numerous techniques have been used in an attempt to understand the deactivation of MDA catalysts ranging from XPS[7, 57] to UV-Raman[58, 59] to TPO-MS.[60, 61] However, carbon deposits are inevitable under a methane stream at high temperatures due to the thermodynamics of the MDA reaction,[2] hence, many groups are working on the regeneration of catalyst under H_2 or O_2.[62-65]

As Zn/ZSM-5 catalysts showed the highest activity for MDA reactions, the carbonaceous deposits present in Zn(IMP)/ZSM-5 and Zn(VD)/ZSM-5 were studied using TPO-MS, UV-Raman and ASAP-MS. Visually, the spent catalysts after 4 h on stream looked very different with the Zn(IMP)/ZSM-5 (Figure 9 left) catalyst looking substantially darker than the Zn(VD)/ZSM-5 (Figure 9 right) catalyst. A speckled appearance post MDA reaction was observed for Zn(VD)/ZSM-5 with particles ranging in colour from white, grey to black. The speckled appearance was present in the catalyst bed highlighting the inhomogeneity of the MDA reaction over the Zn(VD)/ZSM-5. However, despite the visual differences, both catalysts showed very

similar carbon levels, determined by CHN analysis. Further characterisation of the carbonaceous deposits in both Zn(IMP)/ZSM-5 and Zn(VD)/ZSM-5 catalysts was carried out to determine if chemical differences reflecting both the visual appearance of the catalysts and difference in methane to benzene conversion could be observed.

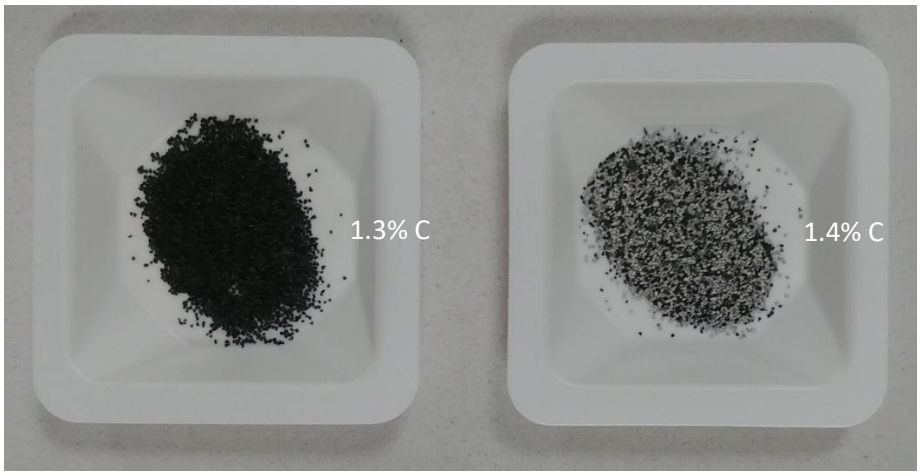

Figure 9: Pictures of spent Zn/ZSM-5 catalysts: Left: Zn(IMP)/ZSM-5 (1.3% C), Right: Zn(VD)/ZSM-5 (1.4%C).

7.2.1.1 ^{13}C NMR spectroscopic analysis of Zn/ZSM-5 catalysts

Hensen *et al.* have characterised carbonaceous deposits in Mo/ZSM-5 through analysis by ^{13}C NMR spectroscopy.[61, 66] Using $^{13}CH_4$ to enhance the quality of the NMR spectra, one signal was observed in the ^{13}C NMR spectrum at 130 ppm corresponding to sp^2 carbon of an aromatic nature on an Mo/ZSM-5 catalyst containing 14% C. [61, 66] Similar analysis was attempted on the Zn/ZSM-5 catalysts. Unfortunately due to the low carbon content present in both catalysts (<1.5 %C) and the use of unlabelled methane, no signals were observed in the ^{13}C NMR spectrum.

7.2.1.2 TPO – MS analysis of Zn/ZSM-5 catalysts

Temperature-programmed techniques have been employed by many research groups to determine the type of carbon present in spent MDA catalysts.[3, 55] For Mo/H-HCM-22, Bao *et al.* established that at least three types of coke were present: molybdenum carbide, molybdenum-associated coke and aromatic coke on acid sites.[54] Hensen *et al.* have also analysed Mo/ZSM-5, which had been exposed to methane for different periods of time, through TPO analysis. The authors establish that the amount carbonaceous deposits associated with BAS increases with time on stream, at the expense of molybdenum-associated coke.[61] The authors also establish that the maximum coke capacity of ZSM-5 is 270 mg of coke per gram of zeolite but practically, spent Mo/ZSM-5 catalysts contain 80 – 180 mg of coke per gram of catalyst.[53, 66-68] Although less analysis has been carried out on spent Zn catalysts, Cheung *et al.* report the

removal of surface coke (5.6 - 10%) through oxidation to CO_2 between 480 – 640 °C on spent Zn/H-ZSM-5. [21] The authors suggest that the zinc catalysts can be regenerated at 640 °C as very little weight loss is measured after this temperature.

Temperature programmed oxidation coupled with mass spectrometery (TPO-MS) was carried out on Zn(VD)/ZSM-5 and Zn(IMP)/ZSM-5 spent catalysts to investigate the coke present in these samples. The analysis was carried out in a 10% O_2, 90% He stream using the temperature program shown in Figure 10 which included a 1 h hold at 150 °C to remove any adsorbed water present in the zeolite catalysts.

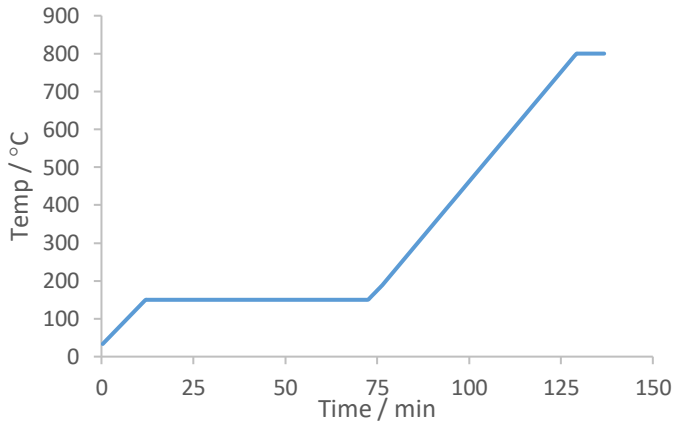

Figure 10: TPO program used to analyse Zn/ZSM-5 spent catalysts. A ramp rate of 10 C min^{-1} from 30 – 800 °C was used with a 1 h hold at 150 °C to remove any surface water. Mass spectra were taken throughout the heating process.

TPO profiles for both catalysts are shown in Figure 11 from 300 °C (so water loss is not included). Both Zn/ZSM-5 catalysts lost about 1 weight% during the TPO experiment. This value is similar to the coke level determined by CHN analysis (1.3 or 1.4 %C).

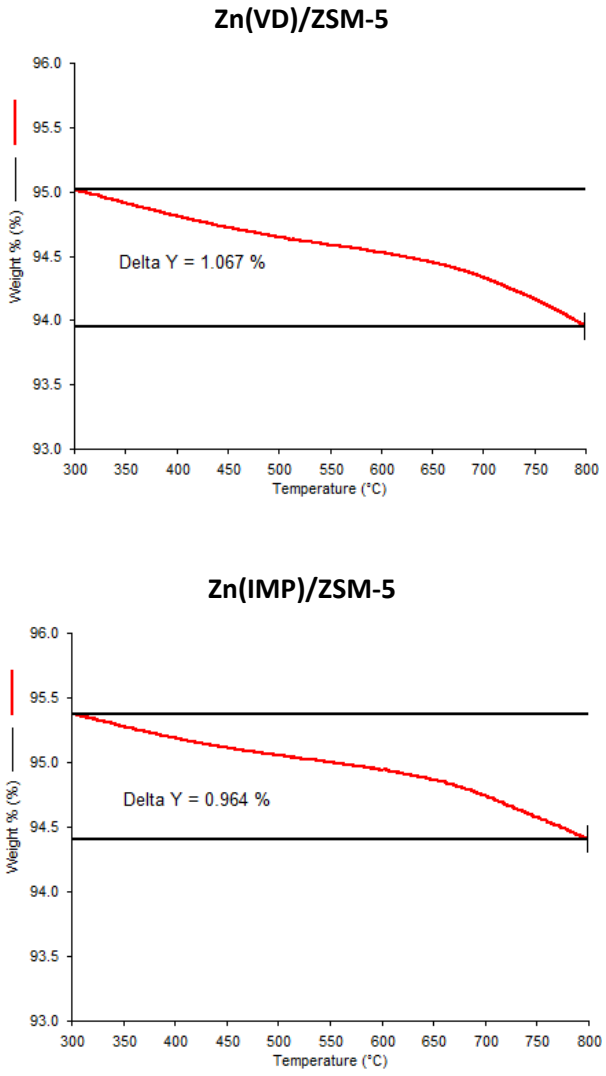

Figure 11: TPO profiles showing %weight loss against temperature from Zn/ZSM-5 spent catalysts. The weight recorded for both samples were very similar to the %C determined for CHN analysis.

Mass spectrometry plots showing ion count against temperature for water, CO and CO_2 are presented in Figure 12. The plots in Figure 12A and Figure 12B corresponding to water loss indicate the majority of the water present in the zeolite was lost after the 150 °C hold for 1 h. The hold is observed as the vertical straight line at 150 °C and the programme used is presented in Figure 10. No CO was produced from the oxidation of coke from either catalysts. Above 350 °C, CO_2 was observed as carbon from the zeolite samples was oxidised. This is similar to the TGA results present by Cheung *et al.*, where most of the surface coke was removed between 480 – 640 °C through oxidation into CO_2.[21] Both Zn/ZSM-5 catalysts behaved very similarly during the oxidation and no significant differences were observed in the mass spectra.

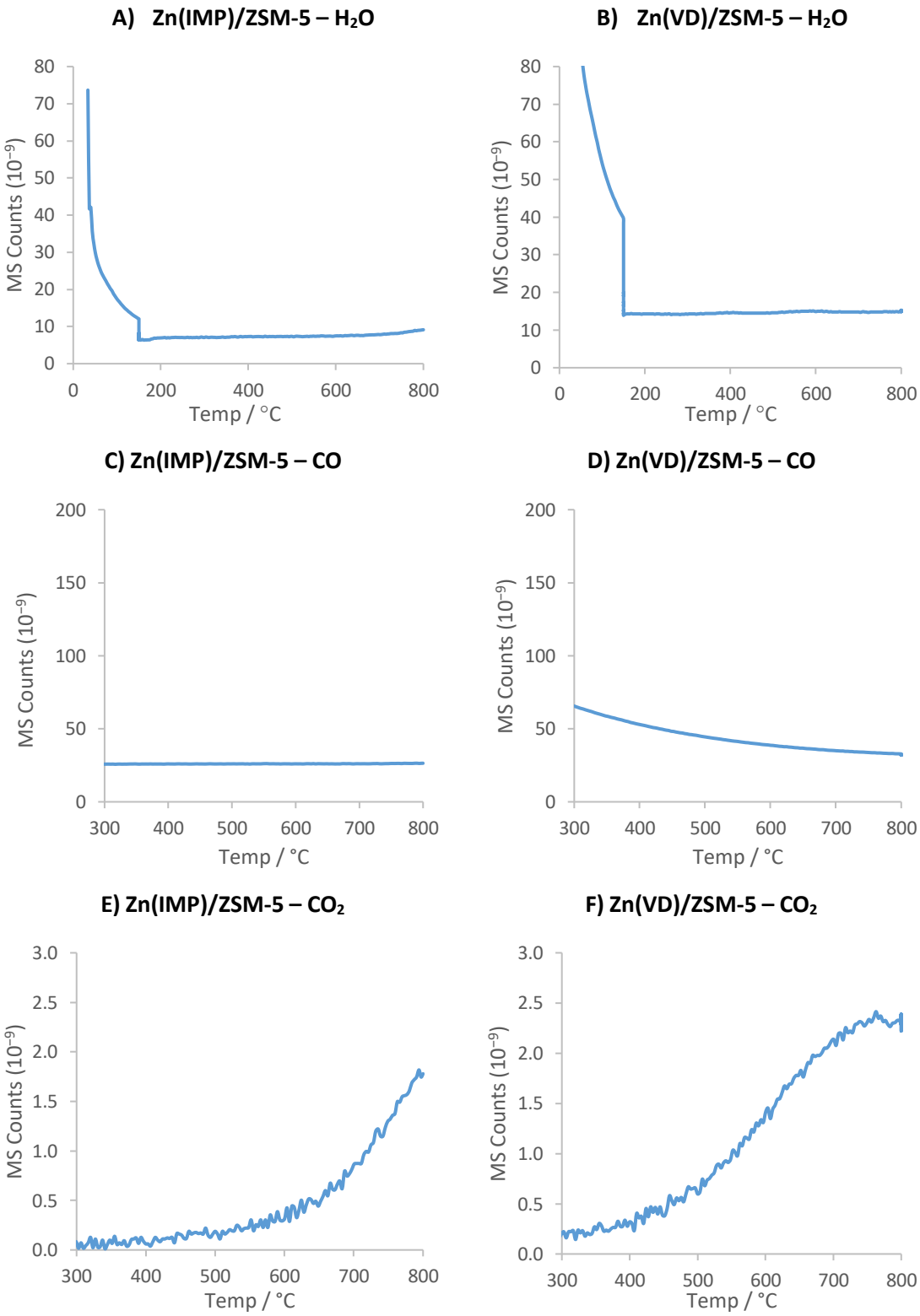

Figure 12: TPO-MS plots for H_2O, CO and CO_2 against temperature under 10 % oxygen stream, 90% He stream showing MS counts against temperature for Zn(IMP)/ZSM-5 and Zn(VD)/ZSM-5.

7.2.1.3 UV-Raman analysis of Zn/ZSM-5 catalysts

UV-Raman spectroscopy has been used to understand the nature of Mo species in Mo catalysts[69, 70] alongside analysing the coke formed during the reaction.[58, 71, 72] Bands observed at around 1600 cm^{-1} are attributed to the coke species formed during the MDA reaction, nominally polyaromatic species.[58] Both Zn/ZSM-5 catalysts produced a band around 1600 cm^{-1} (Figure 13) indicating the presence of polyaromatic coke formed during the MDA reaction. Unfortunately, no differences were observed between the catalysts and similar coke deposits seem to have formed in both Zn(IMP)/ZSM-5 and Zn(VD)/ZSM-5 catalysts despite the difference in catalyst activity.

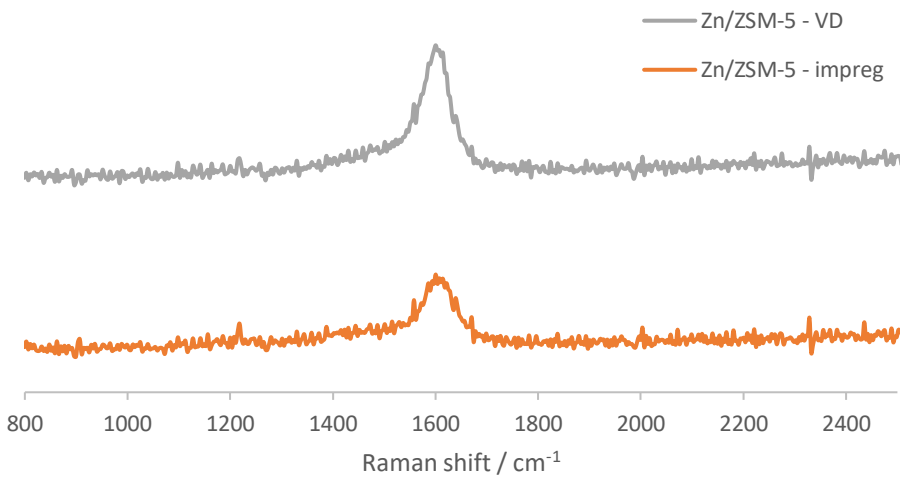

Figure 13: UV-Raman spectra of Zn/ZSM-5 spent catalysts indicating the presence of polyaromatic species. The spectra are not normalised to mass of catalyst.

7.2.1.4 Analysis of internal coke from Zn/ZSM-5 catalysts using ASAP-MS

From the techniques demonstrated above, the carbonaceous deposits present on both Zn(IMP)/ZSM-5 and Zn(VD)/ZSM-5 catalysts have been investigated and no differences were observed between the two catalysts. To try to investigate the internal coke present in both catalysts, attempts were made to dissolve the zeolite framework and extract the carbonaceous deposits following a similar procedure to Olsbye *et al.*[73] Hensen *et al.* have similarly dissolved the zeolite framework using HF, filtered the remaining solid and analysed the carbonaceous deposits.[61] They determined from the TEM images that the carbonaceous deposits remain particulate and the size and shape of the particles are similar to the parent zeolite crystals. The authors suggest that polyaromatic species grow throughout the whole zeolite crystal volume and the structure is similar to those of zeolite-templated carbons as the carbonaceous deposits had a BET surface area of 340 m^2 /g.

The zeolites were dissolved in a solution of HF (Inorganic Ventures digest solution) and an attempt to extract organic material into DCM was carried out. A control sample was also prepared where DCM was added to the HF solution without the presence of zeolite catalyst. After the HF solution was added to the spent catalyst, black solid remained undissolved at the bottom of the flask and upon addition of DCM, the solid remained unchanged. The DCM solution appeared to be slightly coloured black after the extraction and was centrifuged to remove any solid particulates. Atmospheric solids analysis probe mass spectrometry, ASAP-MS, analysis was carried out to try to analyse the carbon content of the DCM solution. The extraction was unsuccessful as the spectra from the catalysts were very similar to the control sample, shown in Figure 15. This could indicate that only polyaromatic coke is present in these Zn/catalysts as this would be too large to be extracted into the DCM solution. These deposits were likely the black solid observed in the bottom of the flask which did not dissolve upon addition of HF, nor did they appear to extract into DCM.

ASAP-MS analysis[3] of the solid zeolite spent catalysts was also carried out, the spectra are shown in Figure 16. Both catalysts have similar mass spectra, potentially showing some fragments of aromatic coke, which are not present in the parent zeolite. Significant peaks are observed at m/z 341 and m/z 354 for Zn(IMP)/ZSM-5 and m/z 457 for Zn(VD)/ZSM-5. Suggested polyaromatic compounds with similar m/z values are presented in Figure 14.

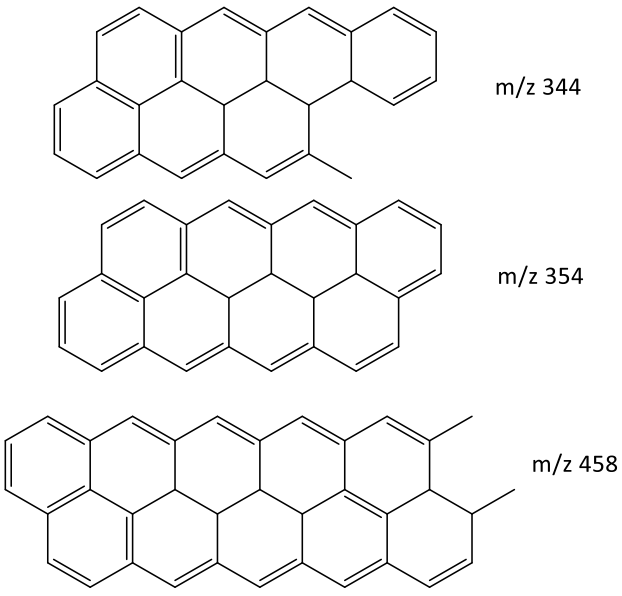

Figure 14: Polyaromatic species with similar m/z values to those observed by ASAP-MS for Zn(IMP)/ZSM-5 and Zn(VD)/ZSM-5

[3] Ions observed using ASAP-MS can include radical cation $M^{+\cdot}$, protonated species $[M+H]^+$ or hydride abstracted species $[M-H^-]^+$.

Overall, despite the visual and catalytic differences between the Zn/ZSM-5 catalysts, the coke present in both samples seems very similar. Analysis indicates the presence of polyaromatic carbon which can be oxidised to CO_2 at temperatures above 350 °C. The carbonaceous deposits formed were sufficiently large that they could not be extracted into DCM. Although several techniques were used to analyse the coke present in the Zn/ZSM-5 spent catalysts, further surface area measurements and TEM imaging could be used to achieve a more complete picture.

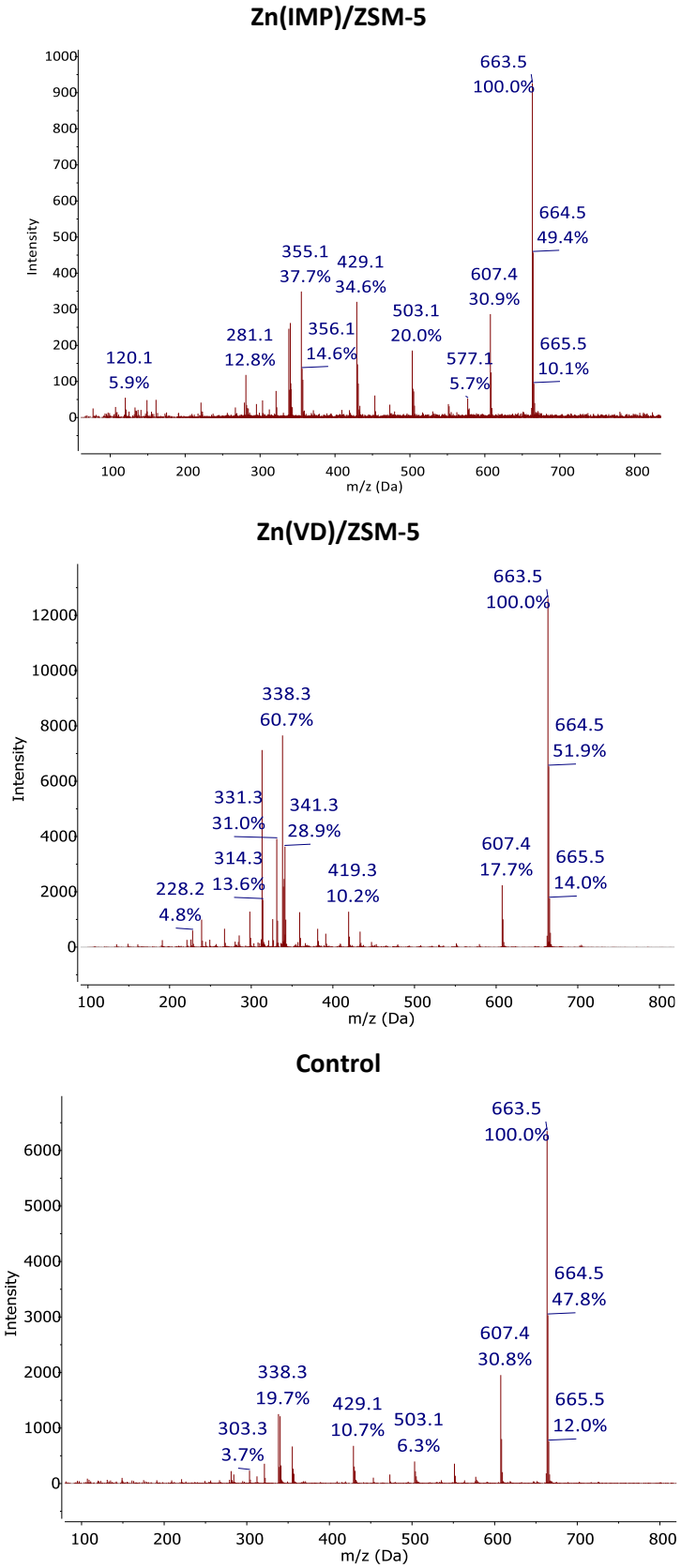

Figure 15: ASAP-MS spectra of coke extracted into DCM from Zn/ZSM-5 catalysts compared to a control sample. No discernible differences are observed between the control and the spent catalysts.

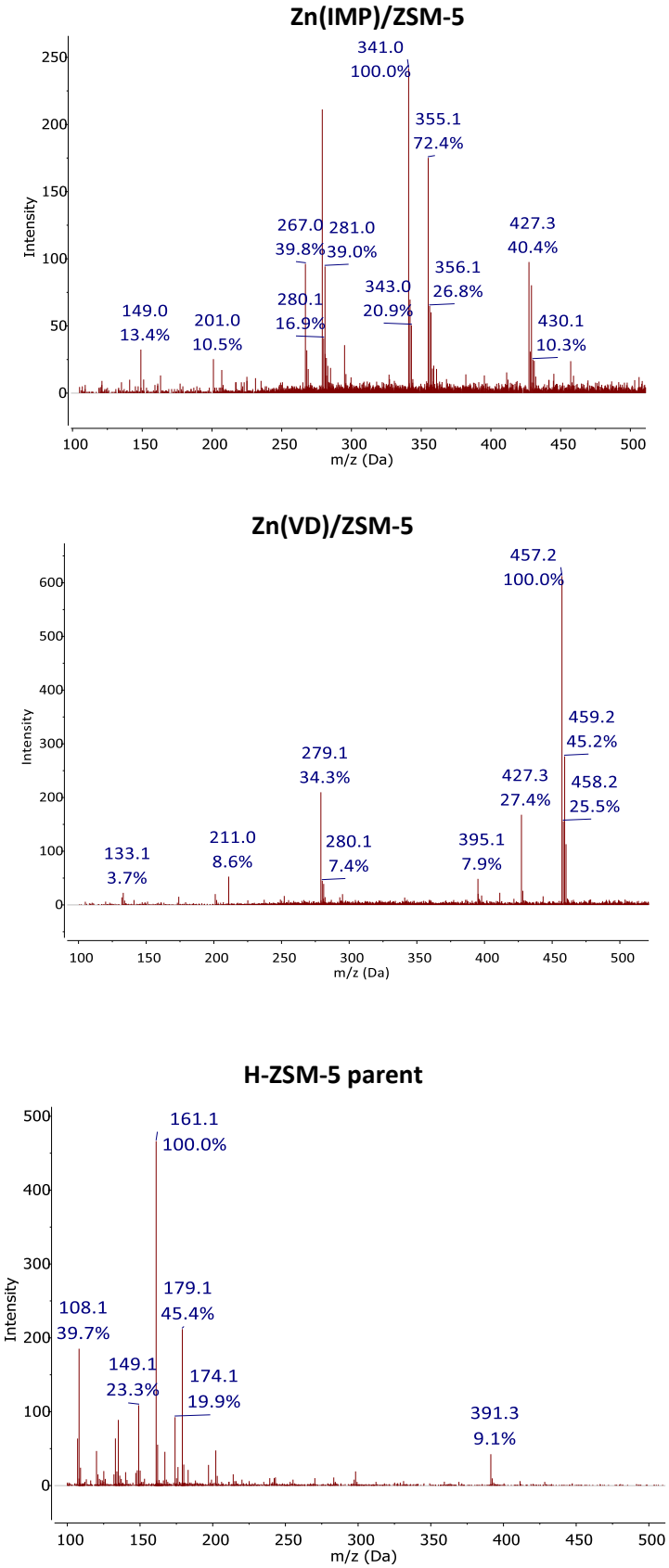

Figure 16: ASAP-MS spectra of Zn/ZSM-5 catalysts compared to the parent H-ZSM-5 zeolite. Both Zn catalysts show signals corresponding to polyaromatic coke.

7.3 Conclusions

Prior literature studies have shown that Zn/ZSM-5 catalysts have not performed as well as Mo/H-ZSM-5 for the MDA reaction, but early work has indicated that zinc catalysts may outperform molybdenum through greater stability and higher activity under certain conditions.[18, 21] We prepared zinc catalysts where the zinc was introduced through zinc vapour deposition, ion exchange and impregnation using four different zeolite frameworks and these were tested for their benzene productivity. Both Zn/ZSM-5 and Zn/Beta catalysts were able to produce detectable levels of benzene at 800 °C. However, Zn/FER and Zn/MOR catalysts were unable to produce liquid products under these catalytic conditions, likely due to pore blockage.

Zn(VD)/ZSM-5 produced the most benzene whilst producing similar levels of carbonaceous deposits to the other less active zinc catalysts. However, the zinc species present was not stable under the high temperature, reducing atmosphere of the MDA reaction as zinc was removed throughout the process. However, after 4 h on stream, the zeolite framework remained intact and little extraframework Al was observed through ^{27}Al NMR spectroscopy. Interestingly, Zn(VD)/Beta (12.5), which was unable to stoichiometrically activate methane, was the worst Zn/Beta catalyst with low activity and high levels of carbonaceous deposits. This supports the idea that in vapour deposition samples, the [Zn^{I}-Zn^{I}] is the active species for the MDA reaction. This is further reinforced by the Zn(VD)/ZSM-5–air catalyst, which is not treated air-sensitively and results in very little benzene formation. Analysis of the carbonaceous deposits using CHN, TPO-MS, UV-Raman, and ASAP-MS techniques indicated that both Zn(VD)/ZSM-5 and Zn(IMP)/ZSM-5 catalysts contained similar polyaromatic coke. The Zn(VD)/ZSM-5 was able to produce 5-10 times more benzene than the Zn(IMP)/ZSM-5 catalyst whilst producing similar levels of carbonaceous deposits, highlighting the potential of this catalyst in MDA reactions.

Cheung *et al.* reported 5.5% methane conversion over Zn(IMP)/H-ZSM-5 whilst Veser *et al.* report lower conversions of 1.2% over Zn(IMP)/H-ZSM-5 and both groups were able to produce benzene at 700 °C.[21, 31] The Zn(VD)/ZSM-5, the best catalyst we have observed, demonstrates less than 1% methane to benzene conversion and requires temperatures of 800 °C. The vapour deposition reaction is limited to 200 mg and the GHSV of our reactor was significantly higher than that of Cheung and Veser which could explain the low methane conversion values that we achieve.

In order to test catalyst lifetime, MDA reactions using Zn(VD)/ZSM-5 and Zn(IMP)/ZSM-5 were carried out for 10 h at 800 °C. Whilst the Zn(VD)/ZSM-5 catalyst once again had high benzene productivity, both catalysts showed significant zinc leaching and loss in crystallinity.

Furthermore, ^{27}Al NMR spectroscopy detected the presence of extraframework Al indicating Al was also being removed from the catalyst during the MDA reaction. The lifetime analysis results indicate that without the stabilisation of the zinc species, potentially as a bimetallic catalyst, [8, 74] Zn/ZSM-5 is unlikely to be viable as an industrial catalyst. However, the low levels of carbonaceous deposits and high benzene selectivity highlight the potential in the Zn(VD)/ZSM-5 catalyst.

7.4 Experimental

NH_4-Beta (12.5) was kindly provided by Clariant. NH_4–ZSM-5 (12.5) was kindly provided by Johnson Matthey. NH_4–MOR (10), NH_4–FER (10) and Zinc nitrate hexahydrate (99%) were purchased from Alfa Aesar. Zinc powder (Goodfellow, 99.9%, max particle size 150 μm) was used as purchased. Acetone-d_6 (99.9 % D) was purchased from Sigma. Tetramethyl silane (99.9+%, NMR grade) was purchased from Acros Organics. SiC (165 μm, 80 grit) was purchased from Fischer scientific. Methane (99.995%), N_2 (oxygen free) and Ar (99.998%) cylinders were purchased from BOC. Zinc powder was stored and used in a PureLab HE glove box under an argon atmosphere.

Ion exchanged samples (IE) were prepared by treating the parent zeolites with an aqueous solution $Zn(NO_3)_2$ based on a method reported by Kuroda *et al.*.[75] Zinc ion exchanges were carried out using 2.5 g of zeolite in a centrifuge tube in contact with 50 ml of 0.3M $Zn(NO_3)_2$ solution for 1 h with constant agitation from a mechanical tube roller. The tube was centrifuged at 4500 rpm for 5.5 min and the resulting supernatant decanted. The zeolite was then re-dispersed into the $Zn(NO_3)_2$ solution and this process was repeated 10 times. The sample was then washed with 50 ml of deionised water 8 times and dried at 80 °C overnight.

Impregnated samples (IMP) were prepared with a target Zn wt% of 3%. The parent zeolite (1 g) was mixed with the appropriate amount of $Zn(NO_3)_2.6H_2O$ in a round bottom flask with 4 ml of water. This was agitated on the rotary evaporator overnight and subsequently all water was removed. The sample was calcined at 550 °C for 5 h in a muffle furnace.

The vapour deposition samples (VD) were prepared by an exchange reaction between metallic zinc vapour and the H-form of the zeolite as reported previously.[47] The zeolite was pressed and sieved to 40-60 mesh before being placed into a quartz u-tube under vacuum (pressure < 10^{-2} mbar) and heated to 150 °C for 1 h followed by 5 h at 550 °C in a tube furnace. A 5 °C min^{-1} ramp rate was used for all furnace program steps. A 100-fold excess of zinc (Zn/Al =100) was used for the zinc metal vapour deposition. To expose the zeolite sample to zinc vapour, the u-tube was sealed and placed in a tube furnace where it was heated to 500 °C at 5 °C min^{-1} and held for 1 h under static vacuum. Excess unreacted zinc vapour was further removed by continued heating at 500 °C for 2 h under dynamic vacuum.

MDA reactions were carried out in a u-tube reactor shown in Figure 1. Catalysts were pressed and sieved to 40-60 mesh before 200 mg was mixed with 1 g SiC to ensure good thermal contact. A 1 g pre-bed and post-bed of SiC was also used. If the catalyst was air-sensitive, the reactor was packed inside the glovebox. The catalyst was held in place with quartz wool plugs

and was positioned in the isothermal zone of the clam-shell furnace. The furnace was heated to 800 °C under a flow of N_2 with a ramp of 5 °C min^{-1}. When the furnace reached temperature, the gas flow was switched from N_2 to CH_4 and held at 800 °C for 4 or 10 h. After 4 h or 10 h at temperature, the furnace was left to cool and the gas flow was returned to N_2. Gas flow was set at approximately 20 ml min^{-1}. Liquid products were collected in a condenser which was placed in a −78 °C dry ice/acetone bath. After the furnace had cooled to below 100 °C, the condenser was removed and rinsed with 0.7 ml of acetone-d_6 containing an internal standard of TMS (100 μl of TMS in 10 ml of acetone-d_6). This was transferred to an NMR tube and quantitative solution state NMR was carried out.

In an attempt to characterise the coke deposited in the interior channels of the zeolites, a method used by Olsbye *et al.* was attempted.[73] Using the Inorganic Ventures HF solution, 10 mg of catalyst was dissolved.[76] Organic material was attempted to be extracted with DCM and the subsequent DCM solution was centrifuged to remove any particles. ASAP-MS was carried out on the DCM solution and solid catalyst samples.

7.5 Chapter 7 References

1. I. Vollmer, I. Yarulina, F. Kapteijn and J. Gascon, *Chem. Cat. Chem*, 2019, **11**, 39-52.
2. J. J. Spivey and G. Hutchings, *Chem. Soc. Rev.*, 2014, **43**, 792-803.
3. Z. R. Ismagilov, E. V. Matus and L. T. Tsikoza, *Energy Environ. Sci.*, 2008, **1**, 526-541.
4. S. Majhi, P. Mohanty, H. Wang and K. K. Pant, *J. Ener. Chem.*, 2013, **22**, 543-554.
5. I. Vollmer, B. van der Linden, S. Ould-Chikh, A. Aguilar-Tapia, I. Yarulina, E. Abou-Hamad, Y. G. Sneider, A. I. Olivos Suarez, J.-L. Hazemann, F. Kapteijn and J. Gascon, *Chem. Sci.*, 2018, **9**, 4801-4807.
6. S. Ma, X. Guo, L. Zhao, S. Scott and X. Bao, *Journal of Energy Chemistry*, 2013, **22**, 1-20.
7. B. M. Weckhuysen, D. Wang, M. P. Rosynek and J. H. Lunsford, *J. Catal.*, 1998, **175**, 347-351.
8. Y. Xu, J. Wang, Y. Suzuki and Z.-G. Zhang, *Appl. Catal., A*, 2011, **409-410**, 181-193.
9. Y. Shu and M. Ichikawa, *Catal. Today*, 2001, **71**, 55-67.
10. W. Ding, S. Li, G. D Meitzner and E. Iglesia, *J. Phys. Chem. B*, 2001, **105**, 506-513.
11. L. Y. Chen, L. W. Lin, Z. S. Xu, X. S. Li and T. Zhang, *J. Catal.*, 1995, **157**, 190-200.
12. Y. Xu, S. Liu, X. Guo, L. Wang and M. Xie, *Catal. Lett.*, 1994, **30**, 135-149.
13. N. Kosinov, F. J. A. G. Coumans, E. A. Uslamin, A. S. G. Wijpkema, B. Mezari and E. J. M. Hensen, *ACS Catal.*, 2017, **7**, 520-529.
14. I. Vollmer, E. Abou-Hamad, J. Gascon and F. Kapteijn, *Chem Cat Chem*, 2020.
15. H. Liu, X. Bao and Y. Xu, *J. Catal.*, 2006, **239**, 441-450.
16. R. W. Borry, Y. H. Kim, A. Huffsmith, J. A. Reimer and E. Iglesia, *J. Phys. Chem. B*, 1999, **103**, 5787-5796.
17. V. T. T. Ha, L. V. Tiep, P. Meriaudeau and C. Naccache, *J. Mol. Catal. A: Chem.*, 2002, **181**, 283-290.
18. L. Wang, L. Tao, M. Xie, G. Xu, J. Huang and Y. Xu, *Catal. Lett.*, 1993, **21**, 35-41.
19. O. Kazuaki, N. Katusmi and O. Yoshio, *Bull. Chem. Soc. Jpn.*, 1993, **66**, 755-759.
20. M. V. Luzgin, V. A. Rogov, S. S. Arzumanov, A. V. Toktarev, A. G. Stepanov and V. N. Parmon, *Angew. Chem. Int. Ed.*, 2008, **47**, 4559-4562.
21. B. S. Liu, Y. Zhang, J. F. Liu, M. Tian, F. M. Zhang, C. T. Au and A. S. C. Cheung, *J. Phys. Chem. C*, 2011, **115**, 16954-16962.
22. V. B. Kazansky and A. I. Serykh, *Phys. Chem. Chem. Phys.*, 2004, **6**, 3760-3764.
23. M. V. Luzgin, D. Freude, J. Haase and A. G. Stepanov, *J. Phys. Chem. C*, 2015, **119**, 14255-14261.
24. A. A. Gabrienko, S. S. Arzumanov, M. V. Luzgin, A. G. Stepanov and V. N. Parmon, *J. Phys. Chem. C*, 2015, **119**, 24910-24918.
25. Y. G. Kolyagin, I. I. Ivanova and Y. A. Pirogov, *Solid State Nucl. Magn. Reson.*, 2009, **35**, 104-112.
26. A. Oda, H. Torigoe, A. Itadani, T. Ohkubo, T. Yumura, H. Kobayashi and Y. Kuroda, *J. Phys. Chem. C*, 2013, **117**, 19525-19534.
27. J. F. Wu, W. D. Wang, J. Xu, F. Deng and W. Wang, *Chem. Eur. J.*, 2010, **16**, 14016-14025.
28. J. Xu, A. Zheng, X. Wang, G. Qi, J. Su, J. Du, Z. Gan, J. Wu, W. Wang and F. Deng, *Chem. Sci.*, 2012, **3**, 2932-2940.
29. V. Abdelsayed, M. W. Smith and D. Shekhawat, *Appl. Catal., A*, 2015, **505**, 365-374.
30. H. Berndt, G. Lietz and J. Völter, *Appl. Catal., A*, 1996, **146**, 365-379.
31. Y. Lai and G. Veser, *Environ. Prog. Sus. Ener.*, 2016, **35**, 334-344.
32. J. Guo, H. Lou and X. Zheng, *J. Nat. Gas Chem.*, 2009, **18**, 260-272.
33. V. R. Choudhary, K. C. Mondal and S. A. R. Mulla, *Angew. Chem. Int. Ed.*, 2005, **44**, 4381-4385.
34. L. B. Pierella, G. A. Eimer and O. A. Anunziata, in *Stud. Surf. Sci. Catal.*, eds. A. Parmaliana, D. Sanfilippo, F. Frusteri, A. Vaccari and F. Arena, Elsevier, 1998, vol. 119, pp. 235-240.

35. O. A. Anunziata, G. V. González Mercado and L. B. Pierella, *Catal. Lett.*, 2003, **87**, 167-171.
36. O. A. Anunziata, G. González Mercado and L. B. Pierella, *Catal. Commun.*, 2004, **5**, 401-405.
37. O. A. Anunziata and G. G. Mercado, *Catal. Lett.*, 2006, **107**, 111-116.
38. G. R. Fulmer, A. J. M. Miller, N. H. Sherden, H. E. Gottlieb, A. Nudelman, B. M. Stoltz, J. E. Bercaw and K. I. Goldberg, *Organometal.*, 2010, **29**, 2176-2179.
39. S. M. T. Almutairi, B. Mezari, P. C. M. M. Magusin, E. A. Pidko and E. J. M. Hensen, *ACS Catal.*, 2012, **2**, 71-83.
40. I. Pinilla-Herrero, E. Borfecchia, J. Holzinger, U. V. Mentzel, F. Joensen, K. A. Lomachenko, S. Bordiga, C. Lamberti, G. Berlier, U. Olsbye, S. Svelle, J. Skibsted and P. Beato, *J. Catal.*, 2018, **362**, 146-163.
41. I. Lezcano-González, R. Oord, M. Rovezzi, P. Glatzel, S. W. Botchway, B. M. Weckhuysen and A. M. Beale, *Angew. Chem. Int. Ed.*, 2016, **55**, 5215-5219.
42. D. Wang, J. H. Lunsford and M. P. Rosynek, *Top. Catal.*, 1996, **3**, 289-297.
43. H. Jiang, L. Wang, W. Cui and Y. Xu, *Catal. Lett.*, 1999, **57**, 95-102.
44. F. Solymosi, J. Cserényi, A. Szöke, T. Bánsági and A. Oszkó, *J. Catal.*, 1997, **165**, 150-161.
45. Y. Nagamori and M. Kawase, *Micro. Meso. Mater.*, 1998, **21**, 439-445.
46. O. Lupan, L. Chow, G. Chai and H. Heinrich, *Chem. Phys. Lett.*, 2008, **465**, 249-253.
47. M. A. Shah, S. Raynes, D. C. Apperley and R. A. Taylor, *Chem. Phys. Chem.*, 2020, **21**, 673-679.
48. A. A. Gabrienko, S. S. Arzumanov, A. V. Toktarev, I. G. Danilova, I. P. Prosvirin, V. V. Kriventsov, V. I. Zaikovskii, D. Freude and A. G. Stepanov, *ACS Catal.*, 2017, **7**, 1818-1830.
49. M. D. Foster, I. Rivin, M. M. J. Treacy and O. Delgado Friedrichs, *Micro. Meso. Mater.*, 2006, **90**, 32-38.
50. Z. Zhu, T. Ruan, Q. Chen, W. Chen and D. Kong, in *Stud. Surf. Sci. Catal.*, eds. A. Galarneau, F. Fajula, F. Di Renzo and J. Vedrine, Elsevier, 2001, vol. 135, p. 271.
51. J. Hagen, in *Industrial Catalysis*, Wiley-VCH Verlag GmbH & Co. KGaA, 2015, DOI: 10.1002/9783527684625.ch7, pp. 239-260.
52. X. Huang, X. Jiao, M. Lin, K. Wang, L. Jia, B. Hou and D. Li, *Catal. Sci. Technol.*, 2018, **8**, 5740-5749.
53. C. H. L. Tempelman and E. J. M. Hensen, *Appl. Catal., B Environ.*, 2015, **176-177**, 731-739.
54. D. Ma, D. Wang, L. Su, Y. Shu, Y. Xu and X. Bao, *J. Catal.*, 2002, **208**, 260-269.
55. P. Schwach, X. Pan and X. Bao, *Chem. Rev.*, 2017, **117**, 8497-8520.
56. Y. Xu, X. Bao and L. Lin, *J. Catal.*, 2003, **216**, 386-395.
57. B. M. Weckhuysen, M. P. Rosynek and J. H. Lunsford, *Catal. Lett.*, 1998, **52**, 31-36.
58. S. Yuan, J. Li, Z. Hao, Z. Feng, Q. Xin, P. Ying and C. Li, *Catal. Lett.*, 1999, **63**, 73-77.
59. Y. Liu, D. Li, T. Wang, Y. Liu, T. Xu and Y. Zhang, *ACS Catal.*, 2016, **6**, 5366-5370.
60. F. Bauer and H. G. Karge, in *Characterization II*, eds. H. G. Karge and J. Weitkamp, Springer Berlin Heidelberg, Berlin, Heidelberg, 2007, DOI: 10.1007/3829_005, pp. 249-364.
61. N. Kosinov, E. A. Uslamin, F. J. A. G. Coumans, A. S. G. Wijpkema, R. Y. Rohling and E. J. M. Hensen, *ACS Catal.*, 2018, **8**, 8459-8467.
62. Y. Shu, R. Ohnishi and M. Ichikawa, *Appl. Catal., A*, 2003, **252**, 315-329.
63. Y. Xu, J. Lu, J. Wang, Y. Suzuki and Z.-G. Zhang, *Chem. Eng. J.*, 2011, **168**, 390-402.
64. A. C. C. Rodrigues and J. L. F. Monteiro, *Catal. Commun.*, 2008, **9**, 1060-1065.
65. M. R. Toosi, B. Sabour, T. Hamuleh and M. H. Peyrovi, *React. Kinet. Mech. Catal*, 2010, **101**, 221-226.
66. N. Kosinov, E. A. Uslamin, L. Meng, A. Parastaev, Y. Liu and E. J. M. Hensen, *Angew. Chem., Int. Ed.*, 2019, **58**, 7068-7072.

67. H. Liu, L. Su, H. Wang, W. Shen, X. Bao and Y. Xu, *Appl. Catal., A*, 2002, **236**, 263-280.
68. H. Liu, Y. Li, W. Shen, X. Bao and Y. Xu, *Catal.*, 2004, **93-95**, 65-73.
69. W. Li, G. D. Meitzner, R. W. Borry and E. Iglesia, *J. Catal.*, 2000, **191**, 373-383.
70. J. Gao, Y. Zheng, J.-M. Jehng, Y. Tang, I. E. Wachs and S. G. Podkolzin, *Science*, 2015, **348**, 686-690.
71. X. Jiao, X. Huang and K. Wang, *Catal. Sci. Technol.*, 2019, **9**, 6552-6555.
72. H. An, F. Zhang, Z. Guan, X. Liu, F. Fan and C. Li, *ACS Catal.*, 2018, **8**, 9207-9215.
73. F. Bleken, W. Skistad, K. Barbera, M. Kustova, S. Bordiga, P. Beato, K. P. Lillerud, S. Svelle and U. Olsbye, *Phys. Chem. Chem. Phys.*, 2011, **13**, 2539-2549.
74. V. Abdelsayed, D. Shekhawat and M. W. Smith, *Fuel*, 2015, **139**, 401-410.
75. A. Oda, H. Torigoe, A. Itadani, T. Ohkubo, T. Yumura, H. Kobayashi and Y. Kuroda, *J. Phys. Chem. C*, 2014, **118**, 15234-15241.
76. P. Gaines, Elemental Analysis of Zeolites, https://www.inorganicventures.com/guides-and-papers/elemental-analysis-of-zeolites, (accessed Jan, 2019).

Chapter 8: Conclusions and Future Work

Chapter 8: Conclusions and Future Work

Methane activation and subsequent reactivity was explored over zinc-modified zeolites in this project and three main questions regarding the role of the zeolite framework and the nature of the zinc active site were investigated.

1) ***What is the role of the zeolite framework on methane activation over zinc-modified zeolites?***

Initially, three zeolite frameworks (ZSM-5 (15), FER (10) and MOR (10)) with very different zeolite topologies were zinc-exchanged using CVD of zinc metal and high levels of zinc exchange were obtained. Upon exposure to $^{13}CH_4$, C-H activation was observed to occur for all three frameworks, as determined by a characteristic signal resulting from [Zn^{II}-CH_3] in ^{13}C MAS NMR spectroscopy studies. Using HMB as an internal standard, the percentage of zinc atoms that resulted in the formation of the [Zn^{II}-CH_3] species was determined; the order was found to be Zn(VD)/CH_4/ZSM-5 (5.7%), Zn(VD)/CH_4/MOR (1.2%) and Zn(VD)/CH_4/FER (0.5%) highlighting that zeolite framework does play a crucial role in methane activation. Furthermore, the vapour deposition sample Zn(VD)/CH_4/ZSM-5 produced significantly higher levels of active zinc sites compared to the Zn(IE)/CH_4/ZSM-5 sample, where the zinc was introduced through ion exchange methods (5.7% compared with 0.9%). Additionally, the reactivity of the [Zn^{II}-CH_3] species in the different zeolite frameworks under oxidative conditions was explored. The three zeolite frameworks demonstrated dissimilar reactivity under different oxidative conditions indicating that the framework also plays a key role in the reactivity post methane activation. The ZSM-5 framework was found to be the most reactive environment for the [Zn^{II}-CH_3] species whilst Zn(VD)/CH_4/air/MOR was selective for methanol.

To explore the role of Al pairing on methane activation using zinc-modified zeolites, CHA samples with different levels of pairing were synthesised by collaborators at KU Leuven. Surprisingly, the Al pairing had no significant impact on the percentage of active sites produced in CHA, contrary to what is expected for ZSM-5.[1] However, whilst Al pairing seemingly had no effect on methane activation, changing the Si/Al ratio of the CHA samples drastically effected the number of zinc active sites produced. In CHA(62), 20% of the zinc sites were able to form the [Zn^{II}-CH_3] species, compared to CHA (12) where only 5.6% of the zinc was active, demonstrating unprecedented reactivity with methane. Though, a Zn/Al ratio of 3 for CHA(62) alongside its remarkable activity remains inexplicable, perhaps indicating a different zinc species is present in high silica CHA.

Methane activation over Zn(VD)/MOR proved to be particularly interesting as two signals were observed in the ^{13}C NMR spectrum after exposure to $^{13}CH_4$. Further NMR spectroscopic experiments determined that the two signals are likely associated with [Zn^{II}-CH_3] species present in the 12 MR channels and the 8 MR side pockets of the MOR framework. Dealumination experiments using nitric acid or steam to selectively remove Al were attempted to further confirm this assignment. Protection of the 8 MRs using partial exchange of a 1+ cation, Na^+, was carried out to achieve selective dealumination of the 12 MRs by steaming whilst nitric acid was used to remove Al primarily from the 8 MR SPs. Zn(VD)/CH_4/MOR-nitric showed a substantial decrease in the signal corresponding to the [Zn^{II}-CH_3] species located in the 8 MRs as expected from the reported selective dealumination of the 8 MR SP by nitric acid.[2-5] Unfortunately, protection by Na^+ was unsuccessful as both steamed samples, Zn(VD)/Na/MOR-deAl and Zn(VD)/MOR-deAl showed a relative decrease in signal corresponding to the [Zn^{II}-CH_3] species located in the 12 MRs suggesting the harsh steaming conditions were able to remove Al from all sites in MOR. It should be noted that post exposure to zinc vapour, all dealuminated MOR samples showed high Zn/Al_{tet} ratio, with values greater than 1 for the steamed samples. This is likely due to the zinc inserting into the silanol nests as determined from ^1H-^{29}Si CP NMR experiments. Overall, from the NMR spectroscopic experiments presented in Chapter 4 and the selective deAl results presented in Chapter 5, it can be concluded that two [Zn^{II}-CH_3] species are present Zn(VD)/MOR associated with the 12 MR channels and the 8 MR side pockets of the MOR framework.

It is clear that zeolite topology plays a crucial role in the activation of methane and subsequent reactivity under oxidative conditions. Whilst ZSM-5 was initially thought to be the most active framework host, CHA(62) has displayed an unparalleled percentage of active zinc sites with a currently inexplicable Zn/Al ratio of 3. Ideally, methane activation should be carried out on a defect free CHA(62) to remove any doubt of the location of the zinc active species and the subsequent reactivity of CHA(62) should be investigated further.

2) What is the nature of the zinc active site for methane activation over zinc-modified zeolites?

The percentage of zinc active sites that are able to form the [Zn^{II}-CH_3]species is dependent on zeolite topology and on the method of zinc introduction. Additionally, Zn/Al ratios higher than the theoretical 0.5 are observed for samples where zinc has been introduced by vapour deposition. To explore these observations further, XAS analysis was performed and XANES analysis of Zn(VD)/ZSM-5 and Zn(VD)/MOR highlighted the presence of a low energy band,

which we assign to a [Zn^{I}-Zn^{I}] dimeric species, supported by previous work by Kuroda *et al*.[6] Zeolite samples prepared by ion exchange or zinc vapour deposition samples that were subsequently evacuated at 600 °C are no longer able to activate methane, do not show this band. Hence, we believe that the [Zn^{I}-Zn^{I}] dimer is the active species in Zn/zeolites where the zinc has been introduced by vapour deposition. EXAFS analysis suggested the data for the VD samples can be fitted using a model containing both Zn-O and [Zn^{I}-Zn^{I}] in the first co-ordination sphere, whilst data for IE and 600 °C samples can only be fitted using Zn-O, providing further evidence that a different active species is present in VD samples. The reaction of methane with the [Zn^{I}-Zn^{I}] dimer is suggested to form a [Zn^{II}-CH_3] species, a new BAS and Zn^0. Additional investigation to confirm the presence of the Zn^0 reaction product should be carried out though detailed analysis of the XANES spectra of Zn(VD)/CH_4/ZSM-5 and Zn(VD)/CH_4/MOR, accompanied by DFT modelling.

To further confirm that the [Zn^{I}-Zn^{I}] dimer is the active zinc species for methane activation, a vapour deposition was carried out on partially exchanged Zn(IE)/Na-ZSM-5 and Zn(IE)/Na-MOR samples. Zinc was able to be added to the zeolite without the presence of BAS and the addition of this zinc led the partially exchanged Zn(IE)/Na-ZSM-5 and Zn(IE)/Na-MOR to be able to activate methane. Analysis of the reaction of the dimer species [Zn^{I}-Zn^{I}] with methane using DR-UV-vis could also provide useful information of the active species.

Whilst there is evidence for the presence of the [Zn^{I}-Zn^{I}] dimer in VD samples from XAS analysis and through the experiments involving Zn(IE)/Na-ZSM-5 and Zn(IE)/Na-MOR samples, without additional analysis the mechanism of methane activation over the [Zn^{I}-Zn^{I}]dimer remains unclear. XAS analysis was limited as the number of active sites present in Zn(VD)/ZSM-5 is only 6%, hence, only a small percent of [Zn^{II}-CH_3] species are formed, potentially undetectable by XAS analysis. However, CHA(62) contains 20% zinc sites, which are able to form the [Zn^{II}-CH_3] species, therefore XAS analysis of this sample may provide more insight into the reaction mechanism occurring. Although, the high Zn/Al ratio of 3 for CHA(62) does imply that perhaps a different active species is present compared to the other zeolite frameworks explored in this thesis.

3) Does the method of zinc introduction or the zeolite topology affect the activity of the zinc catalyst for methane dehydroaromatisation reactions (MDA)?

Zn/ZSM-5 has shown potential for MDA in the literature although one key issues faced is the difficulty stabilising the catalyst due to the reducing reaction conditions.[7-11] Zinc catalysts prepared through zinc vapour deposition, ion exchange or impregnation using four different

zeolite frameworks (ZSM-5 (12.5), BETA (12.5), MOR (10) and FER(10)) were tested for benzene productivity. Both Zn/ZSM-5 and Zn/Beta catalysts were able to produce detectable levels of benzene at 800 °C but Zn/FER and Zn/MOR catalysts were unable to form liquid products, likely due to zeolite topology.

Zn(VD)/ZSM-5 produced the most benzene whilst producing similar levels of carbonaceous deposits to the other less active zinc containing catalysts. However, the zinc species present were not stable under the high temperature, reducing atmosphere of the MDA reaction as zinc was removed throughout the process. After 10 h at 800 °C, the Zn(VD)/ZSM-5 catalyst showed significant zinc leaching and loss in crystallinity, likely due to the formation of extraframework Al. Whilst the Zn(VD)/ZSM-5 was the best perforrming catalyst we observed, it still exhibited less than 1% methane to benzene conversion and required temperatures of 800 °C. However, our vapour deposition reaction is limited to 200 mg of zeolite and the methane flow rate used for the MDA reaction in this thesis was significantly higher compared with the literature, which could explain the low methane conversion values that we achieve.[7, 11]

Overall, ZSM-5 proved to be best framework host for the MDA reaction, as established for Mo catalysts in the literature with the highest yield of benzene and low levels of carbonaceous deposits.[12-18] Zinc introduction by vapour deposition proved superior to both ion exchange and impregnation highlighting that method of zinc introduction, and therefore active zinc species, impacts the MDA reaction. Optimisation of the reactor by reducing the GHSV could yield higher methane conversion results. However, the zinc leaching is a clear issue for industrialisation of this catalyst, therefore, stabilisation of the zinc using a second metal should be explored.[7, 19, 20]

8.1 Conclusion References

1. A. Oda, H. Torigoe, A. Itadani, T. Ohkubo, T. Yumura, H. Kobayashi and Y. Kuroda, *J. Phys. Chem. C*, 2013, **117**, 19525-19534.
2. A. A. C. Reule, J. A. Sawada and N. Semagina, *J. Catal.*, 2017, **349**, 98-109.
3. P. Bodart, J. B. Nagy, G. Debras, Z. Gabelica and P. A. Jacobs, *J. Phys. Chem.*, 1986, **90**, 5183-5190.
4. M.-C. Silaghi, C. Chizallet, J. Sauer and P. Raybaud, *J. Catal.*, 2016, **339**, 242-255.
5. S. Ban, A. N. C. van Laak, J. Landers, A. V. Neimark, P. E. de Jongh, K. P. de Jong and T. J. H. Vlugt, *J. Phys. Chem. C*, 2010, **114**, 2056-2065.
6. A. Oda, T. Ohkubo, T. Yumura, H. Kobayashi and Y. Kuroda, *Dalton Trans.*, 2015, **44**, 10038-10047.
7. Y. Lai and G. Veser, *Environ. Prog. Sust. Ener.*, 2016, **35**, 334-344.
8. M. V. Luzgin, V. A. Rogov, S. S. Arzumanov, A. V. Toktarev, A. G. Stepanov and V. N. Parmon, *Angew. Chem. Int. Ed.*, 2008, **47**, 4559-4562.
9. H. Berndt, G. Lietz and J. Völter, *Appl. Catal., A*, 1996, **146**, 365-379.
10. L. Wang, L. Tao, M. Xie, G. Xu, J. Huang and Y. Xu, *Catal. Lett.*, 1993, **21**, 35-41.
11. B. S. Liu, Y. Zhang, J. F. Liu, M. Tian, F. M. Zhang, C. T. Au and A. S. C. Cheung, *J. Phys. Chem. C*, 2011, **115**, 16954-16962.
12. I. Vollmer, B. van der Linden, S. Ould-Chikh, A. Aguilar-Tapia, I. Yarulina, E. Abou-Hamad, Y. G. Sneider, A. I. Olivos Suarez, J.-L. Hazemann, F. Kapteijn and J. Gascon, *Chem. Sci.*, 2018, **9**, 4801-4807.
13. S. Ma, X. Guo, L. Zhao, S. Scott and X. Bao, *J. Ener. Chem.*, 2013, **22**, 1-20.
14. W. Ding, S. Li, G. D Meitzner and E. Iglesia, *J. Phys. Chem. B*, 2001, **105**, 506-513.
15. L. Y. Chen, L. W. Lin, Z. S. Xu, X. S. Li and T. Zhang, *J. Catal.*, 1995, **157**, 190-200.
16. Y. Xu, S. Liu, X. Guo, L. Wang and M. Xie, *Catal. Lett.*, 1994, **30**, 135-149.
17. N. Kosinov, F. J. A. G. Coumans, E. A. Uslamin, A. S. G. Wijpkema, B. Mezari and E. J. M. Hensen, *ACS Catal.*, 2017, **7**, 520-529.
18. I. Vollmer, E. Abou-Hamad, J. Gascon and F. Kapteijn, *Chem. Cat. Chem*, 2020.
19. J. Guo, H. Lou and X. Zheng, *J. Nat. Gas Chem.*, 2009, **18**, 260-272.
20. V. R. Choudhary, K. C. Mondal and S. A. R. Mulla, *Angew. Chem. Int. Ed.*, 2005, **44**, 4381-4385.

Appendix

Appendix 1: Further NMR spectra for framework effects on methane activation

^{29}Si direct spectra before and after zinc vapour deposition for ZSM-5, FER and MOR frameworks:

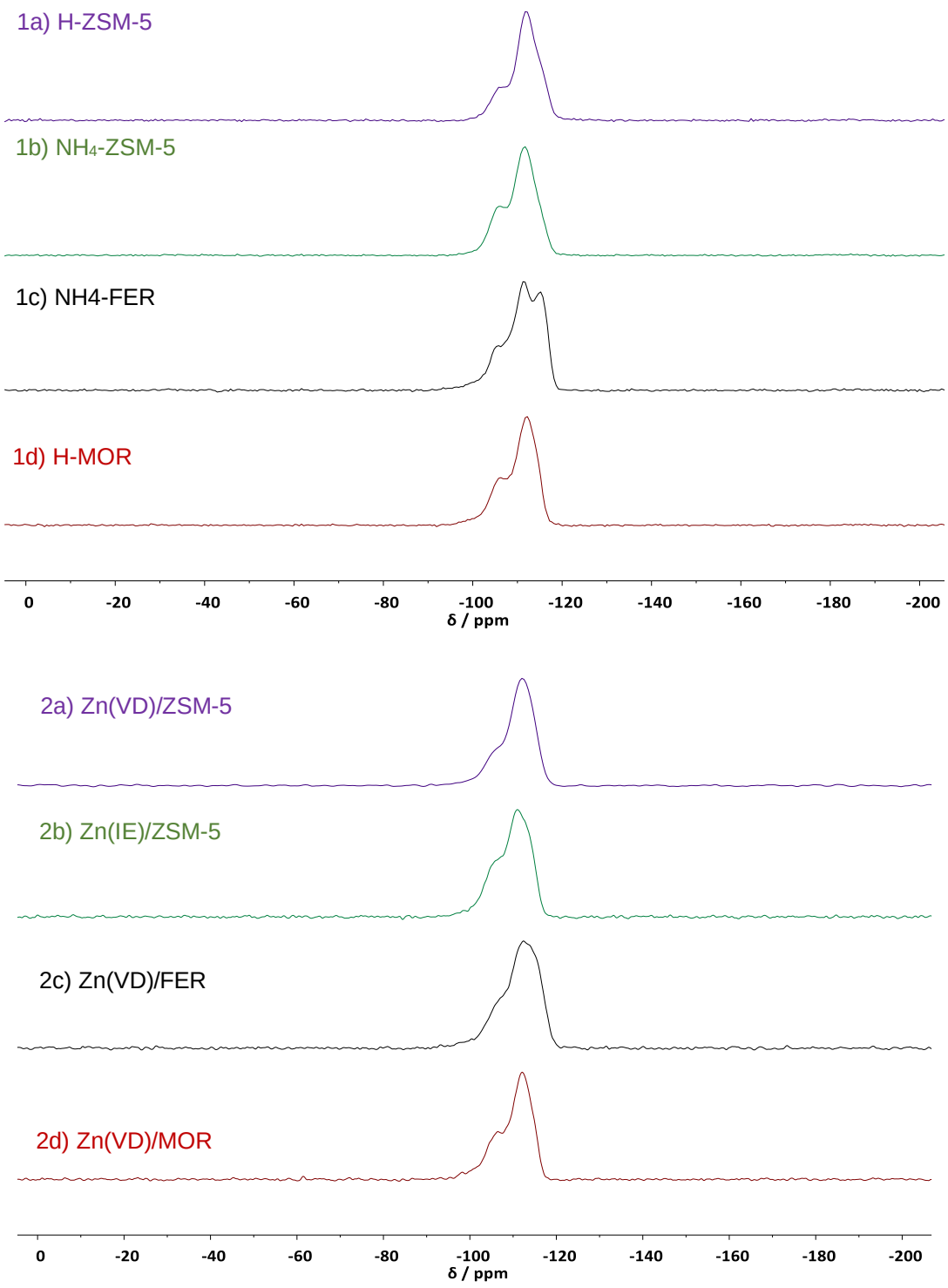

Figure 1: ^{29}Si direct NMR for parent zeolites (1a-d) and Zn/Zeolites (2a-d). (^{29}Si – 79.44 MHz, 8 kHz spin rate)

1.1 ^{1}H-^{27}Al REAPDOR spectra post methane exposure

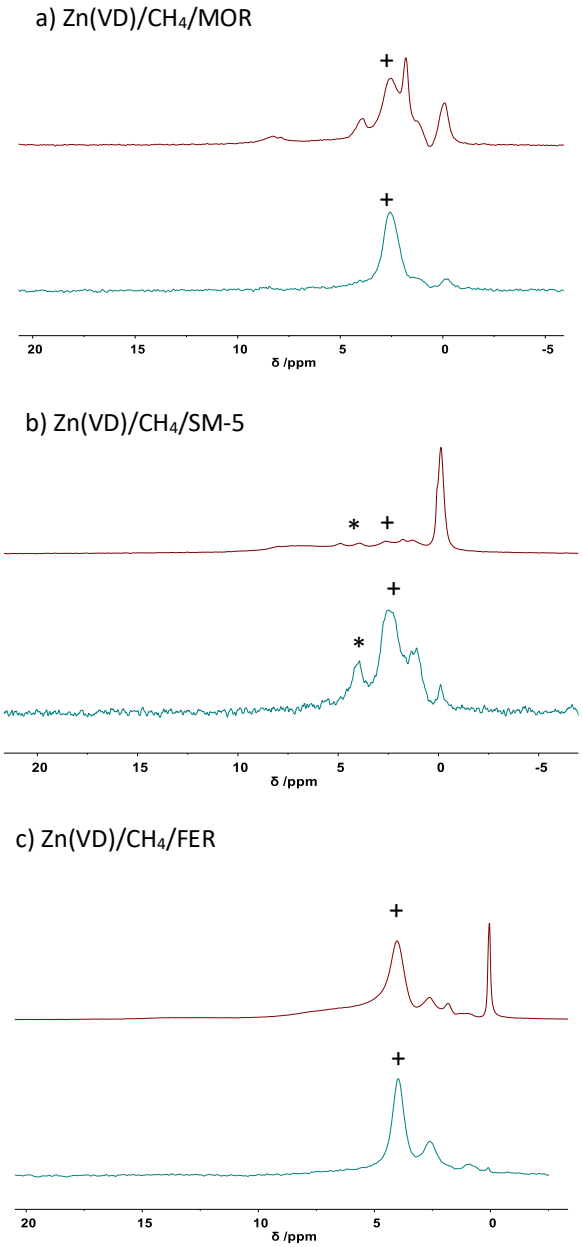

Figure 2: ^{1}H MAS NMR (red) and ^{1}H-^{27}Al REAPDOR difference spectra (green) for Zn(VD)/CH_4/MOR, Zn(VD)/CH_4/ZSM-5 and Zn(VD)/CH_4/FER post reaction with zinc vapour and methane. * Signal at 4 ppm related to BAS (MOR and ZSM-5) and for FER signal due to NH_4^+ (6.6 ppm). $^+$ Signal at 2.5 ppm associated with extraframework Al. Signal at 0 ppm corresponding to [Zn^{II}-CH_3] species which for all three frameworks shows some Al association in the REAPDOR difference spectrum. (^{1}H – 399.88 MHz, 40 kHz spin rate)

1.2 Further analysis on Zn(VD)/CH_4/ZSM-5 (45) and Zn(VD)/CH_4/Y (2.55)

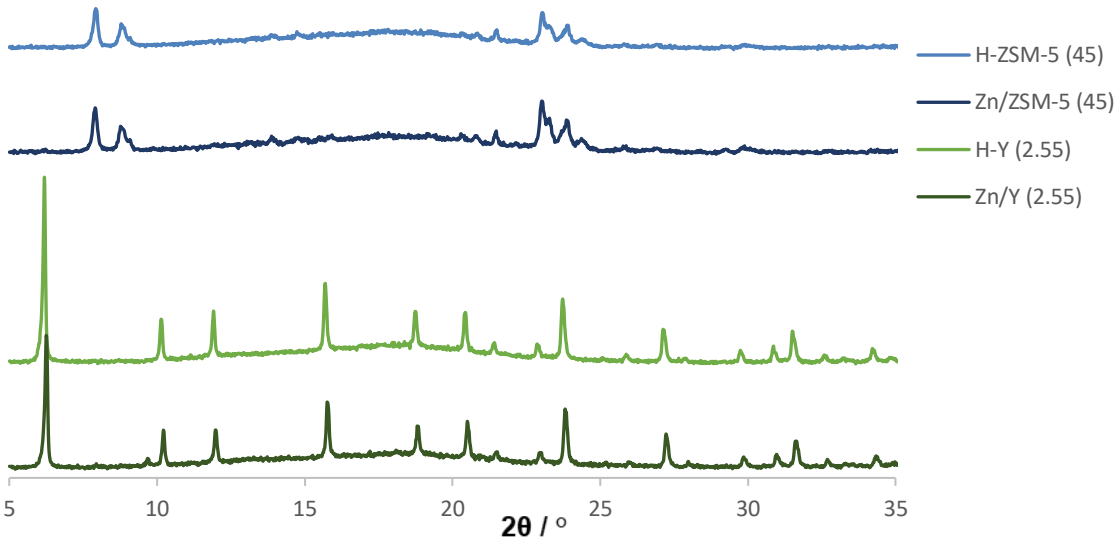

Figure 3: pXRD patterns comparing ZSM (45) and Y (2.55) before and after zinc vapour deposition. No change can be observed post reaction.

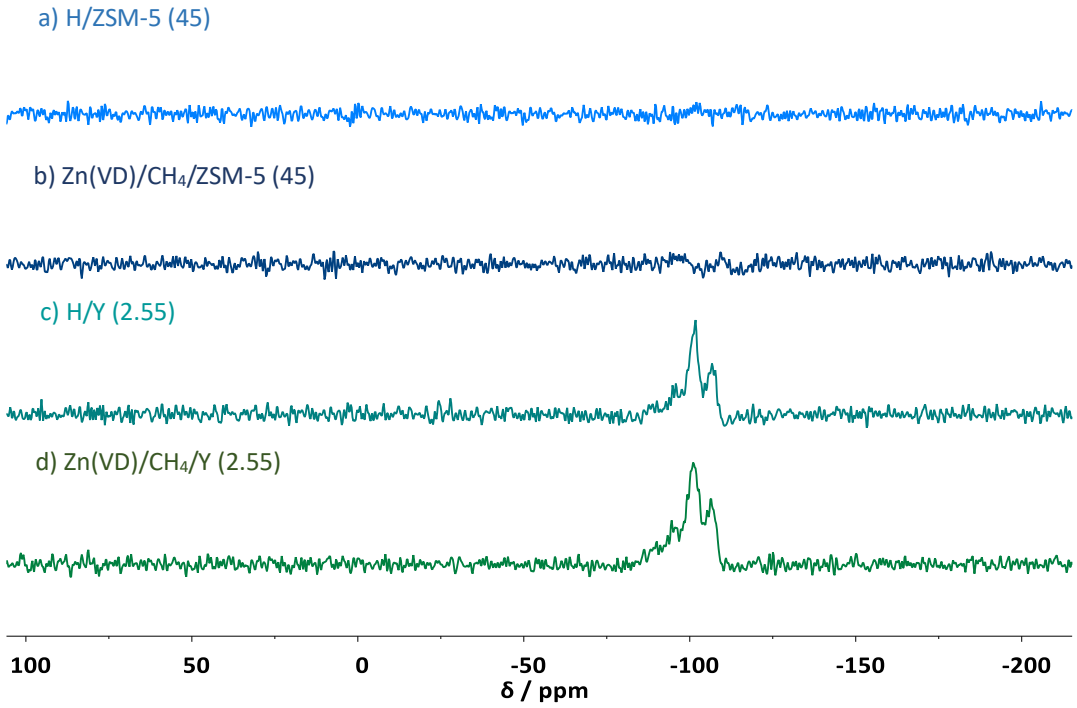

Figure 4: ^{1}H-^{29}Si CP NMR spectra for ZSM-5 (45) and Y (2.55) before and after zinc vapour deposition demonstrating no increase in defect sites after the reaction. (^{29}Si – 79.44 MHz, 8 kHz spin rate)

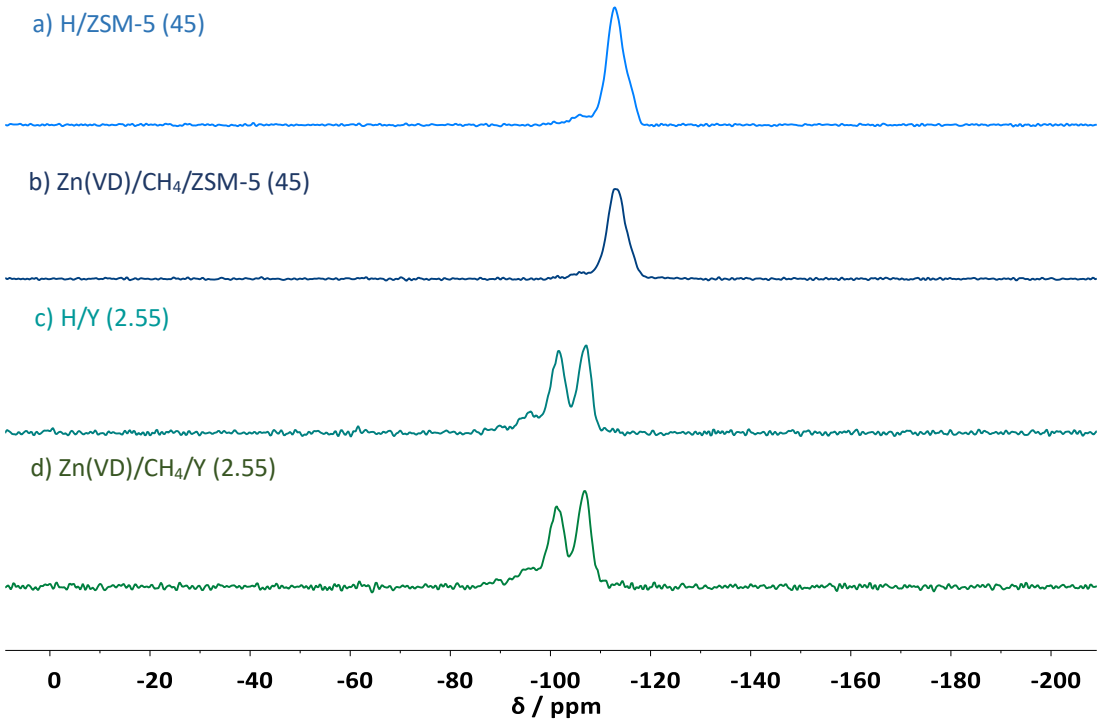

Figure 5: ^{29}Si direct excitation NMR spectra for ZSM-5 (45) and Y (2.55) before and after zinc vapour deposition demonstrating very little change after reaction with zinc. (^{29}Si – 79.44 MHz, 8 kHz spin rate)

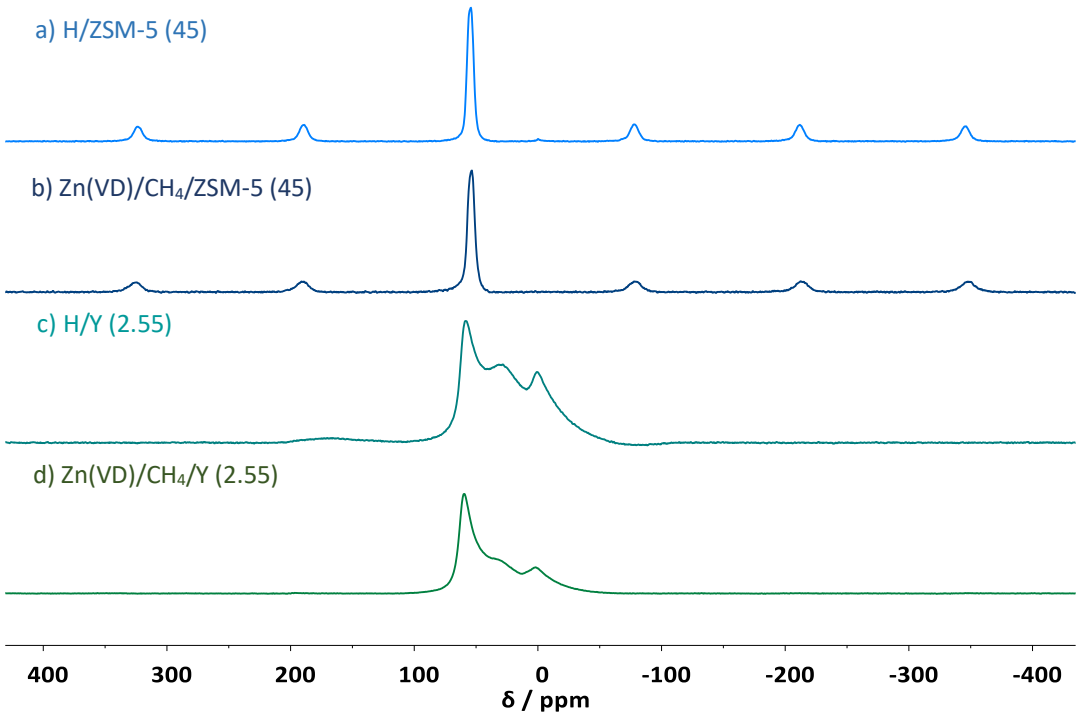

Figure 6: ^{27}Al NMR spectra for ZSM-5 (45) and Y (2.55) before and after zinc vapour deposition. No increases in extra framework Al (0 ppm) is observed post reaction with zinc. A decrease in 5 co-ordinate Al is observed for Zn(VD)/CH$_4$/Y (2.55). (^{27}Al – 104.20 MHz, 14 kHz spin rate)

Appendix 2: Quantification calculations for the number of active Zn sites

To calculate the percentage of active zinc sites, known masses of hexamethylbenzene (HMB) and dehydrated Zn/CH4/ZSM-5 were thoroughly mixed for 3 minutes in a vial in a glovebox. The amount of HMB was targeted at 10 wt%. The mixed sample was split three ways and packed into three 4 mm solid state NMR rotors. A direct excitation ^{13}C NMR experiment with a 10 s recycle, 720 scans at a 10 kHz spin rate was carried out for all quantification measurements. The peak at 17.06 ppm corresponding to the methyl groups in HMB was used to calculate the relationship between Me group and integral value (labelled with an * in Figure 7) In conjunction with elemental analysis (the relative ratios of Zn/Al/Si), the percentage of zinc methyls formed for $Zn/CH_4/ZSM\text{-}5$ can be determined. The calculations for this process are shown in Table 1 and Table 2.

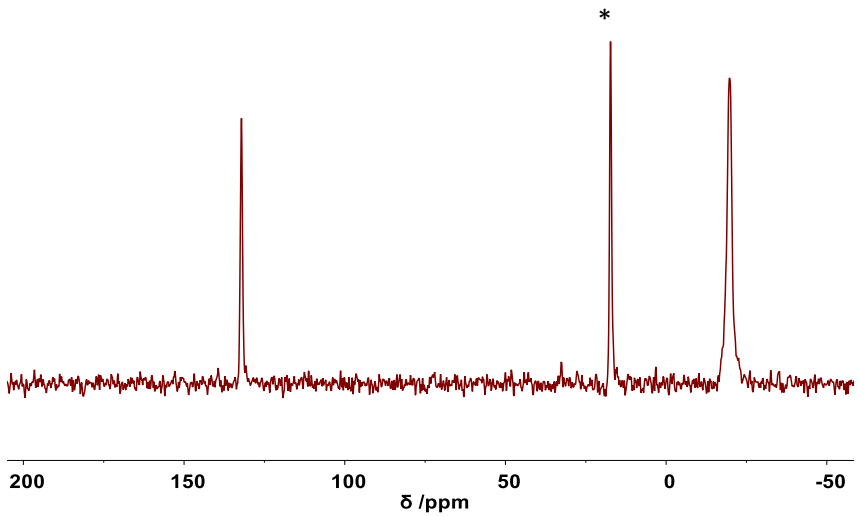

Figure 7: Direct excitation ^{13}C NMR spectrum for 10% HMB in $Zn(VD)/CH_4/ZSM\text{-}5$. * corresponds to Me groups of HMB used in quantification. (^{13}C – 100.57 MHz, 10 kHz spin rate)

Table 1: Calculations to determine the Average Me Integral / mol of HMB using the 17.06 ppm signal from the ^{13}C NMR spectrum

Total mass of HMB across three samples /mg	8.49
Mol of HMB across three samples	5.23×10^{-5}
Sum of integrals for 17.06 ppm peak across three samples	57.83
Integral per Me group (6 Me groups in HMB)	9.64
Integral, accounting for ^{13}C natural abundance	869.10
Me Integral (^{13}C)/ mol of HMB	**15558064.28**

Combing the result for average Me integral per mol of HMB calculated in Table 1 and the Zn/Al ratio and Si/Al ratio determined from ICP-OES and WD-XRF, respectively, the percentage of zinc that forms [Zn^{II}-CH_3] species can be calculated. The example shown below is for the three Zn(VD)/CH_4/ZSM-5 samples mixed with *ca*. 10% HMB (Table 1).

Table 2: Calculations to determine the percentage of Zn in Zn/ZSM-5 that form [Zn^{II}-CH_3] using the average Me Integral/mol calculated in Table 1 and a Zn/Al ratio calculated from ICP-OES data.

Sum of integrals for ZnMe peak for Zn/CH_4/ZSM-5	80.58
Sum of integrals accounting for ^{13}C abundance (99% ^{13}C)	81.40
Mol of methyl across three samples (calculated using Me Integral (^{13}C)/mol of HMB)	5.23×10^{-6}
mg of methyl formed /mg	0.079
Total mass of zeolite across three samples /mg	84.41
Total mass of zeolite (not including methyl groups)/mg	84.33
Zn/Al from ICP-OES	0.73
Si/Al from WD-XRF	12.5
Empirical formula for Zn/ZSM-5	$Zn^{2+}_{5.2}$ $[Al_{7.1}Si_{88.9}O_{192}]$
MW of Zn/ZSM-5 / g mol^{-1}	6131.68
Mol of zinc	7.21×10^{-5}
Percentage of Zn in Zn/ZSM-5 that form [Zn^{II}-CH_3]	**7.3%**

Having established a value for the "Me Integral (^{13}C)/ mol of HMB" this value was used to determine the percentage of Zn active sites for all other experiments. Direct ^{13}C spectra and elemental analysis used to calculate percentage of Zn active sites for the different zeolite frameworks are shown in Table 3.

.

Table 3: Direct excitation ^{13}C spectra, elemental analysis and percentage Zn active sites for ZSM-5, FER and MOR. (^{13}C – 100.57 MHz, 10 kHz spin rate)

Sample	Direct ^{13}C spectra	Si/Al	Zn/Al	Percentage of Zn active sites
Zn(VD)/CH_4/ZSM-5 (15)	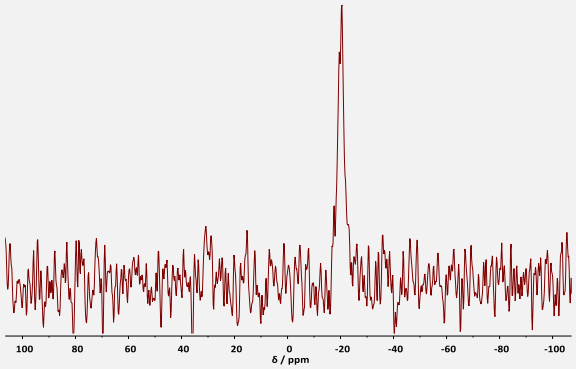	12.5	0.64	4.2%
Zn(VD)/CH_4/FER (10)	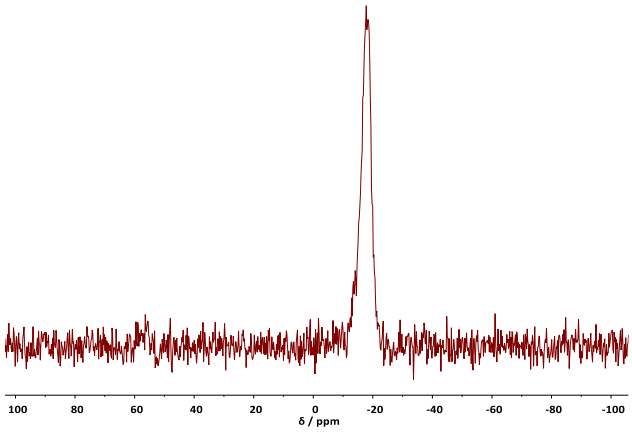	11.2	0.77	0.5%
Zn(VD)/CH_4/FER (10)	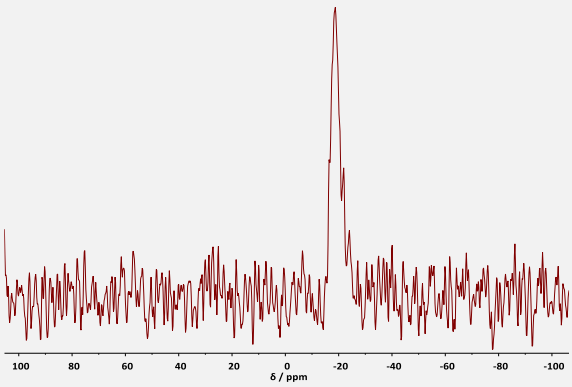	11.2	0.66	0.5%

Zn(VD)/CH_4/MOR (10)	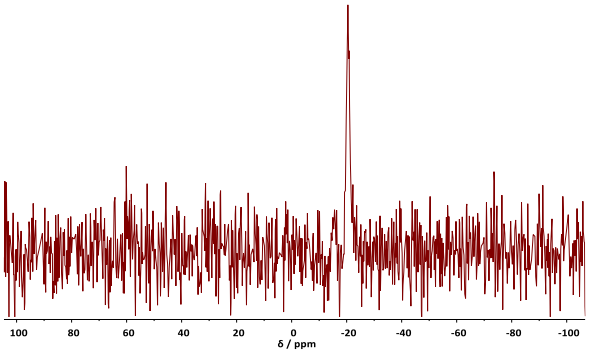	7.9	0.77	1.0%
Zn(VD)/CH_4/MOR (10)	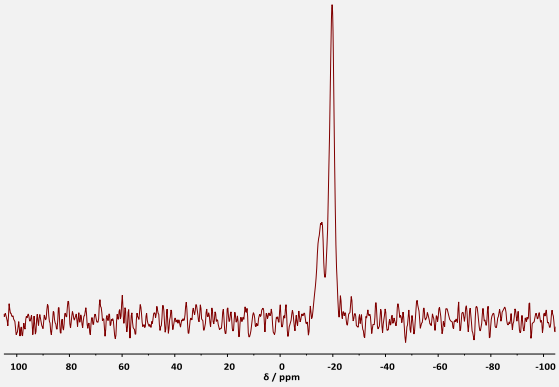	7.9	0.55	1.5%
Zn(IE)/H-ZSM-5 (12.5)	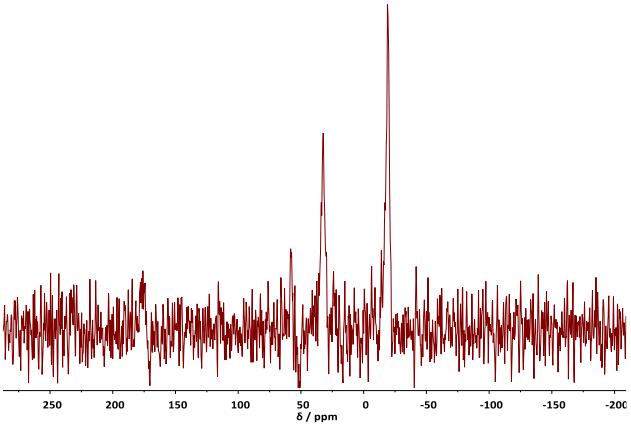 N.B Peak at 34 ppm from rotor	11.6	0.45	0.9%

Appendix 3: ^{27}Al and ^{29}Si spectra for CHA samples, pXRD analysis and Quantification data

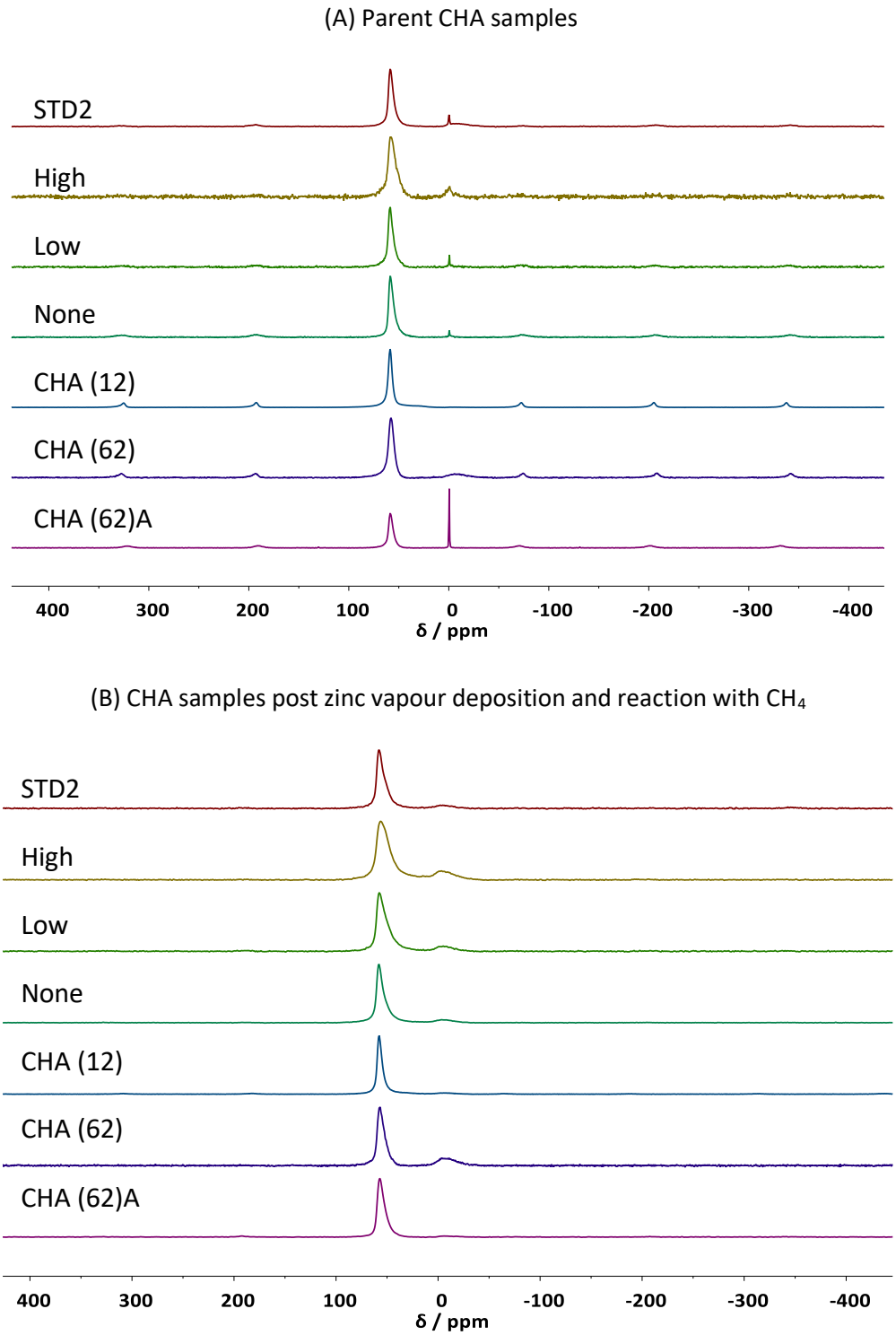

Figure 8: ^{27}Al NMR of CHA samples before (A) and after (B) zinc vapour deposition and reaction with methane for CHA samples. Signals corresponding to octahedral Al (signal at 0 ppm) disappear upon reaction with zinc vapour indicating the parent CHA samples are likely containing octahedral framework Al. (^{27}Al – 104.20 MHz, 14 kHz spin rate)

(A) Parent CHA samples

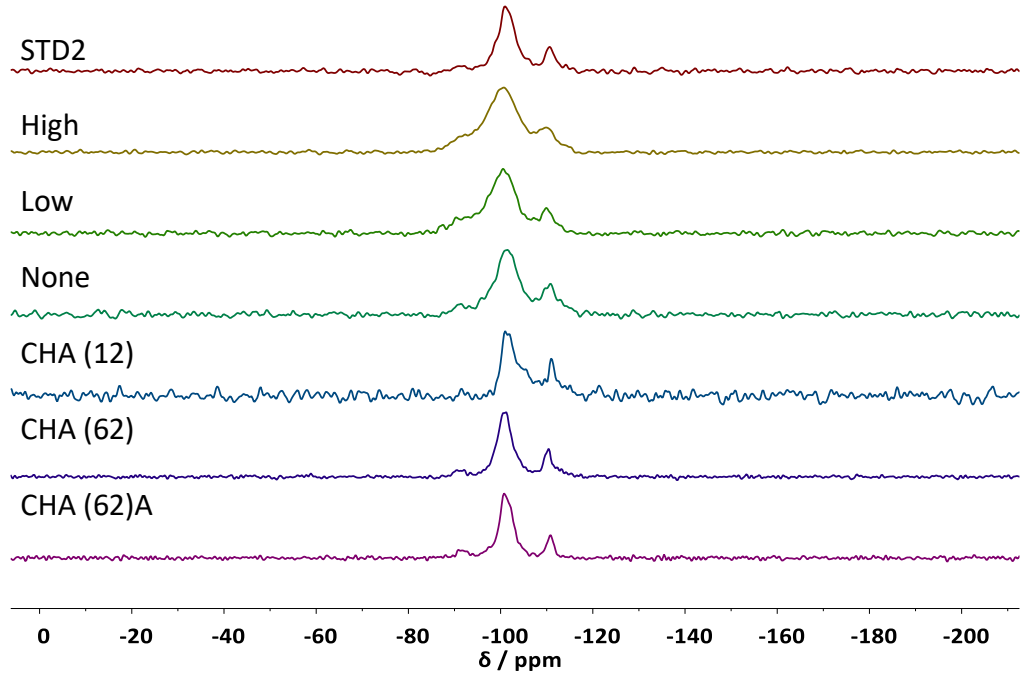

(B) CHA samples post zinc vapour deposition and reaction with CH_4

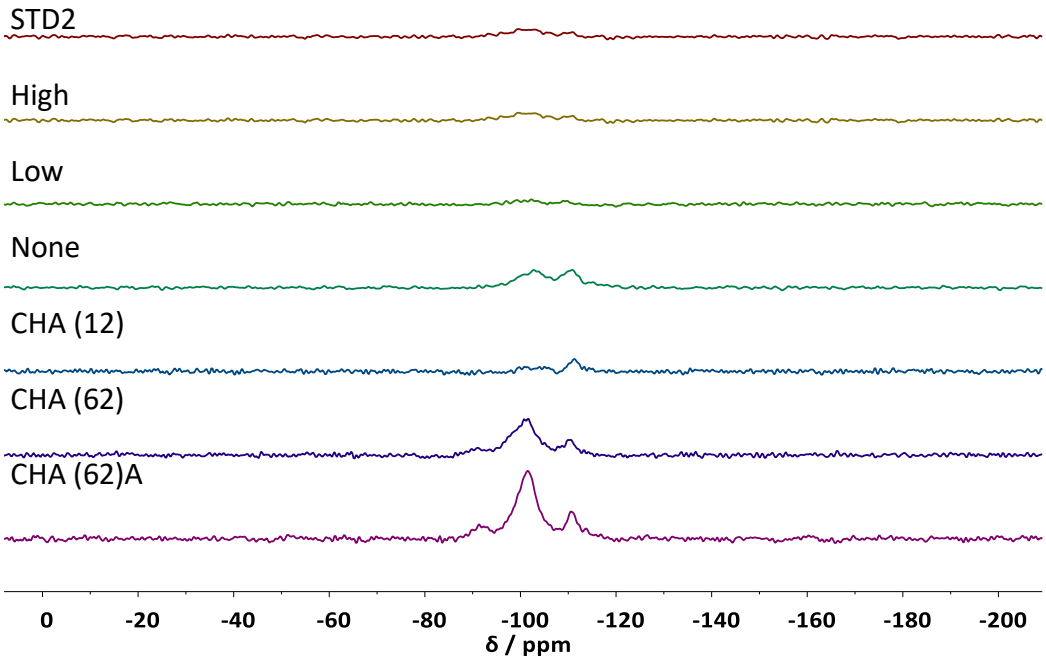

Figure 9: ^{1}H-^{29}Si CP spectra before (A) and after (B) zinc vapour deposition and reaction with methane for CHA samples. All parent samples show the presence of defect sites (Q^3) which are healed to differing degrees after reaction with zinc vapour. (^{29}Si – 79.44 MHz, 8 kHz spin rate)

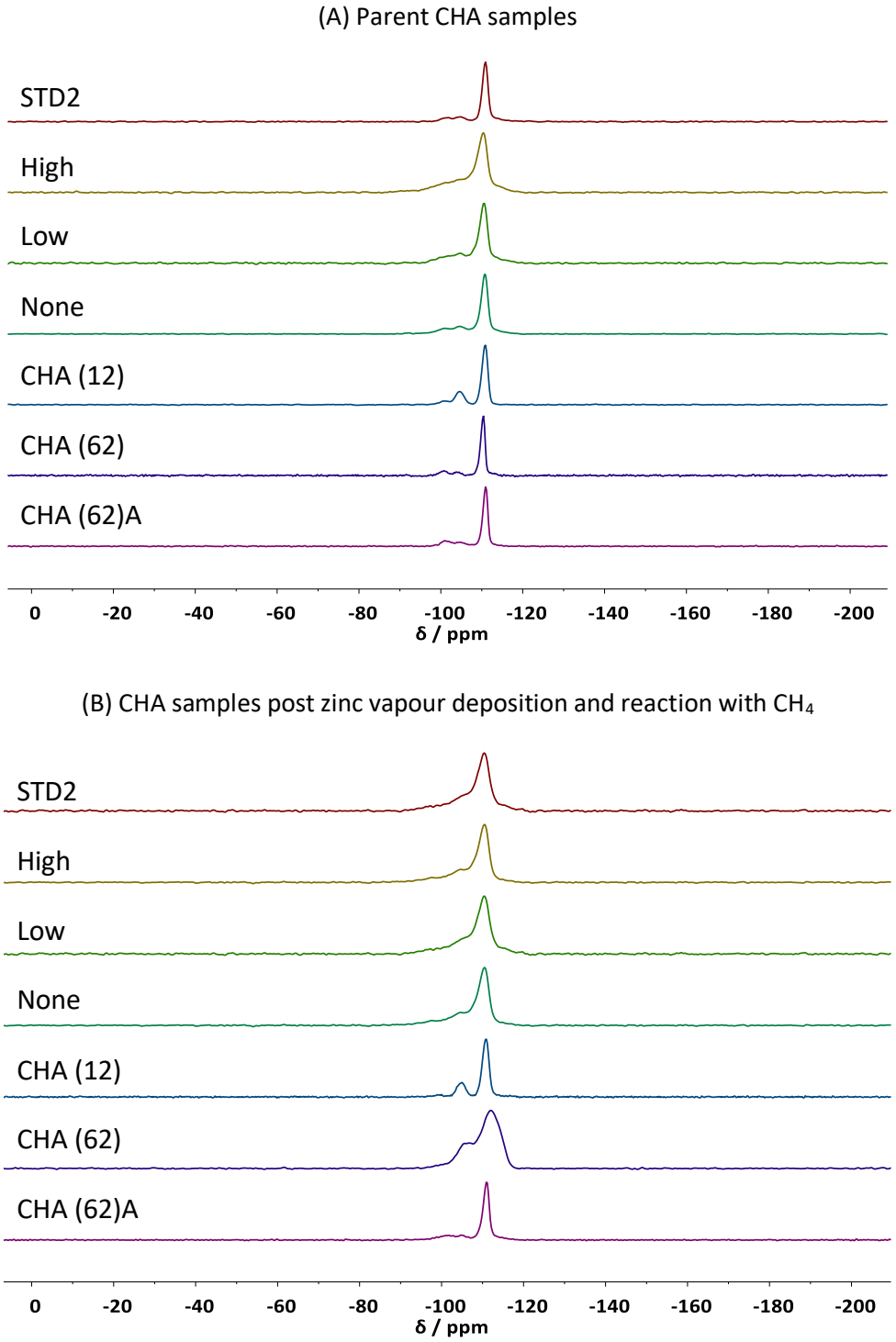

Figure 10: ^{29}Si direct spectra before (A) and after (B) zinc vapour deposition and reaction with methane for CHA samples. Broadening of the signals can be observed for most parent CHA samples after reaction with zinc vapour, likely due to the insertion of zinc into the zeolite framework. (^{29}Si – 79.44 MHz, 8 kHz spin rate)

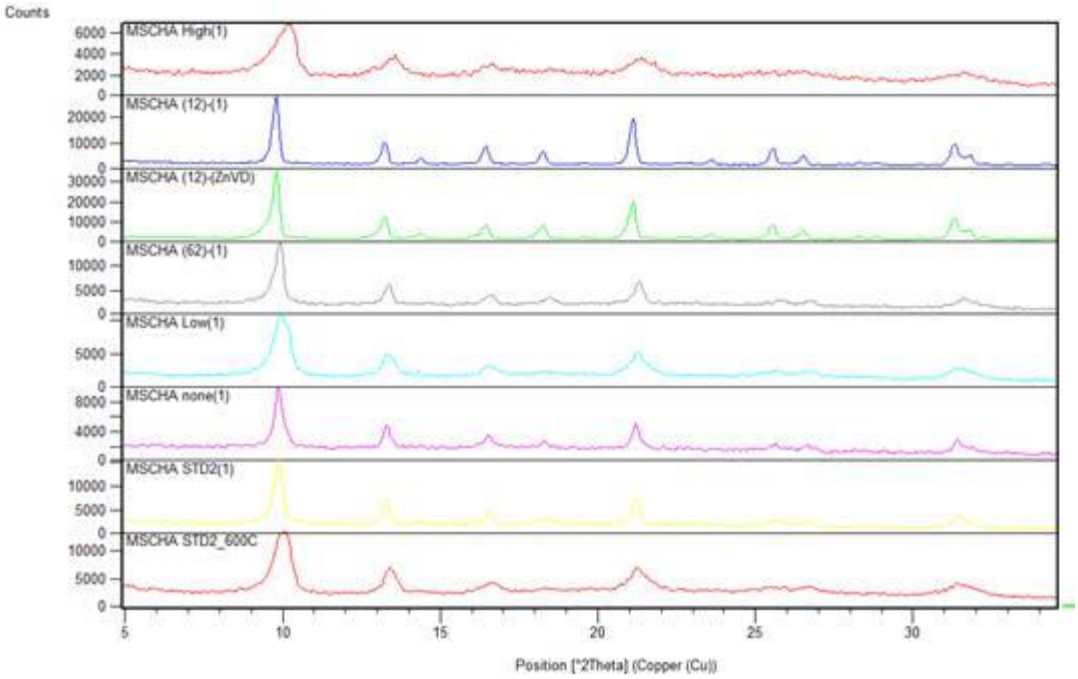

Figure 11: pXRD patterns of CHA samples post zinc vapour deposition and reaction with methane. Analysis was carried out by Julien Devos, KU Leuven and transmission pXRD patterns are shown. All samples show reflections related only to the CHA framework. Varying levels of crystallinity is likely due to crystal size

Table 4: Direct ^{13}C spectra, elemental analysis and percentage Zn active sites for CHA samples. (^{13}C – 100.57 MHz, 10 kHz spin rate)

Sample	Direct ^{13}C spectra	Si/Al	Zn/Al	Percentage of Zn active sites
STD - 1	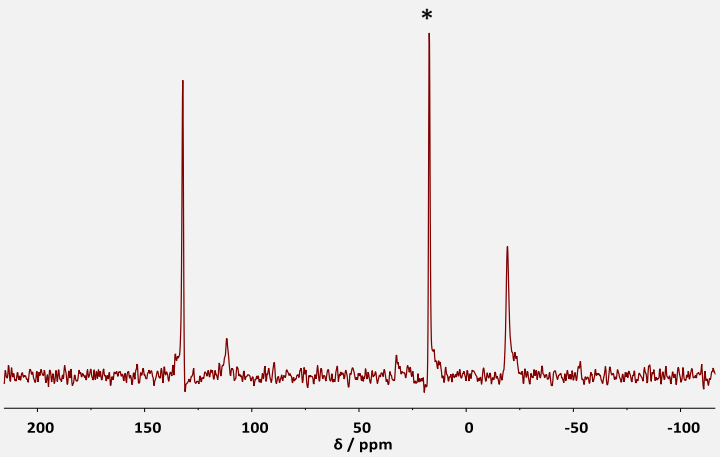 *corresponds to Me groups of HMB used in quantification.	36.0	1.63	3.9
STD - 2	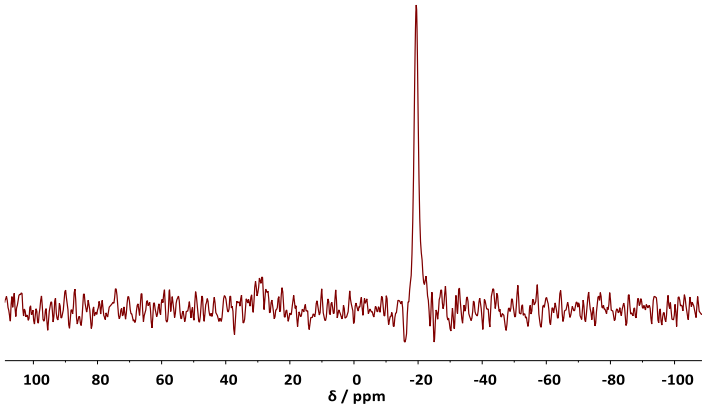	36.6	1.68	4.3

High - 1	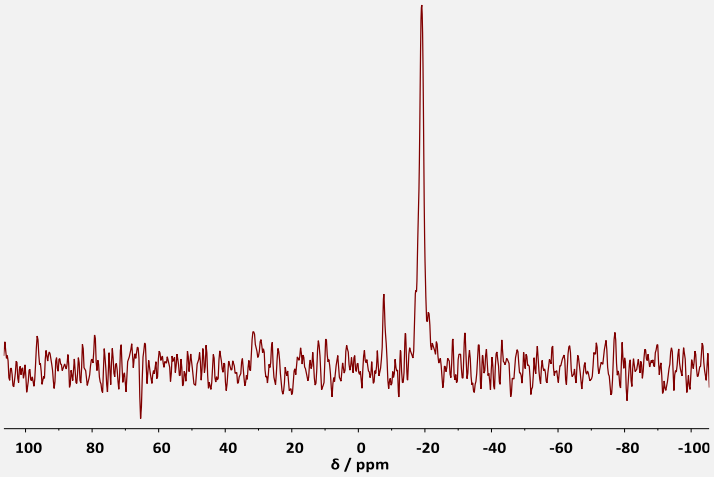	34.5	1.08	3.5
High – 2	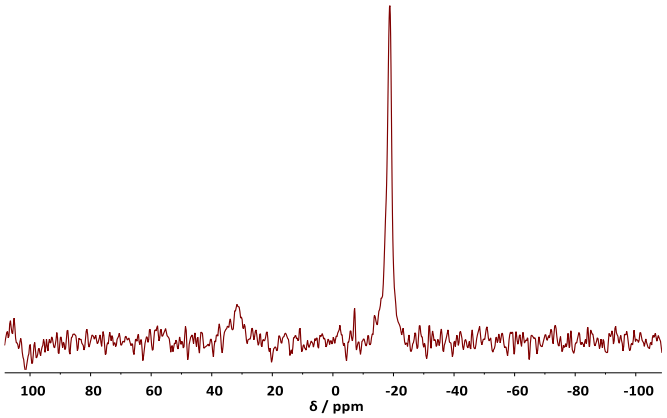	33.4	1.19	2.8
Low – 1	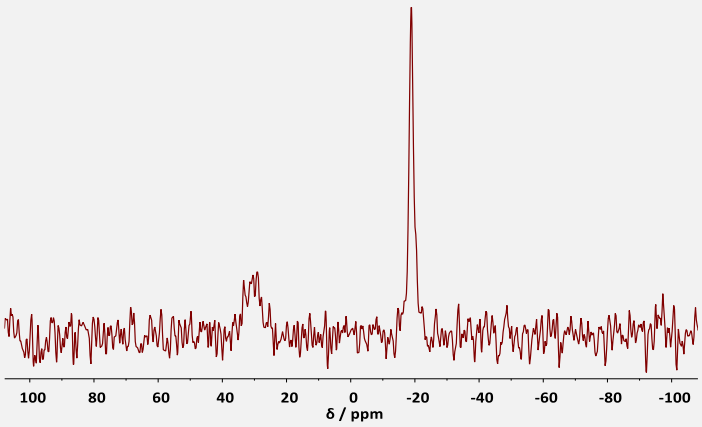	41.9	1.68	3.0

Low – 2	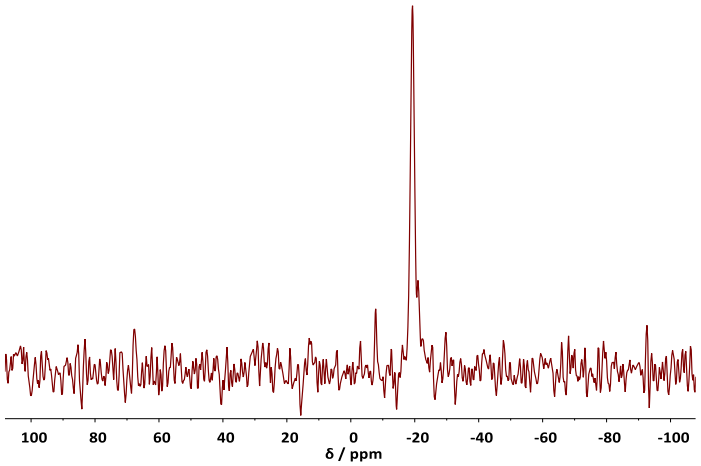	41.3	1.37	4.1
None – 1	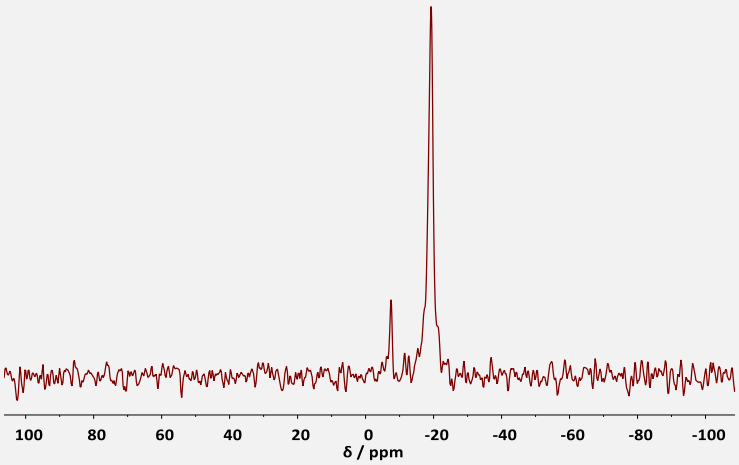	42.3	1.58	2.7
None – 2	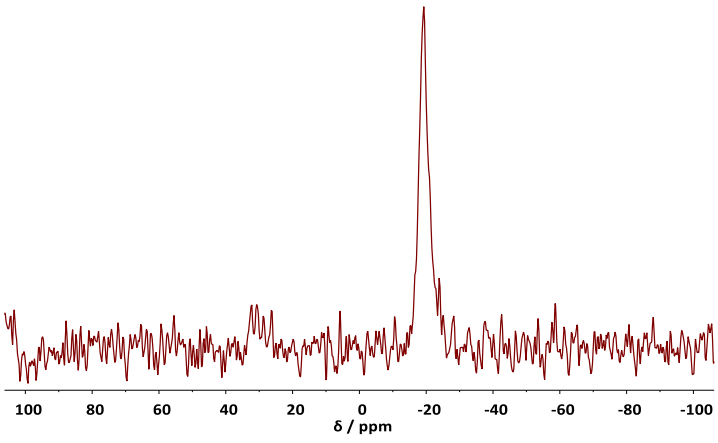	42.9	2.02	3.8

CHA (12) – 1	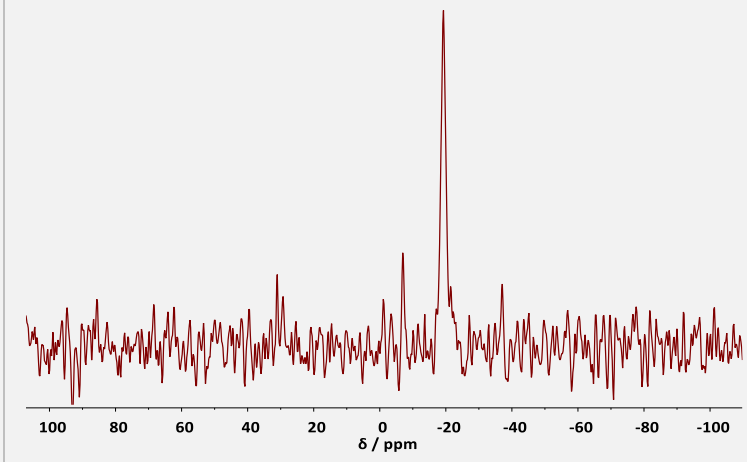	13.5	1.46	6.7
CHA (12) – 2	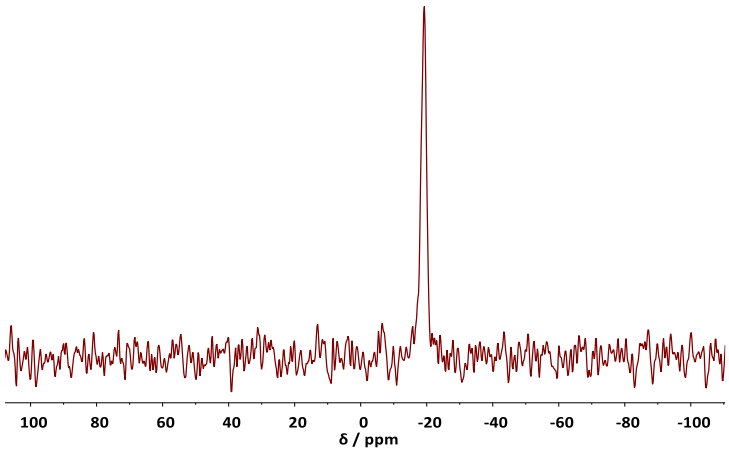	11.9	1.21	4.4
CHA (62) – 1	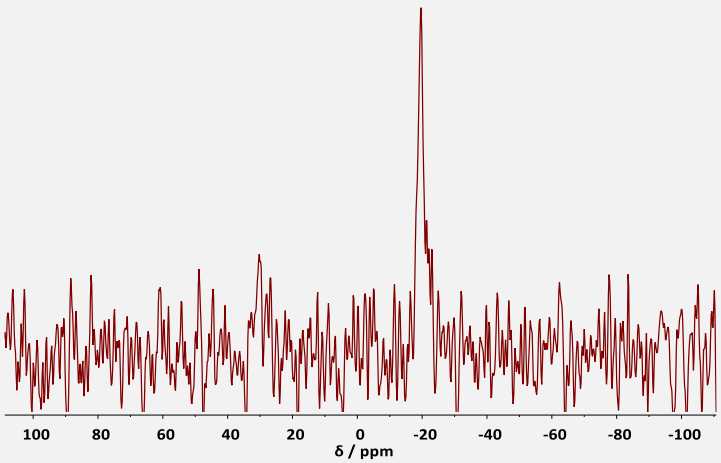	58.3	3.08	22.0

CHA (62) – 2	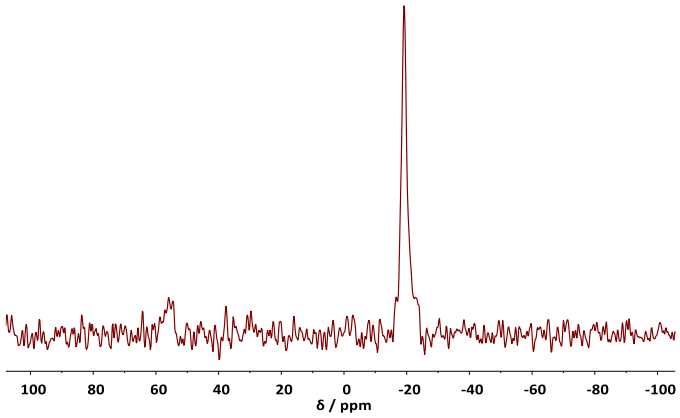	42.3	3.17	16.8
CHA (62)A – 1	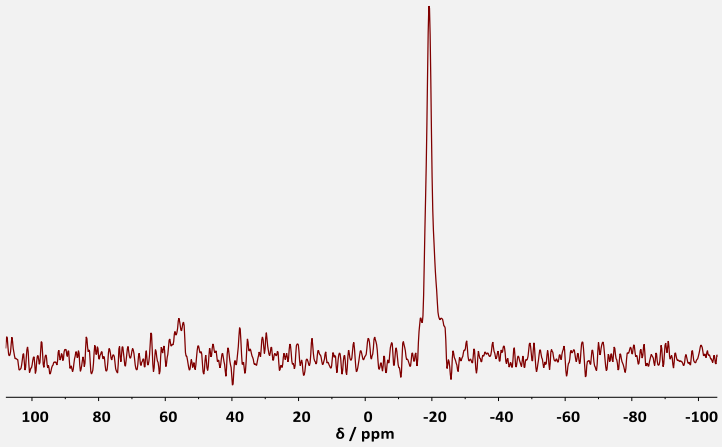	69.8	2.76	32.2
CHA (62)A - 2	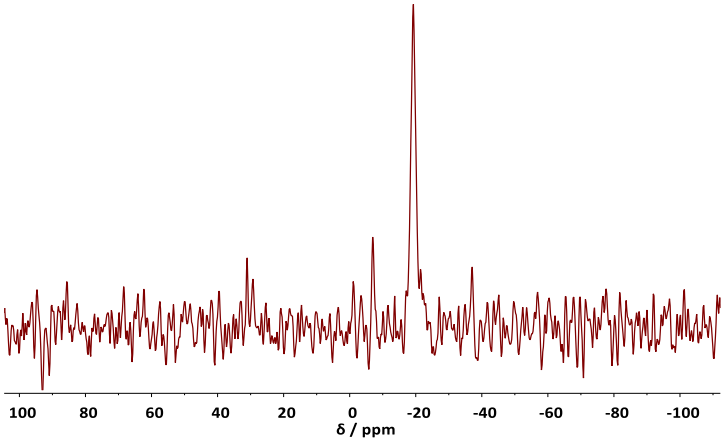	70.0	3.09	13.9

Appendix 4: Further NMR spectra and Deconvolutions for dealuminated MOR samples

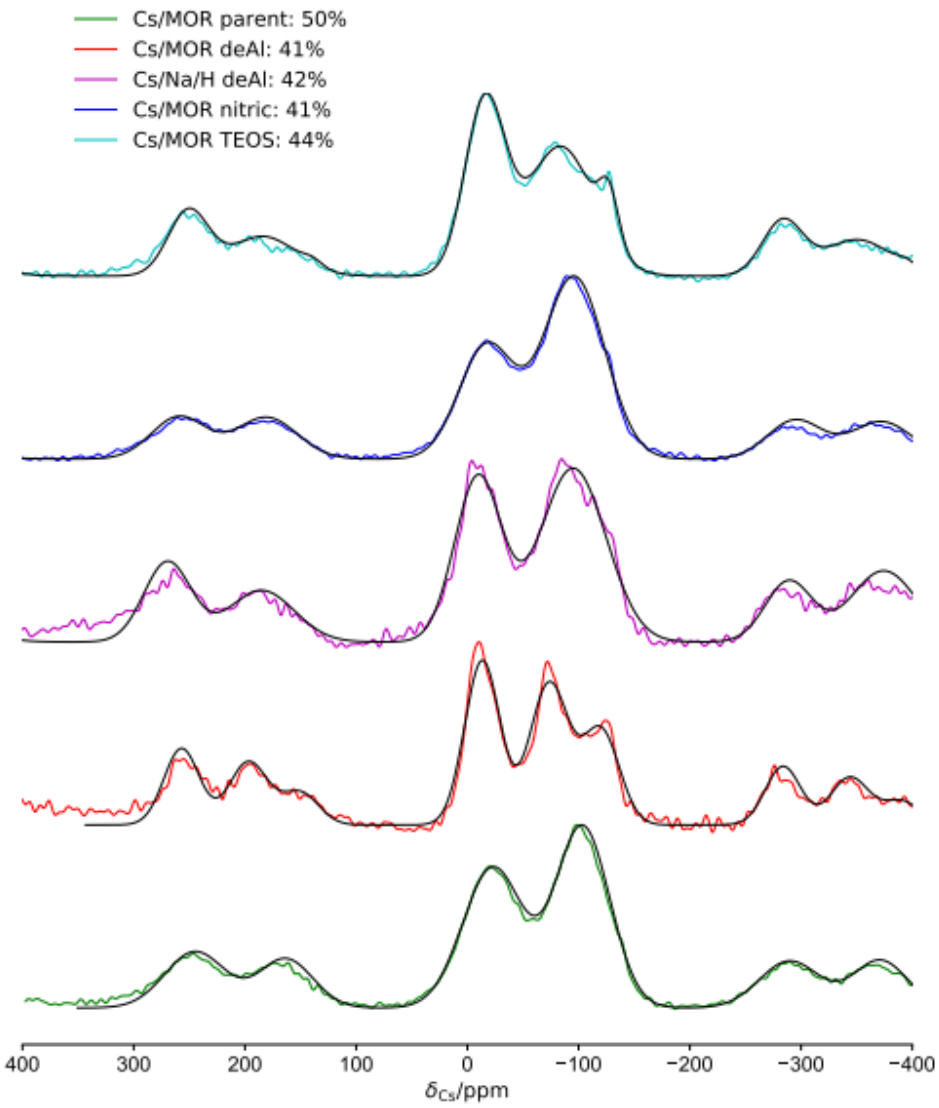

Figure 12: ^{133}Cs NMR spectra comparing real (coloured) and fitted ^{133}Cs data (black).

^{29}Si direct spectra for dealuminated MOR samples:

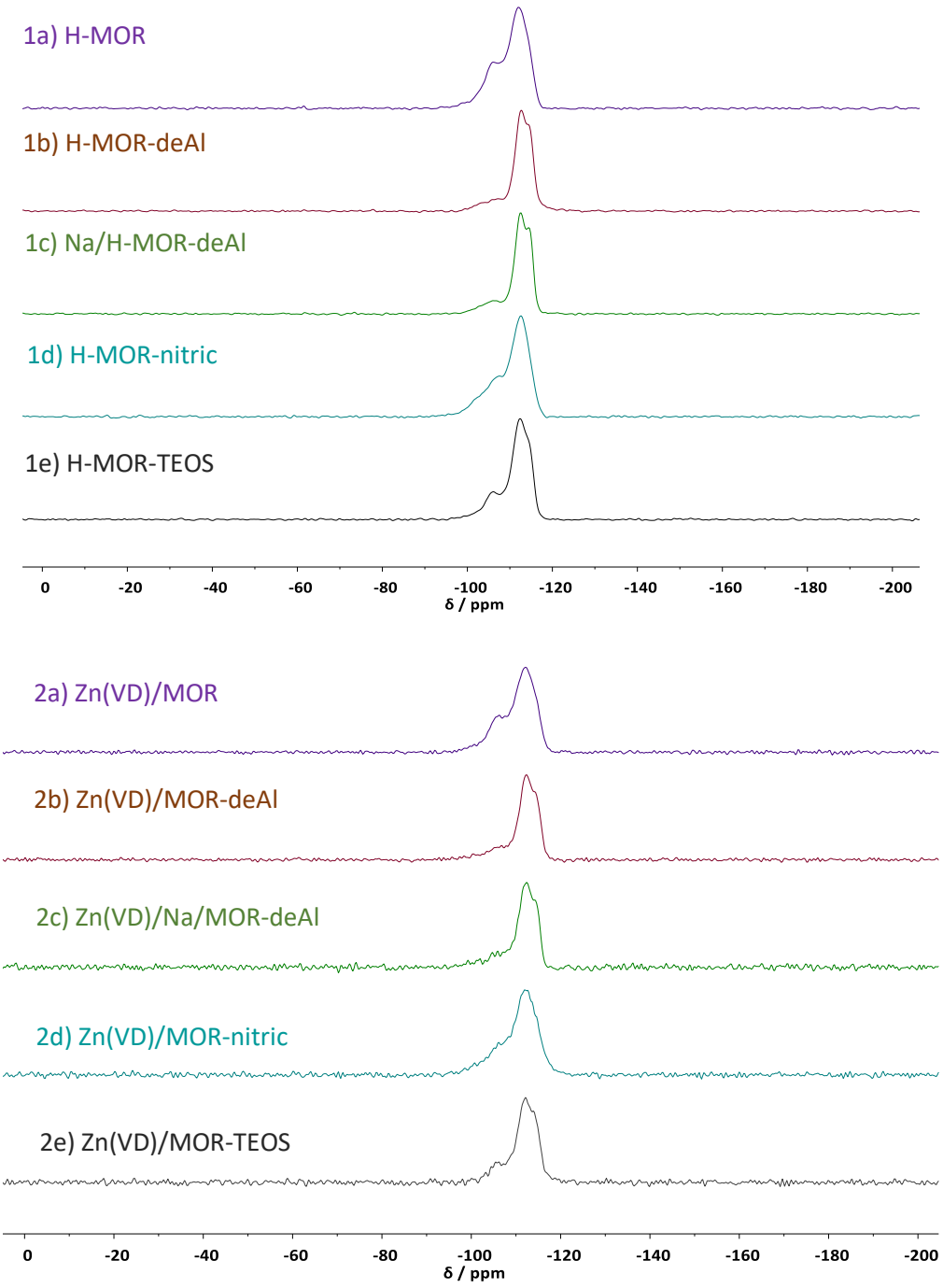

Figure 13: Direct ^{29}Si spectra for MOR dealuminated samples before (1a-e) and after reaction with zinc vapour (2a-e). (^{29}Si – 79.44 MHz, 8 kHz spin rate)

Deconvolution of the 2 peaks of MOR observed in the ^{13}C spectra for Zn(VD)/Na/MOR:

Zn(VD)/CH_4/MOR parent:

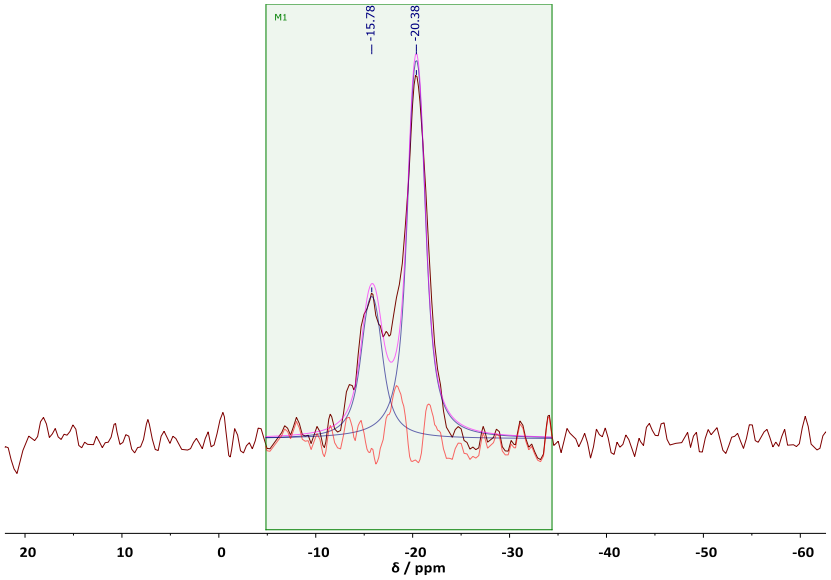

Shift ppm	Height	Width	Area
−15.8	4	259	99
−20.3	11	219	222

Zn(VD)/Na/CH_4/MOR - 38%:

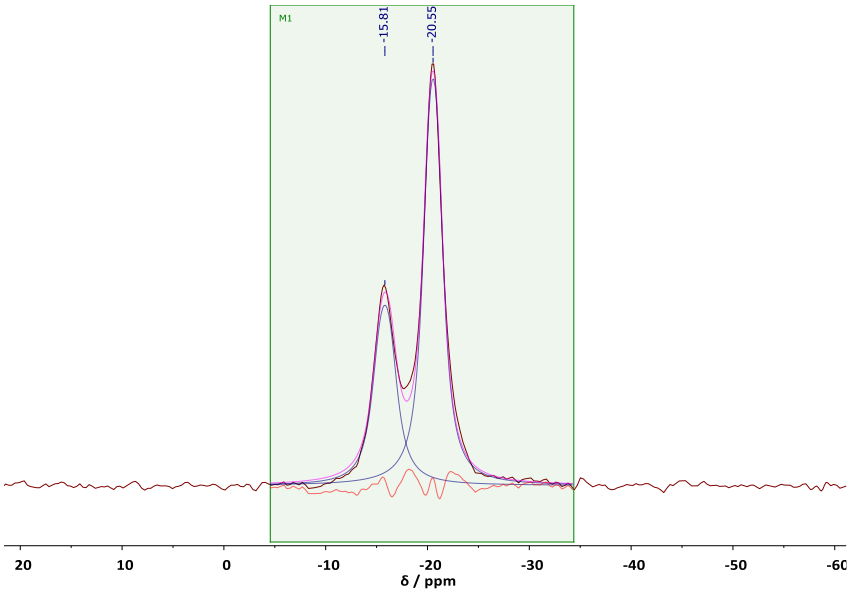

Shift ppm	Height	Width	Area
−15.8	20	259	483
−20.6	46	219	922

Zn(VD)/Na/CH_4/MOR - 58%:

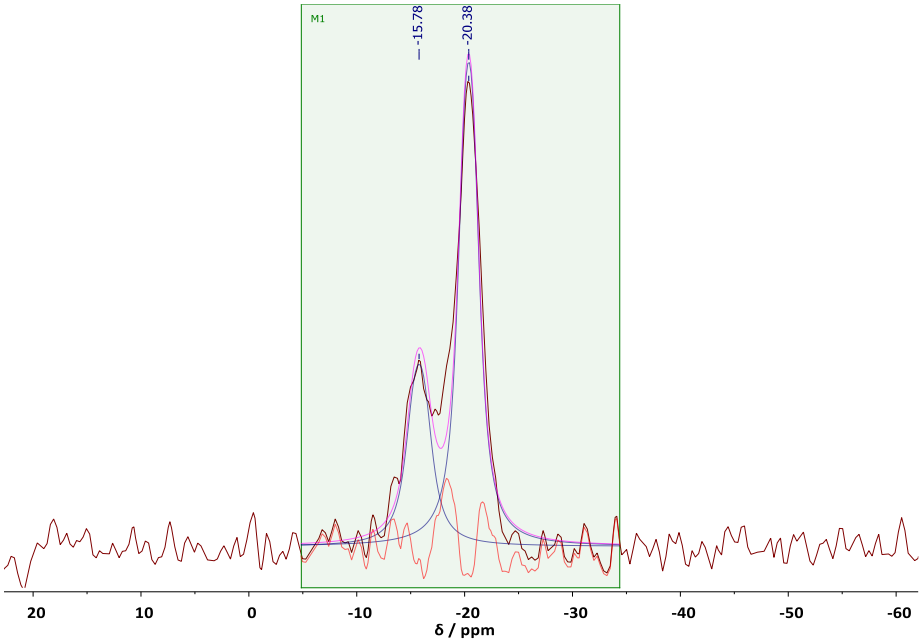

Shift ppm	Height	Width	Area
−15.8	4	259	99
−20.4	11	219	222

Figure 14: Deconvolution of the 2 peaks of MOR observed in the ^{13}C spectra for Zn(VD)/MOR parent, Zn(VD)/Na/MOR (38%) and Zn(VD)/Na/MOR (58%) using MNova

Appendix 5: Further analysis of zinc vapour deposition on partially exchanged Zn(IE)/Na-ZSM-5 and Zn(IE)/Na-MOR

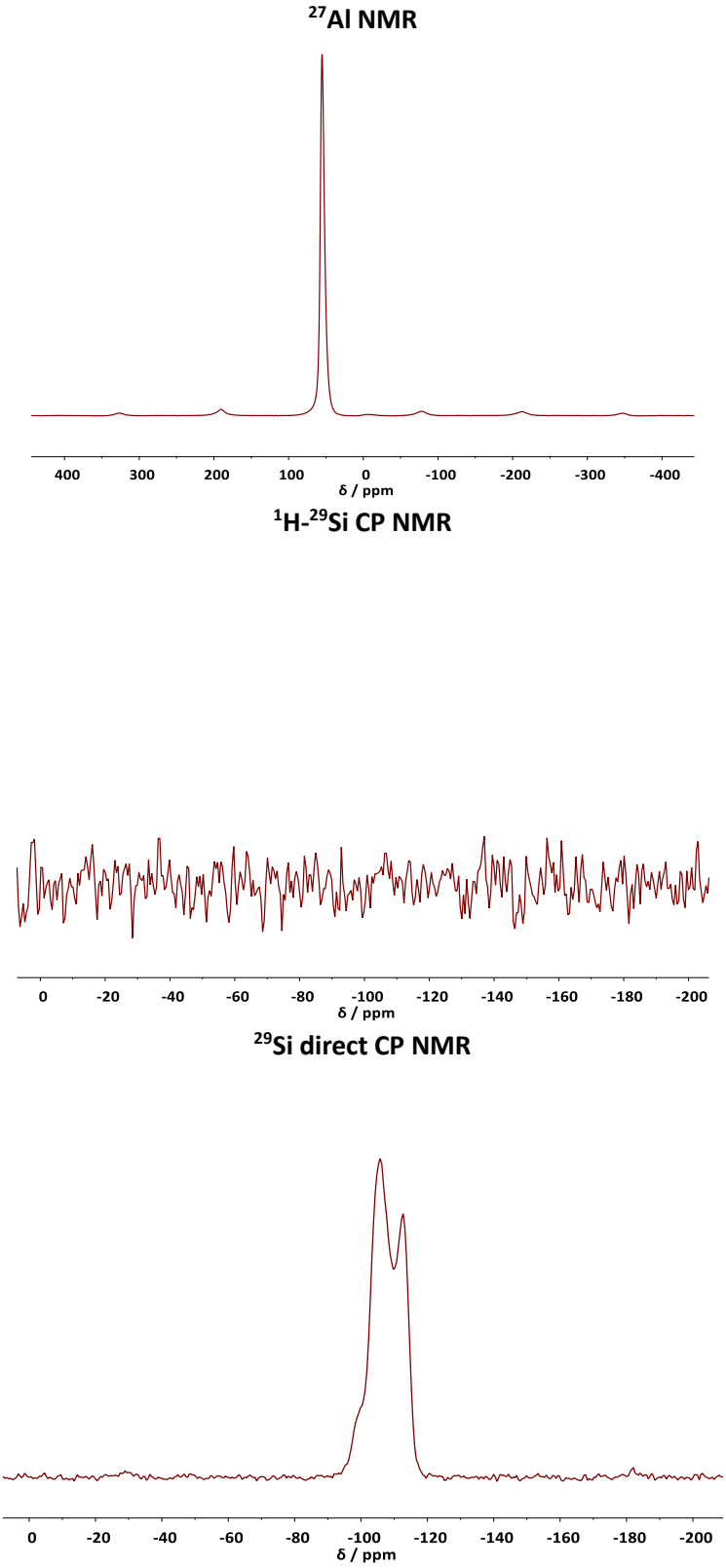

Figure 15: ^{27}Al NMR spectrum and ^{29}Si CP and direct NMR spectra for parent Na-MOR (7) zeolite showing no extraframework Al or defects. (^{27}Al – 104.20 MHz, 14 kHz spin rate and ^{29}Si – 79.44 MHz, 8 kHz spin rate)

Table 5: Direct excitation ^{13}C spectra, elemental analysis and percentage Zn active sites for Zn/Na-ZSM-5 - VD, Zn/MOR and Zn/Na-MOR – VD. *denotes zinc methoxy due to oxygen contamination. (^{13}C – 100.57 MHz, 10 kHz spin rate)

Sample	Direct ^{13}C spectra	Si/Al	Zn/Al	Percentage of Zn active sites
Zn(VD)/Zn(IE)/Na/ ZSM-5 (12.5)	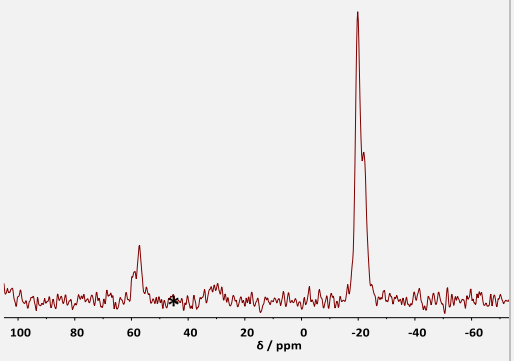	13.1	0.76	3.0%
Zn(VD)/MOR (7)	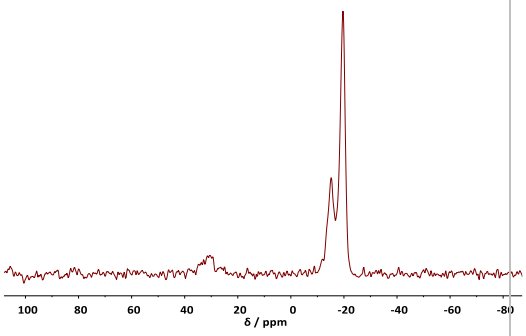	6.6	0.46	1.5%
Zn(VD)/Zn(IE)/Na/ MOR (7)	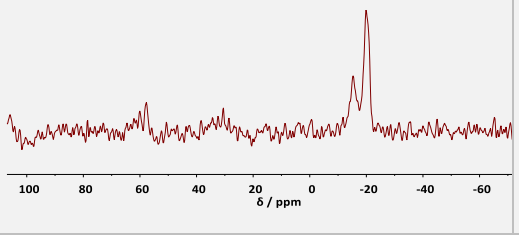	6.6	0.71	1.3%

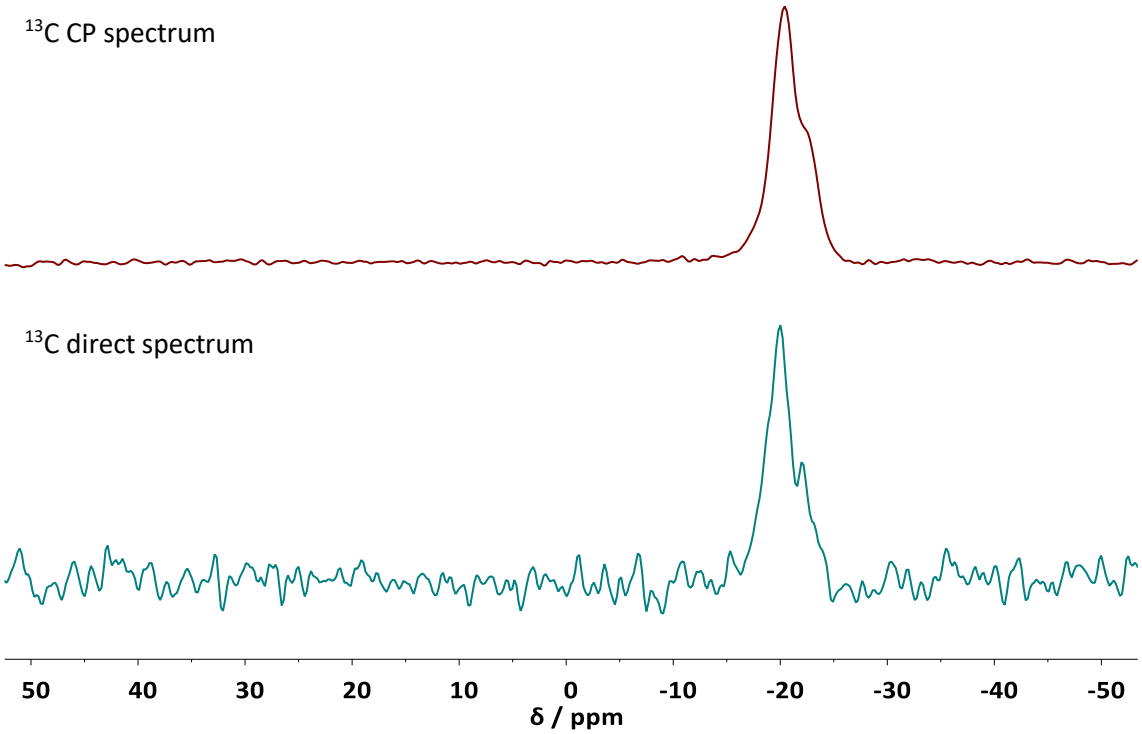

Figure 16: ^{13}C CP and direct excitation NMR spectra for Zn(VD)/Zn(IE)/Na/ZSM-5–2, repeat reaction. The shoulder at −22 ppm is still observed. (^{13}C – 100.57 MHz, 10 kHz spin rate)

Appendix 6: Further analysis on catalysts for MDA reaction

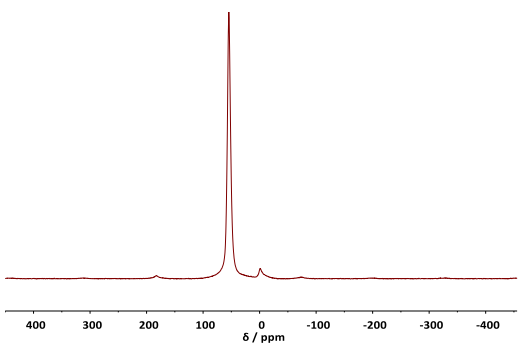

Zn(IMP)/ZSM-5

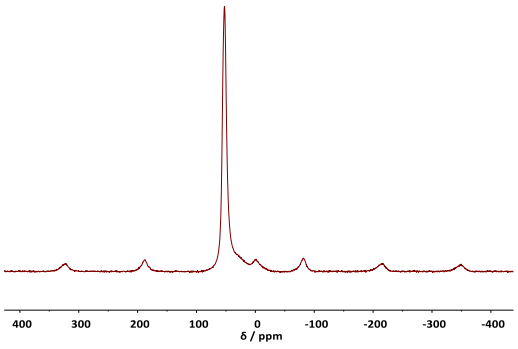

Zn(IMP)/ZSM-5 post MDA reaction

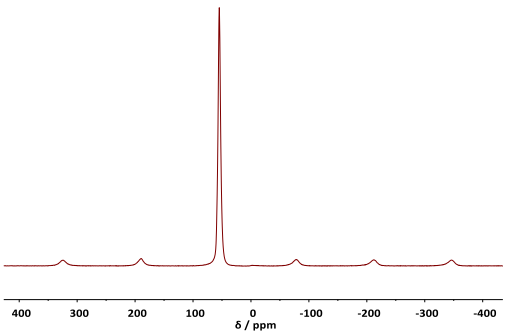

Zn(IE)/ZSM-5

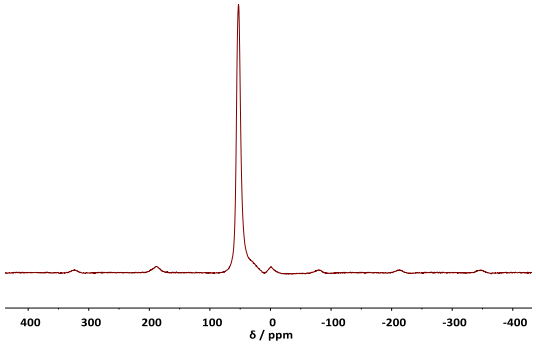

Zn(IE)/ZSM-5post MDA reaction

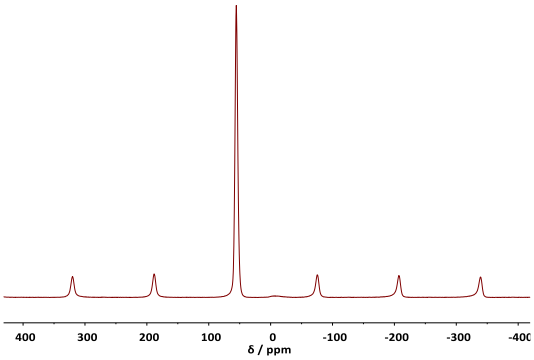

NH_4-ZSM-5 parent

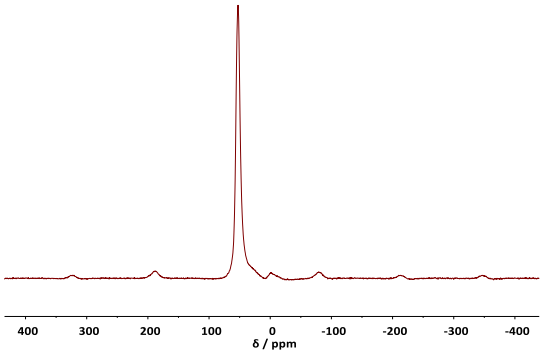

Zn(VD)/ZSM-5 post MDA reaction

Figure 17: ^{27}Al NMR spectra for Zn/ZSM-5 catalyst before and after testing for the MDA reaction. Substantial extraframework Al (demonstrated by a signal at 0 ppm) is not observed after the reaction. (^{27}Al – 104.20 MHz, 14 kHz spin rate)

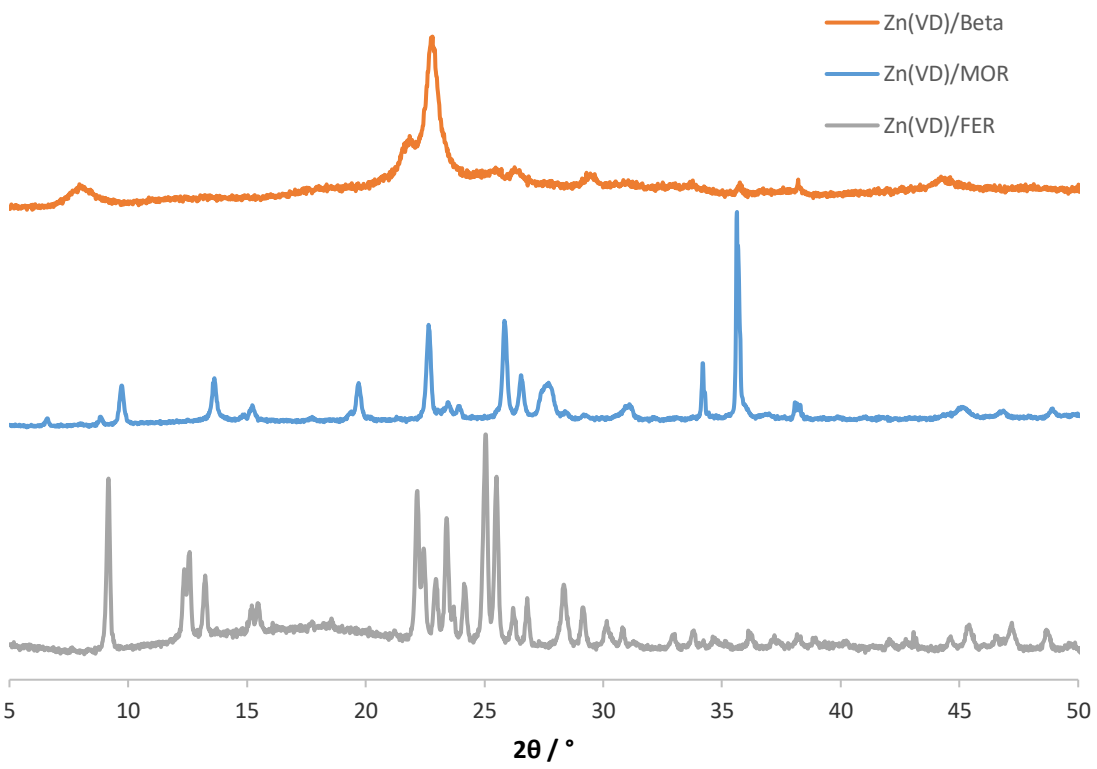

Figure 18: pXRD patterns for Zn/BETA – VD, Zn/MOR – VD and Zn/FER – VD post MDA reaction at 800 °C for 4 h. No framework damage is observed.

Appendix 7: Direct conversion of methane to methanol with zeolites: towards understanding the role of extra-framework d-block metal and zeolite framework type

Samuel Raynes, Meera A. Shah, Russell A. Taylor

Dalton Transactions

PERSPECTIVE

View Article Online
View Journal | View Issue

Cite this: *Dalton Trans.*, 2019, **48**, 10364

Direct conversion of methane to methanol with zeolites: towards understanding the role of extra-framework d-block metal and zeolite framework type

Samuel Raynes, Meera A. Shah and Russell A. Taylor *

The direct conversion of methane to methanol has been an active area of research for over a century, though a viable industrial process is yet to be realised. However, in the last three decades substantial progress has been made in the field through homogeneous and heterogeneous approaches. This perspective article explores the latest advances in the field of direct methane to methanol conversion by zeolites containing extra-framework d-block metals, focussing on first row, d-block metals. The article highlights the similarities and differences in the nature and formation of the active site, the mechanism of methane activation as well as mode of functionalisation, and where appropriate draws on understanding gained from theoretical studies. From the insight obtained into the different roles of the extra-framework metal and zeolite framework we propose new areas of research which the authors believe will be of benefit to the field.

Received 1st March 2019,
Accepted 20th May 2019

DOI: 10.1039/c9dt00922a

rsc.li/dalton

1. Introduction

Methane, the principle component of natural gas, continues to play an ever increasing role as a feedstock for the production of energy and chemicals.[1] While energy production remains the primary use of methane, it is also the feedstock for some of the most important inorganic and organic bulk chemicals produced by the chemical industry. However, bulk chemicals are not produced directly from methane but are instead produced indirectly through the intermediacy of synthesis gas (also known as syngas), a mixture of carbon monoxide and hydrogen. Fig. 1 shows some of the diverse bulk chemicals that are produced from synthesis gas, either by utilising hydrogen or carbon monoxide alone, or by using syngas.

Syngas can be produced from methane in a number of ways[2] but steam reforming (SR) and autothermal reforming (ATR, a combination of steam reforming and partial oxidation) remain the most practised methods.[3,4] Historically it is steam

Department of Chemistry, Durham University, South Road, Durham DH1 3LE, UK. E-mail: russell.taylor@durham.ac.uk

Samuel Raynes

Samuel Raynes received his Masters degree in chemistry from Durham University in 2017. He is now pursuing a Ph.D. with Dr Russell Taylor where his research centres on the use of multifunctional zeolite materials for the cascade conversion of bio-derived small molecules.

Meera A. Shah

Meera A. Shah received her Masters degree in Natural Sciences from Durham University in 2016. She is currently pursuing a Ph.D. with Dr Russell Taylor focusing on methane activation and functionalisation over zinc-modified zeolite materials.

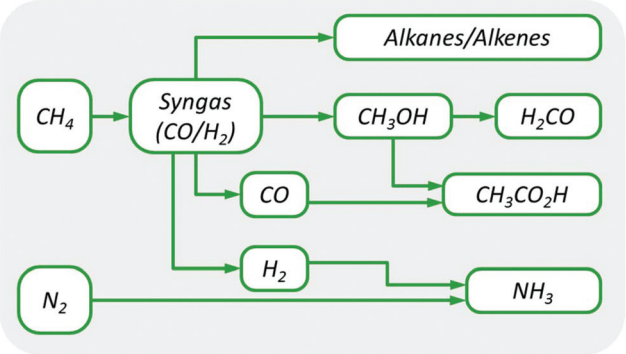

Fig. 1 Flow scheme showing some of the primary products formed from syngas.

reforming that has been most commonly implemented for producing syngas for the manufacture of important basic chemicals (*e.g.*, ammonia and methanol), oil refining, and in many other industrial applications.[5]

The industrially practised approach for converting methane to chemicals *via* syngas has a number of drawbacks. Both SR and ATR of methane utilise catalysts and operate at elevated temperature (800 °C and above) and pressures (30 barg and above).[5] Due to these extreme conditions, plant construction costs are high and the catalysts are prone to deactivation due to sintering or the formation of carbonaceous deposits.[2] Furthermore, depending on the degree of heat exchange, it is estimated that approximately between 20% and 50% of the natural gas feedstock is consumed through energy losses in order to reach the high reaction temperatures required during SR.[3] Further it is reported that trying to improve the energy efficiency of SR would detrimentally impact the syngas production cost.[6] Given the points above, syngas production plants are typically constructed at large scales to optimise material throughput and thus maximise the return on investment. As it stands today, the conversion of methane to chemical products requires a minimum of two chemical manufacturing plants, of which syngas production reportedly accounts for the majority of the investment required. For instance, the production of methanol from methane requires a syngas production plant and a methanol synthesis plant where the latter most commonly utilises a $Cu/ZnO/Al_2O_3$ catalyst to produce the desired product.[7] For methanol production, the syngas plant accounts for approximately 60% of a new production facility.[3] This multistep, large scale approach consequently limits the number of opportunities for deployment of indirect methane conversion technology.

The direct conversion of methane to higher value chemical products has been an area of industrial and academic interest ever since the turn of the 20th century.[8] Moreover the prospect of direct conversion to liquid products has the allure of being able to address two important areas that indirect production cannot. Firstly, associated natural gas (gas produced at oil reservoirs) is often flared on site for environmental and safety reasons, however, in 2015, this amounted to approximately 3.5% of global gas production.[9] Secondly, it is estimated that 40% of natural gas reserves are not economically viable resources as the cost of production is too significant compared to the perceived financial reward.[10] Such reserves are known as stranded gas. The direct conversion of methane to higher value chemicals has the potential to tap into these resources should the requisite plants have lower associated costs than indirect production (such as capital expenditure (CAPEX) and/or operating expenditure (OPEX)). There are of course serious concerns regarding the exploitation of coal, oil and gas for fuels and chemicals, mainly due to the risks of global warming and other environmental issues.[11–13] However, natural gas is regarded as the cleanest of all the fossil based resources and is championed to be the preferred resource in the global transition to lower carbon economies.[14] Therefore, developing technologies that enhance the portfolio of products derived from methane will help to alleviate our reliance on oil for chemical production.

The direct conversion of methane to chemicals has three main areas of interest (1) methane to ethylene, (2) methane to aromatics and (3) methane to methanol (Fig. 2).[15] Substantial progress has been made in all three areas however it is probably methane to ethylene that shows the greatest promise of a commercial process given recent announcements from Siluria Technologies that they have been running a pilot facility in La

Russell A. Taylor

Russell Taylor obtained his PhD in 2007 from Imperial College London (UK) having studied platinum mediated, homogeneous methane oxidation. He subsequently joined BP in 2008, working at the R&D centre in Hull (UK). His research at BP spanned homogeneous catalysis as well as zeolite mediated catalysis and process development. In September 2015 Russell became an Assistant Professor at Durham University (UK), and in 2018 he was awarded an EPSRC Manufacturing Fellowship to develop novel hydrocarbon conversion processes. Research in his group focuses on the development of new catalytic materials and catalytic processes for small molecule conversion.

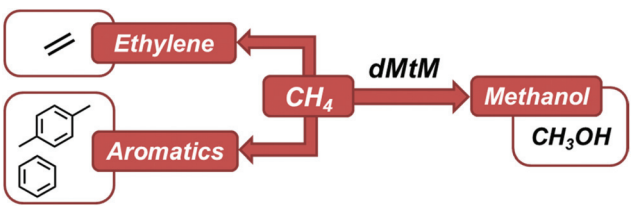

Fig. 2 Schematic showing major products of the direct conversion of methane.

Porte, Texas since 2015[16] and have recently executed a multi-plant technology license with Saudi Aramco to deploy the technology at existing sites.[17]

However it is direct methane to methanol (dMtM) that has been described as the holy grail of catalysis,[18] and has been intensely tackled by both homogeneous and heteregenous catalyst researchers. Perhaps what makes dMtM so tantalising is the very fact that nature has already been able to master this challenging chemistry in the form of methantropic bacteria. These bacteria contain an enzyme, methane monooxygenase (MMO), which is capable of converting methane to methanol at physiological conditions.[19] Two types of MMO enzymes exist, so called particulate and soluble forms, pMMO and sMMO respectively. The sMMO enzyme contains a dinuclear Fe centre in the active site while pMMO contains Cu.[20] The proposed structures of these active sites have inspired much research to develop laboratory mimics and have been a significant source of inspiration in the development of catalysts for dMtM.

The interest in dMtM shows no sign of waning. A number of excellent reviews have been recently published which cover dMtM,[15,19,21–31] adding to the classic reviews in the field.[32–37] Additionally, two opinion pieces proposing methods of overcoming poor reaction selectivity have very recently been written,[38,39] as well as modelling studies detailing optimal temperature and feed compositions for direct methanol production.[40] These articles highlight the collective desire to find a breakthrough that would bring dMtM technology closer to commercialisation.

1.1 Brief history of dMtM

Since the beginning of the 20th century efforts to effect dMtM have been recorded. Articles in 1902 and 1903 reported on gas phase (homogeneous) partial oxidation of methane[8,41] while one of the first dMtM patents dates from 1905 when Lance and Elworthy described the synthesis of methanol by oxidizing methane with hydrogen peroxide in the presence of ferrous sulphate.[42] Although efforts to effect dMtM over heterogeneous catalysts were reported in 1928,[43] the vast majority of subsequent research focussed on dMtM through partial combustion/oxidation in the absence of an added heterogeneous catalyst. However, by the 1960s a range of different supported metals had been identified as competent for dMtM.[31] In 1969, Shilov reported that when methane was heated to 100 °C in a sealed ampoule containing $PtCl_4$ and a D_2O/CH_3COOD mixture, H/D exchange was observed to occur, indicating that methane activation could occur under mild conditions with a homogeneous catalyst.[44] This was the birth of so-called Shilov chemistry and resulted in the first example of direct methane to methanol by homogeneous platinum complexes under remarkably mild conditions (120 °C, in water).[45] Mechanistic studies of the Shilov system elucidated the key steps involved[30] and numerous efforts have been made to improve the system by ligation (see key reviews by Tilset[34] and others[25,29]). However, it has not been possible to bring the aqueous Shilov system close to commercial levels.

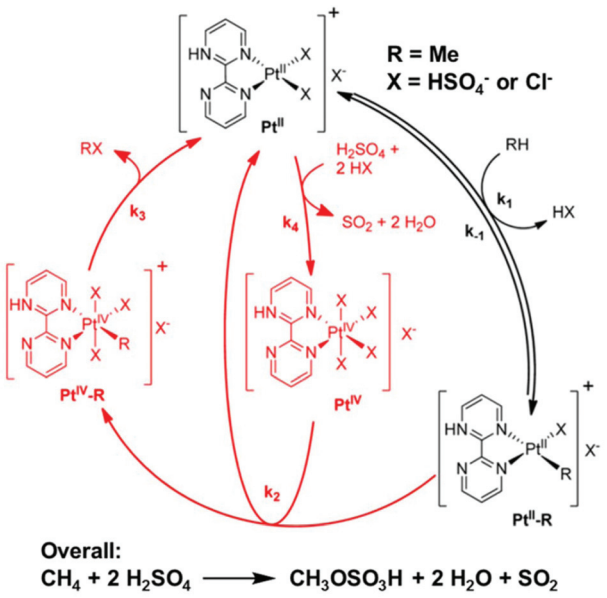

Fig. 3 Proposed mechanism for the functionalisation of methane using (bpym)Pt(TFA)$_2$ in H_2SO_4 in the Catalytica system. Adapted with permission from ref. 46. Copyright 2014 American Chemical Society.

While not a direct conversion process, an important breakthrough in methane conversion came in 1998, with the report from Catalytica which utilised a ligand modified Pt system in fuming sulfuric acid to oxidise methane to methane bisulfate (Fig. 3).[46,47] The system gave a single pass yield of 72% for methane bisulfate. Subsequent hydrolysis of methane bisulfate to methanol gave an overall selectivity of 81%. More recently, Schüth has shown that the Catalytica system can be substantially improved upon by controlling the level of SO_3 in the oleum used and by using K_2PtCl_4 as a catalyst precursor in the absence of additional ligands.[48,49] The improvements led to turnover frequencies (TOFs) three orders of magnitude higher than the original system, giving process parameters which the authors showed are comparable to industrial processes such as the Cativa™ process (methanol carbonylation to acetic acid). However challenges remain in separating methane bisulfate from the reaction mixture and recycling the SO_2 by-product.[48] Furthermore, the inventory of oleum required may be off-putting, though it should be noted that refinery alkylation processes often use concentrated sulfuric acid on very large scales.[50] Although methanol is not produced directly, it is this exact feature of the reaction which prevents over oxidation, giving very high selectivities. This is a result of the methane bisulfate being deactivated with respect to further Pt mediated, electrophilic C–H activation due to the electron withdrawing effect of the sulphate group.

It is unsurprising to note that substantial heterogeneous catalysis research on dMtM has been conducted over early transition metal oxides, which find much use as oxidation catalysts through Mars-van Krevelen type mechanisms.[51] In particular, the commercial production of maleic anhydride *via* partial oxidation of either benzene or n-butane has utilised

oxides of molybdenum or vanadium as catalysts.[52] Correspondingly, both vanadium oxide as well as molybdenum oxide catalysts have been studied for dMtM. Interestingly, catalysts based on MoO_3 and V_2O_5 can also form substantial quantities of formaldehyde during the process.[53–55] By the late 1980s heterogenised molybdenum catalysts were some of the most active materials available for the dMtM reaction.[56–58] In 2008 very impressive methane conversion and methanol selectivity values (13.2% and 78.8% respectively) were reported over an Fe/SiO_2 catalyst.[59] Mössbauer spectroscopic analysis of the catalyst indicated that 81% of the iron is present as supported hematite (Fe_2O_3), while 19% of the iron is embedded into the silica matrix as tetrahedral, Fe^{3+} sites.[59] No further articles on the system have been reported, but these impressive results over Fe/SiO_2 highlight the continuing improvements that are being made using heterogeneous catalyst systems.

By 1990 and beyond, metal-modified zeolites were being reported for the catalytic, direct partial oxidation of methane to methanol with molecular oxygen under flow conditions.[60,61] These pioneering results showed that methanol could be formed selectively under the right conditions. For example, the selectivity reported by Lyons *et al.* was 64% at 4.6% conversion[60] while Walsh reported 20.6% selectivity at 5.5% conversion.[61] However, it should be noted that as early as 1970, metal impregnated zeolites were reported as oxidation catalysts for toluene and xylene in the presence of air.[62] These initial catalytic dMtM studies did not ascertain the nature of the active site but did show that enhanced MeOH yield and selectivity was attainable over such materials (by comparison Walsh reported 47% selectivity at 0.2% conversion over glass beads).[61] In 1995 Panov showed that methanol could be formed from methane by contact with the so-called α-Fe site, supported on ZSM-5.[63] The active site was at this stage unknown. However, the selectivity, after aqueous extraction, was shown to be 75%. This inspired others to further study these stoichiometric reactions in a bid to uncover the mechanism and active site requirements such that the yield and selectivity of the catalytic reaction may be improved. However, as studies have focussed on improving selectivity and mechanistic understanding, the number of studies concerning dMtM catalysis in flow has reduced dramatically. This could be considered detrimental to the industrialisation of dMtM as utilising a cyclical, multistep (and often non-isothermal) approach is less attractive than a continuous flow option, primarily as a multistep process is more complex and has lower thermal efficiency, and therefore a lower economic viability than a continuous flow process.

For a fuller account of the history of the dMtM reaction readers should look at the excellent review by van Bokhoven *et al.*[31]

Despite the progress in heterogeneous and homogeneous systems towards direct (and indirect) methane conversion to methanol, no system has yet been commercialised. This is indicative of the substantial hurdles that remain. In his 2015 article evaluating a dMtM production plant using current catalyst technologies, de Klerk highlights the areas where improvements need to be made in order to challenge the practiced syngas based route.[64] These areas are namely in improving MeOH selectivity/reducing CO_2 selectivity, reducing the need for pure oxygen (which introduces an air fractionation step) as well as keeping the reaction pressure to a minimum to reduce the compressor duty. We note that these areas can all be tackled by catalyst understanding and improvement, and serve as the basis for focus areas for further research. We also note that where methane is a by-product and simply flared it will not be necessary to benchmark against existing syngas based technologies.

1.2 dMtM by metal-modified zeolites

Zeolites are already extensively utilised for refinery and petrochemical processes[65] and are also well known to be able to induce reaction selectivities which differ to those predicted on thermodynamics alone. This can be achieved through the well-known reactant, product and transition state selectivity.[66] Additionally zeolites can impart remarkable reaction selectivity through confinement, where the free energy of the transition state is lowered by interactions with the framework, commonly van der Waals interactions and charge stabilisation by anionic T-sites.[67] The capacity to alter reaction selectivities through subtle substrate-framework interactions has drawn parallels with enzymes,[68] exemplified by the carbonylation of dimethyl ether to methyl acetate, which has been shown to selectively take place in the 8 membered ring (MR) side pockets of MOR.[69,70] Given that zeolites are already made and utilised on industrial scales, and demonstrate a remarkable capacity to control reaction selectivity, it is fair to say that zeolite based catalysts have the potential to be industrial catalysts for dMtM. Subsequently, since Panov reported the highly selective conversion of methane to methanol over iron-modified ZSM-5 (Fe/ZSM-5),[63] although not catalytic, the field has grown enormously to become one of the most promising approaches to dMtM. This perspective focuses on the direct conversion of methane to methanol with first row d-block metal-modified zeolites, and in particular it examines the role of the extra-framework metal and zeolite framework type in the reaction. The perspective will conclude by proposing new areas of research which the authors believe will be of benefit to the field. It should be made clear from the outset that when discussing dMtM in the context of zeolites the reactions are often non-catalytic, *i.e.* substoichiometric reactions, and performed in a multi-step process. In the main body of the text we shall predominantly consider reactions that utilise dioxygen as the source of oxygen as it is the preferred oxygen source for commercialisation. Where appropriate, comparisons may be made to other direct methane conversion reactions over zeolites.

2. Metal-modified zeolites for dMtM

2.1 Fe-Modified zeolites

Perhaps the most historic system within this field, Fe-modified zeolites have been known to be active in the oxidation of

methane since the pioneering work of Panov *et al.* in the early 1990s.[71] Early reports concluded that Fe/ZSM-5 is able to efficiently decompose N_2O at relatively low temperatures (<300 °C) resulting in a highly reactive iron/oxygen species bound to the zeolite surface, termed α-oxygen (α-O) which is active for the direct partial oxidation of benzene to phenol at ambient temperature,[71–73] and was later deduced to be the active species in direct partial oxidation of methane to methanol. The formation of α-O is found to possess first order kinetics with respect to N_2O and cannot be formed by reaction with O_2 or NO.

Due to the presence of inactive spectator iron species, the nature of the active site and factors determining reactivity have been difficult to prove spectroscopically. Originally it was thought that the active precursor associated with the decomposition of N_2O (known as α-Fe) was a binuclear iron species, similar to that observed in MMO enzymes.[74] However, the α-Fe site was later determined to be a mononuclear Fe^{II} species formed *via* irreversible auto-reduction of impregnated Fe^{III} species upon thermal treatment.[75,76] A substantial contribution from Snyder *et al.* reports the use of magnetic circular dichroism (MCD) to elucidate significant structural and electronic information about both the α-Fe and α-O sites in zeolite beta (β).[76] It was found that α-Fe is a mononuclear, high spin Fe^{II} species residing within a square planar co-ordination environment. Further density functional theory (DFT) studies suggest that this square planar environment resides within a β-6MR (see Fig. 4). Similarly, the α-O site is a mononuclear, high spin species which contains an Fe^{IV}═O centre adopting a square pyramidal geometry within the same β-6MR.

The general consensus regarding the methane-to-methanol reaction pathway over α-O sites is that it follows a radical based hydrogen atom abstraction mechanism, although steps following this are debated. Briefly, active α-O species are introduced into the catalyst by N_2O decomposition before methane is subsequently introduced. A hydrogen atom is abstracted from methane by the α-O resulting in an Fe^{III}–O–H fragment and a CH_3 radical. This CH_3 radical may then either react with a further α-O to form Fe^{III}–O–CH_3 that may be extracted *via* hydrolysis or the CH_3 radical may 'rebound' to form an associated Fe^{II}–O(H)–CH_3 which may then desorb forming CH_3OH (Fig. 5).[75,77] Formation of dimethyl ether (DME, CH_3OCH_3) has also been observed *via* the proposed reaction of a CH_3 radical with an already formed Fe^{III}–O–CH_3 group.[75] Kinetic isotope effect experiments suggest that initial C–H bond cleavage is the rate-limiting step in this process.[74] Fourier-transform infrared spectroscopy (FTIR) further supports the presence of the hydrogen atom abstraction process with computational evidence strongly suggesting that the C–H cleavage is performed *via* a radical mechanism with the Fe^{IV}═O species elongating and gaining significant radical character at the transition state, becoming closer to an Fe^{III}–$O^{\bullet-}$ species.[75,76]

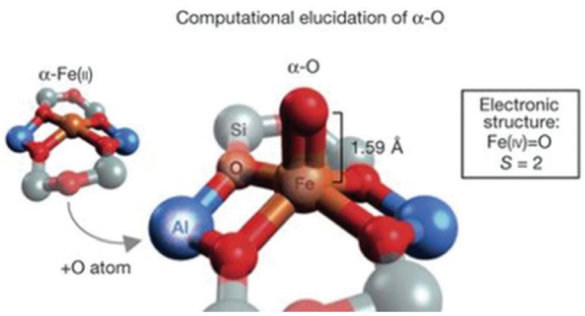

Fig. 4 DFT-optimized structure of α-Fe(IV)═O in the S = 2 ground state and its formation. Adapted with permission from ref. 76. Copyright 2016 Nature.

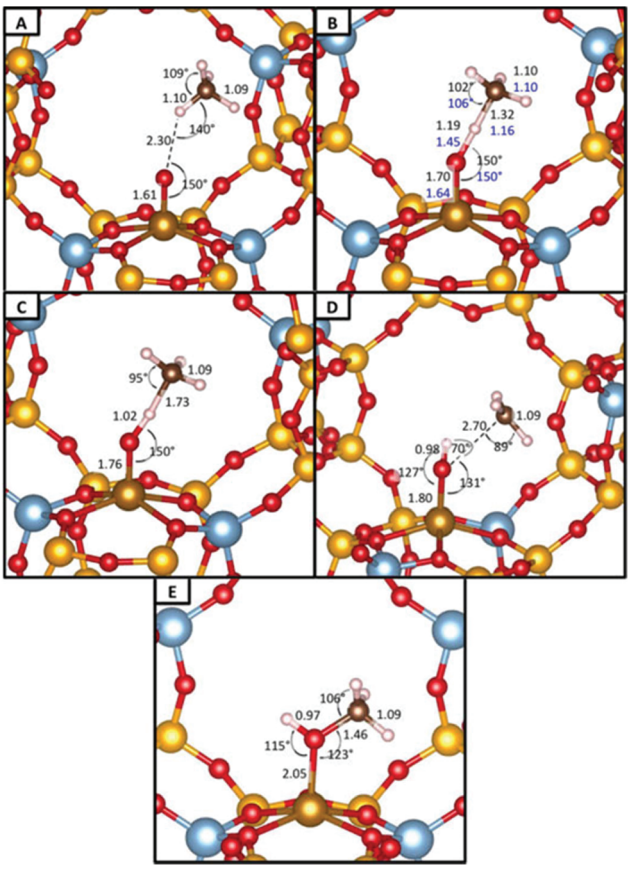

Fig. 5 Structures and the most important intermediates (adsorbed molecule (A), reaction intermediate (C), and adsorbed methanol (E)) and transition states (abstraction transition state (B) and rebound transition state (D)) along the reaction pathway of dMtM over the α-O site. Colour legend: Si atoms, yellow; O atoms, red; Al atoms, blue-grey; Fe atoms, gold; H atoms, white; and C atoms, brown. Black numbers represent PBE-D2 distances (in Å) and angles (in degrees); blue numbers in panel (B) show the optimized RPA geometry. Adapted with permission from ref. 77. Copyright 2016 American Chemical Society.

The remarkable activity of the α-O site is partially attributed to confinement effects within the zeolite channels.[52,77] Periodic and cluster modelling of an α-O site in SSZ-13 have shown that the confining effect of zeolite channels may reduce the energetic barrier to methane activation by over 50%.[77] It is suggested that the confinement effect is predominantly electrostatic in nature and stabilises reaction intermediates and transition states to a further degree than that of the

initially adsorbed methane molecule.[77] The key effect is stated to be the stabilisation of the intermediate species, suggesting that tighter confinement leads to lowered C–H bond activation energy owing to a Brønsted–Evans–Polanyi relationship.

In order to become more viable at large-scale, the requirement for batch-style oxidative pre-treatments and liquid phase extraction should be avoided. Hence, several attempts have been made to produce methanol from methane over Fe-modified zeolites under a continuous or catalytic regime, although success has been limited. The reaction has been reported to occur in a "quasi-catalytic" manner at 160 °C over Fe/ZSM-5 under an atmosphere of CH_4:N_2O with stoichiometry of 1 : 1 and single site turnover number (TON) of 3.6, although liquid phase extraction of products was still required.[78] The >1 TON is attributed to methanol spill over, suggesting that methoxy species can migrate within the framework, reforming the α-Fe site and allowing another catalytic cycle to take place. It is suggested that the reaction temperature (160 °C) is insufficient to promote methanol desorption. A later contribution describes the continuous flow reaction of N_2O and CH_4 over Fe/ZSM-5 at 300 °C.[79] Methanol was observed with only very low selectivity (*ca.* 1%) while CO is observed as the major product. This is attributed to the inability of methanol to desorb from the catalyst, instead migrating to nearby Brønsted acid sites and rapidly producing coke in subsequent reactions akin to those seen in the methanol-to-olefins process. Upon introduction of water in a co-feed, the selectivity to methanol is seen to greatly improve, reaching around 16%. It is thought that the additional water hydrolyses adsorbed methanol and methoxy species, allowing them to leave the catalyst, a hypothesis that is concordant with an observed decrease in coke formation. Activation of N_2O by extra-framework iron species is not experimentally limited to MFI framework types alone with evidence for N_2O decomposition over MOR, FER and FAU having been reported.[80–83] In each case it has been shown that framework oxygen atoms are able to be isotopically exchanged with $N_2{}^{18}O$. N_2O decomposition and subsequent methane activation have also recently been observed to take place on both Fe/BEA and Fe/CHA, resulting in the production of methanol which was able to be recovered by liquid extraction.[76,84] From computational studies, it is found that in the CHA case the α-O site is also stabilised within a 6MR, similar to that of BEA but with subtle differences in their geometries. The mononuclearity of the CHA α-O site was confirmed by Mössbauer spectroscopy.[81] Ferrisilicate, a zeotype material containing only Si and Fe tetrahedral atoms and adopting an MFI framework type, has been shown to be active in the direct conversion of methane to methanol using O_2 as an oxidant as opposed to N_2O.[85] This is of significant interest as α-O sites in aluminosilicates are unable to form from O_2, always requiring N_2O instead. In contrast to Fe-modified aluminosilicate systems which are able to activate methane and form methanol at ambient temperatures, the ferrisilicate systems require much greater temperatures (350 °C) for reaction to take place although the observed methane conversion at this temperature is only around 0.1%. Temperatures even higher still (630 °C) are needed for substantial methane conversion to be observed where methane conversions up to around 30% are seen, although at significant cost of methanol selectivity. The requirement for much higher temperatures to achieve even low-level conversion coupled with the ability to utilise dioxygen as an oxidiser strongly suggest that the ferrisilicates system contains an active site different to that of Fe-modified aluminosilicate zeolites. No mechanism has been suggested as to how this transformation takes place over ferrisilicates and hence a mechanistic comparison with respect to the α-O site cannot be made as yet. For the ferrisilicates system, a higher Si/Fe ratio was shown to result in higher methanol selectivity, although at the expense of percentage methane conversion. Both H- and Na-form ferrisilicates were compared, with Na-forms demonstrating higher selectivity for methanol.

In addition to gaseous phase activation by O_2 or N_2O, several recent contributions have investigated the use of an aqueous phase oxidant, H_2O_2, in the dMtM reaction over Fe-modified zeolites.[86–90] In contrast to what has been highlighted previously, this system is not thought to proceed *via* α-O formation (Fe^{II}/N_2O system) but instead by a mechanism that utilises extra-framework Fe^{III} oxides, intermediately forming methyl hydroperoxide (CH_3–OOH) which is subsequently transformed into the desired methanol product alongside further oxidised products, namely formic acid and carbon oxides.[87]

The initially reported system demonstrated that hydrothermally synthesised Fe-silicalite-1 (0.5 wt% Fe) was able to transform methane into various C_1 oxygenates with a selectivity of 94% at 0.3% conversion within 30 minutes. In terms of oxygenate distribution, 17% of the total selectivity was to the desired methanol product whilst the remaining product was predominantly formic acid.[86] The reaction was carried out in an autoclave under the following conditions: 27 mg of the desired catalyst was stirred in 10 mL of 0.5 M H_2O_2 under a 30.5 bar pressure of CH_4 for 30 minutes at 50 °C. Interestingly, even commercial ZSM-5 containing only trace amounts of Fe (0.014 wt%) was found to be comparably active, achieving 95% total oxygenate selectivity at 0.3% conversion with a similar product distribution. Non-modified silicalite-1 (0 wt% Fe), however, was found to be inactive, achieving 0% conversion under the same reaction conditions. The implication of these results is that at least a low level of framework Fe is required to achieve activity under the employed reaction conditions.

In order to elucidate the role that Fe speciation plays within the catalytic process and to determine whether framework or extra-framework Fe species were the active sites, the nature of the Fe active sites was thoroughly investigated in further reports.[88,89] Although FT-IR, UV-Vis and porosimetry methods demonstrate that the "as-prepared" Fe-silicalite-1 is shown to possess predominantly framework Fe species,[88] it is thought that the active species for methane oxidation is actually extra-framework oligomeric Fe oxide species resulting from high temperature thermal treatment. Upon various thermal treatment temperatures (550, 750, 950 °C) it was observed in the associated UV-Vis spectra that the absorbances corresponding

to framework Fe species decrease upon increasing pre-treatment temperature whilst those resulting from oligomeric and higher extra-framework Fe species increase, suggesting that Fe species are removed from the framework to some degree. The authors suggest that catalytic activity is associated with small oligomeric extra-framework Fe species located within the zeolite micropores. The percentage of Fe species that are oligomeric in nature increases with increasing pre-treatment temperature and a maximum was observed following pre-treatment at 750 °C; treatment at 950 °C was shown to produce fewer oligomeric Fe species and larger Fe clusters and bulk Fe oxides. This data correlates well with catalytic tests which demonstrate that higher temperature pre-treatments result in higher yields of oxygenated products, reaching a maximum at 750 °C and dropping again following pre-treatment at 950 °C.[88] It has been further reported that the presence of other trivalent cations (Al^{3+}, Ga^{3+}) within the system prior to pre-treatment, whilst not constituting catalytically active centres, facilitate Fe removal from the framework and hence increase the formation of active extra-framework Fe species.[89]

It was further demonstrated that addition of Cu^{II} species to the previously described hydrothermally synthesised Fe-silicalite-1 can have a dramatic effect on partial oxygenate selectivity.[86,87] When Cu^{II} was introduced to commercial ZSM-5 (0.014 wt% Fe) by solid-state ion exchange (SSIE), the conversion was seen to remain constant when compared to the unmodified catalyst whereas the selectivity to methanol was seen to increases dramatically from 19% to 83% under the same reaction conditions.[86] Even the introduction of aqueous $Cu^{II}(NO_3)_2$ (10 μmol Cu) to a previously tested system was seen to drastically increase methanol selectivity when compared to the original material at very similar conversions. In contrast, SSIE introduced Cu/silicalite-1 (0 wt% Fe) was seen to be inactive for the conversion of methane under the reaction conditions. This led the authors to conclude that, while Cu^{II} species are not able to perform methane partial oxidation, they are active in preserving the formed methanol and preventing over-oxidation to formic acid and carbon oxides.[87] Under optimised reaction conditions (54 mg catalyst, 20 mL, 1.0 M H_2O_2, $P(CH_4)$ = 3 bar, 30 minutes, 70 °C), Fe-silicalite-1 (0.5 wt% Fe) was seen to produce 8% methanol at 10.5% conversion whilst a bicatalytic system containing Fe-silicalite-1 and SSIE introduced Cu/silicalite-1 was seen to demonstrate a methanol selectivity of 93% at 10.1% conversion.[86] Additionally, the H_2O_2/FeCu-ZSM-5 system has recently been tested in a continuous flow regime under optimised conditions of: 1.5 g catalyst, $P(CH_4)$ 20 bar, Flow (CH_4) = 10 mL min^{-1}, flow (H_2O_2, 0.123 M) = 0.25 mL min^{-1}, 50 °C.[90] In this regime it was observed that high methanol selectivity was able to be retained (92%) at a conversion of 0.5%.

Overall, the active sites (α-Fe and α-O) in Fe-modified zeolite systems have been well characterised, whereas the mechanism of C–O bond formation following initial hydrogen abstraction requires further elucidation. Although a well-established system, potential for exploration of methanol production over different framework types and expansion to continuous flow processes is ripe. A major factor determining the success of Fe-modified zeolite systems will be the ability to use O_2 as an oxidant as opposed to N_2O, which, owing to its energetic nature, is generally undesirable for large-scale industrial usage. In this regard, investigation of methane partial oxidation over ferrisilicates holds promise within this area.

2.2 Cu-Modified zeolites

Since the first report of methane partial oxidation to methanol over copper-modified zeolites in 2005, the field has been subject to intense scientific interest and research.[91] Methanol formation has since been shown to be possible over a wide range of copper-modified zeolite frameworks including: MFI, MOR, FER, CHA, FAU, BEA, LTL, EON, MAZ, MEI, BPH, HEU, SZR, AFX and AEI.[92–94] Within these frameworks, a wide variety of active sites have been proposed for this important transformation.

2.2.1 Active sites for methane partial oxidation in copper-modified zeolites. Unlike iron-modified zeolites in which it is thought that only one site (the so-called α-Fe site) is active for methane partial oxidation to methanol, there have been multiple active sites proposed to exist in copper-modified zeolites. The first site to be proposed for methane C–H bond activation in Cu/ZSM-5 was the bis(μ-oxo)dicopper core (Fig. 6A) that had previously been identified for the decomposition of NO[95] and was thought to be characterised by a strong absorption band at 22 700 cm^{-1} in the ultraviolet-visible-near infrared (UV-Vis-NIR) spectrum.[91] Another active site, a (μ–η^2:η^2-peroxo)dicopper core (Fig. 6B) which is active in nature for O_2 transport by the protein hemocyanin, was also suggested, but was not observed to be active in NO reduction.[91,95,96]

A considerable contribution by Woertink *et al.* utilised resonance enhanced Raman spectroscopy (rR) to further elucidate the active site structure in Cu/ZSM-5.[97] By tuning a laser to the characteristic absorption feature identified with the active site (22 700 cm^{-1}), the Raman vibrations associated with this feature are enhanced, enabling the ~5% active species to be distinguished from spectator Cu. As a result, the bis(μ-oxo) dicopper and (μ-η^2:η^2-peroxo)dicopper cores were able to be discounted due to inconsistencies with the observed rR stretching frequencies. Instead, a bent mono(μ-oxo)dicopper

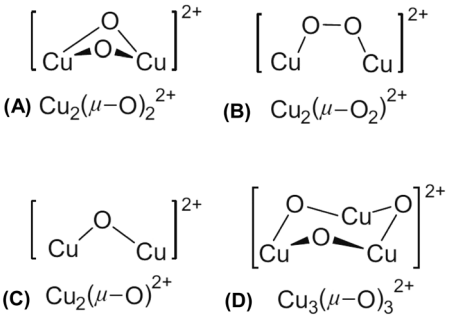

Fig. 6 Cu-Oxo complexes proposed as the active sites for methane activation in Cu-containing high-silica zeolites. Adapted with permission from ref. 122. Copyright 2016 Elsevier.

core (Fig. 6C) was proposed as the active site owing to a series of isotope-sensitive fundamental vibrations at 456 cm^{-1} ($\Delta^{18}O_2$ = 8 cm^{-1}) and 870 cm^{-1} ($\Delta^{18}O_2$ = 40 cm^{-1}) alongside an intense overtone of the latter at 1725 cm^{-1} ($\Delta^{18}O_2$ = 83 cm^{-1}). This intensity pattern closely resembles that seen for mono (μ-oxo)diferric cores.[97,98] The mono(μ-oxo)dicopper species is suggested to exist within the 10MR channel of ZSM-5, bridging two framework aluminium sites separated by two silica tetrahedra. Each copper atom of the mono(μ-oxo)dicopper core is ligated by two oxygen atoms associated with the framework aluminium alongside the bridging oxygen. Normal co-ordinate analysis predicts a Cu–O–Cu bridging angle of 140°. The copper species are proposed to be formally Cu(II), as Cu(III) cannot be stabilised without co-ordination of a further –OH group of which no evidence was detected by rR spectroscopy.[97]

The mono(μ-oxo)dicopper core can be formed by activation in both N_2O and O_2 as evidenced by observation of the UV-Vis-NIR band at 22 700 cm^{-1} that is associated with this active site.[99,100] Activation by N_2O can occur at room temperature by liberation of N_2 with the lowest energy pathway for N–O cleavage—the oxygen bridging mode (μ-1,1-O).[101] Activation by O_2 proceeds at room temperature *via* the formation of a (μ–η^2:η^2-peroxo)dicopper core which can be characterised by a strong UV-Vis-NIR absorption band at 29 000 cm^{-1}.[100] Heat treatment in flowing He or O_2 results in the decrease of the 29 000 cm^{-1} band and a coincidental increase of the 22 700 cm^{-1} band from approximately 448 K, demonstrating formation of the mono(μ-oxo)dicopper core (Fig. 7). This conversion results in the deposition of an oxygen atom on other remote Cu sites within the zeolite as evidenced by $^{18}O_2$ TPD.[100] It has been further proposed that spectator Cu^+ ions in ion exchange sites provide the necessary electrons to reduce the peroxo-bridge.[100]

Larger copper clusters have been both evidenced and predicted as active sites for the partial oxidation of methane in copper-modified zeolite systems. A trinuclear copper core, $[Cu_3(\mu O)_3]^{2+}$, has recently been proposed to exist at the mouth of the 8MR side pocket of Cu/MOR (Fig. 6D).[102] Extended X-ray absorption fine structure (EXAFS) measurements suggest that more than one Cu–Cu scattering path exists within the cluster, suggesting a nuclearity >2. From investigations into the change in acidity of the zeolite upon active site formation, it was shown that two Brønsted acid sites are displaced for every three Cu atoms incorporated into the structure. As a result, it is suggested that the trinuclear cluster is balanced between two aluminium atoms, each separated by three silica tetrahedra.

DFT simulations of mono(μ-oxo)dicopper and $[Cu_3(\mu O)_3]^{2+}$ cores in Cu/ZSM-5 have shown that under standard activation protocols (high temperature calcination in O_2) the trinuclear species is more stable than the binuclear species, whereas the binuclear species is preferentially formed under low partial pressures of O_2.[103] Previously identified binuclear and trinuclear cores alongside clusters of higher nuclearity ($[Cu_nO_{n-1}]^{2+}$ and $[Cu_n(\mu O)_n]^{2+}$, where n = 2,3,4,5) in Cu/MOR have also been simulated by DFT calculations in order to compare their stability and reactivity.[104] It was found that as the cluster increases in size, it becomes both more stable as a cluster and that increased reactivity with methane is strongly correlated with this increased stability.

In small pore zeolites such as CHA, several potential mononuclear extra-framework Cu cations have been identified both experimentally[40] and using DFT calculations.[105,106] Specifically, $[CuOH]^+$ has been suggested to be active for methane partial oxidation in Cu/SSZ-13 and is predicted to be stabilised within an 8MR CHA that contains only one charged aluminium species.[105,106] This species is believed to be formed upon dehydration of hydrated Cu^{2+} species and is characterised by a FTIR stretch at ν(O–H) = 3657 cm^{-1}.[107,108]

2.2.2 Reaction mechanism for the partial oxidation of methane over copper-modified zeolites. Typically, methane partial oxidation over copper-modified zeolites is observed to take place in three distinct steps. Initially, the copper-exchanged zeolite is activated in an oxidative atmosphere using either O_2, at elevated temperature (typically 723–823 K), or N_2O, from as low as room temperature.[91,109,110] The activated material is then exposed to methane at a moderate temperature (approx. 473 K) followed by subsequent extraction of the strongly bound products through contact with water vapour or a suitable solvent, such as a 1 : 1 mixture of acetonitrile and water.[22,91]

Thus far, methane activation over copper-modified zeolites has only been proposed to occur *via* a radical type mechanism with DFT calculations having proved crucial for elucidation of this mechanism and kinetic isotope experiments proving important for determination of the rate-limiting step.[97,103,110,111] The mono(μ-oxo)dicopper core, formally denoted as Cu^{2+}–O^{2-}–Cu^{2+}, is thought to be in resonance with what is effectively a cupric-oxyl species, Cu^{2+}–$O^{\bullet-}$–Cu^{+} (Fig. 8), which possesses significant radical character owing to its singly occupied molecular orbital (SOMO) that is directed into the zeolite channel.[97,103] This resonance form is aptly poised to perform hydrogen atom abstraction from methane to form

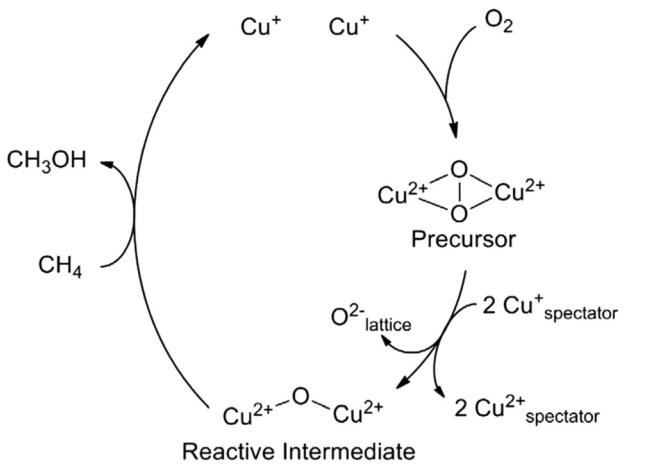

Fig. 7 Formation of the mono(μ-oxo)dicopper core in the presence of O_2. Adapted with permission from ref. 100. Copyright 2010 American Chemical Society.

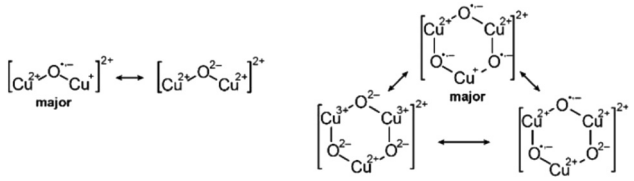

Fig. 8 Possible resonance structures that could be proposed to describe the formal charge configuration in the extra-framework copper species. Adapted with permission from ref. 103. Copyright 2016 Elsevier.

an intermediate Cu–OH–Cu species and a CH_3 radical. This preliminary step shows a considerable H/D kinetic isotope effect of 3.1 at 448 K when the activation energies of CH_4 and CD_4 are compared.[97] This has been further confirmed when the products of a mixed substrate (CH_2D_2) were reacted over Cu/ZSM-5 at 403 K (as analysed by ^{1}H NMR spectroscopy, following extraction into D_2O).[97] In this analysis, a greater product integral is observed for CD_2HOD than for CDH_2OD implying that the rate of C–H cleavage is greater than that of the C–D bond. In a separate study an H/D KIE of 1.6 was determined when CH_4 was substituted by CD_4 in the extracting gas at 483 K over Cu/Na-ZSM-5.[109] These observations alongside DFT predictions show that hydrogen abstraction is the rate limiting step in methanol formation from methane.

The newly formed "free" CH_3 radical intermediate has been predicted to collapse in several ways to form bound intermediates of various stability.[103] Two potential pathways can lead to the formation of a strongly bound, yet desired, methanol molecule (Fig. 9). The first pathway is known as the "rebound mechanism" in which the CH_3 radical reacts directly with the bridging Cu–OH–Cu and forms a sorbed methanol molecule, Cu–(CH_3)OH–Cu. It is also possible that the CH_3 radical reacts with one of the copper atoms before migrating to the bridging oxygen atom; this pathway proceeds *via* an intermediate CH_3–Cu–OH–Cu species. However, the lowest energy pathway calculated proceeds *via* reaction between the CH_3 radical and framework oxygen atoms. This results in formation of a zeolite grafted methoxy group (CH_3–O_{FW}) and reduced copper cluster, Cu^I–O–Cu^I. The production of methanol from this state is predicted to be highly unlikely owing to the need to spontaneously reform the CH_3 radical.[103] It should be noted that alternative mechanistic intermediates have been proposed previously. Prior reports utilised DFT calculations to predict formation of both Cu–OH–Cu and Cu–OCH_3–Cu species as stable intermediates upon hydrogen atom abstraction, resulting in an exothermic methane activation step as opposed to an endothermic step associated with Cu–(CH_3)OH–Cu formation.[97,112] Introduction of water vapour then allows desorption of the methoxy intermediate as methanol.

The mechanism of action for methanol production for the trinuclear $[Cu_3(\mu O)_3]^{2+}$ core is predicted to occur in a similar fashion to the binuclear equivalent. Although formally identified as a mixed Cu(III)/Cu(II) species owing to the formal O(-II) charge of the bridging oxygen atoms, DFT, Bader charge and spin-polarized charge density calculations suggest that the trinuclear species is more aptly described as a radical species, similar to that seen for the binuclear equivalents.[102,103] Therefore this species is proposed to exist as a mixed Cu(II)/Cu(I) system possessing radical anionic oxygen ligands in resonance with the formally charged species and one other form (Fig. 8).

The initial step of methane partial oxidation over $[Cu_3(\mu\text{-}O_3)]^{2+}$ remains to be H-atom abstraction, however, unlike the binuclear mechanism, direct methanol formation (rebound mechanism) is thermodynamically strongly favoured over the formation of grafted, framework methoxy groups (CH_3–O_{FW}) and copper bound methyl species (CH_3–Cu–OH–Cu). The most-energetically favoured pathway in this system, however, is the combination of the CH_3 radical with another μ-oxo bridge associated with the cluster. From this point, adsorbed methanol can be formed by intermolecular proton transfer (Fig. 9).[103]

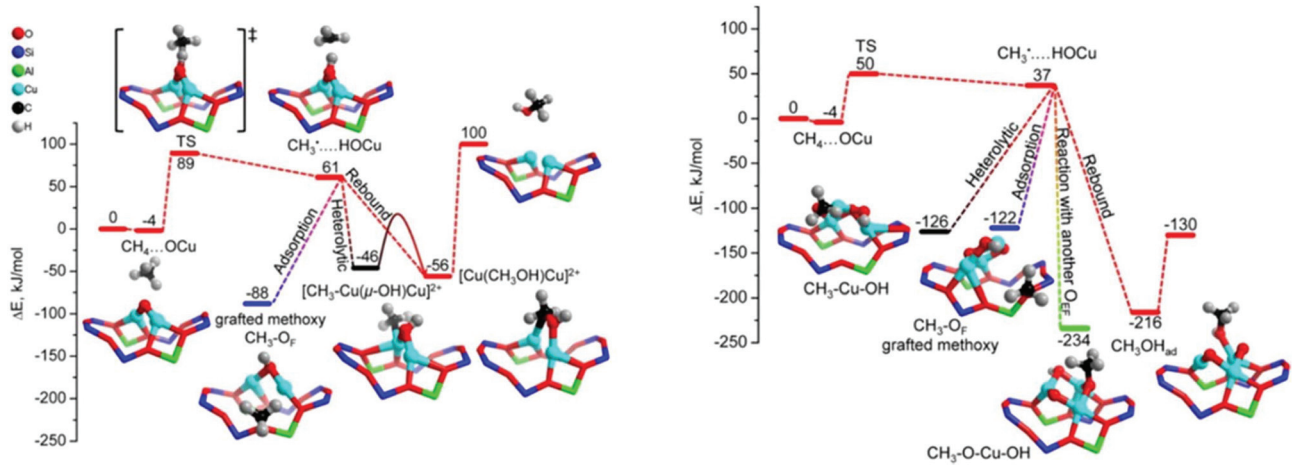

Fig. 9 Reaction pathways for methane oxidation to methanol, and alternative CH_3 recombination routes over binuclear $[Cu_2(\mu O)]^{2+}$ (left) and trinuclear $[Cu_3(\mu O)_3]^{2+}$ (right) sites. Adapted with permission from ref. 103. Copyright 2016 Elsevier.

Methane partial oxidation over mononuclear copper sites, $[CuOH]^+$, has also been predicted by DFT calculations to occur *via* a radical hydrogen atom abstraction pathway.[106] Initially in this pathway, a hydrogen atom is abstracted from methane to form a hydrated copper species and a CH_3 radical. The formed CH_3 radical may then directly insert into $[Cu–OH_2]^+$ to form a bound methanol molecule, although the calculated activation barrier to this transformation renders it unlikely. Formation of $[CH_3–Cu–OH_2]^+$, however, is facile. Experimentally, NIR spectroscopic analysis supports the latter pathway, providing evidence for the existence of a $[CH_3–Cu–OH_2]^+$ or $[CH_3–Cu–OH]^+$ intermediate.[113]

As the methanol produced is strongly adsorbed in all cases, co-adsorption of water is required to either hydrolyse the methoxy intermediate or desorb the formed methanol. It is not considered possible to thermally desorb methanol as increased reaction temperatures may result in further oxidation to CO_2. Following removal of products, it is possible to regenerate both binuclear and trinuclear copper species by reactivation in O_2, hence the reaction pathway may be described as a stepwise cycle as opposed to continuous. In the case of the trimeric active site, $[Cu_3(\mu\text{-}O_3)]^{2+}$, DFT calculations predict that a second C–H activation reaction may occur prior to regeneration of $[Cu_3(\mu\text{-}O_2)]^{2+}$ proceeding *via* an analogous pathway that is similar energetically to the first reaction.[114]

2.2.3 Alternatives to stepwise methanol production: isothermal and direct catalytic conversion of methane to methanol over copper-modified zeolites. As previously stated, most systems that convert methane to methanol over copper-modified zeolites occur in three distinct steps that are performed over a variable temperature range. This represents a significant barrier to commercial exploitation as substantial temperature changes lower both the production efficiency (time is wasted waiting for the reactor to heat or cool) and thermal efficiency (heat is wasted repeatedly heating and cooling the reactor) of the process, hence resulting in reduced profitability.[115] Several recent reports, however, have shown the ability to run this reaction in an isothermal regime using O_2 or NO as an oxidant at 473 K and 423 K respectively.[115,116] Within this mode of operation, both activation and methane exposure steps are run at the same temperature. It is found in the case of isothermal activation with O_2 that methanol yield depends greatly on methane inlet pressure; increasing the inlet pressure from 50 mbar to 37 bar resulted in an increase of methanol yield per gram of catalyst of approximately two orders of magnitude (0.3 μmol g^{-1} and 56.2 μmol g^{-1} respectively). The dependence of methanol yield on methane partial pressure indicates that the active sites present are non-uniform in nature.[115] This may be either due to the presence of additional active species (*e.g.* higher nuclearity clusters, as suggested by the authors),[115] and/or potentially in the extra-framework distribution of the clusters present (such as at channel intersections). It is also feasible that the specific distribution of framework aluminium sites can alter the active site potency as observed for Zn^{2+} sites in ZSM-5.[117]

Recent reports have suggested that certain active sites within copper-exchanged zeolites (specifically Cu/MOR) may be regenerated under step-wise isothermal "anaerobic" conditions, using water as a softer oxidant than O_2.[118] Following initial high temperature activation under He (673 K), the temperature is lowered to 473 K for methane activation and subsequently water is used to concurrently desorb methanol whilst regenerating the active sites at the same temperature.[118] Upon introduction of isotopically labelled water ($H_2{}^{18}O$) into the step-wise reactor, the mass spectrum signal from unlabelled methanol ($CH_3{}^{16}OH$) was seen to decrease whilst that from labelled methanol ($CH_3{}^{18}OH$) increased, suggesting the incorporation of ^{18}O within the active site of Cu/MOR.[118] The suggested mechanism of action for this regeneration is the bridging co-ordination of water between the newly reduced Cu species, $[Cu^{I}–OH_2–Cu^{I}]$, followed by re-oxidation and liberation of H_2, which was observed *via* mass spectrometry.[118] Owing to the bridging nature of this intermediate, it is suggested that only oligomeric copper species (Cu nuclearity ≥2) may be regenerated under these anaerobic conditions.[118] This work, however, has been the subject of strong debate within the associated community, with several technical comments and replies questioning and defending the thermodynamic feasibility of the proposed mechanism.[118–121]

The overarching objective of methane partial oxidation research, however, is to provide a system in which methanol can be produced in a catalytic fashion under continuous flow conditions using O_2 as an oxidant. At the time of writing, literature surrounding methanol production over copper-modified zeolites within a catalytic regime is relatively sparse, yet promising none the less. A recent contribution reports testing of various copper-modified zeolite and silica frameworks for the production of methanol from methane using a feed gas mixture of $CH_4/O_2/H_2O$ at moderate temperatures (483–498 K).[109] Methanol production values of approximately 0.30–3.12 $\mu mol_{MeOH}\ g_{cat}{}^{-1}\ h^{-1}$ were observed over different frameworks and are suggested to be the result of various topologies better stabilising transition states and active sites. Isotopic pulsing by the introduction of $^{13}CH_4$ into the feed gas resulted in detection of a pulse of ^{13}C enriched methanol ($^{13}CH_3OH$) within the mass spectrum; similarly, isotopically enriched $^{13}CO_2$ was observed as a side product during a pulse. While a very valuable contribution to the field, major limitations of the catalytic system are apparent by the fact that approximately 300 hours of time on stream (TOS) were required to generate a cumulative 1.4 $mol_{MeOH}\ mol_{Cu}{}^{-1}$. Furthermore, the high selectivities reported for methanol formation are due to the limited concentration on oxygen in the feed (25 ppm) which clearly limited the maximum possible yield of methanol in order to prevent over-oxidation to carbon oxides.

2.2.4 Effect of framework topology and composition on methane partial oxidation over copper-modified zeolites. The varying topologies and compositions of copper-modified zeolites are thought to have a large effect on not only their ability to produce methanol, but also the nature of the active sites

responsible. As a general observation, frameworks containing a higher Si/Al ratio in which the Al atoms are more dispersed are more likely to support monomeric active sites, whereas those with a lower Si/Al ratio are likely to have several Al atoms within close proximity that are able to stabilise multinuclear copper clusters.[121] Thus far, ZSM-5 and MOR frameworks have been studied most intensively, although many small pore frameworks, such as SSZ-13, have recently been subject to intensified investigation.

2.2.4.1 ZSM-5 (MFI framework). Although not as efficient as other copper-modified zeolites in terms of methanol production, Cu/ZSM-5 has been used to great extent to help characterise the active sites involved in methane partial oxidation, their formation and the reaction mechanism. Cu/ZSM-5 is suggested to host various active sites depending upon the Cu loading and Al distribution with the framework which can have a major effect on methanol production.[122] The major active site within Cu/ZSM-5 is suggested to be the bent mono (μ-oxo)dicopper species, characterised by the UV-Vis-NIR band at 22 700 cm^{-1}.[89] Evidence for the existence of trinuclear active species in Cu/ZSM-5 has been published recently;[122] DFT calculations also predict that the trinuclear species is indeed more stable than the binuclear species in the MFI zeolite framework.[103] At particularly low Cu loadings (or in a zeolite with highly disperse Al atoms) multinuclear species cannot form and mononuclear species are formed instead, resulting in relatively low methane partial oxidation activity. As the loading of copper increases, it becomes more likely that two Cu atoms will be proximal enough to one another to condense and form a binuclear site (providing there are sufficient Al atoms to stabilise it). Upon further increase in Cu loading, the same logic is applied and trinuclear species may form. Once all potential framework sites for cluster formation are occupied, monomeric Cu species may be exchanged onto isolated Al atoms and CuO_x may form.[122] Cu exchanged onto the surface of ZSM-5 is thought to be in the form of CuO_x and inactive in methane partial oxidation.[123] There is an argument to be made, however, that the Cu species within the channel and at channel intersections reside in different local environments, and hence have differing reactivity towards methane partial oxidation.[122]

2.2.4.2 Mordenite. Although ZSM-5 was the first zeolite framework to be investigated for dMtM, the vast majority of the research regarding methane partial oxidation over copper-modified zeolites has been performed with regard to Cu/MOR as it is typically observed to produce a higher methanol yield.[91] At the 8MR windows of the side pockets, Cu/MOR has been suggested to possess both binuclear and trinuclear clusters capable of performing methane partial oxidation.[91,102] Recent spectroscopic observations[124] and DFT simulations[114] have further suggested that Cu/MOR possesses two mono (μ-oxo)dicopper species predicted to be distinct with respect to their siting within the 8MR side pocket.[114] The UV-Vis-IR band originally associated with a single activated Cu/MOR species at approximately 22 000 cm^{-1} has instead been suggested to be comprised of two bands centred at 21 900 cm^{-1} and 23 100 cm^{-1}.[124] Interestingly, these two different sites demonstrate substantial reactivity differences despite very similar geometric and electronic structures. It was further noted that only one of the two active sites is stable above 603 K.[124] Very recently it has been reported that the two species observed are the result of confinement within the multidimensional structure of MOR.[125] Confinement of the $[Cu_2O]^{2+}$ dimer in the 8MR side pocket of MOR gives rise to a lower activation barrier as a result of stabilisation of the transition state through van der Waals contacts with the framework. This effect of confinement, sometimes known as the nest effect,[126] is substantially less well known than the other shape selective effects imparted by zeolite micropores. Interestingly, confinement in the 8MR side pockets of MOR has been shown to give rise to a remarkable increase in reaction rate, and therefore selectivity, in the carbonylation of carbon monoxide to form methyl acetate.[69,127] Additionally, the role of confinement within zeolites in a number of other catalytic systems has been recognised by the Iglesia group.[67,128,129] The ability of confinement to selectively enhance the rate of one reaction over another through transition state stabilisation is an enticing mechanism by which to "break" the themordynamic limitations on methane partial oxidation (or change the selectivity outcome of the partial oxidation of methane).

Owing to the amount of methanol extracted, it was previously determined that approximately 5% of Cu atoms were active in the conversion of methane to methanol over Cu/ZSM-5.[97] However, X-ray adsorption near edge structure (XANES) studies have demonstrated that over Cu/MOR approximately 60% of Cu^{II} species change structure upon methane introduction and are reduced to Cu^{I}.[130,131] In a later contribution, it has been shown that the fraction of copper species that undergo reduction correlates well to the amount of methanol produced.[132] It was also observed that multiple oxidation/reduction cycles were required to obtain a representative view of long-term performance of methane partial oxidation over Cu/MOR, as it is suggested that the copper species present equilibrate over many cycles.

Recent *operando* X-ray absorption spectroscopy (XAS) and high-energy-resolution fluorescence-detected (HERFD) XANES spectroscopy investigations into the active sites of Cu-exchanged MOR strongly suggest that the active species in the systems tested is a dicopper species.[133] This hypothesis is supported by two crucial pieces of evidence; first, a Cu-MOR material was tested in which approximately one methane molecule was activated for every two Cu ions within the material. Subsequently, the methanol productivity across a range of materials and reaction procedures was observed to increase with a slope of 0.5 as the concentration of what is identified spectroscopically as the active Cu species increases. Within this contribution, the highest methanol yield to date over Cu-modified zeolites is reported at 170 $\mu mol_{MeOH}\ g_{cat}^{-1}$ using a Cu-exchanged mordenite with Si/Al = 7 and Cu/Al = 0.18.[133]

The presence of various counter cations has been shown to have a large effect on both the speciation of active sites within

Cu/MOR and subsequent methanol productivity.[121,134,135] It is broadly observed that Cu/MOR samples prepared by ion-exchange from a H-form parent zeolite perform better in terms of methanol productivity than those prepared from a alkali/alkaline earth metal exchanged parents (X-form, where X = Na^+, K^+, Mg^{2+}, Ca^{2+}), a phenomenon that is explained in two ways. Firstly, whilst H^+ ions exhibit a preference for exchange position within the 12MR channel of MOR, it is suggested that both Cu^{2+} and Na^+ ions exhibit a thermodynamic preference for exchange sites within the 8MR pore mouth and hence compete with one another for this exchange position.[134] It can therefore be assumed that the statistical likelihood of two or three Cu^{2+} ions existing within the 8MR at a proximity close enough to form multinuclear active site clusters is greatly diminished in X-form parents when compared to H-form parents.[134] This is supported by an observable decrease in methane conversion over Cu/MOR possessing various counter cations (Na^+, K^+, Mg^{2+}, Ca^{2+}) when compared to H^+ at similar copper concentrations. Secondly, it is argued that the presence of proximal Brønsted acid sites (H^+) increases stability of the produced methanol, preventing over-oxidation to carbon monoxide and dioxide.[135] This conclusion is drawn from an observed maximum methanol selectivity over Cu/MOR species containing the highest proportion of Brønsted acid sites.

2.2.4.3 Small-pore zeolites. Recently, copper-modified small pore zeolites, such as SSZ-13, have gained substantial interest as potential materials to facilitate methane partial oxidation.[94,113,136] In particular, Cu/SSZ-13 has been reported to produce competitive quantities of methanol per copper atom to both previously spotlighted zeolites, Cu/ZSM-5 and Cu/MOR, at similar Si : Al ratios.[94,109,136] Much of the recent literature suggests that isolated copper ions, in the form of $[CuOH]^+$, are responsible for the transformation of methane to methanol over Cu/SSZ-13 (as mentioned in section 2.2.1) as opposed to the multinuclear clusters observed for larger-pore zeolites.[105,106,133]

Importantly, Cu/SSZ-13 has not only been shown to produce methanol in the standard stepwise process, but has also shown great potential in a continuous regime utilising both O_2 [109] and N_2O[136] as oxidants. Maximum methane conversion and methanol production rates over Cu/SSZ-13 (H-form parent) and using N_2O as an oxidant were observed when employing a gas composition of 30% CH_4, 30% N_2O, 3% H_2O (balance He) at 573 K, resulting in production of 55 $\mu mol_{MeOH}\ g_{cat}^{-1}\ h^{-1}$. The greatest methanol selectivity, however, was observed at a lower temperature of 543 K and lower Cu loading, implying that at a higher temperature, selectivity is sacrificed for production rates.[136] When using O_2 as an oxidant and a feed gas mixture of $CH_4/O_2/H_2O$, the maximum yield recorded over several different frameworks was 3.12 $\mu mol_{MeOH}\ g_{cat}^{-1}\ h^{-1}$ as a result of catalysis over Cu/CHA.[109]

Given the potential realised for confinement to promote the partial oxidation of methane, we expect that additional progress in the field will be made by exploiting zeolites which have small pores or more importantly small channels and side pockets. For an in-depth review of 8MR zeolites, readers are suggested to see the excellent review by Dusselier and Davis.[137] Interestingly, until recently, the highest reported methanol yield to date, 86.1 $\mu mol_{MeOH}\ g_{cat}^{-1}$, utilised zeolite omega (MAZ structure), which contains an intersecting 8MR small pore network alongside a discrete 12MR channel.[92] However, this has now been surpassed once again by MOR which notably contains an 8MR side pocket.[133]

2.3 Zn-modified zeolites

In 2004, Kazansky *et al.* reported heterolytic CH_4 bond dissociation over Zn exchanged zeolites.[138] Since then, a number of groups have gone on to show that methane can be partially oxidised in the presence of dioxygen over zinc modified zeolites. A major advantage of these zinc based systems is the ability to form an active species without an initial high temperature oxidation step, which is required for iron and copper modified zeolites. Hence, these materials are of great interest industrially as an isothermal process could be developed.

Framework bound Zn^{2+} cations are believed to be responsible for C–H activation but the mechanism involved is still highly debated. The zinc species introduced in to the zeolite is dependent on a number of factors: the zeolite topology, Si/Al ratio, method of zinc introduction and also any further thermal treatment carried out.[139]

Two key ways of introducing zinc into zeolites are incipient wetness impregnation and ion exchange using a decomposable zinc salt. These methods can introduce a variety of zinc species into the zeolite: isolated Zn^{2+} ions which sit at cation exchange sites within the zeolite, $[Zn–O–Zn]^{2+}$ clusters formed through the condensation of partially hydrolysed $[Zn–OH]^+$ extra-framework ions and ZnO clusters, though ion exchange methods result in predominantly the introduction of Zn^{2+} cations.[139,140] The presence of multiple zinc species makes it difficult to determine which exact species is responsible for C–H activation and subsequently a variety of different mechanisms have been proposed.

Chemical vapour deposition (CVD) methods can also be used to introduce zinc into zeolites. Vapour deposition with Zn^0 powder involves the exchange of Brønsted acid sites (BAS) for Zn^{2+} ions *via* a redox reaction evolving H_2.[141] Under certain zinc vapour deposition conditions, additional zinc species have been detected. A small fraction of paramagnetic isolated Zn^+ ions have also been detected by EPR spectroscopy upon contact of metallic zinc vapours with H-ZSM-5.[142] In the presence of large quantities of zinc, diamagnetic $[Zn_2]^{2+}$ dimers have also been observed which upon UV irradiation increases the number of Zn^+ ions present by one order of magnitude.[143] However, neither the Zn^+ species or $[Zn_2]^+$ dimers have been reported to react with methane. CVD of dimethyl zinc leads to surface grafted $[Zn\text{-}CH_3]^+$ species which can be converted to Zn^{2+} ions through reaction with H_2 or oxidised to ZnO clusters.[139]

The levels of exchange can vary with the method of zinc introduction. Through collection of molecular H_2 produced upon zinc vapour deposition, Kazansky *et al.* showed that full

exchange of BAS occurs.[138] Substitution through impregnation or ion exchange methods normally results in lower exchange levels.[139] This is particularly evident in high silica zeolites where there is a low framework charge and potentially a high degree of separation between Al tetrahedra. Reduced zinc loading is often ascribed to the difficulty of stabilising the formal 2+ charge associated with the Zn^{2+} ions in high silica zeolites.[140,144]

2.3.1 Mechanism of C–H activation in zinc exchanged zeolites. Understanding the mechanism of CH_4 activation in zinc exchanged zeolites is essential for the progress of the fundamental and applied chemistry of these materials. Zinc exchanged into the MFI micropore network, Zn/ZSM-5, has been the most studied system for C–H activation. However, the mechanism of activation is still under debate.

In 2004, Kazansky *et al.* were the first to report that heterolytic CH_4 bond dissociation can occur at room temperature on isolated Zn^{2+} sites in Zn/ZSM-5 as determined through diffuse reflectance infrared fourier transform spectroscopy (DRIFTs) studies, having observed the formation of a zinc methyl species and a framework BAS as demonstrated in Scheme 1.[138]

Solid-state NMR spectroscopy has also been a key technique in confirming the formation of the Zn-CH_3 species. Kolyagin *et al.* were the first to observe a signal at $\delta = -20$ ppm from the reaction of CH_4 within Zn/ZSM-5 at ambient temperature.[145] The upfield chemical shift is characteristic of methyl groups in different organozinc compounds implying the presence of a surface zinc methyl.[146] The peak position was found to be independent of methane loading suggesting the presence of a well-defined surface species. The intensity of the line increased considerably in a ^1H–^{13}C CP/MAS NMR spectrum in comparison to a direct excitation spectrum. This indicates the peak corresponds to a rigid surface species strongly attached to the surface. This evidence presented by Kolyagin *et al.* strongly suggests that methane activation at ambient temperature takes place by dissociative adsorption over Zn sites resulting in the formation of a Zn-CH_3 species and a framework BAS.[145] DRIFTS and NMR spectroscopy have shown that upon initial exposure to methane, an intermediate is formed in which a methane molecule is adsorbed onto an isolated zinc cation.[138,147] Following thermal treatment, a C–H bond of this intermediate is heterolytically cleaved between the zinc centre and a framework oxygen atom. The Zn^{2+} species acts as a Lewis acid with the CH_4 σ(C–H) orbital donating electron density into the Zn-4s orbital, while the framework oxygen atom acts as a Lewis base, leading to C–H bond cleavage.[117] This Zn^{2+} species at the mononuclear active sites, as opposed to other zinc species formed through ion exchange mechanisms, is also active for H_2 dissociation as shown through IR spectroscopy studies.[117]

However, other mechanistic theories have been presented using different active sites. A ^{13}C NMR signal at $\delta = 58$ ppm corresponding to a zinc methoxy species ($ZnOCH_3$) led Xu *et al.* to suggest homolytic C–H bond cleavage is possible over a $[Zn–O–Zn]^{2+}$ cluster.[148] This Zn/ZSM-5 sample was interestingly prepared through Zn vapour deposition which should lead to the presence of predominantly Zn^{2+} ions only. The suggested mechanism involved the formation of a methyl radical ($^{\bullet}CH_3$) which can then interact with the zinc cluster to produce the zinc methoxy species. This zinc methoxy species was reportedly formed in a 3 : 1 ratio to the zinc methyl. As both species are present, Xu *et al.* suggests that both heterolytic cleavage over Zn^{2+} sites forming the zinc methyl species alongside the homolytic cleavage forming the methoxy species on $[Zn–O–Zn]^{2+}$ dimer can occur, with the methoxy species being favoured according to the 3 : 1 ratio stated above.[148]

The concept of both activation mechanisms occurring simultaneously is supported by Wang *et al.* who also observed the presence of oxygenated species (methoxy and formate groups) whilst predominately observing the zinc methyl species in ZSM-5.[149] However, in this case, the zinc was introduced through incipient wetness impregnation which can lead to a variety of zinc species within the zeolite.[149] The signals from the methoxy and formate groups disappeared upon further heating of the sample implying additional reactions occurring at higher temperatures.

On the other hand, Stepanov *et al.* have provided strong evidence that the appearance of zinc methoxy and formate species are in fact not due to the radical based homolytic cleavage suggested above but actually due to the presence of adventitious oxygen shown in Scheme 1.[141] When Zn/ZSM-5 prepared by vapour deposition was exposed to labelled methane ($^{13}CH_4$) at room temperature, two signals at $\delta = -4$ and -6 ppm, corresponding to physisorbed methane, were observed in the ^{13}C NMR spectrum.[141] The two signals correspond to two Zn^{2+} sites of different Lewis acidity caused by a non-homogeneous aluminium distribution.[138] Upon heating to 250 °C, the zinc methyl peak is observed as expected, in the absence of any methoxy or formate species. Oxygenated peaks only appeared through the addition of molecular oxygen at room temperature. The intensity of these NMR signals increased upon heating and the presence of NMR signals from further oxygenated species such as carbonates, ethers and aldehydes were also subsequently detected. This study therefore supports heterolytic cleavage as the principle method of CH_4 activation by Zn^{2+} ions contrary to the findings of Xu *et al.*

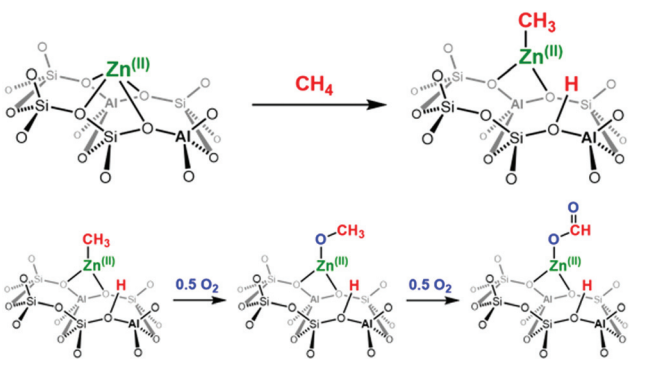

Scheme 1 Top: C–H activation step for dissociative adsorption of methane over Zn^{2+} forming a Zn-CH_3 and new BAS. Bottom: Formation of methoxy and formate species on Zn-CH_3 through addition of O_2.

Understanding the role of Al distribution in zeolites is key to maximising metal-ion exchange levels. It has been determined that as few as 5–15% of ion-exchanged sites are active for CH_4 heterolysis in MFI zeolites.[150] Further, it has been reported that the same zinc active sites are able to activate both CH_4 and H_2.[117,150] DFT studies have suggested this reactivity is dependent on a specific Al array within the zeolite.[151] A recent theoretical paper by Kuroda examines the spontaneous heterolytic cleavage of H_2 on Zn^{2+}/MFI to investigate this dependence.[152] It was found that heterolysis was more favourable on a circumferentially-arrayed Al–Al site compared with a straight channel axis in MFI as shown in Fig. 10. This is due to the formation of a favourably aligned Lewis base-Zn^{2+} pair resulting in a suitable position to activate H_2, even at room temperature. Therefore, the Al arrangement alongside the curvature created by the zeolite pores may be seen to have an impact on the activity of metal ions within zeolite frameworks.

2.3.2 Zinc oxide clusters in zeolites. Zinc oxide clusters in zeolites have been shown to be catalytically active for propane aromatisation.[153,154] Through *in situ* NMR spectroscopy studies, it has been observed that ZnO aggregates, alongside residual BAS, are active for propane aromatisation in a zinc impregnated BEA sample. This is proposed to occur *via* dissociative adsorption of propane on the ZnO species within the pores of the zeolite *via* cleavage of a C–H bond.[153] ZnO clusters have been shown to promote ethane activation but are unable to catalyse the aromatisation of ethane which takes place primarily over Lewis acidic Zn^{2+} or $[Zn–O–Zn]^{2+}$ sites.[155] However, systemic studies of zinc oxide and Zn^{2+} in beta show that zinc oxide is unable to activate methane to form zinc methyl species.

Zinc sites are able to affect H/D exchange of CH_4/CD_4 in Zn/H-BEA with differing reactivity depending on the nature of the active site. Isolated Zn^{2+} cations show pronounced H/D exchange but ZnO clusters are also found to be active, with rate constants of 65×10^{-5} g mol^{-1} min^{-1} and 1.2×10^{-5} g mol^{-1} min^{-1} respectively.[140] This reactivity, however, is limited to H/D exchange with no reaction observed for the alkylation of benzene with methane over these ZnO clusters. On the other hand, Zn^{2+} cations in BEA were able to activate methane to form the zinc methyl species which showed further reactivity with benzene to form substituted aromatics.[147] Similarly, Kazansky *et al.* have found that ZnO clusters in Zn/Na-Y are unable to perform heterolytic dissociative adsorption of methane.[156] The clusters in Zn/Na-Y can be reduced to form isolated Zn^{2+} but this new site is also inactive for C–H cleavage of methane further indicating that the framework plays an important role in mediating the reaction.[154]

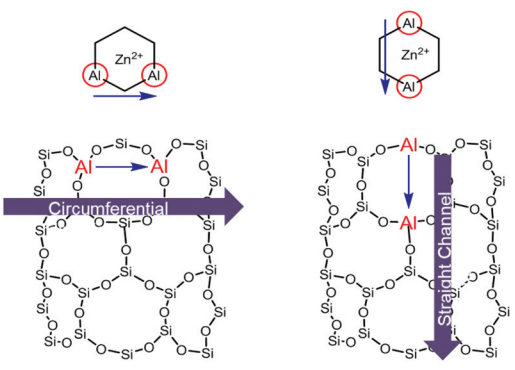

Fig. 10 Representation of Al array direction within a zeolite framework: circumferential and straight channel directions. Adapted with permission from ref. 150. Copyright 2017 Royal Society of Chemistry.

2.3.3 The role of Brønsted acid sites in C–H activation. Stepanov *et al.* have reported that residual BAS after zinc exchange play an interesting role in C–H activation. If BAS are present after zinc exchange on H-ZSM-5, CH_4 activation has been shown to be reversible under reduced pressure.[141] On the other hand, in a fully zinc exchanged ZSM-5 the Zn-CH_3 fragments remain intact after exposure to vacuum.[157]

Conversely, Wu *et al.* found that no reformation of methane with evacuation on a bifunctional Zn/H-ZSM-5 zeolite prepared by impregnation methods.[158] This demonstrates that different methods of zinc introduction can have different reactivity or distribution of zinc species. Wu's sample prepared by impregnation had a variety of zinc species present whereas Stepanov's sample, which showed reversible reactivity, is proposed to have mainly Zn^{2+} present from zinc vapour deposition.

The synergic effect between BAS and zinc Lewis acid sites impacts the temperature required for C–H activation. It has been observed that fully zinc exchanged zeolites require temperatures of 250 °C for activation to take place whereas partially exchanged systems are able to form zinc methyl species at room temperature indicating mechanistic differences caused by the presence of BAS.[141]

High field solid state NMR spectroscopy studies have shown that a synergic effect between BAS and zinc species can promote H/D exchange. In this study, the spatial proximity of these sites is crucial, requiring a BAS-Zn distance <3.5 Å.[159] The enhanced activity of these zinc sites is due to an increase in Brønsted acidity through the spatial proximity between the Zn^{2+} ions and the Brønsted acidic protons of the zeolite. The local electron density on the Zn^{2+} cation is increased (decreasing the electron density on the oxygen atoms around the BAS) leading to a weakening of the interaction between bridging oxygen atoms and acidic protons, overall increasing the acidity of the Zn-modified zeolites.

2.3.4 Reactivity of methane with small molecules on zinc-modified zeolites. As mentioned in section 2.3.1, the formation of methoxy and formate groups are observed when the zinc methyl species are exposed to dioxygen. Reactivity has been observed at ambient temperature, whilst additional heating of the sample results in the formation of higher oxygenates such as acetic acid.[141,149] Further reactivity of zinc methyl species with molecules such as CO, CO_2 and H_2O has been explored by a number of groups and the chemical reactivity has been found to be very similar to that of organozinc compounds.[141,149,158,160]

In situ NMR spectroscopy studies by Deng *et al.* investigated the reactivity of the zinc methyl groups on Zn/H-ZSM-5.[149]

Proton donors such as water, methanol and hydrochloride readily convert the zinc methyl species to methane at room temperature. Deng *et al.* found addition of oxygen to the methyl species results in formation of methoxy and formate groups at 300 °C, in agreement with the findings of Stepanov.[141,149] However, small substoichiometric amounts of methanol are also observed in the NMR spectrum.

The addition of CO and CO_2 to methane over zinc exchanged zeolites has been studied in the context of the formation of acetic acid (Scheme 2). Acetic acid can be formed through two different pathways: CO reacting with surface methoxy species or CO_2 reacting with zinc methyls.[161] The BAS play a key role in the formation of acetic acid *via* proton transfer to the surface acetate species formed upon addition of CO_2.[158]

2.3.5 Differing reactivity between zinc and magnesium. Both Zn^{2+} and Mg^{2+} have similar ionic radii and charge, hence, similar reactivity towards the C–H bond of methane could be expected. However it has been shown that magnesium exchanged ZSM-5 does not form $[Mg\text{-}CH_3]^+$ species under identical conditions to those used for zinc exchanged ZSM-5.[162] Furthermore, H_2 is also not readily chemisorbed on Mg/ZSM-5.[150] Kuroda *et al.* investigated these reactivity differences through IR spectroscopy studies involving the adsorption of CH_4 and CO on Mg/ZSM-5 and Zn/ZSM-5 samples supported by DFT calculations.[162] Stronger perturbation of the adsorbed CH_4 molecule at room temperature was observed through interaction with Zn^{2+} compared with Mg^{2+}. Upon heating, the presence of a zinc methyl group was detected but no change in the IR spectrum of Mg/ZSM-5 was observed. As the electrostatic force of Zn^{2+} is almost identical to that of Mg^{2+}, the authors suggest that the higher activation of the C–H bond observed for Zn^{2+} is due to an electron-transfer interaction rather than based on electrostatics. Similarly, when CO was used as a probe molecule and adsorption studies were undertaken. These studies determined that for Mg^{2+} (and group 2 ions in general), CO adsorption is predominantly governed by electrostatic interaction. However, zinc behaves as an electron acceptor for the CO molecule (as well as for the CH_4 molecule) and this electron-accepting nature is the key electronic feature for CH_4 heterolytic activation. DFT calculations supported that CH_4 dissociation over monomeric Zn^{2+} is derived from the greater electron-accepting power than Mg^{2+} cations.

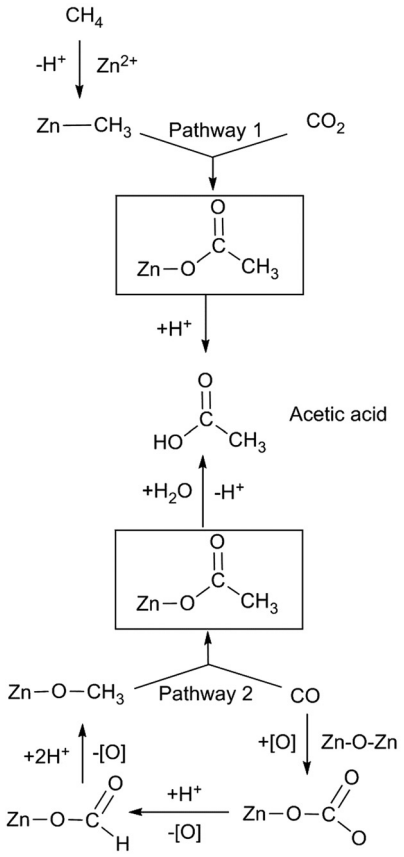

Scheme 2 Proposed reaction pathways for the formation of acetic acid from methane and carbon monoxide on Zn/ZSM-5. Adapted with permission from ref. 161. Copyright 2012 Wiley.

2.4 Other d-block metals in zeolites

2.4.1 Cobalt-modified zeolites. Unlike the previous metals discussed (Fe, Cu, Zn), the literature surrounding the partial oxidation of methane to methanol over Co-modified zeolites is relatively sparse. There are two major products of methane partial oxidation over Co-modified zeolites, methanol and formaldehyde, and their relative selectivities depend upon the active Co species. Cobalt oxide species, Co_3O_4 and CoO, throughout the zeolite are typically selective towards methanol production whilst Co^{2+} cations within the zeolite channels show a general selectivity towards formaldehyde production.[163] As a result, the effect of modification method on methanol selectivity over Co/ZSM-5 may be dramatic; it was found that Co/ZSM-5 prepared by incipient wetness impregnation (IWI) typically contains more surface Co oxide species and is more selective towards methanol, whilst Co/ZSM-5 prepared *via* ion exchange (IE) contains more Co^{2+} species within the zeolite channel system and is more selective towards formaldehyde.[163]

It has been reported that increasing the surface area of Co/ZSM-5 by the introduction of mesoporosity *via* alkaline treatment can improve methanol selectivity by increasing the number of potential Co oxide sites.[164,165] A contribution from Beznis *et al.* shows that a linear correlation between the zeolite surface area and number of Co oxide species can be established and (owing to the selectivity for methanol of Co oxides) a linear correlation between zeolite surface area and methanol selectivity also results.[164] The authors also suggested that increased methanol selectivity could be attributed to the reduced ability to form Co^{2+} sites as a result of extra-framework alumina blocking the channel system. Hence, a subsequent acid treatment to remove extra-framework alumina was applied to the previously alkali treated zeolites before Co introduction. As expected, the relative amounts of Co^{2+} species

within the zeolite channels increased and methanol selectivity decreased.[164]

Partial oxidation of methane conducted in a small-scale batch reactor at 150 °C under an atmosphere of methane (0.75 bar) and 5% oxygen in nitrogen (2 bar) respectively demonstrated the effect of exposure time and oxygen presence on the direct conversion of methane to methanol over Co-impregnated mesoporous H-ZSM-5.[166] It was found that the optimum extracted methanol yield (79%) was obtained at a reaction time of 60 minutes with longer reaction times resulting in a substantial decrease in yield which the authors suggest may be resultant from complete oxidation of methane to CO_2 and water. It is further suggested that the presence of molecular oxygen as an oxidant causes an increased reaction rate when compared to the base reaction in which oxygen (O^{2-}) from cobalt oxides or the ZSM-5 surface acts as the oxidising agent.

In all reports, a preliminary calcination step is required to introduce active oxygen species into Co modified zeolite materials (similar to Cu, *vide supra*) before being exposed to methane at 150 °C. Additionally, it is worth noting that the reaction products remain strongly adsorbed to the catalyst and must be extracted into the liquid phase resulting in a process that, at present, has not been demonstrated to run in a continuous regime.

DFT studies of the direct oxidation of methane to methanol over Co/ZSM-5 in the presence of N_2O have determined a reaction mechanism similar to that observed for α-Fe species.[167] Co/ZSM-5 is predicted to efficiently decompose N_2O resulting in an α-O species which is highly reactive towards radical hydrogen abstraction from methane. The mechanism follows the same pathway as that for Fe (*vide supra*) but with notably lower activation barriers for each step. As with Fe, the presence of water substantially decreases the energy barrier to the methanol formation step.

2.4.2 Other d-block modified zeolites. In addition to the species covered in detail above, several other d-block metal modified zeolite catalysts have been reported to form analogous active sites to those discussed above or activate methane and hence have potential as methane-to-methanol catalysts, although many reports are discrete.

Ni-modified ZSM-5 has been reported to be active for the direct production of methanol from methane with an anchored mono(μ-oxo)dinickel, $[Ni_2(\mu O)]^{2+}$, motif reported as the active site, analogous to that observed for Cu-ZSM-5.[168] The zeolite must be thermally activated in O_2 before methane introduction but produces methanol as the major product at 150 °C, after aqueous extraction into the liquid phase from the catalyst. DFT studies, however, suggest that this active site motif is not plausible, as no activity in methane to methanol conversion was able to be simulated under reasonable conditions.[169] This conclusion corroborates with a recent contribution that utilises DFT+U calculations to simulate an array of plausible Ni-oxo motifs in the periodic MFI framework structure, namely $[NiO]^{2+}$, $[Ni_2(\mu O)]^{2+}$, $[Ni_2(\mu O)_2]^{2+}$, and $[Ni_3(\mu O)_3]^{2+}$ (Fig. 11).[170] It is suggested that the reactivity of the $[Ni_2(\mu O)]^{2+}$ centre is insufficient to be the active site owing to its respective

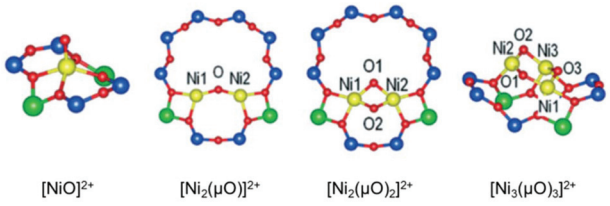

Fig. 11 Optimised ground state structures of $[NiO]^{2+}$, $[Ni_2(\mu O)]^{2+}$, $[Ni_2(\mu O)_2]^{2+}$, and $[Ni_3(\mu O)_3]^{2+}$ in MFI. Adapted with permission from ref. 170. Copyright 2018 Royal Society of Chemistry.

energy of activation for hydrogen atom abstraction from methane being both considerably higher than that observed experimentally and that calculated for the other motifs examined.[168,170] Conversely, the energy of activation for hydrogen atom abstraction calculated for the $[Ni_2(\mu O)_2]^{2+}$, and $[Ni_3(\mu O)_3]^{2+}$ centres is in good agreement with that observed experimentally. Furthermore, the authors suggest that, based on the calculated values for energy of methanol desorption for both active sites, the energetics are within the range that may enable spontaneous, solvent-free and online product extraction.[170] As alluded to in the contribution, the use of experimental resonance Raman spectroscopy (rR) (as used to discern the active species in Cu-modified zeolites) could prove invaluable in assigning the true nature of the active Ni species.

Finally, Mn/ZSM-5 has been shown to be active in the decomposition of N_2O resulting in the suggested formation of an α-O species.[171] Similar to Fe/ZSM-5, this site cannot be generated directly using O_2. At the time of writing, no activation of methane (or any other alkane) over this species has been reported, however the suggested similarity to the α-O in Fe/ZSM-5 could prove promising in methane partial oxidation.

3. Outlook and areas for future research

The development of zeolite based, dMtM catalysts that can compete with the existing two step syngas pathway, remains a major challenge though significant progress has been made in the last 20 years. Competing with the established syngas technology, which has been honed for decades through a combination of chemistry and chemical engineering, will require further substantial effort from the industrial and academic communities. It should be stressed that dMtM technology may not have to compete with the syngas route under certain scenarios; in the monetisation of associated natural gas or other waste methane sources, where it is simply too impractical and/or costly to build a syngas plant and a methanol plant.

At the present time, the single, major improvement that is required to help push dMtM forward as a technology is in preventing unwanted over oxidation to carbon oxides. This remains a major challenge as avoiding thermodynamic fate is no mean feat. However, zeolites are known to give reaction pro-

ducts that differ from thermodynamic predictions (*e.g.* toluene alkylation with methanol to *p*-xylene over ZSM-5)[172] and it stands that zeolites may be able to confer the desired reaction selectivities in dMtM. Conceptually, we believe this could be achieved with metal exchanged zeolite catalysts by exploiting the strategies below which either complement or build on some of the strategies recently suggested by others.[31,38–40]

3.1 Confinement

Zeolites are well known to be able to impart reaction selectivities that differ from those predicted by thermodynamics alone. In the case of dMtM it is unlikely that product selectivity will contribute to improving the selectivity of the reaction due to the similar size of the reactant and the product. On the other hand, exploiting confinement effects which can lower the transition state barrier to C–H activation would enable better activation kinetics and lower process operation temperature. To this end, confinement has very recently been experimentally shown to accelerate methane activation over copper oxide clusters in the MOR framework[23] whilst theoretical studies support this approach for further study.[77] Additionally, it is necessary for confinement effects not to accelerate the activation of the methanol product which could be mitigated by further strategies outlined below.

3.2 $1e^-$ *vs.* $2e^-$ processes

The mechanism of methane oxidation to methanol by the vast majority of materials mentioned in this perspective operate *via* a radical based C–H bond activation process. These $1e^-$ processes are now well understood to result in low methanol selectivities due to the weaker C–H bond of methanol being kinetically more reactive and resulting in over oxidation.[33,38] In the case of functionalisation by $2e^-$ processes, this need not be true. For example, where a Sigma complex is formed prior to C–H bond cleavage (*e.g.* activation by Lewis acid and base or electrophilic activation by transition metals), the more electron rich C–H bond of methane favours coordination, and thus subsequent activation, over the relatively electron poor C–H bond of methanol. Therefore developing and exploring systems where methane complex formation precedes bond cleavage (such as methane activation by Lewis acid–base pairs over zinc exchanged ZSM-5)[147,173] should be a target for future endeavours. In the homogeneous Shilov system, which is capable of converting methane to methanol under remarkably mild conditions (120 °C, in water), the C–O bond forming reaction occurs by nucleophilic attack (a $2e^-$ process) of water at the carbon atom of a Pt(IV)–CH_3 group.[30] While thermodynamics exclude water as a viable oxidant, it highlights alternative mechanisms for C–O bond formation and shows that activation and functionalisation could potentially be separated from a cycle involving dioxygen. This would be akin to the Wacker process, the industrially practised method of acetaldehyde production from ethylene and dioxygen. The process is catalysed by Pd and Cu chloride salts in an acidic, aqueous solution and the C–O bond is in fact formed from water, not dioxygen.[174]

3.3 Hydrophobic pockets

This strategy has been advocated by Román-Leshkov[39] as well as Nørskov,[38] and has parallels in the *modus operandi* of MMO enzymes. In order to prevent over oxidation, rapid release and diffusion of methanol away from the active site is paramount. The non-polar nature of methane compared to the polar and hydrogen bonding properties of methanol can in principle be exploited to engender reaction selectivity. This suggests that ionic active sites (*i.e.* metal-exchanged, aluminosilicate zeolites) may be unsuitable. However, it is conceivable that neutral frameworks with Lewis acid framework sites could serve to activate alkanes. Additionally, minimising diffusion paths indicates that the rapidly developing fields of nano-zeolites[175] and hierarchical zeolites[176] may have a role to play in improving the conversion/selectivity paradigm. In connection, due to the high solubility of methanol in water, recent theoretical work proposes that enhanced reaction selectivity should be observed for dMtM when conducted in water compared to the gas phase, and this is supported by experimental studies.[38]

3.4 Theoretical studies

As has been outlined in this perspective, theoretical studies are making substantial contributions to the field, providing insight into kinetic, mechanistic and thermodynamic considerations (see for example recent contributions from Nørskov,[38,177] Yoshizawa[178] and Sievers[40]). As exemplified and explicitly mentioned by Nørskov,[38] most of these studies are connected to the prevalent radical based, $1e^-$ processes. Additionally, accurate modelling of long-range electrostatic interactions and dispersion in zeolite catalysis is now recognised as key to determining accurate theoretical activation energies. [Bell Catalysis Today 2018 312, P51] Therefore we believe there is substantial scope for theoretical studies to explore $2e^-$ based methane activation and functionalisation processes over metal-exchanged zeolites, and also to explore how the framework can confer optimised confinement effects, both areas for further experimental research that have been highlighted in this section above.

In summary, there remains much to be achieved in dMtM research, though we believe it is likely that zeolites incorporating 3d transition metals will play a prominent role in bringing this long standing challenge to fruition.

Conflicts of interest

There are no conflicts to declare.

Acknowledgements

M. S. and S. R. thank the EPSRC and Durham University for generous financial support for their PhD studentships. R. T. thanks the EPSRC for generous funding of an EPSRC Manufacturing Fellowship (grant number EP/R01213X/1).

References

1 BP Energy Outlook, https://www.bp.com/en/global/corporate/media/press-releases/energy-outlook-2018.html, (accessed 9th November, 2018).
2 K. Aasberg-Petersen, I. Dybkjær, C. V. Ovesen, N. C. Schjødt, J. Sehested and S. G. Thomsen, *J. Nat. Gas Sci. Eng.*, 2011, **3**, 423–459.
3 K. Aasberg-Petersen, J. H. Bak Hansen, T. S. Christensen, I. Dybkjaer, P. S. Christensen, C. Stub Nielsen, S. E. L. Winter Madsen and J. R. Rostrup-Nielsen, *Appl. Catal., A*, 2001, **221**, 379–387.
4 S. C. Reyes, J. H. Sinfelt and J. S. Feeley, *Ind. Eng. Chem. Res.*, 2003, **42**, 1588–1597.
5 R. Reimert, F. Marschner, H.-J. Renner, W. Boll, E. Supp, M. Brejc, W. Liebner and G. Schaub, in *Gas Production 2. Processes, Ullmann's Encyclopedia of Industrial Chemistry*, Wiley-VCH Verlag GmbH & Co. KGaA, 2011.
6 S. A. Bhat and J. Sadhukhan, *AIChE J.*, 2009, **55**, 408–422.
7 J. Ott, V. Gronemann, F. Pontzen, E. Fiedler, G. Grossmann, D. B. Kersebohm, G. Weiss and C. Witte, in *Methanol, Ullmann's Encyclopedia of Industrial Chemistry*, Wiley-VCH Verlag GmbH & Co. KGaA, 2012.
8 W. A. Bone and R. V. Wheeler, *J. Chem. Soc., Dalton Trans.*, 1902, **81**, 535–549.
9 C. Elvidge, M. Zhizhin, K. Baugh, F.-C. Hsu and T. Ghosh, *Energies*, 2016, **9**, 14.
10 BGR, *Energy Study 2013. Reserves, resources and availability of energy resources*, Hannover, 2013.
11 G. L. Foster, D. L. Royer and D. J. Lunt, *Nat. Commun.*, 2017, **8**, 14845.
12 P. G. Levi and J. M. Cullen, *Environ. Sci. Technol.*, 2018, **52**, 1725–1734.
13 OECD, in *Chemicals, OECD Environmental Outlook to 2030*, OECD Publishing, Paris, 2008.
14 IEA, in *The environmental case for natural gas, World Energy Outlook 2017*, OECD/IEA, Paris, 2017.
15 E. V. Kondratenko, T. Peppel, D. Seeburg, V. A. Kondratenko, N. Kalevaru, A. Martin and S. Wohlrab, *Catal. Sci. Technol.*, 2017, **7**, 366–381.
16 Siluria Technologies, http://siluria.com/Technology/Demonstration_Plant, (accessed 15th November 2018).
17 Siluria Technologies, http://siluria.com/Newsroom/Press_Releases, (accessed 15th November 2018).
18 B. A. Arndtsen, R. G. Bergman, T. A. Mobley and T. H. Peterson, *Acc. Chem. Res.*, 1995, **28**, 154–162.
19 V. C. C. Wang, S. Maji, P. P. Y. Chen, H. K. Lee, S. S. F. Yu and S. I. Chan, *Chem. Rev.*, 2017, 8574–8621.
20 M. O. Ross and A. C. Rosenzweig, *J. Biol. Inorg. Chem.*, 2017, **22**, 307–319.
21 Z. Zakaria and S. K. Kamarudin, *Renewable Sustainable Energy Rev.*, 2016, **65**, 250–261.
22 P. Tomkins, M. Ranocchiari and J. A. van Bokhoven, *Acc. Chem. Res.*, 2017, **50**, 418–425.
23 B. E. R. Snyder, M. L. Bols, R. A. Schoonheydt, B. F. Sels and E. I. Solomon, *Chem. Rev.*, 2018, **118**, 2718–2768.
24 M. Ravi, M. Ranocchiari and J. A. van Bokhoven, *Angew. Chem., Int. Ed.*, 2017, **56**, 16464–16483.
25 N. J. Gunsalus, A. Koppaka, S. H. Park, S. M. Bischof, B. G. Hashiguchi and R. A. Periana, *Chem. Rev.*, 2017, **117**, 8521–8573.
26 A. I. Olivos-Suarez, À. Szécsényi, E. J. M. Hensen, J. Ruiz-Martinez, E. A. Pidko and J. Gascon, *ACS Catal.*, 2016, **6**, 2965–2981.
27 W. Taifan and J. Baltrusaitis, *Appl. Catal., B*, 2016, **198**, 525–547.
28 C. Karakaya and R. J. Kee, *Prog. Energy Combust. Sci.*, 2016, **55**, 60–97.
29 J. A. Labinger, *Chem. Rev.*, 2017, **117**, 8483–8496.
30 J. A. Labinger and J. E. Bercaw, *J. Organomet. Chem.*, 2015, **793**, 47–53.
31 M. Ravi, M. Ranocchiari and J. A. van Bokhoven, *Angew. Chem., Int. Ed.*, 2017, **56**, 16464–16483.
32 J. A. Labinger and J. E. Bercaw, *Nature*, 2002, **417**, 507–514.
33 J. A. Labinger, *J. Mol. Catal. A: Chem.*, 2004, **220**, 27–35.
34 M. Lersch and M. Tilset, *Chem. Rev.*, 2005, **105**, 2471–2526.
35 C. L. Rasmussen and P. Glarborg, *Ind. Eng. Chem. Res.*, 2008, **47**, 6579–6588.
36 H. D. Gesser, N. R. Hunter and C. B. Prakash, *Chem. Rev.*, 1985, **85**, 235–244.
37 A. E. Shilov and G. B. Shul'pin, *Chem. Rev.*, 1997, **97**, 2879–2932.
38 A. A. Latimer, A. Kakekhani, A. R. Kulkarni and J. K. Nørskov, *ACS Catal.*, 2018, **8**, 6894–6907.
39 K. T. Dinh, M. M. Sullivan, P. Serna, R. J. Meyer, M. Dincă and Y. Román-Leshkov, *ACS Catal.*, 2018, **8**, 8306–8313.
40 J. N. Jocz, A. J. Medford and C. Sievers, *ChemCatChem*, 2019, **11**, 593–600.
41 W. A. Bone and R. V. Wheeler, *J. Chem. Soc., Dalton Trans.*, 1903, **83**, 1074–1087.
42 D. Lance and H. S. Elworthy, FR352687, 1905.
43 T. E. Layng and R. Soukup, *Ind. Eng. Chem.*, 1928, **20**, 1052–1055.
44 N. F. Gol'dshleger, M. B. Tyabin, A. E. Shilov and A. A. Shteinman, *Zh. Fiz. Khim.*, 1969, **18**, 2174–2175.
45 N. F. Gol'dshleger, V. V. Es'kova, A. E. Shilov and A. A. Shteinman, *Zh. Fiz. Khim.*, 1972, **46**, 1353–1354.
46 R. A. Periana, D. J. Taube, S. Gamble, H. Taube, T. Satoh and H. Fujii, *Science*, 1998, **280**, 560–564.
47 M. M. Konnick, S. M. Bischof, M. Yousufuddin, B. G. Hashiguchi, D. H. Ess and R. A. Periana, *J. Am. Chem. Soc.*, 2014, **136**, 10085–10094.
48 T. Zimmermann, M. Soorholtz, M. Bilke and F. Schüth, *J. Am. Chem. Soc.*, 2016, **138**, 12395–12400.
49 T. Zimmermann, M. Bilke, M. Soorholtz and F. Schüth, *ACS Catal.*, 2018, **8**, 9262–9268.
50 L. F. Albright, *Ind. Eng. Chem. Res.*, 2009, **48**, 1409–1413.
51 J. T. Grant, J. M. Venegas, W. P. McDermott and I. Hermans, *Chem. Rev.*, 2018, **118**, 2769–2815.

52 M. H. Mahyuddin, A. Staykov, Y. Shiota and K. Yoshizawa, *ACS Catal.*, 2016, **6**, 8321–8331.
53 N. D. Spencer and C. J. Pereira, *J. Catal.*, 1989, **116**, 399–406.
54 K. J. Zhen, M. M. Khan, C. H. Mak, K. B. Lewis and G. A. Somorjai, *J. Catal.*, 1985, **94**, 501–507.
55 S. Y. Chen and D. Willcox, *Ind. Eng. Chem. Res.*, 1993, **32**, 584–587.
56 N. D. Spencer, *J. Catal.*, 1988, **109**, 187–197.
57 O. Kiyoshi and H. Masaharu, *Chem. Lett.*, 1992, **21**, 2397–2400.
58 T. Weng and E. E. Wolf, *Appl. Catal., A*, 1993, **96**, 383–396.
59 C. A. G. Fajardo, D. Niznansky, Y. N'Guyen, C. Courson and A.-C. Roger, *Catal. Commun.*, 2008, **9**, 864–869.
60 V. A. Durante, D. W. Walker, S. M. Gussow and J. E. Lyons, US4918249A, 1990.
61 S. Han, E. A. Kaufman, D. J. Martenak, R. E. Palermo, J. A. Pearson and D. E. Walsh, *Catal. Lett.*, 1994, **29**, 27–32.
62 P. S. Landis, US3529020A, 1970.
63 V. I. Sobolev, K. A. Dubkov, O. V. Panna and G. I. Panov, *Catal. Today*, 1995, **24**, 251–252.
64 A. Klerk, *Energy Sci. Eng.*, 2015, **3**, 60–70.
65 W. Vermeiren and J.-P. Gilson, *Top. Catal.*, 2009, **52**, 1131–1161.
66 R. Millini and G. Bellussi, in *Zeolites in Catalysis: Properties and Applications*, The Royal Society of Chemistry, 2017, pp. 1–36.
67 R. Gounder and E. Iglesia, *Chem. Commun.*, 2013, **49**, 3491–3509.
68 A. Corma, *J. Catal.*, 2003, **216**, 298–312.
69 A. Bhan, A. D. Allian, G. J. Sunley, D. J. Law and E. Iglesia, *J. Am. Chem. Soc.*, 2007, **129**, 4919–4924.
70 B. Li, J. Xu, B. Han, X. Wang, G. Qi, Z. Zhang, C. Wang and F. Deng, *J. Phys. Chem. C*, 2013, **117**, 5840–5847.
71 G. I. Panov, V. I. Sobolev and A. S. Kharitonov, *J. Mol. Catal.*, 1990, **61**, 85–97.
72 G. I. Panov, G. A. Sheveleva, A. S. Kharitonov, V. N. Romannikov and L. A. Vostrikova, *Appl. Catal., A*, 1992, **82**, 31–36.
73 V. I. Sobolev, A. S. Kharitonov, Y. A. Paukshtis and G. I. Panov, *J. Mol. Catal.*, 1993, **84**, 117–124.
74 G. I. Panov, V. I. Sobolev, K. A. Dubkov, V. N. Parmon, N. S. Ovanesyan, A. E. Shilov and A. A. Shteinman, *React. Kinet. Catal. Lett.*, 1997, **61**, 251–258.
75 E. V. Starokon, M. V. Parfenov, L. V. Pirutko, S. I. Abornev and G. I. Panov, *J. Phys. Chem. C*, 2011, **115**, 2155–2161.
76 B. E. R. Snyder, P. Vanelderen, M. L. Bols, S. D. Hallaert, L. H. Böttger, L. Ungur, K. Pierloot, R. A. Schoonheydt, B. F. Sels and E. I. Solomon, *Nature*, 2016, **536**, 317.
77 F. Göltl, C. Michel, P. C. Andrikopoulos, A. M. Love, J. Hafner, I. Hermans and P. Sautet, *ACS Catal.*, 2016, **6**, 8404–8409.
78 E. V. Starokon, M. V. Parfenov, S. S. Arzumanov, L. V. Pirutko, A. G. Stepanov and G. I. Panov, *J. Catal.*, 2013, **300**, 47–54.
79 Y. K. Chow, N. F. Dummer, J. H. Carter, R. J. Meyer, R. D. Armstrong, C. Williams, G. Shaw, S. Yacob, M. M. Bhasin, D. J. Willock, S. H. Taylor and G. J. Hutchings, *ChemPhysChem*, 2018, **19**, 402–411.
80 J. Valyon, W. S. Millman and W. K. Hall, *Catal. Lett.*, 1994, **24**, 215–225.
81 J. Leglise, J. O. Petunchi and W. K. Hall, *J. Catal.*, 1984, **86**, 392–399.
82 P. C. Andrikopoulos, Z. Sobalik, J. Novakova, P. Sazama and S. Sklenak, *ChemPhysChem*, 2013, **14**, 520–531.
83 C. M. Fu, V. N. Korchak and W. K. Hall, *J. Catal.*, 1981, **68**, 166–171.
84 M. L. Bols, S. D. Hallaert, B. E. R. Snyder, J. Devos, D. Plessers, H. M. Rhoda, M. Dusselier, R. A. Schoonheydt, K. Pierloot, E. I. Solomon and B. F. Sels, *J. Am. Chem. Soc.*, 2018, **140**, 12021–12032.
85 B. Michalkiewicz, *Appl. Catal., A*, 2004, **277**, 147–153.
86 C. Hammond, M. M. Forde, M. H. Ab Rahim, A. Thetford, Q. He, R. L. Jenkins, N. Dimitratos, J. A. Lopez-Sanchez, N. F. Dummer, D. M. Murphy, A. F. Carley, S. H. Taylor, D. J. Willock, E. E. Stangland, J. Kang, H. Hagen, C. J. Kiely and G. J. Hutchings, *Angew. Chem., Int. Ed.*, 2012, **51**, 5129–5133.
87 C. Hammond, R. L. Jenkins, N. Dimitratos, J. A. Lopez-Sanchez, M. H. ab Rahim, M. M. Forde, A. Thetford, D. M. Murphy, H. Hagen, E. E. Stangland, J. M. Moulijn, S. H. Taylor, D. J. Willock and G. J. Hutchings, *Chem. – Eur. J.*, 2012, **18**, 15735–15745.
88 C. Hammond, N. Dimitratos, R. L. Jenkins, J. A. Lopez-Sanchez, S. A. Kondrat, M. Hasbi ab Rahim, M. M. Forde, A. Thetford, S. H. Taylor, H. Hagen, E. E. Stangland, J. H. Kang, J. M. Moulijn, D. J. Willock and G. J. Hutchings, *ACS Catal.*, 2013, **3**, 689–699.
89 C. Hammond, N. Dimitratos, J. A. Lopez-Sanchez, R. L. Jenkins, G. Whiting, S. A. Kondrat, M. H. ab Rahim, M. M. Forde, A. Thetford, H. Hagen, E. E. Stangland, J. M. Moulijn, S. H. Taylor, D. J. Willock and G. J. Hutchings, *ACS Catal.*, 2013, **3**, 1835–1844.
90 J. Xu, R. D. Armstrong, G. Shaw, N. F. Dummer, S. J. Freakley, S. H. Taylor and G. J. Hutchings, *Catal. Today*, 2016, **270**, 93–100.
91 M. H. Groothaert, P. J. Smeets, B. F. Sels, P. A. Jacobs and R. A. Schoonheydt, *J. Am. Chem. Soc.*, 2005, **127**, 1394–1395.
92 M. B. Park, S. H. Ahn, A. Mansouri, M. Ranocchiari and J. A. van Bokhoven, *ChemCatChem*, 2017, **9**, 3705–3713.
93 P. J. Smeets, M. H. Groothaert and R. A. Schoonheydt, *Catal. Today*, 2005, **110**, 303–309.
94 M. J. Wulfers, S. Teketel, B. Ipek and R. F. Lobo, *Chem. Commun.*, 2015, **51**, 4447–4450.
95 M. H. Groothaert, J. A. van Bokhoven, A. A. Battiston, B. M. Weckhuysen and R. A. Schoonheydt, *J. Am. Chem. Soc.*, 2003, **125**, 7629–7640.
96 M. H. Groothaert, K. Lievens, J. A. van Bokhoven, A. A. Battiston, B. M. Weckhuysen, K. Pierloot and R. A. Schoonheydt, *ChemPhysChem*, 2003, **4**, 626–630.
97 J. S. Woertink, P. J. Smeets, M. H. Groothaert, M. A. Vance, B. F. Sels, R. A. Schoonheydt and

E. I. Solomon, *Proc. Natl. Acad. Sci. U. S. A.*, 2009, **106**, 18908–18913.
98 R. S. Czernuszewicz, J. E. Sheats and T. G. Spiro, *Inorg. Chem.*, 1987, **26**, 2063–2067.
99 M. H. Groothaert, K. Lievens, H. Leeman, B. M. Weckhuysen and R. A. Schoonheydt, *J. Catal.*, 2003, **220**, 500–512.
100 P. J. Smeets, R. G. Hadt, J. S. Woertink, P. Vanelderen, R. A. Schoonheydt, B. F. Sels and E. I. Solomon, *J. Am. Chem. Soc.*, 2010, **132**, 14736–14738.
101 M. L. Tsai, R. G. Hadt, P. Vanelderen, B. F. Sels, R. A. Schoonheydt and E. I. Solomon, *J. Am. Chem. Soc.*, 2014, **136**, 3522–3529.
102 S. Grundner, M. A. C. Markovits, G. Li, M. Tromp, E. A. Pidko, E. J. M. Hensen, A. Jentys, M. Sanchez-Sanchez and J. A. Lercher, *Nat. Commun.*, 2015, **6**, 7546.
103 G. Li, P. Vassilev, M. Sanchez-Sanchez, J. A. Lercher, E. J. M. Hensen and E. A. Pidko, *J. Catal.*, 2016, **338**, 305–312.
104 D. Palagin, A. J. Knorpp, A. B. Pinar, M. Ranocchiari and J. A. van Bokhoven, *Nanoscale*, 2017, **9**, 1144–1153.
105 C. Paolucci, A. A. Parekh, I. Khurana, J. R. Di Iorio, H. Li, J. D. Albarracin Caballero, A. J. Shih, T. Anggara, W. N. Delgass, J. T. Miller, F. H. Ribeiro, R. Gounder and W. F. Schneider, *J. Am. Chem. Soc.*, 2016, **138**, 6028–6048.
106 A. R. Kulkarni, Z.-J. Zhao, S. Siahrostami, J. K. Nørskov and F. Studt, *ACS Catal.*, 2016, **6**, 6531–6536.
107 F. Giordanino, P. N. R. Vennestrøm, L. F. Lundegaard, F. N. Stappen, S. Mossin, P. Beato, S. Bordiga and C. Lamberti, *Dalton Trans.*, 2013, **42**, 12741–12761.
108 E. Borfecchia, K. A. Lomachenko, F. Giordanino, H. Falsig, P. Beato, A. V. Soldatov, S. Bordiga and C. Lamberti, *Chem. Sci.*, 2015, **6**, 548–563.
109 K. Narsimhan, K. Iyoki, K. Dinh and Y. Román-Leshkov, *ACS Cent. Sci.*, 2016, **2**, 424–429.
110 P. Vanelderen, J. Vancauwenbergh, B. F. Sels and R. A. Schoonheydt, *Coord. Chem. Rev.*, 2013, **257**, 483–494.
111 Z.-J. Zhao, A. Kulkarni, L. Vilella, J. K. Nørskov and F. Studt, *ACS Catal.*, 2016, **6**, 3760–3766.
112 E. M. C. Alayon, M. Nachtegaal, A. Bodi and J. A. van Bokhoven, *ACS Catal.*, 2014, **4**, 16–22.
113 R. Oord, J. E. Schmidt and B. M. Weckhuysen, *Catal. Sci. Technol.*, 2018, **8**, 1028–1038.
114 M. H. Mahyuddin, T. Tanaka, Y. Shiota, A. Staykov and K. Yoshizawa, *ACS Catal.*, 2018, **8**, 1500–1509.
115 P. Tomkins, A. Mansouri, S. E. Bozbag, F. Krumeich, B. Park Min, E. M. C. Alayon, M. Ranocchiari and J. A. van Bokhoven, *Angew. Chem., Int. Ed.*, 2016, **55**, 5467–5471.
116 T. Sheppard, C. D. Hamill, A. Goguet, D. W. Rooney and J. M. Thompson, *Chem. Commun.*, 2014, **50**, 11053–11055.
117 A. Oda, H. Torigoe, A. Itadani, T. Ohkubo, T. Yumura, H. Kobayashi and Y. Kuroda, *J. Phys. Chem. C*, 2013, **117**, 19525–19534.
118 V. L. Sushkevich, D. Palagin, M. Ranocchiari and J. A. van Bokhoven, *Science*, 2017, **356**, 523–527.
119 R. A. Periana, *Science*, 2017, **358**, eaan5970.
120 J. A. Labinger, *Science*, 2018, **359**, eaar4968.
121 V. L. Sushkevich, D. Palagin and J. A. v. Bokhoven, *Angew. Chem., Int. Ed.*, 2018, **57**, 8906–8910.
122 M. A. C. Markovits, A. Jentys, M. Tromp, M. Sanchez-Sanchez and J. A. Lercher, *Top. Catal.*, 2016, **59**, 1554–1563.
123 N. V. Beznis, B. M. Weckhuysen and J. H. Bitter, *Catal. Lett.*, 2010, **138**, 14–22.
124 P. Vanelderen, B. E. R. Snyder, M.-L. Tsai, R. G. Hadt, J. Vancauwenbergh, O. Coussens, R. A. Schoonheydt, B. F. Sels and E. I. Solomon, *J. Am. Chem. Soc.*, 2015, **137**, 6383–6392.
125 B. E. R. Snyder, P. Vanelderen, R. A. Schoonheydt, B. F. Sels and E. I. Solomon, *J. Am. Chem. Soc.*, 2018, **140**, 9236–9243.
126 E. G. Derouane, *J. Catal.*, 1986, **100**, 541–544.
127 P. Cheung, A. Bhan, G. J. Sunley and E. Iglesia, *Angew. Chem., Int. Ed.*, 2006, **45**, 1617–1620.
128 A. J. Jones, S. I. Zones and E. Iglesia, *J. Phys. Chem. C*, 2014, **118**, 17787–17800.
129 M. L. Sarazen, E. Doskocil and E. Iglesia, *ACS Catal.*, 2016, **6**, 7059–7070.
130 E. M. C. Alayon, M. Nachtegaal, M. Ranocchiari and J. A. van Bokhoven, *CHIMIA Int. J. Chem.*, 2012, **66**, 668–674.
131 M. A. Newton, A. J. Knorpp, A. B. Pinar, V. L. Sushkevich, D. Palagin and J. A. van Bokhoven, *J. Am. Chem. Soc.*, 2018, 10090–10093.
132 S. E. Bozbag, E. M. C. Alayon, J. Pecháček, M. Nachtegaal, M. Ranocchiari and J. A. van Bokhoven, *Catal. Sci. Technol.*, 2016, **6**, 5011–5022.
133 D. K. Pappas, A. Martini, M. Dyballa, K. Kvande, S. Teketel, K. A. Lomachenko, R. Baran, P. Glatzel, B. Arstad, G. Berlier, C. Lamberti, S. Bordiga, U. Olsbye, S. Svelle, P. Beato and E. Borfecchia, *J. Am. Chem. Soc.*, 2018, 15270–15278.
134 S. Grundner, W. Luo, M. Sanchez-Sanchez and J. A. Lercher, *Chem. Commun.*, 2016, **52**, 2553–2556.
135 V. L. Sushkevich and J. A. v. Bokhoven, *Catal. Sci. Technol.*, 2018, **8**, 4141–4150.
136 B. Ipek and R. F. Lobo, *Chem. Commun.*, 2016, **52**, 13401–13404.
137 M. Dusselier and M. E. Davis, *Chem. Rev.*, 2018, 5265–5329.
138 V. B. Kazansky and A. I. Serykh, *Phys. Chem. Chem. Phys.*, 2004, **6**, 3760–3764.
139 S. M. T. Almutairi, B. Mezari, P. C. M. M. Magusin, E. A. Pidko and E. J. M. Hensen, *ACS Catal.*, 2012, **2**, 71–83.
140 I. Pinilla-Herrero, E. Borfecchia, J. Holzinger, U. V. Mentzel, F. Joensen, K. A. Lomachenko, S. Bordiga, C. Lamberti, G. Berlier, U. Olsbye, S. Svelle, J. Skibsted and P. Beato, *J. Catal.*, 2018, **362**, 146–163.
141 A. A. Gabrienko, S. S. Arzumanov, M. V. Luzgin, A. G. Stepanov and V. N. Parmon, *J. Phys. Chem. C*, 2015, **119**, 24910–24918.

142 E. Morra, G. Berlier, E. Borfecchia, S. Bordiga, P. Beato and M. Chiesa, *J. Phys. Chem. C*, 2017, **121**, 14238–14245.
143 A. Oda, T. Ohkubo, T. Yumura, H. Kobayashi and Y. Kuroda, *Dalton Trans.*, 2015, **44**, 10038–10047.
144 A. Dyer and T. I. Emms, *J. Mater. Chem.*, 2005, **15**, 5012–5021.
145 Y. G. Kolyagin, I. I. Ivanova, V. V. Ordomsky, A. Gedeon and Y. A. Pirogov, *J. Phys. Chem. C*, 2008, **112**, 20065–20069.
146 H. Elmar, *Z. Anorg. Allg. Chem.*, 2000, **626**, 2223–2227.
147 M. V. Luzgin, D. Freude, J. Haase and A. G. Stepanov, *J. Phys. Chem. C*, 2015, **119**, 14255–14261.
148 J. Xu, A. Zheng, X. Wang, G. Qi, J. Su, J. Du, Z. Gan, J. Wu, W. Wang and F. Deng, *Chem. Sci.*, 2012, **3**, 2932–2940.
149 J. F. Wu, W. D. Wang, J. Xu, F. Deng and W. Wang, *Chem. – Eur. J.*, 2010, **16**, 14016–14025.
150 A. Oda, H. Torigoe, A. Itadani, T. Ohkubo, T. Yumura, H. Kobayashi and Y. Kuroda, *Angew. Chem., Int. Ed.*, 2012, **51**, 7719–7723.
151 E. A. Pidko and R. A. van Santen, *J. Phys. Chem. C*, 2007, **111**, 2643–2655.
152 A. Oda, T. Ohkubo, T. Yumura, H. Kobayashi and Y. Kuroda, *Phys. Chem. Chem. Phys.*, 2017, **19**, 25105–25114.
153 A. A. Gabrienko, S. S. Arzumanov, D. Freude and A. G. Stepanov, *J. Phys. Chem. C*, 2010, **114**, 12681–12688.
154 A. A. Gabrienko, S. S. Arzumanov, A. V. Toktarev, I. G. Danilova, I. P. Prosvirin, V. V. Kriventsov, V. I. Zaikovskii, D. Freude and A. G. Stepanov, *ACS Catal.*, 2017, **7**, 1818–1830.
155 A. Mehdad and R. F. Lobo, *Catal. Sci. Technol.*, 2017, **7**, 3562–3572.
156 V. B. Kazansky, V. Yu. Borovkov, A. I. Serykh, R. A. van Santen and P. J. Stobbelaar, *Phys. Chem. Chem. Phys.*, 1999, **1**, 2881–2886.
157 A. G. Stepanov, S. S. Arzumanov, A. A. Gabrienko, V. N. Parmon, I. I. Ivanova and D. Freude, *ChemPhysChem*, 2008, **9**, 2559–2563.
158 J.-F. Wu, S.-M. Yu, W. D. Wang, Y.-X. Fan, S. Bai, C.-W. Zhang, Q. Gao, J. Huang and W. Wang, *J. Am. Chem. Soc.*, 2013, **135**, 13567–13573.
159 G. Qi, Q. Wang, J. Xu, J. Trébosc, O. Lafon, C. Wang, J.-P. Amoureux and F. Deng, *Angew. Chem., Int. Ed.*, 2016, **55**, 15826–15830.
160 Y. Lin, S. Qi, L. Benedict, Z. Junlin, K. Dejing, M. Claire, T. Chiu and T. Edman, *Angew. Chem., Int. Ed.*, 2017, **56**, 10711–10716.
161 X. Wang, G. Qi, J. Xu, B. Li, C. Wang and F. Deng, *Angew. Chem., Int. Ed.*, 2012, **51**, 3850–3853.
162 A. Oda, H. Torigoe, A. Itadani, T. Ohkubo, T. Yumura, H. Kobayashi and Y. Kuroda, *J. Phys. Chem. C*, 2014, **118**, 15234–15241.
163 N. V. Beznis, B. M. Weckhuysen and J. H. Bitter, *Catal. Lett.*, 2010, **136**, 52–56.
164 N. V. Beznis, A. N. C. van Laak, B. M. Weckhuysen and J. H. Bitter, *Microporous Mesoporous Mater.*, 2011, **138**, 176–183.
165 Y. K. Krisnandi, B. A. P. Putra, M. Bahtiar, Zahara, I. Abdullah and R. F. Howe, *Procedia Chem.*, 2015, **14**, 508–515.
166 Y. K. Krisnandi, B. A. Samodro, R. Sihombing and R. F. Howe, *Indones. J. Chem.*, 2015, **15**, 263–268.
167 M. F. Fellah and I. Onal, *J. Phys. Chem. C*, 2010, **114**, 3042–3051.
168 J. Shan, W. Huang, L. Nguyen, Y. Yu, S. Zhang, Y. Li, A. I. Frenkel and F. Tao, *Langmuir*, 2014, **30**, 8558–8569.
169 A. A. Arvidsson, V. P. Zhdanov, P.-A. Carlsson, H. Gronbeck and A. Hellman, *Catal. Sci. Technol.*, 2017, **7**, 1470–1477.
170 M. H. Mahyuddin and K. Yoshizawa, *Catal. Sci. Technol.*, 2018, 5875–5885.
171 D. Radu, P. Glatzel, A. Gloter, O. Stephan, B. M. Weckhuysen and F. M. F. de Groot, *J. Phys. Chem. C*, 2008, **112**, 12409–12416.
172 J. P. Breen, R. Burch, M. Kulkarni, D. McLaughlin, P. J. Collier and S. E. Golunski, *Appl. Catal., A*, 2007, **316**, 53–60.
173 S. S. Arzumanov, A. A. Gabrienko, D. Freude and A. G. Stepanov, *Catal. Sci. Technol.*, 2016, **6**, 6381–6388.
174 J. A. Keith and P. M. Henry, *Angew. Chem., Int. Ed.*, 2009, **48**, 9038–9049.
175 S. Mintova, J.-P. Gilson and V. Valtchev, *Nanoscale*, 2013, **5**, 6693–6703.
176 K. Möller and T. Bein, *Chem. Soc. Rev.*, 2013, **42**, 3689–3707.
177 A. A. Latimer, A. R. Kulkarni, H. Aljama, J. H. Montoya, J. S. Yoo, C. Tsai, F. Abild-Pedersen, F. Studt and J. K. Norskov, *Nat. Mater.*, 2017, **16**, 225–229.
178 M. H. Mahyuddin, Y. Shiota, A. Staykov and K. Yoshizawa, *Acc. Chem. Res.*, 2018, **51**, 2382–2390.

Appendix 8: Framework Effects on Activation and Functionalisation of Methane in Zinc-Exchanged Zeolites

Meera A. Shah, Samuel Raynes, David C. Apperley, Russell A. Taylor

Framework Effects on Activation and Functionalisation of Methane in Zinc-Exchanged Zeolites

Meera A. Shah,[a] Samuel Raynes,[a] David C. Apperley,[a] and Russell A. Taylor*[a]

The first selective oxidation of methane to methanol is reported herein for zinc-exchanged MOR (Zn/MOR). Under identical conditions, Zn/FER and Zn/ZSM-5 both form zinc formate and methanol. Selective methane activation to form $[Zn\text{-}CH_3]^+$ species was confirmed by ^{13}C MAS NMR spectroscopy for all three frameworks. The percentage of active zinc sites, measured through quantitative NMR spectroscopy studies, varied with the zeolite framework and was found to be ZSM-5 (5.7%), MOR (1.2%) and FER (0.5%). For Zn/MOR, two signals were observed in the ^{13}C MAS NMR spectrum, resulting from two distinct $[Zn\text{-}CH_3]^+$ species present in the 12 MR and 8 MR side pockets, as supported by additional NMR experiments. The observed products of oxidation of the $[Zn\text{-}CH_3]^+$ species are shown to depend on the zeolite framework type and the oxidative conditions used. These results lay the foundation for developing structure–function correlations for methane conversion over zinc-exchanged zeolites.

1. Introduction

To date, the selective partial oxidation of methane to methanol remains a 'holy grail' of catalysis.[1] This highly sought after catalytic reaction could provide a more efficient approach to the industrially practiced method of methane to methanol via syngas (CO and H_2).[2] It has been reported that 60% of the capital cost of a methane to methanol facility stems from the syngas plant.[2a] Additionally, given that nature has mastered this conversion through methantropic bacteria, it is tantalising to hope that a similar process could be engineered through modern chemical methods.[3]

Metal-exchanged zeolites have shown great potential for the direct conversion of methane to methanol.[4] In particular, copper-modified zeolites have been intensely studied especially due to catalyst activation being possible under an O_2 atmosphere.[3c,4b,5] The radical based mechanism operative in Cu-modified zeolites has been well established[6] and confinement effects within zeolites containing small pores, promoting the partial oxidation of methane, have traditionally resulted in the greatest methanol yields.[4c,7] In particular, the framework MOR, with 8 membered-ring side pockets (8 MR SP), has particularly shown high selectivity and yield for methanol production from methane.[8]

In 2004, Kazansky et al. reported the heterolytic bond dissociation of CH_4 over zinc-modified ZSM-5.[9] A major advantage of these zinc based systems is the ability to form active species without an initial high temperature oxidation step as required for iron and copper modified zeolites.[3c] As evidenced by DRIFTS and MAS NMR studies, methane activation at Zn^{2+} exchanged ZSM-5 zeolites is generally accepted to result in heterolytic cleavage of the C–H bond in methane, leading to the formation of a $[Zn\text{-}CH_3]^+$ species and a new Brønsted acid site (BAS) (Scheme 1)[9–10] Spectroscopic and theoretical studies have shown that the mechanism proceeds through initial complexation of methane to the Lewis acidic Zn^{2+} species, with the CH_4 δ(C–H) orbital donating electron density into the Zn-4 s orbital (methane sigma complex), after which the framework oxygen atom acts as a Lewis base, leading to C–H bond cleavage.[9–10,11]

Reactivity of the resulting zinc methyl fragment with other small molecules has been explored, in the context of stoichiometric reactions as well as potential catalytic applications. Addition of dioxygen to $[Zn\text{-}CH_3]^+$/ZSM-5 at ambient and elevated temperature has been shown to result in the formation of zinc methoxy and zinc formate species, as monitored through NMR spectroscopic studies.[10b,12] On this basis, it has been shown that the chemical reactivity of $[Zn\text{-}CH_3]^+$ within ZSM-5, with molecules such as CO, CO_2 and H_2O, has been found to be very similar to that of organozinc compounds.[10b,12–13]

Whilst methane activation and oxidation has been explored over zinc-modified ZSM-5, the effect of the zeolite framework on the activation and subsequent functionalisation steps has not yet been investigated. To this end we have conducted a series of studies exploring the C–H activation of methane in

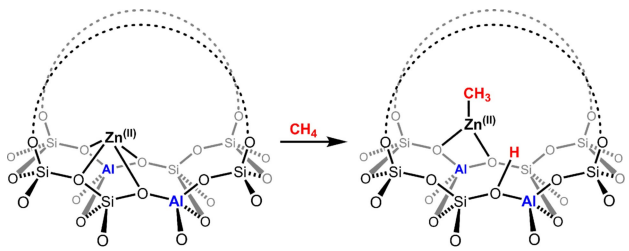

Scheme 1. C–H activation step for dissociative adsorption of methane over Zn^{2+} forming a $[Zn\text{-}CH_3]^+$ and new BAS.

[a] M. A. Shah, S. Raynes, Dr. D. C. Apperley, Dr. R. A. Taylor
Department of Chemistry, Durham University
South Road, Durham, DH1 3LE (United Kingdom)
E-mail: russell.taylor@durham.ac.uk

Supporting information for this article is available on the WWW under https://doi.org/10.1002/cphc.201900973

three different zinc modified frameworks, MFI, MOR and FER, which have intrinsically different micropore topologies. We report that selective methane activation occurs over ZSM-5, FER and MOR zeolites that have been modified by zinc vapour at elevated temperature. Solid state NMR studies have shown that two distinct $[Zn\text{-}CH_3]^+$ species are formed in MOR, due to the very different topological environments within the MOR Framework. Additionally we show that the zeolite framework can influence the observed product(s) when $[Zn\text{-}CH_3]^+$ reacts with O_2 or air. Uniquely, methanol is the sole observable carbon containing product when the $[Zn\text{-}CH_3]^+$ species is exposed to air for Zn/MOR. These results point at the ability of the framework topology to effect the outcome of the reaction in methane oxidation as mediated by zinc exchanged zeolites, hitherto unreported.

2. Results and Discussion

2.1. The Effect of Zeolite Framework on CH_4 Activation

Zinc exchanged zeolites of three differing frameworks, H-ZSM-5, NH_4-FER and H-MOR, were prepared by chemical vapour deposition (CVD) with an excess of zinc metal (100:1 Zn:Al) in a custom designed u-shaped quartz tube (Figure S1 in the Supporting Information). CVD was carried out at 500 °C under reduced pressure (less than 10^{-2} mbar). This was followed by methane activation at 250 °C, based on conditions reported previously by Stepanov et al.[10b] Particular care was taken to prevent aerial oxidation, especially after CH_4 exposure, hence, all the samples was transferred to a glovebox and packed into an NMR rotor in an inert environment (Ar). An additional sample prepared by aqueous ion exchange (IE) was also prepared to provide a comparison to the CVD samples.

CVD methods introduce predominantly Zn^{2+} cations to high exchange levels.[9–,10c] Under certain CVD conditions, additional zinc species have been detected (Zn^+,[14] $[Zn_2]^{2+}$[15]) but these have not been reported to react with methane. To investigate the level of exchange of the BAS for zinc cations after CVD treatment with zinc metal vapour, ^{1}H NMR and ^{1}H-^{27}Al REAPDOR NMR spectroscopic experiments were conducted on the parent zeolites and the products of the CVD reaction. The ^{1}H-^{27}Al REAPDOR experiment probes the aluminium-proton separation by reintroducing the dipolar coupling that is removed by magic angle spinning, thus enabling the determination of which signals in the ^{1}H spectrum are closely associated with ^{27}Al.[16] For the parent zeolites, the signal at 4.0 ppm corresponding to BAS or 6.6 ppm corresponding to $[NH_4]^+$ (in the case of FER), is clearly associated with Al as determined by the appearance in the ^{1}H-^{27}Al REAPDOR difference spectrum (MOR: Figure 1b; ZSM-5: Figure S3a; FER: Figure S4a). Upon exposure to zinc vapour, this peak either disappears indicative of full exchange with Zn^{2+} (MOR, Figure 1c and d, and FER, Figure S4b) or decreases drastically (ZSM-5) (Figure S2b).

Elemental analysis (Table 1) was also used to determine the extent of zinc exchange after CVD and ion exchange. The Zn/Al ratios were found to be over the theoretical maximum exchange value of 0.5 for all CVD samples but values greater than 0.5 have previously been observed and attributed to excess Zn(0) present within the sample.[17] Brunauer-Emmett-Teller (BET) measurements were carried out in order to confirm that the zinc introduction methods did not cause pore blockage of the zeolites, particularly for MOR, which has a unidirectional pore system. A reduction in surface area is observed due to the presence of extraframework zinc (Table 1), similar to the results of Pidko et al.[17] The materials have been additionally analysed by powder X-ray diffraction analysis (pXRD) and ^{29}Si NMR spectroscopy to determine the effect of CVD on the zeolite structure. Figure 2 compares the pXRD patterns of the parent zeolites with the pXRD patterns after vapour deposition confirming that after CVD of zinc metal the framework remains intact. Furthermore, no additional diffraction peaks correspond-

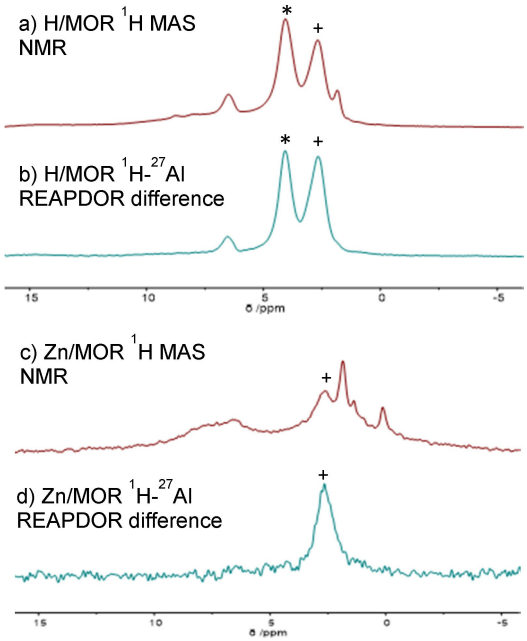

Figure 1. ^{1}H MAS NMR (a and c) and ^{1}H-^{27}Al REAPDOR difference spectra (b and d) for MOR framework. Parent zeolite H/MOR (a and b), Zn/MOR (c and d). *Signal at 4 ppm related to BAS disappears upon vapour deposition of zinc metal. $^+$Signal at 2.5 ppm associated with extraframework Al. Peak at 0 ppm due to adventitious silicon vacuum grease.

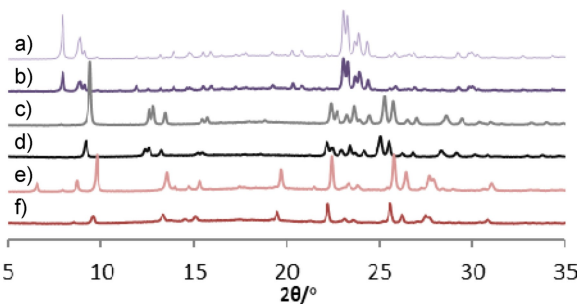

Figure 2. pXRD patterns for a) H-ZSM-5, b) Zn/ZSM-5, c) NH_4-FER, d) Zn/FER, e) H-MOR and f) Zn/MOR.

Table 1. Elemental analysis, BET measurements and C-H activation results for zinc exchanged zeolites.

Sample (given Si/Al)	Measured Si/Al[a]	Zn/Al[b]	BET [m^2/g]	Successful C-H activation	Percentage Zn active sites [c]
H-ZSM-5 (15)	12.5	–	435.0 ± 0.2	N	–
NH_4-ZSM-5 (12.5)	11.6	–	447.3 ± 0.4	N	–
H-MOR (10)	7.9	–	542.2 ± 1.6	N	–
NH_4-FER (10)	11.2	–	404.1 ± 0.5	N	–
Zn/ZSM-5 (15)	12.5	0.78	303.7 ± 0.4	–	–
Zn/CH_4/ZSM-5 (15)	12.5	0.73		Y	5.7%
Zn/FER (10)	11.2	0.69	305.5 ± 0.3	–	–
Zn/CH_4/FER (10)	11.2	0.77		Y	0.5%
Zn/MOR (10)	7.9	0.74	421.9 ± 0.6	–	–
Zn/CH_4/MOR (10)	7.9	0.75		Y	1.2%
Zn/H-ZSM-5-IE (12.5)	11.6	0.45	377.3 ± 0.3	Y	0.9%

[a] determined by WDXRF. [b] determined by ICP-OES. [c] NMR quantification with hexamethylbenzene (HMB) as a standard. Percentage of zinc sites that result in $[Zn\text{-}CH_3]^+$ species. Values given are an average of two independent experiments. Details on quantification can be found in the Supporting Information.

ing to zinc metal were observed in the pXRD patterns. No additional extra framework Al was observed after zinc CVD as determined through ^{27}Al MAS NMR spectroscopy (Figures S8–11). Analysis by ^{1}H-^{29}Si CP NMR spectroscopy demonstrated that no additional defects arose within the zeolites after exposure to zinc metal vapour (Figures S12–14). Overall, the CVD reaction of zinc with ZSM-5, FER and MOR frameworks results in high zinc exchange of the BAS/$[NH_4]^+$ cations and does not damage the zeolite framework or block the pore network.

Having demonstrated successful exchange of BAS for Zn^{2+} cations of ZSM-5, FER and MOR, the materials were studied for the capacity to effect C–H activation of methane, following similar conditions to those reported by Stepanov.[10b] After reaction with zinc vapour at 500 °C, the Zn/Zeolite samples were cooled to 250 °C and then exposed to $^{13}CH_4$ for 15 minutes. When the Zn/CH_4/ZSM-5 CVD sample was analysed by ^{13}C CP MAS NMR spectroscopy we were pleased to observe a signal at −19 ppm (Figure 3a), characteristic of the $[Zn\text{-}CH_3]^+$ fragment, in line with previous reports.[9–10] Gratifyingly, when the Zn/CH_4/FER was likewise analysed, a signal at −20 ppm was also observed (Figure 3c), indicating the successful activation of methane to form the $[Zn\text{-}CH_3]^+$ fragment. Most excitingly, after exposure to $^{13}CH_4$ analysis of the Zn/CH_4/MOR sample showed the presence of two signals at −15 ppm and −20 ppm (Figure 3d). Neither FER or MOR frameworks, modified with zinc, have been previously reported to activate methane. Zn/CH_4/ZSM-5-IE, prepared by aqueous ion exchange (IE) of Zn^{2+} ions, also is able to activate methane, as demonstrated by the ^{13}C NMR signal observed at −19 ppm (Figure 3b), in line with observations reported by other groups.[11a,18] It should be noted that the conditions required to observe C–H activation of methane with the IE sample (Zn/CH_4/ZSM-5-IE) were based on those reported in the literature but are substantially different to those required using samples prepared by CVD with zinc vapour. No change is observed in the pXRD patterns after methane activation and for Zn/ZSM-5-IE (Figures S5–7).

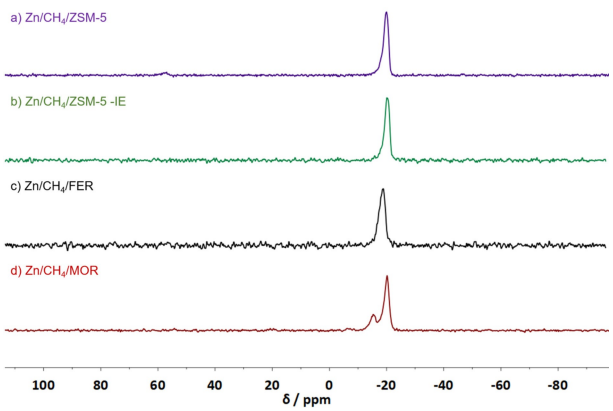

Figure 3. ^{13}C CP MAS NMR spectra of a) Zn/CH_4/ZSM-5, b) Zn/CH_4/ZSM-5-IE, c) Zn/CH_4/FER and d) Zn/CH_4/MOR. A characteristic signal for the $[Zn\text{-}CH_3]^+$ species is observed at a chemical shift of around −19 ppm in all spectra.

Using hexamethylbenzene (HMB) as a standard, further NMR experiments were carried out to determine the percentage of zinc sites that resulted in the formation of the $[Zn\text{-}CH_3]^+$ species (Table 1). Details of the quantification calculations can be found in the Supporting Information. It was found that 5.7% of the zinc sites in ZSM-5 formed $[Zn\text{-}CH_3]^+$, in line with values reported in the literature of 5–10%.[18a] The number of active zinc sites in FER and MOR were found to be substantially fewer, 0.5% and 1.2% respectively. This is potentially due to the difference in topology between the three frameworks but other factors such as Al distribution could play a role in this finding.[19] Interestingly, alongside the $[Zn\text{-}CH_3]^+$ ^{13}C NMR signal observed at −20 ppm in Zn/CH_4/MOR, an unexpected second signal was observed at −15 ppm, also in the range expected for a $[Zn\text{-}CH_3]^+$ species.[20] MOR is a 1D zeolite framework containing 12 MR channels and 8 MR side pockets, both of which are accessible to methane gas (Figure 4a). We hypothesised that the two peaks observed in the ^{13}C NMR spectrum in Zn/CH_4/

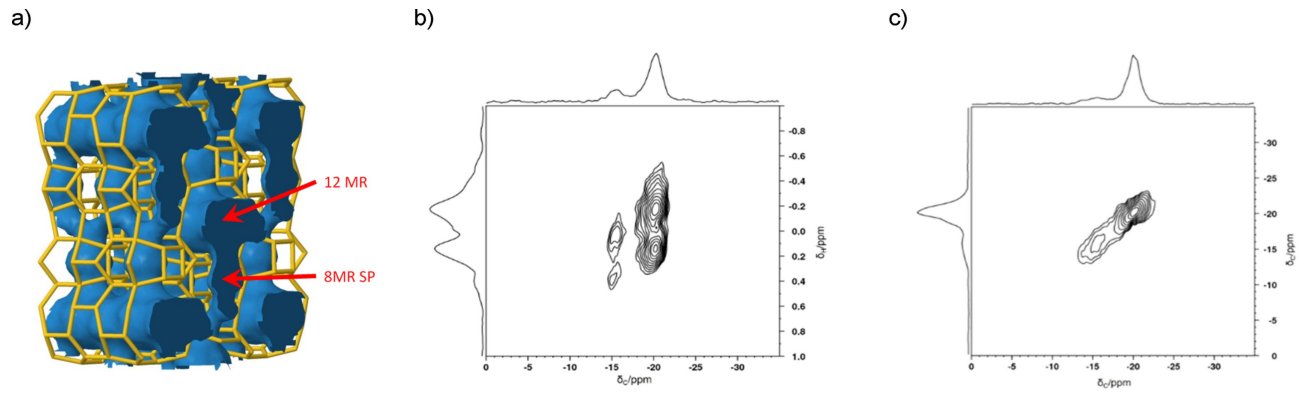

Figure 4. a) Framework representation of MOR framework taken from IZA database highlighting the 12MR channel and 8MR SP. b) ^{1}H-^{13}C heteronuclear correlation (HETCOR) MAS NMR spectrum for Zn/CH_4 MOR indicating two distinct $[Zn\text{-}CH_3]^+$ environments. c) EXSY experiment of Zn/CH_4 MOR highlighting lack of chemical exchange or transfer of magnetisation between the two $[Zn\text{-}CH_3]^+$ sites.

MOR correspond to two $[Zn\text{-}CH_3]^+$ species contained within these two different framework environments.

Further NMR spectroscopic experiments were carried out to investigate the two signals observed for Zn/CH_4 MOR. Through a ^{1}H-^{13}C heteronuclear correlation (HETCOR) MAS NMR experiment (spectrum shown in Figure 4b) it can be seen that there are two discrete $[Zn\text{-}^{13}CH_3]^+$ environments within Zn/CH_4MOR. The ^{1}H signal shows coupling to the ^{13}C nucleus giving a doublet and each environment has a different J-coupling constant: 125 Hz for the main species and 140 Hz for the minor species. Coupling constants are known to be dependent on confinement, therefore, this is likely to correspond to strong confinement of $[Zn\text{-}CH_3]^+$ species in the 8MR side pockets (140 Hz) compared with $[Zn\text{-}CH_3]^+$ in the 12 MR main channel (125 Hz).[21]

To confirm the two $[Zn\text{-}CH_3]^+$ sites could not chemically exchange or transfer magnetisation an EXSY experiment was conducted. The absence of any off-diagonal peaks in Figure 4c indicates no transfer between sites after 200 ms of mixing. This strongly suggests the presence of at least two well separated $[Zn\text{-}CH_3]^+$ environments within Zn/CH_4/MOR.

The distinct topological environments of the 12MR and the 8MR SP within MOR have previously been observed to give rise to two distinct chemical environments, as determined by ^{23}Na and ^{133}Cs MAS NMR spectroscopy studies.[22] Gerstein et al. observed two signals in the ^{133}Cs NMR spectrum of fully dehydrated Cs-exchanged mordenite. The peaks are observed in a 1:3 ratio which the authors assigned to the 12MR main channel and 8MR side pocket within the MOR framework.[22b] Two-dimensional triple-quantum (2D-3Q) ^{23}Na MAS NMR spectroscopy of sodium cations in dehydrated Na/MOR also shows two clear signals assigned to Na cations within the 12MR channels and Na cations located in the 8MR side pockets of the mordenite channels.[22a] Overall, based on NMR spectroscopy studies, the two peaks observed for the $[Zn\text{-}CH_3]^+$ species in MOR correspond to distinct chemical environments likely associated with the 8MR side pocket and 12 MR channels within the zeolite framework.

2.2. Reactivity of $[Zn\text{-}CH_3]^+$ under Oxidative Conditions

Having determined that zinc modified ZSM-5, FER and MOR are able to activate methane to form well defined $[Zn\text{-}CH_3]^+$ species, we subsequently explored the reactivity of these species under oxidative conditions. Upon exposure to 20% O_2 in Ar at room temperature for 20 minutes, the three zeolites Zn/CH_4/O_2/ZSM-5, Zn/CH_4/O_2/FER and Zn/CH_4/O_2/MOR, showed clear differences in reactivity however the $[Zn\text{-}CH_3]^+$ signal is still observed in all spectra in Figure 5 after exposure to 20% O_2/Ar. Two new signals appear in the ^{13}C CP MAS NMR spectrum of Zn/CH_4/O_2 ZSM-5 (Figure 5a). These correspond to a zinc methoxy species (54 ppm) and a zinc formate species (173 ppm) which is in line with previous findings on the exposure of $[Zn\text{-}CH_3]^+$/ZSM-5 to O_2.[10b,12] Conversely, the FER sample shows the presence of a zinc formate peak only (Figure 5b), while the MOR sample exhibits no reactivity towards dioxygen at room temperature after 20 minutes exposure (Figure 6c). This indicates that the framework environ-

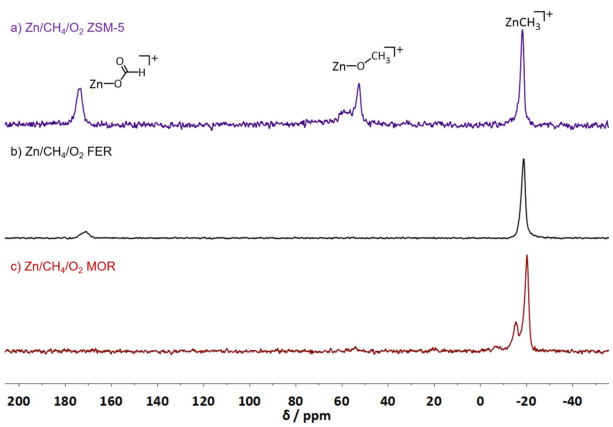

Figure 5. ^{13}C CP MAS NMR spectrum of Zn/CH_4/O_2 ZSM-5 (a), Zn/CH_4/O_2 FER (b) and Zn/CH_4/O_2 MOR (c) after exposure to 20% O_2 in Ar at room temperature. Signals corresponding to a methoxy species (54 ppm) and formate species (173 ppm) are observed for ZSM-5 and FER.

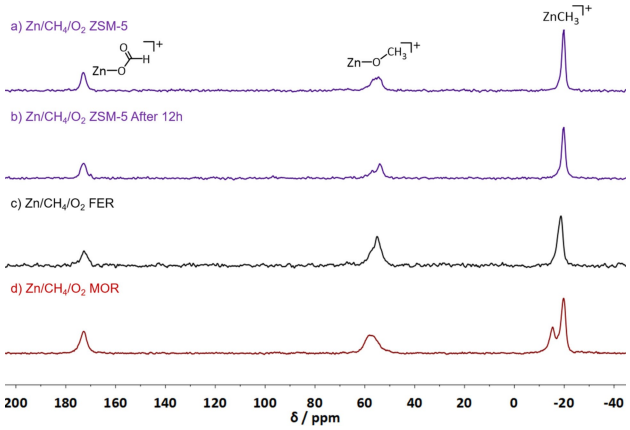

Figure 6. ^{13}C CP MAS NMR spectrum of $Zn/CH_4/O_2$ ZSM-5 (a), $Zn/CH_4/O_2$ ZSM-5 after 12 h (b), $Zn/CH_4/O_2$ FER (c) and $Zn/CH_4/O_2$ MOR (d) after exposure to 20% O_2 in Ar at 200 °C for 15 min. Peaks corresponding to a methoxy species (54 ppm) and formate species (173 ppm) observed in all spectra.

ment plays a key role in the reactivity of $[Zn\text{-}CH_3]^+$ with O_2 at room temperature, with the MFI framework giving rise to more detectable products than either FER or MOR.

Contrary to this, the Zn/CH_4/ZSM-5, Zn/CH_4/FER and Zn/CH_4/MOR show similar reactivity when the $[Zn\text{-}CH_3]^+$ species is exposed to O_2 (20% in Ar) at 200 °C for 15 min, forming zinc methoxy and zinc formate species with similar spectral intensities (Figure 6). After a further 12 hours at room temperature the zinc methoxy and zinc formate species in ZSM-5 are still present at comparable intensity indicating further reaction at room temperature is not substantial (Figure 6b) and that the zinc methoxy and zinc formate species are stable at room temperature. The $[Zn\text{-}CH_3]^+$ species once again does not react fully and can be seen in all spectra. It should also be noted that the two signals discussed previously for the $[Zn\text{-}CH_3]^+$ species in MOR are both present after each reaction with O_2. However, as Figure 7 shows, the species corresponding to the −20 ppm peak appears to be more reactive. The intensity ratio for the −15 ppm and −20 ppm peaks changes from approximately 0.5:1 for the Zn/CH_4/MOR to 0.8:1 for the oxygen exposed sample, $Zn/CH_4/O_2$/MOR. The spectra in Figure 7 are plotted on

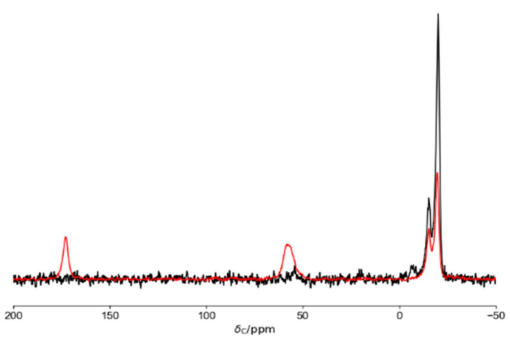

Figure 7. ^{13}C CP MAS spectra from Zn/CH_4/MOR before (black) and after (red) exposure to 20% O_2 in Ar at 200 °C.

equivalent vertical scales after taking into account the differing number of repetitions (800 vs. 4000) and the change in relaxation behaviour involved in exposure to oxygen. The differences in loss of signal intensity indicates that they undergo different rates of reaction. As mentioned previously, the signal at −15 ppm is assigned to the $[Zn\text{-}CH_3]^+$ fragment in the 8MR SP while the signal at −20 ppm is assigned to the $[Zn\text{-}CH_3]^+$ fragment in the 12MR main channel. Our observations for the $[Zn\text{-}CH_3]^+$/MOR system indicated confinement stabilises the $[Zn\text{-}CH_3]^+$ species in the 8MR SP, leading to lower reactivity in the presence of O_2.

The reactivity of the $[Zn\text{-}CH_3]^+$ species was further tested by exposure to air. After zinc vapour deposition and exposure to $^{13}CH_4$, Zn/CH_4/ZSM-5, Zn/CH_4/FER and Zn/CH_4/MOR were left open to the atmosphere overnight by removal of the NMR rotor cap. The three samples exhibited varying reactivity under these conditions. For both the Zn/CH_4/air/ZSM-5 and Zn/CH_4/air/FER (Figure 8a and 8b respectively), the signal corresponding to $[Zn\text{-}CH_3]^+$ is absent and, free MeOH (50 ppm)[12] and zinc formate species have been formed. We note that the Zn/CH_4/air/FER spectrum has a higher signal to noise ratio. Zn/CH_4/air/MOR proves to be the most interesting sample as it is the only framework which still gives a signal from the $[Zn\text{-}CH_3]^+$ species after overnight exposure to the atmosphere. Even after 36 h, there is a signal present from residual $[Zn\text{-}CH_3]^+$ species. The MOR framework is also unique in the fact that predominantly methanol is formed, while trace amounts of zinc formate are observed. The reduced signal intensity of Zn/CH_4/air/FER and Zn/CH_4/air/MOR after 36 h is likely due to loss of the methanol or protonolysis of the $[Zn\text{-}CH_3]^+$ species by water to form methane.[12] Furthermore, we also propose that the complete loss of the signal associated with $[Zn\text{-}CH_3]^+$ in the air exposure experiments compared to O_2/Ar is due to the differences in experimental conditions of O_2/Ar exposure (sample sealed under O_2/Ar in a capped rotor i.e. limited O_2) versus air exposure (sample in an uncapped rotor).

While it is unclear why the differing frameworks display disparate reactivity under different oxidative conditions, these

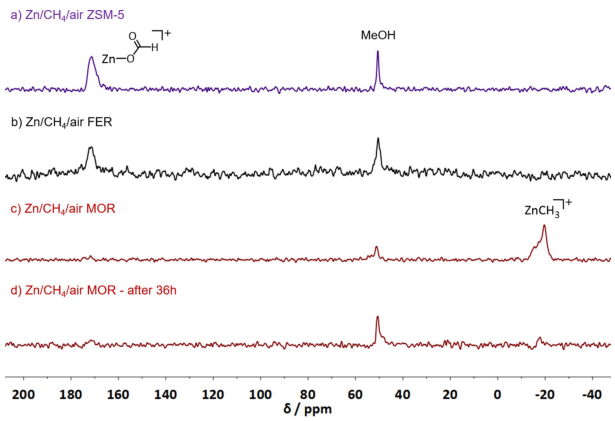

Figure 8. ^{13}C CP MAS NMR spectrum of Zn/CH4/air ZSM-5 (a), Zn/CH4/air FER (b), Zn/CH4/air MOR (c) after exposure to air overnight at room temperature; d) shows reactivity for Zn/CH4/air MOR after 36 h. Signals corresponding to free methanol (50 ppm) and formate species (173 ppm) observed.

findings highlight that the framework plays a crucial role in the reactivity of the $[Zn\text{-}CH_3]^+$. The MFI framework seems to be the most reactive environment for the $[Zn\text{-}CH_3]^+$ species whereas the MOR framework leads to greater methanol selectivity.

3. Conclusions

Using CVD with an excess of zinc metal, zinc-modified zeolites of three frameworks (ZSM-5, FER and MOR) were prepared with high levels of zinc exchange. After CVD, the materials retained high surface areas, good crystallinity and no additional defects were observed. Upon exposure to $^{13}CH_4$, C–H activation was observed to occur for all three frameworks, as determined by a characteristic signal resulting from $[Zn\text{-}CH_3]^+$ in ^{13}C MAS NMR spectroscopy studies. Using HMB as an NMR standard, the percentage of zinc atoms that resulted in the formation of the $[Zn\text{-}CH_3]^+$ species was determined; the order was found to be Zn/CH_4/ZSM-5 (5.7%), Zn/CH_4/MOR (1.2%) and Zn/CH_4/FER (0.5%). At this stage it is unclear why the ZSM-5 framework results in a substantially greater number of active Zn sites than either MOR or FER but this is potentially due to the difference in topology between the three frameworks or differences in Al distribution for example.

The activation of methane over Zn/MOR proved to be particularly interesting as two signals were observed in the ^{13}C NMR spectrum after exposure to $^{13}CH_4$. Further NMR spectroscopy experiments determined that these two signals belonged to two distinct chemical environments which were unable to chemically exchange and had different J-coupling constants. This fitted with our hypothesis that the two signals are associated with $[Zn\text{-}CH_3]^+$ species present in the 12 MR channels and the 8MR side pockets of the MOR framework. Additionally, the two species undergo different rates of reaction upon exposure to O_2.

After establishing stoichiometric methane activation, the reactivity of the $[Zn\text{-}CH_3]^+$ species under oxidative conditions was explored. As expected, methoxy and formate species were formed by all three frameworks after exposure to O_2 at elevated temperatures. However, the three frameworks demonstrated dissimilar reactivity under different oxidative conditions highlighting that the framework plays a key role in the reactivity of the $[Zn\text{-}CH_3]^+$ species. ZSM-5 framework was found to be the most reactive environment for the $[Zn\text{-}CH_3]^+$ species whilst Zn/CH_4/air/MOR is selective for methoxy species.

Further work will be carried out to investigate the catalytic properties of these materials now stoichiometric methane activation and functionalisation has been proven.

Experimental Section

H-MOR (Si/Al = 10), H-ZSM-5 (15) and NH_4-ZSM-5 (12.5) were kindly provided by Clariant. NH_4-FER (10) was purchased from Alfa Aesar. Zinc powder (Goodfellow, 99.9%, max particle size 150 μm) was used as purchased. Zinc nitrate hexahydrate (99%) was used as purchased from Alfa Aesar. Methane-^{13}C (99% ^{13}C) was purchased from Sigma-Aldrich. CH_4 (99.995%), O_2 (99.5%), N_2 (oxygen free) and Ar (99.998%) cylinders were supplied by BOC. Zinc powder was stored and used in a PureLab HE glove box under an argon atmosphere.

The ion exchanged ZSM–5 (Zn/ZSM-5-IE) was prepared by treating NH_4-ZSM-5 (12.5) with an aqueous solution $Zn(NO_3)_2$ based on a method reported by Kuroda et al.[18a] Zinc ion exchanges were carried out using 2.5 g of zeolite in a centrifuge tube in contact with 50 ml of 0.3 M $Zn(NO_3)_2$ solution for 1 h with constant agitation from a mechanical tube roller. The tube was centrifuged at 4500 rpm for 5.5 min and the resulting supernatant decanted. The zeolite was then re-dispersed into the zinc nitrate solution and this process was repeated 10 times. The sample was then washed with 50 ml of deionised water 8 times and dried at 80 °C overnight. The resulting sample is referred to Zn/ZSM–5 IE.

The vapour deposition samples were prepared by an exchange reaction between metallic zinc vapour and the H-form/NH_4-form of the zeolite. This was carried out in a custom quartz u-tube which ensured the separation of the zinc powder and zeolite. All parent zeolites were pre-treated in the same way to dehydrate before exposure to zinc vapour. In a quartz tube, the parent zeolite was placed under vacuum (pressure $< 10^{-2}$ mbar) and heated to 150 °C for 1 h followed by 5 h at 550 °C in a tube furnace. A 5 °C min^{-1} ramp rate was used for all furnace program steps. After dehydration, the zeolites were stored in the glovebox. The vapour deposition conditions were based on a method reported by Stepanov et al.[10b] To achieve maximum ion exchange, a 100-fold excess of zinc (Zn/Al = 100) was used for the vapour deposition. The quartz u-tube and liner used for the reaction are shown in the supplementary information in Figure S1. The u-tube was loaded with zinc metal and zeolite in the glovebox, ensuring the powders were well separated on either sides of the tube (see Figure S1). The u-tube was then attached to a Schlenk line and placed under vacuum (pressure $< 10^{-2}$ mbar). To expose the zeolite sample to zinc vapour, the u-tube was sealed and placed in a tube furnace where it was heated to 500 °C at 5 °C min^{-1} and held for 1 h under static vacuum. Excess unreacted zinc vapour was further removed by continued heating at 500 °C for 2 h under dynamic vacuum. These samples are referred to as Zn/ZSM-5, Zn/MOR, Zn/FER.

Where methane activation took place, the u-tube containing the zinc modified zeolite was cooled to 250 °C in the furnace. The u-tube was filled with 1 atm of $^{13}CH_4$, sealed and held at 250 °C for 15 min. After cooling, the sealed tube was taken into the argon glovebox. These samples, labelled Zn/CH_4/ZSM-5, Zn/CH_4/MOR, Zn/CH_4/FER, were packed into a solid state NMR rotor in the glovebox. NMR experiments were typically conducted immediately after C–H activation.

The ion exchanged sample, Zn/ZSM-5-IE, was activated based on a method by Kuroda et al.[18a] The zeolite was heated to 600 °C for 4 h at 5 °C min^{-1} ramp rate under vacuum. This was cooled to 250 °C after which the tube was sealed under 1 atm of $^{13}CH_4$ and held at 250 °C for 2 h. After cooling, the sealed tube was taken into the argon glovebox. The sample, labelled Zn/CH_4/ZSM–5 IE, was packed into a solid state NMR rotor in the glovebox. NMR experiments were typically conducted immediately after C–H activation.

The $[Zn\text{-}CH_3]^+$ species in Zn/CH_4/ZSM-5, Zn/CH_4/MOR and Zn/CH_4/FER were tested for reactivity with O_2 and air. A solid state NMR rotor containing Zn/CH_4/zeolite was placed in a Schlenk flask under a flow of O_2/Ar, after removing the rotor cap. This was exposed to a mixture of 20% O_2 in Ar flowing at room temperature for 20 min. When testing reactivity at 200 °C, the flask was sealed under the atmosphere of the O_2/Ar mixture, and the samples were heated at 200 °C for 15 min. After cooling to room temperature, the rotor was then re-capped under a nitrogen flow. Reactivity with air was tested

by removing the rotor cap of samples Zn/CH_4/zeolite and leaving the samples exposed to air overnight.

All additional characterisation details are documented in the supplementary information.

Acknowledgements

We would like to thank Malcolm Richardson and Aaron Brown (glassblowers, Department of Chemistry, Durham University) for all their help in developing the quartz tube setup. We would also like to thank Dr. Emily Unsworth for conducting HF digestion and ICP-OES analysis and Dr. Kamal Badreshany for WD-XRF analysis. M.S. and S.R. thank the EPSRC and Durham University for generous financial support for their PhD studentships. R.T. thanks the EPSRC for generous funding of an EPSRC Manufacturing Fellowship (grant number EP/R01213X/1).

Conflict of Interest

The authors declare no conflict of interest.

Keywords: C–H activation · methane · methanol · zeolites · zinc

[1] a) G. A. Olah, *Angew. Chem., Int. Ed.* **2005**, *44*, 2636–2639; b) B. A. Arndtsen, R. G. Bergman, T. A. Mobley, T. H. Peterson, *Acc. Chem. Res.* **1995**, *28*, 154–162.
[2] a) K. Aasberg-Petersen, J. H. Bak Hansen, T. S. Christensen, I. Dybkjaer, P. S. Christensen, C. Stub Nielsen, S. E. L. Winter Madsen, J. R. Rostrup-Nielsen, *Appl. Catal. A* **2001**, *221*, 379–387; b) R. Reimert, F. Marschner, H. J. Renner, W. Boll, E. Supp, M. Brejc, W. Liebner, G. Schaub, in *Gas Production 2. Processes*, *Ullmann's Encyclopedia of Industrial Chemistry*, Wiley-VCH Verlag GmbH & Co. KGaA, **2011**; c) K. Aasberg-Petersen, I. Dybkjær, C. V. Ovesen, N. C. Schjødt, J. Sehested, S. G. Thomsen, *J. Nat. Gas Sci. Eng.* **2011**, *3*, 423–459.
[3] a) V. C. C. Wang, S. Maji, P. P. Y. Chen, H. K. Lee, S. S. F. Yu, S. I. Chan, *Chem. Rev.* **2017**, 8574–8621; b) M. O. Ross, A. C. Rosenzweig, *J. Biol. Inorg. Chem.* **2017**, *22*, 307–319; c) B. E. R. Snyder, M. L. Bols, R. A. Schoonheydt, B. F. Sels, E. I. Solomon, *Chem. Rev.* **2018**, *118*, 2718–2768.
[4] a) M. H. Mahyuddin, A. Staykov, Y. Shiota, K. Yoshizawa, *ACS Catal.* **2016**, *6*, 8321–8331; b) P. Tomkins, M. Ranocchiari, J. A. van Bokhoven, *Acc. Chem. Res.* **2017**, *50*, 418–425; c) M. B. Park, S. H. Ahn, A. Mansouri, M. Ranocchiari, J. A. van Bokhoven, *ChemCatChem* **2017**, *9*, 3705–3713; d) S. Raynes, M. A. Shah, R. A. Taylor, *Dalton Trans.* **2019**, *48*, 10364–10384; e) M. Ravi, M. Ranocchiari, J. A. van Bokhoven, *Angew. Chem. Int. Ed.* **2017**, *56*, 16464–16483; *Angew. Chem.* **2017**, *129*, 16684–16704.
[5] P. J. Smeets, M. H. Groothaert, R. A. Schoonheydt, *Catal. Today* **2005**, *110*, 303–309.
[6] a) J. S. Woertink, P. J. Smeets, M. H. Groothaert, M. A. Vance, B. F. Sels, R. A. Schoonheydt, E. I. Solomon, *Proc. Mont. Acad. Sci.* **2009**, *106*, 18908–18913; b) G. Li, P. Vassilev, M. Sanchez-Sanchez, J. A. Lercher, E. J. M. Hensen, E. A. Pidko, *J. Catal.* **2016**, *338*, 305–312.
[7] a) M. Dusselier, M. E. Davis, *Chem. Rev.* **2018**, 5265–5329; b) M. J. Wulfers, S. Teketel, B. Ipek, R. F. Lobo, *Chem. Commun.* **2015**, *51*, 4447–4450.
[8] D. K. Pappas, A. Martini, M. Dyballa, K. Kvande, S. Teketel, K. A. Lomachenko, R. Baran, P. Glatzel, B. Arstad, G. Berlier, C. Lamberti, S. Bordiga, U. Olsbye, S. Svelle, P. Beato, E. Borfecchia, *J. Am. Chem. Soc.* **2018**, 15270–15278.
[9] V. B. Kazansky, A. I. Serykh, *Phys. Chem. Chem. Phys.* **2004**, *6*, 3760–3764.
[10] a) M. V. Luzgin, D. Freude, J. Haase, A. G. Stepanov, *J. Phys. Chem. C* **2015**, *119*, 14255–14261; b) A. A. Gabrienko, S. S. Arzumanov, M. V. Luzgin, A. G. Stepanov, V. N. Parmon, *J. Phys. Chem. C* **2015**, *119*, 24910–24918; c) Y. G. Kolyagin, I. I. Ivanova, Y. A. Pirogov, *Solid State Nucl. Magn. Reson.* **2009**, *35*, 104–112.
[11] a) A. Oda, H. Torigoe, A. Itadani, T. Ohkubo, T. Yumura, H. Kobayashi, Y. Kuroda, *J. Phys. Chem. C* **2013**, *117*, 19525–19534; b) S. C. Albarracín-Suazo, Y. J. Pagán-Torres, M. C. Curet-Arana, *J. Phys. Chem. C* **2019**, *123*, 16164–16171.
[12] J. F. Wu, W. D. Wang, J. Xu, F. Deng, W. Wang, *Chem. Eur. J.* **2010**, *16*, 14016–14025.
[13] Y. Lin, S. Qi, L. Benedict, Z. Junlin, K. Dejing, M. Claire, T. Chiu, T. Edman, *Angew. Chem. Int. Ed.* **2017**, *56*, 10711–10716; *Angew. Chem.* **2017**, *129*, 10851–10856.
[14] E. Morra, G. Berlier, E. Borfecchia, S. Bordiga, P. Beato, M. Chiesa, *J. Phys. Chem. C* **2017**, *121*, 14238–14245.
[15] A. Oda, T. Ohkubo, T. Yumura, H. Kobayashi, Y. Kuroda, *Dalton Trans.* **2015**, *44*, 10038–10047.
[16] T. Gullion, *Chem. Phys. Lett.* **1995**, *246*, 325–330.
[17] S. M. T. Almutairi, B. Mezari, P. C. M. M. Magusin, E. A. Pidko, E. J. M. Hensen, *ACS Catal.* **2012**, *2*, 71–83.
[18] a) A. Oda, H. Torigoe, A. Itadani, T. Ohkubo, T. Yumura, H. Kobayashi, Y. Kuroda, *J. Phys. Chem. C* **2014**, *118*, 15234–15241; b) A. A. Gabrienko, S. S. Arzumanov, A. V. Toktarev, I. G. Danilova, I. P. Prosvirin, V. V. Kriventsov, V. I. Zaikovskii, D. Freude, A. G. Stepanov, *ACS Catal.* **2017**, *7*, 1818–1830.
[19] a) E. A. Pidko, R. A. van Santen, *J. Phys. Chem. C* **2007**, *111*, 2643–2655; b) A. Oda, T. Ohkubo, T. Yumura, H. Kobayashi, Y. Kuroda, *Phys. Chem. Chem. Phys.* **2017**, *19*, 25105–25114.
[20] a) Y. G. Kolyagin, I. I. Ivanova, V. V. Ordomsky, A. Gedeon, Y. A. Pirogov, *J. Phys. Chem. C* **2008**, *112*, 20065–20069; b) H. Elmar, *Z. Anorg. Allg. Chem.* **2000**, *626*, 2223–2227.
[21] J. Geertsen, J. Oddershede, W. T. Raynes, G. E. Scuseria, *J. Magn. Reson.* **1991**, *93*, 458–471.
[22] a) M. Hunger, P. Sarv, A. Samoson, *Solid State Nucl. Magn. Reson.* **1997**, *9*, 115–120; b) P. J. Chu, B. C. Gerstein, J. Nunan, K. Klier, *J. Phys. Chem.* **1987**, *91*, 3588–3592.

Manuscript received: October 7, 2019
Accepted manuscript online: November 27, 2019
Version of record online: January 17, 2020